Physics of the Solid State, Vol. 46, No. 8, 2004, pp. 1383–1385. Translated from Fizika Tverdogo Tela, Vol. 46, No. 8, 2004, pp. 1345–1347.
Original Russian Text Copyright © 2004 by Smirnova, Isaev, Vekilov.

METALS
AND SUPERCONDUCTORS

Effect of Vanadium Doping on the Structure of TiAl: *Ab initio* Calculations

E. A. Smirnova, É. I. Isaev, and Yu. Kh. Vekilov
Moscow State Institute of Steel and Alloys (Technological University), Leninskiĭ pr. 4, Moscow, 119049 Russia
Received October 28, 2003

Abstract—The degree of tetragonality of TiAl and the effect of vanadium doping on it are studied theoretically in the framework of the coherent-potential approximation using *ab initio* potentials. It is shown that substitution of vanadium for Ti increases the degree of tetragonality, whereas substitution of vanadium for aluminum decreases the degree of tetragonality of the TiAl : V alloy and the lattice becomes virtually cubic when the vanadium content is about 8 at. %; this, in turn, can increase the plasticity of TiAl, which is brittle at low temperatures. © *2004 MAIK "Nauka/Interperiodica".*

1. INTRODUCTION

Intermetallic compounds are of considerable interest from both the fundamental and practical standpoint because of their possible application under high-temperature conditions. Among these compounds are transition-metal aluminides, which are of importance in modern technologies and possess many valuable properties, such as low density, high melting temperature, and high load resistance. The TiAl-based intermetallic systems have been the subject of many studies in recent years [1–7].

Due to their low density and fluidity, these alloys are an alternative to nickel alloys and other compounds based on heat-resistant metals used in the aerospace industry. However, in many cases, the former alloys are not sufficiently plastic and, hence, are of limited usefulness. Because the deformation properties of these alloys depend heavily on their crystal structure, elemental composition, and the character of interatomic interaction, the electronic structure plays a great role in the formation of their plastic properties. Therefore, it is important to study the electronic structure of these alloys in the framework of the current theory.

At low temperatures, TiAl crystallizes in the $L1_0$ (CuAu) structure with a feebly marked tetragonality, $c/a = 1.02$. To decrease its tetragonality and improve its low-temperature plasticity, TiAl is lightly doped with transition metals [2–5]. However, the experimental data from those publications are not sufficient to reveal regularities in the dependence of the alloy structure on doping with different metals, such as V, Cr, and Mn. Furthermore, there are inconsistencies between the results obtained by different groups of researchers, which is probably due to the specific features of the sample preparation techniques used.

In this paper, we perform an *ab initio* study on γ-TiAl and the vanadium-doped binary alloy TiAl : V. The dependence of the degree of alloy tetragonality on the concentration of vanadium substituting for Ti or Al is determined. It is shown that, contrary to expectations, substitution of V for Ti increases the alloy tetragonality. However, substitution of vanadium for part of the Al atoms causes the degree of tetragonality to decrease.

2. DETAILS OF THE CALCULATIONS

We applied two different methods for calculating the electronic structure. For disordered alloys, we used the method of exact MT orbitals (TMTO) [8] in combination with the coherent potential approximation (CPA). The contributions from exchange-correlation effects are calculated within the local density approximation with inclusion of generalized gradient corrections [9]. The *s*, *p*, and *d* orbitals are used as a basis. Integration over energy in the complex plane is performed using 16 points on a semicircle. The Ti, V, and Al atomic sphere radii are taken to be equal to the average radius of the Wigner–Seitz cell of the alloy. The core states of all alloy components are recalculated in each iterative cycle of the self-consistent procedure (the unfrozen-core approximation). Integration over the Brillouin zone is performed by involving 969 *k* points in this zone. The equation of state for each case is obtained by performing a cubic-spline interpolation of the calculated total energies.

Using the VASP software package [0, 11] based on *ab initio* pseudopotentials, we also carried out calculations for pure TiAl and for supercells containing 5.5 at. % vanadium at Ti or Al sites. The many-electron (pseudo)potentials used in the calculations are generated with allowance for all nodes of the wave functions of the valence states and for the gradient corrections to the local electron density [11, 12]. To determine the electron density that minimizes the total energy of the system according to the Hohenberg–Kohn theorem [13], we calculated the wave functions using the Davidson method. Integration over the Brillouin zone is per-

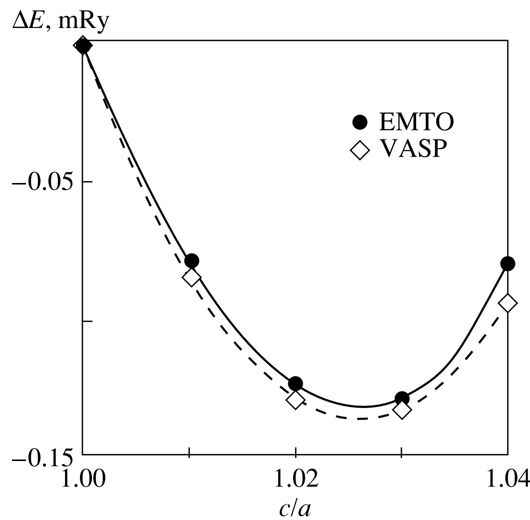

Fig. 1. Total energies calculated using the TMTO (EMTO) and VASP methods.

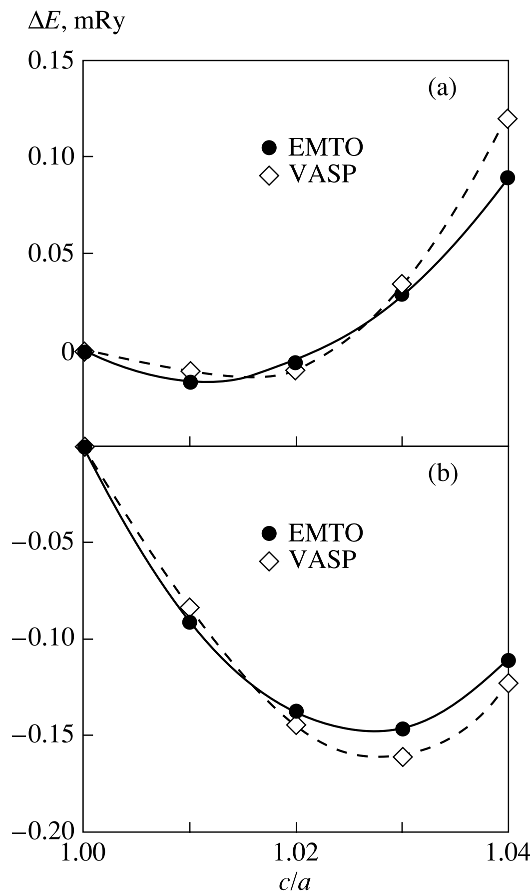

Fig. 2. Total energies of (a) $Ti_{18}(Al_{17}V_1)$ and (b) $(Ti_{17}V_1)Al_{18}$ supercells as a function of c/a at a fixed unit cell volume of 218.36 au^3.

formed using the tetrahedron method with inclusion of the Blöchl corrections [14] and involving 315 k points in an irreducible part of the Brillouin zone (approximately 4600 tetrahedra).The convergence criterion in calculating the total energy is chosen to be 1 meV.

3. RESULTS

Using the TMTO method, we calculated the total energy of γ-TiAl for several values of the unit cell volume and different values of the c/a ratio. At a fixed value of c/a, the total energy reaches a minimum for a unit cell volume of 218.36 au^3, which is very close to the experimental value (218.32 au^3). For this value of the unit cell volume, we calculated the total energy of $L1_0$ TiAl using *ab initio* pseudopotentials (VASP). The dependence of the total energy of γ-TiAl on the ratio c/a at a fixed value of the unit cell volume ($V = 218.36$ au^3) is shown in Fig. 1. The results of TMTO and VASP calculations virtually coincide, which lends additional support to the adequacy of the methods used by us. The equilibrium values of c/a calculated using the TMTO and VASP methods are 1.0252 and 1.025, respectively, and agree well with the experimental value $c/a = 1.02$ [15]. Therefore, the calculated equilibrium values of the lattice parameters of TiAl are $a = 3.988$ Å and $c = 4.0877$ Å, which are close to the x-ray diffraction data, $a = 3.991$ Å and $c = 4.081$ Å [16].

We also calculated the electronic structure of vanadium-doped TiAl alloys. Using the coherent potential approximation makes it possible to study a disordered alloy that forms when part of the atoms on one or both sublattices of a binary alloy are replaced by atoms of a third element. The available experimental data do not give a decisive answer as to which sublattice is "preferred" by vanadium. For this reason, we calculated the total energies of alloys $(Ti_{99}V_1)(Ti_1Al_{99})$ and $Ti(Al_{99}V_1)$. It is found that the energy of the $Ti(Al_{99}V_1)$ alloy is lower. From comparing the calculated total energies of alloys $(Ti_{99}Al_1)(Al_{99}V_1)$ and $(Ti_{99}V_1)Al$, it follows that the energy of $(Ti_{99}V_1)Al$ is lower. Thus, the formation of antisite defects, i.e., the shift of Ti atoms to Al sublattice sites or of Al atoms to Ti sublattice sites, requires a greater energy than the substitution of V atoms for Al and Ti atoms, respectively. Based on these results, one might expect that neither of the two sublattices will be preferred by vanadium (which agrees with the conclusions made in [17]).

We performed calculations for the case where vanadium substitutes for atoms of only one (Ti or Al) sublattice and its concentration x varies from 0 to 10 at. % on the sublattice, i.e., for alloys $(Ti_{100-x}V_x)Al$ and $Ti(Al_{100-x}V_x)$. Since the addition of a small amount of V has virtually no effect on the equilibrium unit cell volumes, the TMTO–CPA calculations of the total energy are carried out at the same value of the unit cell volume, 218.36 au^3. The VASP calculations are performed for supercells $3 \times 3 \times 2$ in size (with the same unit cell volume as for pure TiAl) containing 36 atoms each. In one supercell, a V atom is placed at a Ti site, and in the other, at an Al site; i.e., the supercells are

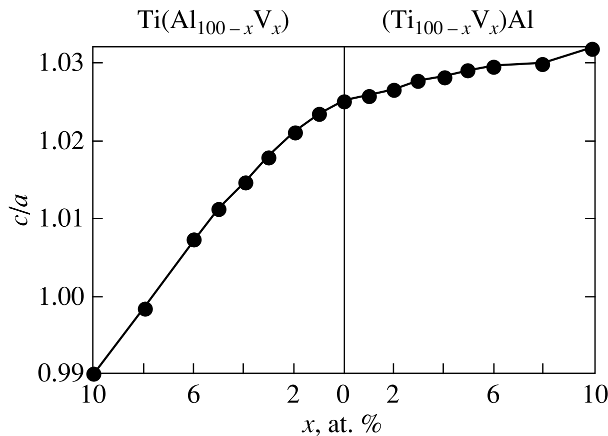

Fig. 3. Variation in the degree of tetragonality with vanadium concentration x. At $x \approx 8$, the lattice becomes cubic.

$(Ti_{17}V)Al_{18}$ and $Ti_{18}(Al_{17}V)$, respectively. Figures 2a and 2b show the dependences of the total energy on the ratio c/a at a fixed volume for alloys containing 5 at. % V at Ti and Al sites, respectively. As is the case for pure TiAl, the results obtained by the two methods for vanadium-doped alloys are in close agreement. Thus, the total energy of alloys can be calculated by the TMTO method within the coherent potential approximation with the same accuracy as by the full-potential method.

Figure 3 shows the dependence of the ratio c/a of TiAl : V alloys on the vanadium concentration on one of the sublattices. The parameter c/a is seen to vary smoothly. In the case where vanadium atoms are at Ti sites, the c/a ratio increases monotonically from 1.025 to 1.03, which corresponds to the addition of 10 at. % vanadium. In the case where vanadium substitutes for Al atoms, the change in the c/a ratio is more significant, $c/a = 1.011$ for alloy $Ti(Al_{95}V_5)$. As can be seen from the left-hand part of Fig. 3, the lattice becomes virtually cubic on addition of 8 at. % V.

4. CONCLUSIONS

Thus, using the *ab initio* methods for calculating the electronic structure, we have investigated γ-TiAl and vanadium-doped TiAl alloys. It has been shown that doping changes the degree of tetragonality of the alloys. In the case where vanadium substitutes for Al atoms, the c/a ratio decreases and the lattice becomes virtually cubic as the V concentration reaches 8 at. %, which can improve the plasticity of the alloy. Note that the tetragonality decreases when vanadium substitutes for Al rather than Ti atoms.

ACKNOWLEDGMENTS

The authors are grateful to A.V. Ruban and I.A. Abrikosov for useful discussions.

This study was supported by the Russian Foundation for Basic Research (project no. 03-02-16970) and the Royal Swedish Academy of Sciences.

REFERENCES

1. S. D. Chebb, D. A. Papaconstantopolus, and B. M. Klein, Phys. Rev. B **38** (12), 120 (1988).
2. K. Lie, R. Holmestad, K. Martinsen, and R. Hoier, Phys. Rev. B **57**, 1585 (1998).
3. M. J. Blackburn and M. P. Smith, U.S. Patent No. 42946615 (1981).
4. R. Yu, L. L. He, and H. Q. Ye, Phys. Rev. B **65**, 184102-1 (2002).
5. C. Woodward, S. Kajihara, and L. H. Yang, Phys. Rev. B **57**, 13549 (1998).
6. R. E. Watson and M. Weinert, Phys. Rev. B **58**, 5981 (1998).
7. P. K. Khowash, D. L. Prise, and B. R. Cooper, Phys. Rev. B **47**, 9884 (1993).
8. L. Vitos, H. L. Skriver, B. Johansson, and J. Kollar, Comput. Mater. Sci. **18**, 24 (2000).
9. J. P. Perdew, K. Burke, and M. Ernzerhof, Phys. Rev. Lett. **77**, 3865 (1996).
10. G. Kresse and J. Furthmüller, Phys. Rev. B **54**, 11169 (1996).
11. G. Kresse and J. Furthmüller, Comput. Mater. Sci. **6**, 15 (1996).
12. P. E. Blöchl, Phys. Rev. B **50**, 17953 (1994).
13. P. Hohenberg and W. Kohn, Phys. Rev. B **136**, 864 (1964).
14. P. E. Blöchl, O. Jepsen, and O. K. Andersen, Phys. Rev. B **49**, 16223 (1994).
15. W. B. Peason, *A Handbook of Lattice Spacing and Structure of Metals and Alloys* (Pergamon, Oxford, 1987), Vols. 1, 2.
16. T. Sikora, G. Hug, M. Jaouen, and J. J. Rehr, Phys. Rev. B **62**, 1723 (2000).
17. A. V. Ruban and H. L. Skriver, Phys. Rev. B **55**, 856 (1997).

Translated by Yu. Epifanov

Physics of the Solid State, Vol. 46, No. 8, 2004, pp. 1386–1393. Translated from Fizika Tverdogo Tela, Vol. 46, No. 8, 2004, pp. 1348–1355.
Original Russian Text Copyright © 2004 by Grishkov, Lotkov, Dubinin, Teploukhov, Parkhomenko.

METALS
AND SUPERCONDUCTORS

Short-Wavelength Atomic-Displacement Modulation Preceding the *B*2 ⟶ *B*19' Martensitic Transformation in a TiNi-Based Alloy

V. N. Grishkov*, A. I. Lotkov*, S. F. Dubinin, S. G. Teploukhov**, and V. D. Parkhomenko****

**Institute of Strength Physics and Materials Science, Siberian Division, Russian Academy of Sciences, pr. Akademicheskiĭ 2/1, Tomsk, 634021 Russia*

e-mail: lotkov@ispms.tsc.ru

***Institute of Metal Physics, Ural Division, Russian Academy of Sciences, ul. S. Kovalevskoĭ 18, Yekaterinburg, 620219 Russia*

e-mail: dubinin@uraltc.ru

Received December 16, 2003

Abstract—Neutron diffraction studies of the fine structure of a $Ti_{49}Ni_{51}$ single crystal are performed before the onset of the *B*2 ⟶ *B*19' martensitic transformation (temperature of the onset of the transformation M_s = 200 K). Upon cooling below 460 K, extra reflections are found to form; their positions in the *B*2-phase reciprocal lattice correspond to the full non-Lifshitz star of the wave vector $\mathbf{q} = 0.225\langle 112\rangle$. At temperatures below 430 K, $0.45\langle 110\rangle$ extra reflections appear, corresponding to second-order diffraction effects. In the temperature range 300–460 K, reversible and nonhysteretic changes in the intensities and positions of both types of extra reflections are observed. Analysis of the intensities and spatial distribution of the extra reflections in the *B*2-phase reciprocal lattice indicates that a displacive superstructure dominated by longitudinally polarized atomic-displacement waves with $\mathbf{q} = 0.225\langle 112\rangle$ arises in the single crystal in the pretransition temperature range.
© 2004 MAIK "Nauka/Interperiodica".

1. INTRODUCTION

Binary titanium nickelide–based alloys undergo two basic sequences of martensitic transformations (MTs):

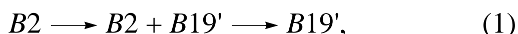

$$B2 \longrightarrow B2 + B19' \longrightarrow B19', \quad (1)$$

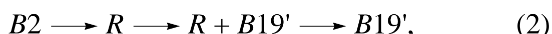

$$B2 \longrightarrow R \longrightarrow R + B19' \longrightarrow B19', \quad (2)$$

where *B*2 is the high-temperature phase with a CsCl-type long-range order and *B*19' and *R* are the martensite phases having monoclinic and rhombohedral structures, respectively [1, 2]. MT sequence (1) is characteristic of an equiatomic alloy (irrespective of heat treatment) and similar alloys that have a higher Ni content and are quenched from the *B*2 field. As the temperature decreases, the concentration range of the *B*2 field decreases sharply from ~57 at. % Ni at 1370 K [3] to ≤50.8 at. % Ni at 773 K [3, 4]. Thus, nickel-rich TiNi-based alloys are aging alloys and undergo MT sequence (2) upon heat treatment at temperatures below 770–800 K [4]. In a wide temperature range preceding the formation of the *R* and *B*19' martensitic phases, pretransition structures are formed, which can change the physical–mechanical properties of binary TiNi-based alloys [1, 2, 5]. The formation of the intermediate displacive structure (IDS) preceding the *B*2 ⟶ *R* transformation has been studied in great detail using various methods, such as electron microscopy [1, 5, 6], x-ray diffraction [5, 7], and neutron diffraction [2, 8, 9]. The formation of IDS1 is characterized by the appearance of $(1/3)\langle 111\rangle$, $(1/3)\langle 112\rangle$, and $(1/3)\langle 110\rangle$ extra reflections in the electron, neutron, and x-ray diffraction patterns. This structure is believed to be due to correlation of the transverse waves of $1/3\langle 110\rangle_{\mathbf{q}}\langle 1\bar{1}0\rangle_{\mathbf{u}}$ atomic displacements (where **q** and **u** are the wave vector and polarization vector, respectively), which appear as a consequence of the softening of the corresponding transverse phonon mode $TA_2\xi[110]$ near $\xi = 1/3$ [10, 11].

The formation of the second-type of intermediate displacive structure (IDS2) preceding the *B*2 ⟶ *B*19' transformation has been studied in less detail than IDS1; it was mainly studied using electron diffraction [1, 5, 6, 12]. Structure IDS2 is identified by diffuse extra reflections that appear near the $(1/2)\langle 110\rangle$ positions in the *B*2–phase reciprocal lattice and are strongly broadened along the related directions. The broadening of the extra reflections of IDS2 is assumed to be due to its incommensurate structure with respect to the *B*2-phase lattice; however, this assumption was not confirmed directly in [5]. The incommensurate IDS2 structure was directly detected in [9, 13], where the pretransition phase in a massive $Ti_{49}Ni_{51}$ single crystal was studied using neutron diffraction. After quenching from 1073–1123 K, this crystal underwent the *B*2 ⟶ IDS2 ⟶ *B*19' phase transformations. Below 420 K, extra doublet reflections appeared in the $(1/2 \pm \delta_2)\langle 110\rangle$ positions along radial

directions ⟨110⟩ and the incommensurability parameter $\delta_2$was as high as 0.09–0.10. Later [14], the same authors showed that similar extra reflections also appeared at temperatures below 420 K along nonradial directions ⟨110⟩. However, the results from [13, 14] are insufficient to correctly describe the IDS2 structure using only the correlation of incommensurate transverse waves of atomic displacements with wave vectors close to (1/2)⟨110⟩. One of the reasons for this conclusion is the presence of weak but reliably identified $(1/2 - \delta_2)\langle 110\rangle$ extra reflections in the neutron diffraction patterns near the zero site of the reciprocal lattice; these reflections must have zero intensity in the case of purely transverse polarization. The appearance of these reflections can be caused by either the longitudinal component of atomic-displacement waves or second-order (or higher-order) diffraction effects of neutron scattering by correlated atomic displacements of other types. Thus, to simulate the IDS2 structure, it is necessary to study reflections located in other planes or in other directions of the $B2$-phase reciprocal lattice or to make certain that they are absent. The (110) and (111) planes of the reciprocal lattice, which include the high-symmetry ⟨112⟩ directions, are of great importance, because, for example, longitudinal (2/3)⟨111⟩ atomic-displacement waves, whose correlation induces the $\beta \longrightarrow \omega$ transformation in bcc alloys [5], are equivalent to $(1/3)\langle 112\rangle_{\mathbf{q}}\langle \bar{1}\bar{1}1\rangle_{\mathbf{u}}$ transverse waves. Moreover, in the ideal bcc structure, $(1/2)\langle 110\rangle_{\mathbf{q}}\langle 1\bar{1}1\rangle_{\mathbf{u}}$ longitudinal atomic-displacement waves and $(1/2)\langle 110\rangle_{\mathbf{q}}\langle 1\bar{1}0\rangle_{\mathbf{u}}$ transverse waves are equivalent to a $(1/2)\langle \bar{1}\bar{1}2\rangle_{\mathbf{q}}\langle 1\bar{1}0\rangle_{\mathbf{u}}$ transverse wave; however, this equivalence is absent for incommensurate atomic-displacement waves with **q** along the ⟨110⟩ directions.

The goal of this work is to apply neutron diffraction to study the reflections in the ⟨112⟩ and ⟨110⟩ directions of the $B2$-phase reciprocal lattice that appear when IDS2 forms in a $Ti_{49}Ni_{51}$ single crystal as a result of the $B2 \longrightarrow$ IDS2 $\longrightarrow B19'$ transformations.

2. EXPERIMENTAL

The initial $Ti_{49}Ni_{51}$ alloy was produced from electrolytic nickel N–0 and titanium iodide. A single crystal was grown following the Bridgman technique in a helium atmosphere with a preliminary vacuum of 10^{-3} Pa. The technique for preparing a single-crystal sample 10 mm in diameter and 15 mm high, with its axis being close to the $B2$-phase [001] direction, is described in [8, 9, 13, 14]. The misorientation angle of mosaic blocks was smaller than 1.2°. The initial structural state of the single-crystal sample, as in [9, 13, 14], was produced by water-quenching from 1120 K. The surface layer of the quenched sample was removed by chemical polishing to a depth of ~0.25 mm. Upon cooling, the sample underwent the $B2 \longrightarrow B19'$ transformation (M_s = 200 K). The results from [9, 13, 14] indicate that, in the temperature range from 420 K to M_s, IDS2 is formed; it is identified by the appearance of incommensurate extra reflections near (1/2)⟨110⟩ in the neutron diffraction patterns.

Elastic scattering of thermal neutrons was studied on a special-purpose multidetector diffractometer intended for examination of the fine structure of single crystals in the temperature range 1070–120 K. The wavelength of neutrons incident upon the sample was controlled by a double-crystal monochromator made of pyrolytic graphite and germanium and was equal to 0.1567 nm. The monochromatized primary beam and the chosen neutron wavelength allowed us to suppress the effects of multiple diffraction harmonics and, thus, substantially increase the sensitivity of the neutron diffraction apparatus.

3. EXPERIMENTAL RESULTS

Neutron diffraction patterns taken from the $Ti_{49}Ni_{51}$ single crystal at T = 295 K along the ⟨110⟩ directions and the nonradial ⟨011⟩ direction between the (011) and (022) fundamental reflections of the $B2$ phase are found to be qualitatively similar to the patterns taken in [8, 9, 13, 14]. A neutron diffraction pattern along the ⟨011⟩ direction that was not published earlier is shown in Fig. 1. This pattern contains a pronounced extra-reflection doublet near (1/2)⟨011⟩, which is characteristic of the incommensurate IDS2. The reproducibility of the extra-reflection profiles near (1/2)[110] and a similar extra-reflection profile near (1/2)[011] indicate that the structural state of the single-crystal sample at 295 K in our studies [8, 9, 13, 14] is the same and characterized by the presence of the incommensurate IDS2. The incommensurability parameter δ_2 characterizing the positions of the $(1/2 \pm \delta_2)\langle 110\rangle$ extra reflections with respect to the centers of the corresponding zones of the $B2$-phase reciprocal lattice is equal to $\sim 0.05 \pm 0.01$.

New results were obtained when studying neutron diffraction patterns taken along various ⟨112⟩ directions

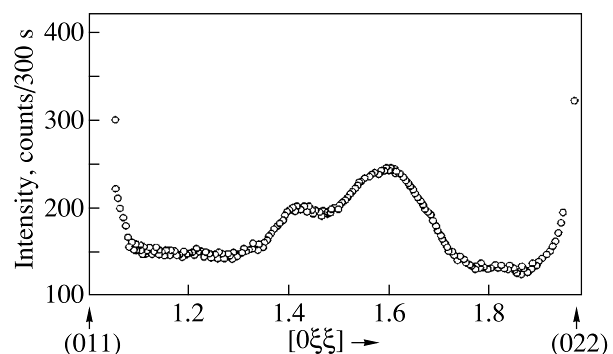

Fig. 1. Neutron diffraction pattern along the [011] direction of the $B2$-phase reciprocal lattice at 295 K.

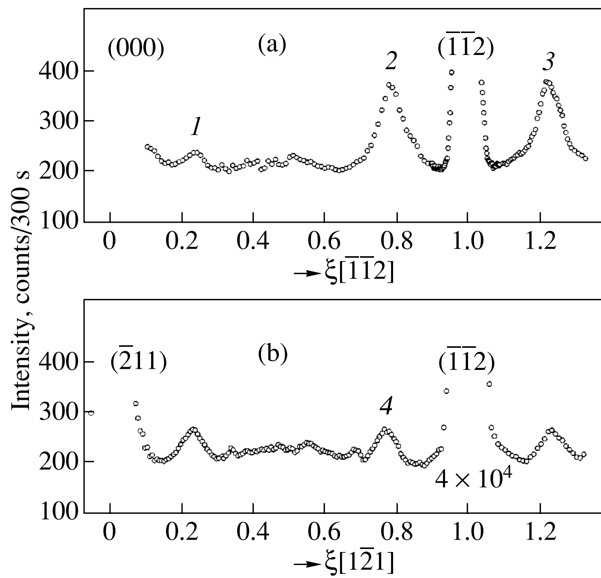

Fig. 2. Neutron diffraction patterns taken at 295 K along (a) the radial [$\bar{1}\bar{1}2$] direction and (b) the [$1\bar{2}1$] direction, which passes through the ($\bar{2}11$) and ($\bar{1}\bar{1}2$) sites of the $B2$–phase reciprocal lattice.

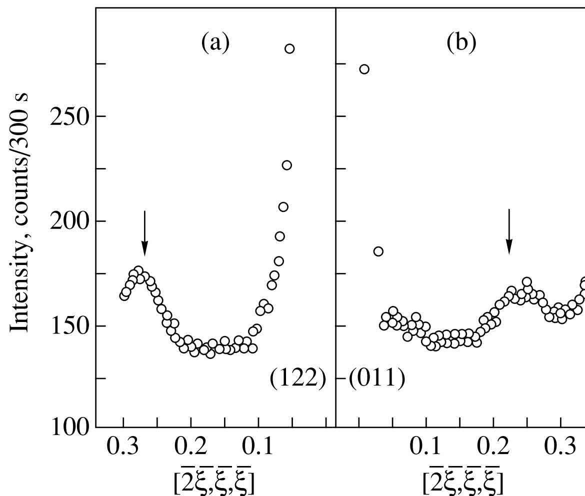

Fig. 3. Extra reflections in the nonradial ⟨211⟩ directions, which pass through various sites of the $B2$-phase reciprocal lattice: (a) from (122) to ($\bar{1}11$) and (b) from (011) to (222).

of the $B2$-phase reciprocal lattice. Figure 2a shows a neutron diffraction pattern for the [$\bar{1}\bar{1}2$] direction that is typical of the radial ⟨112⟩ directions. Figure 2b shows a neutron diffraction pattern along the nonradial [$1\bar{2}1$] direction, which intersects the ($\bar{2}11$)and ($\bar{1}\bar{1}2$) sites of the $B2$-phase reciprocal lattice. Figure 3 gives fragments of neutron diffraction patterns taken along the nonradial equivalent ⟨211⟩ directions, which go through the (122) superstructure site (Fig. 3a) and the (011) structure site (Fig. 3b) of the $B2$-phase reciprocal lattice. A characteristic feature of these neutron diffraction patterns is the presence of extra reflections (Fig. 2, numerals *1–4*; Fig. 5, numerals *1–7*) near the reciprocal-lattice structure and superstructure sites. Analysis of the neutron diffraction patterns shows that the positions of these extra reflections are determined by

$$\mathbf{G}_m = \mathbf{G}_{hkl} + \mathbf{q}_m, \tag{3}$$

where $\mathbf{q}_m$ is a 0.225⟨112⟩ vector and m is the number of the extra reflection. The profiles of the $\mathbf{G}_m$ extra reflections exhibit a significant dependence on orientation. Figure 4 shows the profiles of the $\mathbf{G}_2 = \langle\overline{0.775}, \overline{0.775}, 1.55\rangle$ extra reflection measured along the $\langle\bar{1}\bar{1}2\rangle$ direction and along the perpendicular $\langle 1\bar{1}0\rangle$ direction. A comparison of these profiles reveals that the half-width of the $\mathbf{G}_2$ extra reflection in the $\langle\bar{1}\bar{1}2\rangle$ direction is noticeably smaller than that in the $\langle 1\bar{1}0\rangle$ direction. As follows from our studies, the shape of the $\mathbf{G}_m$ extra reflections is close to a disk, with the disk plane being normal to the ⟨112⟩ directions. The $\mathbf{G}_m$ extra reflections are diffuse; their half-widths measured along the ⟨112⟩ directions are greater than those of the nearest fundamental and superstructure reflections of the $B2$ phase by a factor of 1.5–2.

The distributions of the $\mathbf{G}_m$ extra reflections in the (001)*, ($0\bar{1}1$)*, and (111)* planes of the $B2$-phase reciprocal lattice are given in Fig. 5. The extra reflections near the (1/2)⟨110⟩ positions (open contours), which appear upon cooling below $T_{01} = 430(\pm 10)$ K, are also shown in Fig. 5 [9, 13, 14]. To analyze the nature of the $\mathbf{G}_m$ extra reflections, we have to study the temperature dependences of their intensities and positions in the reciprocal space and to find the temperature range of their existence.

Figure 6 shows the evolution of the profile of the $\mathbf{G}_2 = \langle\overline{0.775}, \overline{0.775}, 1.55\rangle$ extra reflection upon heating, and Fig. 7 shows the temperature dependences of its maximum intensity $I_{\max}$, half-width $\Delta\xi$, and position ξ. It is seen that $I_{\max}$ decreases almost linearly upon heating and that ξ increases insignificantly (~0.015 ± 0.005). In other words, the extra reflection shifts from the nearest Bragg reflection ($\bar{1}\bar{1}2$) upon heating and its half-width increases noticeably. As follows from the temperature dependence of $I_{\max}$, the temperature of disappearance of $\mathbf{G}_2$ upon heating is $T_{02} = 460(\pm 10)$ K. Note that T_{02} is higher than T_{01} by about 40 K. Upon repeated cooling to 295 K, the intensities and positions of the $\mathbf{G}_m$ extra reflections are recovered (Fig. 8a). Thus, both the extra reflections near (1/2)⟨110⟩ and the $\mathbf{G}_m$ extra reflections coexist in a temperature range preceding the $B2 \longrightarrow B19'$ transformation and character-

ize the pretransition IDS2 phase. This phase is sufficiently stable in this temperature range: there are no substantial changes in the profiles and positions of the $\mathbf{G}_m$ extra reflections in the neutron diffraction patterns taken after 1.5 years of storage of the sample at 295 K (Fig. 8b).

4. DISCUSSION OF THE RESULTS

It is known [6, 16] that the positions of extra reflections near reciprocal-lattice sites of an initial phase in which a modulated structure appears due to a correlation of atomic-displacement waves of different types with an amplitude u are determined by the scattering vector

$$\mathbf{G}_j = \mathbf{b}_j + \sum p_i \mathbf{q}_i, \quad (4)$$

where $\mathbf{b}_j$ is the jth reciprocal-lattice site; $\mathbf{q}_i$ is the ith ray of, e.g., the non-Lifshitz star of a wave vector characterizing the spectrum of atomic-displacement waves; and p_i are integers (0, 1, 2, …). First-order diffraction effects (in the case where one p_i is ±1 and the others are zero) correspond to the regular appearance of pair extra reflections near reciprocal-lattice sites at the points

$$\mathbf{G}_{ji} = \mathbf{b}_j \pm \mathbf{q}_i. \quad (5)$$

The intensities I_{ji} of extra reflections of this type are proportional to the square of a Bessel function of the argument $Z_p = (\mathbf{G}_{ij}, \mathbf{u}_p)$. Extra reflections in the positions $\mathbf{b}_j + \mathbf{q}_i$ and $\mathbf{b}_j - \mathbf{q}_i$ have the same intensities, and, for small values of Z, we have

$$I_{ji} \sim (\mathbf{G}_{ji}, \mathbf{u}_i)^2. \quad (6)$$

Second-order diffraction effects can appear at the reciprocal-lattice points

$$\mathbf{G}'_{ij} = \mathbf{b}_j \pm 2\mathbf{q}_i \quad (7)$$

(one p_i is 2, the others are zero).

Their intensities I'_{ji} have a more complex form and, at small Z, can be estimated from the expression

$$I'_{ji} = (\mathbf{G}_{ji}, \mathbf{u}_i)^4. \quad (8)$$

As a rule, I'_{ji} are much less intense than I_{ji}.

Another type of second-order diffraction effects corresponds to extra reflections whose positions are characterized by the scattering vectors

$$\mathbf{G}''_{jkl} = \mathbf{b}_j \pm \mathbf{q}_k \pm \mathbf{q}_l \quad (9)$$

(two p_i, e.g., p_k and p_l, are equal to ±1, and the others are zero). The intensities of these extra reflections are close to I'_{ji} in order of magnitude. The intensities of higher order extra reflections are well below I'_{ji} and I''_{ji}; hence, the probability of their detection is very low.

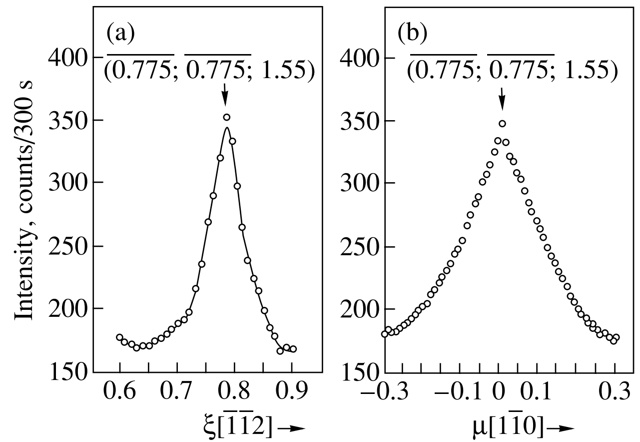

Fig. 4. Intensity profiles of the ($\overline{0.775}$, $\overline{0.775}$, 1.55) extra reflection measured at 295 K along (a) the radial [$\bar{1}\bar{1}2$] direction and (b) the perpendicular [$1\bar{1}0$] direction. $\Delta\mu = \Delta\xi/\sqrt{3}$.

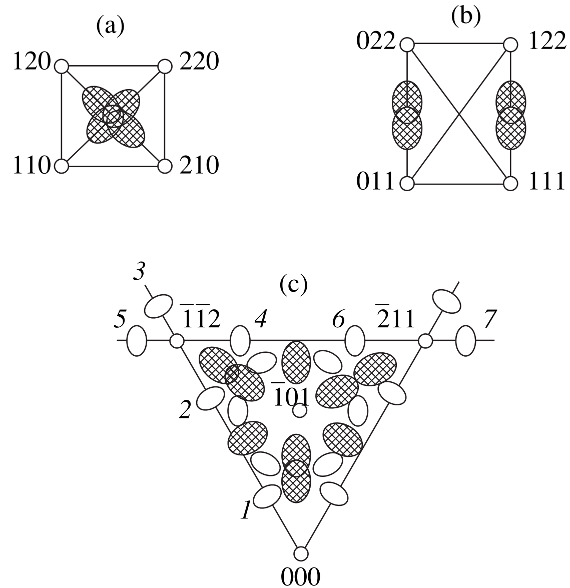

Fig. 5. Distribution of extra reflections along the ⟨110⟩ and ⟨112⟩ directions of the $B2$-phase reciprocal lattice at 295 K: (a) (001)*, (b) ($0\bar{1}1$)*, and (c) (111)*. The designations are identical to those in Fig. 2.

A comparison of our experimental data and the theory developed in [17] suggests that the extra reflections along the ⟨112⟩ directions of the $B2$-phase reciprocal lattice are first-order diffraction effects corresponding to the full non-Lifshitz star of the wave vector,

$$\mathbf{q} = 0.225\langle 112\rangle, \quad (10)$$

each of whose rays is incommensurate with the translations of the initial cubic crystal. In accordance with the theory [16, 17], the intensities of the extra reflections

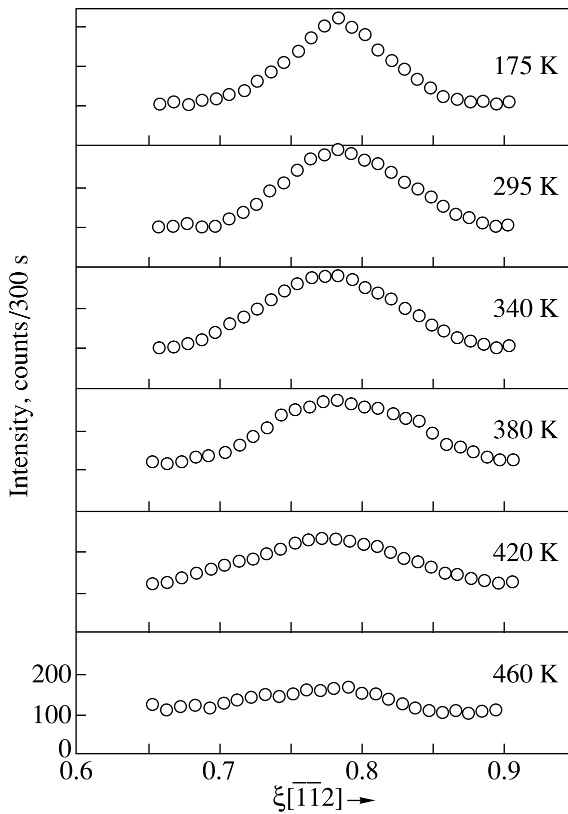

Fig. 6. Effect of temperature on the intensity profile of the($\overline{0.775}$, $\overline{0.775}$, 1.55) extra reflection.

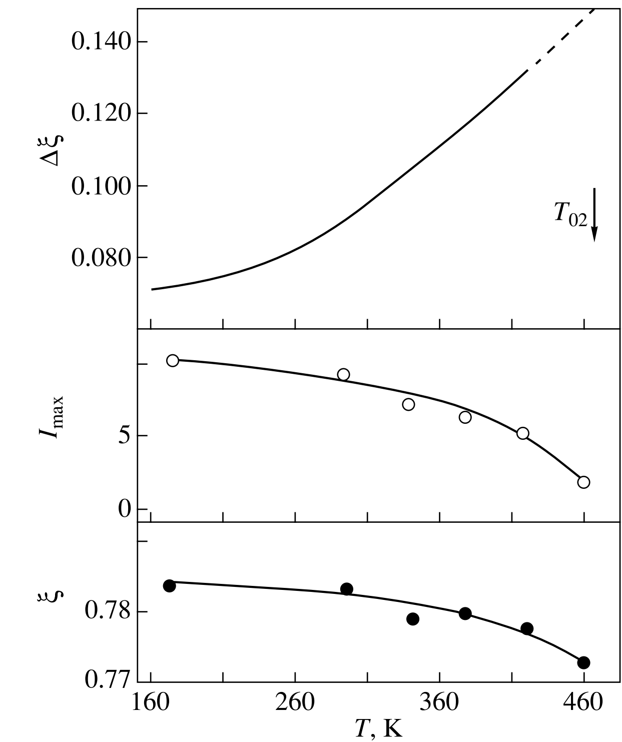

Fig. 7. Effect of temperature on the position ξ of the ($\overline{0.775}$, $\overline{0.775}$, 1.55) extra reflection, its maximum intensity I_{max}, and its half-width Δξ upon heating from 295 K.

with $\mathbf{b}_j + \mathbf{q}_i$ and $\mathbf{b}_j - \mathbf{q}_i$ are virtually the same if we take into account the difference (which can reach ~10%) in the angular intensity factors. For example, these are pairs of extra reflections *2*, *3* and *4*, *5* in different ⟨112⟩ directions near the ($\bar{1}\bar{1}2$) fundamental reflection of the *B*2 phase (Fig. 2). The theory is also supported by the presence of very weak diffuse maxima near (1/2 ± 0.05)⟨112⟩ (Fig. 2), which should correspond, according to [16, 17], to the second-order $\mathbf{G}'_{ji}$ reflections (see Eqs. (7), (8)). The doublet incommensurate extra reflections $(1/2 \pm \delta_2)\langle 110\rangle$ with $\delta_2 \approx 0.05$, whose intensities are 30–40% lower than the intensity of the extra reflections characterized by Eq. (10) and which appear at temperatures lower than T_{02}, also correspond to second-order diffraction effects (two-beam effects) but belong to their second type, $\mathbf{G}''_{jkl}$, defined by Eq. (9). For example, the extra reflections in the (100)* plane (Fig. 1) appear as a result of the correlation of atomic-displacement waves of the type

$$\mathbf{q}_{\langle 011\rangle} = 0.225\langle \bar{2}11\rangle + 0.225\langle 211\rangle = 0.45\langle 011\rangle \quad (11)$$

(in the reduced zone). The extra reflections near (1/2)⟨110⟩ in the (001)* plane, which were earlier described in [9, 13, 14], also correspond to correlations of a similar type,

$$\mathbf{q}_{\langle 110\rangle} = 0.225\langle 112\rangle + 0.225\langle 11\bar{2}\rangle = 0.45\langle 110\rangle, \quad (12)$$

$$\mathbf{q}_{\langle 0\bar{1}1\rangle} = 0.225\langle 1\bar{1}2\rangle + 0.225\langle 1\bar{1}\bar{2}\rangle = 0.45\langle 0\bar{1}1\rangle. \quad (13)$$

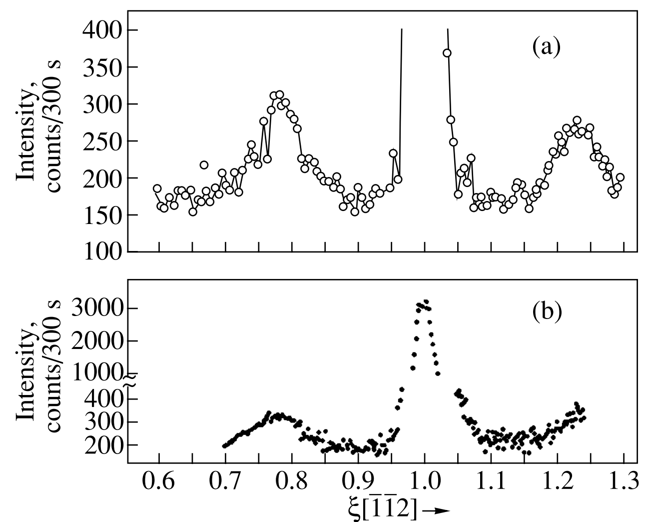

Fig. 8. Extra-reflection profiles near the ($\bar{1}\bar{1}2$) reflection of the *B*2 phase at 295 K: (a) after heating to 460 K and (b) after 1.5 year.

Thus, the analysis of the experimental diffraction effects detected in the $\langle 112 \rangle$ and $\langle 110 \rangle$ directions of the *B*2-phase reciprocal lattice suggests that all 24 rays of the star of the wave vector in Eq. (10) are involved in the formation of the neutron diffraction patterns of IDS2 in the quenched $Ti_{49}Ni_{51}$ single crystal. In this case, according to [16], the $B2 \longrightarrow$ IDS2 phase transformation is characterized by a double-beam transformation channel and the IDS2 has a multidomain structure.

Another important problem, which can be discussed using the experimental data obtained, is related to the character (transverse or longitudinal) of displacement waves appearing in the pretransition temperature range. Based on the distribution of the extra reflections in the reciprocal space, we can assume that the spectrum of the atomic-displacement waves involved in the formation of IDS2 contains waves with clearly pronounced longitudinal polarization. This assumption is based on the presence of the weak but clearly visible $0.225\langle 112 \rangle$ extra reflections in the radial $\langle 112 \rangle$ directions near the zero site of the *B*2-phase reciprocal lattice. The intensities of these extra reflections should be zero for any type of transverse polarization $\mathbf{u}$ of the atomic-displacement waves with $\mathbf{q} = 0.225\langle 112 \rangle$, e.g., for $\mathbf{u}$ directed along $\langle 111 \rangle$, $\langle 1\bar{1}0 \rangle$, and $\langle 31\bar{2} \rangle$.

An argument for the involvement of longitudinal waves in the formation of IDS2 is the presence of the $(1/2 - \delta_2)\langle 110 \rangle$ extra reflections in the neutron diffraction patterns in the radial $\langle 110 \rangle$ directions near the zero site of the reciprocal lattice; according to Eq. (9), these are two-beam effects of neutron scattering by a modulated structure corresponding to the star of the wave vector given by Eq. (10).

The existence of longitudinal displacement waves of this type does not exclude the simultaneous presence of components with transverse polarization and the same wave vector along $\langle 110 \rangle$ in the premartensitic state of the alloy and, in general, the presence of atomic-displacement waves with other wave vectors and other displacement polarization, whose diffraction effects will completely or partly correspond to the extra-reflection distribution in the neutron diffraction patterns obtained in this work.

First of all, transversely polarized waves with $\mathbf{q} = 0.225\langle \bar{1}\bar{1}2 \rangle$ and polarization vectors of the $\langle 1\bar{1}0 \rangle$ and $\langle 111 \rangle$ types can be present. The $(1/2)\langle \bar{1}\bar{1}2 \rangle_{\mathbf{q}}\langle 1\bar{1}0 \rangle_{\mathbf{u}}$ transverse waves in the CsCl structure are equivalent to transverse waves of the TA_2 [110] phonon branch at $\xi = 1/2$. In [10, 11], it was found experimentally that, on the whole, the $TA_2\xi$ [110] phonon branch in TiNi-based alloys is low-energy, and the authors of [10, 18, 19] found that, near the Brillouin zone boundary, there is a deep minimum, which covers a rather wide range of wave vectors (from $\xi \approx 0.4$ to 1/2). The development of anomalous softening of the $TA_2\xi$ [110] phonon branch in the vicinity of $\xi = 1/2$ was observed upon cooling in the pretransition temperature range [10]. The diffuse pretransition effects that appear in electron diffraction patterns of TiNi-based alloys were comprehensively discussed in [1, 2, 5, 12] in terms of the development of weakly incommensurate correlated $(1/2)\langle 110 \rangle_{\mathbf{q}}\langle 1\bar{1}0 \rangle_{\mathbf{u}}$ atomic-displacement waves. Thus, the first- and second-order diffraction effects that appear upon neutron scattering by the correlated $(1/2 - \delta_2)\langle 110 \rangle_{\mathbf{q}}\langle 1\bar{1}0 \rangle_{\mathbf{u}}$ atomic-displacement waves can substantially overlap (in the *B*2-phase reciprocal lattice) second-order diffraction effects described by Eqs. (7) and (9) and belonging to the star of the wave vector in Eq. (10). In particular, at $1/2 - \delta_2 = 0.45$, the space positions of these reflections coincide completely.

In TiNi-based alloys, there exists a high probability of appearance of diffraction effects induced by the correlation of quasi-transverse atomic-displacement waves of the so-called special phonon mode, which is close to the transversely polarized $T_2\langle 112 \rangle_{\mathbf{q}}\langle 11\bar{1} \rangle_{\mathbf{u}}$ mode (their misorientation is ~5° [20]). Softening of the specific elastic modulus C_s, which characterizes the beginning of this phonon-spectrum branch, was observed upon cooling TiNi-based [21] and other alloys with the initial *B*2 structure (AuCd [22], NiAl [19, 22], Au–Ag–Cd [23]) in the pretransition temperature range. A significant decrease in the $T_2\xi$ [112] phonon energy at $\xi \approx 1/3$ was detected experimentally only in the pretransition temperature range of the $\beta \longrightarrow 9R$ martensitic transformation in a Cu–19.3 wt % Zn–13 wt % Al alloy [24]; in most other alloys with the initial *B*2 structure, this phonon-spectrum branch has not yet been studied. In [25–27], it was assumed that, in β-Ti, β-Zn, and the related alloys, the energy of $T_2\xi$ [112] phonons at $\xi = 1/3$ should also decrease. In this case, these phonons are equivalent to phonons of the $LA\xi$ [111] longitudinal mode at $\xi = 2/3$, whose softening was observed in all these alloys when approaching the $\beta \longrightarrow \omega$ martensitic transformation [5, 25] and the $\beta \longrightarrow 9R$ transformation [24].

The complex structure of the phonon spectrum of titanium nickelide–based alloys [28, 29] suggests various scenarios of the development of correlated atomic-displacement waves of different types and, hence, the possible formation of various pretransition IDS2 structures (dominated by longitudinal waves, transverse waves, or various combinations of them). Therefore, it is important to study the second-order diffraction effects, whose spatial distribution and intensity give additional information on each of these structures. At the same time, we can qualitatively estimate the ratios of the integrated intensities of extra reflections using Eq. (6) even without regard to the possible presence of displacement waves other than longitudinally polarized waves with $\mathbf{q} = 0.225\langle 112 \rangle$. Estimates indicate that the most intense extra reflections in the cubic field of the reciprocal space bound by (200)-type sites should exist near the (112) structural sites, which are located in the

radial ⟨112⟩ directions. The ratio of the integrated intensities of the extra reflections located in these directions near the zero site should be about 8.6 : 1.0. The integrated intensities of the extra reflections localized in the nonradial ⟨112⟩ directions should be weaker than the extra reflections located in the radial directions near the (112) sites by a factor of 2–4. The experimental ratios of the extra reflections considered above and partly given in Figs. 2, 3, and 5 are close to the calculated values; their differences do not exceed 20%. The differences between the experimental and calculated values are satisfactory, making allowance for the fact that Eq. (6) was obtained under the assumption that the argument of the corresponding Bessel functions describing the extra-reflection intensities was small [16, 17]. However, the amplitudes of atomic displacements in the premartensitic temperature range (including TiNi-based alloys [1, 5, 10]) can be 10% or more of the values corresponding to the interplanar spacings; therefore, Eq. (6) is applied near the boundary of its range of application. The agreement between the calculated and experimental values of such subtle parameters as the ratios of the integrated intensities of the extra reflections supports the assumption regarding the dominating role of the $0.225\langle 112\rangle_{\mathbf{q}}\langle 112\rangle_{\mathbf{u}}$ longitudinal displacement waves in the formation of IDS2 in the alloy under study.

In concluding, we note that the diffraction effects in the form of strongly incommensurate $(1/2 - \delta_2)\langle 110\rangle$ (with δ_2 varied from 0.05 to 0.1) extra reflections are not a unique phenomenon that can exist only in TiNi-based alloys undergoing the $B2 \longrightarrow B19'$ martensitic transformation. In particular, electron diffraction patterns corresponding to the (110)* planes of the reciprocal lattice of $Ti_{54}Ni_{46-x}Fe_x$ (x = 0–16 at. %) and $Ti_{50}Pd_{50-x}Fe_x$ (x = 0–16 at. %) alloys contain pairs of $\Delta_i\langle 110\rangle$ extra reflections (i = 1, 2) in the pretransition temperature range before the $B2 \longrightarrow B19$ martensitic transformation. Depending on the alloy composition and the recording temperature ($T > M_s$), the positions of these reflections change from $\Delta_1 \approx 0.22$ to $\Delta_1 \approx 1/3$ and from $\Delta_2 \approx 1/2$ to $\Delta_2 \approx 1/3$ (for the first and second extra reflection of each pair, respectively) [30]. In [31], neutron diffraction patterns of a $Ti_{50}Pd_{42}Cr_8$ alloy also exhibit 0.22⟨110⟩ extra reflections in the pretransition temperature range of the $B2 \longrightarrow B19$ martensitic transformation. No softening of the $TA_2\xi$ [110] phonon mode at $\xi = 0.22$ was detected in [31]. Other planes and directions were not studied in [31]. The reasons for the appearance of these extra reflections in TiPd-based alloys are unknown. However, the fact that the positions of the extra reflections in the ⟨110⟩ directions in TiPd-based alloys doped with Fe and Cr [30, 31] are close to the second-order reflections ($\mathbf{G}''_{jkl}$) belonging to the star of the wave vector in Eq. (8) suggests that the results of a detailed study of these effects in TiNi-based alloys could prove important not only for simulating the IDS2 structure in them but also for the development of general concepts on IDS structures that appear in various alloys undergoing the $B2 \longrightarrow B19'$ (or $B2 \rightleftarrows B19$) martensitic transformation.

5. CONCLUSIONS

(1) We have performed a neutron diffraction study of a quenched $Ti_{49}Ni_{51}$ single-crystal alloy with a single-phase $B2$ structure that undergoes the $B2 \longrightarrow B19'$ martensitic transformation upon cooling below M_s = 200 K. The alloy is known to have a pretransition intermediate displacive structure (IDS2) at about 300 K. Neutron diffraction patterns revealed 0.225⟨112⟩ first-order reflections belonging to the complete 24-ray star of the wave vector $\mathbf{q} = 0.225\langle 112\rangle$.

(2) Second-order diffraction effects in the form of 0.45⟨112⟩ and 0.45⟨110⟩ extra reflections, which are close to the (1/2)⟨110⟩ commensurate equivalent vectors of the $B2$-phase reciprocal lattice, have been revealed and studied.

(3) Based on the experimentally found spatial distribution of the diffraction effects and analysis of the intensities of the extra reflections in both radial and nonradial directions of the $B2$ reciprocal lattice, we have shown that these diffraction effects are caused by the correlation of longitudinally polarized atomic-displacement waves with $\mathbf{q} = 0.225\langle 112\rangle$ in the temperature range of IDS2.

(4) Neutron diffraction studies at various temperatures have indicated that the 0.225⟨112⟩ extra reflections appear upon cooling below $T_{02} = 470 \pm 10$ K and that the 0.45⟨110⟩ extra reflections appear upon cooling below $T_{01} = 430 \pm 10$ K. The intensities of all the extra reflections detected increase upon cooling to M_s, then decrease to zero without hysteresis upon subsequent heating above T_{01} (for the 0.45⟨110⟩ reflection) and T_{02} (for 0.225⟨112⟩), and again increase during repeated cooling below these temperatures.

(5) We assumed that the correlation of longitudinally polarized atomic-displacement waves plays a dominating role in the formation of IDS2 in the alloy under study. The $(1/2 - \delta_2)\langle 110\rangle_{\mathbf{q}}\langle 1\bar{1}0\rangle_{\mathbf{u}}$ transversely polarized atomic-displacement waves (where δ_2 can vary from 0 to 0.1) can also take part in this process. Since the contributions from atomic-displacement waves of different types can vary because of the complex structure of the acoustic-phonon spectrum in TiNi-based alloys, various IDS2 can arise that differ in terms of their fine crystal structure.

ACKNOWLEDGMENTS

This work was supported by the Russian Foundation for Basic Research (project no. 02-02-17849), the Complex Integration Project of the Siberian Division of the Russian Academy of Sciences (project no. 24, SO

RAN Presidium decision no. 62 of Feb. 21, 2003), and State Contract no. 40.012.1.1.1150 ("Neutron Diffraction Studies of Condensed Matter").

REFERENCES

1. V. N. Khachin, V. G. Pushin, and V. V. Kondrat'ev, *Titanium Nickelide: Structure and Properties* (Nauka, Moscow, 1992) [in Russian].
2. A. I. Lotkov, Doctoral Dissertation (Tomsk, 1991).
3. S. T. Kindzoku, Met. Technol. **59** (8), 11 (1989).
4. A. I. Lotkov and V. N. Grishkov, Izv. Vyssh. Uchebn. Zaved., Fiz., No. 5, 68 (1985).
5. V. G. Pushin, V. V. Kondrat'ev, and V. N. Khachin, *Pretransition Phenomena and Martensitic Transformations* (Ural. Otd. Ross. Akad. Nauk, Yekaterinburg, 1998).
6. C. M. Hwang, M. Meichle, M. B. Salamon, and C. M. Wayman, Philos. Mag. A **47**, 9 (1983).
7. S. M. Shapiro, Y. Noda, Y. Fujii, and U. Yamada, Phys. Rev. B **30** (8), 4314 (1984).
8. S. F. Dubinin, A. I. Lotkov, S. G. Teploukhov, V. N. Grishkov, and V. P. Scorobogatov, Phys. Met. Metallogr. **73** (4), 401 (1992).
9. A. I. Lotkov, S. F. Dubinin, S. G. Teploukhov, V. N. Grishkov, and V. P. Scorobogatov, J. Phys. Colloq. **5** (C8), C8-551 (1995).
10. P. Moine, J. Allain, and B. Renker, J. Phys. F: Met. Phys. **14**, 2517 (1984).
11. G. Herget, M. Mullner, G. Eckold, H. Tietze, and W. Assmus, IKF Annu. Rep. **47**, 77 (1987).
12. P. Moine, G. M. Michal, and R. Sinclair, Acta Metall. **30**, 109 (1982).
13. S. F. Dubinin, A. I. Lotkov, S. G. Teploukhov, and V. N. Grishkov, Izv. Vyssh. Uchebn. Zaved., Fiz. **38** (1), 56 (1995).
14. A. I. Lotkov, S. F. Dubinin, V. N. Grishkov, and S. G. Teploukhov, Materialovedenie, No. 10, 11 (2000).
15. A. I. Simons and C. M. Varma, Solid State Commun. **35**, 317 (1980).
16. R. W. James, *The Optical Principles of the Diffraction of X-rays* (Bell, London, 1962; Mir, Moscow, 1966).
17. Yu. A. Izyumov, V. E. Naĭsh, and R. P. Ozerov, *Neutron Diffraction of Magnetic Materials* (Atomizdat, Moscow, 1981; Consultants Bureau, New York, 1991).
18. T. Ohba, T. Fukuda, T. Tabata, and T. Kakeshita, J. Phys. IV **112**, 639 (2003).
19. X. Ren, K. Taniwaki, K. Otsuka, and Y. Mori, J. Phys. Soc. Jpn. **70**, 280 (2001).
20. A. Nagasawa, N. Nakanishi, and K. Enami, Philos. Mag. A **43** (6), 1345 (1981).
21. A. I. Lotkov, V. A. Goncharova, V. P. Lapshin, V. A. Chernyshova, V. N. Grishkov, and D. R. Dmitriev, Dokl. Ross. Akad. Nauk **343** (2), 187 (1995) [Phys. Dokl. **40**, 340 (1995)].
22. A. Nagasawa and Y. Ueda, J. Phys. Soc. Jpn. **45** (4), 1249 (1978).
23. A. Nagasawa, N. Nakanishi, H. Morimoto, M. Takano, Y. Matsuo, and T. Suzuki, J. Phys. Soc. Jpn. **47** (2), 535 (1979).
24. G. Guenin, D. R. Jara, M. Morin, L. Delaey, R. Pynn, and P. F. Gobin, J. Phys. (Paris) **43**, C4-597 (1982).
25. W. Petry, A. Heiming, J. Trampenau, and G. Vogl, Trans. Tech. Publ. **66–69**, 365 (1989).
26. W. Petry, T. Flottmann, A. Heiming, J. Trampenau, and M. Alba, Phys. Rev. Lett. **61** (6), 722 (1988).
27. J. A. Krumhansl and R. J. Gooding, Phys. Rev. B **39** (5), 3047 (1989).
28. X. Huang, C. Bungaro, V. Godlewsky, and K. M. Rabe, Phys. Rev. B **65**, 014108-1 (2002).
29. K. Parlinski and M. Parlinska-Wojtan, Phys. Rev. B **66**, 064307-1 (2002).
30. K. Enami, T. Yoshida, and S. Nenno, in *Proceedings of International Conference on Martensitic Transformations, ICOMAT'86* (JIM, Japan, 1986), p. 103.
31. B. L. Winn, S. M. Shapiro, R. Erwin, D. L. Schlagel, and T. Lograsso, Appl. Phys. A **74** (Suppl. 1), 182 (2002).

Translated by K. Shakhlevich

Physics of the Solid State, Vol. 46, No. 8, 2004, pp. 1394–1397. Translated from Fizika Tverdogo Tela, Vol. 46, No. 8, 2004, pp. 1356–1359.
Original Russian Text Copyright © 2004 by Anshukova, Golovashkin, Ivanova, Krynetskiĭ, Rusakov, Shulyatev.

METALS AND SUPERCONDUCTORS

Low-Temperature Thermal-Expansion Anomaly in $Bi_2Sr_2CuO_6$

N. V. Anshukova*, A. I. Golovashkin*, L. I. Ivanova, I. B. Krynetskiĭ***, A. P. Rusakov**, and D. A. Shulyatev****

**Lebedev Physical Institute, Russian Academy of Sciences, Leninskiĭ pr. 53, Moscow, 119991 Russia*
e-mail: golov@sci.lebedev.ru
***Moscow Institute of Steel and Alloys, Leninskiĭ pr. 4, Moscow, 117936 Russia*
****Moscow State University, Vorob'evy gory, Moscow, 119899 Russia*

Received November 24, 2003

Abstract—Single-crystal samples of the $Bi_{2+x}Sr_{2-x-y}Cu_{1+y}O_{6+\delta}$ system revealed anomalous (negative) thermal expansion in the temperature range 10–20 K. Magnetic fields of 1–3 T were found to strongly affect the position and width of the anomaly region. A thermal-expansion singularity was detected at temperatures $T \approx 30$–50 K, which may be related to the formation of a pseudogap. © *2004 MAIK "Nauka/Interperiodica".*

The temperature dependence of the thermal expansion coefficient, $\alpha(T)$, of a number of HTSCs shows anomalies at low temperatures [1]. Cuprate HTSC systems $La_{2-x}Sr_xCuO_4$, $YBa_2Cu_3O_{7-x}$, and $Bi_2Sr_2CaCu_2O_8$; the bismuthates $Ba_{1-x}K_xBiO_3$, $BaPb_xBi_{1-x}O_x$; and MgB_2 [2] reveal $\alpha(T) < 0$ within a certain temperature interval. Magnetic fields of a few teslas strongly affect the position and width of the $\alpha(T)$ anomaly region [3]. These effects were generally observed on as-prepared high-quality samples. It was shown in [1] (with the $Ba_{1-x}K_xBiO_3$ system) that the anomaly of thermal expansion is manifested most strongly in the light-doping region and disappears under heavy doping. This anomaly is apparently a fundamental property of all HTSC systems; therefore, it should be related to the mechanism of high-temperature superconductivity. A final conclusion on this point would require additional studies in systems where the $\alpha(T)$ dependence at low temperatures (in particular, in magnetic fields) has not yet been investigated.

Recent studies have revealed the particular place the $Bi_2Sr_2CuO_6$ (Bi-2201) system holds in the investigation of HTSCs [4]. These studies produced the first clear indication that the superconducting gap Δ and the pseudogap Δ^* differ strongly in magnitude and coexist down to the lowest temperatures reached. In other HTSC systems, the pseudogap Δ^* at low temperatures is comparable in magnitude to Δ to such an extent that they are practically indistinguishable. Various explanations of the nature of the pseudogap have been offered. The unique data quoted in [4] considerably narrow the area on which the search for the mechanism of pseudogap formation in HTSC systems should be focused.

We carried out measurements of the thermal expansion of single-crystal $Bi_{2+x}Sr_{2-x-y}Cu_{1+y}O_{6+\delta}$ samples with different doping levels in the temperature region 4.2–80 K and studied its response to magnetic fields of up to 2.8 T. We investigated samples prepared by two methods, namely, radiation-heated skull melting [5] and growth in a gas cavern in a melt solution [6]. Thermal expansion was investigated on samples of two types. Samples of the first type, with the composition $x = 0.30$–0.32, $y = 0.01$–0.04, and $\delta = 0.18$–0.19, are subsequently referred to as Bi-*A*, and samples of the second type, with the composition $x = 0.19$–0.20, $y = 0.10$–0.12, and $\delta = 0.10$, are referred to as Bi-*B*. The composition of a sample was determined by electron probe microanalysis (EPMA) and energy-dispersive x-ray analysis (EDX). The compositions of the samples studied here are known [4, 7] to be classed among heavily doped materials, with the Bi-*A* samples being more strongly doped. Preliminary results of these studies were reported earlier [8].

X-ray characterization showed the samples under study to be of very high quality. Diffractograms of the crystals contained only one series of very strong (001) reflections. The lattice parameters of the Bi-*A* samples are $a = 5.410$ Å and $c = 24.55$ Å; for the Bi-*B* samples, they are $a = 5.390$ Å and $c = 24.60$ Å. The rocking curve halfwidths attest to the high structural perfection of the crystals. For instance, the halfwidth of the rocking curve for the main lattice ($00\underline{16}$) reflection in Bi-*A* samples was 0.1°–0.2°. Samples of both types revealed superstructural modulation correlating with the critical temperature. From the known dependence of the lattice parameters of the Bi-2201 system on composition, it follows that the x-ray measurements agree well with the data derived from EPMA and EDX. The critical temperatures T_c of the samples were derived from measurements of the differential magnetic susceptibility. It was found that for the Bi-*B* samples $T_c = 7.2 \pm 0.1$ K and for the Bi-*A* crystals $T_c < 4$ K.

1063-7834/04/4608-1394$26.00 © 2004 MAIK "Nauka/Interperiodica"

The change in sample length $\Delta L/L$ was measured dilatometrically with a sensitivity of ~10^{-7} [9]. The magnetic field was oriented parallel to the direction in which the strain was determined. The setup was calibrated by measuring the thermal expansion of samples of rare-earth oxides with a well-known $\alpha(T)$ dependence.

Figure 1 shows typical temperature dependences of $\Delta L/L$ obtained for samples of both types (Bi-*A*, Bi-*B*) at $H = 0$. The curve for the Bi-*B* sample clearly exhibits two features, a low-temperature one at $T \le 30$ K and a "high-temperature" feature in the region of $T \sim 50$ K. For Bi-*A* samples with a higher doping level, the temperature dependence of $\Delta L/L$ has only one, high-temperature, feature in the region $T = 25$–35 K. At lower temperatures, the thermal expansion of such samples is practically zero (below the sensitivity level of the sensor). Above the high-temperature feature, the temperature dependences of $\Delta L/L$ for both samples exhibit a behavior typical of metals, with a positive coefficient of thermal expansion.

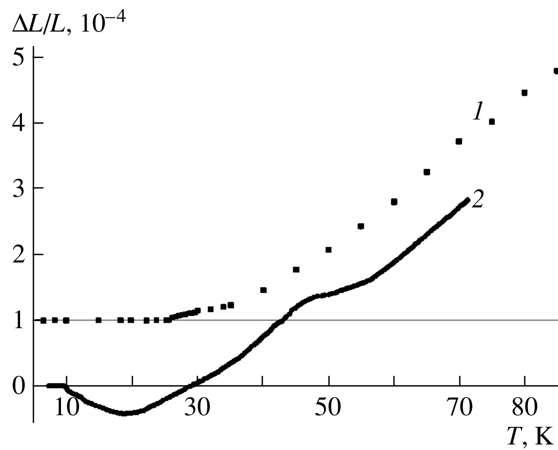

Fig. 1. Typical temperature behavior of thermal expansion $\Delta L/L$ in a zero magnetic field obtained on samples (*1*) Bi-*A* and (*2*) Bi-*B*. For convenience, the curve for the Bi-*A* sample was translated vertically by 1×10^{-4}.

The temperature behavior of the thermal expansion coefficient $\alpha = (1/L)dL/dT$ in the region of the low-temperature anomaly and the effect of a magnetic field on this anomaly are illustrated in Fig. 2 for Bi-*B* samples. We readily see that the region with $\alpha < 0$ shifts to lower temperatures with increasing magnetic field. The dependence of the temperature of the minimum in $\alpha(T)$ on magnetic field is presented graphically in Fig. 3.

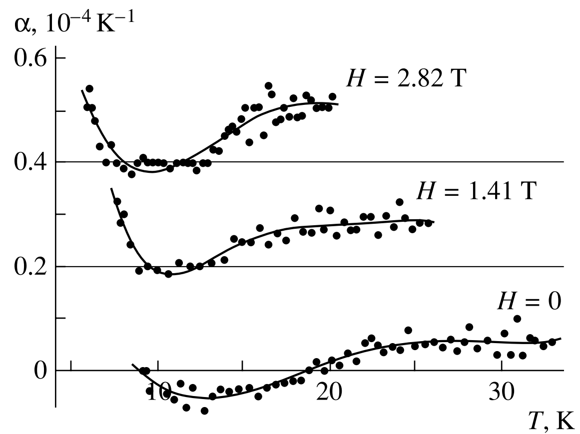

Fig. 2. Temperature dependences of the thermal expansion coefficient $\alpha(T) = (1/L)dL/dT$ in the region of the low-temperature anomaly obtained for Bi-*B* samples in different magnetic fields. The points are our experimental data, and the curves are least square interpolations. For convenience, the $\alpha(T)$ curves corresponding to different magnetic fields are translated vertically by multiples of 0.2×10^{-4} K^{-1}.

The positions of the $\Delta L/L$ anomalies observed in Bi-*B* samples in the higher temperature region (30–55 K) are shown in Fig. 4 for various magnetic fields *H*. These results were obtained by subtracting from the experimental data the linear relation extrapolated from the low-temperature region (here, experimental data are fitted with good accuracy by a linear relation; see Fig. 4). The onset of the anomaly is seen to shift toward lower temperatures with increasing magnetic field. Figure 5 plots the dependence of the temperature of the anomaly onset on *H*.

Analysis of these results should be performed with due account of the fact that an increase in bismuth concentration in a sample in itself entails a decrease in the hole concentration. On the other hand, this growth is accompanied by an increase in the oxygen concentration, which gives rise to an increase in the hole concentration. This complicates analysis of the phase diagram in the region where the bismuth concentration is over 2. Substitution of bismuth for strontium and insertion of oxygen likewise result in a change in the distance between the CuO_2 and SrO planes. Strong changes in the interatomic distances lead to a noticeable change in T_c [4, 7]. At $x \sim 0.4$, the samples even become semiconducting. Therefore, a study of the phase diagrams of HTSC systems should take into account, in addition to the variation in the carrier concentration with doping, the effect of a variation in interatomic distance and the ensuing distortion of the crystal lattice.

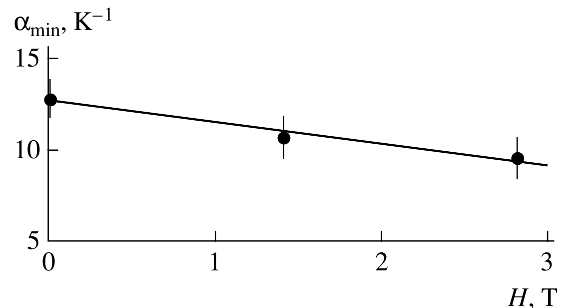

Fig. 3. Magnetic field dependence of the temperature of the minimum in $\alpha(T)$.

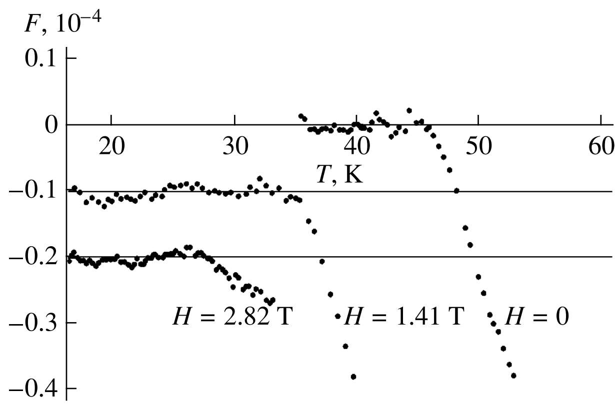

Fig. 4. Positions of the $\Delta L/L$ anomalies observed in the temperature interval 30–55 K in different magnetic fields H. The quantity F was obtained by subtracting the linear dependence (extrapolated from the low-temperature region) from the experimental data. For convenience, the data for $\Delta L/L$ corresponding to different magnetic fields are translated vertically by multiples of 0.1×10^{-4}.

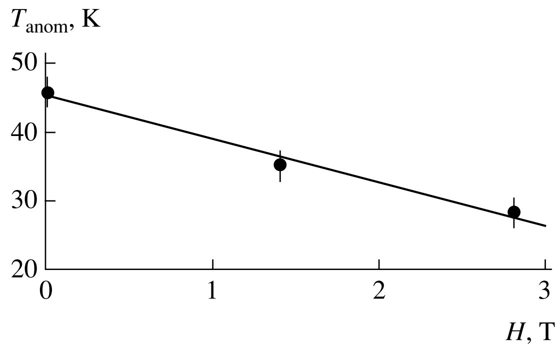

Fig. 5. Temperature of the onset of the high-temperature anomaly plotted vs. H.

Figure 6a shows a schematic phase diagram for the Bi-2201 HTSC system drawn in the T vs. p coordinates, where T is the temperature and p is the hole concentration reduced to one copper ion [10]. The solid line is a plot of $T_c(p)$, and the dashed line is the graph of the $T^*(p)$ dependence, where T^* is the temperature of the pseudogap formation. Our samples belong to the heavy-doping region with $p \gtrsim 0.2$. Figure 6b shows the positions of the high-temperature anomalies obtained by us for the two types of samples and plotted versus T_c, as well as the data on T^* taken from [4, 7, 11]. We readily see that this dependence is linear in the zero approximation (actually, the best fitting dependence also contains a small quadratic term, but, because of the limited number of available points, this result is not reliable). It is conceivable that the high-temperature thermal expansion anomaly observed by us at $T \approx 30$–50 K is due to pseudogap formation. Thus, if we subscribe to this conclusion, a pseudogap in the $Bi_{2+x}Sr_{2-x-y}Cu_{1+y}O_{6+\delta}$ system should be observable up to carrier concentrations $p \gtrsim 0.2$, i.e., to the boundary of the superconductivity region. This point was taken into account in constructing the phase diagram in Fig. 6a.

Generally speaking, in this experiment, one observes the so-called dielectric pseudogap Δ_D^*, which forms, according to our model [12], for certain reciprocal lattice directions and results in an increase in T_c. Experiments [4] convincingly showed the pseudogap and the superconductivity in the bismuth system to differ in physical nature. In other words, the pseudogap observed in our experiments and in [4] is not related to superconductivity. According to our model [12], the formation of a dielectric pseudogap Δ_D^* should be accompanied by a structural distortion and observed in thermal-expansion experiments (Fig. 1). At the same time, a "superconducting" pseudogap Δ_c^* (appearance of incoherent carrier pairs), which is observed in some experiments, may, in principle, also form in the system. Despite the dielectric pseudogap Δ_D^* and the superconducting gap Δ being of different origin, they are intimately related because both are of electronic nature.

It was shown in [4] that, in contrast to other HTSC systems, in Bi-2201 both the superconducting gap and the pseudogap are observed to exist down to the lowest temperatures reached. This should be assigned to them differing strongly in magnitude. This is why they do not coalesce, as they do in other HTSCs. It was also shown that such a large gap difference originates from deformation of the CuO_2 sheets caused by a strong modulation in the BiO planes. This deformation suppresses the superconducting gap and decreases T_c while affecting the magnitude of the pseudogap only weakly. This implies that superconductivity (the value of T_c) depends not only on the hole carrier concentration but also on the degree of deformation D of the CuO_2 sheets. Therefore, a more complete phase diagram of HTSC systems should be constructed in the T–p–D coordinates. This manifests itself most vividly in the Bi-2201 system, where T_c was successfully increased from 7 to 47 K by reducing the deformation (through doping by lanthanum and lead) [13].

It should be pointed out that, in the case of heavy doping, similarly to other HTSC systems (for instance, $Ba_{1-x}K_xBiO_3$ [3]), the coefficient α in the $Bi_{2+x}Sr_{2-x-y}Cu_{1+y}O_{6+\delta}$ system is positive throughout the temperature range covered. As the doping level decreases, however, a thermal expansion anomaly ($\alpha < 0$) appears in the low-temperature range. The temperature region of the α anomaly grows in extent as the hole concentration decreases.

As in other HTSC systems [1–3], $Bi_{2+x}Sr_{2-x-y}Cu_{1+y}O_{6+\delta}$ exhibits an anomalously strong dependence of negative thermal expansion on a magnetic field. This suggests that the anomalous (negative) coefficient α is of electronic nature [14].

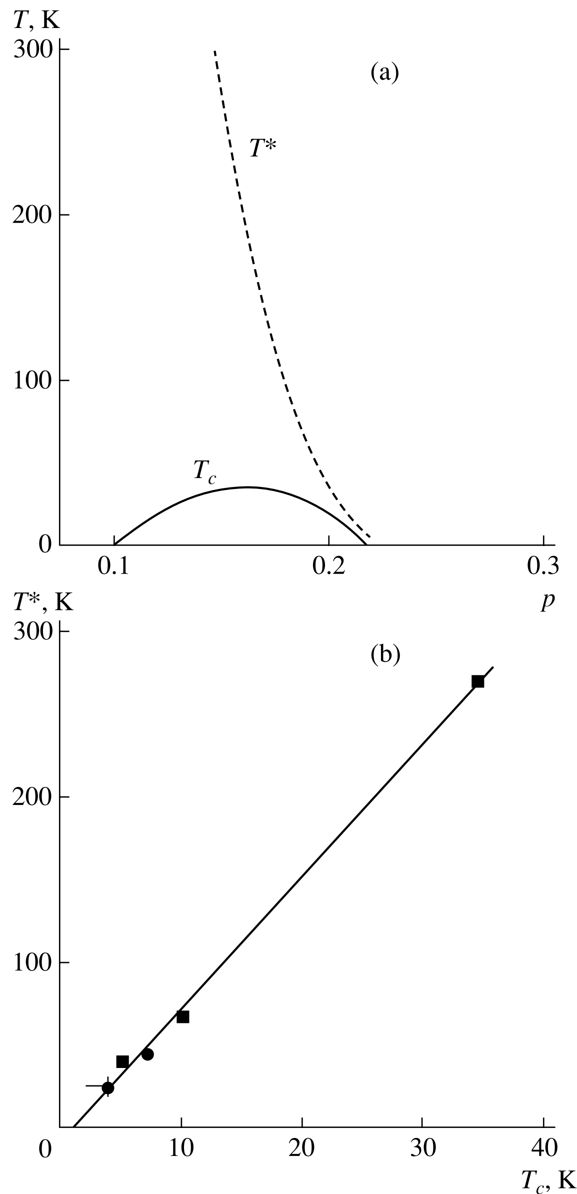

Fig. 6. (a) Phase diagram of the HTSC plotted in the T–p coordinates (T is the temperature; p is the hole concentration reduced to one copper ion). Solid line is the $T_c(p)$ dependence; dashed line is the $T^*(p)$ plot (T^* is the temperature of pseudogap formation). (b) Dependence of T^* on T_c; the circles identify the positions of the high-temperature anomalies obtained by us, and the squares relate to the data on T^* taken from [4, 7, 11].

Figures 3 and 5 plot the variation of the temperature of the minimum in $\alpha(T)$ and the position of the high-temperature anomaly versus the magnetic field. In a first approximation, these relations are linear and we can readily estimate the field in which the anomalies should vanish. It was found that the magnetic field required to suppress both anomalies is 7–11 T. Unfortunately, we did not have facilities for producing such fields and, thus, could not verify this conclusion experimentally.

The results obtained in this work offer additional grounds to believe that the observed anomalies in the thermal characteristics, including their dependence on magnetic field and doping level, are a fundamental property of HTSC systems.

ACKNOWLEDGMENTS

The authors are indebted to G.A. Kalyuzhnaya for providing the samples grown in a gas cavity inside a melt solution, V.P. Martovitskiĭ for performing x-ray characterization, and S.A. Zver'kov and S.G. Chernook for measuring the sample composition.

This study was supported by the Russian Foundation for Basic Research (project no. 01-02-16395) and the Ministry of Industry, Science, and Technology of the Russian Federation (program "Theoretical and Experimental Studies of HTSC Mechanisms").

REFERENCES

1. A. I. Golovashkin, N. V. Anshukova, L. I. Ivanova, I. B. Krinetskiy, and A. P. Rusakov, Int. J. Mod. Phys. B **12** (29–31), 3251 (1998).
2. N. V. Anshukova, B. M. Bulychev, A. I. Golovashkin, L. I. Ivanova, I. B. Krynetskiĭ, and A. P. Rusakov, Zh. Éksp. Teor. Fiz. **124** (1), 80 (2003) [JETP **97**, 70 (2003)].
3. N. V. Anshukova, A. I. Golovashkin, L. I. Ivanova, I. B. Krynetskiĭ, and A. P. Rusakov, Pis'ma Zh. Éksp. Teor. Fiz. **71**, 550 (2000) [JETP Lett. **71**, 377 (2000)].
4. A. Yurgens, D. Winkler, T. Claeson, S. Ono, and Y. Ando, cond-mat/0212562 (2002).
5. A. M. Aprelev, V. A. Grazhulis, and G. A. Shulyatev, Phys. Low-Dimens. Semicond. Struct. **10**, 31 (1994).
6. Y. I. Gorina, G. A. Kaljushnaia, N. N. Senturina, and V. A. Stepanov, Solid State Commun. **126**, 557 (2003).
7. M. Kugler, Ø. Fischer, C. Renner, S. Ono, and Y. Ando, Phys. Rev. Lett. **86**, 4911 (2001).
8. N. V. Anshukova, A. I. Golovashkin, L. I. Ivanova, I. B. Krynetskiĭ, A. P. Rusakov, and D. A. Shulyatev, Kratk. Soobshch. Fiz., No. 8, 32 (2003).
9. N. V. Anshukova, A. I. Golovashkin, Y. U. Bugoslavskii, L. I. Ivanova, A. P. Rusakov, and I. B. Krinetskii, J. Supercond. **7**, 427 (1994).
10. Y. Ando, Y. Hanaki, S. Ono, T. Murayama, K. Segawa, N. Miyamoto, and S. Komiya, Phys. Rev. B **61**, R14956 (2000).
11. X. H. Hou, W. J. Zhu, J. Q. Li, J. W. Xiong, F. Wu, Y. Z. Huang, and Z. X. Zhao, Phys. Rev. B **50**, 496 (1994).
12. N. V. Anshukova, A. I. Golovashkin, L. I. Ivanova, and A. P. Rusakov, Zh. Éksp. Teor. Fiz. **123** (6), 1188 (2003) [JETP **96**, 1045 (2003)].
13. Z. Jianwu, Z. Changjin, T. Shun, X. Gaojie, and Z. Yuheng, Supercond. Sci. Technol. **14**, 599 (2001).
14. N. V. Anshukova, B. M. Bulychev, A. I. Golovashkin, L. I. Ivanova, I. B. Krynetskiĭ, and A. P. Rusakov, Fiz. Tverd. Tela (St. Petersburg) **45** (1), 8 (2003) [Phys. Solid State **45**, 6 (2003)].

Translated by G. Skrebtsov

Physics of the Solid State, Vol. 46, No. 8, 2004, pp. 1398–1403. Translated from Fizika Tverdogo Tela, Vol. 46, No. 8, 2004, pp. 1360–1365.
Original Russian Text Copyright © 2004 by Berezin, Tulin.

METALS
AND SUPERCONDUCTORS

Dynamics of the Magnetic Flux Component Normal to the Layers of $Bi_2Sr_2CaCu_2O_8$ in a Tilted Field

V. A. Berezin and V. A. Tulin
Institute of Microelectronics Technology and High Purity Materials, Russian Academy of Sciences, Chernogolovka, Moscow oblast, 142432 Russia
e-mail: berezin@ipmt-hpm.ac.ru, tulin@ipmt-hpm.ac.ru
Received July 17, 2003; in final form, December 16, 2003

Abstract—High-frequency losses in the strongly anisotropic layered superconductor $Bi_2Sr_2CaCu_2O_8$ are measured at 600 MHz under a magnetic field rocking about the **ab** plane. Anomalies in losses and hysteretic phenomena are found while performing periodic rocking, i.e., cycling the magnetic field component normal to the sample surface. Based on these observations, conclusions are drawn about the nature of magnetic-flux penetration into the superconductor. It is found that, in the range between 60 K and T_c, the dynamics of magnetic-flux vortex lines normal to the **ab** plane in the presence of a constant magnetic field applied parallel to this plane is governed by the critical penetration field $H_c^{\perp *}$ and the surface barrier in the presence of thermally activated vortex motion (giant flux creep). The dependences of $H_{c1}^{\perp *}$ and the characteristic field of the surface barrier on the magnitude of the parallel magnetic field are measured. *© 2004 MAIK "Nauka/Interperiodica".*

1. INTRODUCTION

Interest in strongly anisotropic superconductors remains strong because of the many striking features exhibited by high-temperature superconductors. These features are related, to a great extent, to the anisotropy of these semiconductors and to the layered nature of their lattices. $Bi_2Sr_2CaCu_2O_8$ is a prominent example of this class of materials. Each half of its unit cell along the **c** axis ($a = 30.5$ Å) contains one double CuO_2 layer, which supports conductivity and superconductivity. The critical current densities along the CuO_2 layers (i.e., along the **ab** plane of the crystal) and along the normal to them differ by up to four orders of magnitude or greater, depending on the composition in the homogeneity region and on the conditions of thermal treatment.

Strong anisotropy of the electrical properties of the superconductors in question leads to anisotropy of their magnetic properties. Magnetic flux can penetrate into a layered superconductor with a weak, supposedly Josephson coupling between layers in the form of vortices of two different types. Vortex lines parallel to the **c** axis of the crystal run through superconducting layers and are similar to Abrikosov vortices in conventional isotropic superconductors, but they can be represented as a column of two-dimensional vortices or pancakes [1]. Vortex lines parallel to the **ab** planes of the crystal (to the superconducting layers) are coreless and similar to the Josephson vortices present in wide tunnel junctions [2].

Coexistence of the two types of magnetic-flux vortices gives rise to a variety of compound vortex structures in a slanted magnetic field depending on the degree of anisotropy and the relation between the Josephson and magnetic energies [3–6]. Interaction between Josephson vortices and pancakes in a compound vortex structure modifies their total energies, thus affecting the values of the critical fields governing the dynamics of magnetic flux in strongly anisotropic superconductors. At present, there are a number of theoretical and experimental publications devoted to the study of the influence of a compound vortex structure arising in a slanted magnetic field on the properties of pancake and Josephson vortex lattices and on the melting line of the pancake vortex lattice [7–9].

The magnetization of $Bi_2Sr_2CaCu_2O_8$ in magnetic fields up to 1 kOe directed at a small angle to the **ab** plane was studied in [10]. In that work, experimental observations were explained in terms of two critical magnetic fields, namely, $H_{c1}^{\parallel}$ corresponding to the onset of penetration of magnetic flux parallel to the **ab** plane into the sample and $H_p^{\perp}$ corresponding to the onset of penetration of flux parallel to the **c** axis. The field $H_p^{\perp}$ was found to be independent of the magnetic field projection onto the **ab** plane. Several theoretical papers [3] have discussed the behavior of an intersecting vortex lattice in strongly anisotropic layered superconductors placed in a slanted magnetic field (phase diagram in the $H^{\perp}$ vs. $H^{\parallel}$ coordinates). It was shown that, if $H^{\perp} < H_{c1}^{\perp *}$ (where $H_{c1}^{\perp *}$ is the critical field for the penetration of magnetic flux parallel to the **c** axis

1063-7834/04/4608-1398$26.00 © 2004 MAIK "Nauka/Interperiodica"

with inclusion of the demagnetization factor), then the vortex lattice consists only of Josephson vortices parallel to the superconducting layers; that is, the sample is locked in. At $H^{\perp} > H_{c1}^{\perp *}$, the magnetization vector deviates from the **ab** plane and pancakes appear. These results are in agreement with those from [1] (if we set $H_{c1}^{\perp *} \equiv H_{p}^{\perp}$).

In the present work, we studied high-frequency electromagnetic field absorption in $Bi_2Sr_2CaCu_2O_8$ single crystals at a frequency of 600 MHz. Fixed magnetic fields ranging from zero to several kilooersteds were applied along the **ab** plane, and a slowly varying magnetic field with a peak value of about 20 Oe was applied normally to the **ab** plane along the **c** axis. From the observed features of the high-frequency absorption, we made conclusions regarding the behavior of the magnetic flux in the sample.

2. EXPERIMENTAL

To study high-frequency losses in a sample, we employed a technique based on measuring the transmission signal of a spiral resonator with the sample placed inside it [11, 12]. The measurement circuit consisted of a decimeter-range FM generator, a spiral resonator, an mw detector, and a peak detector. The measured signal was proportional to the maximal transmitted mw power during the period of frequency modulation. If the resonance frequency of the loaded resonator is within the modulation range, the variation of the peak signal is proportional to the variation of the quality factor of the resonator, which, in turn, is proportional to the absorption in the sample. The resonance frequency in our experiments was about 600 MHz. The axis of the spiral resonator (which coincided with the polarization of the mw magnetic field) was horizontal, normal to the **c** axis, and parallel to the vertically aligned **ab** plane of the sample (Fig. 1). The magnetic field was created by an electromagnet, which could rotate in the horizontal plane. This made it possible to accurately align the field direction with the **ab** plane of the sample by rotating the magnet and watching for features of the loss behavior. An additional split coil powered by a sawtooth current at a frequency of about 0.01 Hz created a magnetic field normal to the sample surface. The spiral resonator was placed in the center of the coil such that their axes were orthogonal. Measurements were performed at temperatures near the liquid-nitrogen temperature with the use of a heater, which made it possible to achieve temperatures ranging from 80 to 100 K. Most of the measurements were made at 80 K. A detailed description of the measurement technique can be found in [12].

We studied two sets of $Bi_2Sr_2CaCu_2O_8$ single crystals. One (first) set was grown at Moscow State Institute of Steel and Alloys by using the floating zone melting method and had $T_c = 91$ K; samples from the other (second) set were prepared at the Royal Institute of Technology (Stockholm) by slow solidification of a nonstoichiometric melt of a mixture of Bi, Sr, Ca, and Cu oxides (composition 2.4 : 2 : 1 : 2) and had $T_c = 86$ K. Samples were about 1 mm across with a thickness of less than 1 μm. The superconducting transition width obtained in resistance measurements was about 1 K.

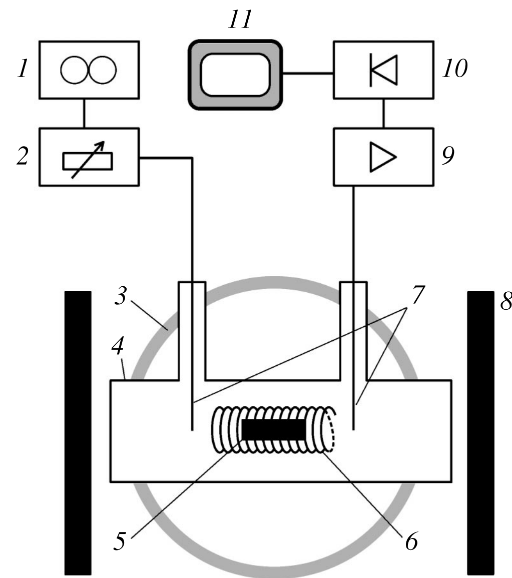

Fig. 1. Experimental setup. (*1*) High-frequency generator, (*2*) attenuator, (*3*) split-coil magnet, (*4*) cell, (*5*) sample, (*6*) spiral resonator, (*7*) coaxial cables, (*8*) electromagnet, (*9*) high-frequency detector and amplifier, (*10*) peak detector, and (*11*) computer.

3. EXPERIMENTAL RESULTS

Figure 2 presents dependences of the high-frequency losses on a normal magnetic field at several values of the parallel field. The curve at zero parallel field corresponds to the beginning of penetration of magnetic flux vortices normal to the **ab** plane. By using this curve and extrapolating it, we determined $H_{c1}^{\perp}(1 - N_{\perp}) \approx 13 \pm 3$ Oe, where $H_{c1}^{\perp}$ is the lower critical field normal to the **ab** plane and $N_{\perp}$ is the demagnetization factor for the direction perpendicular to the plate. Taking into account the crystal geometry ($N_{\perp} \approx 0.9$), we obtained $H_{c1}^{\perp}$ ($T = 80$ K) $\approx$ 100 ± 20 Oe. All other curves exhibit two kinds of features. One of them arises in the vicinity of zero normal field in the form of a peak in the high-frequency losses after the zero value of the field is passed. The evolution of this feature is evident at low parallel fields (Fig. 2a). The other feature appears after the sweep direction of the normal field is reversed. This feature can be clearly seen at high enough parallel fields (Fig. 2b) and corresponds to the development of hysteretic behavior close to the maximum and minimum values of the normal magnetic field. The field dependence of high-frequency

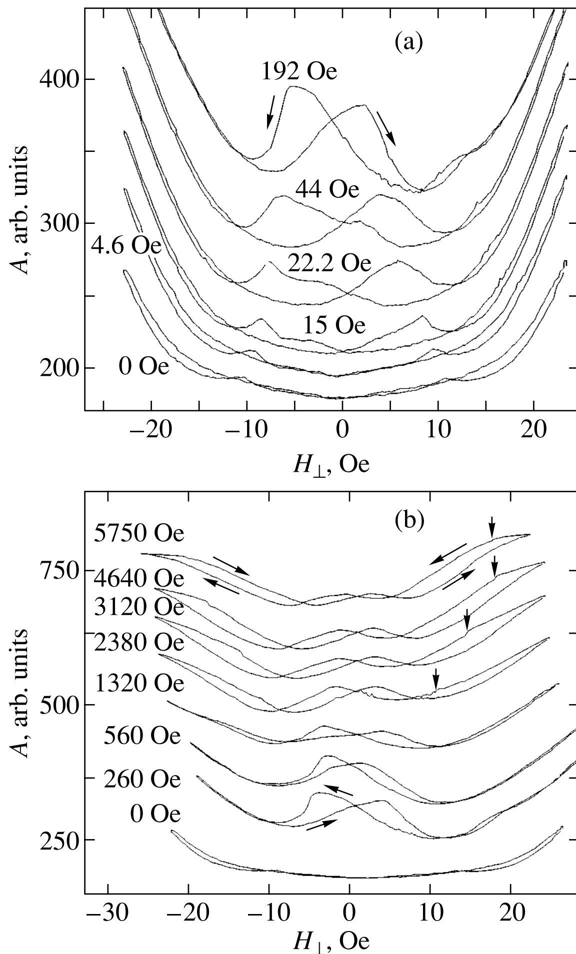

Fig. 2. High-frequency absorption in a $Bi_2Sr_2CaCu_2O_8$ single crystal vs. magnetic field normal to the **ab** plane at (a) low parallel fields and (b) high parallel fields. The values of the parallel field are indicated on the curves; arrows show the sweep direction and features of the absorption curves.

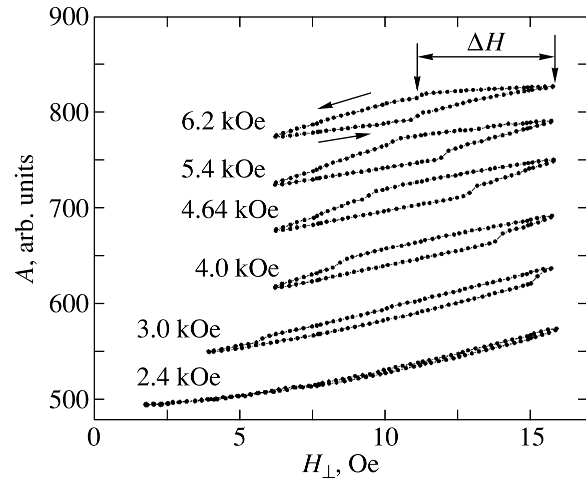

Fig. 3. High-frequency absorption in a $Bi_2Sr_2CaCu_2O_8$ single crystal vs. magnetic field normal to the **ab** plane for sweeps performed around a nonzero normal-field value that is larger than the modulation amplitude.

losses becomes weaker in a short range after the sweep direction is reversed (at the highest or lowest value of the perpendicular field) than prior to the reversal. This range is terminated by a small jump in the high-frequency losses, and its width depends on the parallel-field value.

In order to study the second feature in further detail, we adjusted the measurement procedure. For a certain value of the parallel field, the amplitude of the perpendicular field was chosen to be sufficient for full realization of this feature and the field was swept around a nonzero value in order to get a clear picture without interference from the other feature. Examples of dependences of high-frequency losses on a perpendicular field for this case are shown in Fig. 3. We are interested in the width of the slightly sloping part of the hysteresis curve (from the maximal field value down to the field at which the absorption undergoes a jump); this part is denoted by ΔH in Fig. 3.

4. DISCUSSION

A magnetic field penetrates into a superconductor of the second kind as magnetic flux vortices, whose dynamics governs the high-frequency response of the superconductor. In this case, the real part of the impedance is given by

$$\mathrm{Re}\,Z = (2\pi\omega\rho_f/\mu c^2)^{1/2}, \qquad (1)$$

where ρ_f is the flux flow resistance, μ is the magnetic permeability, c is the speed of light, and ω is the radian frequency of an electromagnetic wave [13]. The principal quantity here is the flux flow resistance, which depends on the vortex dynamics. The strong anisotropy and layered structure of $Bi_2Sr_2CaCu_2O_8$ put additional twist on the vortex system by producing Josephson vortices and pancakes. Various vortex structures can occur in strongly anisotropic layered superconductors at small angles between the direction of the magnetic field and the **ab** plane [3–6]. At present, the intersecting structure of Josephson vortices between CuO planes and pancake columns running through these planes and localized at Josephson vortex positions is accepted as the most plausible case [9].

It was shown in [5] that there are two contributions to the high-frequency losses in single crystals at liquid-nitrogen temperatures ($T > 77$ K). One contribution is related to the Josephson vortex dynamics; it is observed when a magnetic field is applied parallel to the **ab** plane and has a characteristic maximum at a field value of about 10–100 Oe. This contribution is suppressed at liquid-nitrogen temperature because of the presence of a small number of pancakes in a sample (typical suppressing field $H_\perp \approx 1$–10 Oe). The other contribution is due to vortices normal to the **ab** plane; it is observed at

sufficiently high temperatures, from 60 K to T_c, and steadily increases as the vortex concentration increases.

The magnetic flux kinetics can be inferred from the behavior of the high-frequency losses as $H_\perp$ is varied. As for the first feature, it is related to the absorption of the electromagnetic field by Josephson components of magnetic flux vortices and to suppression of this absorption by vortices normal to the **ab** plane [12]. The maximum of absorption in this case corresponds to the minimum concentration of vortices normal to the **ab** plane in the region of penetration of the mw field (in other words, to the maximal length of pancake-free segments of Josephson vortices). The decrease in absorption observed after the maximum is due to the beginning of penetration of normal vortices into the sample as $H_\perp$ is increased.

In this work, a sample is subjected to a relatively strong parallel magnetic field ($H > H_{c1}^{\parallel}$) and a weak normal field ($H_\perp < H$). For a low perpendicular field, the orientation of magnetic flux vortices parallel to the **ab** plane is favorable in energy because of the additional positive energy that pancakes have in the local magnetic field $H_L < H_{c1}$. The energy of Abrikosov vortices in a superconductor has two terms, namely, the positive energy of the normal vortex core and the negative energy of the magnetic field:

$$W_p = H_c^2\xi^2 - H^2\lambda^2, \quad (2)$$

where H_c is the thermodynamic critical field, ξ is the coherence length, and λ is the magnetic-field penetration depth. The lower critical field H_{c1} is defined as the field in which these terms are equal. For strongly anisotropic layered superconductors, Eq. (2) should be adjusted by replacing ξ by ξ_{ab}, λ by λ_{ab}, and $H_\perp$ by H. As shown theoretically in [3], in this case, the right-hand side of Eq. (2) is independent of the parallel magnetic field up to fairly large values. Accordingly, the mixed and Meissner states of perpendicular vortices are separated in the $H_\perp$–$H_\parallel$ phase diagram by a straight line parallel to the $H_\parallel$ axis at a value $H_\perp = H_{c1}^{\perp}$ (with allowance for the demagnetization factor of the sample). When vortices begin entering the sample and absorption starts to fall off after the maximum, the energy of pancakes becomes negative. At this point, $H_{c1}^{\perp}$ is equal to $H_{c1}^{\perp *}$ (with allowance for the demagnetization factor of the sample). The dependence of $H_\perp$ corresponding to the absorption drop after the maximum on the parallel magnetic field is shown in Fig. 4. As we consider this quantity to be $H_{c1}^{\perp}$, we conclude that significant suppression of the lower critical field occurs in a parallel field of about 100 Oe. As the parallel field is increased further, the field $H_{c1}^{\perp *}$ remains unchanged (Fig. 2b). Hence, we conclude that the positive part of the pancake energy in a magnetic field parallel to the **ab** plane decreases as the field increases from zero to 200 Oe. This result contradicts the data from [10]. We performed measurements at a high temperature, where all hindrances to the magnetic flux flow are overcome due to thermal activation and the critical fields and barriers manifest themselves as specific features in the measured curves. In [10], the main measurements were performed at 54 K, where thermal activation phenomena rapidly subside and effects of barriers become pronounced.

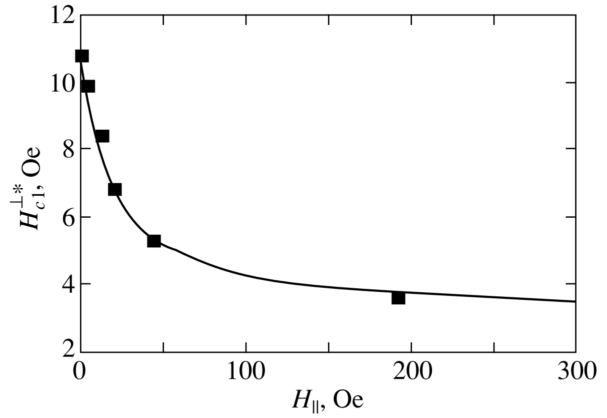

Fig. 4. $H_{c1}^{\perp *}$ corresponding to the absorption drop after the maximum vs. parallel magnetic field.

Our data show that a critical change in the field dependence of absorption also takes place in the vicinity of the reverse point of the $H_\perp$ sweep, where the sign of dH/dt changes. The experimental curves plotted for high parallel fields clearly show that, as one approaches the extreme point of the curve, the rate of change of high-frequency losses $(dA/dH)_f$ is higher than in the case where one goes away from this point. The lower rate persists in a magnetic field range $\Delta H_\perp$ after passing through the extreme value and then returns to (dA/dH) in a small jump. The range $\Delta H_\perp$ increases with decreasing H, covers the entire range of the variation in $H_\perp$, and then exceeds it (dA/dH does not change when the sweep direction is reversed at 560 Oe; see Fig. 2b).

On these grounds, we presume that the magnetic flux inside the sample is screened from changes in the external field after reversal of the $H_\perp$ sweep. An analogous phenomenon is observed in superconductors of the second kind with a surface barrier [14] and in hard superconductors of the second kind featuring bulk pinning and a critical state [15]. Vortices normal to the **ab** plane absorb a noticeable amount of high-frequency power [12] at frequencies well below the depinning frequency. Therefore, these vortices are fairly free in the bulk and we can conclude that the surface barrier dominates over the bulk pinning in the observed phenomenon. As one approaches the extreme point, the flux flows through the surface. In this case, the surface cur-

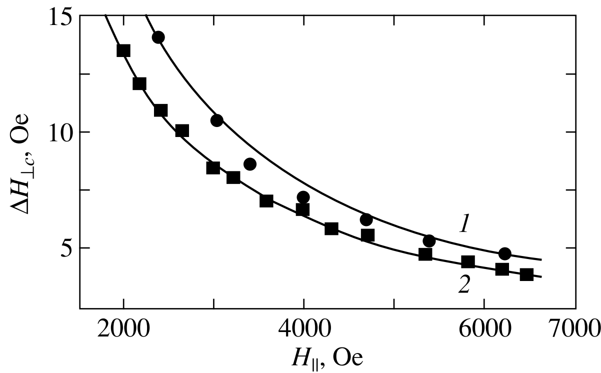

Fig. 5. Critical value of the change $\Delta H_{\perp c}$ in the perpendicular field vs. applied parallel magnetic field. Points are experimental data and solid lines are fitting curves for (*1*) the first and (*2*) second set of samples.

rent density is equal to the critical value and there is no barrier for vortices normal to the **ab** plane entering or exiting the sample. After reversal of the magnetic field sweep direction, the surface current density becomes lower than the critical value and vortices cannot exist in a sample surface layer of thickness λ. As the field is swept further, the surface current density passes through zero and again reaches the critical value in the opposite direction. Now, vortices can again flow through the surface instead of jumping over a surface barrier. This happens in a magnetic field where a jump in the high-frequency losses is observed. A nonzero surface barrier exists over this span of the normal component of the magnetic field.

Analogous experiments with conventional superconductors, such as PbIn alloys [14], demonstrated a minimum of high-frequency absorption after the change in the sign of dH/dt. This minimum was related to the expulsion of magnetic flux vortices from the region of penetration of the magnetic field at currents below the critical value. In this case, absorption decreases and reaches a minimum at zero induced surface current. In high-temperature superconductors (including strongly anisotropic layered ones), in contrast to conventional superconductors, thermally activated vortex motion (so-called giant flux creep) exists, which can both cause depinning of vortices and make them overcome the surface barrier [16]. The presence or absence of a surface barrier affects the rate at which vortices enter or leave the sample and their ability to stay in the surface layer of thickness λ_{ab}. Because samples are in the shape of a thin plate and the applied field is not parallel to its surface, there is no absorption minimum in the region where the surface barrier exists.

The energy factor plays the main role in the thermally activated motion over barriers. Consider a sample in the form of a thin plate placed in a strong magnetic field almost parallel to the plate plane. Variation of the normal component of the magnetic field is equivalent to rocking of the total field through a small angle relative to the plate plane (for small angles, we have $H \gg H_{c1}^{\perp}$). This problem coincides with minute rocking of the sample in a nearly parallel magnetic field. Magnetic field lines are distorted when the plate turns away from the original position when in the subcritical state. The distortion affects not only the small normal field but also the large parallel field, giving rise to additional positive energy of the magnetic field:

$$W_m \approx \frac{H^2}{8\pi} a l^2 \sin\alpha \approx \frac{H^2}{8\pi} a l^2 \frac{\Delta H_{\perp}}{H} \approx \frac{H \Delta H_{\perp} a l^2}{8\pi}, \quad (3)$$

where a is the width of the sample, l is the sample length, and α is the angle between the sample plane and the external magnetic field. We express the tilt angle via the variation in the normal component. The distortion of the magnetic field is caused by supercurrents flowing on the sample surface. When the current density reaches the critical value at any point, magnetic flux starts to enter the sample and the field distortion subsides. At this moment, one of the differences, $(H_{\perp\max} - H_{\perp})$ or $(H_{\perp} - H_{\perp\min})$, reaches the critical value $\Delta H_{\perp c}$ and normal vortices (pancakes) start to pass through the surface of the superconductor. The quantity $\Delta H_{\perp c}$ depends on the critical current and is proportional to its doubled value. According to Eq. (3), if W_m is constant (i.e., the critical current is independent of the parallel field) the critical variation in the normal magnetic field $\Delta H_{\perp c}$ is proportional to $1/H_{\parallel}$. An experimental dependence of the critical variation in the normal magnetic field $\Delta H_{\perp c}$ on the parallel field can be derived from the data shown in Figs. 2b and 3. This dependence is presented in Fig. 5. The experimental data agree well with the inverse proportion law at high fields but deviate from this law in the low-field region. The field dependence of $\Delta H_{\perp c}$ can be approximated as

$$\Delta H_{\perp c} \sim 1/(H - H_a),$$

where H_a is a fitting parameter. The parameter H_a describes deviation from the simple $1/H_{\parallel}$ dependence in the low-field region. The deviation may be due to the increase in the critical current with a decrease in the field in this range. For a sample from the set with T_c = 91 K, the fitting parameter H_a was 350 ± 100 Oe, and for samples from the set with T_c = 86 K, it was H_a = 140 ± 50 Oe (all measurements were performed at 80 K). The values of H_a obtained using the above approximation are close in order of magnitude to the lower critical field normal to the **ab** plane, $H_{c1}^{\perp}$. Estimations of the quantity $H_{\perp c}(dH_{c1}/dT)$ from magnetization curves measured for different BSCCO samples even by one research group [17, 18] differ significantly but are comparable to our data. Theoretical calculations are needed for more detailed discussion of this result.

5. CONCLUSIONS

We have studied the behavior of high-frequency losses in a $Bi_2Sr_2CaCu_2O_8$ single crystal at a frequency of 600 MHz. We observed maxima of absorption at fields of about several oersteds and hysteretic phenomena arising after the change of the sweep direction (after reaching the extreme value of the normal magnetic field). The maxima of absorption correspond to the minimum concentration of normal vortices [12], which is achieved just before the normal field reaches $H_{c1}^{\perp *}$. Hysteretic phenomena are related to the reduction of the induced surface current below the critical value for the magnetic flux vortex formation and to the formation of a surface barrier for the vortex entrance [14]. From these data, we derived the dependence of the lower critical field $H_{c1}^{\perp *}$ on the parallel field (Fig. 4) and the dependence of the magnetic field difference characterizing the critical current for the formation of vortices (surface barrier) on the parallel field (Fig. 5). The characteristic magnetic field was achieved by applying a sufficiently high magnetic field parallel to the **ab** plane and subsequently applying a periodic normal field with a certain amplitude.

Strong thermally activated vortex motion in $Bi_2Sr_2CaCu_2O_8$ at high temperature causes a lack of phase coherence over large distances. However, the coherence is preserved over distances of the order of the vortex spacing. As a result, all features of the superconducting state are manifested to some extent and there are no critical phenomena, such as pinning or surface barrier, that are able to totally suppress magnetic flux motion. This makes it possible to derive the quantities characterizing the magnetic flux dynamics from the features of the behavior of a measured variable (high-frequency losses in our case).

ACKNOWLEDGMENTS

This work was supported by the program of Russian Academy of Sciences "Quantum Macrophysics" (subprogram "Strongly Correlated Electron Systems").

REFERENCES

1. A. I. Buzdin and D. Feinberg, J. Phys. (Paris) **51**, 1971 (1990); S. N. Artemenko and A. N. Kruglov, Phys. Lett. A **143**, 485 (1990); J. R. Clem, Phys. Rev. B **43**, 7837 (1991).
2. L. N. Bulaevskiĭ, Zh. Éksp. Teor. Fiz. **65**, 1278 (1973) [Sov. Phys. JETP **38**, 634 (1973)]; J. R. Clem and M. W. Coffey, Phys. Rev. B **42**, 6209 (1990).
3. L. N. Bulaevskii, M. Ledvij, and V. G. Kogan, Phys. Rev. B **46**, 366 (1992); D. Feinberg and C. Villard, Phys. Rev. Lett. **65**, 919 (1990); D. Feinberg, Physica C (Amsterdam) **194**, 126 (1992).
4. A. E. Koshelev, Phys. Rev. B **48**, 1180 (1993); D. Feinberg and A. M. Ettouhami, Int. J. Mod. Phys. B **7**, 2085 (1993).
5. A. I. Buzdin and A. Yu. Simonov, Zh. Éksp. Teor. Fiz. **98**, 2074 (1990) [Sov. Phys. JETP **71**, 1165 (1990)]; W. A. M. Morgado, M. M. Doria, and G. Carniero, Physica C (Amsterdam) **349**, 196 (2001).
6. L. L. Daemen, L. J. Campbell, A. Ju. Simonov, and V. G. Kogan, Phys. Rev. Lett. **70**, 2948 (1993); E. Sardella, Physica C (Amsterdam) **257**, 231 (1997).
7. A. E. Koshelev, Phys. Rev. Lett. **83**, 187 (1999).
8. J. Mirkovoch, S. E. Savelev, E. Sugahara, and K. Kadovaki, Phys. Rev. Lett. **86**, 886 (2001).
9. A. E. Koshelev, Phys. Rev. B **68**, 094520 (2003).
10. N. V. Zavaritskiĭ and V. N. Zavaritskiĭ, Pis'ma Zh. Éksp. Teor. Fiz. **53**, 212 (1991) [JETP Lett. **53**, 226 (1991)].
11. K. V. Baginskiĭ, V. A. Berezin, S. A. Govorkov, and V. A. Tulin, Pis'ma Zh. Éksp. Teor. Fiz. **60**, 60 (1994) [JETP Lett. **60**, 61 (1994)].
12. V. A. Berezin and V. A. Tulin, Zh. Éksp. Teor. Fiz. **110** (3), 1054 (1996) [JETP **83**, 582 (1996)].
13. L. P. Gor'kov and N. B. Kopnin, Usp. Fiz. Nauk **116** (3), 413 (1975) [Sov. Phys. Usp. **18**, 496 (1975)].
14. B. L. Walton, B. Rosenblum, and F. Bridges, Phys. Rev. Lett. **32** (19), 1047 (1974).
15. C. P. Bean, Phys. Rev. Lett. **8**, 250 (1962).
16. L. Burlachkov, Physica C (Amsterdam) **209**, 203 (1993).
17. Y. Yamaguchi, N. Aoki, F. Iga, and Y. Nishihara, Physica C (Amsterdam) **246**, 216 (1995).
18. Y. Yamaguchi, Dong Han Ha, F. Iga, and Y. Nishihara, Physica C (Amsterdam) **228**, 141 (1994).

Translated by G. Tsydynzhapov

Physics of the Solid State, Vol. 46, No. 8, 2004, pp. 1404–1409. Translated from Fizika Tverdogo Tela, Vol. 46, No. 8, 2004, pp. 1366–1371.
Original Russian Text Copyright © 2004 by Luk'yanova, Kutasov, Popov, Konstantinov.

Galvanomagnetic and Thermoelectric Properties of p-$Bi_{2-x}Sb_xTe_{3-y}Se_y$ Solid Solutions at Low Temperatures (<220 K)

L. N. Luk'yanova, V. A. Kutasov, V. V. Popov, and P. P. Konstantinov
Ioffe Physicotechnical Institute, Russian Academy of Sciences, Politekhnicheskaya ul. 26, St. Petersburg, 194021 Russia
e-mail: lidia.lukyanova@mail.ioffe.ru
Received November 18, 2003

Abstract—The galvanomagnetic and thermoelectric properties of p-$Bi_{2-x}Sb_xTe_{3-y}Se_y$ solid solutions ($x \leq 1.2$, $y \leq 0.09$) are studied for various carrier concentrations. The degeneracy parameter β_d governing the scattering processes in solid solutions was calculated in terms of the many-valley energy spectrum model. The data on the degeneracy parameter and the Seebeck coefficient α were used to calculate the effective scattering parameter r_{eff} and the reduced Fermi level η. The parameter r_{eff} was found to depend on the carrier concentration in the materials studied. The temperature dependences of the effective density-of-states mass m/m_0 and mobility μ_0 in samples with various carrier concentrations were determined. *© 2004 MAIK "Nauka/Interperiodica".*

1. INTRODUCTION

Solid solutions based on bismuth and antimony chalcogenides are high-efficiency thermoelectric materials for operation at low temperatures ($T < 220$ K) [1–3]. These materials have a complex band structure described in terms of the many-valley energy-spectrum model, and a two-band model is customarily invoked to interpret the galvanomagnetic effects observed in them [4–9]. In analyzing the parameters governing the thermoelectric efficiency, the conduction and valence bands are generally described in terms of a simple parabolic model under the assumption of the effective density-of-states mass m/m_0 being isotropic. This model usually includes scattering of carriers by acoustic phonons (scattering parameter $r = -0.5$), which is predominant in these materials. The relaxation time is approximated by a power-law function $\tau = aE^r$, where a = const. The carrier degeneracy is taken into account through the parameter $\beta_d(\eta)_{r=-0.5}$ (η is the reduced Fermi level).

Due to the inclusion of degeneracy in the form $\beta_d(\eta)_{r=-0.5}$, the parameters of the ellipsoidal constant-energy surfaces and their orientation relative to the crystallographic axes in n- and p-Bi_2Te_3 derived from galvanomagnetic effects in weak magnetic fields differ from those determined by studying oscillatory phenomena in strong magnetic fields [10–13]. This difference was eliminated for n-Bi_2Te_3 in [14], where the scattering parameter r was not set in advance in calculating $\beta_d(\eta)$ and determining the shape and orientation of the constant-energy ellipsoids. Results analogous to those reported in [14] were obtained by us for p-Bi_2Te_3 in analyzing the results from [12, 13]. For the p-Bi_2Te_3 sample studied in [12], the value of $\beta_d(\eta)$ varied from ~0.9 for $r = -0.5$ to 0.7 when calculated following the method used in [14]; i.e., the sample was more degenerate at $r = -0.5$. Thus, in analyzing the thermoelectric and galvanomagnetic properties of Bi_2Te_3-based materials, irrespective of the actual conduction type, it is insufficient to include the scattering mechanism by putting $r = -0.5$.

2. THEORY

The many-valley model of the energy spectrum establishes the following relation between the electrical resistivity (ρ_{ii}), Hall effect (ρ_{ijk}), and magnetoresistance (ρ_{ijkl}) tensor components and fitting parameters u, v, and w determining the shape of constant-energy ellipsoids [10, 14]:

$$\frac{\rho_{312}}{\rho_{123}} = \frac{(w+uv)(1+u)}{4uv}, \quad (1)$$

$$\frac{\rho_{11}\rho_{1133}}{\rho_{123}^2} = \frac{1+u^2}{4u\beta_d} - 1, \quad (2)$$

$$\frac{\rho_{11}\rho_{1122}}{\rho_{123}^2} = \frac{(3w+uw+uw+3u^2v)(1+u)}{16\beta_d u^2} - \frac{2v}{a^2(1+u)}, \quad (3)$$

$$\rho_{11}\rho_{1111}/\rho_{123}^2 = (w-5uw+3uv+u^2v)(1+u/16\beta_d u^2), \quad (4)$$

where $a = \rho_{312}/\rho_{123}$.

1063-7834/04/4608-1404$26.00 © 2004 MAIK "Nauka/Interperiodica"

Table 1. Thermoelectric and galvanomagnetic properties of p-$Bi_{2-x}Sb_xTe_{3-y}Se_y$ solid solutions

Sample no.	T, K	x, y	α, μV/K	σ, Ω^{-1} cm^{-1}	ρ_{1133}/ρ_{1122}	ρ_{1133}/ρ_{1111}	ρ_{1122}/ρ_{111}	ρ_{312}/ρ_{123}
1	77	1.2, 0.09	134	2600	1.34	1.89	1.4	1.89
	290		290	226	1.3	3.0	2.3	2.07
2	77	1.1, 0.06	117	2990	1.32	1.69	1.26	1.77
	290		280	273	1.2	1.98	1.65	1.84
3	77	1.1, 0.09	99	3920	1.2	1.65	1.38	1.45
	290		266	348	1.2	1.97	1.67	1.36
4	77	1.2, 0.06	93	4100	1.42	2.33	1.65	1.39
	290		260	355	1.28	1.72	1.34	1.35

The degeneracy parameter can be written as $\beta_d = \frac{I_1^2}{I_0 I_2}$, where I_n are isotropic factors in the expressions for the electrical conductivity (I_0), Hall conductivity (I_1), and magnetoconductivity (I_2). In the case of an isotropic relaxation time, where $\tau = \tau_0 E^r$ is an energy-independent factor), the parameter β_d is [15]

$$\beta_d(r, \eta) = \frac{(2r + 3/2)^2 F_{2r+1/2}^2(\eta)}{(r + 3/2)(3r + 3/2)F_{r+1/2}(\eta)F_{3r+1/2}(\eta)}, \quad (5)$$

where $F_r(\eta)$ are Fermi integrals of the type

$$F_s(\eta) = \int_0^{\infty} \frac{x^s}{e^{x-\eta} + 1} dx. \quad (6)$$

To find the quantities u, v, w, and β_d, we solved the coupled equations (1)–(4) by minimizing the following objective function $\chi(u, v, w, \beta_d)$, which determines the quality of optimization:

$$\chi(u, v, w, \beta_d) = \sum_{i=1}^{4} \left(\frac{y_i^e - y_i(u, v, w, \beta_d)}{y_i^e} \right)^2. \quad (7)$$

Here, y_i^e are the ratios of the experimental galvanomagnetic coefficients and $y_i^e(u, v, w, \beta_d)$ are the analogous ratios calculated from Eqs. (1)–(4).

Next, we used Eq. (5) for $\beta_d(r, \eta)$ and the Seebeck coefficient α

$$\alpha = \frac{k}{e}\left[\frac{(r + 5/2)F_{r+3/2}(\eta)}{(r + 3/2)F_{r+1/2}(\eta)} - \eta\right] \quad (8)$$

to calculate the scattering parameter r (which is referred to as the effective parameter, r_{eff}) and the reduced Fermi level η in the same way as for materials based on n-type bismuth and antimony chalcogenides [15, 16].

The objective function $R(r, \eta)$ used in calculating r_{eff} and η has the form

$$R(r, \eta) = \frac{(\alpha_c(r, \eta) - \alpha_e(r, \eta))^2 + (\beta_c(r, \eta) - \beta_e(r, \eta))^2}{\alpha_e^2(r, \eta) + \alpha_e^2(r, \eta)}, \quad (9)$$

where $\alpha_e(r, \eta)$ and $\alpha_c(r, \eta)$ are the experimental and calculated [from Eq. (8)] values of the Seebeck coefficient, respectively; $\beta_e(r, \eta)$ are the values of the degeneracy parameter derived from the coupled equations (1)–(4); and $\beta_c(r, \eta)$ are the values calculated from Eq. (5).

3. EXPERIMENT

We studied the galvanomagnetic and thermoelectric properties of p-$Bi_{2-x}Sb_xTe_{3-y}Se_y$ solid solutions ($x \leq 1.2$, $y \leq 0.09$) with various carrier concentrations. Samples of solid solutions grown by oriented crystallization consisted of single-crystal blocks elongated along the growth axis. The galvanomagnetic properties were measured in weak magnetic fields (up to 28 kOe) on single-crystal samples cut from such blocks. The temperature dependences of thermopower and electrical conductivity were obtained on "oriented" block crystals similar to single crystals in terms of their characteristics.

The carrier concentration in the samples was varied by adding excess Te (with respect to the stoichiometric solid solution composition). Adding excess Te to a solid solution reduces the concentration of antisite defects (i.e., reduces the number of Sb atoms in Te sublattice sites) and favors a decrease in the concentration of intrinsic acceptor-type point defects [17].

Table 1 lists the results from investigating the thermoelectric and galvanomagnetic effects in $Bi_{2-x}Sb_xTe_{3-y}Se_y$ solid solutions ($x \leq 1.2$, $y \leq 0.09$). The anisotropy of the magnetoresistance is in accord with the data obtained for n-type materials. The anisotropy in the Hall coefficients decreases with decreasing thermopower, i.e., with increasing carrier concentration.

Table 2. Degeneracy parameter β_d, effective scattering parameter r_{eff}, and reduced Fermi level η of p-$Bi_{2-x}Sb_xTe_{3-y}Se_y$ solid solutions

Sample no.	T, K	x, y	β_d	r_{eff}	η	p, 10^{19} cm^{-3}
1	77	1.2, 0.09	0.89	–0.45	1.5	0.4
	290		0.31	–0.75	–1.6	
2	77	1.1, 0.06	0.83	–0.57	1.5	0.85
	290		0.42	–0.72	–1.4	
3	77	1.1, 0.09	0.46	–0.7	1.8	1.4
	290		0.4	–0.78	–1.1	
4	77	1.2, 0.06	0.44	–0.76	2	1.9
	290		0.36	–0.78	–1.15	

Data on the galvanomagnetic effects were used to determine the degeneracy parameter β_d by solving Eqs. (1)–(4) (see Table 2). The variation of β_d with thermopower (carrier concentration) is similar in behavior to that observed in studies on n-type solid solutions [15]. The effective scattering parameter r_{eff} and the reduced Fermi level were calculated by solving Eqs. (5) and (8). The values of the objective functions $\chi(u, v, w, \beta_d)$ in Eq. (7) and $R(r, \eta)$ in Eq. (9) involved in the solution of Eqs. (1)–(4) and Eqs. (5) and (8) did not exceed 10^{-4}, which indicates a high accuracy of determination of the fitting parameters.

The solution of the coupled equations (5) and (8) can be represented in graphical form. Figure 1 plots the objective functions $R(r, \eta)$ for p-$Bi_{2-x}Sb_xTe_{3-y}Se_y$ samples. The function $R(r, \eta)$ is seen to have a single minimum; i.e., the coupled equations (5) and (8) have a unique solution.

The dependence of the quantity r_{eff} on carrier concentration and temperature in p-$Bi_{2-x}Sb_xTe_{3-y}Se_y$ solid solutions (Table 2, Fig. 1) is similar to that observed in n-type materials [18]. The values of r_{eff} also agree with the data available on p-$Bi_2Te_{2.85}Se_{0.15}$ [19]. The variation in r_{eff} with the Seebeck coefficient α obtained in this study suggests that the scattering mechanism in p-$Bi_{2-x}Sb_xTe_{3-y}Se_y$ solid solutions changes because of the influence of the additional valence band [4–9]. The values of the reduced Fermi level presented in Table 2 indicate the solid-solution samples to be weakly degenerate.

Equations (5) and (8) enable one to calculate the $\alpha(\eta)$ and $\beta_d(\eta)$ relations for broad ranges of r_{eff} and η variation (Fig. 2). We readily see from Fig. 2 that using a constant value for the scattering parameter, $r = -0.5$, in analyzing the temperature and concentration dependences of the thermoelectric properties of Bi_2Te_3-based materials gives rise to errors in the determination of the reduced Fermi level.

When measuring the Hall tensor components in weak magnetic fields, the carrier concentration is usually calculated from a relation used for anisotropic materials [10],

$$p = \frac{A(r_{eff}, \eta)B(r_{eff}, \eta)}{\rho_{123}e} = \frac{A(r_{eff}, \eta)}{\rho_{123}e}\frac{4u}{1+u^2}, \quad (10)$$

$$B(r_{eff}, \eta) = \left(\left(\frac{\rho_{11}\rho_{1133}}{\rho_{123}^2} + 1\right)\beta(r_{eff}, \eta)\right)^{-1}. \quad (11)$$

Here, $B(r_{eff}, \eta)$ is the anisotropy parameter and $A(r_{eff}, \eta)$ is the Hall factor

$$A(r_{eff}, \eta) = \frac{3/2(2r+3/2)F_{1/2}(\eta)F_{2r+1/2}(\eta)}{(r+.)^2F_{r+1/2}^2(\eta)}. \quad (12)$$

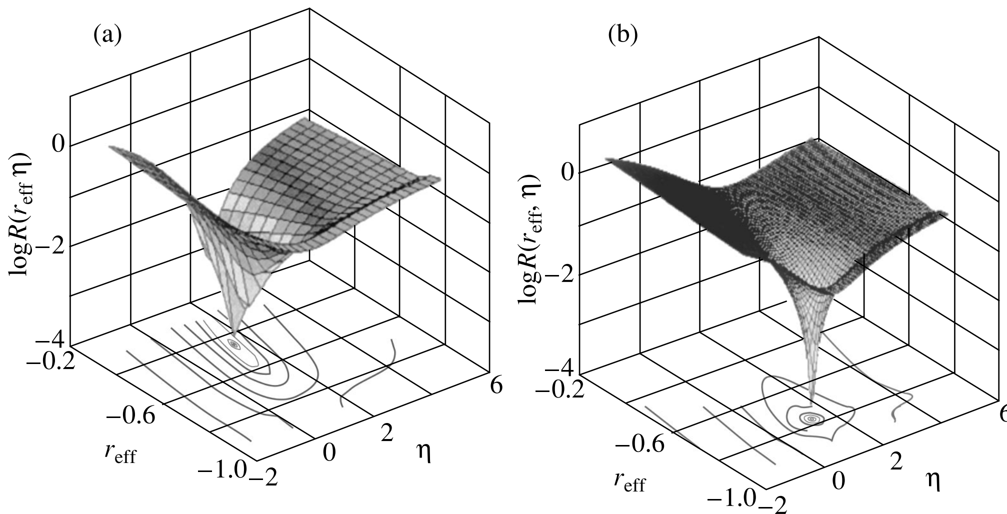

Fig. 1. Objective functions $R(r, \eta)$ calculated for samples (a) 1 and (b) 4 at $T = 77$ K (see Table 1).

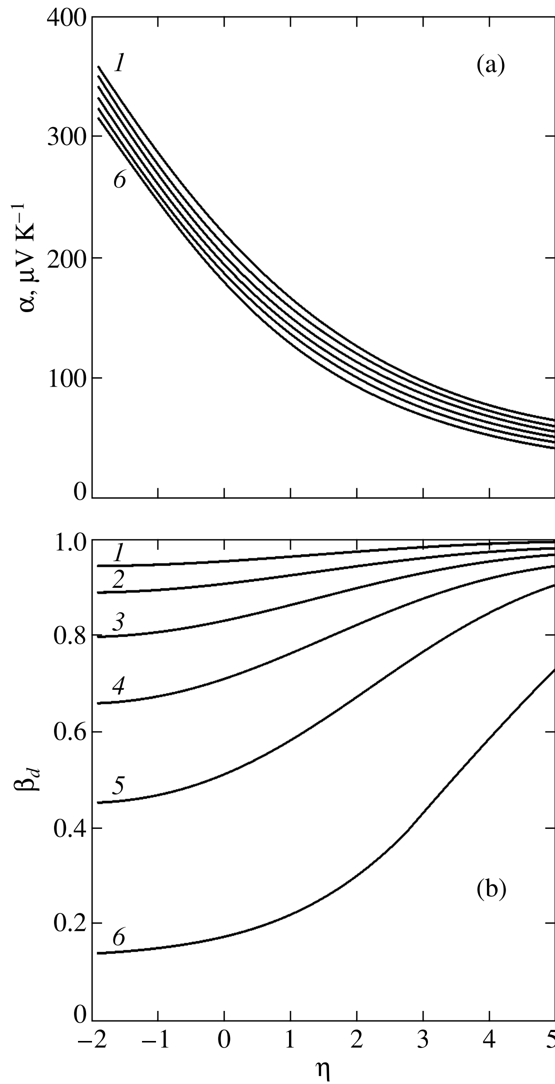

Fig. 2. (a) Seebeck coefficient α and (b) degeneracy parameter β_d plotted vs. reduced Fermi level η for various values of $r_{\rm eff}$: (*1*) –0.3, (*2*) –0.4, (*3*) –0.5, (*4*) –0.6, (*5*) –0.7, and (*6*) –0.8. Curves in panel (a) are numbered from *1* to *6* down.

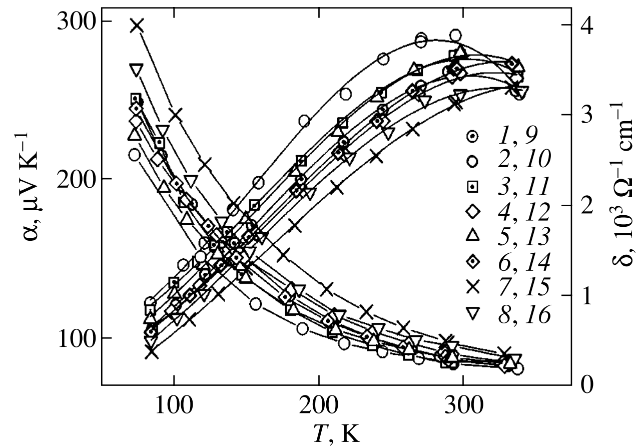

Fig. 3. (*1–8*) Temperature behavior of the Seebeck coefficient α and (*9–16*) electrical conductivity σ in p-$Bi_{2-x}Sb_xTe_{3-y}Se_y$ solid solutions for different values of p (in units of 10^{19} cm^{-3}): (*1*, *9*) 1.5 for $x = 1.0$, $y = 0.06$; (*2*, *10*) 0.4, (*3*, *11*) 0.9, and (*4*, *12*) 1.5 for $x = 1.2$, $y = 0.06$; (*5*, *13*) 0.8, (*6*, *14*) 1.5, and (*7*, *15*) 2 for ($x = 1.2$, $y = 0.09$); and (*8*, *16*) 2 for $x = 1.1$, $y = 0.09$.

The values of the carrier concentration listed in Table 2 correlate well with the data obtained for n-$Bi_{2-x}Sb_xTe_{3-y}Se_y$ ($x = 0.08, 0.12$; $y = 0.24, 0.36$) [18] when we have similar values of the Seebeck coefficient and can be employed in analyzing the thermoelectric properties of p-$Bi_{2-x}Sb_xTe_{3-y}Se_y$ solid solutions. Note that the room-temperature carrier concentration calculated for p-$Bi_{2-x}Sb_xTe_{3-y}Se_y$ is higher than that obtained for $T = 77$ K by 20–30%, as is the case in n-type materials (a growth in the carrier concentration with temperature was also revealed earlier in calculations for $r = -0.5$).

The variation in the concentration with temperature is possibly due to additional emfs generated by attendant effects that appear when galvanomagnetic properties are measured [20]. Variations in the carrier concentration can also be brought about by electrically active point defects; however, the corresponding mechanism operating in the temperature interval under study remains unclear. Because the increase in concentration with temperature was very small and its inclusion has no noticeable effect on the behavior of the properties of the solid solutions we are interested in, the concentration needed for the subsequent calculations is taken to be equal to that obtained for $T = 77$ K.

Figure 3 plots the temperature dependences of the Seebeck coefficient α and the electrical conductivity σ in p-$Bi_{2-x}Sb_xTe_{3-y}Se_y$ ($x \le 1.2$, $y \le 0.09$) obtained for various carrier concentrations. The measurements were performed for the case where the current was passed along the crystal growth axis parallel to the [1010] cleavage planes, which corresponds to measurements of the components α_{11} and σ_{11} for single-crystal samples. Room-temperature measurements of electrical conductivity carried out on single-crystal and block samples of p-$Bi_{2-x}Sb_xTe_{3-y}Se_y$ solid solutions showed that the values of σ in these materials differ by no more than 5%, which is comparable to the measurement error.

As the carrier concentration and the number of substituted atoms (Sb ⟶ Bi, Se ⟶ Te) in the p-$Bi_{2-x}Sb_xTe_{3-y}Se_y$ solid solutions increase, the temperature dependences of α and σ become weaker (Fig. 3) because of additional scattering from lattice distortions, as is the case with n-type materials. The weakening of the $\alpha = f(T)$ dependences brings about a decrease in the slopes $s_1 = d\ln\alpha/d\ln T$ determined for the low-temperature region. As the Sb and Se concentrations in the solid

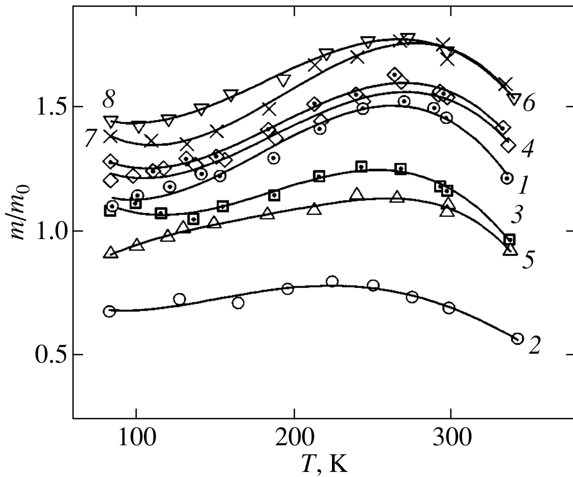

Fig. 4. Temperature dependences of the effective density-of-states mass m/m_0 in p-$Bi_{2-x}Sb_xTe_{3-y}Se_y$ solid solutions for different values of p (in units of 10^{19} cm^{-3}): (*1*) 1.5 for $x = 1.0$, $y = 0.06$; (*2*) 0.4, (*3*) 0.9, and (*4*) 1.5 for $x = 1.2$, $y = 0.06$; (*5*) 0.8, (*6*) 1.5, and (*7*) 2 for $x = 1.2$, $y = 0.09$; and (*8*) 2 for $x = 1.1$, $y = 0.09$.

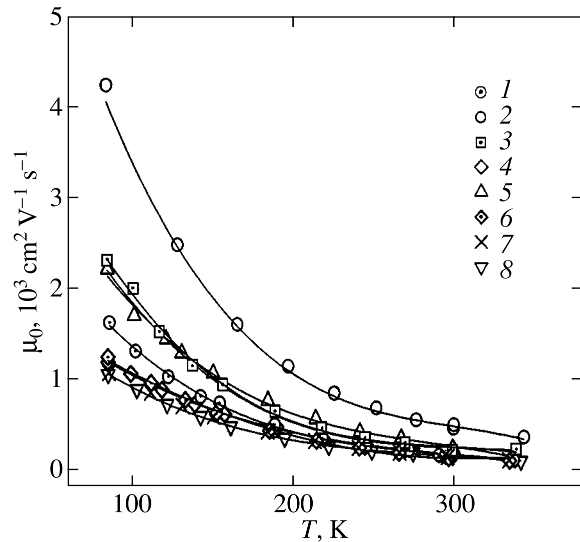

Fig. 5. Temperature dependences of mobility μ_0 in p-$Bi_{2-x}Sb_xTe_{3-y}Se_y$ solid solutions. Sample notation is the same as in Fig. 4.

solutions increase from 1.0 to 1.2 and from 0.06 to 0.09, respectively, the values of s_1 decrease from 0.81 to 0.72.

The temperature dependences of α and σ (Fig. 3) and the data on the carrier concentration (Table 2) were used to calculate the average effective density-of-states mass m/m_0 and the carrier mobility μ_0 (with due account of the degeneracy). The temperature dependences of the effective mass m/m_0 in the p-$Bi_{2-x}Sb_xTe_{3-y}Se_y$ solid solutions in the temperature range 77–200 K were found to be weaker than those for the n-type materials [18, 20] (Fig. 4).

As the carrier concentration increases, m/m_0 in samples of the same composition increases, as it does in n-type solid solutions. As the Sb content in a solid solution increases, m/m_0 grows with concentration for the same number of Se atoms in samples with similar concentrations.

Note that, within the framework of the many-valley model of the energy spectrum, the effective mass is $m = N^{2/3}(m_1m_2m_3)^{1/3}$, where m_1, m_2, and m_3 are the effective masses along the ellipsoid axes in the case of isotropic carrier scattering.

Because the anisotropy in the kinetic properties of the materials under study (both n and p type) originated from that of elastic crystal vibrations, the many-valley model is sometimes generalized to include anisotropic scattering [21–23] described by a tensor $\overleftrightarrow{\tau}$, with τ_0 in the energy dependence of the relaxation time being replaced by τ_{ij}.

The changes in the expressions relating the galvanomagnetic coefficients (ρ_{ii}, ρ_{ijk}, ρ_{ijkl}) to the inverse effective mass tensor components (α_{ij}) in the model with anisotropic carrier scattering reduce to the replacement of α_{ij} by matrix products $(\alpha\tau)_{ij}$ [21, 22]. The tensors $\overleftrightarrow{\alpha}$ and $\overleftrightarrow{m}$ are related through

$$\overleftrightarrow{\tau} = m_0\overleftrightarrow{T}(\Theta)\overleftrightarrow{m}^{-1}\overleftrightarrow{T}^{-1}(\Theta), \tag{13}$$

where $\overleftrightarrow{T}(\Theta)$ is given by

$$\overleftrightarrow{T}(\Theta) = \begin{bmatrix} 1 & 0 & 0 \\ 0 & \cos\theta & \sin\theta \\ 0 & -\sin\theta & \cos\theta \end{bmatrix}. \tag{14}$$

Thus, the concentration and temperature dependences of the effective mass m/m_0 in p-$Bi_{2-x}Sb_xTe_{3-y}Se_y$ solid solutions originate not only from changes in the shape of constant-energy surfaces but also from anisotropy of the carrier scattering.

As the carrier concentration and the Sb and Se contents in samples with similar carrier concentrations increase, the mobility in p-$Bi_{2-x}Sb_xTe_{3-y}Se_y$ (Fig. 5), as well as the electrical conductivity, decreases as the number of scatterers increases. For $p > 0.4 \times 10^{19}$ cm^{-3}, the mobility falls off considerably because of the effect exerted by the additional band.

The effective mass m/m_0 and mobility μ_0, together with the lattice thermal conductivity κ_L, define the refrigerating factor β, which increases in p-$Bi_{2-x}Sb_xTe_{3-y}Se_y$ solid solutions ($x \le 1.2$, $y \le 0.09$) for temperatures <200 K as compared to the value of β for p-$Bi_{2-x}Sb_xTe_3$ ($x = 0.5$), a composition employed widely in the room-temperature region in various refrigerating devices.

4. CONCLUSIONS

Our studies provide supportive evidence for the validity of the methods used to determine the scattering mechanism, effective mass, and mobility, as well as the lattice thermal conductivity κ_L. The latter were shown to enable one to establish changes in the refrigerating factor β and the figure of merit of thermoelectric materials Z with composition, temperature, and carrier concentration in *p*-type bismuth- and antimony-chalcogenide-based solid solutions.

ACKNOWLEDGMENTS

This study was supported in part by the Russian Foundation for Basic Research, project no. 03-02-17605a.

REFERENCES

1. E. Müller and H. Süβmann, in *Proceedings of the XVII International Conference on Thermoelectrics* (Nagoya, Japan, 1998), p. 85.
2. A. I. Anukhin, S. Ya. Skipidarov, and O. B. Sokolov, in *Proceedings of the XII International Conference on Thermoelectrics* (Yokogama, Japan, 1993), p. 97.
3. M. N. Ettenberg, W. A. Jesser, and F. D. Rosi, in *Proceedings of the XV International Conference on Thermoelectrics* (Passadena, CA, USA, 1996), p. 52.
4. V. V. Sologub, A. D. Goletskaya, and R. V. Parfen'ev, Fiz. Tverd. Tela (Leningrad) **14** (3), 915 (1972) [Sov. Phys. Solid State **14**, 783 (1972)].
5. H. Kohler and A. Feudenberger, Phys. Status Solidi B **84**, 195 (1977).
6. V. A. Kulbachinskii, M. Inoue, M. Sasaki, H. Negishi, W. X. Gao, K. Takase, J. Giman, P. Lostak, and J. Horak, Phys. Rev. B **50** (23), 16921 (1994).
7. V. A. Kulbachinskii, Z. M. Dashevskii, M. Inoue, M. Sasaki, H. Negishi, W. X. Gao, P. Lostak, and J. Horak, Phys. Rev. B **52** (15), 10915 (1995).
8. G. Simon and W. Eichler, Phys. Status Solidi B **107**, 210 (1981).
9. F. Borghese and E. Donato, Nuovo Cimento B **53**, 283 (1968).
10. J. R. Drabble, R. D. Groves, and R. Wolfe, Proc. Phys. Soc. London **71** (3), 430 (1958).
11. R. B. Mallinson, J. A. Rayne, and R. W. Ure, Phys. Rev. **175** (3), 1049 (1968).
12. J. R. Drabble, Proc. Phys. Soc. London **72** (3), 380 (1958).
13. R. B. Malinson, J. A. Rayne, and R. W. Ure, Phys. Lett. **19**, 545 (1965).
14. L. P. Caywood and G. R. Miller, Phys. Rev. B **2** (8), 3209 (1970).
15. V. A. Kutasov and L. N. Luk'yanova, Fiz. Tverd. Tela (Leningrad) **28** (3), 899 (1986) [Sov. Phys. Solid State **28**, 502 (1986)].
16. V. A. Kutasov and L. N. Luk'yanova, Fiz. Tverd. Tela (Leningrad) **26** (8), 2501 (1984) [Sov. Phys. Solid State **26**, 1515 (1984)].
17. R. R. Shvangiradze and E. P. Sabo, Neorg. Mater. **36** (11), 1316 (2000).
18. V. A. Kutasov and L. N. Luk'yanova, Phys. Status Solidi B **154**, 669 (1989).
19. H. Kaibe, M. Sakata, L. J. Ohsugi, and I. Nishida, in *Proceedings of the VIII International Conference on Thermoelectrics* (Nancy, France, 1989), p. 195.
20. E. V. Kuchis, *Methods for Studying the Hall Effect* (Sovetskoe Radio, Moscow, 1974) [in Russian].
21. B. A. Efimova, I. Ya. Korenblit, V. I. Novikov, and A. G. Ostroumov, Fiz. Tverd. Tela (Leningrad) **3** (9), 2746 (1961) [Sov. Phys. Solid State **3**, 2004 (1961)].
22. H. A. Ashworth, J. A. Rayne, and R. W. Ure, Phys. Rev. B **3** (8), 2646 (1971).
23. V. A. Kutasov, L. N. Luk'yanova, and P. P. Konstantinov, Fiz. Tverd. Tela (St. Petersburg) **41** (2), 187 (1999) [Phys. Solid State **41**, 164 (1999)].

Translated by G. Skrebtsov

Physics of the Solid State, Vol. 46, No. 8, 2004, pp. 1410–1419. Translated from Fizika Tverdogo Tela, Vol. 46, No. 8, 2004, pp. 1372–1380.
Original Russian Text Copyright © 2004 by Kagan, Red'ko, Rodionov, Pol'shin, Zotova.

SEMICONDUCTORS AND DIELECTRICS

Phonon Drag Thermopower in Doped Bismuth

V. D. Kagan, N. A. Red'ko, N. A. Rodionov, V. I. Pol'shin, and O. V. Zotova

Ioffe Physicotechnical Institute, Russian Academy of Sciences, Politekhnicheskaya ul. 26, St. Petersburg, 194021 Russia

e-mail: nikolaj.a.redko@mail.ioffe.ru

Received December 24, 2003

Abstract—The low-temperature ($2 < T < 80$ K) thermopower in bismuth doped by tellurium, a donor impurity ($0 < c \leq 0.07$ at. % Te), is dominated by the phonon component, which shifts to higher temperatures with increasing dopant concentration. The temperature and concentration dependences of the phonon thermopower of doped bismuth are satisfactorily described by the theory of phonon drag of electrons. The theory is developed for a strongly anisotropic electron spectrum and includes both direct and two-step phonon drag. *© 2004 MAIK "Nauka/Interperiodica".*

1. INTRODUCTION

Doping bismuth with the tellurium impurity destroys charge compensation in the semimetal, and the concentration of electrons can increase compared to that of the holes to the extent where electrons may become the only carriers determining the transport phenomena. As a result, the thermopower originating from the phonon drag of electrons increases strongly at low temperatures [1]. Theoretical studies have shown [2–4] that, in semimetals and semiconductors, in which the thermal phonon momentum substantially exceeds the characteristic momentum of electrons and, hence, that of phonons interacting with electrons, the drag of electrons by phonons may acquire a two-step character. An important part in this process is played by the nonequilibrium state of thermal phonons transferring additional momentum (in normal phonon–phonon collisions) to low-energy phonons, which, in turn, transfer this momentum to electrons. In the conditions where normal phonon collisions dominate over resistive collisions, the drag thermopower is due primarily to two-step phonon drag.

The phonon thermopower and the Nernst–Ettingshausen phonon coefficient studied in pure and perfect bismuth samples at low temperatures ($3 < T < 9$ K) exhibit an exponential temperature dependence [5–8]. This dependence is characteristic of the relaxation time associated with Umklapp processes, which in pure bismuth are resistive phonon processes. In the above experimental studies, this dependence is assigned to two-step phonon drag of charge carriers.

This communication reports on the phonon drag thermopower observed in doped bismuth at low temperatures.

2. SAMPLES AND EXPERIMENTAL TECHNIQUES

The temperature behavior of the thermopower, thermal conductivity, and electrical resistivity was studied on single-crystal samples of bismuth doped by the tellurium donor impurity. The samples were spark-eroded from the central part of a single-crystal ingot grown through horizontal zone recrystallization. The samples were rectangular parallelepipeds $2.5 \times 2.5 \times 30$ mm in size whose faces were perpendicular to the C_1, C_2, and C_3 crystallographic axes. The largest dimension of the samples was along either the bisector axis C_1 or the trigonal axis C_3. The samples were etched in a C_2H_5OH–HNO_3 (1 : 1) solution.

A sample to be studied, with heaters attached to its ends, was soldered to the bottom of a vacuum chamber ≈18 mm in diameter immersed in a thermostatting liquid (helium, hydrogen, nitrogen). The heater at the chamber bottom served to control the average temperature, and the heater at the other end of the sample produced a temperature gradient (∇T) across the sample. The temperature was measured in two cross sections of the sample spaced by $l_T \cong 15$ mm (at a constant heat flux) with carbon resistance thermometers in the $1.5 < T < 40$ K region and with copper–constantan thermocouples in the range $30 < T < 80$ K. The thermopower of the samples was measured in relation to copper, whose absolute thermopower did not exceed 1 μV/K throughout the temperature region covered. The experimental thermopower data are presented below without inclusion of this small quantity.

3. EXPERIMENTAL RESULTS

Doping bismuth with tellurium destroys charge compensation, because the concentration of electrons in pure bismuth is equal to that of holes ($n_0 = p_0 \cong 3 \times 10^{17}$ cm^{-3}). In our experiments, the electron concentra-

1063-7834/04/4608-1410$26.00 © 2004 MAIK "Nauka/Interperiodica"

tion in doped bismuth samples increases from 3.5×10^{17} to 1.5×10^{19} cm^{-3}. The main parameters of the doped bismuth samples studied are listed in the table.

As bismuth is doped, its conductivity first decreases sharply from $\sim 4 \times 10^6\ \Omega^{-1}$ cm^{-1} in pure bismuth to $\sim 4 \times 10^4\ \Omega^{-1}$ cm^{-1} for a doping level of $\sim 4 \times 10^{-3}$ at. % Te. Further doping brings about a slow rise in the conductivity. The minimum in the conductivity as a function of tellurium concentration can be identified with the Fermi level approaching the top of the hole band in bismuth. When the degree of doping is higher, the Fermi level rises above the hole band top and the electrons become the sole charge carriers involved in the transport phenomena. Increasing the electron concentration in the course of bismuth doping does not give rise to a proportional increase in the conductivity because the mobility of electrons decreases as a result of their scattering from the dopant ($\sigma = en\mu$, where n and μ are the concentration and mobility of electrons, respectively).

In the region of impurity conductivity in our bismuth samples ($T < 60$ K), the electron gas is degenerate and the Fermi surface consists of three electronic ellipsoids centered at the L points of the Brillouin zone, which are located on the reflection planes. One of the minor ellipsoid axes coincides with the binary axis C_2 of the crystal, about which the ellipsoids are tilted through a small angle $\varphi = 6.38°$. As a result of this turn, the two other ellipsoid axes make an angle φ with the C_1 and C_3 axes. The three electron ellipsoids are equivalent, in accordance with the bismuth crystal symmetry, and the electron effective masses are strongly anisotropic.

Doping bismuth with tellurium also results in a decrease in phonon thermal conductivity, because phonons are scattered by dopant atoms (Fig. 1). The maximum in the phonon thermal conductivity decreases in magnitude and shifts toward higher temperatures. In a sample of pure bismuth, phonon scattering from the boundaries results in a $\kappa \sim T^3$ scaling at low temperatures. In addition to phonon scattering on the sample boundaries, the scattering from impurities and electrons appears in doped bismuth, which changes the temperature dependence of thermal conductivity from cubic to close to quadratic, with the maximum shifted toward high temperatures. Doping bismuth to $\sim 4 \times 10^{-3}$ at. % Te reduces the low-temperature conductivity by approximately two orders of magnitude, with the phonon thermal conductivity decreasing by an order of magnitude. Further doping of bismuth with tellurium causes a slight rise in conductivity as a result of the increase in the concentration of electrons outweighing the decrease in their mobility. Indeed, doping of bismuth to an electron concentration of 1.5×10^{19} cm^{-3} reduces the conductivity as compared to the case of pure bismuth by approximately 50 times, while the phonon thermal conductivity at low temperatures decreases by two orders of magnitude. Note that, for $T < 20$ K, the electronic component of thermal conductivity is negligible as compared to the phonon component.

Main parameters of samples of bismuth doped by the tellurium donor impurity

Sample no.	c, 10^{-2} at. % Te	n_L, 10^{17} cm^{-3}	p_T, 10^{17} cm^{-3}	E_{FL}, meV	E_{FT}, meV	Θ_{1e}, K	Θ_{2e}, K
1	0.06	3.5	2.4	33	11	1.1	16
2	0.25	5.9	0.48	40	4	1.3	19
3	0.4	7.2	0.05	43	0.8	1.4	20
4	1	22	–	64	–	2	29
5	2	47	–	84	–	2.6	38
6	3.6	69	–	96	–	2.9	43
7	5	111	–	113	–	3.4	50
8	7	149	–	125	–	3.8	55
9	1	22	–	64	–	2	29

Note: c, n_L, and p_T are the concentrations of tellurium, L electrons, and T holes, respectively; E_{FL} and E_{FT} are the Fermi energies of L electrons and T holes, respectively; and Θ_{1e} and Θ_{2e} are the electron Debye temperatures. The largest dimension of samples 1–8 is along the C_1 crystallographic axis, and that of sample 9, along the C_3 axis.

We studied the temperature dependence of thermopower α_{22} ($\nabla \mathbf{T} \parallel C_1$) and α_{33} ($\nabla \mathbf{T} \parallel C_3$) in samples of doped bismuth. Figure 2 plots the temperature behavior of the thermopower α_{22} obtained on the samples of doped bismuth studied. The low-temperature thermopower consists of two components, one due to diffusion (α_{22}^{dif}) and one due to phonons (α_{22}^{ph}). The electron gas in our samples of doped bismuth is degenerate at low temperatures ($T < 60$ K), and the diffusion component of thermopower is given by [10]

$$\alpha_{22}^{\text{dif}} = -\frac{\pi^2 k^2 T}{3e\zeta}\left\{\frac{3 + 8\dfrac{\zeta}{\mathcal{E}_g} + 8\dfrac{\zeta^2}{\mathcal{E}_g^2}}{2\left(1 + \dfrac{\zeta}{\mathcal{E}_g}\right)\left(1 + \dfrac{2\zeta}{\mathcal{E}_g}\right)} - \frac{d\ln\left(\dfrac{1}{\tau_i(\zeta)}\right)}{d\ln\zeta}\right\}, \quad (1)$$

where e is the absolute value of electronic charge, k is the Boltzmann constant, and ζ is the chemical potential. The parameter $d\ln(1/\tau_i(\zeta))/d\ln\zeta = \beta_i$ takes on the following values, depending on the scattering mechanism involved:

$$\beta_{e\text{–ph}} = \frac{1 + 8(\zeta/\mathcal{E}_g) + 8(\zeta^2/\mathcal{E}_g^2)}{2(1 + \zeta/\mathcal{E}_g)(1 + 2\zeta/\mathcal{E}_g)}$$

for electron scattering from acoustic phonons and

$$\beta_{e\text{–imp}} = -\frac{3 + 8(\zeta/\mathcal{E}_g) + 8(\zeta^2/\mathcal{E}_g^2)}{2(1 + \zeta/\mathcal{E}_g)(1 + 2\zeta/\mathcal{E}_g)}$$

for electron scattering on ionized impurities.

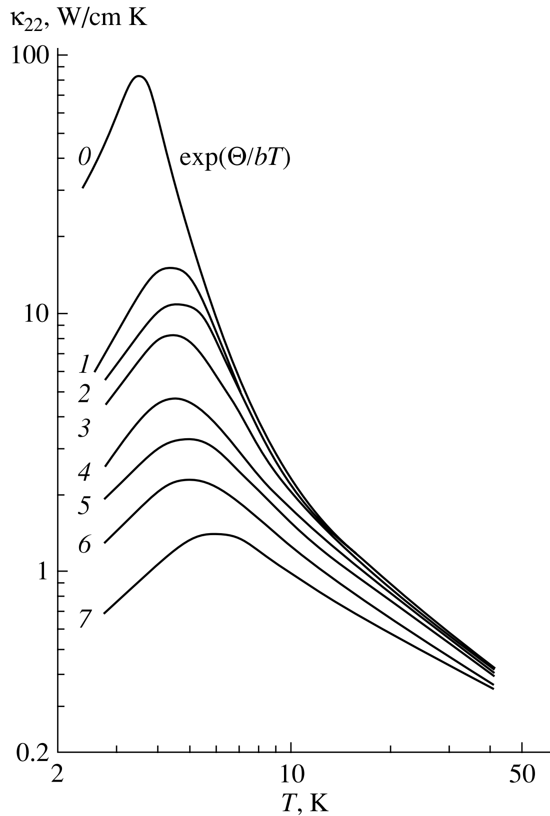

Fig. 1. Thermal conductivity κ_{22} ($\nabla T \parallel C_1$) plotted vs. temperature for samples of pure bismuth (curve *0*) [9] and of bismuth doped by the tellurium donor impurity. The numerals on the curves indicate the sample numbers (see table).

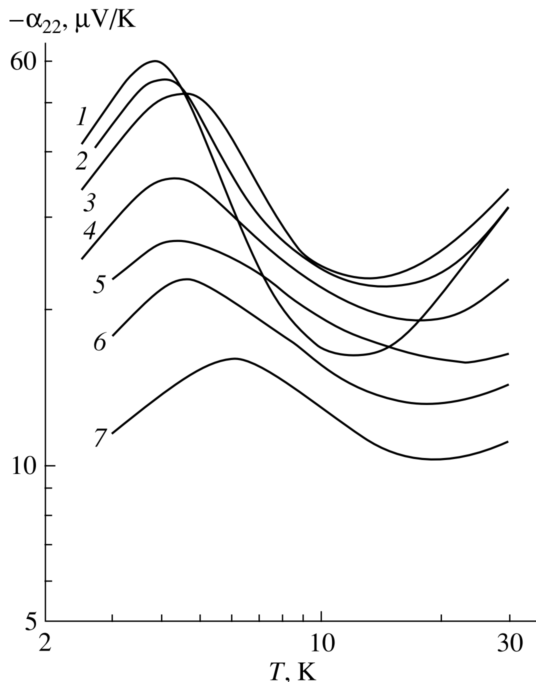

Fig. 2. Temperature dependence of thermopower for samples of doped bismuth. The numerals on the curves indicate the sample numbers (see table).

The diffusion component of thermopower for the samples of doped bismuth studied was found by linearly extrapolating the thermopower from the high temperature region $T > 30$ K, where the diffusion component dominates over the phonon component, to the low-temperature region. Figure 3 shows (for sample 1) the temperature dependence of total thermopower (curve *1*) and of its diffusion (straight line *2*) and phonon (curve *3*) components, with the latter derived by subtracting the diffusion component from the total thermopower. A similar procedure for isolating the phonon component of thermopower was applied to the other samples of doped bismuth. The temperature behavior of the phonon thermopower in samples of doped bismuth is presented graphically in Figs. 4 and 5. Comparing the experimentally found diffusion components of thermopower of doped bismuth samples with the results of calculations from Eq. (1) using the parameters characteristic of electron scattering on acoustic phonons and ionized impurities leads to the following conclusion. At low temperatures, doped bismuth features a mixed electron scattering mechanism; i.e., electrons scatter from both acoustic phonons and ionized impurities, with the latter process being predominant.

At temperatures above that of the maximum (Figs. 4, 5), the phonon component of thermopower follows a power law, $\alpha_{22}^{ph} \sim T^{-m}$. For sample 1 (Fig. 4), the exponent is $m \cong 3$ at low temperatures $T < 10$ K) and $m \cong 4$ at high temperatures ($T > 10$ K). An increase in the concentration of electrons entails an increase in their momentum p, which brings about an increase in the number of phonons interacting with electrons ($2p \leq \hbar q$, where $\hbar q$ is the phonon momentum). As a result, as the electron concentration in bismuth increases under doping, the phonon component shifts toward higher temperatures (Figs. 4, 5). Figure 6 plots the dependence of the temperature T_0 at which the phonon thermopower is 1 μV/K on electron concentration for the samples studied. The temperature T_0 grows with increasing electron concentration as $T_0 \sim n^{0.17}$. Furthermore, the exponent m in the temperature dependence of the phonon thermopower at low temperatures decreases when the electron concentration is increased from $m \cong 3$ for sample 1 ($n = 3.5 \times 10^{17}$ cm^{-3}) to $m \cong 1$ for sample 8 ($n = 1.5 \times 10^{19}$ cm^{-3}). At high temperatures, the exponent for the phonon thermopower remains unchanged for all samples and is equal to $m \cong 4$.

Figure 7 presents temperature dependences of both phonon thermopower components, α_{22}^{ph} and α_{33}^{ph}, for samples 4 and 9 having equal electron concentrations $n = 2.2 \times 10^{18}$ cm^{-3}. These dependences were used to estimate the anisotropy of the phonon thermopower, $\alpha_{22}^{ph}/\alpha_{33}^{ph} \cong 2$, which varies only weakly with temperature.

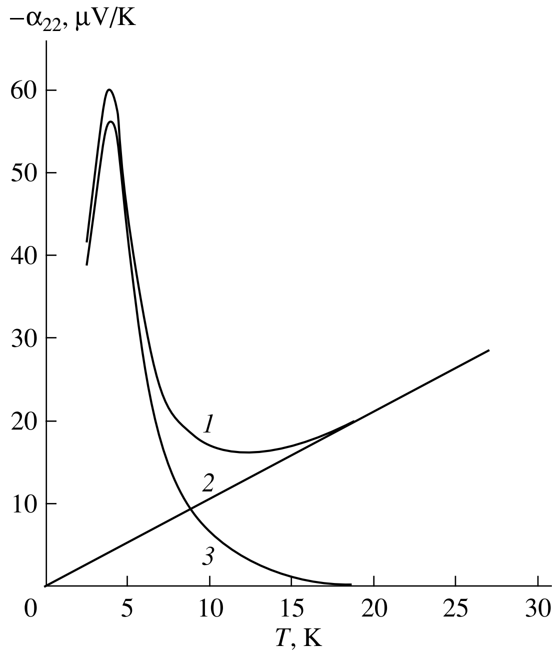

Fig. 3. Temperature dependence of the total thermopower (curve *1*) and of its (*2*) diffusion and (*3*) phonon components for sample 1.

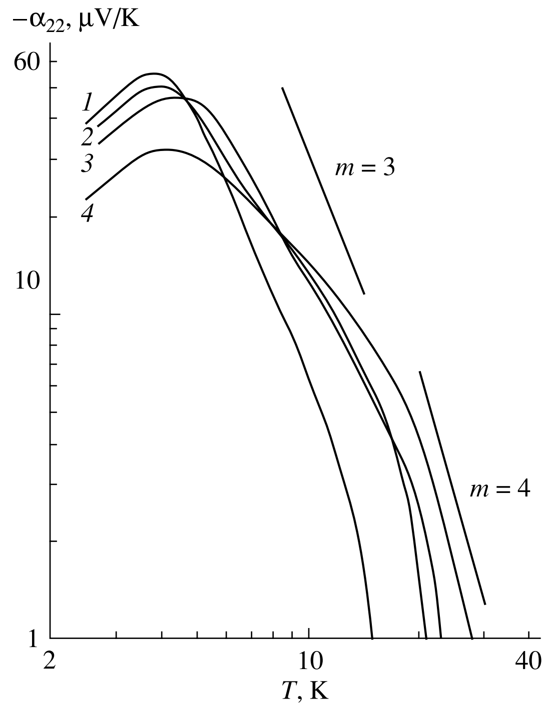

Fig. 4. Temperature dependence of the phonon component of thermopower plotted for doped bismuth samples. The numerals on the curves indicate the sample numbers.

The temperature of the maximum in phonon thermopower for doped bismuth samples lies in the interval 3.8–5.5 K (Figs. 4, 5). As the dopant concentration c increases, this temperature shifts toward higher temperatures as $T_{\max} \sim c^{0.08}$, with the maximum of the phonon thermopower decreasing gradually as $\alpha_{\max} \sim c^{-0.12}$.

The experimental temperature and concentration dependences of the phonon thermopower component in doped bismuth will now be analyzed in terms of a theory that includes both direct and two-step phonon drag of electrons.

4. THEORY OF PHONON DRAG OF ELECTRONS

The phonon thermopower tensor was found by solving the kinetic equation for bismuth L electrons with a strongly anisotropic nonparabolic dispersion described in terms of the Lax model:

$$\mathcal{E}_{\mathbf{p}} = \left[\left(\frac{\mathcal{E}_g}{2}\right)^2 + \frac{\mathcal{E}_g}{2}\left(\frac{p_1^2}{m_1} + \frac{p_2^2}{m_2} + \frac{p_3^2}{m_3}\right)\right]^{1/2} - \frac{\mathcal{E}_g}{2}, \quad (2)$$

where $\mathcal{E}_{\mathbf{p}}$ is the energy of an electron with momentum $\mathbf{p}$, whose components along the ellipsoid axes are p_1, p_2, and p_3; m_i are the electron effective masses in an ellipsoid; and $\mathcal{E}_g$ is the energy band gap.

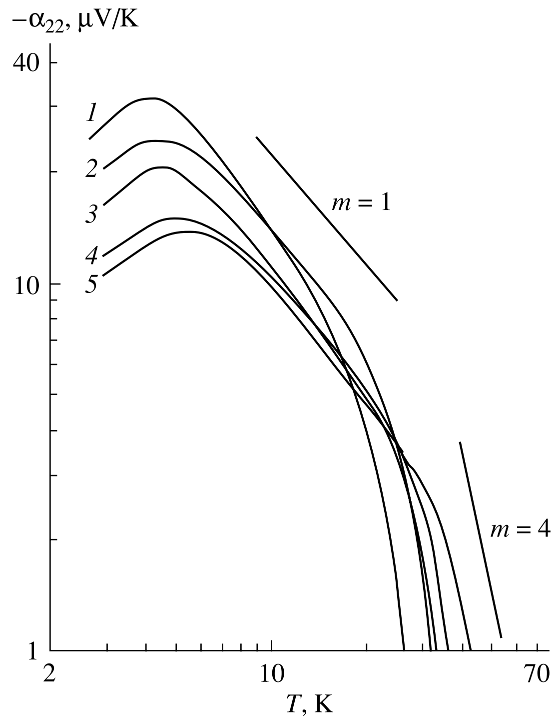

Fig. 5. Temperature dependence of the phonon component of thermopower plotted for different doped bismuth samples: (*1*) 4, (*2*) 5, (*3*) 6, (*4*) 7, and (*5*) 8.

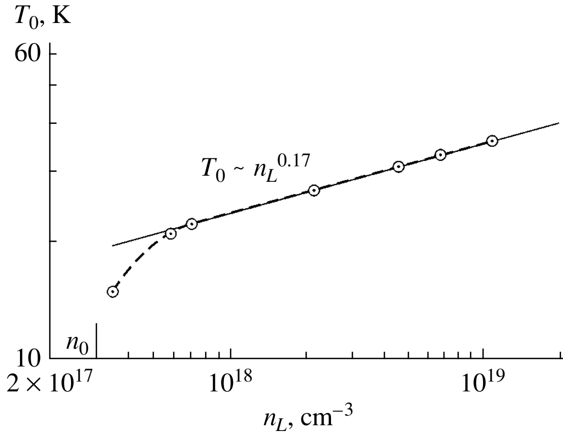

Fig. 6. Temperature T_0 for which the phonon thermopower is 1 μV/K in samples of doped bismuth plotted vs. electron concentration; $n_0 = 3 \times 10^{17}$ cm^{-3} is the electron concentration in pure bismuth.

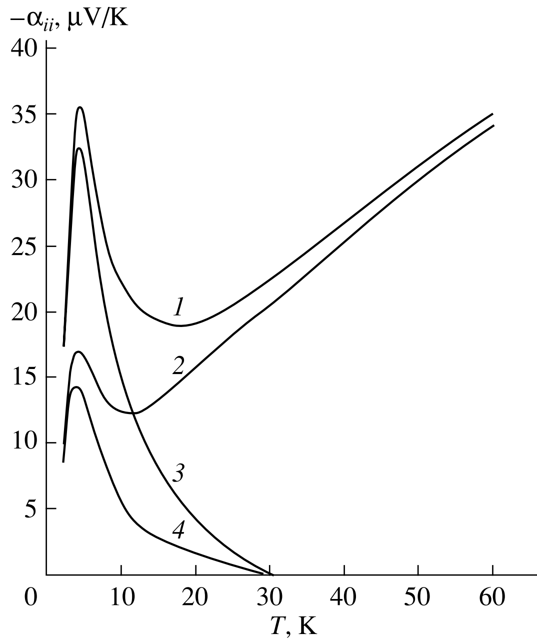

Fig. 7. Temperature dependence of thermopower α_{22} ($\nabla T \parallel C_1$) for sample 4 (curve *1*), of α_{33} ($\nabla T \parallel C_3$) for sample 9 (curve *2*), and of their phonon components (curves *3*, *4*, respectively).

The electron distribution function found by solving the linearized kinetic equation is

$$\frac{f_{\mathbf{p}}}{\tau_e(\mathscr{E}_{\mathbf{p}})} = \sum_{s=1}^{3} \int \frac{d^3 q}{(2\pi)^3} \frac{2\pi}{\hbar} |C_{\mathbf{q}}|^2 n_{\mathbf{q}} \tag{3}$$
$$\times \{ [F_0(\mathscr{E}_{\mathbf{p}} - \hbar\omega_{\mathbf{q}}^{(s)}) - F_0(\mathscr{E}_{\mathbf{p}})] \delta(\mathscr{E}_{\mathbf{p}} - \mathscr{E}_{\mathbf{p}-\hbar\mathbf{q}} - \hbar\omega_{\mathbf{q}}^{(s)})$$
$$+ [F_0(\mathscr{E}_{\mathbf{p}} + \hbar\omega_{\mathbf{q}}^{(s)}) - F_0(\mathscr{E}_{\mathbf{p}})] \delta(\mathscr{E}_{\mathbf{p}} - \mathscr{E}_{\mathbf{p}+\hbar\mathbf{q}} + \hbar\omega_{\mathbf{q}}^{(s)}) \},$$

where $f_{\mathbf{p}}$ and $n_{\mathbf{q}}$ are nonequilibrium terms added to the equilibrium distribution functions of electrons and phonons, $F_{\mathbf{p}} = F_0 + f_{\mathbf{p}}$ and $N_{\mathbf{q}} = N_0 + n_{\mathbf{q}}$ ($f_{\mathbf{p}}$ depends on the electron momentum **p**, and $n_{\mathbf{q}}$ is a function of the phonon wave vector **q**); $F_0(\mathscr{E}_{\mathbf{p}}) = [\exp((\mathscr{E}_{\mathbf{p}} - \zeta)/kT) + 1]^{-1}$ is the equilibrium Fermi distribution function of electrons with chemical potential ζ; $N_0 = [\exp(\hbar\omega_{\mathbf{q}}/kT) - 1]^{-1}$ is Planck's equilibrium distribution function; $\omega_{\mathbf{q}}^{(s)}$ is the frequency of *s*-mode phonons with wave vector **q**; $\tau_e(\mathscr{E}_{\mathbf{p}})$ is the total electron relaxation time for scattering from acoustic phonons and ionized impurities; and $C_{\mathbf{q}}$ is the electron–phonon coupling constant.

The phonon distribution function is obtained from the kinetic equation for *s*-mode phonons

$$\frac{\partial\omega_{\mathbf{q}}}{\partial\mathbf{q}} \frac{\partial N_0}{\partial T} \nabla T + \left(\frac{1}{\tau_{\text{ph-im}}(\omega_{\mathbf{q}})} + \frac{1}{\tau_{\text{ph-}e}(\omega_{\mathbf{q}})} \right) n_{\mathbf{q}} + \frac{1}{\tau_{\text{ph-ph}}(\omega_{\mathbf{q}})} \left(n_{\mathbf{q}} + \mathbf{qV} \frac{\partial N_0}{\partial\omega_{\mathbf{q}}} \right) = 0. \tag{4}$$

The kinetic equation for phonons includes the scattering from impurities ($\tau_{\text{ph-im}}$), electrons ($\tau_{\text{ph-}e}$), and phonons ($\tau_{\text{ph-ph}}$). By applying the Callaway method for solving the kinetic equation, one can include conservation of the total momentum in phonon–phonon collisions through the term involving the average drift velocity of phonons **V**. This term is derived from the condition of total-momentum conservation in normal phonon–phonon collisions:

$$\sum_{s=1}^{3} \int d^3 q \frac{\mathbf{q}}{\tau_{\text{ph-ph}}(\omega_{\mathbf{q}}^{(s)})} \left(n_{\mathbf{q}} + \mathbf{qV} \frac{\partial N_0}{\partial\omega_{\mathbf{q}}^{(s)}} \right) = 0. \tag{5}$$

The above consideration disregards the influence of the nonequilibrium distribution function of electrons on that of phonons; in other words, the mutual electron and phonon drag is neglected. Mutual drag will appear only when, for both electrons and phonons, the mutual collisions prevail over collisions with other scatterers. In doped bismuth, these requirements for the onset of mutual electron and phonon drag cannot be met.

Since kinetic equation (4) is independent of Eq. (3), we first solve the former equation subject to condition (5). Next, the solution is substituted into kinetic equation (3), in which the phonon energy (on the order of *kT*) is much less than the average electron energy (which is equal to the Fermi energy); therefore, we can expand the right-hand part of Eq. (3) in a small parameter $\hbar\omega_{\mathbf{q}}/\mathscr{E}_{\mathbf{p}}$. Solving Eqs. (3) and (4) yields the electron distribution function $f_{\mathbf{p}}$, which is antisymmetric in momentum and proportional to ∇T. With this function, we can calculate the thermoelectric tensor (which is the coefficient of proportionality between the electric current and the temperature gradient) by summing the contributions to this tensor due to the three equivalent ellipsoids tilted to the C_3 axis at an angle φ. By multiplying

this tensor by the resistivity tensor (following a procedure analogous to that employed to derive the diffusion component in [11]), we obtain the phonon thermopower tensor. The components of the phonon thermopower $\alpha_{11} = \alpha_{22}$ and α_{33} for n-type bismuth are found to be

$$\alpha_{11} = \left(-\frac{1}{e}\right)\frac{3\hbar(1+2\zeta/\mathcal{E}_g)}{4\rho(2\zeta)^{3/2}(1+\zeta/\mathcal{E}_g)^{3/2}} \times \sum_{s=1}^{3}\int\frac{d^3q}{(2\pi)^2}\frac{\tau_{\mathrm{ph}}(\Lambda_{ik}q_i l_k^{(s)})^2}{\left(\frac{q_1^2}{m_1}+\frac{q_2^2}{m_2}+\frac{q_3^2}{m_3}\right)^{1/2}}$$

$$\times\left[\left(q_1\frac{\partial\omega_{\mathbf{q}}^{(q)}}{\partial q_1}\frac{\partial N_0}{\partial T}-\frac{b_1}{a_1}\frac{q_1^2}{\tau_{\mathrm{ph-ph}}}\frac{\partial N_0}{\partial\omega_{\mathbf{q}}^{(s)}}\right)\right. \quad (6)$$

$$+\frac{m_1\cos^2\varphi}{m_2}\left(q_2\frac{\partial\omega_{\mathbf{q}}^{(s)}}{\partial q_2}\frac{\partial N_0}{\partial T}-\frac{b_2}{a_2}\frac{q_2^2}{\tau_{\mathrm{ph-ph}}}\frac{\partial N_0}{\partial\omega_{\mathbf{q}}^{(s)}}\right)$$

$$\left.+\frac{m_1\sin^2\varphi}{m_3}\left(q_3\frac{\partial\omega_{\mathbf{q}}^{(s)}}{\partial q_3}\frac{\partial N_0}{\partial T}-\frac{b_3}{a_3}\frac{q_3^2}{\tau_{\mathrm{ph-ph}}}\frac{\partial N_0}{\partial\omega_{\mathbf{q}}^{(s)}}\right)\right],$$

$$\alpha_{33} = \left(-\frac{1}{e}\right)\frac{3\hbar(1+2\zeta/\mathcal{E}_g)}{4\rho(2\zeta)^{3/2}(1+\zeta/\mathcal{E}_g)^{3/2}} \times \sum_{s=1}^{3}\int\frac{d^3q}{(2\pi)^2}\frac{\tau_{\mathrm{ph}}(\Lambda_{ik}q_i l_k^{(s)})^2}{\left(\frac{q_1^2}{m_1}+\frac{q_2^2}{m_2}+\frac{q_3^2}{m_3}\right)^{1/2}} \quad (7)$$

$$\times\left[\cos^2\varphi\left(q_3\frac{\partial\omega_{\mathbf{q}}^{(s)}}{\partial q_3}\frac{\partial N_0}{\partial T}-\frac{b_3}{a_3}\frac{q_3^2}{\tau_{\mathrm{ph-ph}}}\frac{\partial N_0}{\partial\omega_{\mathbf{q}}^{(s)}}\right)\right.$$

$$\left.+\frac{m_3\sin^2\varphi}{m_2}\left(q_2\frac{\partial\omega_{\mathbf{q}}^{(s)}}{\partial q_2}\frac{\partial N_0}{\partial T}-\frac{b_2}{a_2}\frac{q_2^2}{\tau_{\mathrm{ph-ph}}}\frac{\partial N_0}{\partial\omega_{\mathbf{q}}^{(s)}}\right)\right],$$

where

$$a_i = \int d^3q\frac{q_i^2\tau_{\mathrm{ph}}}{\tau_{\mathrm{ph-ph}}\tau_R}\left(-\frac{\partial N_0}{\partial\omega_{\mathbf{q}}^{(s)}}\right), \quad (8)$$

$$b_i = \int d^3q\frac{\tau_{\mathrm{ph}}}{\tau_{\mathrm{ph-ph}}}\left(q_i\frac{\partial\omega_{\mathbf{q}}^{(s)}}{\partial q_i}\right)\left(\frac{\partial N_0}{\partial T}\right), \quad (9)$$

$$i = 1,2,3, \quad \frac{1}{\tau_R(q)} = \frac{1}{\tau_{\mathrm{ph-im}}(q)}+\frac{1}{\tau_{\mathrm{ph-}e}(q)}, \quad (10)$$

$$\frac{1}{\tau_{\mathrm{ph}}(q)} = \frac{1}{\tau_R(q)}+\frac{1}{\tau_{\mathrm{ph-ph}}(q,T)}. \quad (11)$$

Here, e is the absolute value of the electronic charge, ρ is the density of doped Bi⟨Te⟩, ζ is the electron chemical potential, Λ_{ik} is the deformation-potential tensor, $\mathbf{l}$ is the polarization vector of s-mode phonons, $\tau_R(q)$ is the resistive phonon relaxation time characterizing the momentum relaxation in the phonon system, $\tau_{\mathrm{ph}}(q)$ is the total phonon relaxation time, and $\tau_{\mathrm{ph-ph}}(q, T)$ is the phonon–phonon relaxation time.

It should be pointed out that integration over wave vector $\mathbf{q}$ in Eqs. (6) and (7) is performed within a limited volume of phonon momentum space determined by the energy and momentum conservation laws for phonons interacting with electrons and by dispersion relation (2) for the L electrons:

$$\frac{\hbar^2q_1^2}{m_1}+\frac{\hbar^2q_2^2}{m_2}+\frac{\hbar^2q_3^2}{m_3} \le 8\zeta\left(1+\frac{\zeta}{\mathcal{E}_g}\right). \quad (12)$$

The integrands in Eqs. (6) and (7) contain terms with coefficients b_i/a_i that are associated with the gain in phonons due to phonon–phonon collisions [the second term in parentheses in Eq. (5)] and appear when the phonon kinetic equation is solved using the Callaway method. The integrals determining the coefficients a_i and b_i in Eqs. (8) and (9), respectively, do not have any bearing on the electron–phonon coupling. Therefore, constraint (12) on the domain of integration in the phonon momentum space does not extend to them; i.e., the integration in Eqs. (8) and (9) is performed over the whole phonon wave vector space.

According to Eq. (12), the constraint on the region in phonon momentum space where phonons interact with electrons in an isotropic degenerate semiconductor defines the maximum momentum of a phonon interacting with electrons, $\hbar q_{\max} = [8m\zeta(1+\zeta/\mathcal{E}_g)]^{1/2}$. This momentum can be identified with the electronic Debye temperature $\Theta_e = s[8m\zeta(1+\zeta/\mathcal{E}_g)]^{1/2}/k$, where s is the sound velocity. In the case of anisotropic n-type bismuth with the electron Fermi surface approximated by ellipsoids of revolution with effective masses $m_1 \cong m_3$ and m_2, one may limit oneself to two different electronic Debye temperatures, Θ_{1e} and Θ_{2e}. Taking into account the anisotropy of the electronic spectrum in pure bismuth, we obtain $\Theta_{1e} \cong 1$ K and $\Theta_{2e} \cong 15$ K. The corresponding data on Θ_{ie} for our samples of doped bismuth are listed in the table. Because the values of Θ_{1e} and Θ_{2e} differ strongly, it would be wrong to use an average Debye temperature to estimate integrals (6) and (7); therefore, another approach is employed to calculate these integrals. If in Eq. (12) we neglect the small term with large effective mass m_2, the constraint will be imposed only on the wave vector components q_1 and q_3. Because q_2 is not constrained, integration over q_2 is performed over an unlimited region of the phonon wave vector component. In this case, Planck's distribution function for phonons makes the integral over q_2 converge; this integral will be determined by the thermal

wave vector $kT/\hbar s$. This value is larger than the maximum value $q_{1m} = [8m_1\zeta(1 + \zeta/\mathscr{E}_g)]^{1/2}/\hbar$. Therefore, everywhere in the integrals of Eqs. (6) and (7) except the square root in the denominators, we can neglect the variables q_1 and q_3 as compared to q_2. This approach is applicable to intermediate temperatures, i.e., in the region between Θ_{1e} and Θ_{2e}. In the high- and low-temperature regions, integration proceeds in standard fashion. For high temperatures, $T \gg \Theta_{2e}$, we integrate over q_2 only up to $q_{2m} = [8m_2\zeta(1 + \zeta/\mathscr{E}_g)]^{1/2}/\hbar$ because of condition (12); here, q_{2m} is much less than the thermal momentum. Note that Planck's distribution function for phonons can be replaced by the Rayleigh distribution function. For low temperatures, $T \ll \Theta_{1e}$, there is no need to worry about the constraint on the integration region for phonon wave vectors, because in Planck's distribution function the most important wave vectors are those corresponding to thermal phonons, which are substantially smaller than q_{1m} and, even more so, than q_{2m}.

5. DISCUSSION OF THE EXPERIMENTAL RESULTS

The resistive processes for the phonon gas in pure bismuth are the Umklapp processes and phonon scattering from impurities in doped bismuth. Although normal phonon–phonon collisions dominate over resistive processes in bismuth, the small resistive scattering cannot be neglected. Despite the validity of the inequality

$$1/\tau_{\text{ph-ph}}(q_T) \gg 1/\tau_R(q_T), \tag{13}$$

the terms containing the coefficients b_i/a_i in Eqs. (6) and (7) are proportional to $\tau_R(q_T)$ and are predominant. In the high-temperature region, $T \gg \Theta_{2e}$, these terms, according to [2–4], describe two-step phonon drag. For lower temperatures, $T < \Theta_{2e}$, interpretation of these terms as reflecting two-step phonon drag is no longer valid; indeed, thermal phonons are now coupled to electrons. This contribution to the phonon thermopower originates, according to inequality (13), only from the weak resistive scattering and can be directly related to Peierls' ideas. We denote this part of the phonon thermopower by α_R; it is determined by the terms containing the coefficients b_i/a_i [the second terms in parentheses in Eqs. (6) and (7)]. This part of the phonon thermopower is completely analogous to the part of the thermal conductivity that, according to inequality (13), is determined by weak resistive scattering. For pure bismuth, τ_R is closely connected with Umklapp processes and, thus, depends exponentially on temperature. This dependence holds for temperatures below the Debye temperature for the bismuth crystal, $\Theta \cong 120$ K; i.e., it is in no way related to Θ_{2e} and is applicable for temperatures both above and below Θ_{2e} and even for temperatures on the order of Θ_{1e}. At low temperatures, the power-law temperature dependences for pure bismuth are hard to distinguish from the exponential relation. Therefore, an exponential temperature dependence of the phonon thermopower will hold for both the two-step phonon drag ($T \gg \Theta_{2e}$) and the resistive phonon part of the thermopower ($T < \Theta_{2e}$). Exponential temperature dependences of the phonon thermopower (α^{ph}) and the Nernst–Ettingshausen phonon coefficient (Q^{ph}) were observed in [5–8] in pure bismuth in the region below Θ_{2e}, which follows from the above estimates. Therefore, α^{ph} and Q^{ph} can be related to the electronic characteristics associated with resistive phonon scattering. The electrons serve here as a probe for revealing the exponential that governs the phonon thermal conductivity of pure bismuth.

A resistive process for the phonon gas in doped bismuth is Rayleigh phonon scattering from impurities, for which $1/\tau_{\text{ph-im}} \sim c\omega_{\mathbf{q}}^4$, where c is the tellurium dopant concentration in bismuth. In addition to this power law, one has to take into account the variation of all quantities under the integral in Eqs. (6) and (7) as functions of the phonon wave vectors. In this case, in view of condition (12), the dependences on temperature and impurity concentration in different temperature intervals will be different.

As for the concentration behavior of the phonon thermopower, one has to bear in mind that there is a direct and an indirect dependence. The direct concentration dependence for the phonon thermopower is the dependence of $1/\tau_{\text{ph-im}}$ on c. There is also an indirect dependence, because q_{1m} and q_{2m} are related to the chemical potential ζ determined by the electron concentration n. In doped bismuth, the concentration of electrons is the sum of two parts, namely, the electron concentration in pure bismuth, $n_0 = 3 \times 10^{17}$ cm^{-3}, and the concentration of electrons formed in the ionization of the tellurium dopant atoms present in concentration c. The dependence of the chemical potential on the electron concentration in doped bismuth is given by [10, 11]

$$n = n_0 + c = \frac{1}{\pi^2\hbar^3}\left\{m_1m_2m_3\left[2\zeta\left(1 + \frac{\zeta}{\mathscr{E}_g}\right)\right]^3\right\}^{1/2}. \tag{14}$$

Now, we will analyze the phonon thermopower of doped bismuth for temperatures above that of the maximum, as well as in the temperature region of the maximum.

5.1. Phonon Thermopower above the Temperature of the Maximum

5.1.1. Resistive phonon drag of electrons. Because of the strong nonparabolicity of the L band in doped bismuth ($\zeta/\mathscr{E}_g \gg 1$), we have $\zeta \sim (n_0 + c)^{1/3}$. For temperatures above Θ_{2e} ($T \gg \Theta_{2e}$), theory predicts the follow-

ing dependence of the resistive phonon thermopower on temperature and impurity concentration:

$$\alpha_R \sim \frac{(1+2\zeta/\mathscr{E}_g)[\zeta(1+\zeta/\mathscr{E}_g)]^{1/2}}{cT^4} \sim \frac{(n_0+c)^{2/3}}{cT^4}. \quad (15)$$

The temperature dependence of α_R (15) is determined by the cross section of phonon scattering from impurities and is in agreement with experiment (Figs. 4, 5). However, according to Eq. (15), the phonon thermopower should decrease with increasing impurity concentration, whereas experiment shows a growth in the phonon thermopower. Thus, two-step phonon drag of electrons described by Eq. (15) does not fit with the experimentally observed concentration dependence of the phonon thermopower.

5.1.2. Direct phonon drag of electrons. In what follows, we assume that resistive phonon scattering in doped bismuth is not weak: $1/\tau_{\text{ph-ph}}(q_T) \geq 1/\tau_{\text{ph-im}}(q_T)$, where q_T is the wave vector of thermal phonons. Therefore, the total phonon thermopower is determined by direct drag. This drag is represented in Eqs. (6) and (7) by the first terms in the parentheses, with $\tau_{\text{ph}}(q_T) \cong \tau_{\text{ph-ph}}(q_T)$. We denote this contribution to the phonon thermopower by α_n.

Now, we analyze all mechanisms of normal phonon–phonon scattering to establish the temperature and concentration dependences of the phonon thermopower α_n.

5.1.2.1. Accepting Herring's model for $\tau_{\text{ph-ph}}(q)$, we obtain, for the crystal symmetry of bismuth,

$$\frac{1}{\tau_{\text{ph-ph}}(q)} \cong a_1 q^3 T^2. \quad (16)$$

In this case, for the phonon direct-drag thermopower in bismuth, we have

$$\alpha_n \sim \frac{(1+2\zeta/\mathscr{E}_g)}{\zeta(1+\zeta/\mathscr{E}_g)T^2}. \quad (17)$$

The temperature and concentration dependences of Eq. (17) for the phonon thermopower do not correlate with the experimental relations (Figs. 4, 5).

5.1.2.2. Inclusion for the transverse phonon modes in bismuth of normal phonon–phonon collisions determined by the Landau–Rumer processes yields

$$\frac{1}{\tau_{\text{ph-ph}}(q)} \cong a_2 q T^4. \quad (18)$$

Equation (18) is also applicable to the longitudinal phonon branch for Simons' processes. In this case, the contribution from all phonon modes to the phonon thermopower turns out to be

$$\alpha_n \sim \frac{(1+2\zeta/\mathscr{E}_g)}{T^4}. \quad (19)$$

The temperature dependence of the phonon thermopower $\alpha_n \sim T^{-4}$, given by Eq. (19), agrees with the experimental data presented graphically in Figs. 4 and 5. As a result of the strong nonparabolicity of the bismuth L band, the phonon thermopower depends on the dopant concentration:

$$\alpha_n \sim \frac{(n_0+c)^{1/3}}{T^4}. \quad (20)$$

One can also theoretically find the concentration dependence of the temperature T_0 for a given value of the phonon thermopower using the sample parameters. The experimental data for our samples of doped bismuth are plotted in Fig. 7 for a phonon thermopower $\alpha = 1$ μV/K. As follows from Eq. (20), $T_0 \sim (n_0 + c)^{1/12}$, which correctly reflects the trend of a slow growth in T_0 with increasing dopant concentration and deviates only slightly from the experimental relation.

Let us discuss now the behavior of phonon thermopower at lower temperatures ($T < 15$ K).

For dopant concentrations $c < 0.01$ at. % Te in bismuth, the temperature behavior of phonon thermopower above the temperature of the maximum is approximated by the intermediate-temperature model ($\Theta_{1e} < T < \Theta_{2e}$):

$$\alpha = \alpha_n + \alpha_R, \quad \text{where} \quad \alpha_n \sim \frac{(1+2\zeta/\mathscr{E}_g)}{T^3[\zeta(1+\zeta/\mathscr{E}_g)]^{1/2}},$$
$$\alpha_R \sim \frac{(1+2\zeta/\mathscr{E}_g)}{cT^2[\zeta(1+\zeta/\mathscr{E}_g)]^{1/2}}. \quad (21)$$

Here, α_n is the phonon thermopower mediated by direct drag and α_R is that due to resistive drag. The experimentally observed temperature dependence of phonon thermopower (Fig. 4) correlates with the dominant part being played by the direct drag, as in Eq. (21).

For dopant concentrations in bismuth of $c > 0.02$ at. % Te, the temperature behavior of phonon thermopower is approximated by the low-temperature model ($T < \Theta_{1e}$):

$$\alpha = \alpha_n + \alpha_R, \quad \text{where} \quad \alpha_n \sim \frac{(1+2\zeta/\mathscr{E}_g)}{T[\zeta(1+\zeta/\mathscr{E}_g)]^{3/2}},$$
$$\alpha_R \sim \frac{(1+2\zeta/\mathscr{E}_g)}{c[\zeta(1+\zeta/\mathscr{E}_g)]^{3/2}}. \quad (22)$$

The temperature dependence of phonon direct-drag thermopower given by Eq. (22) also agrees with the experimental relation plotted in Fig. 5.

According to Eq. (22), at low temperatures, α_n decreases with increasing impurity concentration c, while at high temperatures, according to Eq. (20), α_n increases. As a result of the different concentration dependences of the phonon thermopower, the graphs of the temperature dependence of phonon thermopower

obtained on bismuth with different dopant concentrations cross in the intermediate temperature region, which is in agreement with the experimental data plotted in Fig. 5.

5.2. Phonon Thermopower in the Region of the Temperature of the Maximum

To consider the phonon thermopower below the temperature of the maximum, we assume the phonon scattering to be dominated by the phonon–electron scattering [12] and phonon scattering from sample boundaries:

$$\frac{1}{\tau_{\text{ph}-e}(T)} \cong a_3 T\left(1+\frac{\zeta}{\mathcal{E}_g}\right)^2, \quad \frac{1}{\tau_{\text{ph}-d}} \approx \frac{s}{L}, \tag{23}$$

where s is the sound velocity and L is the transverse size of the sample. Because of the strong nonparabolicity of the bismuth L band, $\tau_{\text{ph}-e}$ contains an indirect concentration dependence. For the phonon thermopower, we obtain the following relation:

$$\alpha \sim \frac{(1+2\zeta/\mathcal{E}_g)}{[\zeta(1+\zeta/\mathcal{E}_g)]^{3/2}} \frac{T^4}{[a_4 + a_5 T(1+\zeta/\mathcal{E}_g)^2]}. \tag{24}$$

The first term in the second denominator in Eq. (24), a_4, is determined by phonon–boundary scattering, and the second term, by phonon–electron collisions. As the temperature increases, the rising temperature dependence of the phonon thermopower should be replaced, according to Eq. (24), by the dropping relation described by Eq. (22). Thus, according to theory, the temperature dependence of the phonon thermopower should pass through a maximum, which is confirmed experimentally (Figs. 4, 5).

If the phonon–electron scattering is insignificant, the temperature of the maximum is concentration-independent and

$$\alpha_{\max} \sim \frac{(1+2\zeta/\mathcal{E}_g)}{[\zeta(1+\zeta/\mathcal{E}_g)]^{3/2}} \sim (n_0 + c)^{-2/3}, \qquad T_{\max} \sim \text{const}. \tag{25}$$

By contrast, if the maximum of the phonon thermopower is dominated by phonon–electron scattering, we have

$$\alpha_{\max} \sim \frac{(1+2\zeta/\mathcal{E}_g)}{\zeta^{3/2}(1+\zeta/\mathcal{E}_g)^2} \sim (n_0 + c)^{-5/6}, \qquad T_{\max} \sim \left(1+\frac{\zeta}{\mathcal{E}_g}\right)^{1/2} \sim (n_0 + c)^{1/6}. \tag{26}$$

Equations (25) and (26) reflect the trend of increasing $T_{\max}$ and decreasing $\alpha_{\max}$ for the phonon thermopower with increasing impurity concentration, and this trend is in accord with the experimental data available for the phonon thermopower of doped bismuth (Figs. 4, 5).

Now, we consider the anisotropy of the phonon thermopower observed experimentally (Fig. 6). According to theory, the main contribution to the phonon thermopower components α_{22} and α_{33} [given by Eqs. (6), (7)] are due to the first terms. Due to elastic anisotropy, these terms are not equal are close in order of magnitude, which does not contradict (and does not corroborate) the noticeable anisotropy observed experimentally.

6. CONCLUSIONS

In doped bismuth, in contrast to pure bismuth, the mechanism of two-step phonon drag of electrons is not realized. The temperature and concentration dependences of the phonon thermopower observed in doped bismuth samples are described by the mechanism of direct phonon drag, with allowance made for phonon scattering through the Landau–Rumer mechanism for transverse phonon branches and through the Simons mechanism for the longitudinal phonon branch. It has been shown that the phonon thermopower calculations using Herring's model for phonon scattering do not correspond with the experimentally observed behavior of the phonon thermopower. At low temperatures, the temperature behavior of the phonon thermopower of doped bismuth reveals a maximum, which also finds explanation. According to theory, the maximum is due to the dominant role of phonon–phonon scattering prevailing for $T > T_{\max}$ being replaced by the predominance of the phonon–electron and phonon–boundary scattering for $T < T_{\max}$. The satisfactory description of the behavior of the phonon thermopower component observed in our doped bismuth samples in terms of direct phonon drag suggests the conclusion that the phonon–phonon collision frequency in such samples does not dominate over that of resistive scattering.

ACKNOWLEDGMENTS

This study was supported in part by the program of support of leading scientific schools, project no. NSh-2200.2003.2.

REFERENCES

1. I. Ya. Korenblit, M. E. Kuznetsov, and S. S. Shalyt, Zh. Éksp. Teor. Fiz. **56** (1), 8 (1969) [Sov. Phys. JETP **29**, 4 (1969)].
2. V. A. Kozlov and É. L. Nagaev, Pis'ma Zh. Éksp. Teor. Fiz. **13** (11), 639 (1971) [JETP Lett. **13**, 455 (1971)].
3. V. A. Kozlov, N. S. Lidorenko, and É. L. Nagaev, Fiz. Tverd. Tela (Leningrad) **15** (5), 1458 (1973) [Sov. Phys. Solid State **15**, 982 (1973)].
4. A. A. Bel'chik and V. A. Kozlov, Fiz. Tekh. Poluprovodn. (Leningrad) **20** (1), 53 (1986) [Sov. Phys. Semicond. **20**, 31 (1986)].

5. V. N. Kopylov and L. P. Mezhov-Deglin, Pis'ma Zh. Éksp. Teor. Fiz. **15** (5), 269 (1972) [JETP Lett. **15**, 188 (1972)].
6. V. N. Kopylov and L. P. Mezhov-Deglin, Zh. Éksp. Teor. Fiz. **65** (8), 720 (1973) [Sov. Phys. JETP **38**, 357 (1973)].
7. É. S. Medvedev, V. N. Kopylov, and L. P. Mezhov-Deglin, Fiz. Nizk. Temp. **1** (9), 1192 (1975) [Sov. J. Low Temp. Phys. **1**, 572 (1975)].
8. V. N. Galev, V. A. Kozlov, N. V. Kolomoets, S. Ya. Skipidarov, and N. A. Tsvetkova, Pis'ma Zh. Éksp. Teor. Fiz. **33** (2), 112 (1981) [JETP Lett. **33**, 106 (1981)].
9. J.-P. Issi and J. Hermans, in *Proceedings of XV International Conference on Thermal Conductivity* (Ottawa, 1977), p. 63.
10. V. D. Kagan, N. A. Red'ko, N. A. Rodionov, and V. I. Pol'shin, Zh. Éksp. Teor. Fiz. **122** (2), 377 (2002) [JETP **95**, 325 (2002)].
11. V. D. Kagan, N. A. Red'ko, N. A. Rodionov, and V. I. Pol'shin, Fiz. Tverd. Tela (St. Petersburg) **42** (8), 1376 (2000) [Phys. Solid State **42**, 1414 (2000)].
12. N. A. Red'ko and V. D. Kagan, Fiz. Tverd. Tela (St. Petersburg) **36** (7), 1978 (1994) [Phys. Solid State **36**, 1081 (1994)].

Translated by G. Skrebtsov

Physics of the Solid State, Vol. 46, No. 8, 2004, pp. 1420–1424. Translated from Fizika Tverdogo Tela, Vol. 46, No. 8, 2004, pp. 1381–1385.
Original Russian Text Copyright © 2004 by Belyaev, Gritskikh, Zhikharev, Kara-Murza, Korchikova.

Mixed (Ionic and Hole) Conductivity of Tl_3VS_4 Crystals

B. V. Belyaev*, V. A. Gritskikh*, I. V. Zhikharev, S. V. Kara-Murza*, and N. V. Korchikova***

** Shevchenko National Pedagogical University, Lugansk, 91011 Ukraine*

*** Donetsk Physicotechnical Institute, National Academy of Sciences of Ukraine, Donetsk, 83055 Ukraine*

e-mail: mark@bm.dsip.net

Received November 10, 2003

Abstract—A model of mixed (ionic and hole) conductivity in Tl_3VS_4 crystals at close-to-room temperatures is proposed. The significant fraction of the ionic conductivity component (~70% of the total conductivity) is explained by the nonstoichiometric electrically active thallium vacancies, whose acceptor levels provide *p*-type conductivity. The characteristic time dependence of the voltage developing across a sample due to its polarization and depolarization is described using the diffusion theory of mixed conductivity previously developed by Yokota. The charge transport phenomena in Tl_3VS_4 are studied experimentally, and the data are processed according to the theoretical model. *© 2004 MAIK "Nauka/Interperiodica".*

1. INTRODUCTION

Crystals of the $Tl_3B^VC_4^{VI}$ type (B^V is V, Nb, Ta; C^{VI} is S, Se), belonging to the space symmetry group $I\bar{4}3m$, were synthesized, grown, and described for the first time by Crevecouer in 1964 [1]. Subsequent papers in the 1970s were mostly devoted to experimental studies of their electric and optical properties. Emphasis was placed on Tl_3VS_4 crystals as the most prominent representative of the class mentioned above. In the mid-1980s, the interest in Tl_3VS_4 sharply increased due to the discovery of unique properties in this compound, namely, a pronounced piezoelectric effect at low velocities of slow elastic waves (800–1000 m/s) and a low electrical conductivity [2–4]. Furthermore, it was in Tl_3VS_4 crystals that the crystallographic planes and polarizations of surface acoustic waves (SAWs) with zero temperature coefficients of velocity were identified. This suggested promising application of this material in acoustoelectronic devices. Due to the increased interest expressed by developers of SAW-based electronic equipment in Tl_3VS_4 and other compounds of this class, a significant number of studies were devoted to the problems of growth of large single crystals and the development of filters and delay lines based on them using SAWs [2, 3, 5]. However, the application of Tl_3VS_4 crystals encountered many difficulties, such as nonreproducible and unstable parameters of the SAW-based devices, changes in the condition of the substrate surface, and the switching effect (a sharp decrease in the resistivity almost to zero followed by its partial recovery). These phenomena (in addition to the small elastic constant C_{44} and its positive temperature coefficient) and the features of the temperature dependence of the dc and ac conductivity [6–8] suggest a significant influence of thallium ions on the properties of these materials. Our calculations showed that the ionicity of the Tl^+–$(VS_4)^{3-}$ bond is 75% [9]. From direct measurements of mass transfer, it was concluded in [10] that the ionic component accounts for 85% of the total Tl_3VS_4 conductivity at 30°C. However, despite a significant number of studies into the Tl_3VS_4 conductivity mechanism, a convincing model of charge transfer in crystals of this compound has not yet been developed.

In this paper, we propose a model of the mixed conductivity in Tl_3VS_4 at close-to-room temperatures. Furthermore, we report new experimental results and a number of quantitative characteristics of the charge transport phenomena in Tl_3VS_4.

2. MODEL OF THE MIXED CONDUCTIVITY OF Tl_3VS_4

Since Tl_3VS_4 exhibits an appreciable ionic conductivity already at room temperature, we may assume that this conductivity is not associated with thermally activated structural defects. The features of Tl_3VS_4 growth (an excess of sulfur relative to the stoichiometric composition) suggest the existence of electrically active Tl vacancies, whose acceptor levels provide *p*-type conductivity. Indeed, it is unlikely that interstitial sulfur ions exist in the close-packed Tl_3VS_4 structure; $(VS_4)^{3-}$ complex anions form a bcc lattice, and Tl^+ ions are at the centers of faces and edges of the cubic elementary cell. There are crystallographic directions ([200] and those equivalent to this direction) in which thallium ions form linear chains, and vacancies provide facilitated motion of mobile thallium ions along these channels. We note that the ionic conductivity in isostructural Cu_3VS_4 compounds was explained in [11] by the presence of interstitial Cu^+ ions. We believe this explanation to be inconsistent for Tl_3VS_4, since Cu_3VS_4 crystallizes

1063-7834/04/4608-1420$26.00 © 2004 MAIK "Nauka/Interperiodica"

in the simple cubic $P\bar{4}3m$ structure, whereas Tl_3VS_4 crystallizes in the close-packed $I\bar{4}3m$ structure. Moreover, the Tl^+ ion radius significantly exceeds that of the Cu^+ ion.

Distinctive features of the direct current flowing in mixed-conductivity semiconductors are a noticeable time dependence of the potential distribution along the sample and nonlinearity of this distribution. It should be noted that, under these conditions, measurements should be carried out without any irreversible processes; i.e., the current intensity must be insufficient for electrolytic deposition of ions on electrodes. These features are described well in terms of the diffusion theory of mixed conductivity developed by Yokota [12]. This theory is based on the electrical quasi-neutrality concept; i.e., any local change in the concentration of mobile charges of one type must be compensated by a corresponding change in the concentration of mobile charges of other types. In general, the condition of electrical quasineutrality imposed on the equilibrium charge concentrations for Tl_3VS_4 crystals can be written in the form

$$n_h + N_{i^+} = N_{A^-} + n_{v^-} + n, \qquad (1)$$

where n_h is the hole concentration in the valence band, N_{i^+} is the concentration of ionized donor levels of interstitial thallium atoms, N_{A^-} is the concentration of ionized shallow acceptor levels of impurities, n_{v^-} is the concentration of ionized acceptor levels of thallium vacancies, and n is the electron concentration in the conduction band.

We assume that thermal activation of defects can be neglected near room temperature. Moreover, the quantities n and N_{A^-} can also be neglected in the temperature range under consideration, since the intrinsic conductivity is not yet excited and shallow acceptor levels are completely ionized but $N_A \ll n_v$ [8]. Then, Eq. (1) takes on the form

$$n_h \cong n_{v^-}, \qquad (2)$$

with

$$n_{v^-} \cong \alpha n_v, \qquad (3)$$

where n_v is the equilibrium concentration of thallium vacancies. The coefficient α depends only on temperature and is defined by the conventional expression

$$\alpha = \left(\frac{N_v}{V g_v}\exp(E_a/kT) + 1\right)^{-1}, \qquad (4)$$

where N_v is the number of nonstoichiometric Tl vacancies in the sample, V is the sample volume, E_a is the activation energy of acceptor vacancy levels, and g_v is the density of states in the valence band.

As a weak external electric field is applied, the concentration of vacancies and, hence, that of holes become functions of the coordinates and time that differ from the equilibrium values of n_v and n_h. For a sample in the form of a thin bar, we introduce the nonequilibrium concentrations

$$\tilde{n}_v = n_v(x, t), \quad \tilde{n}_h = n_h(x, t), \qquad (5)$$

where the x coordinate is measured from the positive electrode. In this notation, the electrical quasi-neutrality condition for any sample point at any instant of time can be written as

$$\tilde{n}_h = \alpha \tilde{n}_v. \qquad (6)$$

We note that the coefficient α depends only on temperature in this case as well [see Eq. (4)].

In terms of diffusion theory, the charge transport in mixed-conductivity semiconductors is described by the equations for the current densities

$$J = J_i + J_h, \qquad (7)$$

$$J_i = -\frac{\tilde{n}_v \mu_i}{e}\nabla\eta_i = e\tilde{n}_v\mu_i E + \mu_i kT\frac{\partial n_v}{\partial x}, \qquad (8a)$$

$$J_h = -\frac{\tilde{n}_h \mu_h}{e}\nabla\eta_h = e\tilde{n}_h\mu_h E + \mu_h kT\frac{\partial \tilde{n}_h}{\partial x} \qquad (8b)$$

and the continuity equations for vacancies

$$\frac{\partial \tilde{n}_v}{\partial t} = \frac{1}{e}\frac{\partial J_i}{\partial x}. \qquad (9)$$

In Eqs. (7)–(9), J_i and J_h are the ionic and hole components of the current density J; η_i and η_h are the electrochemical potentials of ions and holes, respectively; μ_i and μ_h are the mobilities of ions and holes, respectively, which are considered independent of the coordinate and time under weakly nonequilibrium conditions; and E is the electric field, which is almost uniform at low currents.

In Eqs. (8a) and (8b), the Einstein relation for the diffusivity $D = \mu kT/e$ is used.

In the case of electron electrodes, the voltage across the sample is defined by the difference in the electrochemical potentials for holes. By eliminating E from Eqs. (7) and (8) and taking into account relations (3) and (6), one can derive the following expression for the voltage U under the condition $J = \text{const}$:

$$U = \frac{\eta_h(0, t) - \eta_h(L, t)}{e} = \frac{J}{\sigma_i + \sigma_h}\int_0^L \frac{dx}{\tilde{n}_v/n_v} + \frac{2kT}{e}\frac{\sigma_i}{\sigma_i + \sigma_h}\ln\frac{\tilde{n}_v(0, t)}{\tilde{n}_v(L, t)}, \qquad (10)$$

where $\sigma_i = en_v\mu_i$ and $\sigma_h = en_h\mu_h$ are the ionic and hole conductivities, respectively, with $\sigma_i + \sigma_h = \sigma$ being the total conductivity of the material.

In turn, $\tilde{n}_v$ is a solution to Eq. (9), which, after certain substitutions, can be reduced to a diffusion equation with the initial conditions

$$\tilde{n}_v(x, 0) = n_v, \quad \tilde{n}_h(x, 0) = n_h$$

and the boundary conditions at the electron electrodes defined by the absence of electrolytic deposition of the ions,

$$J_i(0, t) = J_i(L, t) = 0.$$

In this case,

$$\frac{\tilde{n}_v}{n_v} = 1 - 2A\left[\left(\frac{x}{L} - \frac{1}{2}\right) + F\left(\frac{t}{\tau}, \frac{x}{L}\right)\right], \quad (11)$$

where

$$A = \frac{eJL}{4kT\sigma_h},$$

$$F\left(\frac{t}{\tau}, \frac{x}{L}\right) = \frac{4}{\pi^2}\sum_{m=0}^{\infty}(2m+1)^2 \exp\left[-(2m+1)^2\frac{t}{\tau}\right] \times \cos\left[(2m+1)\pi\frac{x}{L}\right]. \quad (12)$$

The characteristic time τ is related to the ion diffusivity D_i as

$$D_i = \frac{L^2\sigma}{2\pi^2\tau\sigma_h}, \quad (13)$$

and the theory parameter A should be less than unity, as follows from the positiveness condition imposed on $\tilde{n}_v$ in Eq. (11). Thus, in the measurements, the current density J should satisfy the condition

$$\frac{eJL}{4kT\sigma_h} < 1. \quad (14)$$

Under steady-state conditions ($t \longrightarrow \infty$), we have

$$\frac{\tilde{n}_v}{n_v} = 1 - 2A\left(\frac{x}{L} - \frac{1}{2}\right), \quad (15)$$

and the voltage across the sample is given by

$$U_{st} = \frac{2kT}{e}\frac{\sigma_h}{\sigma_i + \sigma_h}\ln\frac{1+A}{1-A} + \frac{2kT}{e}\frac{\sigma_i}{\sigma_i + \sigma_h}\ln\frac{1+A}{1-A} = \frac{2kT}{e}\ln\frac{1+A}{1-A}. \quad (16)$$

We note that, in Eq. (16), the first term is the ohmic part and the second term is due to ion (vacancy) redistribution.

As the current is turned off (depolarization conditions), the voltage initially drops abruptly to the value

$$U_{d0} = \frac{2kT}{e}\frac{\sigma_i}{\sigma_i + \sigma_h}\ln\frac{1+A}{1-A}, \quad (17)$$

and then slowly decreases to zero following the law

$$U_d(t) = \frac{2kT}{e}\frac{\sigma_i}{\sigma_i + \sigma_h}\ln\frac{\tilde{n}(0, t)}{\tilde{n}_v(L, t)}, \quad (18)$$

where, as before, $\tilde{n}_v(x, t)$ is the solution to the diffusion equation, but now in the absence of current in the external circuit and with the initial voltage U_{d0} across the sample:

$$\frac{\tilde{n}_v(x, t)}{n_v} = 1 + 2AF\left(\frac{x}{L}, \frac{t}{\tau}\right). \quad (19)$$

Thus, by studying the time dependence of the voltage on the sample under polarization conditions (J = const) followed by depolarization ($J = 0$) at various temperatures, one can determine the basic characteristics of charge transport in the sample. For example, the parameter A (and, hence, σ_h) can be determined from Eq. (16) and the ratio $\sigma_i/(\sigma_i + \sigma_h)$ and, hence, σ_i can be found from Eqs. (16) and (17):

$$\frac{\sigma_i}{\sigma_i + \sigma_h} = \frac{U_{d0}}{U_{st}}. \quad (20)$$

In the depolarization regime, the characteristic time τ and diffusivity D can be easily determined using tabulated values of $F(x/L; t/\tau)$ [12] and Eq. (18). Knowing the values of σ_h, σ_i, and D_i, one can determine μ_i and then n_v, n_h, and μ_h. From the temperature dependences of these quantities, one can find the corresponding activation energies.

3. EXPERIMENTAL RESULTS

The applicability of the proposed model of charge transport in Tl_3VS_4 near room temperature was determined by the absence of intrinsic-defect conductivity. To this end, the temperature dependence of the specific heat of Tl_3VS_4 was studied up to the melting point at a fixed pressure (Fig. 1). The sharp increase in the specific heat at $T \geq 400°C$ is caused by absorption of the energy expended for the generation of statistically equilibrium defects. From the slope of the characteristic dependence $\ln(T^2\Delta C)$ on the inverse temperature (Fig. 2), the activation energy for intrinsic defects was found to be $W \cong 4.5$ eV. We can see in Fig. 1 that the temperature range of intrinsic-defect conductivity excitation is much higher than room temperature and seems to coincide with the excitation range of the intrinsic electronic conductivity ($W/2 \cong E_g$, where $E_g = 1.9$ eV is the band gap in Tl_3VS_4 [1, 8, 10]). Thus, the ionic component of the room-temperature conductivity of Tl_3VS_4 is caused by temperature-independent defects due to a

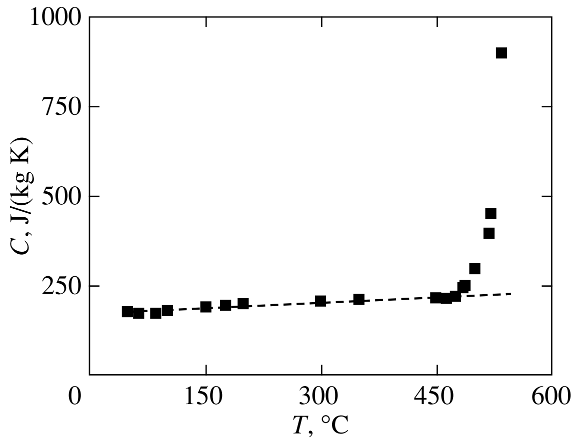

Fig. 1. Temperature dependence of the specific heat of Tl_3VS_4 at a fixed pressure.

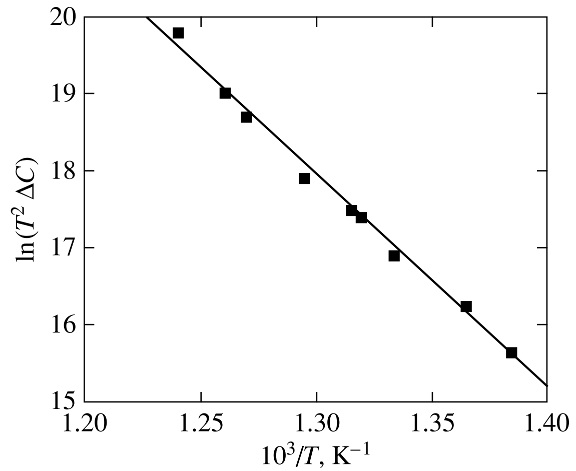

Fig. 2. Dependence of $\ln(T^2\Delta C)$ on inverse temperature.

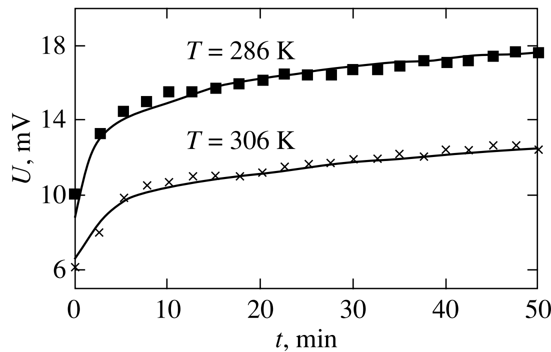

Fig. 3. Time dependence of the polarization voltage across the Tl_3VS_4 sample. Solid curves represent calculations.

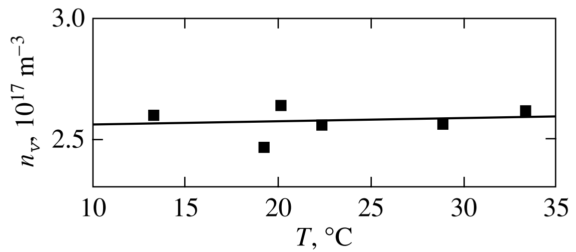

Fig. 4. Temperature dependence of the vacancy concentration.

deviation from stoichiometry (which arises in the course of the material fabrication) rather than by thermal excitation of defects.

The mixed-conductivity parameters were experimentally studied under dc conditions, $J \cong 5 \times 10^{-8}$ A/m^2. A sample in the form of a thin bar of length $L = 16$ mm with a cross section of 2×2 mm was placed into a vacuum thermostat, whose temperature was maintained constant by a temperature controller with an accuracy of 0.1 K. Ohmic contacts were deposited onto sample ends through thermal evaporation of aluminum in vacuum. The dc conditions were maintained using a load resistor with $R = 2 \times 10^{10}$ Ω ($R_{\rm load} \gg R_{\rm sample}$). The voltage on the sample was fed to an electrometric amplifier and then measured using an electronic recording potentiometer. The time dependence of the voltage on the sample was measured in the polarization (J = const) and depolarization ($J = 0$) regimes in the temperature range 280–306 K.

By processing the experimental curves of polarization and depolarization according to the above technique, we determined the main characteristics of charge transport in Tl_3VS_4. The table lists these characteristics for $T = 300$ K, Fig. 3 shows the polarization curves for $T = 286$ and 306 K, and Fig. 4 shows the temperature dependence of the vacancy concentration n_v.

Characteristics of the charge transport in Tl_3VS_4

σ_i, 10^{-7} Ω^{-1} m^{-1}	σ_h, 10^{-7} Ω^{-1} m^{-1}	σ, 10^{-7} Ω^{-1} m^{-1}	σ_i/σ	$\tilde{n}_v \cong n_h$, 10^{17} m^{-3}	μ_i, 10^{-6} m^2 s^{-1} V^{-1}	μ_h, 10^{-7} m^2 s^{-1} V^{-1}	D_i, 10^{-8} m^2 s^{-1}
1.28	0.55	1.8	0.7	6.6	1.9	5	5

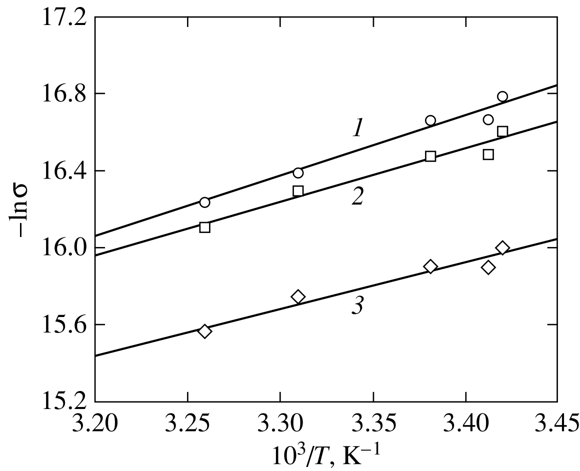

Fig. 5. Dependence of conductivity on inverse temperature: (*1*) hole component, (*2*) ionic component, and (*3*) total conductivity.

It is noteworthy that n_v is virtually temperature-independent and $n_h \cong n_v$ in the entire temperature range under consideration, which confirms the validity of the proposed model of charge transport, namely, the statistical relation between the electronic subsystem and the subsystem of defects due to a deviation from stoichiometry. The increase in diffusivity D_i with temperature leads to an exponential dependence of the ion mobility and, hence, of the ionic conductivity component σ_i (Fig. 5). Figure 5 also shows the dependences of the hole and total conductivities on inverse temperature. Since $n_h \cong n_v$, the exponential growth of σ_h is caused only by the corresponding increase in the hole mobility μ_h. This means that the *p*-type hole conductivity in Tl_3VS_4 near room temperature is hopping in character. The activation energies for the hole, ionic, and total conductivities are almost identical and equal to ≅0.25 eV, which is in good agreement with the values previously obtained using alternative methods [8, 10, 12]; the fraction of the ionic component $\sigma_i/\sigma = 0.7$ also agrees well with the data from [8].

The authors hope this paper will revive interest in $Tl_3B^{V}C_4^{VI}$ compounds and stimulate possible applications with them.

REFERENCES

1. C. Crevecouer, Acta Crystallogr. **17**, 757 (1964).
2. T. J. Isaacs, M. Gottlieb, and M. R. Daniel, J. Electron. Mater. **4**, 67 (1975).
3. M. Gottlieb, T. J. Isaacs, J. D. Feitchner, and G. J. Roland, Appl. Phys. **45** (12), 5145 (1974).
4. B. V. Belyaev, S. V. Kara-Murza, and V. P. Rombakh, Ukr. Fiz. Zh. **23** (6), 1038 (1978).
5. T. I. Golovnina, V. N. Zubov, and S. V. Kara-Murza, in *Proceedings of 11th All-Union Conference on Acoustic Electronics and Quantum Acoustics* (Dushanbe, 1981), Part 2, p. 243.
6. V. A. Gritskikh, S. V. Kara-Murza, V. A. Korotun, and A. L. Rapoport, in *Abstracts of 1st All-Union Conference on Materials of Optoelectronics* (Uzhgorod, 1980), p. 78.
7. V. I. Valyukenas, V. M. Rubish, V. V. Khiminets, I. D. Turyanitsa, V. F. Mikuchenis, and S. B. Aukyalis, in *Proceedings of 3rd Scientific Seminar on Ionics of Solids* (Vilnius, 1984), p. 55.
8. B. V. Belyaev and V. P. Rombakh, in *Solid State Physics* (Kiev, 1975), No. 5, p. 40.
9. S. V. Kara-Murza and V. P. Rombakh, in *Abstracts of 1st All-Union Conference on Actual Problems of Production and Application of Ferro- and Piezoelectric Materials* (Moscow, 1981), p. 155.
10. K. Wacher and P. Buck, Z. Kristallogr. **172**, 121 (1985).
11. H. Arribart and B. Sapoval, Electrochem. Acta **24**, 751 (1979).
12. I. Yokota, J. Phys. Soc. Jpn. **16** (11), 2213 (1961).

Translated by A. Kazantsev

Physics of the Solid State, Vol. 46, No. 8, 2004, pp. 1425–1431. Translated from Fizika Tverdogo Tela, Vol. 46, No. 8, 2004, pp. 1386–1392.
Original Russian Text Copyright © 2004 by Malashkevich, Semkova, Stupak, Sukhodolov.

SEMICONDUCTORS AND DIELECTRICS

Silica Gel Glasses with a High Efficiency of Luminescence Sensitization in the Ce^{3+}–Tb^{3+} System

G. E. Malashkevich, G. I. Semkova, A. P. Stupak, and A. V. Sukhodolov

Institute of Molecular and Atomic Physics, Belarussian Academy of Sciences, pr. F. Skoriny 70, Minsk, 220072 Belarus

e-mail: malash@imaph.bas-net.by

Received October 27, 2003

Abstract—Terbium- and (Ce, Tb)-containing glasses prepared using the direct sol–gel–glass transition are studied. It is shown that glasses doped with one activator contain two main types of optical centers, namely, isolated and complex centers, which are characterized by weak and strong cross-relaxation quenching of luminescence from the $^5D_3$ state of Tb^{3+} ions, respectively. The Ce^{4+}–Tb^{3+} (Tb^{4+}) complex centers are formed during sintering of coactivated xerogels in oxygen and can be transformed into Ce^{3+}–Tb^{3+} centers through saturation of the samples with hydrogen. The Ce^{3+}–Tb^{3+} centers exhibit efficient luminescence from the $^5D_4$ state upon excitation into the absorption bands of Ce^{3+} ions. *© 2004 MAIK “Nauka/Interperiodica”.*

1. INTRODUCTION

For many decades, particular interest has been expressed by researchers in glasses activated with Tb^{3+} ions due to their extensive use as materials for fabricating various optical reradiators and cathodoluminescent screens [1–6]. The main features of luminescence in these materials have already been established. In particular, it has been found that, at high activator contents, the cross-relaxation quenching of luminescence from the $^5D_3$ state proceeds according to the $Tb^{3+}(^5D_3 \longrightarrow {}^7F_{0,1})$–$Tb^{3+}(^7F_6 \longrightarrow {}^5D_4)$ and $Tb^{3+}(^5D_3 \longrightarrow {}^5D_4)$–$Tb^{3+}(^7F_6 \longrightarrow {}^7F_{0,1})$ schemes with excitation of the $^5D_4$ state [6–8]. However, the important problem of increasing the light output of terbium-containing glasses upon UV excitation still remains unsolved. The point is that the light output of these materials is limited by the occurrence of intense absorption bands in the high-frequency range due to the $4f^8 \longrightarrow 4f^7(^8S_{7/2})5d^1(T_2)$ and $4f^7(^8S_{7/2})5d^1(E)$ interconfigurational transitions [6] and a relatively low efficiency of excitation transfer from the luminescence sensitizers. For example, when Ce^{3+} [9, 10] and Sn^{2+} [3] ions are used as luminescence sensitizers, the efficiency of excitation transfer does not exceed 40 and 20%, respectively.

In this work, we attempted to solve the above problem for silica gel glasses by way of producing Ce–O–Tb chains with a nearly collinear configuration that provides a maximum overlap of “optical” orbitals of energy donors and energy acceptors [7]. As is known [11–15], such a configuration can be formed in Ce^{4+}–Ln^{3+} complex centers, i.e., CeO_2 nanoparticles in which Ce^{4+} ions are partially replaced by Ln^{3+} ions [16]. In our earlier work [17], we showed that, in the case when silica glasses containing similar complex centers are saturated with hydrogen at relatively low temperatures ($T \leq 1000°C$), the Ce^{4+} ions are completely reduced to Ce^{3+} without relaxation of their local environment to an equilibrium configuration with a new charge state. This makes it possible to create conditions for the most efficient intracenter sensitization of luminescence by labile photoreduced ions $(Ce^{4+})^-$ [11–15] and their stable analogs. Moreover, we elucidated the concentration features of the spectroscopic behavior of Tb^{3+} ions in silica gel glasses.

2. SAMPLE PREPARATION AND EXPERIMENTAL TECHNIQUE

Samples were prepared using the direct sol–gel–glass transition according to the procedure described in [12]. The glasses were activated by impregnating porous xerogels[1] with solutions of cerium and terbium oxides at different activator contents C_{Ln} in H_2SO_4 + HCl + H_2O. All the reactants used were of reagent grade. The terbium-containing glasses were sintered in air, whereas the coactivated glasses were sintered predominantly in oxygen in order to decrease the fraction of Ce^{4+}–O–Ce^{3+} groups (cerium-containing clusters) absorbing in the visible range [18]. In all cases, the sintering temperature was equal to 1250°C. The coactivators were reduced by annealing the prepared glasses in hydrogen at a temperature $T \approx 950°C$.

The absorption spectra were recorded on a Cary-500 spectrophotometer in the form of the dependence of the absorption coefficient k on the wavelength λ. The luminescence spectra and luminescence excitation spectra were measured on an SDL-2 spectrofluorimeter and were then corrected for the spectral sensitivity of the

[1] We are grateful to B.V. Plyushch for synthesizing the xerogels used in our experiments.

recording system and spectral density of exciting radiation, respectively [19]. These spectra were normalized to unity at the maximum of the intensity and represented as the dependence of the number of photons per unit range of wavelengths $dN/d\lambda$ on the wavelength λ. In order to reduce the reabsorption and luminescence quenching, the frontal excitation was used for coactivated samples and, if required, their thickness was decreased to 100 µm. The barycenters of complex spectral contours were calculated from their moments according to the standard formula $\bar{\nu} = \int \nu k(\nu) d\nu / \int k(\nu) d\nu$, where ν is the wave number. The luminescence kinetics was investigated with the use of an S9-8 digital oscilloscope upon excitation of the third (λ = 355 nm) and fourth (λ = 266 nm) harmonics of a single-pulse neodymium laser. The time constant of the measuring circuit did not exceed 0.02 of the mean time of the process under investigation. The mean time of luminescence decay was calculated from the relationship $\bar{\tau} = I_{max}^{-1} \int I(t) dt$. The quantum yield of luminescence η for Tb^{3+} ions was determined by the comparative method [19]. The tin-containing glass was used as a reference sample. The quantum yield of luminescence η for the tin-containing glass was determined using the absolute method [20]. All spectral measurements were performed at T = 298 K.

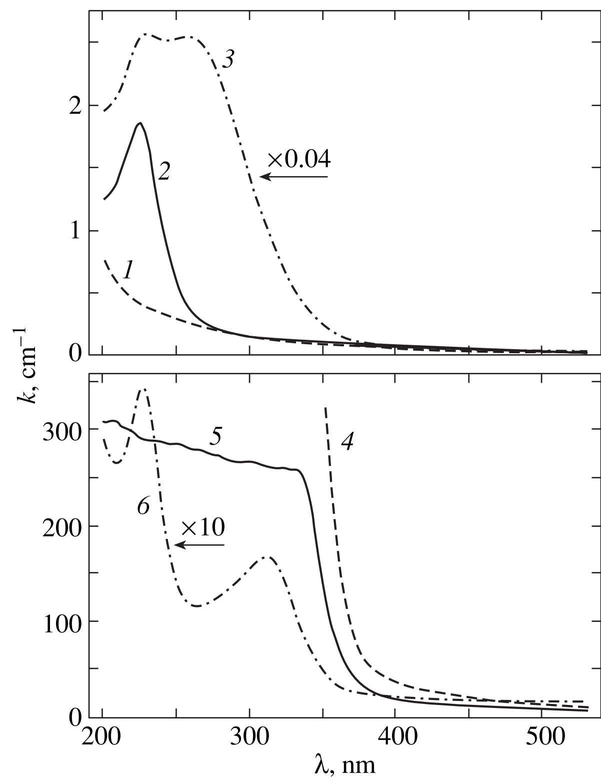

Fig. 1. Absorption spectra of (*1*) undoped, (*2*) Tb-containing, and (*3–6*) (Ce, Tb)-containing glasses sintered in (*1–3*, *6*) air or (*4*, *5*) oxygen (*4*) before and (*5*, *6*) after annealing in hydrogen. C_{Ce} = (*3*, *6*) 1.0 and (*4*, *5*) 4.0 wt %. C_{Tb} = (*2–6*) 1.0 wt %.

3. RESULTS

The absorption spectra of Tb- and (Ce, Tb)-containing glasses are depicted in Fig. 1. For comparison, this figure shows the absorption spectrum of the nonactivated glass (curve *1*). It can be seen that the spectrum of the terbium-containing glass (C_{Tb} = 1 wt %) exhibits a broad structureless band with the maximum at a wavelength $\lambda \approx$ 225 nm (curve *2*). The shape of the structureless band is virtually independent of the activator content C_{Tb}, whereas the intensity of this band varies proportionally with C_{Tb} in the range 0.1–3.0 wt %. The spectrum of the coactivated glass ($C_{Ce} = C_{Tb}$ = 1.0 wt %) sintered in air contains one more intense broad band at a wavelength $\lambda \approx$ 260 nm (curve *3*). A fourfold increase in the cerium content in the coactivated glass upon sintering in oxygen is accompanied by a multiple increase in the intensity of absorption at λ < 400 nm and gives rise to a relatively weak absorption in the long-wavelength range (curve *4*), which imparts a brown hue to the glass. Annealing of this glass in hydrogen brings about the disappearance of absorption at λ > 400 nm and a considerable decrease in the intensity of the UV band absorption (curve *5*). Annealing of the glass at an activator content $C_{Ce} = C_{Tb}$ = 1.0 wt % in hydrogen leads to the appearance of a deep spectral dip at wavelength $\lambda \approx$ 260 nm (curve *6*).

The luminescence spectra of the Tb- and (Ce, Tb)-containing glasses are shown in Fig. 2. It can be seen from this figure that the spectrum of the terbium-containing glass (C_{Tb} = 0.1 wt %) measured at the excitation wavelength λ_{exc} = 220 nm (curve *1*) consists of a series of narrow bands in the UV and visible ranges due to transitions from the $^5D_3$ and $^5D_4$ states [8]. An increase in the terbium content C_{Tb} to 3.0 wt % is attended by a multiple decrease in the intensity of the luminescence bands associated with the $^5D_3 \longrightarrow {}^7F_j$ transition, a substantial redistribution of their relative intensities, and a small shift in the barycenters toward the short-wavelength range (curve *2*). A shift in the excitation wavelength λ_{exc} from the maximum to the UV absorption band edge for the glass at an activator content C_{Tb} = 0.1 wt % leads to a noticeable decrease (by approximately 20%) in the relative intensity of the bands attributed to the $^5D_3 \longrightarrow {}^7F_j$ transition. The luminescence spectrum of the coactivated glass (C_{Ce} = 4.0 wt %, C_{Tb} = 1.0 wt %) measured at the excitation wavelength λ_{exc} = 330 nm (curve *3*) exhibits a broad band with the maximum at a wavelength $\lambda \approx$ 450 nm. Moreover, it can be seen that the long-wavelength wing of this band overlap with the narrow bands associated with the $^5D_4 \longrightarrow {}^7F_j$ transition. Annealing of the glass at activator contents C_{Ce} = 4.0 wt % and C_{Tb} = 1.0 wt %

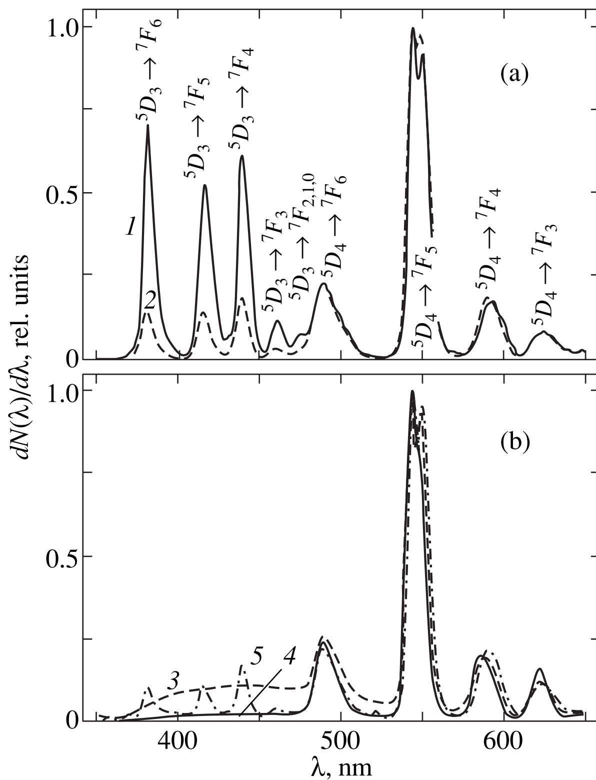

Fig. 2. Corrected normalized luminescence spectra of (a) Tb-containing glasses sintered in air and (b) (Ce, Tb)-containing glasses sintered in oxygen (*1–3*) before and (*4*, *5*) after annealing in hydrogen. C_{Tb} = (*1*) 0.1, (*2*) 3.0, and (*3–5*) 1.0 wt %. C_{Ce} = (*3*, *4*) 4.0 and (*5*) 1.0 wt %. λ_{exc} = (*1*, *2*, *5*) 220 and (*3*, *4*) 330 nm. $\Delta\lambda_{exc}$ = 5 nm. $\Delta\lambda_{rec}$ = 1 nm.

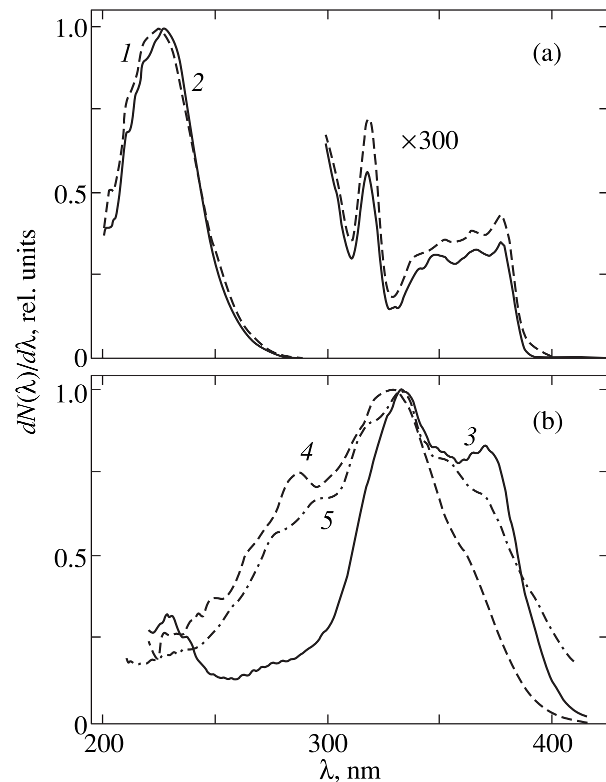

Fig. 3. Corrected normalized luminescence excitation spectra of (a) Tb-containing glasses sintered in air and (b) (Ce, Tb)-containing glasses sintered in oxygen (*1–3*) before and (*4*, *5*) after annealing in hydrogen. C_{Tb} = (*1*, *2*) 0.1 and (*3–5*) 1.0 wt %. C_{Ce} = (*3–5*) 4.0 wt %. λ_{rec} = (*1*, *3*, *4*) 545, (*2*) 438, and (*5*) 450 nm. $\Delta\lambda_{exc} = \Delta\lambda_{rec}$ = 5 nm.

in hydrogen results in a considerable decrease in the relative intensity of the broad band (λ_{exc} = 330 nm) and an insignificant redistribution and a change in the location and shape of the narrow bands (curve *4*). A variation in the excitation wavelength λ_{exc} in the range of the UV absorption band of this glass is accompanied only by a small redistribution of the relative intensities of the spectral bands. A decrease in the cerium content in the hydrogen-saturated coactivated glass to 1.0 wt % does not affect the shape of the luminescence spectrum but leads to an increase in the fraction of photons emitted within the broad band at wavelength $\lambda \approx 450$ nm (λ_{exc} = 330 nm) and the appearance of weak bands associated with the $^5D_3 \longrightarrow {}^7F_j$ transition at λ_{exc} = 220 nm (curve *5*).

Figure 3 shows the luminescence excitation spectra of Tb- and (Ce, Tb)-containing glasses. As can be seen from Fig. 3, the spectrum of the terbium-containing glass with an activator content C_{Tb} = 0.1 wt % at the recording wavelength λ_{rec} = 545 nm consists of an intense broad band at $\lambda_{max} \approx 225$ nm and a number of weak narrow bands at $\lambda > 300$ nm (curve *1*). Upon recording the spectra at λ_{rec} = 438 nm, the barycenter of the intense band is substantially shifted (by approximately 2 nm or 350 cm^{-1}) toward the short-wavelength range and the contour of the narrow bands in the long-wavelength range transforms insignificantly (curve *2*). An increase in the terbium content to 3.0 wt % does not result in a radical change in the luminescence excitation spectra. A variation in the recording wavelength λ_{rec} within the most intense bands of luminescence also has no noticeable effect on the luminescence excitation spectra. In the luminescence excitation spectrum of the coactivated glass (C_{Ce} = 4.0 wt %, C_{Tb} = 1.0 wt %) at the recording wavelength λ_{rec} = 545 nm (curve *3*), there arises a new relatively intense broad double-peaked band with a barycenter at $\lambda \approx 550$ nm. After annealing of the coactivated glass in hydrogen, this band transforms into a broad weakly structured band with the maximum at $\lambda \approx 330$ nm (curve *4*). The excitation spectrum of the broadband luminescence of this glass at λ_{rec} = 450 nm (curve *5*) differs from spectrum *4* primarily in the substantial increase in the intensity of the long-wavelength wing. As the cerium content decreases to 1.0 wt %, the spectrum of the annealed coactivated glass becomes similar to spectrum *6* in Fig. 1 in outline; i.e., it resembles the absorption spectrum.

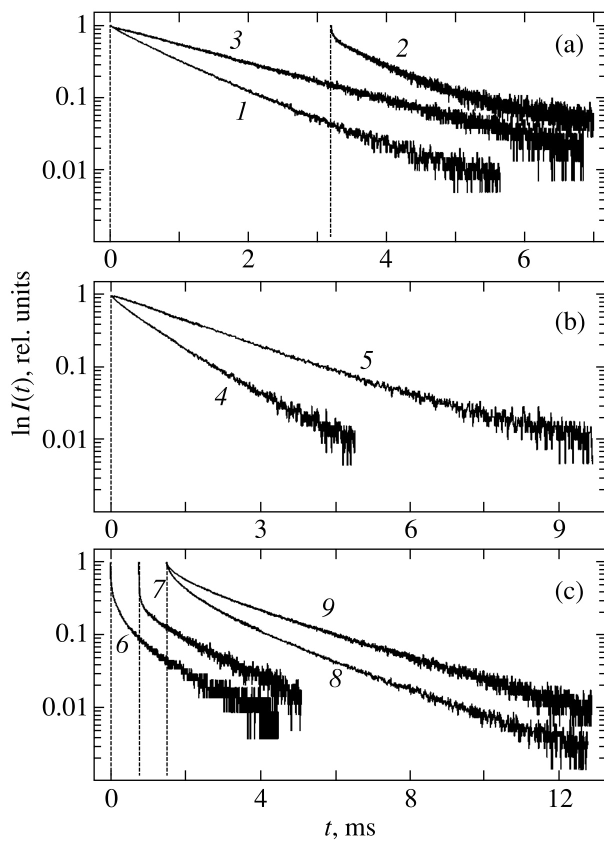

Fig. 4. Decay kinetics of luminescence in (a, b) Tb- and (c) (Ce, Tb)-containing glasses (*1–7*) before and (*8*, *9*) after annealing in hydrogen. C_{Tb} = (*1–3*) 0.1, (*4*, *5*) 3.0, and (*6–9*) 1.0 wt %. C_{Ce} = (*6–9*) 4.0 wt %. λ_{exc} = (*1*, *4*, *5*, *7*, *9*) 266 and (*2*, *3*, *6*, *8*) 355 nm. λ_{rec} = (*1*, *2*, *4*) 380 and (*3*, *5–9*) 545 nm. $\Delta\lambda_{exc}$ = 0.1 nm. $\Delta\lambda_{rec}$ = 5 nm. Curves *1–5* and *6–9* are measured with delay times of 1 and 10 μs after excitation, respectively. Dashed lines indicate the instants of excitation.

The decay kinetics of luminescence of trivalent terbium ions in the Tb- and (Ce, Tb)-containing glasses is illustrated in Fig. 4. It should be noted that complete suppression of the scattered exciting radiation presents considerable difficulties. Moreover, in this case, it is necessary to cut off the luminescence of cerium ions. For these reasons, the decay kinetics of luminescence for the monoactivated and coactivated glasses was measured at delay times of 1 and 10 μs, respectively. It can be seen from Fig. 4 that, in the terbium-containing glass (C_{Tb} = 0.1 wt %) at the recording wavelength λ_{rec} = 380 nm and excitation wavelength λ_{exc} = 266 nm, the luminescence decay occurs according to an approximately exponential law at a mean time $\bar{\tau} \approx 0.92$ ms (curve *1*). An increase in the excitation wavelength to λ_{exc} = 355 nm leads to a substantial deviation from exponential behavior of the luminescence decay (curve *2*) and to a decrease in the mean time $\bar{\tau}$ to 0.68 ms. However, the time constant of the final stage τ_1 increases from 1.06 to 2.00 ms. At λ_{rec} = 545 nm, the decay curve exhibits almost exponential behavior with $\tau \approx 1.75$ ms (curve *3*). For the terbium-containing glass (C_{Tb} = 3.0 wt %) at λ_{rec} = 380 nm and λ_{exc} = 266 nm, the decay kinetics of luminescence (curve *4*) is virtually identical to that observed at λ_{exc} = 355 nm and is characterized by an insignificant deviation from exponential behavior with $\bar{\tau} \approx 0.87$ ms. For λ_{exc} = 266 nm and λ_{rec} = 545 nm, the kinetic curve exhibits almost exponential behavior with $\tau \approx 1.80$ ms (curve *5*) and only slightly differs from the curve measured at the excitation wavelength λ_{exc} = 355 nm. In the coactivated glass (C_{Ce} = 4.0 wt %, C_{Tb} = 1.0 wt %) at the recording wavelength λ_{rec} = 545 nm, the luminescence decay occurs according to a nonexponential law at both wavelengths λ_{exc} = 355 nm (curve *6*) and λ_{exc} = 266 nm (curve *7*) with mean times $\bar{\tau} \approx 0.25$ and 0.34 ms, respectively. After annealing of this glass in hydrogen, the decay curves exhibit a similar behavior but the decay time $\bar{\tau}$ increases to 0.97 ms ($\tau_f \approx$ 2.15 ms) at λ_{exc} = 355 nm (curve *8*) and to 1.63 ms ($\tau_f \approx$ 2.50 ms) at λ_{exc} = 266 nm (curve *9*). The decay kinetics of the broadband luminescence is characterized by a substantial deviation from exponential behavior ($\bar{\tau} \approx$ 40 ns at λ_{exc} = 355 nm and λ_{rec} = 440 nm) and only slightly differs from the decay kinetics in the cerium-containing glasses prepared under identical conditions.

Furthermore, it should be noted that the integrated intensity of luminescence in terbium-containing glasses is proportional to the terbium content and that the measured quantum yields of the sensitized luminescence from the $^5D_4$ state for the coactivated glass at activator contents C_{Ce} = 4.0 wt % and C_{Tb} = 1.0 wt % (λ_{exc} = 330 nm) before and after annealing in hydrogen are equal to 5 and 95%, respectively. It is worth noting that the quantum yield η for an identical coactivated glass sintered in hydrogen does not exceed 40%. The quantum yield of luminescence for the annealed glass at activator contents $C_{Ce} = C_{Tb}$ = 1 wt % is also relatively small (≈ 50%).

4. DISCUSSION

According to [6], the broad UV absorption band of the terbium-containing glass (Fig. 1, curve *2*) can be assigned to the $4f^8 \longrightarrow 4f^7(^8S_{7/2})5d^1(E)$ interconfigurational transition of the activator. The probability of this transition is almost three orders of magnitude higher than that of parity-forbidden intraconfigurational transitions. The appearance of an intense band at $\lambda \approx$ 260 nm in the spectrum of the glass ($C_{Tb} = C_{Ce}$ = 1 wt %) sintered in air (Fig. 1, curve *3*) is associated with the $O^{2-} \longrightarrow Ce^{4+}$ charge transfer [12]. The intensity of the UV absorption for the glass at activator contents C_{Ce} = 4.0 wt % and C_{Tb} = 1.0 wt % increases nonlinearly with an increase in the cerium content (Fig. 1, curve *4*). This can be explained by the formation of Ce–Ce and Ce–Tb

complex centers, in which differently charged lanthanide ions are involved in exchange interactions [18, 21], and also by a partial oxidation of Tb^{3+} ions to Tb^{4+} ions, which are characterized by the $O^{2-} \longrightarrow Tb^{4+}$ charge-transfer band at $\lambda \approx 360$ nm with $\Delta\lambda = 150$ nm [22]. The absorption of this glass in the visible range predominantly manifests itself in the long-wavelength wing of the $O^{2-} \longrightarrow Tb^{4+}$ band and is associated with the residual coloring Ce^{4+}–O–Ce^{3+} groups [18]. The considerable weakening of absorption in the UV and visible ranges after annealing of the glass in hydrogen (Fig. 1, curve *5*) is caused by the reduction of coactivator ions to the triply charged state. In this case, the absence of the bands attributed to individual Ce^{3+} and Tb^{3+} ions in the spectrum, which clearly manifest themselves in the spectrum of the glass at activator contents $C_{Tb} = C_{Ce} = 1.0$ wt % (Fig. 1, curve *6*), can be treated as another argument in support of the formation of Ce–Tb complex centers. On the other hand, we cannot rule out the possible effect of partial relaxation of the local environment of reduced ions $(Ce^{4+})^-$ in cerium-containing clusters to an equilibrium state [17].

The close values of the integrated intensities of the $^5D_3 \longrightarrow {}^7F_j$ and $^5D_4 \longrightarrow {}^7F_j$ bands attributed to Tb^{3+} ions in the luminescence spectra of the glass at a terbium content $C_{Tb} = 0.1$ wt % (Fig. 2, curve *1*) and the considerable decrease in the intensity of the former bands with an increase in the terbium content to $C_{Tb} = 3.0$ wt % (Fig. 2, curve *2*) can be explained by the increase in the efficiency of cross-relaxation deactivation of the $^5D_3$ state with an increase in the activator content. The redistribution of the relative intensities of the $^5D_3 \longrightarrow {}^7F_j$ spectral bands and the short-wavelength shift of their barycenters with the aforementioned increase in the terbium content suggest that at least two types of optical centers are formed in the terbium-containing glasses. The Tb^{3+} luminescence observed in the coactivated glass ($C_{Ce} = 4.0$ wt %, $C_{Tb} = 1.0$ wt %) sintered in oxygen upon excitation in the range in which $k_{Ce} \gg k_{Tb}$ ($\lambda_{exc} = 330$ nm) can be caused by the sensitization of Tb^{3+} ions by labile photoreduced ions $(Ce^{4+})^-$. The absence of the $^5D_3 \longrightarrow {}^7F_j$ bands in this spectrum can be due to the nonradiative transfer of excitations from the $^5D_3$ state to the lowest sublevels of the $4f5d$ state of the sensitizer. The broad luminescence band with a maximum at approximately 450 nm is most likely associated with the presence of Ce^{3+} residual isolated ions. The substantial increase in the fraction of photons emitted by Tb^{3+} ions as compared to that of photons emitted by Ce^{3+} ions after annealing of this glass in hydrogen (compare curves *3*, *4* in Fig. 2) can be attributed to the high efficiency of luminescence sensitization and the loss of quenching properties by Ce^{4+}–O–Ce^{3+} groups and Tb(IV) oxo complexes upon reduction of Ce^{4+} and Tb^{4+} ions to the triply charged state. The appearance of sufficiently intense bands due to the $^5D_3 \longrightarrow {}^7F_j$ transition in the luminescence spectrum measured for the annealed glass at activator contents $C_{Tb} = C_{Ce} = 1.0$ wt % and $\lambda_{exc} = 220$ nm (Fig. 2, curve *5*) indicates that this glass contains Tb^{3+} isolated optical centers with a weak cross-relaxation deactivation of the $^5D_3$ state and an inefficient transfer of excitations from Tb^{3+} isolated centers to Ce–Tb complex centers.

The short-wavelength shift of the $4f^8 \longrightarrow 4f^7(^8S_{7/2})5d^1(E)$ band in the luminescence excitation spectrum of the terbium-containing glass when changing over from the recording of the luminescence from the $^5D_4$ state to the recording of the luminescence from the $^5D_3$ state (Fig. 3, curves *1*, *2*) indicates a decrease in the degree of covalence of Tb–O bonds [23]. This suggests that optical centers characterized by a high intensity of luminescence from the $^5D_3$ state have Si^{4+} ions in the first coordination sphere of the cationic environment (i.e., they are isolated centers), whereas centers with a low luminescence intensity have Tb^{3+} ions in the first coordination sphere (these centers will be referred to as Tb–Tb complex centers). Actually, the relative strength of a single chemical bond with oxygen is equal to 1.54 for Si^{4+} and only 1.25 for Tb^{3+} [24]. This should lead to displacement of the oxygen ion toward the silicon ion in the Si–O–Tb chain, a decrease in the overlap of the Tb^{3+} and O^{2-} electron shells, and the observed shift of the band under consideration. It is unlikely that the insignificant difference between the contours of the intraconfigurational bands can contradict the assumption regarding the formation of isolated and complex centers due to the deep location of the f electron shell of Tb^{3+} ions. The broad double-peaked band (Fig. 3, curve *3*) revealed in the luminescence excitation spectrum of the coactivated glass sintered in oxygen ($\lambda_{rec} = 545$ nm) can be assigned to the transfer of excitations from photoreduced ions $(Ce^{4+})^-$ to Tb^{3+} ions in Ce^{4+}–Tb^{3+} complex centers. As is known [11–15], this transfer can be observed in the case when Ce^{4+} and Ln^{3+} ions are linked by a bridging oxygen atom with the formation of a nearly collinear configuration. It is reasonable to assume that this band strongly shields the $^7F_6 \longrightarrow {}^5D_3$ band ($\lambda \approx 380$ nm) of Tb^{3+} ions. As a consequence, the luminescence from the $^5D_3$ state is quenched and only the $^5D_4 \longrightarrow {}^7F_j$ transitions manifest themselves in the luminescence spectra. It is also evident that the short-wavelength portion of the double-peaked band is distorted as a result of luminescence quenching by Ce(IV) and Tb(IV) oxo complexes and coloring Ce^{4+}–O–Ce^{3+} groups. The considerable broadening of this band toward the short-wavelength range after hydrogen saturation of the coactivated glass (Fig. 3, curve *4*) is predominantly associated with the transformation of the above oxo complexes and groups due to the reduction of Ln^{4+} ions. The substantial difference between the band under consideration and the luminescence excitation bands in the spectra of cerium-containing silica gel

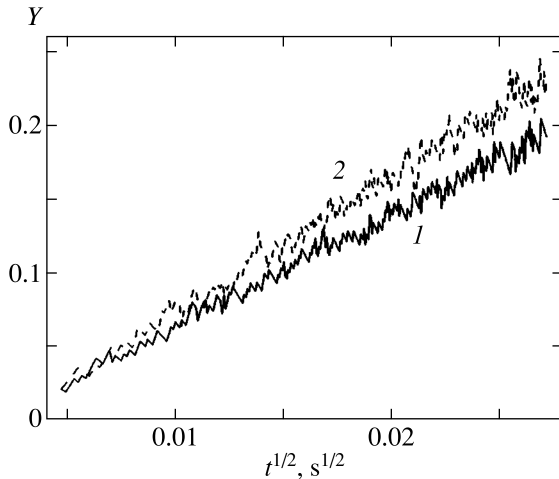

Fig. 5. Dependences of the function $Y = \ln I_{max}/I(t) - t/\tau_f$ on $t^{1/2}$ for the decay kinetics of luminescence in Tb-containing glasses. C_{Tb} = (*1*) 0.1 and (*2*) 3.0 wt %.

glass annealed under identical conditions with a close cerium content [17] can be treated as evidence of the formation of Ce–Tb complex centers. In turn, the difference between the excitation band of these centers and the spectrum obtained at λ_{rec} = 440 nm (compare curves *4*, *5* in Fig. 3) indicates that the broad short-wavelength luminescence band corresponds to Ce^{3+} ions not involved in Ce–Tb centers.

The fundamental difference between the decay kinetics of luminescence from the $^5D_3$ state at wavelengths λ_{exc} = 266 and 355 nm for the terbium-containing glass with C_{Tb} = 0.1 wt % (Fig. 4, curves *1*, *2*) confirms the above inference regarding the formation of centers of two types. The analysis of kinetic curves *1* and *4* shows that the function characterizing the rate of nonexponential luminescence decay $Y = \ln I_{max}/I(t) - t/\tau_f$ is linear in $t^{1/2}$ coordinates in both cases (Fig. 5). This suggests the dipole–dipole mechanism of interaction between energy donors and energy acceptors and provides a way of determining the macroparameter of the Forster decay γ from the slopes of straight lines *1* and *2*. These parameters for the glasses at terbium contents C_{Tb} = 0.1 and 3.0 wt % are calculated to be 7.7 and 9.0 $s^{-1/2}$, respectively. Such a small difference between these parameters with an almost fourfold decrease in the relative intensity of luminescence from the $^5D_3$ state for the heavily doped glass (compare curves *1*, *2* in Fig. 2) is a weighty argument in support of the formation of isolated centers and indicates a considerable decrease in their fraction with an increase in the terbium content C_{Tb}. Therefore, we can argue that the pronounced nonexponential behavior of the luminescence decay (Fig. 4, curve *2*) is associated with the dominant contribution of Tb–Tb centers to the decay kinetics. The independence of the decay rate of the $^5D_3$ state from λ_{exc} for the glass at a terbium content C_{Tb} = 3.0 wt % suggests an almost complete cross-relaxation quenching of the $^5D_3 \longrightarrow {}^7F_j$ luminescence of Tb–Tb centers at high terbium contents and a very insignificant transfer of excitations from isolated centers to complex centers. It is this efficient cross-relaxation in complex centers that can be responsible for the considerable decrease in the decay rate of luminescence from the $^5D_4$ state for the heavily doped glass at the initial instants of time (Fig. 4, curve *5*). Note that attempts to obtain a linear dependence of the function *Y* with different multipolarity parameters [8] for curve *2* in Fig. 4 have not been successful. This circumstance, together with the absence of indications that Tb–Tb centers of different types are formed, counts in favor of the exchange interaction between Tb^{3+} ions in these centers. A substantial decrease in the decay time $\bar{\tau}$ for the luminescence corresponding to the $^5D_4 \longrightarrow {}^7F_j$ transitions for the coactivated glass sintered in oxygen (Fig. 4, curves *6*, *7*) indicates that the Tb^{3+} luminescence is effectively quenched by cerium-containing clusters and Tb(IV) oxo complexes. The nonexponential decay of the $^5D_4$ state at a high quantum yield η and the dependence of this decay on λ_{exc} after elimination of the aforementioned quenching groups (Fig. 4, curves *8*, *9*) can be explained by the wide scatter in the radiation-decay times of luminescence of Tb^{3+} ions in an activator ensemble of Ce–Tb complex centers. It should be noted that an increase in τ_f by 20–40% for the coactivated glass saturated with hydrogen as compared to τ_f for the terbium-containing glass is in agreement with the high (cubic) symmetry of Ln(III) oxo complexes in Ce^{4+}–Ln^{3+} centers [14–16]. Furthermore, an insignificant difference between the decay kinetics of the broadband luminescence in the Ce- and (Ce, Te)-containing glasses annealed in hydrogen confirms the inference (drawn in the analysis of the luminescence excitation spectra) that this luminescence is associated with the Ce^{3+} ions not involved in Ce–Tb centers.

In our opinion, the main factors responsible for the high quantum yield of luminescence η for the coactivated glass at activator contents C_{Ce} = 4.0 wt % and C_{Tb} = 1.0 wt % after annealing in hydrogen are as follows: the efficient intracenter sensitization of luminescence due to the “conservation” of the collinear configuration of Ce–O–Tb bonds, the lower position of the lowest 4*f*5*d* sublevel of Ce(III) in Ce–Tb complex centers as compared to that in Ce^{3+} isolated ions (compare curve *4* in Fig. 3, for example, with curve *3* in Fig. 4 in [12]), and the large fraction of complex centers. Apparently, the absence of conditions for the formation of these complex centers upon sintering of the coactivated glass in hydrogen or the small fraction of complex centers formed upon sintering in air can explain the relatively low quantum yield η of Tb^{3+} luminescence upon excitation through Ce^{3+} ions in the corresponding glasses.

5. CONCLUSIONS

Thus, terbium-containing silica gel glasses contain optical centers of two main types, namely, Tb isolated centers and Tb–Tb complex centers, which exhibit weak and strong cross-relaxation quenching of the luminescence from the $^5D_3$ state of the activator, respectively. The Ce^{4+}–Tb^{3+} complex centers are formed in glasses sintered under oxidizing conditions and activated by cerium ions. These centers are characterized by efficient intracenter transfer of excitations from labile photoreduced ions $(Ce^{4+})^-$ to Tb^{3+} ions in the $^5D_4$ state and quenching of the luminescence from this state by cerium-containing clusters and Tb(IV) oxo complexes absorbing in the visible range. The hydrogen saturation of the glasses under investigation leads to complete suppression of the quenching factors and a multiple increase in the quantum yield of the sensitized luminescence of Tb^{3+} ions. The transfer of excitations from Tb isolated centers to Tb–Tb and Ce–Tb complex centers has a low efficiency. The radiation-decay time of luminescence of Tb^{3+} ions in Ce–Tb complex centers is longer than that in Tb isolated centers and Tb–Tb complex centers.

ACKNOWLEDGMENTS

This work was supported in part by the "Science for Peace" NATO program (grant no. SfP 977980), the Belarussian Foundation for Basic Research (project no. F02R-003), and the NANOTECH Belarussian Republican Program for Basic Research (project no. 4.14).

REFERENCES

1. G. O. Karapetyan and S. G. Lunter, Zh. Prikl. Spektrosk. **5**, 310 (1966).
2. D. M. Krol, R. P. van Stapele, J. H. Haanstra, T. J. A. Popma, G. E. Ghomas, and A. T. Vink, J. Lumin. **37**, 293 (1987).
3. A. L. Blinov, M. A. Borik, G. E. Malashkevich, I. V. Prusova, and A. P. Stupak, Zh. Prikl. Spektrosk. **65** (1), 83 (1998).
4. G. S. Maciel, A. Biswas, and P. N. Prasad, Opt. Commun. **178**, 65 (2000).
5. G. S. Martin, A. C. Yanes, J. Mendez-Ramos, M. E. Torres, and V. D. Rodriguez, J. Appl. Phys. **89** (5), 2520 (2001).
6. V. I. Arbuzov, V. Ya. Grabovskis, N. S. Kovaleva, U. T. Rogulis, and M. N. Tolstoĭ, Opt. Spektrosk. **65** (4), 943 (1988) [Opt. Spectrosc. **65**, 555 (1988)].
7. N. S. Poluéktov, N. P. Efryushina, and S. A. Gava, *Determination of Tracer Amounts of Lanthanides from Luminescence of Phosphor Crystals* (Naukova Dumka, Kiev, 1976) [in Russian].
8. V. A. Anisimov, A. V. Dmitryuk, and G. O. Karapetyan, Zh. Prikl. Spektrosk. **43** (1), 62 (1985).
9. R. Reisfeld and Ch. K. Jörgensen, *Laser and Excited States of Rare Earths* (Springer-Verlag, Berlin, 1977), p. 178.
10. L. Huang, X. Wang, H. Lin, and X. Liu, J. Alloys Compd. **316**, 256 (2001).
11. G. E. Malashkevich, E. N. Poddenezhnyĭ, I. M. Mel'nichenko, A. A. Boĭko, and L. G. Brazhnik, Opt. Spektrosk. **78** (1), 84 (1995) [Opt. Spektrosk. **78**, 74 (1995)].
12. G. E. Malashkevich, E. N. Poddenezhny, I. M. Melnichenko, and A. A. Boiko, J. Non-Cryst. Solids **188**, 107 (1995).
13. G. E. Malashkevich, I. M. Mel'nichenko, E. N. Poddenezhnyĭ, and A. V. Semchenko, Fiz. Tverd. Tela (St. Petersburg) **40** (3), 458 (1998) [Phys. Solid State **40**, 420 (1998)].
14. G. E. Malashkevich, A. G. Makhanek, A. V. Semchenko, V. E. Gaĭshun, I. M. Mel'nichenko, and E. N. Poddenezhnyĭ, Fiz. Tverd. Tela (St. Petersburg) **41** (2), 229 (1999) [Phys. Solid State **41**, 202 (1999)].
15. G. E. Malashkevich, G. I. Semkova, V. E. Gaĭshun, and A. V. Mudryĭ, Pis'ma Zh. Éksp. Teor. Fiz. **74**, 426 (2001) [JETP Lett. **74**, 388 (2001)].
16. G. E. Malashkevich, V. N. Sigaev, G. I. Semkova, and B. Champagnon, Fiz. Tverd. Tela (St. Petersburg) **46** (3), 534 (2004) [Phys. Solid State **46**, 552 (2004)].
17. G. E. Malashkevich, E. N. Poddenezhny, I. M. Melnichenko, and A. A. Boiko, J. Non-Cryst. Solids **260**, 141 (1999).
18. G. Malashkevich, G. Semkova, and W. Strek, J. Alloys Compd. **341**, 244 (2002).
19. C. A. Parker, *Photoluminescence of Solutions* (Elsevier, Amsterdam, 1968; Mir, Moscow, 1972).
20. Yu. A. Voĭtukevich, V. V. Kuz'min, and M. G. Livshits, in *Collected Papers on Physics* (Grodnen. Gos. Univ., Grodno, 1988), p. 85.
21. A. V. Anan'ev, V. I. Skorospelova, and S. A. Stepanov, Fiz. Khim. Stekla **19**, 134 (1993).
22. H. Ebendorff-Heidepriem and D. Ehrt, Opt. Mater. **15**, 7 (2000).
23. H. Ebendorff-Heidepriem and D. Ehrt, J. Non-Cryst. Solids **248**, 247 (1999).
24. N. N. Ermolenko, in *Glass, Glass Ceramics, and Silicate Materials* (Minsk, 1976), No. 5, p. 3 [in Russian].

Translated by O. Borovik-Romanova

Physics of the Solid State, Vol. 46, No. 8, 2004, pp. 1432–1437. Translated from Fizika Tverdogo Tela, Vol. 46, No. 8, 2004, pp. 1393–1397.
Original Russian Text Copyright © 2004 by Maslyuk, Skordeva, Puga, Arsova, Pamukchieva.

SEMICONDUCTORS AND DIELECTRICS

Concentration Dependence of Radiation-Induced Changes in the Optical Properties of $Ge_xAs_{40-x}S_{60}$ Films

V. T. Maslyuk*, E. Skordeva, P. P. Puga*, D. Arsova**, and V. Pamukchieva****

** Institute of Electronic Physics, National Academy of Sciences of Ukraine, Universitetskaya ul. 21, Uzhgorod, 88016 Ukraine*

e-mail: maslyuk@univ.uzhgorod.ua

*** Institute of Solid-State Physics, Bulgarian Academy of Sciences, Sofia, 1784 Bulgaria*

Received November 12, 2003

Abstract—Radiation-induced changes in the optical properties of chalcogenide glasses in the Ge–As–S system are investigated as a function of the concentration. Theoretical calculations are performed with due regard for possible constraints on the range of variation in the number of homobonds and heterobonds upon their switching in the structural network of chalcogenide glasses. The experimental data are obtained upon irradiation of $Ge_xAs_{40-x}S_{60}$ thin films with fast electrons (6 MeV). The possible mechanism of structural transformations responsible for the specific features in the concentration dependence of the change in the band gap of chalcogenide glasses is discussed. © *2004 MAIK "Nauka/Interperiodica".*

1. INTRODUCTION

Dependences of the range of variation in a number of physicochemical parameters of chalcogenide glasses on the ratio of chemical components are of considerable importance for several reasons. First and foremost, the analysis of these dependences makes it possible to choose the optimum media for data recording, on the one hand, and the optimum compositions of chalcogenide glasses resistant to radiation, on the other hand. At the same time, the correct interpretation of the experimental data can serve as a criterion for the adequacy of theoretical models for the vitreous state, the specific features of the glass structure, and the mechanisms of structural transformations.

Modern concepts of the nature of the vitreous state are based on the assumption of a stochastic agglomeration of structural units [1, 2]. The type of structural glass network containing atoms with different valences is very sensitive to the ratio of chemical components or the mean coordination number $\bar{Z}$. It has been assumed that there are two characteristic coordination numbers $\bar{Z}$ determining the stability of the glass structure: $\bar{Z}$ = 2.4 and 2.67. For the former coordination number, the problem associated with the rigidity of connection of atoms by chemical bonds is described within the classical (Lagrangian) formalism [3]. The latter coordination number corresponds to a change in the topological connectivity of a glass upon the $2D \rightleftharpoons 3D$ topological transformation [4]. In more recent theoretical and experimental studies, it has been demonstrated that, in amorphous materials, the aforementioned coordination numbers more likely determine the ranges of critical values of the mean coordination number.

For quantitative estimations of the physical parameters of a glass, it is of interest to consider models allowing for the local structure and statistical distribution of chemical bonds. One of the first approaches to solving this problem is the chemical–structural method proposed by Myuller [5]. Within this approach, parameters of multicomponent glasses assumed to be additive with respect to the ratio of structural units. In [6], it was shown that the Myuller method can be used to evaluate the concentration dependence of the range of induced variations in the physical parameters of binary chalcogenide glasses.

In this work, we performed similar calculations for Ge–As–S ternary chalcogenide glasses. The experimental data on the radiation-induced change in the optical properties as a function of the concentration were obtained for $Ge_xAs_{40-x}S_{60}$ thin films (along the As_2S_3–Ge_2S_3 join) irradiated with fast electrons. The choice of this join is explained by the possibility of changing the mean coordination number $\bar{Z}$ from 2.4 to 2.8 with an increase in the germanium content from 0 to 40 at. %. We investigated the change in the band gap E_g under irradiation. A comparison of the experimental data with the results of calculations performed with allowance made for the relation of the band gap E_g to the mean energy $\bar{E}_c$ of the structural network [7] allowed us to draw an inference regarding the induced structural transformations in thin films of chalcogenide glasses.

2. THEORY

The theoretical model chosen for our calculations allows for the fact that, under the action of different fac-

1063-7834/04/4608-1432$26.00 © 2004 MAIK "Nauka/Interperiodica"

tors (optical radiation, nuclear particle beams, etc.), the optical properties of chalcogenide glasses vary in a similar way. In this case, the weak EPR signal measured for these glasses indicates the absence of dangling chemical bonds [8]. It is assumed that atomic displacements in chalcogenide glasses even under irradiation with fast electrons at an energy $E_e = 6.5$ MeV (i.e., when an energy of 500–900 eV is transferred to atoms) are "healed" through the switching of chemical bonds with the formation of a new, more stable configuration.

Within this model, the changes observed in the characteristics of chalcogenide glasses upon irradiation will be interpreted under the assumption that the homobond $\rightleftarrows$ heterobond switching is a dominant mechanism. A number of switchings are accompanied by spatial displacements and rotations of atoms in the structure of the chalcogenide glass. After irradiation, a new metastable state is characterized by a change in the homobond-to-heterobond ratio depending on the initial state of the chalcogenide glass and the accumulation of radiation energy [9]. This approach makes it possible to estimate quantitatively the radiation-induced changes in complex systems, such as Ge–As–S glasses.

According to Manca [7], the band gap E_g depends linearly on the mean bond energy $\bar{E}_c$ for a chalcogenide glass. Arsova [10] established that, for $Ge_xAs_{40-x}S_{60}$ glasses, these quantities are related by the expression

$$E_g = 2.26\bar{E}_c - 1.62 \text{ [eV]}. \quad (1)$$

The irradiation leads to changes in the degree of ordering, the homobond-to-heterobond ratio, and, hence, the mean bond energy $\bar{E}_c$. According to formula (1), this results in a change in the band gap E_g, which enables us to estimate the concentration dependence of the optical parameters of chalcogenide glasses.

Further calculation will be performed for a cluster consisting of N atoms of the A, B, and C types, whose coordination numbers are m, n, and l, respectively. It is assumed that, in the cluster, the ratio of atoms corresponds to the structural formula $A_\alpha B_\beta C_{1-\alpha-\beta}$ and the numbers of the A–A, B–B, C–C, A–B, A–C, and B–C bonds are x_1, x_2, x_3, y_1, y_2, and y_3, respectively. In the absence of dangling bonds, the quantities x_i and y_i (i = 1–3) are related by the expressions

$$\begin{aligned} 2x_1 + y_1 + y_2 &= mN\alpha, \\ 2x_2 + y_1 + y_3 &= nN\beta, \\ 2x_3 + y_2 + y_3 &= lN(1-\alpha-\beta). \end{aligned} \quad (2)$$

From expressions (2), we can determine the total number of chemical bonds in the cluster $N_b = N/2[(m-l)\alpha + (n-l)\beta + l]$. Under the condition that, in the chalcogenide glass, the bond energies are additive respect to the number and energy of chemical bonds, the mean

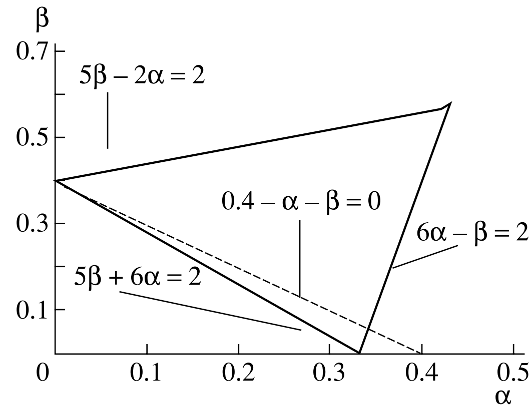

Fig. 1. Graphical solution of Eq. (2) for determining the composition region of $Ge_\alpha As_\beta S_{1-\alpha-\beta}$ chalcogenide glasses in which the number of heterobonds reaches a maximum. The dashed line corresponds to the $Ge_xAs_{40-x}S_{60}$ composition.

bond energy (per chemical bond) can be written in the form

$$\bar{E}_c = (-C_0 + \Delta_{A-B}y_1 + \Delta_{A-C}y_2 + \Delta_{B-C}y_3)/N_b. \quad (3)$$

Here, the quantity $C_0 = E_{A-A}mN_\alpha/2 + E_{B-B}nN\beta/2 + E_{C-C}lN(1-\alpha-\beta)$ is determined only by the ratio of components $\Delta_{i,j}$ ($i, j = A, B, C, i \neq j$) in the chalcogenide glass and has the meaning of the accumulated energy per chemical bond formed by atoms of the ith and jth types: $\Delta_{i-j} = E_{i-j} - (E_{i-i} + E_{j-j})/2$. According to Pauling [11], the accumulated energy Δ_{i-j} depends on the difference between the electronegativities χ_i and χ_j (i, $j = A, B, C$) of atoms of the Ath, Bth, and Cth types; that is,

$$\Delta_{i-j} = 1.06(\chi_i - \chi_j)^2 - 0.06(\chi_i - \chi_j)^4 \text{ [eV]}. \quad (4)$$

It follows from relationships (3) and (4) that the range of variation in the mean bond energy $\bar{E}_c$ is determined by the limits of variation in the number of heterobonds and the type of atoms in the chalcogenide glass. Formulas (1)–(4) make it possible to estimate the range of variation in the mean bond energy $\bar{E}_c$ under different constraints imposed on the range of variation in the number of heterobonds and homobonds. These constraints account for the specific features observed in the course of transformations of the structural network for thin-film and bulk samples of chalcogenide glasses under irradiation.

Figure 1 schematically represents the composition region of $Ge_\alpha As_\beta S_{1-\alpha-\beta}$ chalcogenide glasses in which the number of heterobonds can reach a maximum due to induced transformations and, according to expressions (3) and (1), the band gap E_g can vary over the widest range. This region was determined by assuming that homobonds are not formed in the course of induced

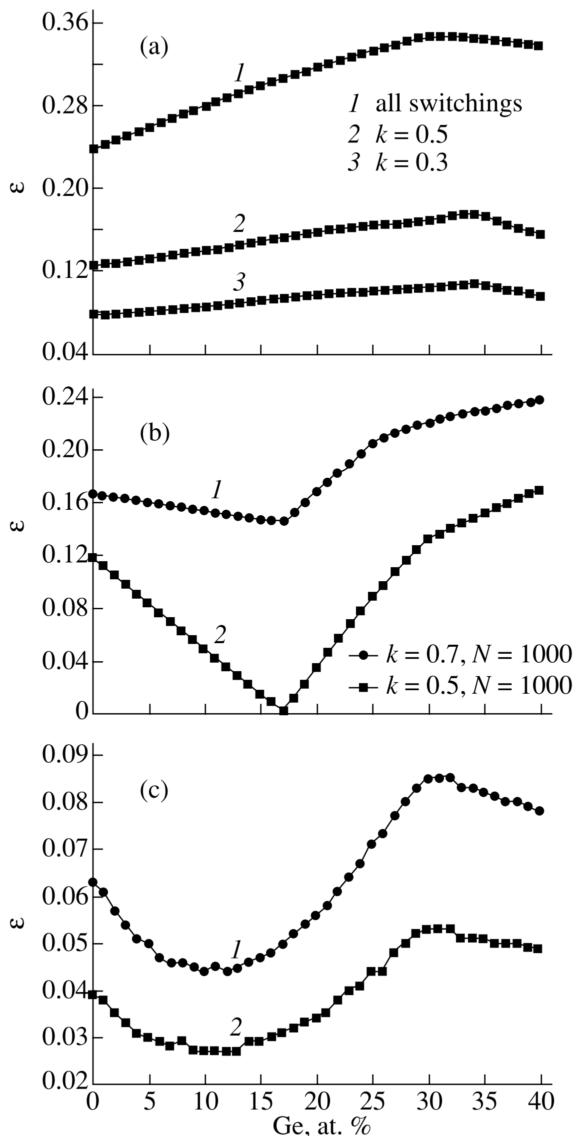

Fig. 2. Concentration dependences of the range of variation in the band gap $\varepsilon = (E_{g\,\max} - E_{g\,\min})/E_{g\,\max}$ (rel. units) for different variants of constraints on the numbers of homobonds and heterobonds x_i and y_i (i = 1–3). Curve *1* in panel (a) is constructed without constraints on the possible switchings of chemical bonds. Curves *2* and *3* in panel (a) correspond to variant **2** ($k = k_i = p_i$) at k = 0.5 and 0.3, respectively. Curves *1* and *2* in panel (b) represent the dependences for variant **3** at t = 0.7 and 0.5 ($t = t_i$), respectively. Curves *1* and *2* in panel (c) are the dependences for variant **4** at k = 0.5 and 0.3 ($k = k_i$), respectively.

transformations in the chalcogenide glass. Under this assumption, the number density of heterobonds should be maximum. In particular, it can be seen from Fig. 1 that, for the $Ge_xAs_{40-x}S_{60}$ composition, the region under consideration (triangle) corresponds to concentrations $x < 33$ at. % Ge.

In order to obtain quantitative estimates, we consider in more detail the possible constraints on the range of variation in the number of homobonds and heterobonds x_i and y_j (i, j = 1–3).

Variant 1. All possible switchings of homobonds and heterobonds are taken into account. In this case, the state with the lowest bond energy of the chalcogenide glass is achieved in the absence of heterobonds, which corresponds to the phase separation of the material.

Variant 2. The initial state of the chalcogenide glass is assumed to be statistically probable and is characterized by the following numbers of chemical bonds of different types (see [12]):

$$\bar{x}_1 = N(\alpha m)^2/(2N_s),\ \bar{x}_2 = N(\beta n)^2/(2N_s),$$
$$\bar{x}_3 = N(1-\alpha-\beta)^2/(2N_s), \tag{5}$$
$$\bar{y}_1 = N\alpha m\beta n/N_s,\ \bar{y}_2 = N\alpha m(1-\alpha-\beta)l/N_s,$$
$$\bar{y}_3 = N\beta n(1-\alpha-\beta)l/N_s.$$

Under the action of external factors, the numbers of chemical bonds vary in the ranges $|x_i - \bar{x}_i| < k_i\bar{x}_i$, $|y_i - \bar{y}_i| < p_i\bar{y}_i$ (i = 1–3).

Variant 3. In this variant, the initial state of the chalcogenide glass is characterized by the maximum number of heterobonds $y_{i\,\max}$ (i = 1–3) [5]. The numbers of heterobonds are represented by the relationships

$$y_{1\,\max} = \begin{Bmatrix} mN\alpha, & m\alpha \le n\beta \\ nN\beta, & m\alpha > n\beta \end{Bmatrix},$$

$$y_{2\,\max} = \begin{Bmatrix} mN\alpha, & m\alpha \le l(1-\alpha-\beta) \\ lN(1-\alpha-\beta), & m\alpha > l(1-\alpha-\beta) \end{Bmatrix}, \tag{6}$$

$$y_{3\,\max} = \begin{Bmatrix} nN\beta, & n\beta \le l(1-\alpha-\beta) \\ nN(1-\alpha-\beta), & n\beta > l(1-\alpha-\beta) \end{Bmatrix}.$$

The effect of external factors is reduced to a decrease in the number of heterobonds in the chalcogenide glass in the range $|y_{i\,\max} - y_i| < t_i y_{i\,\max}$ (i = 1–3). Here, as in the preceding case, the coefficients t_i satisfy the inequality $t_i < 1$.

Variant 4. The numbers of heterobonds in the chalcogenide glass fall in the ranges $[\bar{y}_i, y_{i\,\max}]$, where $\bar{y}_i$ and $y_{i\,\max}$ are determined by relationships (5) and (6), respectively. It is assumed that the inequality $|x_i - \bar{x}_i| < k_i\bar{x}_i$ holds for the number of homobonds.

Figure 2 shows the calculated concentration dependences of the range of variation in the band gap E_g expressed in terms of the parameter ε for the above variants of constraints on the numbers of homobonds and heterobonds in the chalcogenide glass. The parameter ε is defined by the expression $\varepsilon = (E_{g\,\max} - E_{g\,\min})/E_{g\,\max}$, where $E_{g\,\max}$ and $E_{g\,\min}$ are the maximum and minimum

band gaps E_g determined from formula (1), respectively. The cluster consists of $N = 1000$ atoms. The results of calculations account for the specific features in the behavior of the function $\varepsilon = \varepsilon(\alpha)$ depending on the range of induced variations in the number of homobonds and heterobonds in the chalcogenide glass. It can be seen from curve *1* in Fig. 2a that, even with allowance made for all the possible structural combinations of the chalcogenide glass at $\alpha \geq 30$ at. % Ge, the range of variation in the energy $\bar{E}_c$ becomes narrower upon switching of the chemical bonds. This is associated with the general tendency toward a decrease in the degrees of freedom in the space of possible numbers of chemical bonds in a cluster of the chalcogenide glass (Fig. 1). Under the assumption that structural transformations in the chalcogenide glass occur in accordance with variant **2**, the behavior of the parameter ε remains unchanged (Fig. 2a, curves *2*, *3*). On the other hand, by assuming that the initial state of the chalcogenide glass is characterized by the maximum number of high-energy heterobonds, whose number decreases during induced structural transformations (variant **3**), the concentration dependence of the parameter ε exhibits a strong minimum (Fig. 2b) in the concentration range α ~ 15–17 at. % Ge. Finally, the concentration dependence of the parameter ε for variant **4** (Fig. 2c) is characterized by a minimum in the range of low germanium concentrations and a maximum at ≈30 at. % Ge.

3. EXPERIMENTAL TECHNIQUE AND RESULTS

Radiation-induced changes in the optical properties of chalcogenide glasses as a function of the concentration were experimentally investigated using $Ge_xAs_{40-x}S_{60}$ thin films ($0 \leq x \leq 40$). The initial glasses were synthesized from elemental substances of V5 purity grade. After holding evacuated tubes with the initial substances at 950°C for 20 h and cooling in air, the prepared glasses were ground to powder. The powder was thermally evaporated at a deposition rate of ≈8 nm/s chosen such that the compositions of the deposited film and the initial glass would be as similar as possible. The deposition rate and the film thickness (1.2–1.5 μm) were checked *in situ* with a piezoelectric quartz sensor. The films were deposited on substrates from fused silica, whose transparency very weakly varies under irradiation with high-energy particle beams.

Irradiation of film samples was performed at room temperature on an M-30 microtron (Institute of Electronic Physics, National Academy of Sciences of Ukraine) at an electron energy of 6.5 MeV and flux density $\varphi_e = 5 \times 10^{11}$ electrons cm^{-2} s^{-1}. The energy homogeneity of the electron beam was equal to 0.02%. The nonuniformity of the irradiation field was checked *in situ* and did not exceed 5–7%. Films of different compositions were fixed in a holder and were then simultaneously irradiated with a uniform electron beam. The integrated particle flux per unit irradiation area was equal to 10^{15}–10^{16} electrons cm^{-2}.

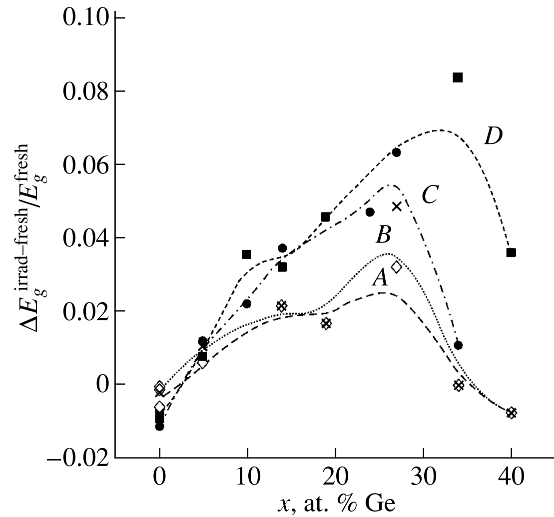

Fig. 3. Experimental concentration dependences of the relative change in the band gap for $Ge_xAs_{40-x}S_{60}$ films at different irradiation doses.

The transmittance of the samples in the range from 350 nm to 3 μm was measured before and after irradiation on Specord 61 NIR, Specord UV/Vis, and Shimadzu UV 910 spectrophotometers. The absorption coefficients and the refractive indices were calculated by the Swanepoel method, and the optical band gaps were determined by the Tautz technique.

Electron-induced changes in the optical properties were predominantly investigated by irradiating as-prepared (unannealed) films. Moreover, several annealed films of different composition were irradiated with the aim of observing reversible changes. The concentration dependences of the relative change in the band gap [or the parameter $\varepsilon = (E_g^{\text{irrad}} - E_g^{\text{fresh}})/E_g^{\text{fresh}}$] calculated from the experimental data are plotted in Fig. 3. Since the surface of some samples under irradiation at high doses became rough, the optical transmission could not be measured to sufficient accuracy. For this reason, the corresponding compositions are not presented in this figure. The lines in Fig. 3 are drawn in order to illustrate tendencies in the dependences of the electron-induced changes on the film composition. The data presented for irradiated films were obtained at four integrated electron fluxes. Curves *A*, *B*, *C*, and *D* correspond to integrated electron fluxes of 10^{15}, 2.5×10^{15}, 5×10^{15}, and 10^{16} electrons cm^{-2}, respectively.

It can be seen from Fig. 3 that the changes induced in the band gap of chalcogenide glasses upon irradiation under conditions *A* and *B* are rather small and comparable in magnitude to those observed in chalcogenide films due to ageing. The curves are almost identical in shape and exhibit a maximum at $x = 30$ at. % Ge and a weak feature (minimum) at $x = 17$ at. % Ge. This fea-

ture manifests itself differently depending on the irradiation dose.

Note that the above changes in the band gap E_g under irradiation with high-energy electrons and photons at energies close to the band gap identically depend on the germanium content x [13–15]. The reversible photoinduced changes are accompanied by a darkening of the samples (an increase in the band gap), whereas the irradiation with high-energy electrons and irreversible photoinduced changes are attended by a bleaching of the samples.

4. DISCUSSION

Therefore, experimental investigations demonstrate that all the compositions are sensitive to irradiation with electrons. (The maximum changes in the band gap and the refractive index are of the order of 6–8%.) According to Savchenko *et al.* [16], noticeable changes in the structure-sensitive properties of glasses are observed at integrated fluxes of higher than 10^{17} cm^{-2}. Owing to the considerable looseness of the film structure, similar changes occur in films at substantially lower integrated electron fluxes ($\geq 10^{12}$ cm^{-2}) [16, 17]. For the $Ge_xAs_{40-x}S_{60}$ films, the threshold sensitivity lies in the range 2.5×10^{15}–5×10^{15} electrons cm^{-2}. The composition dependence of the electron-induced change in the optical properties of the films is similar to that of the photoinduced change in the optical properties of glasses [13] and exhibits a maximum at high germanium contents (25–30 at. %). Judging from the similarity of the dependences of the photoinduced and electron-induced changes in the optical band gap, we can assume that the structural transformations induced under irradiation proceed through the same mechanism.

In our earlier work [13], the higher sensitivity of $Ge_xAs_{40-x}S_{60}$ glasses in the concentration range x = 27 at. % was explained by the loose atomic packing of chalcogenide glasses (the large free volume). It was assumed that this state of the chalcogenide glass is favorable for manifestation of different mechanisms of structural transformations, such as rotation of chalcogen atoms around Ge and As atoms [4] and switching of homopolar and heteropolar bonds in chalcogenide glasses [18].

The aforementioned theoretical model of structural combinations allows for the possibility of these processes occurring through both mechanisms. It can be seen from Fig. 2 that, for each variant of constraints on the range of variation in the number of bonds, the dependence of the parameter ε for the $Ge_xAs_{40-x}S_{60}$ films exhibits a maximum in the range of 30 at. % Ge. This can be explained by the fact that the largest number of chemical bonds, especially of bonds with a high bond energy, such as the Ge–S and As–S bonds (≈0.5 and ≈0.26 eV per bond, respectively), can be switched in chalcogenide glasses in the concentration range under consideration. In particular, at a germanium content of 30 at. %, the bonds formed by Ge and S atoms become comparable in number and the highest energy is accumulated upon switching of the Ge–S bonds into Ge–Ge and S–S bonds. As can be seen from Fig. 1, a further increase in the germanium content leads to a decrease in the energy accumulated by the structural network of the chalcogenide glass upon switching of the chemical bonds.

The origin of the feature observed in the concentration dependence of the parameter ε at a germanium content of 17 at. % is of particular interest. As follows from the results of our calculations (Fig. 2), the above feature manifests itself only for models in which the initial state of the chalcogenide glass is characterized by a maximum number of heterobonds and the degree of manifestation of this feature is determined by the range of variation in the number of heterobonds with respect to their maximum number $y_{i\,\max}$ (i = 1–3). In the framework of the proposed model, this feature is associated with the competition between the effects caused by the increase in the number of Ge–S heterobonds and, correspondingly, the decrease in the number of As–S heterobonds (having a lower bond energy) with an increase in the germanium content. Specifically, the number of chemical bonds formed by Ge atoms becomes comparable to the number of chemical bonds formed by As atoms at 17.3 at. % Ge (Fig. 2b) and the total bond energy of Ge–S heterobonds is comparable to that of As–S heterobonds at 10 at. % Ge (Fig. 2c).

In our specific case, the absence of a pronounced minimum in the concentration dependence of ε can be explained by both the insufficient irradiation dose and the larger number of homobonds as compared to the number assumed within the model (variants **3**, **4**). Indeed, our IR spectroscopic measurements showed that a relatively large number of As–As bonds are formed in as-prepared As_2S_3 films [18]. According to [19], there are grounds to believe that the introduction of Ge into As_2S_3 in small amounts does not lead to the incorporation of Ge into the structural clusters.

5. CONCLUSIONS

Thus, a model allowing for the switching of chemical homobonds and heterobonds in a chalcogenide glass matrix offers a satisfactory explanation of the specific features of radiation-induced changes in the optical properties of $Ge_xAs_{40-x}S_{60}$ films. In particular, a comparison of the experimental and theoretical data lends support to the validity of variants **3** and **4**, according to which the $Ge_xAs_{40-x}S_{60}$ films in the initial state involve $GeS_{4/2}$ and $AsS_{3/2}$ structural units. The irradiation brings about the formation of new, weaker As–As, Ge–Ge, and S–S homobonds. In as-deposited films, part of these bonds can be formed in the course of synthesis. This can affect the specific features in the concentration dependence of the induced changes in the

optical properties of films. For example, unlike bulk samples, the as-prepared films already contain homobonds bonds, which is explained by the features of the preparation technique. However, according to the model, the initial state of the films is characterized by the maximum number of heterobonds.

The proposed approach makes it possible to estimate the physicochemical parameters of multicomponent chalcogenide glasses quantitatively, including the ranges of their variation, and to predict the optimum composition of amorphous materials that are promising, for example, for optical data recording.

ACKNOWLEDGMENTS

This work was performed in the framework of the agreement on scientific cooperation between the Bulgarian and Ukrainian Academies of Sciences.

REFERENCES

1. R. Kerner, Physica B (Amsterdam) **215** (2), 267 (1995).
2. R. Kerner and M. Micoulaut, J. Phys.: Condens. Matter **9** (12), 2551 (1997).
3. J. C. Phillips, Phys. Rev. B **54** (10), R6807 (1996).
4. K. Tanaka, Phys. Rev. B **39** (2), 1270 (1989).
5. R. L. Myuller, *The Nature of Electrical Conductivity in Vitreous Semiconductors* (Leningr. Gos. Univ., Leningrad, 1965) [in Russian].
6. V. T. Maslyuk, L. I. Doĭnikov, and P. P. Puga, Fiz. Khim. Stekla **27** (5), 627 (2001).
7. P. Manca, J. Phys. Chem. Solids **20** (3/4), 268 (1961).
8. L. N. Blinov, Fiz. Khim. Stekla **29** (3), 289 (2003).
9. V. T. Maslyuk and L. I. Doĭnikov, Dokl. Akad. Nauk Ukr. SSR, Ser. A, No. 8, 61 (1986).
10. D. Arsova, J. Phys. Chem. Solids **57** (9), 1279 (1996).
11. L. Pauling, *General Chemistry*, 3rd ed. (Freeman, San Francisco, 1970; Nauka, Leningrad, 1974).
12. T. T. Nang, M. Okuda, and T. Matsushita, Phys. Rev. B **19** (2), 947 (1979).
13. E. Vateva, D. Arsova, E. Skordeva, and E. Savova, in *Electronic, Optoelectronic, and Magnetic Thin Films* (Wiley, Singapore, 1994), p. 604.
14. E. Vateva and E. Skordeva, J. Optoelectron. Adv. Mater. **4** (1), 3 (2002).
15. D. Arsova, V. Pamukchieva, E. Vateva, and E. Skordeva, J. Mater. Sci.: Mater. Electron. (2003) (in press).
16. N. D. Savchenko, N. I. Dovgosheĭ, and L. G. Kesler, *Optoelectronic Materials* (Tekhnika, Kiev, 1992), No. 1, p. 64 [in Russian].
17. K. Golovchak, in *Proceedings of the 7th International Seminar on Physical Chemistry of Solids* (Prace Naukowe-Chemia, Warszawa, 2001), Vol. 5, p. 199.
18. E. Skordeva, K. Christova, M. Tzolov, and Z. Dimitrova, Appl. Phys. A **66**, 103 (1998).
19. T. Velinov, M. Gateshki, D. Arsova, and E. Vateva, Phys. Rev. B **55** (17), 11014 (1997).

Translated by O. Borovik-Romanova

Physics of the Solid State, Vol. 46, No. 8, 2004, pp. 1438–1441. Translated from Fizika Tverdogo Tela, Vol. 46, No. 8, 2004, pp. 1398–1401.
Original Russian Text Copyright © 2004 by Bobrovskiĭ, Glazkov, Kichanov, Kozlenko, Savenko, Somenkov.

SEMICONDUCTORS AND DIELECTRICS

Effect of High Pressure on the Crystal Structure of $Sr_{1-x}La_xCuO_2$ Compounds

V. I. Bobrovskiĭ*, V. P. Glazkov, S. E. Kichanov***, D. P. Kozlenko***, B. N. Savenko***, and V. A. Somenkov****

** Institute of Metal Physics, Ural Division, Russian Academy of Sciences, ul. S. Kovalevskoĭ 18, Yekaterinburg, 620219 Russia*

*** Russian Research Centre Kurchatov Institute, pl. Kurchatova 1, Moscow, 123182 Russia*

**** Joint Institute for Nuclear Research, Dubna, Moscow oblast, 141980 Russia*

Received August 13, 2003; in final form, January 8, 2004

Abstract—The effect of high pressure on the tetragonal structure of infinite-layer compounds $Sr_{1-x}La_xCuO_2$ ($x = 0.07, 0.13$) and the orthorhombic structure of the $SrCuO_2$ compound is investigated using powder neutron diffraction. It is found that infinite-layer compounds are characterized by strong compression anisotropy. The mechanism of the phase transition from the orthorhombic phase to the tetragonal phase is discussed. *© 2004 MAIK "Nauka/Interperiodica".*

1. INTRODUCTION

Under normal conditions, the $SrCuO_2$ compound has an orthorhombic structure (space group *Cmcm*) (Fig. 1) consisting of copper-deficient layers (or so-called double zigzag Cu–O chains) alternating with $(SrO)_2$ layers [1]. At high pressures $P \sim 5$ GPa and temperatures $T \sim 1000$ K, this compound undergoes a phase transition from the orthorhombic low-pressure phase to the tetragonal infinite-layer phase, which is also referred to as the high-pressure phase [2]. The mechanism of the transition from the orthorhombic phase to the tetragonal phase is not clearly understood. Moreover, it is still not known which external factor (temperature or pressure) plays the key role in this phase transition.

Infinite-layer compounds of the general formula $Sr_{1-x}Ln_xCuO_2$, where *Ln* is a rare-earth element (La, Nd, etc.), have a simple crystal structure (space group *P*4/*mmm*) (see Fig. 2) [3–5] in which atoms occupy only special positions. These compounds undergo a transition to the superconducting state at a temperature $T_c \sim 20$–110 K [4, 5]. The considerable interest expressed by researchers in infinite-layer compounds with a tetragonal structure stems from the fact that the unit cell parameters *a* and *c*, which are related to the intralayer and interlayer Cu–Cu interactions, respectively, can serve as criteria for determining the temperature T_c of the superconducting transition in these compounds [6]. A change in the intralayer Cu–O distance is observed when the Sr^{2+} ion with ionic radius $r_{eff} = 1.26$ Å is replaced by ions with a smaller radius, for example, La^{3+} ($r_{eff} = 1.16$ Å) or Nd^{3+} ($r_{eff} = 1.11$ Å) [6, 7]. X-ray diffraction investigations of infinite-layer compounds $Sr_{1-x}La_xCuO_2$ ($0.05 < x < 0.12$) have revealed [6] that, under normal conditions, the parameters *a* and *c* of the tetragonal unit cell decrease linearly with an increase in the lanthanum content. However, at higher lanthanum

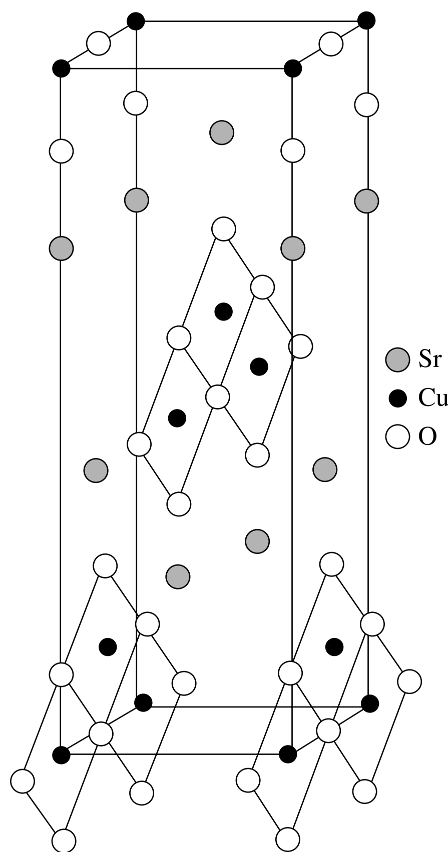

Fig. 1. Orthorhombic structure of the $SrCuO_2$ compound with copper-deficient Cu–O layers (double zigzag Cu–O chains) alternating with $(SrO)_2$ layers.

contents ($x > 0.12$), the behavior of the unit cell parameters considerably deviates from linearity; similar deviations are observed for $Sr_{1-x}Nd_xCuO_2$ compounds [7]. Therefore, it can be assumed that there is a critical doping level x_c at which the ratio of the unit cell parameters c/a ceases to decrease with an increase in the content of lanthanum or neodymium. It should be noted that changes in the lattice parameters under pressure can substantially exceed those observed upon doping. However, the effect of high pressure on the structure and properties of infinite-layer superconductors has not been adequately investigated. In this work, we performed a powder neutron diffraction investigation of the orthorhombic structure of the $SrCuO_2$ compound and the tetragonal structure of infinite-layer compounds $Sr_{1-x}La_xCuO_2$ at lanthanum contents $x = 0.07$ and 0.13 under high pressure.

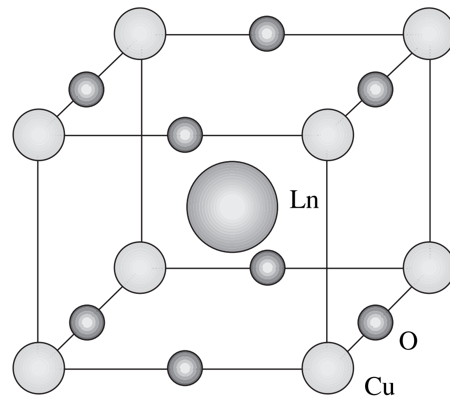

Fig. 2. Tetragonal structure of infinite-layer compounds $Sr_{1-x}Ln_xCuO_2$ (*Ln* is a rare-earth element).

2. SAMPLE PREPARATION AND EXPERIMENTAL TECHNIQUE

Samples of $Sr_{1-x}La_xCuO_2$ (x = 0.07, 0.13) compounds were synthesized according to the original procedure developed in [6] from $SrCuO_2$ and $LaCuO_2$ precursors with the use of preliminary magnetic pulsed compaction of batch pieces, which ensured a high density (~95%) and homogeneity of the samples and a high degree of accuracy of their geometrical dimensions. The final synthesis was carried out at a temperature of 1273 K and a pressure of 7 GPa (Institute of High-Pressure Physics, Russian Academy of Sciences, Troitsk). The neutron diffraction experiments were performed on a DN-12 spectrometer [8] installed on an IBR-2 pulsed high-flux reactor (Joint Institute for Nuclear Research, Dubna). Polycrystalline samples approximately 2.5 mm^3 in volume were placed in a high-pressure chamber with sapphire anvils [9]. The pressure in the chamber was determined from the shift of the ruby luminescence line with an accuracy of 0.05 GPa. The characteristic time taken for one spectrum to be measured was equal to 20 h. The experimental data were processed with the MRIA program [10] based on the standard Rietveld method [11]. When processing the neutron diffraction spectra measured at different pressures, we refined the unit cell parameters *a* and *c* for the tetragonal phase of infinite-layer compounds and the unit cell parameters *a*, *b*, and *c* and positional parameters of strontium, copper, and oxygen atoms for the orthorhombic phase of the $SrCuO_2$ compound. The refinement was performed in the space group *P*4/*mmm* for infinite-layer compounds and in the space group *Cmcm* for the $SrCuO_2$ compound. The results of the structure refinement are summarized in the Table 1.

3. RESULTS AND DISCUSSION

Figure 3 shows the pressure dependences of the unit cell parameters of the orthorhombic phase of the $SrCuO_2$ compound. The positional parameters of strontium, copper, and oxygen atoms are weakly dependent on pressure; their variations do not exceed the experimental error. However, pressure substantially affects the distance between the copper-deficient layers in the orthorhombic structure. The ratio of the Cu–Cu interlayer distance to the Cu–Cu intralayer distance decreases from 0.9138(8) to 0.9012(6). According to calculations, the phase transition from the orthorhombic low-pressure phase to the tetragonal infinite-layer phase (high-pressure phase) should occur at a pressure of 13.5 GPa. However, the pressure exerts a weak effect on the positional parameters of the atoms in the structure. Therefore, the above phase transition can proceed only at high temperatures. This suggests that the pressure and temperature affect the point of the phase tran-

Table 1. Structural parameters of infinite-layer compounds $Sr_{1-x}La_xCuO_2$ (x = 0.07, 0.13) and the orthorhombic phase of the $SrCuO_2$ compound under normal pressure

	$Sr_{0.93}La_{0.07}CuO_2$	$Sr_{0.87}La_{0.13}CuO_2$	$SrCuO_2$
a, Å	3.939(5)	3.948(7)	3.573(4)
b, Å	3.939(5)	3.948(7)	16.316(6)
c, Å	3.417(6)	3.408(5)	3.910(2)
Sr	(1/2, 1/2, 1/2)	(1/2, 1/2, 1/2)	(0, *y*, 0)
			y = 0.327(5)
Cu	(0, 0, 0)	(0, 0, 0)	(0, *y*, 0)
			y = 0.058(6)
O(1)	(1/2, 0, 0)	(1/2, 0, 0)	0, *y*, 0
			y = 0.175(4)
O(2)	–	–	(0, *y*, 0)
			y = 0.941(7)

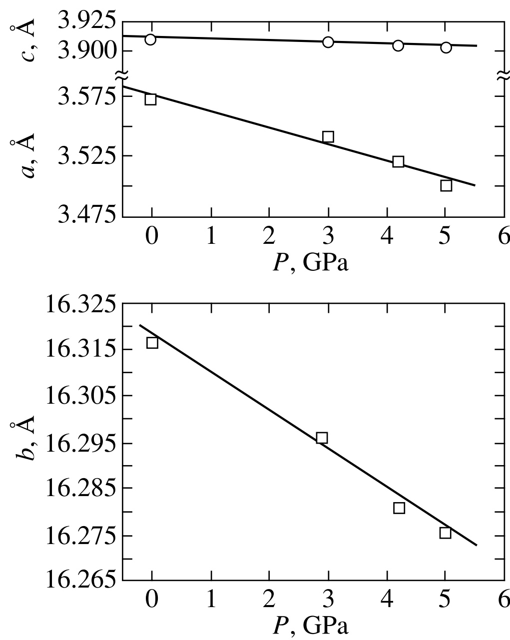

Fig. 3. Pressure dependences of the unit cell parameters *a*, *b*, and *c* for the $SrCuO_2$ orthorhombic phase. Solid straight lines represent linear approximations by the least-squares method. The experimental errors do not exceed the symbol sizes.

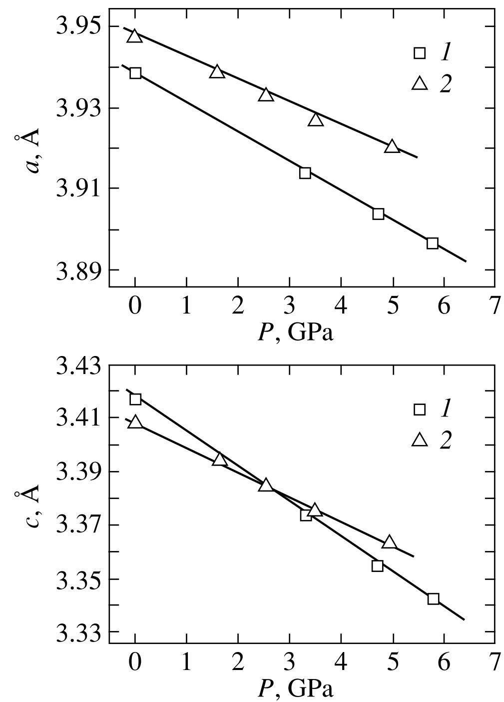

Fig. 4. Pressure dependences of the unit cell parameters *a* and *c* for the tetragonal phase of infinite-layer compounds $Sr_{1-x}La_xCuO_2$ at lanthanum contents x = (*1*) 0.07 and (*2*) 0.13. Solid straight lines represent linear approximations by the least-squares method. The experimental errors do not exceed the symbol sizes.

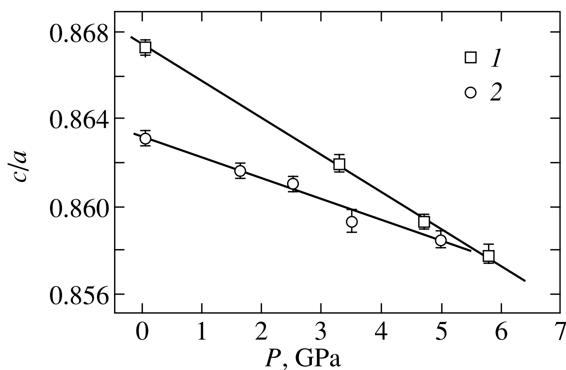

Fig. 5. Pressure dependences of the ratio *c*/*a* for the tetragonal unit cell of infinite-layer compounds $Sr_{1-x}La_xCuO_2$ at lanthanum contents x = (*1*) 0.07 and (*2*) 0.13. Solid straight lines represent linear approximations by the least-squares method.

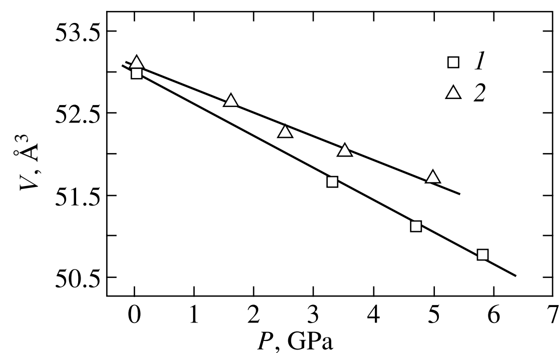

Fig. 6. Pressure dependences of the unit cell volume of infinite-layer compounds $Sr_{1-x}La_xCuO_2$ at lanthanum contents x = (*1*) 0.07 and (*2*) 0.13. Solid straight lines represent linear approximations by the least-squares method. The experimental errors do not exceed the symbol sizes.

sition from the orthorhombic phase to the tetragonal phase independently.

It can be seen from the Fig. 4 that the unit cell parameters of infinite-layer compounds at different lanthanum contents decrease linearly with an increase in pressure in the range up to 5.8 GPa. This behavior of the unit cell parameters indicates the absence of saturation observed in the case of doping [4, 5]. An increase in the pressure leads to a more noticeable decrease in the unit cell parameter *c* as compared to the parameter *a*. Therefore, the compressibility of infinite-layer compounds is anisotropic in nature (Figs. 5, 6; Table 2).

Table 2. Linear compressibilities and bulk moduli of infinite-layer compounds $Sr_{1-x}La_xCuO_2$ ($x = 0.07, 0.13$) and the orthorhombic phase of the $SrCuO_2$ compound

Parameter	$Sr_{0.93}La_{0.07}CuO_2$	$Sr_{0.87}La_{0.13}CuO_2$	$SrCuO_2$
k_a, 10^{-3} GPa^{-1}	2.10(3)	1.93(2)	1.03(4)
k_b, 10^{-3} GPa^{-1}	2.10(3)	1.93(2)	5.22(9)
k_c, 10^{-3} GPa^{-1}	4.08(5)	4.20(4)	1.81(5)
k_v, 10^{-3} GPa^{-1}	8.28(4)	8.06(6)	8.00(7)
B, GPa	120(9)	124(11)	125(9)

4. CONCLUSIONS

Thus, the results obtained in this study demonstrate that infinite-layer structures undergo anisotropic compression. The compression anisotropy of infinite-layer compounds is less pronounced than that for other types of oxide superconductors that crystallize in structures characterized by positional parameters, with one of them being more compliant [12–16]. In infinite-layer structures in which atoms occupy only special positions, the structural transformations and, possibly, changes in the electrical characteristics under pressure are associated only with the anisotropic compression of the unit cell.

ACKNOWLEDGMENTS

This work was supported by the Russian Foundation for Basic Research (project nos. 00-02-17077 and 00-02-17370), the Ministry of Industry, Science, and Technology of the Russian Federation (state contract nos. 40.012.1.1.1148 and 40.012.1.1.1166, agreement no. 10/02), the grant in support of unique facilities in Russia, and the International Association of Assistance for the promotion of cooperation with scientists from the New Independent States of the former Soviet Union (project INTAS no. 99-00256).

REFERENCES

1. Y. Taguchi, T. Matsumoto, and Y. Tokura, Phys. Rev. B **62**, 7015 (2000).
2. A. Podlesnyak, A. Mirmelstein, V. Bobrovskii, V. Voronin, A. Karkin, I. Zhdakhin, B. Goshchitskii, E. Midberg, V. Zubkov, T. D'yachkova, E. Khlbov, J.-Y. Genoud, S. Rosenkranz, F. Fauth, W. Henggeler, and A. Furrer, Physica C (Amsterdam) **258**, 159 (1996).
3. T. Siegrist, S. M. Zahurak, D. W. Murphy, and R. S. Roth, Nature (London) **334**, 231 (1988).
4. M. Takano, Y. Takeda, H. Okada, and Z. Hiroi, Physica C (Amsterdam) **159**, 231 (1988).
5. M. Takano, M. Azuma, Z. Hiroi, Y. Bando, and Y. Takeda, Physica C (Amsterdam) **176**, 441 (1991).
6. N. Ikeda, Z. Hiroi, M. Azuma, M. Takano, Y. Bando, and Y. Takeda, Physica C (Amsterdam) **210**, 367 (1993).
7. A. Podlesnyak, A. Mirmelstein, V. Voronin, B. Goshchitskii, T. D'yachkova, H. Kadyrova, V. Zubkov, Y. Zainulin, V. Kochetkov, E. Khlybov, R. Rosenkranz, and A. Furrer, Physica C (Amsterdam) **230**, 311 (1994).
8. V. L. Aksenov, A. M. Balagurov, V. P. Glazkov, D. P. Kozlenko, I. V. Naumov, B. N. Savenko, D. V. Sheptyakov, V. A. Somenkov, A. P. Bulkin, V. A. Kudryashev, and V. A. Trounov, Physica B (Amsterdam) **265**, 258 (1999).
9. V. P. Glazkov and I. N. Goncharenko, Fiz. Tekh. Vys. Davleniĭ, No. 1, 181 (1991).
10. V. B. Zlokazov, Comput. Phys. Commun. **85**, 415 (1995).
11. H. M. Rietveld, J. Appl. Crystallogr. **2**, 65 (1969).
12. V. L. Aksenov, A. M. Balagurov, V. P. Glazkov, D. V. Sheptyakov, V. A. Somenkov, and S. Sh. Shilshtein, High Press. Res. **14**, 127 (1995).
13. V. L. Aksenov, A. M. Balagurov, V. P. Glazkov, D. V. Sheptyakov, V. A. Somenkov, S. Sh. Shilshtein, and E. V. Antipov, Physica C (Amsterdam) **275**, 87 (1997).
14. V. L. Aksenov, A. M. Balagurov, V. P. Glazkov, D. V. Sheptyakov, V. A. Somenkov, S. Sh. Shilshtein, and E. V. Antipov, Physica B (Amsterdam) **234–237**, 940 (1997).
15. S. Sh. Shil'shteĭn, Fiz. Tverd. Tela (St. Petersburg) **40**, 1980 (1998) [Phys. Solid State **40**, 1793 (1998)].
16. V. P. Glazkov, B. N. Savenko, V. A. Somenkov, D. V. Sheptyakov, and S. Sh. Shilstein, High Press. Res. **17**, 201 (2000).

Translated by I. Volkov

Physics of the Solid State, Vol. 46, No. 8, 2004, pp. 1442–1448. Translated from Fizika Tverdogo Tela, Vol. 46, No. 8, 2004, pp. 1402–1408.
Original Russian Text Copyright © 2004 by Lemanov, Smirnova, Sotnikov, Weihnacht.

DEFECTS, DISLOCATIONS, AND PHYSICS OF STRENGTH

Dielectric Relaxation in $SrTiO_3$: Mn

V. V. Lemanov[1], E. P. Smirnova[1], A. V. Sotnikov[1, 2], and M. Weihnacht[2]

[1] *Ioffe Physicotechnical Institute, Russian Academy of Sciences, Politekhnicheskaya ul. 26, St. Petersburg, 194021 Russia*
e-mail: lemanov@mail.ioffe.ru
[2] *Leibnitz Institute of Solid State and Materials Research, Dresden, D-01069 Germany*
Received December 16, 2003

Abstract—Dielectric relaxation (activation energy $U \approx 0.03$ eV, relaxation time $\tau_0 \approx 5 \times 10^{-11}$ s) has been observed in $SrTiO_3$: Mn solid solutions at low temperatures. It is assumed that the relaxation is related to reorientation of the polarons localized at defects of the $\{Mn^{2+}_{Ti}–O^-\}$ type and that the deviations from classical thermally activated behavior at the lowest temperatures reached are due to the quantum tunneling mode. *© 2004 MAIK “Nauka/Interperiodica”.*

1. INTRODUCTION

Impurity centers in perovskite crystals have been studied starting from the late 1950s (see [1] and references therein). Strontium titanate crystals doped with manganese ($SrTiO_3$: Mn) revealed cubic ESR spectra of Mn^{4+}_{Ti} and Mn^{2+}_{Ti} and axial spectra of the $\{Mn^{2+}_{Ti}–V_O\}$ and $\{Mn^{3+}_{Ti}–V_O\}$ complexes (after high-temperature reduction of the crystals), where V_O denotes a vacancy of oxygen ions O^{2-} and the manganese ions substitute for the main ion Ti^{4+}. Additional information on impurity centers of this type, as well as on impurity centers with localized polarons, can be derived by means of dielectric spectroscopy [3–6].

We report here on a dielectric spectroscopy study of ceramic samples of strontium titanate doped by manganese ions with different valences, which was aimed at clarifying the dielectric relaxation mechanisms and obtaining additional information on the structure of impurity centers.

2. EXPERIMENTAL

$SrTiO_3$: Mn samples were prepared using standard ceramic technology. The starting materials were the high-purity reagents $SrCO_3$, TiO_2, MnO, and MnO_2. The typical heat treatment regime consisted of a preliminary annealing at 1100–1200°C for 20 h and final annealing at 1350–1450°C for 1.5 h.

The quadrivalent manganese was introduced into $SrTiO_3$ in the form of manganese dioxide (MnO_2) or preliminarily synthesized $SrMnO_3$. For the manganese ions to remain in the Mn^{4+} charge state, $SrTiO_3$–$SrMnO_3$ ceramics were annealed in an oxygen flow at 1000°C for 20 h. Introduction of MnO resulted in an excess of oxygen in the ceramics, and part of these samples were annealed in an oxygen flow at 1000°C for 21 h. In all these cases, cooling was performed in two regimes, namely, slow (at a rate of about 1 K/min) and fast (5–10 K/min). We note immediately that all these changes in the ceramic preparation regimes did not affect the dielectric relaxation parameters (activation energy U, relaxation time τ_0) observed experimentally under thermal-activation conditions.

The density of all samples was 0.92 to 0.96 of the value determined from x-ray diffraction.

X-ray diffraction measurements were performed on a DRON-2 diffractometer at room temperature. The samples with a Mn concentration of less than 5 at. % were single-phase with the perovskite structure. The lattice parameters were measured on powders with a Ge internal reference.

The permittivity was studied on a Solartron SI 1260 in the frequency range from 10 Hz to 1 MHz and at temperatures ranging from 4.2 to 300 K. The samples prepared for the measurements were about 10 mm in diameter and 0.4 mm thick. Silver paste fired into the samples served as electrodes.

3. EXPERIMENTAL RESULTS

Figure 1 plots the lattice parameter a versus the molar concentration x of Mn^{2+} ions. We readily see that the solubility limit for this system is no greater than 0.05 and that the lattice parameter of $SrTiO_3$: Mn is closer to that of the solid solution $(1 - x)SrTiO_3 + xSrMnO_3$ than of $(1 - x)SrTiO_3 + xMnTiO_3$.

Note that doping with Mn^{4+} results in approximately the same $a(x)$ relation, with two cubic perovskite phases observed for $x \geq 0.05$. This fits with the results from [7], where two phases with perovskite structure were also observed and where the antiferromagnetic

1063-7834/04/4608-1442$26.00 © 2004 MAIK “Nauka/Interperiodica”

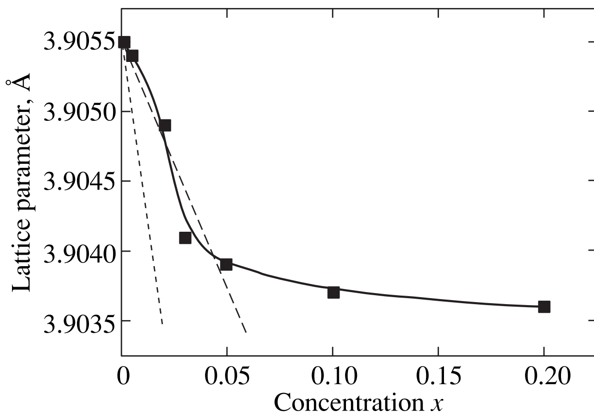

Fig. 1. Concentration dependence of the lattice parameter in $SrTiO_3 : Mn^{2+}$. Solid line is experiment. Dotted line is Vegard's law for $(1 - x)SrTiO_3 + xMnTiO_3$ solid solutions, and dashed line is Vegard's law for $(1 - x)SrTiO_3 + xSrMnO_3$ solid solutions; the lines are drawn under the assumption that the reduced perovskite cell parameters for the second components of the solid solutions are 3.791 and 3.868 Å, respectively.

properties of the system were related to excess manganese present at grain boundaries of the ceramic.

Figures 2–4 display temperature dependences of ε' and ε'' obtained at different frequencies on $SrTiO_3 : Mn^{2+}$ samples with concentrations $x = 0.005$ and 0.02 and on $SrTiO_3 : Mn^{4+}$ with $x = 0.01$. Figures 5–7 show ε'(ω) and ε''(ω) spectra measured at different temperatures.

As follows from the treatment of our experimental data, our samples exhibit, on the whole, Debye relaxation, with the relaxation frequencies (times) obeying the Arrhenius law in the region of relatively high temperatures.

For the Debye relaxation, we have

$$\varepsilon^*(\omega) = \varepsilon_\infty + (\varepsilon_0 - \varepsilon_\infty)/(1 + i\omega\tau), \quad (1)$$

$$\varepsilon' = \varepsilon_\infty + (\varepsilon_0 - \varepsilon_\infty)/(1 + \omega^2\tau^2), \quad (2)$$

$$\varepsilon'' = (\varepsilon_0 - \varepsilon_\infty)\omega\tau/(1 + \omega^2\tau^2). \quad (3)$$

Here, ε_0 is the permittivity in the case where it receives all of the relaxing-center contribution ($\omega\tau \ll 1$) and ε_∞ is the lattice permittivity in the case where the relaxation does not occur ($\omega\tau \gg 1$). For $\omega\tau = 1$, we have

$$\varepsilon' = (\varepsilon_0 + \varepsilon_\infty)/2, \quad \varepsilon'' = \varepsilon''_{max} = (\varepsilon_0 - \varepsilon_\infty)/2.$$

It is known that Eq. (1) for the Debye relaxation is a particular case of the Cole–Cole function

$$\varepsilon^*(\omega) = \varepsilon_\infty + (\varepsilon_0 - \varepsilon_\infty)/[1 + (i\omega\tau)^\beta]. \quad (4)$$

Figures 8 and 9 plot (on a semilogarithmic scale) the dependence of the relaxation times on reciprocal temperature. The relaxation times were found by fitting the ε'(ω) and ε''(ω) spectra with Cole–Cole function (4).

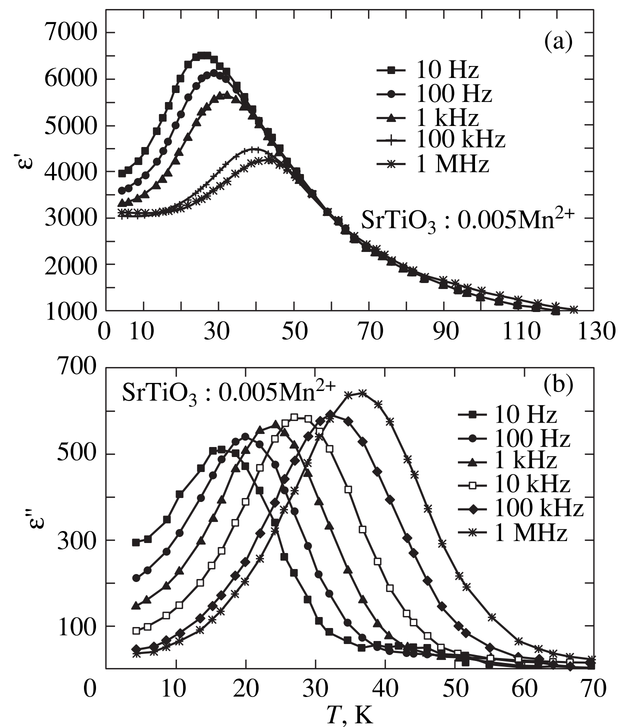

Fig. 2. Temperature dependence of the permittivity (a) ε' and (b) ε'' of $SrTiO_3 : Mn^{2+}$ measured at different frequencies for $x = 0.005$.

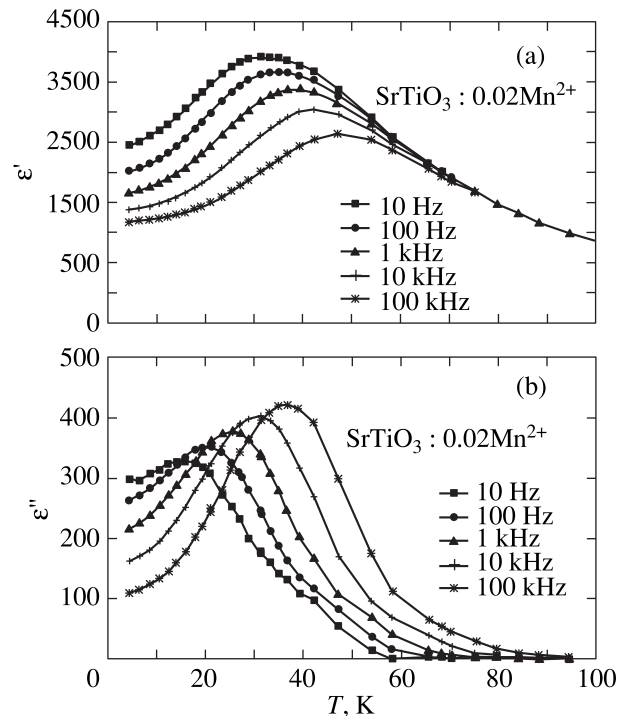

Fig. 3. Temperature dependence of the permittivity (a) ε' and (b) ε'' of $SrTiO_3 : Mn^{2+}$ measured at different frequencies for $x = 0.02$.

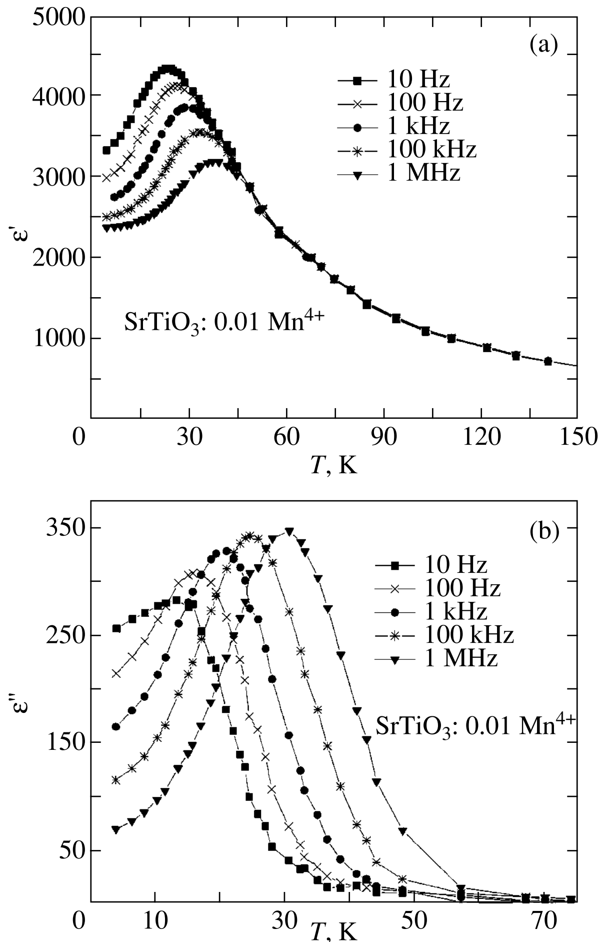

Fig. 4. Temperature dependence of the permittivity (a) ε' and (b) ε" of $SrTiO_3 : Mn^{4+}$ measured at different frequencies for $x = 0.01$.

The quantity β varies from sample to sample within a fairly broad range and, in addition, depends on temperature. The average values of β are about 0.4.

The smallness of β shows that the ε(ω) spectra are considerably more diffuse than the pure Debye spectra, in other words, that there is a wide range of relaxation times.

As follows from the figures, the experimental points obtained at relatively high temperatures obey the Arrhenius relation

$$\tau = \tau_0 \exp(U/kT). \quad (5)$$

The relaxation parameters U and $\tau_0 = 1/\omega_0$ extracted from these experimental data are listed in Tables 1 and 2 (the deviation of experimental points from a linear relation at low temperatures is discussed in the next section).

We may add that the relaxation parameters U and τ_0 obtained using $\varepsilon''(T)$ relations measured at different frequencies (Figs. 2–4) are the same.

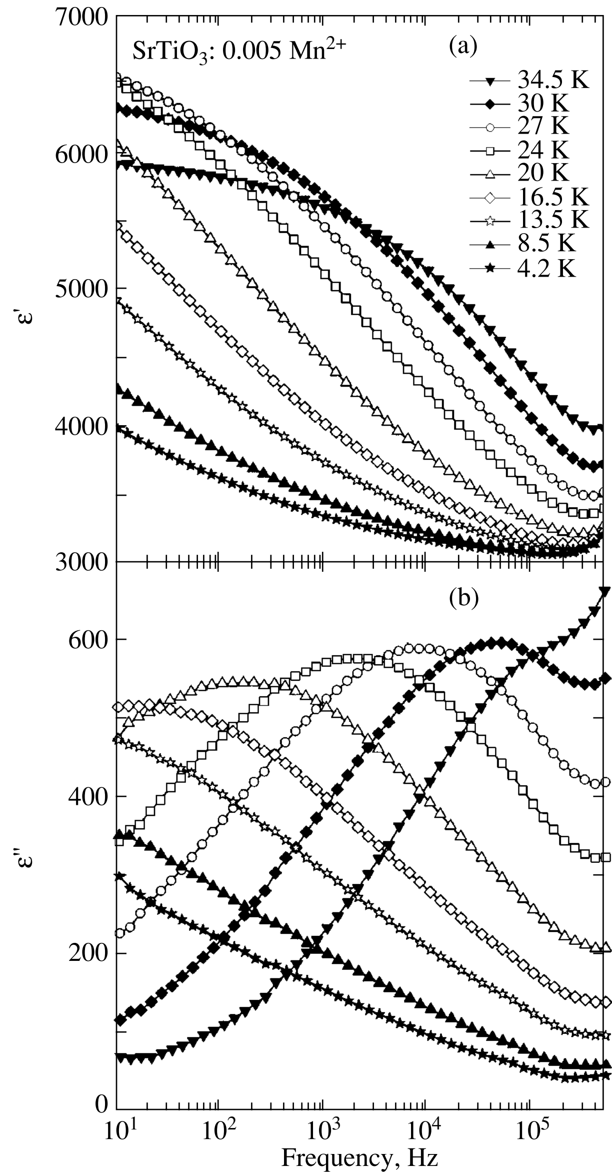

Fig. 5. Frequency dependences of the permittivity (a) ε' and (b) ε" of $SrTiO_3 : Mn^{2+}$ measured at different temperatures for $x = 0.005$.

4. DISCUSSION OF THE RESULTS

We start our discussion with Fig. 1. If $SrTiO_3 : Mn^{2+}$ is considered a $(1 - x)SrTiO_3 + xMnTiO_3$ solid solution, a question arises as to the validity of Vegard's law for the lattice constant. The tolerance factor t for the ABO_3 perovskite structure is given by

$$t = \sqrt{2}/2(R_A + R_O)/(R_B + R_O), \quad (6)$$

where R_A, R_B, and R_O are the corresponding ionic radii.

For $MnTiO_3$, the tolerance factor is $t = 0.93$. This means it is unlikely that $MnTiO_3$ can have a perovskite structure. Nevertheless, if the parameter of the reduced

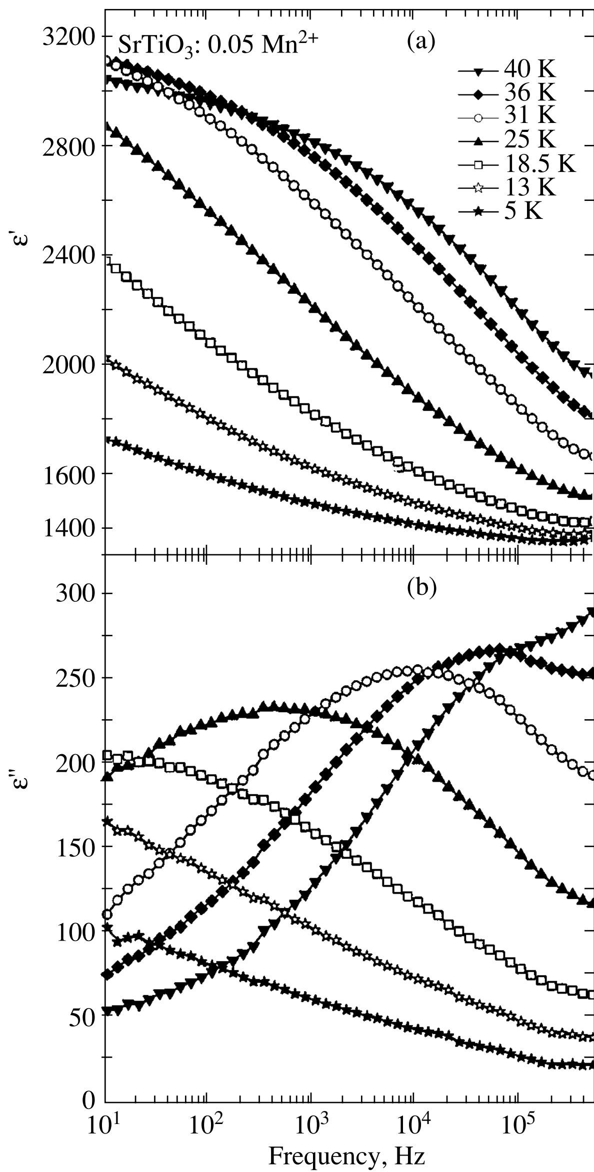

Fig. 6. Frequency dependences of the permittivity (a) ε' and (b) ε'' of $SrTiO_3 : Mn^{2+}$ measured at different temperatures for $x = 0.05$.

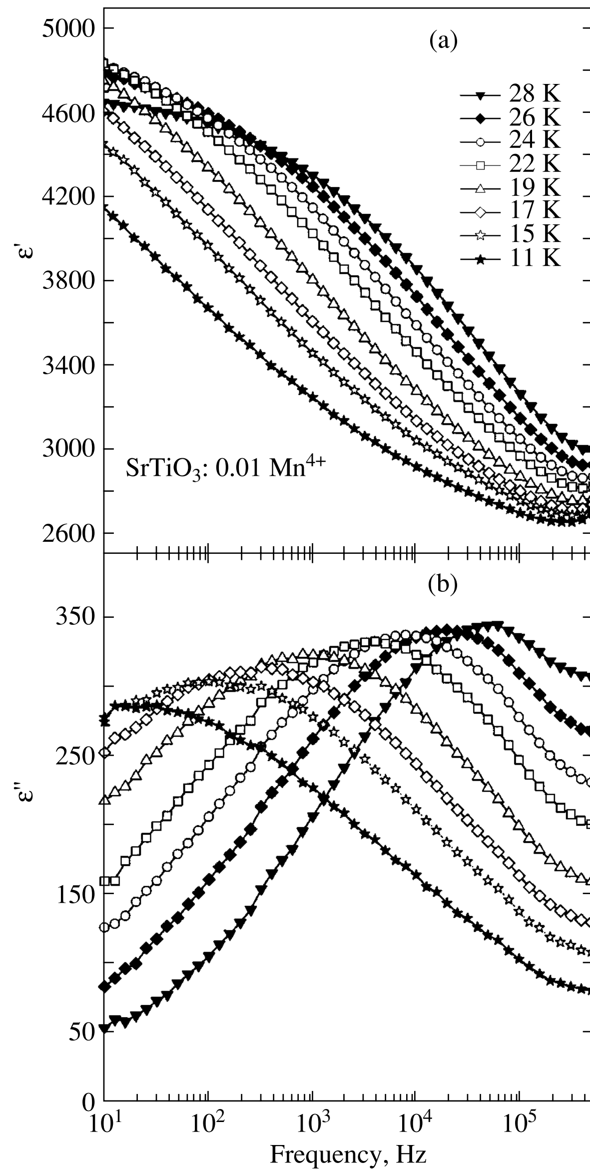

Fig. 7. Frequency dependences of the permittivity (a) ε' and (b) ε'' of $SrTiO_3 : Mn^{4+}$ measured at different temperatures for $x = 0.01$.

perovskite cell is estimated based on the volume of the $MnTiO_3$ hexagonal cell, we obtain for this parameter $a_p = [((\sqrt{3}/2)a^2c)/Z]^{1/3}$, where $a = 5.1396$ Å and $c = 14.2902$ Å are the tabulated values of the $MnTiO_3$ hexagonal cell parameters and $Z = 6$ is the number of formula units in the cell. In this case, we come to $a_p = 3.791$ Å.

On the other hand, if $SrTiO_3 : Mn^{2+}$ is considered a $(1 - x)SrTiO_3 + xSrMnO_3$ solid solution, the second component is $SrMnO_3$ with a tolerance factor of 1.04. Despite this tolerance factor being very favorable for the perovskite structure, $SrMnO_3$ usually has a hexagonal lattice with the tabulated parameters $a = 5.460$ Å and $c = 13.45$ Å. In this case, the parameter of the reduced perovskite cell is $a_p = 3.868$ Å.

In Fig. 1, the solid line displays experimental data obtained for the lattice parameter of $SrTiO_3 : Mn^{2+}$ solid solutions, the dotted straight line plots Vegard's law for a $(1 - x)SrTiO_3 + xMnTiO_3$ solid solution, and the dashed straight line plots this law for a $(1 - x)SrTiO_3 + xSrMnO_3$ solid solution; these lines were drawn under the assumption that the parameters a_p of the reduced perovskite cell for the second solid-solution components are 3.791 and 3.868 Å, respectively. We readily see that the experimental values of the $SrTiO_3 : Mn^{2+}$ lattice parameter are

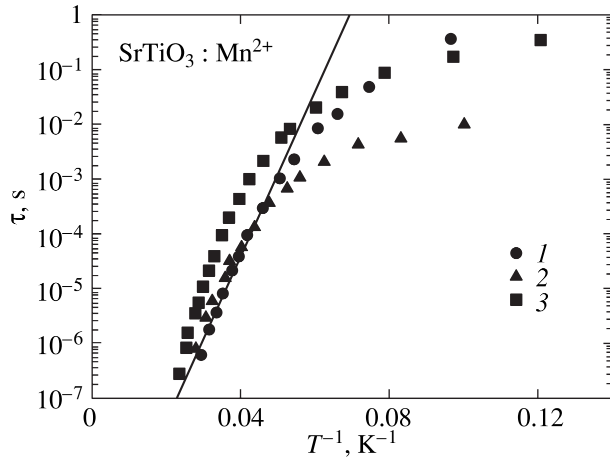

Fig. 8. Relaxation time τ plotted vs. reciprocal temperature for $SrTiO_3 : Mn^{2+}$ for (*1*) $x = 0.005$, (*2*) 0.02, and (*3*) 0.03. Straight line is a plot of the Arrhenius law for $U = 0.03$ eV and $\tau_0 = 4.2 \times 10^{-11}$ s.

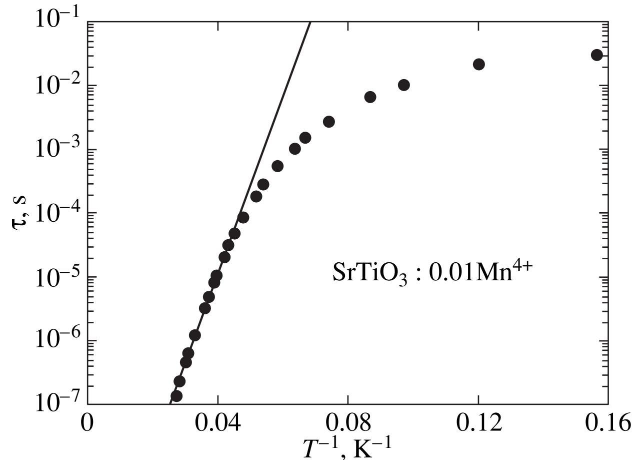

Fig. 9. Relaxation time τ plotted vs. reciprocal temperature for $SrTiO_3 : Mn^{4+}$ for the concentration $x = 0.01$. Straight line is a plot of the Arrhenius law for $U = 0.028$ eV and $\tau_0 = 2 \times 10^{-11}$ s.

closer to Vegard's law for the $(1 - x)SrTiO_3 + xSrMnO_3$ solid solution than to that for $(1 - x)SrTiO_3 + xMnTiO_3$.

Consider further which positions in the $SrTiO_3$ lattice can be occupied by manganese ions with different valences. Consider first the ionic radii. We use for this purpose the data obtained by Shannon [8]. These data do not contain values of the ionic radii for the coordination number $N_k = 12$; these values are obtained by extrapolating the data for smaller N_k (it is well known that the coordination numbers N_k for the *A*, *B*, and O ions in an ABO_3 perovskite lattice are 12, 6, and 8, respectively). Shannon gives two values of an ionic radius for $N_k = 6$, namely, 0.67 and 0.83 Å for Mn^{2+} and 0.58 and 0.645 Å for Mn^{3+}, with the second value in each pair considered more reliable. It is these values that we use here. The ionic radii for the $SrTiO_3$: Mn system are listed in Table 3.

As seen from Table 3, the ionic radii differ strongly (except for the Mn^{3+} and Ti^{4+} ions, which have similar radii). Nevertheless, the Sr^{2+} and Ti^{4+} ions of the main lattice can be replaced by a manganese ion in any valence state. However, ESR studies [1, 2, 7] revealed

Table 1. Relaxation parameters in $SrTiO_3 : Mn^{2+}$

x	U, eV	τ_0, 10^{-11} s
0.001	0.03	5.0
0.005	0.03	4.2
0.01	0.03	3.2
0.02	0.03	7.9
0.03	0.035	3.5
0.05	0.036	2.5

Mn ions of various valences only in the Ti^{4+} position. Furthermore, it was established that paramagnetic centers with Mn^{3+} arise only in samples calcined at a high temperature in a mixture of nitrogen with hydrogen and subsequently quenched to room temperature. Because our samples were not subjected to this treatment, we will not discuss centers with Mn^{3+} in what follows. We will discuss instead in detail only the Mn^{2+} and Mn^{4+} ions in the Ti^{4+} position, i.e., Mn_{Ti}^{2+} and Mn_{Ti}^{4+}.

We start with the Mn^{2+} ion. The Mn^{2+} ion substitutes for the titanium ion. The vacancy V_O of the O^{2-} ion with an effective charge of +2 appears to compensate the charge, and a $\{Mn_{Ti}^{2+} - V_O\}$ dipole forms (the formula of the solid solution can in this case be written as $SrTi_{1-x}Mn_x^{2+}O_{3-x}$). In another case, there are two oxygen ions with a unit negative charge per Mn_{Ti}^{2+} ion ($SrTi_{1-x}Mn_x^{2+}O_{3-2x}^{2-}O_{2x}^{-}$), with one or two O^- ions located in the immediate vicinity of the Mn^{2+} ion (at a distance of $a/2$). This formation may be treated as a localized hole polaron (bipolaron). (One could consider one more conceivable compensating center, namely, neutral oxygen ($SrTi_{1-x}Mn_x^{2+}O_{3-x}^{2-}O_x$) with a radius of about 1 Å, but the probability of formation of such a center is apparently very low.)

In $SrTiO_3 : Mn^{4+}$, the Mn^{4+} ion substitutes for the titanium ion, Mn_{Ti}^{4+} (the formula of the solid solution is now $SrTi_{1-x}Mn_x^{4+}O_3$). In this case, no charge compensation is needed, but the manganese ion may occupy an off-center position because $R_i/R_h = 0.88$ (for the classical off-center ion Li^+ in a $KTaO_3$ lattice, $R_i/R_h = 0.76$).

Table 2. Relaxation parameters in $SrTiO_3 : Mn^{4+}$

x	U, eV	τ_0, 10^{-11} s
0.001	0.03	4.7
0.005	0.025	4.1
0.01	0.028	2.0

All of the three above centers, namely, $\{Mn_{Ti}^{2+}-V_O\}$, $\{Mn_{Ti}^{2+}-O^-\}$ (or $\{O^- - Mn_{Ti}^{2+}-O^-\}$), and the off-center Mn_{Ti}^{4+} ion, possess an electric dipole moment and, hence, can contribute to dielectric relaxation.

As follows from Tables 1 and 2, the activation energy U in our experiments is about 0.03 eV and the relaxation time is $\tau_0 \approx 5 \times 10^{-11}$ s. The values of the activation energy and the relaxation time listed in Tables 1 and 2 suggest the conclusion that we have one relaxation center in all cases. For the relaxation associated with motion of the oxygen ions, this energy is substantially larger than 0.1 eV and quite frequently is about 1 eV (see [6] and references therein). The experimentally observed activation energy of 0.03 eV can be related only to motion in the electronic subsystem. From this viewpoint, the most appropriate of the above centers appears to be the $\{Mn_{Ti}^{2+}-O^-\}$ (or $\{O^- - Mn_{Ti}^{2+} - O^-\}$) center. Relaxation associated with this center involves an electron (hole) hopping over six O^{2-} ions surrounding the Mn_{Ti}^{2+} ion. Such an electron dressed in a phonon coat is actually a polaron. As for the Mn_{Ti}^{4+} ion, an off-center position does not appear likely for it; furthermore, the activation energy required to reorient such an off-center ion may constitute about 0.1 eV, as in the case of the Li^+ ion in $KTaO_3$ (where the activation energy is about 0.09 eV).

Thus, out of the above centers in $SrTiO_3$: Mn that can account for the observed relaxation, only one center, $\{Mn_{Ti}^{2+}-O^-\}$ (or $\{O^- - Mn_{Ti}^{2+}-O^-\}$), is left. The activation energy for this center should be fairly low (a few tens of millielectronvolts), in agreement with Tables 1 and 2, and the relaxation time should lie between the electronic and phonon relaxation times, which is approximately what is observed. Thus, we assume that the dielectric relaxation observed in our $SrTiO_3$: Mn samples at relatively high temperatures is related to thermally activated polaron dynamics. We note that the existence of polarons in $SrTiO_3$ is still a subject of debate [9].

An obvious question arises as to why we did not observe the relaxation associated with the $\{Mn_{Ti}^{2+}-V_O\}$ center. Two answers to this question can be offered; namely, either the concentration of the $\{Mn_{Ti}^{2+}-V_O\}$ centers in our samples is very low (because they were not subjected to high-temperature calcination in a reducing atmosphere [1, 2, 7]) or the parameters of the relaxation, U and τ_0, are such that this relaxation does not fall into the frequency and temperature ranges studied by us (the lowest frequency was 10 Hz, and the highest temperature, 300 K). Indeed, as follows from Eq. (5), for a high enough activation energy and/or long enough relaxation time τ_0, the relaxation should be seen at temperatures above 300 K. For instance, for U = 0.55 eV and $\tau_0 = 10^{-10}$ s, the maximum value of ε'' for a frequency of 10 Hz should be observed at 370 K.

As follows from Figs. 8 and 9, the experimental points deviate from the Arrhenius plot at low temperatures. This can be accounted for by the fact that at low temperatures the classical thermally activated regime switches to quantum tunneling, with the hopping rate becoming dependent on temperature, as was first observed in nominally pure $SrTiO_3$ crystals [4]. The tunneling relaxation mode was also observed to occur in $SrTiO_3$: Ca [10] and $KTaO_3$: Li [11] and was assigned to tunneling of the off-center Ca_{Sr}^{2+} and Li_K^+ ions, respectively. An attempt was made in [12] to relate the tunneling in the same crystals doped by Ca and Li to bipolaron tunneling, but without invoking any particular (bi)polaron model. As for the results of our experiments on dielectric relaxation with a transition from the classical thermally activated to quantum tunneling mode, they will be described in detail elsewhere [13].

Consider now the relaxation strength $\varepsilon_0 - \varepsilon_\infty$. The largest relaxation strength in our $SrTiO_3$: Mn samples is $(\varepsilon_0 - \varepsilon_\infty) \approx 3500$. This quantity can be estimated following the approach used in [6].

Table 3. Ionic radii following Shannon [8] (N_k is the coordination number; R_i and R_h are the radii of the impurity and the main ion)

N_k	Sr^{2+}	Ti^{4+}	O^{2-}	Mn^{2+}		Mn^{3+}		Mn^{4+}	
	12	6	8	6	12	6	12	6	12
R, Å	1.44	0.605	1.42	0.83	1.25	0.645	1.0	0.53	0.96
R_i/R_h				1.37	0.87	1.07	0.69	0.88	0.67

Note: The values of the ionic radii of manganese ions for $N_k = 12$ were obtained by extrapolating the data available for smaller N_k.

The polarization induced by a field E is given (in CGSE units) by

$$P = (p^2 n/3kT)[(\varepsilon_\infty + 2)/3]E, \quad (7)$$

where p is the dipole moment of the defect under study, n is the defect concentration, ε_∞ is the permittivity for $\omega\tau \gg 1$ (i.e., at frequencies too high for the defects to contribute to the permittivity), and the factor $(\varepsilon_\infty + 2)/3$ accounts for the enhancement of the local electric field compared to the applied field [14].

From Eq. (7), the permittivity ε_0 is found to be

$$\varepsilon_0 = 4\pi(p^2 n/9kT)(\varepsilon_\infty + 2). \quad (8)$$

The dipole moment of the defects of interest here is $p \approx ea \approx 2 \times 10^{-17}$ CGSE = 20 D. For $x = 0.01$, we have $n = 1.7 \times 10^{20}$ cm^{-3}, so that, for $\varepsilon_\infty = 2000$ and $T = 100$ K, Eq. (8) yields $\varepsilon_0 = 8000$ and the relaxation strength becomes $\varepsilon_0 - \varepsilon_\infty = 6000$. Thus, even such a rough estimate shows that this approach can be employed for describing experimental results.

We note in conclusion that, in studying $SrTiO_3$–$SrMnO_3$ solid solutions, we expected to detect ferroelectric properties in this system. The tolerance factor for the $SrMnO_3$ compound, as already mentioned, is $t = 1.04$. Because the tolerance factors of the classical ferroelectrics $BaTiO_3$ and $PbTiO_3$ are 1.06 and 1.02, respectively (for $SrTiO_3$, $t = 0.998$), it appears only natural to assume that the cubic $SrMnO_3$ with the perovskite structure is also a ferroelectric. In this case, the $SrTiO_3$–$SrMnO_3$ system should undergo a ferroelectric phase transition. No such transition has been observed, however; therefore, this point requires further study.

ACKNOWLEDGMENTS

The authors are indebted to N.V. Zaĭtseva for performing the x-ray measurements and to B.T. Melekh, P.P. Syrnikov, V.V. Krasovskaya, and V.A. Yankovskaya for preparing the samples. One of the authors (E.P.S.) acknowledges the financial support of the Ministry of Science of Sachsen.

This study was supported by the President of the Russian Federation (project no. NSh-2168.2003.2), the program "Physics of Solid-State Nanostructures," and a program of the DPS RAS.

REFERENCES

1. R. A. Serway, W. Berlinger, K. A. Müller, and R. W. Collins, Phys. Rev. B **16**, 4761 (1977).
2. K. W. Blazey, J. M. Cabrera, and K. A. Müller, Solid State Commun. **45**, 903 (1983).
3. E. Iguchi, N. Kubota, T. Nakamori, N. Yamamoto, and K. J. Lee, Phys. Rev. B **43**, 8646 (1991).
4. R. Viana, P. Lukenheimer, J. Hemberger, R. Böhmer, and A. Loidl, Phys. Rev. B **50**, 601 (1994).
5. O. Bidault, M. Maglione, M. Actis, M. Kchikech, and B. Salce, Phys. Rev. B **52**, 4191 (1995).
6. V. V. Lemanov, A. V. Sotnikov, E. P. Smirnova, and M. Weihnacht, Fiz. Tverd. Tela (St. Petersburg) **44**, 1948 (2002) [Phys. Solid State **44**, 2039 (2002)].
7. C. B. Azzoni, M. C. Mozzati, A. Paleari, V. Massarotti, M. Bini, and D. Capsoni, Solid State Commun. **114**, 617 (2000).
8. R. D. Shannon, Acta Crystallogr. A **32**, 751 (1976).
9. J. F. Scott, A. Q. Jiang, S. A. T. Redfern, Ming Zhang, and M. Dawber, J. Appl. Phys. **94**, 3333 (2003).
10. W. Kleemann and H. Schremmer, Phys. Rev. B **40**, 7428 (1989).
11. W. Kleemann, V. Schönknecht, D. Sommer, and D. Rytz, Phys. Rev. Lett. **66**, 762 (1991).
12. A. Levstik, C. Filipic, V. Bobnar, and R. Pirc, Appl. Phys. Lett. **81**, 4046 (2002); Appl. Phys. Lett. **82**, 4843(E) (2003).
13. V. V. Lemanov, A. V. Sotnikov, E. P. Smirnova, and M. Weihnacht (in preparation).
14. Ch. Kittel, *Introduction to Solid State Physics*, 4th ed. (Wiley, New York, 1971; Nauka, Moscow, 1978).

Translated by G. Skrebtsov

Physics of the Solid State, Vol. 46, No. 8, 2004, pp. 1449–1455. Translated from Fizika Tverdogo Tela, Vol. 46, No. 8, 2004, pp. 1409–1415.
Original Russian Text Copyright © 2004 by Kardashev, Plaksin, Stepanov, Chernov.

DEFECTS, DISLOCATIONS, AND PHYSICS OF STRENGTH

Effect of Proton and Laser Irradiation on the Elastic and Inelastic Properties of a V–Ti–Cr Alloy

B. K. Kardashev*, O. A. Plaksin, V. A. Stepanov**, and V. M. Chernov*****

** Ioffe Physicotechnical Institute, Russian Academy of Sciences, Politekhnicheskaya ul. 26, St. Petersburg, 194021 Russia*
e-mail: b.kardashev@mail.ioffe.ru

*** Leĭpunskiĭ Institute of Physics and Power Engineering, Russian Federal Research Center, pl. Bondarenko 1, Obninsk, Kaluzhskaya oblast, 249020 Russia*

**** Federal State Unitary Enterprise Bochvar All-Russia Research Institute of Inorganic Materials, ul. Rogova 5, Moscow, 123060 Russia*

Received December 30, 2003

Abstract—The behavior of Young's modulus E and the decrement of ultrasonic vibrations δ in a V–4Ti–4Cr alloy is studied during proton (8-MeV protons, dose rate 10^4 Gy/s) or IR laser (YAG : Nd^{3+} laser, wavelength 1.06 μm, intensity up to 10^2 W/cm^2) irradiation. Measurements are performed using the method of a composite piezoelectric oscillator (longitudinal 100-kHz resonance vibrations). The sizes of the irradiated surface regions of a sample in the proton and laser experiments are the same in order to provide the same thermal conditions in the sample–quartz transducer system. The amplitude, time, and temperature dependences of E and δ are measured before and after preliminary plastic deformation, as well as before, during, and after irradiation of a sample. The process of postdeformation aging (the kinetics of recovery of internal friction after deformation) during proton irradiation is shown to differ substantially from that during laser irradiation. The specific features detected can be explained by the more intense evolution of the defect structure during proton irradiation. Analysis shows that radiation annealing is related to the ionizing component of proton irradiation, which excites the electronic subsystem of the metallic alloy and, thus, creates hot electrons and plasmons. The electron excitations relax at lattice defects (dislocations) and increase the dislocation mobility; this results in a relatively rapid decrease in the dislocation density and in a more significant (as compared to the laser irradiation) decrease in the level of internal stresses in the material. *© 2004 MAIK "Nauka/Interperiodica".*

1. INTRODUCTION

Metallic alloys of the V–Ti–Cr system are of practical interest as promising materials for the first wall and a blanket in a novel fusion reactor [1, 2]. The structural materials of the reactor are subjected to various radiations, such as neutrons, protons, and γ rays. As a result of irradiation by neutrons or ions, cascades of atom–atom collisions occur in the materials. Depending on the energy, temperature, and the type of materials involved, the cascades are either a set of regions consisting of isolated Frenkel pairs or a compact region where the energy of the atoms that are primarily knocked-out is spent for both atomic ionization and displacements. Calculations show [3] that dense cascades with an energy of primarily knocked-out atoms of about 0.1 MeV can be as large as 6–7 nm. Late in the development of the dense cascades, a shock wave (traveling distances that are longer than the cascade size and even longer than the projective ion range) forms in them [4]. This wave induces pressures as high as 10^{11} Pa. As a result, plastic deformation occurs in a volume that significantly exceeds the cascade volume. The evolution of the dislocation structure that appears during this deformation has a substantial effect on the behavior of the material upon irradiation.

In this paper, we present the results of *in situ* acoustic studies of the dislocation structure evolution in V–4Ti–4Cr alloy samples (the numerals indicate the percentage of titanium and chromium in the alloy). This work is a continuation of studies [5, 6], where it was found that, when the alloy is irradiated by 8-MeV protons, its elastic modulus (Young's modulus), as a rule, decreases and the decrement of acoustic vibrations increases. This behavior is mainly caused by the heating of the material during irradiation. However, there is another cause that can result in changes in the acoustic parameters to be measured; namely, the changes can be related to the appearing (radiation) defects and/or the evolution of the defect structure existing in the material. As shown in [5, 6], the sample temperature T measured with a thermocouple often differs significantly from the temperature estimated using the thermoelastic coefficient $\Delta E/\Delta T$ determined experimentally upon conventional heating of the material.

The main problem in studying the behavior of a material during irradiation consists in separating the effects that influence the mechanical properties of the material, namely, defect formation and the evolution of a defect structure; the latter can occur upon heating and as a result of radiation stimulation. This problem is

1063-7834/04/4608-1449$26.00 © 2004 MAIK "Nauka/Interperiodica"

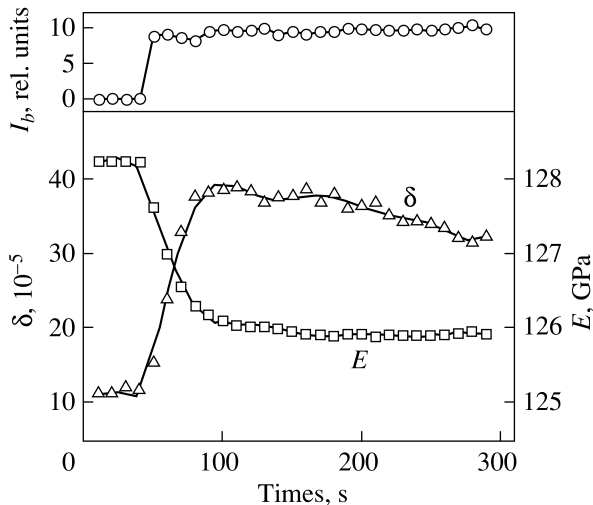

Fig. 1. Initial portion of the experimental time dependences of the decrement δ and Young's modulus *E* measured during irradiation by 8-MeV protons with intensity I_b of a V–4Ti–4Cr alloy sample that was first bent and then straightened.

rather complex and can be solved by carrying out *in situ* acoustic experiments. The thermal conditions of such experiments (the temperature and temperature gradients in a sample) must be the same in both proton experiments and conventional heating. In this work, we meet this requirement using a laser beam, which imitates the thermal heating of a sample during proton irradiation.

We study the acoustic properties of a V–4Ti–4Cr alloy after laser heating and proton irradiation and the recovery of internal friction (ultrasonic damping) during the proton and laser action on a material subjected to preliminary plastic deformation.

2. EXPERIMENTAL

We studied samples of a V–4Ti–4Cr alloy prepared in the United States. Samples in the form of 22.8 × 2.5 × 1.0-mm rods were cut from plates and vacuum-annealed at 1075°C for 1 h.

We applied the acoustic technique described in [5, 6]. For measurements, the method of a composite piezoelectric oscillator was used. Longitudinal resonance vibrations with a frequency *f* of about 100 kHz were excited in a sample with a quartz transducer. The parameters to be measured were the Young's modulus $E \propto f^2$ and the vibration decrement δ. These parameters and the sample temperature during irradiation were measured every 10 s at a fixed amplitude $\varepsilon = 1.0 \times 10^{-6}$, which falls in the range of amplitude-independent damping for vanadium alloys [6, 7]. The amplitude was automatically stabilized with an error of less than 5%. The $E(\varepsilon)$ and $\delta(\varepsilon)$ amplitude dependences before and after deformation and before and after irradiation were measured at room temperature in the amplitude range from $\sim 10^{-6}$ to 3×10^{-4}.

To separate the thermal effect of radiation, we also performed measurements under laser-heating conditions. The geometry of laser irradiation coincided with that of proton irradiation. The same sample was used for the measurements. An 8-MeV proton beam or a laser beam (wavelength 1.06 μm) was directed onto the central part of the wide face of a rod. The spot diameter in both cases was about 1 cm. For temperature measurements, a thermocouple was attached (by spot welding) to the center of the rod sample from the side opposite to the irradiated side. For irradiation, we used an ÉGP-10M proton accelerator (RFRC IPPE, Obninsk) and a YAG : Nd^{3+} continuous laser. As the intensity of irradiation was varied, the sample temperature varied from 20 to 200°C. Thus, we obtained $E(T)$ and $\delta(T)$ temperature dependences, as well as $E(t)$ and $\delta(T)$ time (dose) dependences at various temperatures. The measurements were carried out upon heating and cooling.

During the testing, samples were in air at atmospheric pressure. For deformation, we applied three-point bending, which allowed us to study the same sample in its undeformed and deformed states without unsticking it from the quartz transducer. We studied bent samples (the plastic bending flexure at the center of a sample was 0.3 mm) and also samples that were first bent and then straightened.

Three types of procedures were applied in the experiments: (1) A sample in the undeformed state was irradiated by protons; then a laser beam; again by protons, but after the sample was deformed; and finally by a laser beam. (2) A second sample was first plastically bent, then irradiated by protons, and finally irradiated by a laser beam. (3) A third sample was first annealed and deformed, then heated by a laser beam, and finally irradiated by protons.

3. EXPERIMENTAL DATA

Figures 1 and 2 show the initial portions of time diagrams recorded during the proton irradiation of two samples of the V–4Ti–4Cr alloy. Figure 1 shows how the acoustic parameters (Young's modulus *E*, decrement δ) change in a bent and then straightened sample during proton irradiation at a constant intensity. Figure 2 shows the variation of the temperature *T* of a plastically bent sample and the variation of its decrement δ early in the irradiation.

The results of studying the effect of proton and laser irradiation show that all deformed samples behave qualitatively similarly at a constant radiation intensity. Young's modulus decreases and then levels off if the sample temperature is constant, and the decrement increases significantly upon heating and then gradually decreases with time. The so-called recovery of internal friction is observed, which is related to aging after deformation. This process is irreversible, as indicated

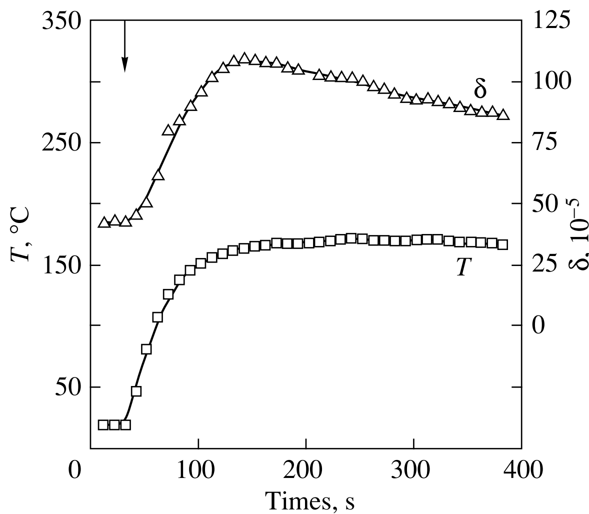

Fig. 2. Time dependences of the decrement δ and temperature T of a bent V–4Ti–4Cr alloy sample measured during irradiation by 8-MeV protons. The arrow shows the instant of the beginning of irradiation.

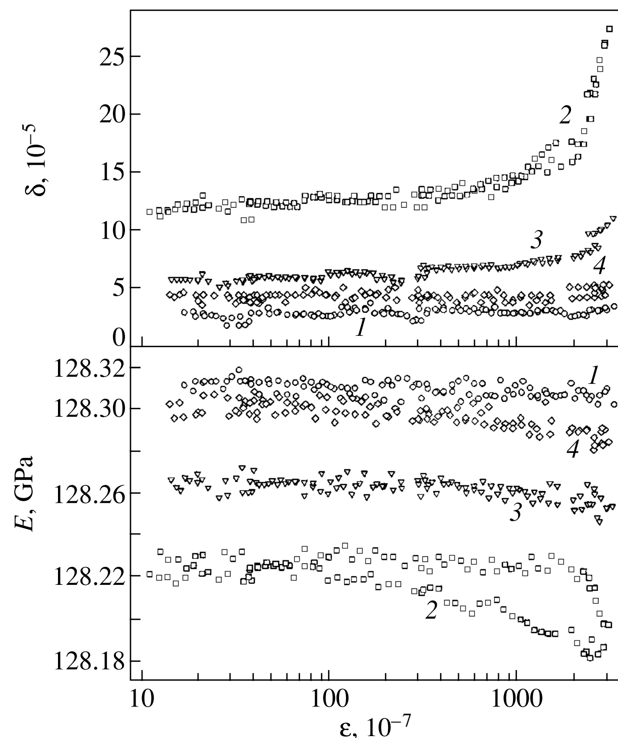

Fig. 3. Amplitude dependences of the decrement δ and Young's modulus E of a nonirradiated V–4Ti–4Cr alloy sample (*1*) before and (*2*) after preliminary deformation by bending followed by unbending. (*3*, *4*) The same but after proton irradiation at doses of 2.8×10^{15} and 9.4×10^{16} protons/cm^2, respectively. The measurements were performed by increasing and then decreasing ε.

by both the amplitude (Figs. 3, 4) and temperature (Figs. 5, 6) dependences of Young's modulus and the decrement. As a result of irradiation, the decrement and elastic modulus tend to return to their initial values measured before deformation.

It should be noted that the recovery of $\delta(t)$ in the alloy under study follows a linear law in most cases. This behavior is illustrated by Fig. 7, which shows the time dependences of the relative change in the decrement for various samples irradiated by protons and a laser beam (δ_0 is the maximum decrement for each sample in the experiment at a steady-state temperature, and the time $t = 0$ corresponds to the instant of the maximum decrement). The parameters characterizing the recovery of internal friction in all samples of the V–4Ti–4Cr alloy are given in Table 1. In addition to the data on δ_0, Table 1 contains the values of $\Delta\delta/\Delta t$ (which reflect the rate of change in the absolute value of the decrement in various experiments) and the values of the characteristic time $\tau = \Delta t/(\Delta\delta/\delta_0)$ corresponding to the slopes of the straight lines in Fig. 7 (τ is the time it takes for the quantity δ/δ_0 to change twofold). The temperature dependences of this parameter for all V–4Ti–4Cr samples irradiated by both protons and a laser beam are given in Fig. 8.

The behavior of Young's modulus during the proton and laser irradiation can be judged from Figs. 5 and 6 and Table 2. Figures 5 and 6 are plotted with allowance for the complete time diagrams for the sample temperature T, Young's modulus E, and the decrement δ. Table 2

Table 1. Damping characteristics of deformed V–4Ti–4Cr alloy samples under irradiation by protons and a laser beam

Sample no.	Deformation	Irradiation	Irradiation temperature, °C	δ_0, 10^{-5} rel. units	$\Delta\delta/\Delta t$, 10^{-5} s^{-1}	$\tau = \Delta t/(\Delta\delta/\delta_0)$, s
1	Bending	Protons	170	120	0.102	1180
2	″	″	125	195	0.082	2380
3	″	″	121	110	0.070	1560
4	Bending–unbending	″	181	40	0.029	1370
5	Bending	Laser	91	51	0.0042	12100
6	″	″	135	65	0.0074	9100
7	″	″	188	240	0.104	2310

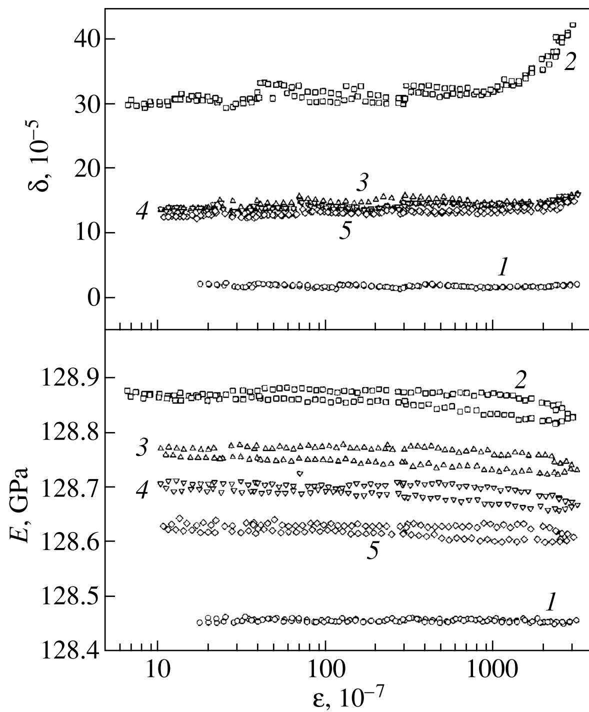

Fig. 4. Amplitude dependences of the decrement δ and Young's modulus E of a nonirradiated V–4Ti–4Cr alloy sample (*1*) before and (*2*) after preliminary deformation by bending. (*3–5*) The same but after proton irradiation at doses of 3.0×10^{15}, 6.4×10^{15}, and 9.5×10^{16} protons/cm^2, respectively. The measurements were performed by increasing and then decreasing ε.

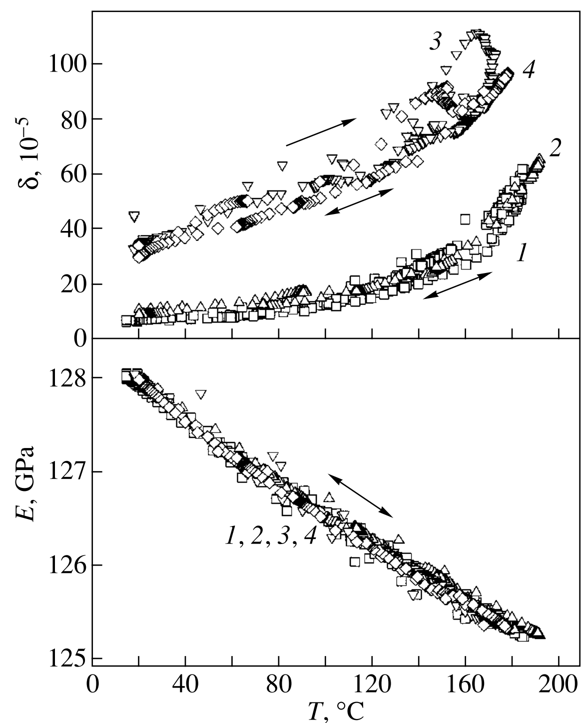

Fig. 5. Temperature dependence of Young's modulus E and decrement δ of a V–4Ti–4Cr alloy irradiated by (*1*, *3*) protons and (*2*, *4*) a laser beam. (*1*, *2*) Undeformed sample and (*3*, *4*) the same sample after preliminary deformation by bending. The arrows show the direction of temperature variation.

lists the data on the temperature coefficients $\Delta E/\Delta T$ obtained on samples before and after plastic deformation by bending.

Figures 5 and 6 show that the modulus varies linearly with temperature with a correlation coefficient of no less than 0.994 for all experiments and all samples. Thus, analysis of the $E(T)$ dependences can be reduced to a comparison of the thermoelastic coefficients $\Delta E/\Delta T$ determined in various experiments. Possible error in the estimation of $\Delta E/\Delta T$ was determined experimentally on one of the annealed undeformed samples, which exhibited no noticeable irreversible structural changes. The error in the estimation of $\Delta E/\Delta T$ was found to be smaller than 2–3%. Table 2 gives the absolute errors in determining $\Delta E/\Delta T$ for each sample in various experiments.

Table 2. Thermoelastic coefficients $\Delta E/\Delta T$ reflecting changes in Young's modulus E with temperature T in a V–4Ti–4Cr alloy irradiated by protons or a laser beam (numerals in parentheses are the ordinal numbers of experiments with the given sample; the signs = and > mean approximately equal or different values of $\Delta E/\Delta T$, respectively, in the proton and laser experiments)

Sample no.	Sample state	$\Delta E/\Delta T$, MPa/K	
		proton irradiation	laser irradiation
1	Undeformed	16.0 ± 0.3 (1) =	15.6 ± 0.3 (2)
1	Bent	16.9 ± 0.3 (3) =	16.5 ± 0.3 (4)
2	Bent	22.5 ± 0.5 (1) >	18.4 ± 0.4 (2)
3	Undeformed	–	17.4 ± 0.3 (1)
3	Bent	19 ± 0.4 (3) >	16.3 ± 0.3 (2)

A comparison of the data from Figs. 5 and 6 indicates that the results for the deformed samples differ from each other: the data in Fig. 5 are obtained using procedure 1, and the data in Fig. 6, using procedure 2 (see above). The decrement of the deformed sample (Fig. 6) increases with temperature, and this sample undergoes more intense aging upon proton irradiation as compared to the sample that is preliminarily subjected to irradiation and then deformed (Fig. 5). As seen from Fig. 6, the modulus E decreases with increasing temperature during proton irradiation more rapidly than during laser heating performed later on the same sample.

The data obtained indicate that the radiation (thermal) and deformation histories of the samples are important for the acoustic parameters, which reflect the evolution of the defect structure of the material under various external conditions.

4. DISCUSSION OF THE RESULTS

The behavior of the decrement δ (Figs. 1, 2, 7) in the experiments with proton and laser irradiation qualitatively resembles the peaking effect that was detected in unalloyed fcc and hcp metals irradiated by 1–2-MeV electrons and γ rays and discussed extensively in the 1970s–1980s [8, 9]. Review [9] contains a number of models for explaining this effect; these models, as a rule, reduce to taking into account the interaction of dislocations with point (radiation) defects. For example, in one of the models (according to [9], it describes the experimental characteristics of this effect most precisely), certain defects serve as pinning centers for dislocations (which decrease the damping), while other radiation defects, located at a certain distance from slip planes, cause an increase in the viscous retardation of dislocations, which explains the increase in the decrement early during irradiation. The temperature of a sample is thought to be virtually unchanged after switching the beam on. This is likely to be true, since a possible change in the sample temperature during irradiation was not discussed in the papers reviewed in [9] (the measurements were mainly carried out using the flexural vibrations of thin foils made of copper, aluminum, silver, and magnesium).

The authors of [9] only mentioned that pinning centers can break away from dislocations into the lattice under the action of irradiation, which should increase the dislocation mobility and usually occurs with increasing temperature.

Our experiments differ significantly from the experiments described above in terms of both the material (bcc alloy) and the level of irradiation (8-MeV protons or intense laser radiation). The irradiation heats a sample such that its temperature differs dramatically from the ambient temperature. Nevertheless, the behavior of $\delta(t)$ is qualitatively the same: there is a maximum in the damping curve. Undoubtedly, the increase in the decrement under the action of a proton or laser beam in our experiments is mainly caused by the increase in the temperature of the sample. The subsequent decrease in the decrement with time can be due to both dislocation pinning by point defects (including radiation defects) and possible annihilation of dislocations (radiation annealing). During irradiation (heating), the annihilation can occur because of an increase in the dislocation mobility (slip velocity). In this case, dislocation motion can be caused by residual internal stresses. This can also be related to dislocation climb due to the damping of proton-induced point defects. We think that the effect of recrystallization annealing, which appears because of an increase in the slip velocity, is the main factor. This opinion can be supported as follows. First, our experiments show that any irreversible change in the decrement can be achieved by conventional heating, in the absence of radiation point defects in the material. Second (most important), the effects of irradiation on Young's moduli of bent samples and of samples that

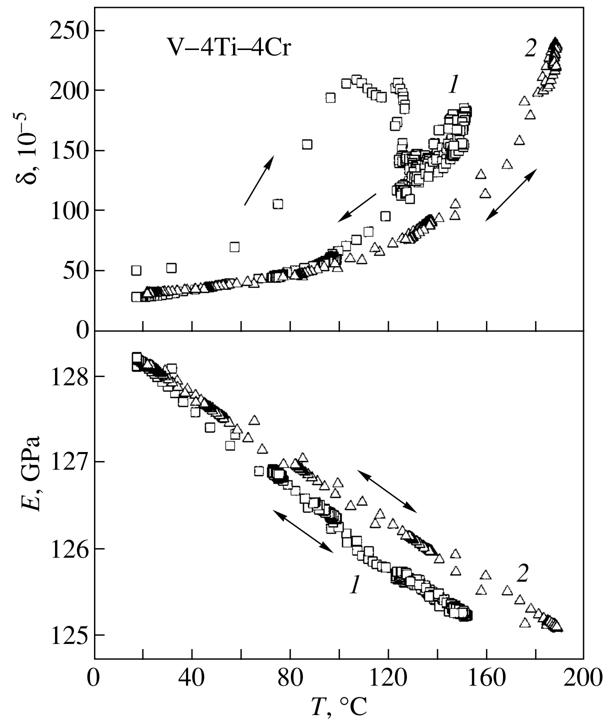

Fig. 6. Temperature dependence of Young's modulus E and decrement δ of a bent V–4Ti–4Cr alloy sample irradiated by (*1*) protons and (*2*) a laser beam upon heating followed by cooling. The arrows show the direction of temperature variation.

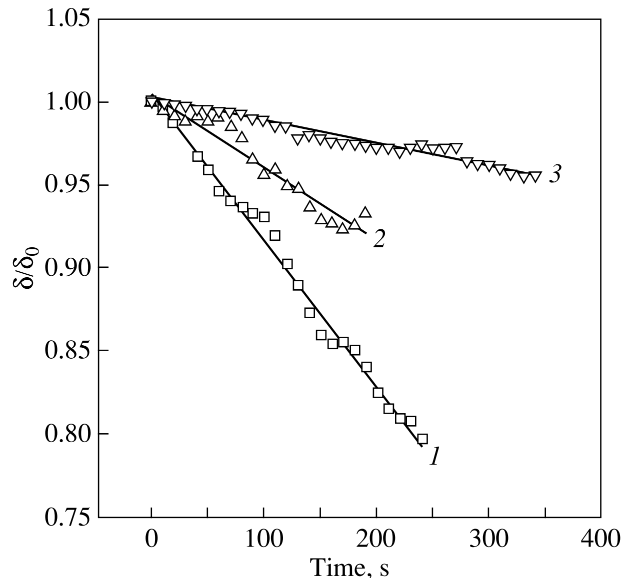

Fig. 7. Relative change in the decrement δ of bent V–4Ti–4Cr alloy samples as a function of the time of irradiation by (*1*) protons and (*2*, *3*) a laser beam. The irradiation temperature is (*1*) 170, (*2*) 188, and (*3*) 135°C.

were first bent and then straightened differ in sign (compare Figs. 3, 4), which cannot be explained in terms of a model where dislocations are pinned and/or viscously retarded by point defects. Indeed, the effects

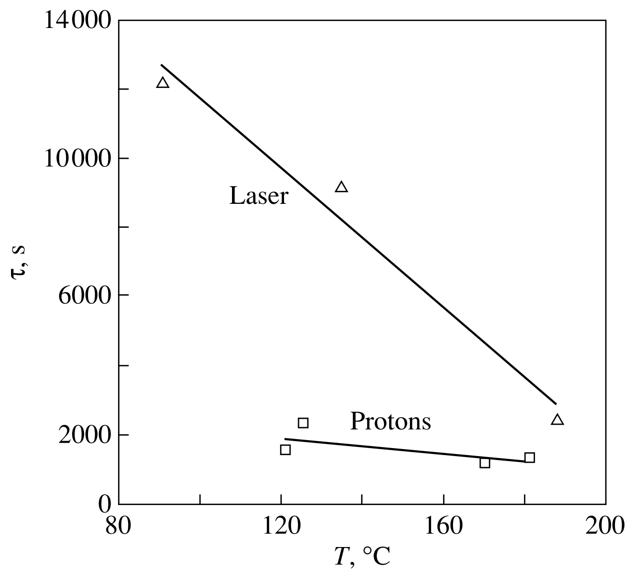

Fig. 8. Temperature dependences of the characteristic time τ of irreversible changes in the decrement (recovery of internal friction after preliminary deformation) for a V–4Ti–4Cr alloy irradiated by protons or a laser beam.

of proton and laser irradiation on the decrement (Figs. 7, 8; Table 1) differ only in the characteristic recovery times τ: for protons, this time is noticeably shorter (by almost an order of magnitude at low temperatures). Analysis indicates that this difference is due to radiation annealing, which increases the dislocation mobility.

For the detected change in the decrement of acoustic vibrations to be caused by dislocation climb, the displacement of each dislocation should be $\sim\rho^{-1/2}$ in a time of $\sim 10^2$ s. According to [10], the supersaturation with point defects in this case should be $\Delta n = b\rho^{1/2} \sim 10^{-4}$ (here, $\rho \sim 10^8$ cm^{-2} is the density of dislocations involved in the process and $b \sim 10^{-8}$ cm is the Burgers vector). However, calculations with the TRIM-90 computer program give $\Delta n \sim 4 \times 10^{-6}$ for vacancies (interstices) created by protons in vanadium alloys along a free path of 220 μm in a time of 10^2 s (proton energy 8 MeV, intensity 10^{12} cm^{-2} s^{-1}). This value is seen to be well below the concentration of radiation defects required for dislocation climb. Therefore, the increase in the rate of relaxation of the decrement should be related to the ionizing rather than the damaging effect of proton irradiation, which stimulates dislocation slip.

As a result of the ionizing effect of proton irradiation, the electron subsystem of the metal becomes excited and virtually all the energy of the protons is consumed to form hot electrons and, eventually, plasmons [11]. The electron excitations are likely to relax mainly at lattice defects, including dislocations, thereby increasing their mobility. The high dislocation mobility increases the rate of their annihilation, which results in a decrease in the decrement of acoustic vibrations.

Like the decrement, the elastic modulus, which is measured with a high accuracy, is a structure-sensitive parameter of the material. From the standpoint of any theory on the interaction between dislocations and point defects (see, e.g., reviews [12, 13]), the decrement, as a rule, increases and the elastic modulus decreases when dislocations are introduced in a sample. Irradiation, which creates additional point defects (dislocation pinning centers) should lead to the opposite effects. In this work, such a result was obtained only for the sample that was first bent and then straightened (Fig. 3). A slightly bent sample exhibits anomalous behavior of the Young's modulus (Fig. 4); namely, it increases after deformation and decreases upon irradiation.

The effect of an increase in *E* after bending deformation in alloys of the V–Ti–Cr system was first observed by us in [7]. An analysis showed that this effect is related to residual internal stresses, whose relaxation in an alloy with a high amount of defects is hindered. Owing to the anharmonicity of atomic vibrations (i.e., higher order elastic constants), these stresses increase the elastic modulus to be measured. Obviously, relaxation of the internal stresses, if it can be realized, should significantly decrease the modulus *E*. The decrease in *E* with increasing radiation dose (illustrated in Fig. 4) suggests annealing of dislocations. Indeed, in terms of our model, a decrease in the dislocation density during irradiation should decrease both the modulus and the decrement.

Annealing of an alloy with a low level of internal stresses (where the effect of higher order elastic constants on the modulus is virtually absent) should increase the modulus and decrease the decrement. In this case, dislocation annihilation and dislocation pinning by point defects produce effects having the same sign. This behavior is likely to explain the finding that, at similar radiation doses, the degree of recovery of the decrement and modulus to their initial (before deformation) values for the bent-and-straightened sample (Fig. 3) is higher than that for the bent sample (Fig. 4).

5. CONCLUSIONS

Using a structural metallic V–4Ti–4Cr alloy as an example, we were the first to detect the effect of a decrease in the elastic modulus upon irradiation. This effect has been found to occur only in materials where the dislocation-assisted relaxation of internal stresses is hindered, e.g., by impurities.

The ionizing component of irradiation has been shown to be important, because it excites the electron subsystem of the alloy (thereby increasing the dislocation slip velocity), results in dislocation annihilation, and, hence, rapidly decreases the level of internal stresses in the material.

REFERENCES

1. R. J. Kurtz, K. Abe, V. M. Chernov, V. A. Kazakov, G. E. Lucas, H. Matzui, T. Muroga, G. R. Odette, D. L. Smith, and S. J. Zinkle, J. Nucl. Mater. **283–287**, 70 (2000).
2. M. I. Solonin, V. M. Chernov, V. A. Gorokhov, A. G. Ioltukhovskiy, A. K. Shikov, and A. I. Blokhin, J. Nucl. Mater. **283–287**, 1468 (2000).
3. V. V. Kirsanov, A. L. Suvorov, and Yu. V. Trushin, *Processes of Radiation Damage in Metals* (Énergoatomizdat, Moscow, 1985) [in Russian].
4. V. P. Zhukov, A. V. Demidov, and A. A. Boldin, in *Materials Technological Problems in Atomic Engineering* (Énergoatomizdat, Moscow, 1991), p. 58 [in Russian].
5. V. M. Chernov, Yu. A. Burenkov, B. K. Kardashev, O. A. Plaksin, V. A. Stepanov, and L. P. Zavialski, in *Proceedings of 4th IEA Vanadium Workshop* (Argon National Laboratory, USA, 1999), p. 759.
6. B. K. Kardashev, V. M. Chernov, O. A. Plaksin, V. A. Stepanov, and L. P. Zavialski, J. Alloys Compd. **310** (1–2), 102 (2000).
7. V. M. Chernov, B. K. Kardashev, L. M. Krjukova, L. I. Mamaev, O. A. Plaksin, A. E. Rusanov, M. I. Solonin, V. A. Stepanov, S. N. Votinov, and L. P. Zavialsky, J. Nucl. Mater. **257**, 263 (1998).
8. H. M. Simpson, A. Sosin, and D. F. Johnson, Phys. Rev. B **5**, 1393 (1972).
9. C. Minier, J. Lauzier, C. Esnouf, and G. Fantozzi, J. Phys. (Paris) **44** (S12), C9 (1983).
10. M. A. Shtremel', *Strength of Alloys: Lattice Defects* (Metallurgiya, Moscow, 1982), Part 1 [in Russian].
11. A. S. Davydov, *Solid-State Theory* (Nauka, Moscow, 1976) [in Russian].
12. S. P. Nikanorov and B. K. Kardashev, *Elasticity and Dislocation Inelasticity of Crystals* (Nauka, Moscow, 1985) [in Russian].
13. G. Gremaud, Mater. Sci. Forum **366–368**, 178 (2001).

Translated by K. Shakhlevich

Physics of the Solid State, Vol. 46, No. 8, 2004, pp. 1456–1461. Translated from Fizika Tverdogo Tela, Vol. 46, No. 8, 2004, pp. 1416–1421.
Original Russian Text Copyright © 2004 by Mazilkin, Kamalov, Myshlyaev.

Structure and Phase Composition of an Al–Mg–Li–Zr Alloy under High-Rate Superplasticity Conditions

A. A. Mazilkin, M. M. Kamalov, and M. M. Myshlyaev

Institute of Solid State Physics, Russian Academy of Sciences, Chernogolovka, Moscow oblast, 142432 Russia

e-mail: mazilkin@issp.ac.ru

Received January 12, 2004

Abstract—Uniaxial-tensile tests are performed on samples of a commercial aluminum–lithium alloy subjected to equal-channel angular extrusion. It is found that the material under study has a highly fine–grain structure and exhibits superplasticity under tension. The microstructure of the samples is studied during their plastic deformation. *© 2004 MAIK "Nauka/Interperiodica".*

1. INTRODUCTION

Nano- and submicrocrystalline materials are of great interest, because they have a number of advantages over conventional coarse-grained materials (higher strength, high-rate superplasticity, etc. [1–3]). Ultrafine-grain materials can be obtained, in particular, through severe plastic deformation. One of the methods for producing such deformations is equal-channel angular (ECA) extrusion. This method was developed by Segal [4, 5] and allows one to obtain bulk submicrocrystalline samples. An important advantage of the ECA extrusion method over the other methods for producing submicrocrystalline materials is that the materials obtained are nonporous and uniform in structure.

In this work, we studied aluminum–lithium alloy 1420 with submicrocrystalline structure produced through ECA extrusion. Because of its unique physical properties (low density, corrosion resistance, weldability [6]), this alloy is of interest and has been studied intensively in recent years [2, 7–9]. It should also be noted that the study of plastic deformation of submicrocrystalline materials may help in predicting their properties at later stages of deformation [10]. In this paper, we report data on the evolution of the structure of alloy 1420 in the course of tensile tests carried out under the conditions of superplasticity.

2. SAMPLES AND EXPERIMENTAL TECHNIQUE

Experiments were performed using rods of alloy 1420 (Al–5.5 wt % Mg–2.2 wt % Li–0.12 wt % Zr) subjected to tenfold ECA extrusion to obtain a microcrystalline grain structure. ECA extrusion was carried out at 370°C. After each passage, the rod was rotated through 90° about its axis (route *B*), which produced the most uniform texture and microstructure in the material [11].

From the rods thus treated, flat samples were prepared for mechanical tests. The thickness of the samples was 0.85 mm, and the length of their gage portion was 5 mm. The samples were deformed in an Instron testing machine under uniaxial-tension conditions at a constant rate of 5 mm/min at 370°C. The temperature was maintained constant to within ±2.5 K in the course of testing. A more detailed description of the study of the mechanical properties can be found in [9].

The structure and phase composition of the alloy in the initial state (after ECA extrusion) and after mechanical tests were examined with a JEM-100CX transmission electron microscope (accelerating voltage 100 kV). The substructure was investigated using **gb** analysis and trace analysis [12]. X-ray phase analysis of the alloy was carried out with a Siemens diffractometer (CuK_α radiation).

3. RESULTS AND DISCUSSION

Figure 1 shows a photograph of the microstructure of the alloy subjected to ECA extrusion. The sample is seen to consist of separate grains. The image of each grain is a dark-field picture taken with one of the zone reflections corresponding to the grain in question. Selected-area diffraction patterns of the grains are also shown in Fig. 1. It can be seen that the structure of the alloy subjected to ECA extrusion is fairly uniform. The grains are equiaxial, and the average grain size is ~1.5 μm. The grains exhibit a developed substructure consisting of isolated dislocations, pileups of dislocations, and dislocation subboundaries. Therefore, because of the presence of subboundaries, the material under study can be characterized as submicrocrystalline.

The average dislocation density in the material is $\sim 10^9$ cm^{-2}. The structure contains precipitations of intermetallic phases, namely, S_1 phase (Al_2LiMg) and δ' phase (Al_3Li). S_1-phase precipitations arise near grain boundaries and triple interface junctions, as well as in the grains themselves, and make up colonies (Fig. 1).

The series of photographs in Fig. 2 illustrates the change in the structure of the alloy caused by its deformation in the course of mechanical tests. The images were obtained in the same way as those in Fig. 1. As already mentioned, the grains in the alloy in the initial state are typically equiaxial in shape. In the alloy with strain $\varepsilon = 110\%$ (Fig. 2a), the structure is dominated by elongated grains. This is also the case for samples with $\varepsilon = 300\%$ (Fig. 2b). In samples with higher strains (900, 1200%), the structure is again characterized by equiaxial grains (Figs. 2c, 2d, respectively).

As the alloy strain is increased, the average grain size slightly increases (up to 2 μm) and the dislocation density decreases down to 10^6–10^7 cm^{-2}. No changes were observed in the size, shape, or distribution of the secondary phases.

We performed a detailed study of the structure of subboundaries with dislocations forming the structure of grains in both the initial material and the samples subjected to mechanical tests. Certain distortions were observed in the structure of the subboundaries. For the most part, these distortions were fairly regular, even though the material was subjected to severe plastic deformations, which indicates that the subboundaries were formed not only through dislocation glide but also through nonconservative motion of dislocations. Figures 3 and 4 show typical examples of dislocation subboundaries observed in alloy samples.

Figure 3 shows photographs of a subboundary (dislocation wall) corresponding to different diffraction conditions (the foil lies horizontally). According to selected-area diffraction data, the projection of the subboundary onto the foil plane corresponds to the (112) plane, the line of intersection of the subboundary and the foil plane is parallel to $[1\bar{3}1]$, and the projections of the dislocations onto the foil plane are approximately parallel to $[11\bar{1}]$.

The foil thickness t near a dislocation wall was determined (for the horizontal film position) by measuring the number of oscillations n in contrast on images of tilted dislocations for $\mathbf{g} = [11\bar{1}]$ and $s \approx 0$, where $\mathbf{g}$ is the diffraction vector and s is a parameter characterizing the deviation from the exact reflection position. The foil thickness is $t = n\xi_{\mathbf{g}} = 0.17$ μm, where $\xi_{\mathbf{g}}$ is the extinction distance corresponding to the reciprocal lattice vector $\mathbf{g}$.

The intersections of the subboundary with the upper and lower foil surfaces were determined using a dark-field image of the subboundary for $s < 0$. Under these conditions, the contrast at dislocation lines is stronger near the upper foil surface than near the lower one [13]. In Fig. 3b, the letters T and B indicate the portions of the subboundary that cross the upper and lower foil surfaces, respectively. The width of the subboundary projection onto the plane of the figure is approximately 0.7 μm. Therefore, the plane of the subboundary is

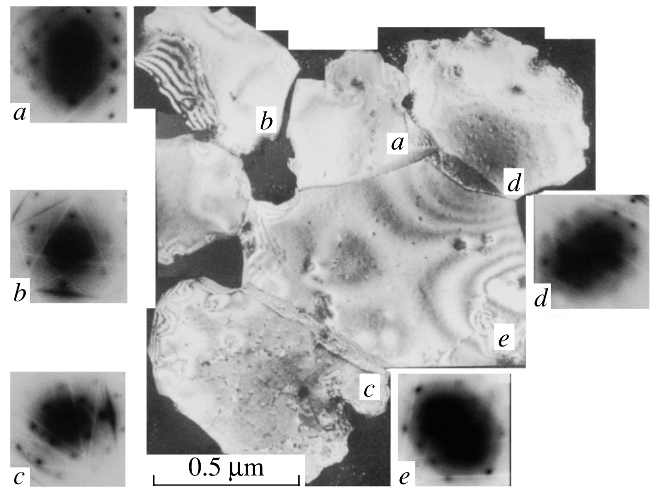

Fig. 1. Composed dark-field picture of the structure of aluminum alloy 1420 taken after ECA extrusion. Identical letters indicate grains and the corresponding diffraction patterns.

tilted at an angle of 19° to the plane of the figure and coincides with the $(10\bar{1})$ plane and the dislocations forming the wall are virtually parallel to the [101] direction.

The Burgers vector $\mathbf{b}$ of dislocations was determined from the reflections $\mathbf{g}$ in which no dislocations were observed or the contrast of dislocations was minimal ($\mathbf{gb} = 0$). This is the case in Fig. 3c. Note that, according to diffraction intensity calculations based on dynamic theory [14], the criterion for the absence of contrast of dislocations with an edge component in the case of $\mathbf{gb} = 0$ is that $m = \mathbf{g}[\mathbf{b} \times \mathbf{u}]/8 \le 0.08$, where $\mathbf{u}$ is a unit vector in the positive direction of a dislocation line. In the case in question, $m = 0.125$; therefore, a low contrast should be observed.

Thus, the dislocation wall at hand consists of mixed ~60° glide dislocations with Burgers vector $\mathbf{b} = (a/2)[110]$ and slip plane $(11\bar{1})$.

A subboundary consisting of a hexagonal network formed by dislocations of three families is illustrated in Fig. 4, where several photographs are shown corresponding to different conditions that determine the subboundary contrast. Analysis of the dislocation composition of the subboundary was performed following the above technique used to analyze the dislocation wall.

As seen from Fig.4 (the foil is in horizontal position), the foil surface coincides with the (110) plane, the line of intersection of the dislocation network with the foil plane is parallel to $[1\bar{3}\bar{1}]$, and the projections of dislocations onto the foil plane are directed along $\mathbf{v}_1 = [\bar{1}11]$, $\mathbf{v}_2 = [1\bar{1}1]$, and $\mathbf{v}_3 = [002]$; the width of the projection of the network onto the plane of the figure is approximately 0.5 μm.

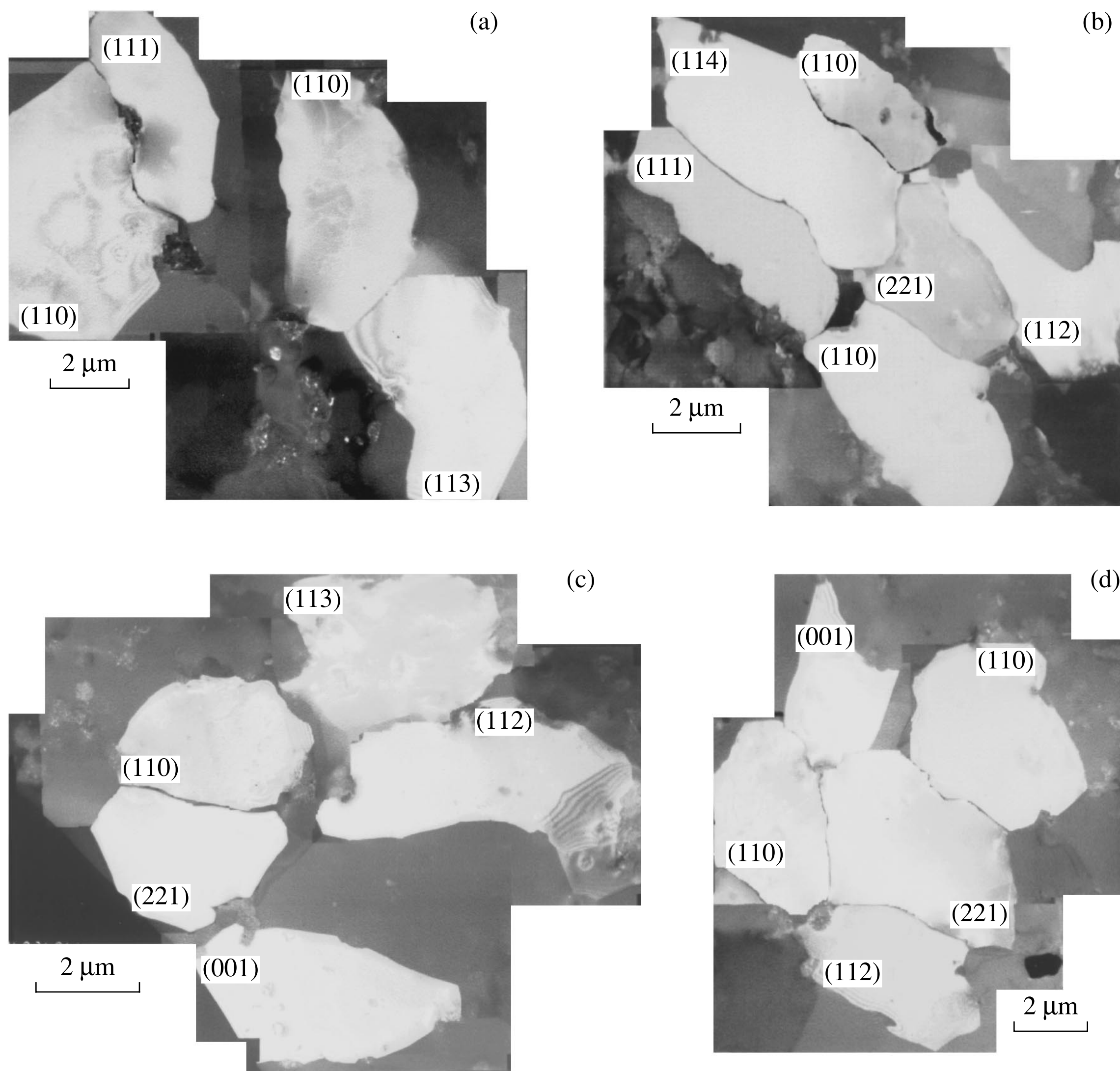

Fig. 2. Composed dark-field pictures of the structure of aluminum alloy 1420 taken during tensile tests for (a) ε = 110, (b) 300, (c) 900, and (d) 1200%. The zone axes are indicated for each grain.

The foil thickness near the dislocation network was determined from the number of thickness extinction profiles on a grain boundary image for $s \approx 0$ (Fig. 4a) and was 0.34 μm. The position of the network plane was determined from the character of the contrast of a dark-field image of dislocations for $s < 0$ (Fig. 4b). This plane was found to coincide with the $(1\bar{2}1)$ plane. Therefore, the dislocation lines are approximately parallel to $\mathbf{u}_1 = [135]$, $\mathbf{u}_2 = [210]$, and $\mathbf{u}_3 = [\bar{1}10]$.

The photographs in Fig. 4 correspond to the cases where the reflecting planes are (002), $(\bar{1}11)$, and $(1\bar{1}1)$. In each of these photographs, only the contrast of two families of dislocations is normal. Therefore, the Burgers vectors for one family of dislocations lie in a reflecting plane in each case. With allowance for the value of the parameter m, it can be found that, for the first family of dislocations, the Burgers vector is $\mathbf{b}_1 = (a/2)[011]$; for the second, $\mathbf{b}_2 = (a/2)[\bar{1}0\bar{1}]$; and for the third, $\mathbf{b}_3 = (a/2)[\bar{1}10]$. All dislocations of the subboundary in question are mixed, and the angles between the vectors **b** and **u** are $\varphi_1 = 18°$, $\varphi_2 = 51°$, and $\varphi_3 = 60°$, respectively. For the third family of dislocations, the slip plane is (111).

These and other similar subboundaries are typical of both the material in the initial state and samples subjected to mechanical tests.

As mentioned above, the material under study contained two of the intermetallic phases known for the Al–Li–Mg system [15, 16], namely, the equilibrium cubic S_1 phase and the nonequilibrium δ' phase (the $L1_2$ structure). Precipitations of the δ' phase are highly dis-

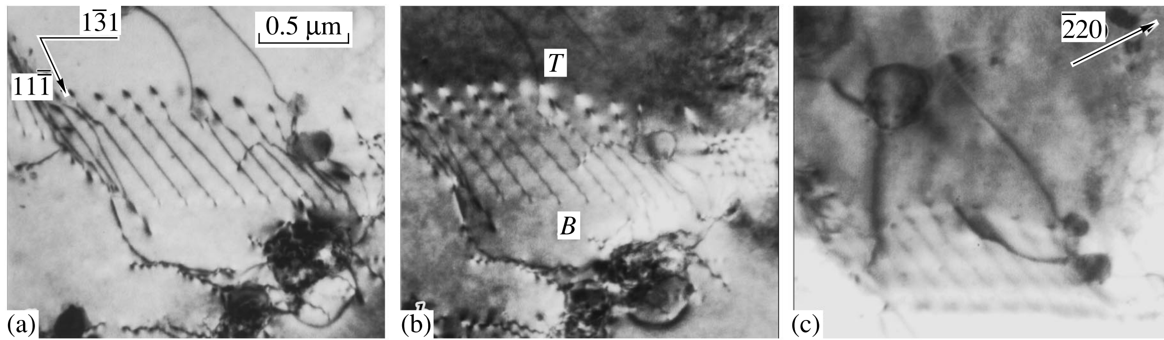

Fig. 3. Photomicrographs of a dislocation wall taken with (a) the $\mathbf{g} = [\bar{1}\bar{1}1]$ reflection, $s \approx 0$; (b) $\mathbf{g} = [\bar{1}\bar{1}1]$, dark field, $s < 0$; and (c) $\mathbf{g} = [\bar{2}20]$.

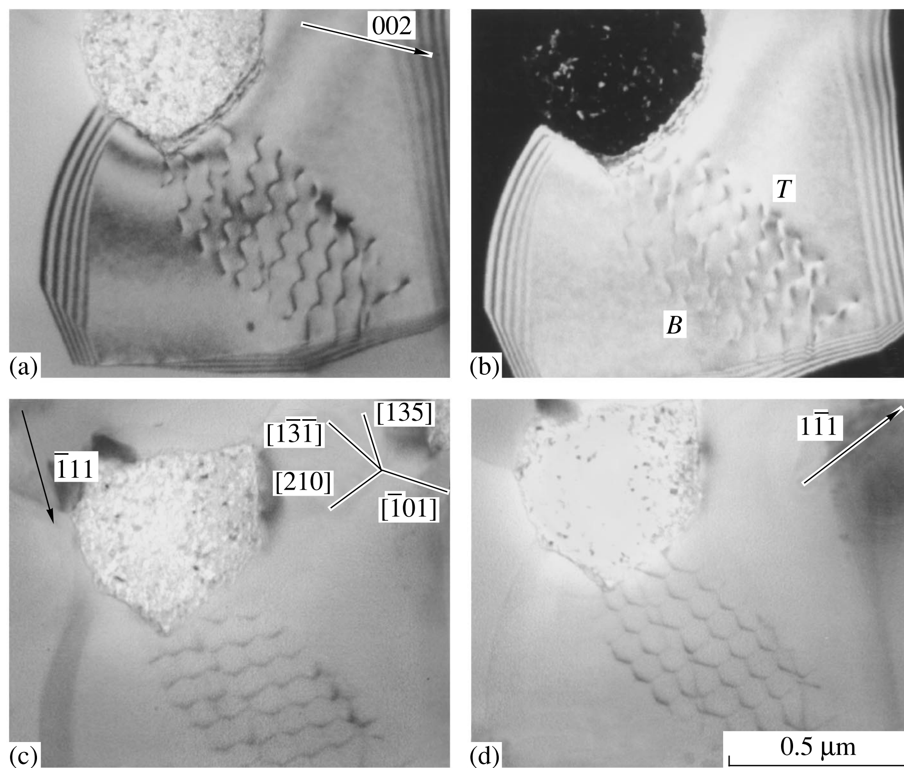

Fig. 4. Pictures of a hexagonal dislocation network taken with (a) the $\mathbf{g} = [002]$ reflection, $s \approx 0$; (b) $\mathbf{g} = [002]$, dark field, $s < 0$; (c) $\mathbf{g} = [\bar{1}11]$; and (d) $\mathbf{g} = [1\bar{1}1]$.

persed, and the presence of this phase can often be detected only through additional reflections in a selected-area diffraction pattern. Precipitations of the S_1 phase are arbitrary in shape, and their size is 0.2–0.3 μm. According to electron-microscopic examinations, the volume fraction of this phase in the material can be as large as 15%. However, an x-ray diffraction study showed that the content of this phase in the alloy is less than 1% (Fig. 5). The positions of the Al and Al_2LiMg reflections are indicated in the bar diagram at the bottom of Fig. 5.

Figure 6 shows a dark-field picture of a portion of the foil containing an S_1-phase precipitation and the corresponding diffraction pattern. The picture was taken with one of the reflections of the phase. The S_1 phase is seen to precipitate in the form of colonies of randomly oriented small (~25-nm) Al_2LiMg crystallites. The contrast of regions containing crystallites of

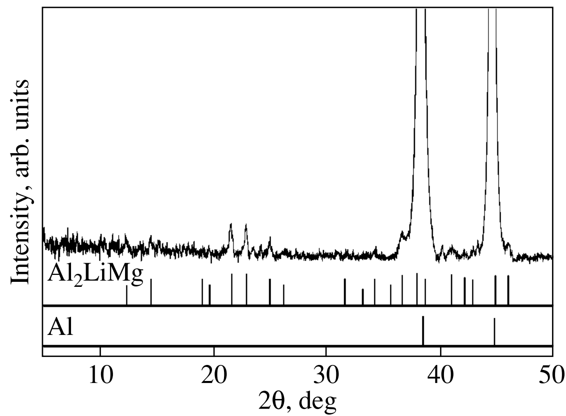

Fig. 5. Diffraction pattern of aluminum alloy 1420 (CuK_α radiation).

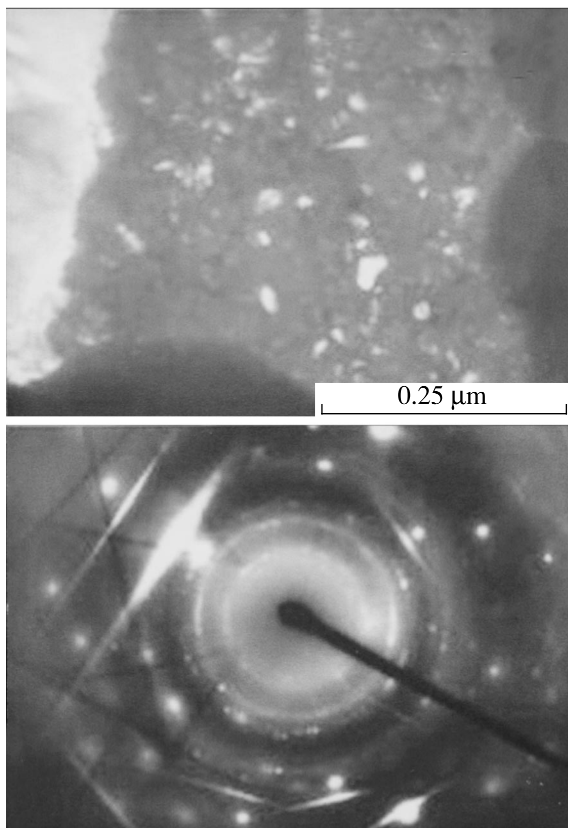

Fig. 6. Dark-field picture and the corresponding selected-area diffraction pattern of a portion of the alloy structure containing S_1-phase particles.

this phase differs from the contrast of other regions of the material (without this phase). The material between crystallites in a colony is, apparently, a Li- and Mg-lean solid solution in an aluminum matrix.

It is instructive to compare the data on the structure of the superplastic aluminum alloy with the results of its mechanical tests performed in [9]. By analyzing the true stress–true strain curve, it was concluded in [9] that the deformation of alloy 1420 is characterized by two main stages: elastic deformation is followed by a relatively short portion of the curve associated with hardening of the material, after which a prolonged softening stage is observed. For the hardening and softening stages, the activation energy was determined to be 1.4 and 0.98 eV, respectively. Based on these values of the activation energy, it was supposed that the dominant mechanism of superplastic deformation in the first stage is self-diffusion in the bulk of grains (which corresponds to dislocation slip in grains) and in the second stage, grain-boundary self-diffusion (i.e., slip along grain boundaries).

Our study of the evolution of the alloy grain structure provides support for the conclusion concerning the dominant mechanisms of deformation. Indeed, in the hardening stage, the grain shape changes from equiaxial to elongated, which indicates the occurrence of intragrain dislocation slip. Since the dislocation density in grains is fairly high at this stage, intragrain dislocation slip can be considered the dominant mechanism of deformation.

Examinations of the alloy structure showed that, at the softening stage ($\varepsilon = 900$, 1200%), grains become equiaxial in shape and the dislocation density in them decreases significantly. Such a structure is typical of superplastic deformation through grain boundary slip [17].

Our electron-microscopic studies of the dislocation boundaries of building blocks indicate that the structure is dominated by various nonequilibrium subboundaries. The subboundary nonequilibrium is associated, first, with the breaking of their structural regularity and, second, with the fact that the dislocations making up dislocation walls have an appreciable screw component and that the dislocations forming a dislocation network have an edge component [18, 19]. Such nonequilibrium boundaries have a higher energy and can undergo thermally activated breakdown when samples are heated and deformed. They produce long-range stress fields in grains, which, in turn, can destroy other subboundaries by causing dislocations to emerge from them.

ACKNOWLEDGMENTS

This study was supported by the Russian Foundation for Basic Research, project nos. 03-02-16947, 01-02-16505, and 02-02-81021.

REFERENCES

1. P. G. Sanders, J. A. Eastman, and J. R. Weertman, Acta Mater. **45** (10), 4019 (1997).
2. M. V. Markushev, C. C. Bampton, M. Y. Murashkin, and D. A. Hardwick, Mater. Sci. Eng. A **234–236**, 927 (1997).
3. K. Neishi, Z. Horota, and T. G. Langdon, Scr. Mater. **45**, 965 (2001).

4. V. M. Segal, V. I. Reznikov, A. E. Drobyshevskiĭ, and V. I. Kopylov, Fiz. Met. Metalloved. **1**, 99 (1981).
5. V. M. Segal, Mater. Sci. Eng. A **197**, 157 (1995).
6. I. N. Fridlyander, Metalloved. Term. Obrab. Met. **4**, 2 (1990).
7. S. Lee, P. B. Berbon, M. Furukava, Z. Horita, M. Nemoto, N. K. Tsenev, R. Z. Valiev, and T. G. Langdon, Mater. Sci. Eng. A **272**, 63 (1999).
8. M. Furukava, Z. Horita, M. Nemoto, and T. G. Langdon, Mater. Sci. Eng. A **324**, 82 (2002).
9. M. M. Myshlyaev, V. V. Shpeĭzman, and M. M. Kamalov, Fiz. Tverd. Tela (St. Petersburg) **43**, 2015 (2001) [Phys. Solid State **43**, 2099 (2001)].
10. V. V. Rybin, *Large Plastic Deformations and Fracture of Metals* (Metallurgiya, Moscow, 1986) [in Russian].
11. M. Furukava, Y. Iwahashi, Z. Horita, M. Nemoto, and T. G. Langdon, Mater. Sci. Eng. A **257**, 328 (1998).
12. *Electron Microscopy of Thin Crystals*, Ed. by P. B. Hirsch, A. Howie, R. B. Nicholson, D. W. Pashley, and M. J. Whelan (Plenum, New York, 1965; Mir, Moscow, 1968).
13. W. L. Bell and G. Thomas, Phys. Status Solidi **12**, 843 (1965).
14. A. Howie and M. J. Whelan, Proc. R. Soc. London, Ser. A **267**, 206 (1962).
15. L. F. Mondolfo, *Aluminum Alloys: Structure and Properties* (Butterworths, London, 1976; Metallurgiya, Moscow, 1979).
16. I. N. Fridlyander, K. V. Chuistov, A. L. Berezina, and N. I. Kolobnev, *Aluminum–Lithium Alloys: Structure and Properties* (Naukova Dumka, Kiev, 1992) [in Russian].
17. O. A. Kaĭbyshev, *Plasticity and Superplasticity of Metals* (Metallurgiya, Moscow, 1975), p. 280 [in Russian].
18. J. C. M. Li, in *Electron Microscopy and Strength of Crystals*, Ed. G. Thomas and J. Washburn (Interscience, New York, 1963).
19. V. K. Lindroos and H. M. Miekkoja, Philos. Mag. **16**, 593 (1967); Philos. Mag. **17**, 117 (1968).

Translated by Yu. Epifanov

Physics of the Solid State, Vol. 46, No. 8, 2004, pp. 1462–1468. Translated from Fizika Tverdogo Tela, Vol. 46, No. 8, 2004, pp. 1422–1427.
Original Russian Text Copyright © 2004 by Ivanova, Kazak, Markov, Ovchinnikov, Rudenko, Abd-Elmeguid.

Analysis of the Electrical and Optical Properties of VBO_3 Single Crystals and $Fe_{1-x}V_xBO_3$ Solid Solutions on the Basis of a Many-Electron Model of Energy Band Structure

N. B. Ivanova*, N. V. Kazak, V. V. Markov**, S. G. Ovchinnikov**, V. V. Rudenko**, and M. M. Abd-Elmeguid*****

**Krasnoyarsk State Technical University, Krasnoyarsk, 660074 Russia*
***Kirenskiĭ Institute of Physics, Siberian Division, Russian Academy of Sciences, Akademgorodok, Krasnoyarsk, 660036 Russia*
e-mail: nat@iph.krasn.ru
**** II. Physikalisches Institut, Universität zu Köln, Köln, 50937 Germany*
Received November 24, 2003

Abstract—A many-electron model of the energy band structure of VBO_3 and of $Fe_{1-x}V_xBO_3$ solid solutions is proposed with strong electron correlations taken into account. Experimental optical absorption spectra and data on the resistivity are discussed in the framework of the suggested model. Variation in the magnetic and electronic properties of VBO_3 and $Fe_{1-x}V_xBO_3$ under high pressure is predicted. For VBO_3, a Mott–Hubbard (insulator–metal) transition is expected in the high-pressure phase. In $Fe_{1-x}V_xBO_3$ solid solutions, a nontrivial variation in the properties is predicted, leading to the appearance of a different magnetic state. © *2004 MAIK "Nauka/Interperiodica".*

1. INTRODUCTION

After the discovery of high-temperature superconductivity in copper oxides, interest in the study of strongly correlated electronic systems has increased substantially. Transition-metal borates form yet another class of oxides, whose magnetic and electrical properties are determined by strong electron correlations in narrow d bands. Transition-metal oxyborates MBO$_3$ (where M = Fe, V, Cr, Ti) crystallize in the calcite structure [space group $R\bar{3}c$ (D^6_{3d})]. In this class of materials, iron borate, $FeBO_3$, has been studied most extensively. This compound was first synthesized in 1963 [1], but correct interpretation of its magnetic properties was given only in 1968, when Joubert and coworkers showed that $FeBO_3$ belongs to a large class of antiferromagnets with weak ferromagnetism [2]. $FeBO_3$ is one of the few compounds that have a spontaneous magnetic moment at room temperature and, at the same time, are transparent in the visible part of the spectrum [3, 4]. Such a combination of magnetic and optical properties makes this material rather promising for applications in magnetooptics [5–7]. Although $FeBO_3$ has been intensively studied for a long time, there are only a few theoretical and experimental investigations into the other representatives of this class, as well as of $FeBO_3$-based solid solutions. In particular, there is no information about their electronic and, in some cases, magnetic structure. The optical properties and anisotropy of these compounds have been studied to an even lesser extent. The VBO_3, $CrBO_3$, and $TiBO_3$ isostructural compounds were synthesized for the first time in 1964 [8]. Further measurements have shown that $CrBO_3$ is a low-temperature antiferromagnet (T_N = 15 K); according to [9], the magnetic moments of the sublattices are oriented along the third-order C_3 axis. The magnetic and electrical properties of $TiBO_3$ were recently studied in [10], and it was assumed that this compound is a weak ferromagnet (T_N = 25 K). To date, the following systems among the $FeBO_3$-based solid solutions have been synthesized and partly investigated: $Fe_{1-x}Ga_xBO_3$ [1, 11–14], $Fe_{1-x}Al_xBO_3$ [13–15], $Fe_{1-x}Cr_xBO_3$ [1, 13, 14, 16, 17], and $Fe_{1-x}M_xBO_3$ with M = Mn, In [14] and M = Mg, Cu [18, 19])

A few studies of $FeBO_3$-based solid solutions containing a transition metal as a substitution ion are restricted to the $Fe_{1-x}M_xBO_3$ (M = Mn, Cr) series; however, by synthesizing solid solutions of isostructural compounds having different transport and magnetic properties, one can intentionally create a situation where competing mechanisms and interactions result in the establishment of magnetic order accompanied by a modification of the electrical properties of the sample. Earlier, we performed a complex study of the electrical, magnetic, and optical properties of $Fe_{1-x}V_xBO_3$ solid solutions [20, 21]. The choice of the V^{3+} ion as a substitution ion is motivated by the large difference in the electrical and magnetic properties of the final compounds. For example, $FeBO_3$ is an antiferromagnet

with weak ferromagnetism (T_N = 348 K) and an insulator with an optical absorption edge E_g = 2.9 eV [22], while VBO_3 is a ferromagnet (T_C = 32 K) and a semiconductor [9].

In spite of the significant advances made in simulation methods, there are no consistent calculations of the energy band structure of transition-metal borates that would even qualitatively account for the interrelation of the observed effects. For this reason, the experimental results were mainly interpreted on the basis of a model. In the case of 3*d*-metal borates, this model was the Mott–Hubbard model. Theoretical studies of the electronic structure of the materials in question are quite scarce and deal mainly with iron borate, $FeBO_3$. One-electron *ab initio* calculations of $FeBO_3$ using the method of the local spin density functional (LDA) and the generalized gradient approximation (GGA) taking into account nonlocal corrections to the L-DA were performed in [23] and [24], respectively. Calculations of the molecular orbitals for the VB_6O_6 and FeB_6O_6 clusters have shown that for both compounds a strong hybridization of *s* and *p* cation states with oxygen *p* states and boron *sp* states occurs [20]. The valence band is formed by strongly hybridized boron and oxygen *s* and *p* states. At the same time, hybridization of the cation *d* electrons with oxygen *s* and *p* electrons is very weak, much weaker than in 3*d*-metal oxides. This is due to strong hybridization in the trigonal BO_3 group. Recently, a collapse of the magnetic moment was observed in iron borate, which was accompanied by a structural transition and modification of the electrical properties of the sample under pressure [25–27]. A many-electron model of the energy band structure of $FeBO_3$ with allowance for strong electron correlations that adequately describes the transition under pressure was given in [28]. However, up to now, there has been no model of the electronic structure of solid solutions describing the observed properties of these systems and the dynamics of their variation at different concentrations x and pressures.

In this study, we discuss the electrical and optical properties of VBO_3 and $Fe_{1-x}V_xBO_3$ single crystals on the basis of the many-electron theory of energy band structure taking into account strong electron correlations for these crystals.

2. SAMPLES AND EXPERIMENTAL TECHNIQUE

We studied single crystals of VBO_3 and $Fe_{1-x}V_xBO_3$ solid solutions grown by spontaneous crystallization from a melt solution [20]. It should be noted that we previously listed the concentrations x determined from the content of the components in the charge (x_s) [20, 21]. To determine the exact amount of the components, we used energy dispersive x-ray analysis (EDAX ZAF Quantification). The values of x obtained and, for comparison, the values of x_s used previously are listed in Table 1.

Table 1. Vanadium concentrations in $Fe_{1-x}V_xBO_3$ solid solutions (x_s is determined from the charge composition; x, from the data from energy dispersive x-ray analysis)

x_s	x
0.25	0.02
0.5	0.13
0.6	0.18
0.75	0.3
0.95	0.95

Since the intermediate contact resistance is rather small, resistance measurements were performed by the two-probe method using a teraohmmeter E6-13A, which made it possible to measure resistances of up to 10^{13} Ω. Samples were heated and cooled at a rate of 1 K/min in order to prevent a parasitic temperature gradient.

Single crystals of the $Fe_{1-x}V_xBO_3$ series were transparent hexahedral plates with the optical C_3 axis perpendicular to the plate plane. The color of the samples varied from light green ($FeBO_3$) to dark brown (VBO_3). The optical absorption of the crystals was measured using a single-beam technique in the spectral range 4000–20000 cm^{-1}. The spectral width of the slit of a grating monochromator was 10 cm^{-1}. The accuracy of the absorption measurements was 3%. The spectral resolution varied from 20 cm^{-1} at 20000 cm^{-1} to 13 cm^{-1} at 4000 cm^{-1}.

3. MODEL OF THE VBO_3 BAND STRUCTURE

To calculate the one-electron density of states $N(E)$ in VBO_3 with allowance for strong electronic correlations in the framework of many-electron theory [28], we consider the occupied term V^{3+} ($3d^2$) and the $3d^1$ and $3d^3$ terms describing the annihilation and creation of an electron from the d^2 state. The Hamiltonian of the model is

$$H_{am} = \sum_{\lambda\sigma}\left(\varepsilon_\lambda n_{\lambda\sigma} + \frac{U_\lambda}{2} n_{\lambda\sigma} n_{\lambda\bar{\sigma}}\right) + \sum_{\substack{\lambda,\lambda' \\ (\lambda\neq\lambda')}} \sum_{\sigma\sigma'} (V_{\lambda\lambda'} n_{\lambda\sigma} n_{\lambda'\sigma'} - J_{\lambda\lambda'} a^{+}_{\lambda\sigma} a_{\lambda'\sigma} a^{+}_{\lambda'\sigma'} a_{\lambda'\sigma}), \quad (1)$$

where $n_{\lambda\sigma} = a^{+}_{\lambda\sigma} a_{\lambda\sigma}$, $a_{\lambda\sigma}$ is the *d* electron creation operator in one of the five orbitals λ with spin projection σ, and $\bar{\sigma} = -\sigma$. The first term describes the atomic *d* levels in the crystalline field; we neglect the small uniaxial

Table 2. Energies $E_s(n)$ of the ground and first excited states of vanadium ions (the subscript denotes spin; n is the electronic configuration)

d^1	d^2	d^3
$E_{1/2}(1) = \varepsilon_d - \frac{2}{5}\Delta$	$E_1(2) = 2\varepsilon_d - \frac{4}{5}\Delta + V - J$	$E_{3/2}(3) = 3\varepsilon_d - \frac{6}{5}\Delta + 3V - 3J$
$E'_{1/2}(1) = \varepsilon_d + \frac{3}{5}\Delta$	$E'_1(2) = 2\varepsilon_d + \frac{1}{5}\Delta + V - J$	$E'_{3/2}(3) = 3\varepsilon_d - \frac{1}{5}\Delta + 3V - 3J$

component of the crystalline field and set $\varepsilon(t_{2g}) = \varepsilon_d - 2\Delta/5$ and $\varepsilon(e_g) = \varepsilon_d + 3\Delta/5$. The remaining terms in Eq. (1) correspond to the Coulomb intraorbit repulsion U_λ, interorbit repulsion $V_{\lambda\lambda'}$, and Hund exchange $J_{\lambda\lambda'}$. For simplicity, we disregard the orbital dependence of the Coulomb matrix elements and assume that there are three parameters, U, V, and J, related by the well-known formula $U = 3V + J$, which follows from the spherical symmetry of the atom.

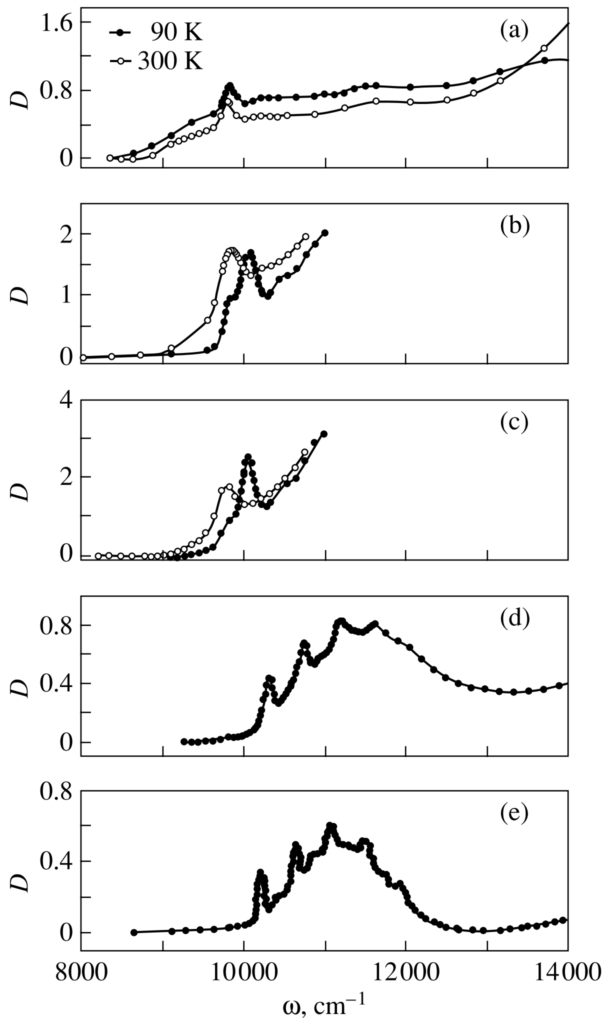

Fig. 1. Optical absorption spectra of solid solutions of the system $Fe_{1-x}V_xBO_3$. (a) VBO_3, (b) $Fe_{0.7}V_{0.3}BO_3$, (c) $Fe_{0.82}V_{0.18}BO_3$, (d) $Fe_{0.98}V_{0.02}BO_3$, and (e) $FeBO_3$.

Since the M–O distances in the VBO_3 and $FeBO_3$ octahedrons are approximately equal, we assume that the Coulomb parameters U, V, and J have the same values as in $FeBO_3$. Furthermore, we assume that the energy of the crystalline field Δ for VBO_3 is close to $\Delta = 1$ eV for $FeBO_3$. Strongly hybridized s and p states of the BO_3 group show almost no change [20]. Thus, we can assume that the bottom of the conduction band ε_c and the top of the valence band ε_c in VBO_3 are also close in energy, with the energy distance between them (the absorption threshold) being $E_{g0} = 2.9$ eV.

Table 2 lists the energies $E_S(n)$ of the ground and first d^n excited terms with $n = 1, 2, 3$ for vanadium ions with spin S calculated in the strong crystalline field approximation. We find the crystalline field parameter from the optical absorption spectrum of VBO_3 (Fig. 1a), where a low-intensity peak is observed at the energy $\omega_0 = 9800$ cm^{-1} [20]. If we assume, by analogy with $FeBO_3$, that this peak is related to d–d transitions (in this case, transitions occur from the ground-state term $^3T_1$ of the V^{3+} ion to the first excited term $^3T_2$ with energy $\omega_0 = E'_1(2) - E_1(2) = \Delta$), then we obtain $\Delta = 1.21$ eV. This value is smaller than the quantity $\Delta = 1.57$ eV for $FeBO_3$ [29]. Furthermore, we assume that the values of the Coulomb parameters U, V, and J are close to the analogous parameters for $FeBO_3$; according to [30], $U = 3$ eV, $V = 1.15$ eV, and $J = 0.7$ eV.

The levels Ω_v and Ω_c are analogous to the lower and upper Hubbard bands for a zero interatomic hopping parameter t:

$$\Omega_v = E_1(2) - E_{1/2}(1) = \varepsilon_d - \frac{2}{5}\Delta + V - J,$$
$$\Omega_c = E_{3/2}(3) - E_1(2) = \varepsilon_d - \frac{2}{5}\Delta + 2V - 2J. \quad (2)$$

The effective Hubbard energy is defined as the energy of transitions between the lower and upper Hubbard bands:

$$U_{\text{eff}} = \Omega_c - \Omega_v = E_{3/2}(3) + E_{1/2}(1) - 2E_1(2) = V - J. \quad (3)$$

Using the parameters U, V, and J defined above, we obtain $U_{\text{eff}} = 0.45$ eV. The lower level Ω_v is occupied, and the upper level Ω_c is empty; this follows from the self-consistency condition on the chemical potential, which can be written in the x representation in the form

$$n_e = \frac{N_e}{N} = 1\sum_p X^{1p,1p} + 2\sum_p X^{2p,2p} + 3\sum_p X^{3p,3p}. \quad (4)$$

Here, $X^{np,n'p'} \equiv |np\rangle\langle n'p'|$ are the Hubbard operators constructed using the many-electron basis of terms $|np\rangle$ (p is the set of spin and orbital indices for an n-electron term).

To correlate the level positions with that of the valence band top of the oxygen p states, we use the data on the conductivity, according to which the activation energy is $E_a = 0.9$ eV. Since the Ω_v and Ω_c states are localized and do not contribute to the conductivity, the quantity $2E_a$ can be correlated with the energy of charge transfer excitations with $\Omega_c - \varepsilon_v$ ($p^6d^2 \longrightarrow p^5d^3$) (in this case, a hole appears on an oxygen atom at the top of the valence band and an electron appears at the level Ω_c; i.e., a V^{2+} ion is formed). Measuring the one-particle energy from the valence band top, we obtain $\Omega_c = 1.8$ eV and $\Omega_v = 1.35$ eV. The density of states $N(E)$ for VBO_3 is represented schematically in Fig. 2. According to the classification used by Zaanen *et al.* [31], VBO_3 can be considered a Mott–Hubbard insulator.

In addition to the levels Ω_v and Ω_c with a spectral weight of 1, virtual levels with zero spectral weight in the stoichiometric ground state appear in the many-electron approach [32]. Such states acquire a nonzero spectral weight at deviations from stoichiometry or under optical pumping of excited levels. In the case of VBO_3, inside the band gap, we have the virtual level

$$\Omega'_v = E'_1(2) - E_{1/2}(1) = \Omega_v + \Delta = 2.56 \text{ eV},$$

shown by the dashed line in Fig. 2. Such levels do not contribute to $N(E)$, but optical transitions involving these levels are possible; therefore, they can be expected to appear in the absorption spectrum.

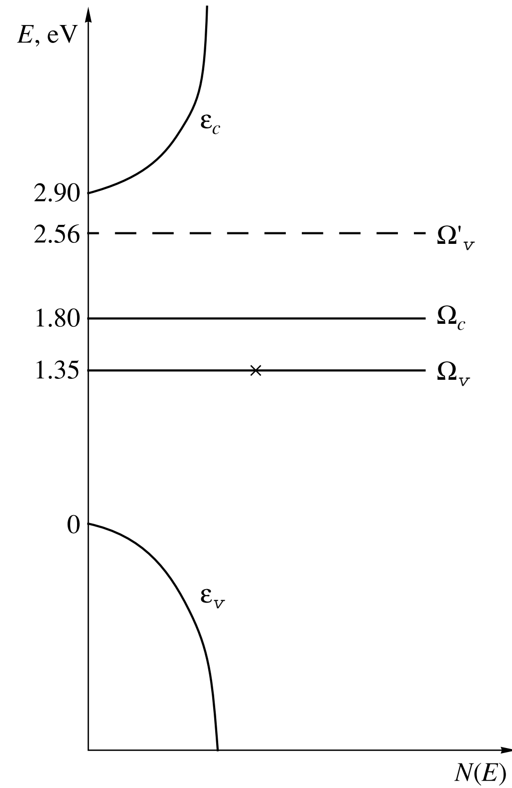

Fig. 2. Density of states for VBO_3 (schematic).

4. BAND STRUCTURE OF $Fe_{1-x}V_xBO_3$ SOLID SOLUTIONS

When simulating the electronic structure of $Fe_{1-x}V_xBO_3$ solid solutions, we make the following assumptions. First, the BO_3 states and, therefore, the parameters ε_c, ε_v, and $E_{g0} = \varepsilon_c - \varepsilon_v$ are assumed to be constant for all x. Second, the distribution of d electrons in the crystal can be spatially homogeneous or inhomogeneous; in any case, the average concentration of d electrons is $n_d = 5 - 3x$. We consider both possibilities.

In the case of a homogeneous distribution, the electron concentration per cation is $\langle n_d\rangle = n_d$. Such a distribution could be established in a metal alloy due to hopping of d electrons between the cations. However, in our case, where the hopping integral t_d is almost zero, there is no reason to expect the electron distribution to be homogeneous. Nevertheless, we consider a possible optical spectrum for the "homogeneous scenario." As follows from the self-consistency condition for the chemical potential, the occupation probability for the d^5 configuration with spin 5/2 is $N_{5/2}(d^5) = 1 - 3x$ for $x < 1/3$. The lower term d^4 with spin $S = 2$ is occupied with the probability $N_2(d^4) = 3x$. Thus, the optical absorption spectrum can be written in the form

$$I(\omega) = N_{5/2}(d^5)\delta(\omega - \varepsilon_A) + N_2(d^4)\delta(\omega - \tilde{\varepsilon}), \quad (5)$$

where $\varepsilon_A = E_{3/2}(5) - E_{5/2}(5)$ is the energy of an exciton ${}^6A_{1g}(S = 5/2) \longrightarrow {}^4T_{1g}(S = 3/2)$, which determines the A absorption band in $FeBO_3$, and $\tilde{\varepsilon} = E({}^3T_1) - E({}^5E)$ is the exciton energy for the d^4 configuration. Using Tanabe–Sugano diagrams and the above value of the parameter Δ, we find $\tilde{\varepsilon} = 0.97$ eV. We did not detect an exciton with this energy in the $Fe_{1-x}V_xBO_3$ optical spectra. Thus, the assumption of a homogeneous distribution does not agree with the experimental data.

In the model of an inhomogeneous distribution, we assumed a random spatial distribution of the two types of cations: V^{3+} (d^2) with probability x and Fe^{3+} (d^5) with

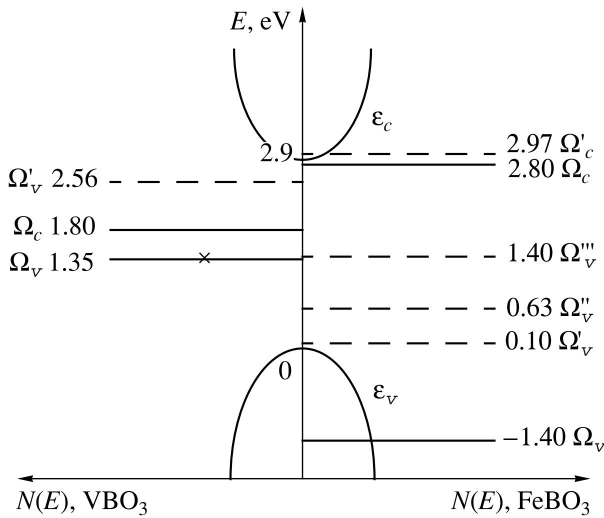

Fig. 3. Density of states for $Fe_{1-x}V_xBO_3$ solid solutions (schematic). The left part is to be taken with weight x, and the right part, with weight $(1 - x)$.

probability $1 - x$. In this model, characteristics such as the density of states, the optical spectrum, and the Mössbauer effect can be written in the form

$$\begin{aligned} N(E) &= xN_V(E) + (1-x)N_{Fe}(E), \\ D(\omega) &= xD_V(E) + (1-x)D_{Fe}(E), \end{aligned} \qquad (6)$$

where $N_V(N_{Fe})$ and $D_V(D_{Fe})$ are the density of states and the absorption intensity for VBO_3 ($FeBO_3$). The density of states for $Fe_{1-x}V_xBO_3$ solid solutions is shown schematically in Fig. 3; the density of states for $FeBO_3$ is taken from [30].

Let us consider the concentration dependence of the optical absorption spectra for solid solutions of the $Fe_{1-x}V_xBO_3$ series. For $x = 0.02$, the contribution from I_V is negligible and the spectrum in Fig. 1d practically coincides with the spectrum for $FeBO_3$. For comparison, Figs. 4 and 5 show the experimental absorption spectra for the solid solutions and the simulated spectra calculated by using Eq. (6) under the assumption of independent V^{3+} and Fe^{3+} absorption centers. For $x = 0.18$, we can distinguish the same spectral lines A_1–A_4 as for $FeBO_3$, but these lines are strongly broadened (Fig. 4a). The absorption line $\varepsilon_A = 9800$ cm^{-1} for VBO_3 is seen as a wide shoulder on the slope of the peak A_1; the latter is shifted by 100 cm^{-1} to lower energies as compared to $FeBO_3$. We believe that the reason for this shift is a change in the magnetic order. Indeed, due to the interatomic exchange interaction I, the energy of the $E_S(n)$ term depends on the spin projection M:

$$E_{S,M}(n) = E_S - I\langle S^Z\rangle M. \qquad (7)$$

Estimation of the exchange integral yields a value of $I \approx 120$ cm^{-1} [30]. Accordingly, the maximum shift of the exciton energy is $\varepsilon_A \approx I\langle S^Z\rangle \approx \frac{5}{2}I = 300$ cm^{-1}. In the original $FeBO_3$ at low temperatures, we have $\varepsilon_A = 10250$ cm^{-1}, whereas at $T > T_N = 348$ K we have $\varepsilon_A =$

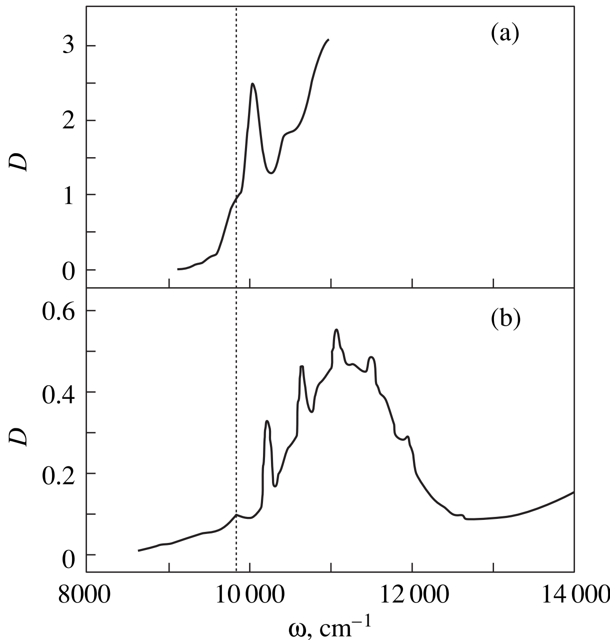

Fig. 4. Optical absorption spectra of $Fe_{0.82}V_{0.18}BO_3$ at T = 90 K. (a) Experimental data, and (b) the calculated spectrum.

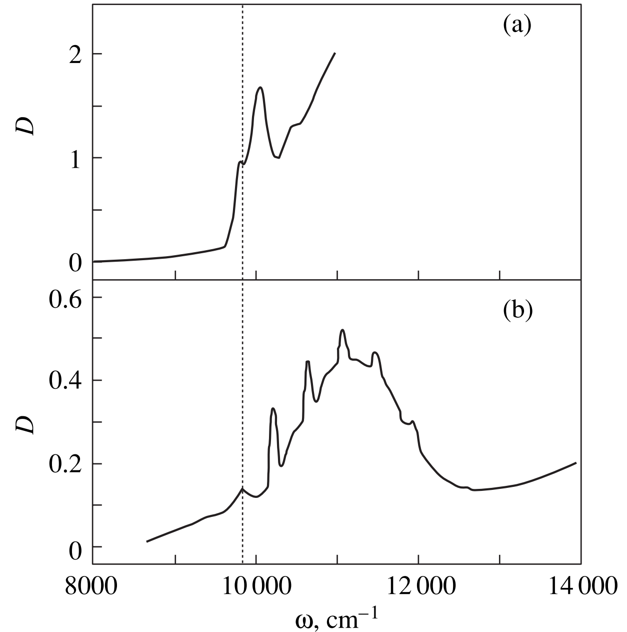

Fig. 5. Optical absorption spectra of $Fe_{0.7}V_{0.3}BO_3$ at T = 90 K. (a) Experimental data, and (b) the calculated spectrum.

9950 cm^{-1}. For the $Fe_{0.82}V_{0.18}BO_3$ composition, the magnetic order is partially suppressed and T_N drops to 200 K; therefore, the shift $\delta\varepsilon_A$ equal to 1/3 of the maximum value agrees with the partial suppression of the magnetic order.

For the $Fe_{0.7}V_{0.3}BO_3$ composition, the magnetic order is suppressed even more strongly and there is no magnetic order above 180 K. We note that, in a magnetically ordered state of $FeBO_3$, the line ε_A = 9950 cm^{-1} is very close to the absorption line ε_A = 9800 cm^{-1} for VBO_3; therefore, for $Fe_{0.7}V_{0.3}BO_3$, the two lines close in energy are superimposed and a broad peak is seen in the absorption spectrum (Fig. 1b). With a decrease in temperature to 90 K, the line ε_A is shifted to the energy region near 10050 cm^{-1} due to magnetic ordering and the lines in the absorption spectrum of the $Fe_{0.7}V_{0.3}BO_3$ solid solution are split (Fig. 5a). The peak lying lower in energy corresponds to the absorption line of the V^{3+} ion, and the upper peak corresponds to that of the Fe^{3+} ion.

5. VARIATION IN THE BAND STRUCTURE OF VBO_3 AND $Fe_{1-x}V_xBO_3$ SOLID SOLUTIONS UNDER PRESSURE

Recent experiments [25–27] have revealed nontrivial variations in the magnetic and electronic properties of $FeBO_3$ at high pressures, which consist in a collapse of the magnetic moment and a tendency toward metallization. These variations were interpreted in [28] as a result of the crossover of the high-spin term d^5 ($S = 5/2$) and the low-spin term d^5 ($S = 1/2$) with an increase in the crystalline field parameter Δ under pressure. Therefore, possible variations in the properties of VBO_3 and $Fe_{1-x}V_xBO_3$ solid solutions with increasing pressure, i.e., with increasing parameter Δ, are of interest.

For VBO_3, there is no crossover between the ground-state high-spin and low-spin excited terms in any of the sectors of the Hilbert space (d^1, d^2, d^3). The magnitude of the Mott–Hubbard band gap $U_{\text{eff}} = \Omega_c - \Omega_v$ does not depend on the parameter Δ. In this case a change in the energy band structure under pressure can only occur through broadening of the d bands and the Mott–Hubbard (insulator–metal) transition.

For $Fe_{1-x}V_xBO_3$ solid solutions, an unusual situation is possible where there is a crossover of the Fe^{3+} terms and there is no crossover of the V^{3+} terms. This situation implies that there exists a mixture of $S = 5/2$ (Fe) and $S = 1$ (V) spins below the critical pressure $P_c \approx$ 50 GPa and a mixture of $S = 1/2$ (Fe) and $S = 1$ (V) spins above P_c. Since VBO_3 is a ferromagnet and $FeBO_3$ is expected to be antiferromagnetically ordered above P_c, we may expect that, in the $Fe_{1-x}V_xBO_3$ system, ferromagnetic and antiferromagnetic bonds are randomly distributed and are of the same order of magnitude. Such a situation can give rise to disordered magnetic phases, in particular, to a spin glass.

ACKNOWLEDGMENTS

One of the authors (M.M.A.) would like to thank the Deutsche Forschungsgemeinschaft (SFB608) for financial support.

This study was supported by the Russian Foundation for Basic Research (project no. 03-02-16286), the program “Integration” (project no. B0017), and the program of the Division of Physical Sciences of the Russian Academy of Sciences “Strongly Correlated Electrons.”

REFERENCES

1. I. Bernal, C. W. Struck, and J. G. White, Acta Crystallogr. **16**, 849 (1963).
2. J. C. Joubert, T. Shirk, W. B. White, and R. Roy, Mater. Res. Bull. **3**, 671 (1968).
3. A. J. Kurtzig, R. Wolfe, R. C. LeCraw, and J. W. Nielsen, J. Appl. Phys. **14**, 350 (1969).
4. R. Wolfe, A. J. Kurtzig, and R. C. LeCraw, J. Appl. Phys. **41**, 1218 (1970).
5. B. Andlauer, J. Schneider, and W. Wettling, Appl. Phys. **10**, 189 (1976).
6. V. N. Zabluda, A. V. Malakhovskiĭ, and I. S. Édel’man, Fiz. Tverd. Tela (Leningrad) **27**, 133 (1985) [Sov. Phys. Solid State **27**, 77 (1985)].
7. J. Haisma, H. J. Prins, and K. L. L. van Mierlo, J. Phys. D: Appl. Phys. **7**, 162 (1974).
8. H. Schmid, Acta Crystallogr. **17**, 1080 (1964).
9. T. A. Bither, C. G. Frederick, T. E. Gier, J. F. Weiher, and H. S. Young, Solid State Commun. **8**, 109 (1970).
10. Xu Ziguang, Matam Mahesh Kumar, and Ye Zuo Guang, in *Proceedings of Annual March Meeting* (Am. Phys. Soc., New York, 2001).
11. N. M. Salanskii, E. A. Glozman, and V. N. Seleznev, Phys. Status Solidi A **36**, 779 (1976).
12. I. W. Shepherd, Phys. Rev. B **5**, 4524 (1972).
13. M. Vithal and R. Jagannathan, J. Solid State Chem. **63**, 16 (1986).
14. O. Muller, M. P. O’Horo, and J. F. O’Neill, J. Solid State Chem. **23**, 115 (1978).
15. T. A. Bither and H. S. Young, J. Solid State Chem. **6**, 502 (1973).
16. M. P. O’Horo and O. Muller, J. Appl. Phys. **49**, 1516 (1978).
17. M. W. Ruckman, R. A. Levy, and R. Chennette, J. Appl. Phys. **53**, 1694 (1982).
18. A. A. Karaev, B. Yu. Sokolov, and Yu. M. Fedorov, Fiz. Tverd. Tela (St. Petersburg) **42**, 2036 (2000) [Phys. Solid State **42**, 2097 (2000)].
19. De Lacklison, J. Chadwick, and J. L. Page, J. Phys. D: Appl. Phys. **5**, 810 (1972).
20. N. B. Ivanova, V. V. Rudenko, A. D. Balaev, N. V. Kazak, V. V. Markov, S. G. Ovchinnikov, I. S. Édel’man, A. S. Fedorov, and P. V. Avramov, Zh. Éksp. Teor. Fiz. **121**, 354 (2002) [JETP **94**, 299 (2002)].
21. V. V. Markov, V. V. Rudenko, I. S. Edel’man, N. B. Ivanova, N. V. Kazak, A. D. Balaev, and S. G. Ovchinnikov, Phys. Met. Metallogr. **93**, 114 (2002).

22. I. S. Édel'man, A. V. Malakhovskiĭ, T. I. Vasil'eva, and V. N. Seleznev, Fiz. Tverd. Tela (Leningrad) **14**, 2810 (1972) [Sov. Phys. Solid State **14**, 2442 (1972)].
23. A. V. Postnikov, St. Bartkowski, M. Neumann, R. A. Rupp, E. Z. Kurmaev, S. N. Shamin, and V. V. Fedorenko, Phys. Rev. B **50**, 14849 (1994).
24. K. Parlinski, Eur. Phys. J. B **27**, 283 (2002).
25. I. N. Troyan, A. G. Gavrilyuk, V. A. Sarkisyan, I. S. Lyubutin, R. Rüffer, O. Leupold, A. Barla, B. Doyle, and A. I. Chumakov, Pis'ma Zh. Éksp. Teor. Fiz. **74**, 26 (2001) [JETP Lett. **74**, 24 (2001)].
26. A. G. Gavriliuk, I. A. Trojan, R. Boehler, M. Eremets, A. Zerr, I. S. Lyubutin, and V. A. Sarkisyan, Pis'ma Zh. Éksp. Teor. Fiz. **75**, 25 (2002) [JETP Lett. **75**, 23 (2002)].
27. V. A. Sarkisyan, I. A. Troyan, I. S. Lyubutin, A. G. Gavrilyuk, and A. F. Kashuba, Pis'ma Zh. Éksp. Teor. Fiz. **76**, 788 (2002) [JETP Lett. **76**, 664 (2002)].
28. S. G. Ovchinnikov, Pis'ma Zh. Éksp. Teor. Fiz. **77**, 808 (2003) [JETP Lett. **77**, 676 (2003)].
29. A. V. Malakhovskii and I. S. Edelman, Phys. Status Solidi B **74**, K145 (1976).
30. S. G. Ovchinnikov and V. N. Zabluda, Zh. Éksp. Teor. Fiz. (in press).
31. J. Zaanen, G. A. Sawatzky, and J. W. Allen, Phys. Rev. Lett. **55**, 418 (1985).
32. V. V. Val'kov and S. G. Ovchinnikov, *Quasiparticles in Strongly Correlated Systems* (Sib. Otd. Ross. Akad. Nauk, Novosibirsk, 2001) [in Russian].

Translated by I. Zvyagin

Physics of the Solid State, Vol. 46, No. 8, 2004, pp. 1469–1473. Translated from Fizika Tverdogo Tela, Vol. 46, No. 8, 2004, pp. 1428–1432.
Original Russian Text Copyright © 2004 by Ovchinnikov, Shneĭder.

MAGNETISM AND FERROELECTRICITY

Spectral Functions in the Hubbard Model with Half-Filling

S. G. Ovchinnikov and E. I. Shneĭder

Kirenskiĭ Institute of Physics, Siberian Division, Russian Academy of Sciences, Akademgorodok, Krasnoyarsk, 660036 Russia

e-mail: shneyder@iph.krasn.ru, sgo@iph.krasn.ru

Received November 24, 2003

Abstract—Under the assumption of long-range antiferromagnetic order at low temperatures, the spectral functions and the density of states are calculated in the two-dimensional Hubbard model with half-filling in the Hubbard-I approximation. The results are compared with the data obtained using an exact numerical technique, namely, the quantum Monte Carlo method. The influence of hopping to the next-to-nearest neighbor on the formation of the electronic structure is considered. © *2004 MAIK "Nauka/Interperiodica".*

1. The Hubbard model taking into account electron motion in solids along with the electron–electron interaction is one of the basic models in the theory of systems with strong electron correlations (SECs). The point is that this model does reflect important effects characteristic of systems with SECs, even though it is insufficient for describing the properties of specific materials quantitatively [1]. It is interesting to study approximations in the atomic limit, because, as is known, it is simpler to describe such systems by starting with the local approach than with the theory of the Hartree–Fock band limit [2]. In the limit of $t \ll U$, the Hubbard-I approximation yields a simple description of a system in terms of two energy bands separated by a Mott–Hubbard gap [1]. As the ratio t/U increases, this approximation becomes incorrect a priori; however, it is quite applicable to systems with SECs. In a diagram technique based on Hubbard X operators [2, 3], the Hubbard-I solution is a result of the Hartree–Fock approximation. Using the quantum Monte Carlo (QMC) method, one can compare the electronic structure of the Hubbard model obtained in the limit $t \ll U$ in the Hubbard-I approximation and the results of exact numerical calculations (see, e.g., [4, 5]). Such a comparison was performed in [4] to show that, at high temperatures, the spectral functions $A(\mathbf{k}, \omega)$ are sufficiently well described by the Hubbard-I paramagnetic solution. At low temperatures, neither the Hubbard-I paramagnetic solution nor the solution in the form of a spin density wave (SDW) can even approximately reproduce the model electronic structure. It is known that the SDW solution is applicable under conditions of weak electron correlations, when $U \ll W = zt$, but this solution is inapplicable to systems with SECs. In this paper, the spectral functions of the two-dimensional (2D) Hubbard model with half-filling are calculated in the Hubbard-I approximation under the assumption of long-range antiferromagnetic order at low temperatures.

Comparison of our results with the data obtained using the QMC method showed that the spectral functions are in reasonable agreement with the exact numerical calculations, despite the disadvantages of the approximation used. These disadvantages are as follows.

(i) According to the Mermin–Wagner theorem, there is no antiferromagnetic order in a 2D system at finite temperatures; hence, an interplane interaction or certain anisotropy should be assumed. Nevertheless, the approximation used is appropriate, since we compare the results of this study with QMC data for finite systems, for which the above-mentioned theorem is invalid.

(ii) The Hubbard-I approximation does not yield a self-consistent description of the antiferromagnetic state; indeed, there is only a zero solution for the sublattice magnetization m. For this reason, in the limit $t \ll U$ for a system with $n_e = 1$, we construct an effective Heisenberg Hamiltonian with the antiferromagnetic interaction constant $J = 4t^2/U$ and calculate the magnetization self-consistently in the Heisenberg model. At $T = 0$, m decreases from a nominal value due to zero quantum fluctuations and we get $m = 0.3$ under the assumption that the interplane interaction is weak in comparison with the in-plane interaction.

It should be noted that going beyond the mean-field approximation requires consideration of self-energy one-loop diagrams [2, 3]. In the magnetically ordered phase, the largest contribution comes from diagrams describing spin-wave excitations. The main effect of spin excitations consists in a renormalization of the occupation numbers. According to [6], we define the occupation numbers as

$$\begin{aligned} n_{f,\sigma} + n_{f,\bar{\sigma}} &= n_e, \\ n_{f,\sigma} - n_{f,\bar{\sigma}} &= 2m = (1 - 2n_{sf}). \end{aligned} \qquad (1)$$

where $2n_{sf}$ is the magnon concentration and $n_{f,\sigma}$ is the number of electrons at a site with a specified spin projection. Thus, the introduction of the nonzero magnetization of sublattices corresponds to consideration of the first significant correction to the mean-field approximation.

2. The Hubbard model Hamiltonian can be written as

$$\hat{H}-\mu\hat{N}_e = \sum_{f,\sigma}\left[(\varepsilon-\mu)n_{f,\sigma}+\frac{1}{2}Un_{f,\sigma}n_{f,\bar{\sigma}}\right] + \sum_{f,g,\sigma}(t_{f,g}a^{+}_{f,\sigma}a_{g,\sigma}+\text{H.c.}), \quad (2)$$

where $a^{+}_{f,\sigma}$ ($a_{f,\sigma}$) is the creation (annihilation) operator of an electron at site f with spin $\sigma = \pm 1/2$, $n_{f\sigma} = a^{+}_{f\sigma}a_{f\sigma}$, ε is the one-electron energy in the crystal field, μ is the chemical potential, U is the intra-atomic repulsion matrix element, and $t_{f,g}$ is the hopping integral between sites f and g in the nearest neighbor approximation.

In what follows, we analyze a simple spatially inhomogeneous solution to the above Hamiltonian for a 2D square lattice with antiferromagnetic ordering of the spins (the antiferromagnetic order near half-filling is caused by kinetic superexchange in the system). In the case of two sublattices, the Green's function [7] is written as

$$G(\mathbf{k},\omega) = \frac{1}{N}\begin{pmatrix} \sum_{f,f'}\exp\{i\mathbf{k}(\mathbf{f}-\mathbf{f}')\}\langle\langle a_f|a^{+}_{f'}\rangle\rangle & \sum_{f,g}\exp\{i\mathbf{k}(g-\mathbf{f})\}\langle\langle a_g|a^{+}_{f}\rangle\rangle \\ \sum_{f,g}\exp\{i\mathbf{k}(\mathbf{f}-\mathbf{g})\}\langle\langle a_f|a^{+}_{g}\rangle\rangle & \sum_{g,g'}\exp\{i\mathbf{k}(\mathbf{g}-\mathbf{g}')\}\langle\langle a_g|a^{+}_{g'}\rangle\rangle \end{pmatrix}. \quad (3)$$

Analytical expressions for the Green's functions are derived in the Hubbard-I approximation, which corresponds to the following uncoupling of averages [1]:

$$\langle\langle a_{f+h,\sigma}n_{f,\sigma}|a^{+}_{f',\sigma}\rangle\rangle \longrightarrow \langle n_{f,\bar{\sigma}}\rangle\langle\langle a_{f+h,\sigma}|a^{+}_{f',\sigma}\rangle\rangle. \quad (4)$$

In the atomic limit, it is more convenient to use the representation of Hubbard operators, with which the conventional Fermi operators are related through the linear combination

$$a^{+}_{f,\sigma} = X^{\sigma,0}_f + 2\sigma X^{2,\bar{\sigma}}_f, \quad a_{f,\sigma} = X^{0,\sigma}_f + 2\sigma X^{\bar{\sigma},2}_f. \quad (5)$$

Therefore, the Green's functions can be written in the new representation (A, B are intersublattice indices) as

$$G^u_{AA} = \langle\langle X^{\bar{\sigma},2}_A|X^{2,\bar{\sigma}}_A\rangle\rangle = F^{\bar{\sigma},2}_A((E-\varepsilon_1)^2[\nu+F^{\bar{\sigma},2}_B t(\mathbf{k})] - F^{0,\sigma}_A t^2(\mathbf{k})(E-\varepsilon_1-F^{0,\sigma}_B U))/\prod_{i=1}^{4}(E-E_i),$$

$$G^u_{AB} = \langle\langle X^{\bar{\sigma},2}_A|X^{2,\bar{\sigma}}_B\rangle\rangle = F^{\bar{\sigma},2}_B((E-\varepsilon_1)^2[\nu+F^{\bar{\sigma},2}_A t(\mathbf{k})] - F^{0,\sigma}_B t^2(\mathbf{k})(E-\varepsilon_1-F^{\bar{\sigma},2}_A U))/\prod_{i=1}^{4}(E-E_i),$$

$$G^l_{AA} = \langle\langle X^{0,\sigma}_A|X^{\sigma,0}_A\rangle\rangle = F^{0,\sigma}_A((E-\varepsilon_1)[\nu^2 - F^{\bar{\sigma},2}_A F^{\bar{\sigma},2}_B t^2(\mathbf{k})] + F^{0,\sigma}_B t(\mathbf{k})[\nu^2 - F^{\bar{\sigma},2}_A t(\mathbf{k})\nu])/\prod_{i=1}^{4}(E-E_i), \quad (6)$$

$$G^l_{AB} = \langle\langle X^{0,\sigma}_B|X^{\sigma,0}_A\rangle\rangle = F^{0,\sigma}_B((E-\varepsilon_1)[\nu^2 - F^{\bar{\sigma},2}_A F^{\bar{\sigma},2}_B t^2(\mathbf{k})] + F^{0,\sigma}_A t(\mathbf{k})[\nu^2 - F^{\bar{\sigma},2}_B t(\mathbf{k})\nu])/\prod_{i=1}^{4}(E-E_i),$$

where $F^{0,\sigma}_A = \langle X^{0,0}_A + X^{\sigma,\sigma}_A\rangle$ and $F^{\bar{\sigma},2}_A = \langle X^{2,2}_A + X^{\bar{\sigma},\bar{\sigma}}_A\rangle$ are the filling factors, $\varepsilon_1 = (\varepsilon-\mu)$, $\nu = (E-\varepsilon_1-U)$, and superscripts l and u correspond to the lower and upper Hubbard bands, respectively.

We restrict the analysis to the half-filling region, where the chemical potential is described by the well-known expression $\mu = \varepsilon + U/2$ [8], which is valid for any temperature and all values of the model parameters. In this case, the equation defining the spectrum of quasiparticles in the 2D antiferromagnetic lattice has the analytical solution

$$E^{l,u}_{\pm} = \pm\frac{1}{2}(t^2(\mathbf{k}) \pm \sqrt{t^4(\mathbf{k})+4U^2t^2(\mathbf{k})n_{f,\sigma}n_{f,\bar{\sigma}}} - 2\varepsilon_1(\varepsilon_1+U))^{1/2}. \quad (7)$$

Since the Brillouin zone becomes twice as small in the antiferromagnetic phase, each Hubbard subband in the paraelectric phase is split into two. If the bands obtained had been ordinary one-electron bands with a

number of states per atom equal to unity, the total number of states would have been equal to four. However, these bands correspond to quasiparticles with a fractional spectral weight, which can be explicitly calculated using the QMC method. In our calculations, the spectral weight is defined by the filling factor $F_g^{m,n} = \langle X_g^{m,m} + X_g^{n,n} \rangle$.

It is noteworthy that the quasiparticle spectrum (7) can be rewritten using the well-known solution for the paramagnetic phase. In this case, it turns out that the dispersion in the antiferromagnetic state has a form similar to that for SDWs,

$$E_{\pm}^{l,u} = \pm\sqrt{(\xi^{\pm})^2 + \Delta^2}, \quad (8)$$

where $\Delta = Um$ is the gap parameter, $m = (1/2)(n_{f,\sigma} - n_{f,\bar{\sigma}})$ is the sublattice magnetization, $\varepsilon_{\mathbf{k}}^{\pm}$ is the dispersion of the upper and lower Hubbard bands in the paramagnetic phase with the renormalized Coulomb repulsion parameter $\tilde{U} = U\sqrt{1-4m^2}$, and

$$\xi_{\mathbf{k}}^{\pm} = \frac{1}{2}(t(\mathbf{k}) \pm \sqrt{t^2(\mathbf{k}) + \tilde{U}^2}). \quad (9)$$

If the magnetization is zero, the obtained bands exactly correspond to the upper and lower Hubbard bands in the paraelectric phase. In the one-electron SDW state, the quasiparticle dispersion is described by a formula similar to Eq. (9), with $\xi^{\pm}$ being the dispersion of free electrons.

Now, we consider the full spectral function of the system, which is the sum of the imaginary parts of the Green's functions in Eq. (6),

$$A(\mathbf{k}, \omega) = -\frac{1}{\pi}\mathrm{Sp}(\mathrm{Im}\,G(\mathbf{k}, \omega)) = -\frac{1}{\pi}\mathrm{Im}(G_{AA}^{l}(\mathbf{k}, \omega) + G_{BB}^{l}(\mathbf{k}, \omega) + G_{AA}^{u}(\mathbf{k}, \omega) + G_{BB}^{u}(\mathbf{k}, \omega)) \quad (10)$$

and the one-electron density of states,

$$N(\omega) = \frac{1}{N}\sum_{\mathbf{k}} A(\mathbf{k}, \omega). \quad (11)$$

The approximation used does not contain information on the spectral linewidths (the spectral density contains delta functions). To compare our results with the numerical QMC data, we approximate the delta functions by a Lorentzian with the most appropriate parameter δ. This renormalization of the width and weight of the quasiparticle spectral lines corresponds to the introduction of a certain nonzero imaginary part of the self-energy $\Sigma(\mathbf{k}, \omega)$. We note that there is no one-to-one correspondence between the parameter δ and temperature; however, this parameter tends to zero as the temperature decreases. Despite the fact that the Mermin–Wagner theorem forbids the existence of antiferromagnetic

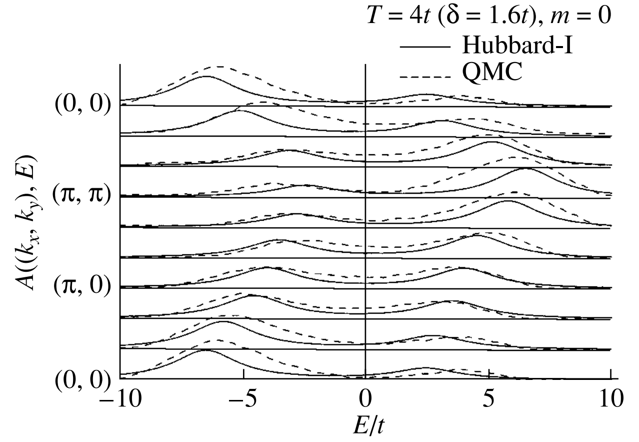

Fig. 1. Spectral functions of the Hubbard model at high temperatures $T = 4t$ (Hubbard-I and QMC [4] calculations).

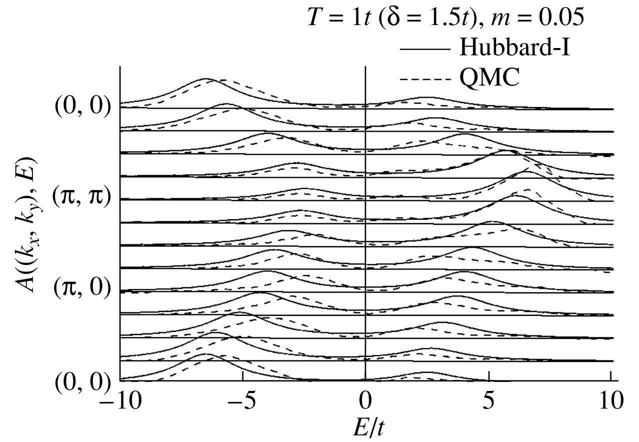

Fig. 2. Spectral functions of the Hubbard model at high temperatures $T = 1t$ (Hubbard-I and QMC [4] calculations).

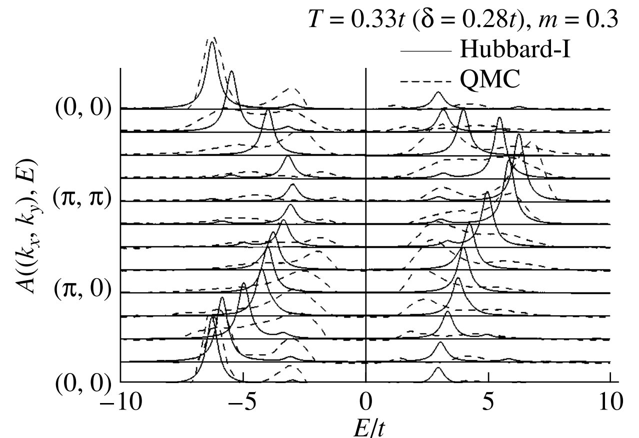

Fig. 3. Spectral functions of the Hubbard model at intermediate temperatures $T = 0.33t$ (Hubbard-I and QMC [4] calculations).

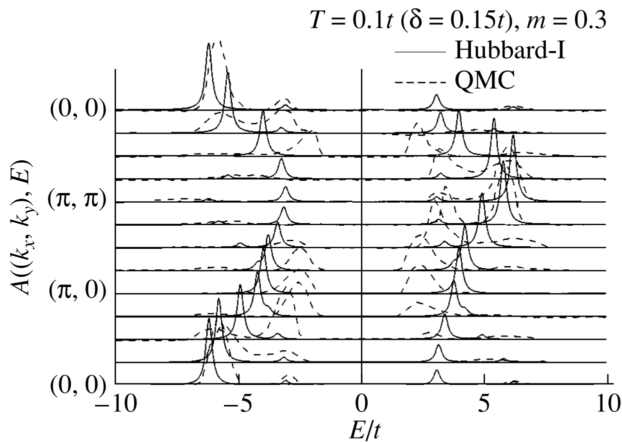

Fig. 4. Spectral functions of the Hubbard model at low temperatures $T = 0.1t$ (Hubbard-I and QMC [4] calculations).

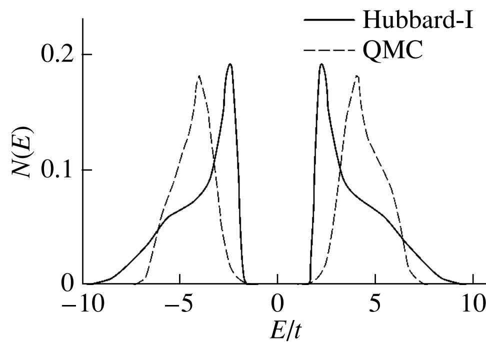

Fig. 5. Density of states in the Hubbard model with half-filling (Hubbard-I and QMC [5] calculations).

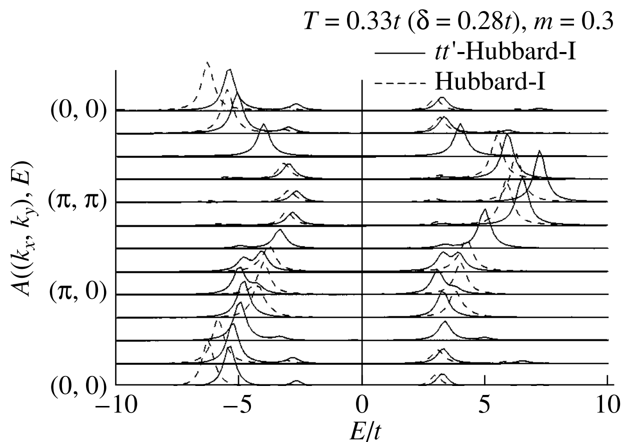

Fig. 6. Spectral functions of the Hubbard model (Hubbard-I and tt'-Hubbard-I, $t'/t = 0.3$).

order in 2D systems at finite temperatures, it is generally assumed that the system is "effectively ordered" if the spin correlation length becomes comparable to the system size.

Figures 1–5 show the determined spectral functions and the density of states, as well as the results of exact numerical QMC calculations from [4, 5]. In this case, the following values of the system parameters were used: $U = 8t$, $\varepsilon - \mu + U/2 = 0$, and $t(\mathbf{k}) = -2t(\cos k_x + \cos k_y)$. We assume that the sublattice magnetization parameter m is equal to 0.3 in the low-temperature range.

At high temperatures (Figs. 1, 2), the Hubbard-I approximation reproduces the position and weight of the spectral peaks corresponding to the upper and lower Hubbard bands to sufficient accuracy. This is explained by the fact that the spin correlation effects (disregarded in this approximation) become insignificant above the Néel temperature.

At $T = 1.00t$, QMC calculations [4] indicate very weak satellites for an unoccupied state at the $\mathbf{k} = (0, 0)$ point and for an occupied state at the $\mathbf{k} = (\pi, \pi)$ point. These satellites correspond to the calculated bands E_{+}^{u} and E_{-}^{l} with a very small spectral weight. Of course, long-range antiferromagnetic ordering does not exist in the system at such temperatures; however, we think that there is a short-range magnetic order, which gives rise to weak satellites in the function $E(\mathbf{k})$.

At intermediate and low temperatures (Figs. 3, 4), each Hubbard band in the paramagnetic state is split into two subbands $E_{1,2}^{l,u}$. In this case, one of the subbands has the largest spectral weight, while the other appears as a weak satellite. A nontrivial result obtained using the QMC method and the Hubbard-I approximation is the spectral weight redistribution between strong and weak peaks. The tendencies toward redistribution of the spectral weight in our calculations and the QMC calculations are retained. In some regions of the Brillouin zone [near $\mathbf{k} = (0, 0)$ and $\mathbf{k} = (\pi, \pi)$], reasonable agreement is observed in the shape and position of the peaks in $A(\mathbf{k}, \omega)$. However, the QMC and Hubbard-1 data significantly differ in other $\mathbf{k}$-space regions [$\mathbf{k} = (\pi/2, \pi/2)$and $\mathbf{k} = (\pi, 0)$].

The one-electron density of states (Fig. 5) at low temperatures has two peaks corresponding to the occupied (l) and unoccupied (u) Hubbard bands. The weak satellites in the spectral density give rise to shoulders on both peaks. Our results and the QMC data from [6] are in qualitative agreement.

We also considered the influence of the next-to-nearest neighbor on the formation of the electronic structure. The Hamiltonian of the tt' model includes hopping on a sublattice described by the term $\sum_{f, f' \in A, \sigma} (t'_{f, f'} a^{+}_{f, \sigma} a_{g, \sigma} + \text{H.c.})$. In the simplest case, the $\mathbf{k}$ dependence of the parameter t' is described by the formula $t'(\mathbf{k}) = 4t'\cos k_x \cos k_y$. The spectral functions of the Hubbard model, corresponding to the Hubbard-I antiferromagnetic solution, are shown in Fig. 6 for the ratio $t'/t \approx 0.3$. A comparison of the solutions shows that

the most significant effect is the formation of additional quasiparticle states at points (π, 0) and (π, π/4) of the Brillouin zone. At the (π, 0) point, these states appear as small satellites located near the main peak. The position of the additional peaks is controlled by spin fluctuations and the parameter t'. When the magnon concentration $2n_{sf}$ is zero and $t' = 0$, there are two dispersionless levels in the electronic structure, which lie above the valence band top and below the conduction band bottom.

3. Thus, it was shown that the spectral function at low temperatures, determined using the Hubbard model in the Hubbard-I approximation, as well as that obtained using exact numerical QMC calculations, consists of four peaks corresponding to antiferromagnetic Hubbard subbands. The approximation used retains the basic tendencies toward redistribution of the spectral weight; however, quantitative disagreement is observed in some regions of the **k** space. The density of states in the Hubbard-I solution agrees with the QMC calculations. A significant effect resulting from the inclusion of the next-to-nearest neighbor leads in calculating the electronic structure is the formation of additional quasiparticle states at certain points of the Brillouin zone.

ACKNOWLEDGMENTS

This study was supported by the program "Strongly Correlated Electrons" (Department of Physical Sciences, Russian Academy of Sciences).

REFERENCES

1. J. Hubbard, Proc. R. Soc. London, Ser. A **276**, 238 (1963).
2. R. O. Zaĭtsev, Zh. Éksp. Teor. Fiz. **68** (1), 207 (1975) [Sov. Phys. JETP **41**, 100 (1975)].
3. Yu. A. Izyumov and Yu. N. Skryabin, *Statistical Mechanics of Magnetically Ordered Systems* (Nauka, Moscow, 1987) [in Russian].
4. C. Grober, R. Eder, and W. Hanke, Phys. Rev. B **62** (7), 4336 (2000).
5. N. Bulut, D. J. Scalapino, and S. R. White, Phys. Rev. Lett. **73** (5), 748 (1994).
6. A. N. Podmarkov and I. S. Sandalov, Zh. Éksp. Teor. Fiz. **86** (4), 1461 (1984) [Sov. Phys. JETP **59**, 856 (1984)].
7. S. V. Tyablikov, *Methods in the Quantum Theory of Magnetism*, 2nd ed. (Nauka, Moscow, 1975; Plenum, New York, 1967).
8. C. Castellani, C. Di Castro, D. Feinberg, and J. Ranniger, Phys. Rev. Lett. **43** (26), 1957 (1979).

Translated by A. Kazantsev

Physics of the Solid State, Vol. 46, No. 8, 2004, pp. 1474–1481. Translated from Fizika Tverdogo Tela, Vol. 46, No. 8, 2004, pp. 1433–1440.
Original Russian Text Copyright © 2004 by Vecherskiĭ, Batalov, Esina, Shekhtman.

MAGNETISM AND FERROELECTRICITY

Region of Existence and Electrical Properties of $La_{1-x}Li_xFeO_3$ Solid Solution

S. I. Vecherskiĭ, N. N. Batalov, N. O. Esina, and G. Sh. Shekhtman

Institute of High-Temperature Electrochemistry, Ural Division, Russian Academy of Sciences, ul. S. Kovalevskoĭ 20, Yekaterinburg, 620219 Russia

e-mail: batalov@ihim.uran.ru

Received December 2, 2003

Abstract—$La_{1-x}Li_xFeO_3$ solid solution prepared by solid-phase synthesis in an air environment at atmospheric pressure is found to exist only for $x \lesssim 0.1$. All single-phase samples are *p*-type semiconductors. An increase in lithium concentration brings about a decrease in their electrical resistivity and thermopower. The results are discussed in terms of the small polaron (SP) model. The SP concentration and mobility are calculated from data on the electrical resistivity and thermopower in the presence of an antiferromagnetic–paramagnetic phase transition. It is shown that the decrease in electrical resistivity of the samples is connected with the increase in both the concentration and mobility of SPs. *© 2004 MAIK "Nauka/Interperiodica".*

1. INTRODUCTION

Perovskite-like $La_{1-x}A_xMO_3$ solid solutions (where *A* stands for an alkaline-earth metal; *M* stands for Mn, Fe, or Co; and $x \leq 0.5$) form throughout the above interval of *x* and attract considerable interest because their electrical and magnetic properties depend substantially on the species and concentration of the *A* atoms [1–10]. For illustration, one may be referred to the colossal-magnetoresistance effect observed in lanthanum manganites partially substituted by alkaline-earth metals [1–5, 7, 8], as well as to the insulator–metal transitions occurring, for instance, in $La_{1-x}Sr_xMnO_3$ [8, 9] and $La_{1-x}Sr_xCoO_3$ [5, 6, 10]. Interestingly, a "stable" transition (i.e., occurring throughout the temperature range studied) to the metallic phase takes place in both systems for $x \geq 0.3$ and is identified with a rhombohedral lattice distortion and ferromagnetic ordering below the Curie temperature.

In the series of perovskite-like lanthanum oxides containing a transition metal ion, $LaFeO_3$ occupies an intermediate position between $LaMnO_3$ and $LaCoO_3$. However, the properties of $LaFeO_3$ and the related oxides $La_{1-x}A_xFeO_3$ differ from those of partially substituted lanthanum manganites and cobaltites. It is known [11, 12] that $LaFeO_3$ has an orthorhombic crystal lattice and resides in the antiferromagnetic (AFM) state below the Néel temperature $T_N = 750$ K. At low temperatures, this crystal is an insulator, while at higher temperatures it exhibits semiconducting properties (a *p*-type semiconductor, with charge transport mediated by small-polaron hopping) [13]. $La_{1-x}Sr_xFeO_3$ [5, 6, 9, 14] is one of the best studied oxide systems based on this compound. As is evident from the phase diagram of this system [9], single-phase samples can be prepared within a broad interval of *x*. It was shown that, within the interval $0 \leq x \leq 0.5$ (which is the interval in which $LaFeO_3$ may be considered a starting oxide), samples do not convert to the metallic phase and that their crystal structure and electrical and magnetic properties are similar to those of $LaFeO_3$. Partial substitution of strontium for La brings about, however, a decrease in the Néel temperature and an increase in the electrical conductivity of samples. This phenomenon was assigned in [14] to an increase in the concentration of small polarons (SPs).

Unlike the $La_{1-x}A_xMO_3$ oxides, where *A* stands for an alkaline-earth metal, solid solutions in which La is replaced by a monovalent metal have been studied to a much lesser extent. The properties of these compounds are however no less interesting, although the region of their existence is substantially narrower [15, 16]. To cite just one example, a study of $La_{1-x}A_xMnO_3$ solid solutions (where *A* denotes Na, K, Rb) revealed [15] that they also undergo an insulator–metal transition. However, single-phase samples with a perovskite-like structure can be prepared only for $x \leq 0.2$ when the lanthanum is replaced by sodium or potassium and only for $x \leq 0.1$ when rubidium is substituted for lanthanum. A study of the magnetic properties of $La_{1-x}Ag_xMnO_3$ showed that the region of existence of this solid solution is also relatively narrow ($x < 0.3$) [16].

Unfortunately, data on the possibility of formation, region of existence, and electrical properties of lithium-containing solid solutions, in particular, of $La_{1-x}Li_xFeO_3$, are lacking. Therefore, one of the goals of this study was to establish the region of existence of this solid solution as prepared in an air environment. Another goal was to investigate the behavior of the

1063-7834/04/4608-1474$26.00 © 2004 MAIK "Nauka/Interperiodica"

electrical resistivity and thermopower of this solid solution as functions of Li concentration and temperature.

2. EXPERIMENTAL

With this goal in mind, we prepared six $La_{1-x}Li_xFeO_3$ samples with x varied from 0 to 0.25 in steps of 0.05 (samples 1 through 6, respectively). We studied their phase composition, ran derivatographic measurements, and obtained the temperature dependences of the electrical resistivity ρ and of the thermopower (the Seebeck coefficient) α.

The starting components were powders of iron carbonyl, lithium carbonate (Li_2CO_3), and lanthanum oxide (La_2O_3). $La_{1-x}Li_xFeO_3$ samples were synthesized for 18 h at temperatures of 1523 K ($0.05 \le x \le 0.25$) and 1623 K ($LaFeO_3$) following the technique described earlier in [17]. To prepare samples for measurements of the electrical resistivity and thermopower, the powders thus obtained were pressed into the shape of parallelepipeds and sintered for 12 h under the conditions of their synthesis.

Phase analysis of the samples was performed by x-ray diffractometry (CuK_α radiation). Silicon was chosen as a reference in determining the lattice parameters. The error in determining the parameters and volume of the unit cell was less than ±0.001 nm and ±0.001 nm^3, respectively. The porosity of the samples was estimated by comparing their apparent density with the density determined from x-ray diffraction and was found to vary from 15 to 20%. Differential thermal analysis (DTA) of the samples was carried out in the range 290–1073 K in air with a Q-1500D derivatograph at a heating rate of 5 K/min.

The electrical resistivity was measured in the range 77–1073 K in air following the dc four-probe technique. The correction coefficients needed to reduce the measured electrical resistivity of porous samples ρ^{eff} to the resistivity of dense samples ρ were calculated using the method described earlier in [17].

The thermopower was measured relative to Ag in the steady state in air in the range 300–1073 K following the standard technique [18]. The temperature of the cell containing a sample was set by means of a tubular electric heater. The sample was placed between two silver plates, one of which was heated additionally with an electric heater insulated from the plate. The temperatures of the "hot" (T_1) and "cold" (T_2) ends of a sample were measured with chromel–alumel thermocouples. The thermopower was derived from the expression $\alpha = U/\Delta T$ (where U is the potential difference between the hot and cold sample ends and $\Delta T = T_1 - T_2$) and reduced to the average sample temperature, $T = (T_1 + T_2)/2$, with the Ag thermopower taken into account[19]. The value of ΔT varied from 8 to 12 K, depending on the actual sample temperature.

3. EXPERIMENTAL RESULTS

3.1. Phase Composition, Electrical Resistivity, and Thermopower

X-ray diffraction patterns of samples 1–5 contained only the diffraction maxima characteristic of an orthorhombically distorted perovskite structure. A diffractogram of sample 6 also exhibited the strongest peak belonging to the cubic modification of $LiFeO_2$. Table 1 lists the parameters a, b, and c and the volume V_c of the orthorhombic unit cell of the samples. In the case of $LaFeO_3$, they agree satisfactorily with the literature data [11]. It is seen from Table 1 that, as the lithium concentration x increases from 0 to 0.1, the cell volume decreases and then becomes stable at a value of 0.241 nm^3. This gave us grounds to conclude that single-phase samples formed in the concentration region $x \le 0.1$. The samples obtained at higher Li concentrations are apparently two-phase, although the small amount of the second phase ($LiFeO_2$) precluded observation of the corresponding x-ray peaks in the diffractograms of samples 4 and 5.

The DTA curves of the samples prepared in the range 290–1073 K did not contain any features indicative of first-order phase transformations.

Figure 1 displays temperature dependences of the electrical resistivity ρ of the samples. All of them bear a semiconductor signature. It should be pointed out that the $\rho(T)$ curve for sample 1 (curve *1*) has a distinct feature associated with a crossing of the Néel temperature. Immediately below and above $T \approx 750$ K, however, one can isolate quasi-linear portions within which the derivative $d(\log\rho)/dT$ is constant. As one crosses T_N, the derivative changes in magnitude. A similar feature is present in the $\rho(T)$ graphs of samples 2–6 near T = 750 K (curves *2*–*6*).

The inset to Fig. 1 shows the concentration dependences of ρ obtained for 220, 530, and 1050 K. They pass through a minimum at $x = 0.1$. A further increase in x causes the electrical resistivity to increase. Recalling the sensitivity of the electrical resistivity of the samples to phase composition, one may conjecture that

Table 1. Parameters a, b, and c and volume V_c of the orthorhombic unit cell of the perovskite phase in $La_{1-x}Li_xFeO_3$ samples

Sample	Compound	$a \times 10$, nm	$b \times 10$, nm	$c \times 10$, nm	$V_c \times 10^3$, nm^3
1	$LaFeO_3$	5.56	5.57	7.86	243
2	$La_{0.95}Li_{0.05}FeO_3$	5.55	5.56	7.86	242
3	$La_{0.90}Li_{0.10}FeO_3$	5.53	5.54	7.85	240
4	$La_{0.85}Li_{0.15}FeO_3$	5.54	5.55	7.85	241
5	$La_{0.80}Li_{0.20}FeO_3$	5.54	5.55	7.85	241
6	$La_{0.75}Li_{0.25}FeO_3$	5.54	5.55	7.85	241

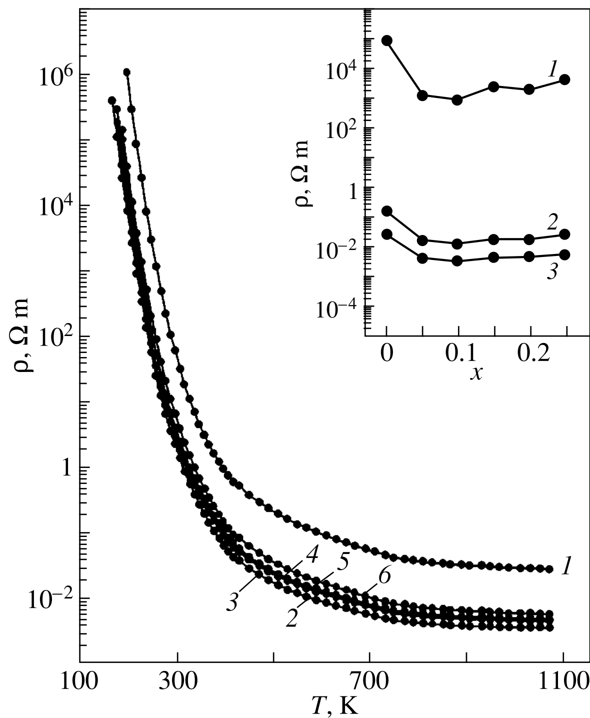

Fig. 1. Temperature dependences of the electrical resistivity of $La_{1-x}Li_xFeO_3$ for different values of x: (*1*) 0, (*2*) 0.05, (*3*) 0.1, (*4*) 0.15, (*5*) 0.2, and (*6*) 0.25. Inset shows concentration dependences of the electrical resistivity of $La_{1-x}Li_xFeO_3$ at different temperatures: (*1*) 220, (*2*) 530, and (*3*) 1050 K.

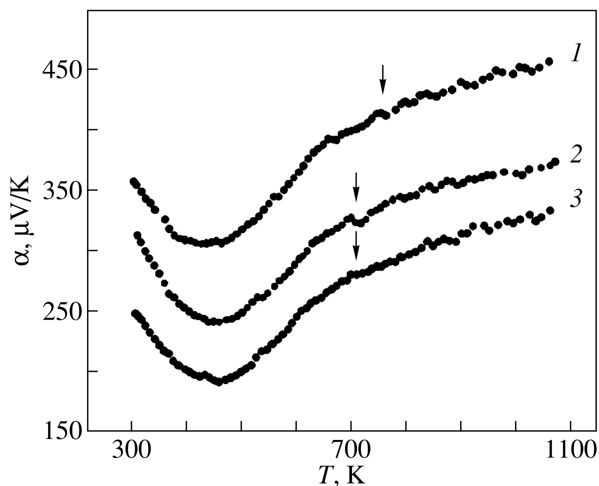

Fig. 2. Temperature dependences of the thermopower of $La_{1-x}Li_xFeO_3$ for different values of x: (*1*) 0, (*2*) 0.05, and (*3*) 0.1. Arrows identify the Néel temperature T_N.

the increase in ρ for $x > 0.1$ is associated with the formation of a second phase, $LiFeO_2$, whose electrical resistivity is two orders of magnitude larger than that of $LaFeO_3$ [20].

It was established in [13, 17] that conduction in $LaFeO_3$ is mediated by SP hopping. In view of the similarity between the temperature dependences of electrical resistivity for samples 1–3 (Fig. 1), we suggest that charge transport in samples 2 and 3 also involves SP hopping, so the $\rho(T)$ relations in various temperature intervals can be written in the form [21]

$$\rho = A_1 T \exp\left(\frac{E}{kT}\right), \quad (1)$$

where A_1 is a constant factor, E is the activation energy for electrical resistivity, and k is the Boltzmann constant. Plotted in the $\ln(\rho/T)$ vs. T^{-1} coordinates, the temperature dependences of the resistivity can be approximated by three sections, whose slope varies with increasing T^{-1}. The values of E are listed in Table 2. Note that the upper boundary of the range 420–780 K, within which the electrical resistivity can be described by Eq. (1) with a constant activation energy E, lies above the Néel temperature for $LaFeO_3$ and the lower boundary of the next temperature range is 810 K (Table 2). These ranges are separated by an intermediate region within which the $\ln(\rho/T)$ vs. T^{-1} dependence is not linear.

Figure 2 presents temperature dependences of the thermopower α in single-phase samples 1–3 ($0 \le x \le 0.1$). The analogous dependences for the two-phase samples ($0.15 \le x \le 0.25$) are similar to $\alpha(T)$ for sample 3. The thermopower of all samples is positive, which is a signature of p-type conduction. In the temperature interval studied, $\alpha(T)$ for sample 1 passes through a minimum at $T_0 \approx 430$ K. At higher temperatures, α increases. In the vicinity of T_N, a barely discernible feature is seen (identified by an arrow in Fig. 2).

The $\alpha(T)$ dependences of samples 2 and 3 also have a minimum. It shifts in position, however, toward higher temperatures ($T_0 \approx 470$ K). Furthermore, the feature which we associate with a crossing of the Néel temperature manifests itself at a lower temperature, $T_N \approx 712$ K (Fig. 2), and does not coincide with the onset of the $d(\log\rho)/dT$ variation (Fig. 1).

If the conduction in the samples originates from SP hopping over localized states, the thermopower in a p-type semiconductor can be written as [22, 23]

$$\alpha = \frac{\xi + \Delta}{eT} + C = -\frac{k}{e}\ln\frac{p}{N_V} + C, \quad (2)$$

where $e > 0$ is the electronic charge, $C < 10$ μV/K is a constant, ξ is the Fermi level energy, Δ is the energy gap separating the conduction band from the valence band (which will be discussed in more detail in the next section), p is the concentration of mobile polarons, and N_V is the number of polaron states over which SPs can hop.

Equation (2) relates the thermopower and the concentration of mobile polarons. If N_V and the $\alpha(T)$ rela-

tion are known, one can estimate p (neglecting the small constant C [22]) and then, using the well-known expression [24] $\sigma = epu$ (where $\sigma = 1/\rho$), calculate the SP mobility u. Obviously enough, in order to find N_V throughout the temperature interval studied, one has to know the spectrum of electronic states of the semiconductor both below and above the Néel temperature.

3.2. Carrier Concentration and Mobility

We suggested in [17] that the scheme of the electronic density of states $N(E)$ in $LaFeO_3$ for temperatures $T > T_N$ is similar to that for $LaCoO_3$ [25] in the temperature region where the lanthanum cobaltite is semiconducting. We took into account the distinctive features of $LaFeO_3$ [26, 27], as well as the theoretical *ab initio* calculations of the electronic density of states in $LaFeO_3$ [28]. Figure 3a presents a fragment of the scheme taken from [17]. The dashed areas identify occupied states. According to this scheme, in the gap separating the valence band from the conduction band (CB) of $LaFeO_3$, there is a narrow energy band (π^* band) deriving from the hybridized t_{2g} orbitals of Fe and the $2p$ orbitals of oxygen. In $LaFeO_3$, all Fe^{3+} ions are in a high-spin state [28] and the electron configuration of the d electrons can be written as $t_{2g}^3 e_g^2$. The localized d-electron t_α^3 and e_α^2 levels (here and subsequently, the state indices $2g$ and g are dropped and the indices α and β denote the spin-up and spin-down directions, respectively) overlap the valence band and are not directly involved in the charge transport process (these levels and the valence band are not shown in Fig. 3). On the other hand, the localized t_β^3 and e_β^2 levels lie in the energy region between the π^* band and the conduction band. The lower lying t_β^3 states are separated from the π^* band by a comparatively narrow energy gap E_g, whereas the energy gap between the conduction band and the π^* band, Δ, is a few electron-volts [13, 28, 29].

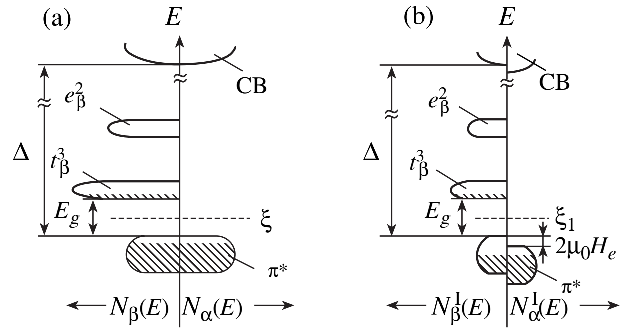

Fig. 3. Schematic diagrams of the electronic density of states $N(E)$ for $La_{1-x}Li_xFeO_3$ at (a) $T \geq T_N$ and (b) $T < T_N$ (for magnetic sublattice I).

If we neglect the AFM ordering below the Néel temperature, then in this model at $T = 0$ all localized t_α^3 and e_α^2 states, as well as the states in the π^* band, will be occupied by electrons and the t_β^3 and e_β^2 states will be vacant. In the absence of impurities, the conductivity of $LaFeO_3$ is zero. At higher temperatures, the occupation of the t_β^3 levels will be nonzero due to carriers being thermally activated from the π^* band. Because these levels are localized, the electrons in them will be trapped and charge transport will be effected by holes forming in the π^* band (p conduction) [17, 25]. To reconcile the data on the hopping character of conduction in $LaFeO_3$ [13, 17], which implies carrier localization, with the model of electronic densities of state given in Fig. 3, one has to assume that the holes apparently form in the π^* band tail beyond the mobility edge [21, 30]. Accepting the aforesaid, we note that this situation is similar to that in a nondegenerate acceptor semiconduc-

Table 2. Activation energies for $La_{1-x}Li_xFeO_3$ samples derived from data on the electrical resistivity (E) and the carrier mobility (W)

Sample	Electrical resistivity		Mobility	
	temperature range, K	E, eV	temperature range, K	W, eV
1	200–350	0.53	300–350	0.38 ± 0.02
	410–780	0.27	350–810	0.28 ± 0.01
	810–1073	0.16	810–1073	0.14 ± 0.03
2	180–350	0.45	300–370	0.25 ± 0.02
	420–780	0.23	370–810	0.22 ± 0.01
	810–1073	0.14	810–1073	0.12 ± 0.02
3	200–370	0.44	300–370	0.28 ± 0.01
	420–780	0.23	370–810	0.21 ± 0.01
	810–1073	0.13	810–1073	0.13 ± 0.02

tor (this assumption appears to be justified because the orthorhombic crystal field in $LaFeO_3$ lifts the t_{2g} and e_g level degeneracy). The intrinsic t_β^3 levels now act as impurity levels, and the π* band acts as the valence band.

The quantity N_V in a nondegenerate semiconductor with hole conduction is given by [22, 23]

$$N_V = 2\left(\frac{2\pi m_h kT}{h^2}\right)^{3/2}, \tag{3}$$

where h is Planck's constant and m_h is the effective hole mass in the lattice not distorted by electron–phonon coupling. From Eq. (2), the hole concentration above T_N is found to be

$$p \approx N_V \exp\left(-\frac{e}{k}\alpha\right). \tag{4}$$

After a sample has crossed to the AFM state, all magnetic atoms (Fe) will be distributed over the two magnetic sublattices [24]. To understand the situation on a qualitative footing, we neglect the iron ion spins in $LaFeO_3$ being noncollinear [31] and consider the simple case where the magnetic moments of all atoms on one of the sublattices are oriented parallel to one another while the total magnetizations of the sublattices are oppositely directed, which makes the net magnetic moment of a sample zero.

We consider one of the sublattices and denote it by I. All its atoms are in a constant effective magnetic field $\mathbf{H}_e$ generated by atoms of the other sublattice (denoted by II). Figure 3b gives a schematic representation of a fragment of the single-particle density of electronic states in sublattice I, which is acted upon by the effective magnetic field $\mathbf{H}_e$ of sublattice II. The electronic density of states of sublattice II is a mirror reflection of that of sublattice I in a plane parallel to the E axis.

The internal magnetic field $\mathbf{H}_e$, similar to an external field, affects the electron energy. In particular, the energy of electrons with spin α aligned with the magnetic field $\mathbf{H}_e$ will be reduced by $-\mu_0 H_e$ as compared to their energy at $\mathbf{H}_e = 0$ (μ_0 is the electron magnetic moment) [24]. Accordingly, the energy of electrons with spin β oriented opposite to the magnetic field $\mathbf{H}_e$ will increase by $+\mu_0 H_e$. The energy difference between them is $2\mu_0 H_e$ (Fig. 3b). The problem consists in estimating the concentration of holes in the π* band, which appear as a result of the thermal activation of electrons into the t_β^3 levels.

The procedure for calculating the hole concentration in a nondegenerate, magnetically disordered semiconductor is described in detail, for instance, in [23, 32]. If the semiconductor is in the AFM state, this calculation differs primarily in that each of the sublattices is treated separately. As a consequence, the density of states of electrons (holes) with spin α or β in the π* band of sublattice I (or II) is $N_V/4$. In addition, one has to take into account the energy difference $2\mu_0 H_e$ between electrons (holes) with different spin directions on each sublattice. The calculation performed for the density-of-states scheme in Fig. 3b yielded the following expression for the hole concentration on sublattice I, assuming a parabolic dispersion relation and the Boltzmann approximation for the distribution function:

$$p^{\mathrm{I}} = \frac{N_V}{2}\exp\left(-\frac{\xi_1 + \Delta}{kT}\right)\left(1 + \tanh\frac{\mu_0 H_e}{kT}\right)^{-1}, \tag{5}$$

where ξ_1 is the Fermi energy for sublattice I. In the same way, one can calculate the hole concentration p^{II} on sublattice II. Since the values of Δ and of the Fermi energy ξ_1 on both sublattices are equal, we obtain $p^{\mathrm{I}} = p^{\mathrm{II}} = p_{\mathrm{AFM}}/2$ (p_{AFM} is the total hole concentration in the sample).

Consider the argument of the function $\tanh(\mu_0 H_e/kT)$ on the right-hand side of Eq. (5). In the Weiss molecular field approximation, we have $H_e = \lambda M$, where M is the average magnetization of one of the sublattices and λ is a constant. Following [33], we introduce the reduced magnetization $m(T) = M(T)/M(0)$ and reduced temperature $t = T/T_N$, where $M(0) = N^{\mathrm{I}} g S \mu_B$, $T_N = N^{\mathrm{I}} g^2 S(S+1)\lambda\mu_B^2/3k$, N^{I} is the number of magnetic atoms (Fe) on sublattice I (or II), g is the spectroscopic splitting factor for electrons, S is the average spin per atom, and μ_B is the Bohr magneton. In this case, the total hole concentration in a sample below T_N is

$$p_{\mathrm{AFM}} = N_V \exp\left(-\frac{\xi_1 + \Delta}{kT}\right)\left[1 + \tanh\left(D\frac{m}{t}\right)\right]^{-1}, \tag{6}$$

where $D = 3\mu_0/\mu_B g(S+1)$. For $S = 5/2$ (for the Fe^{3+} ion in $LaFeO_3$), $g = 2.0023$, and $\mu_0 \approx \mu_B$ [33], we obtain $D \approx 0.4285$.

Since the thermopower of a sample in the AFM state is $\alpha_{\mathrm{AFM}} \approx (\xi_1 + \Delta)/eT$, we can write

$$p_{\mathrm{AFM}} = N_V \exp\left(-\frac{e}{k}\alpha_{\mathrm{AFM}}\right)\left[1 + \tanh\left(D\frac{m}{t}\right)\right]^{-1}. \tag{7}$$

Knowing the temperature dependence of reduced magnetization $m(T)$ for one of the sublattices and the Néel temperature for the sample, one can calculate the hole concentration p_{AFM} for $T < T_N$ from Eq. (7). In the case where the formation of a hole in the spectrum of electronic states of a semiconductor is accompanied by the appearance of an SP, the concentration of holes will apparently be equal to that of SPs.

Figure 4 plots temperature dependences of the SP concentration $p(T)$ in samples 1–3 calculated with allowance for (points and solid lines) and disregarding (dashed lines) the transformation of their electronic spectrum in crossing from the paramagnetic to the AFM state. The $m(T)$ relation is approximated as [33]

$$m = B_S\left(\frac{m}{t}\right), \quad (8)$$

where the Brillouin function

$$B_S = \frac{2S+1}{2S}\coth\frac{3(2S+1)m}{2(S+1)t} - \frac{1}{2S}\coth\frac{3m}{2(S+1)t}.$$

The SP concentration in sample 1 is calculated assuming that $T_N \approx 750$ K [12]. The Néel temperature in samples 2 and 3 is derived from the position of the feature observed in the $\alpha(T)$ plots at 712 K (Fig. 2).

As the Li concentration increases, the number of carriers grows and reaches a maximum value in sample 3. In all the samples, an increase in temperature from 300 to 430–470 K brings about an increase in the SP concentration, after which it remains practically constant to the end of the temperature interval studied. The concentration first attains a maximum at the temperature T_0 corresponding to the minimum in $\alpha(T)$.

Figure 5 displays temperature dependences of the carrier mobility $u(T)$ in samples 1–3. An increase in Li concentration results in a substantial increase in the SP mobility in samples 2 and 3 (compared to sample 1). This dependence is not, however, a monotonically rising function. The calculated carrier mobilities in sample 2 are somewhat higher than those in sample 3, although the electrical resistivity of the samples decreases monotonically with increasing Li concentration (Fig. 1). The values of the mobility in samples 2 and 3 are apparently similar; the observed difference should be assigned to errors in the determination of ρ and α.

In all the samples, the SP mobility increases with temperature. The $u(T)$ dependence can be fitted in different temperature intervals by an exponential [22],

$$u = \frac{A_2}{T}\exp\left(-\frac{W}{kT}\right), \quad (9)$$

where A_2 is a constant, $W = (W_p + W_D)/2$ is the activation energy for the mobility, W_p is the energy of SP formation, and W_D is the disordering energy. However, the boundaries of the temperature intervals within which the $u(T)$ relation is characterized by a constant activation energy W differ somewhat from those of the corresponding intervals identified in the $\rho(T)$ plots (Table 2), because the electrical resistivity depends not only on u but also on the SP concentration. In each of the above temperature intervals, the inequality $E \geq W$ holds, which is the necessary condition for SP hopping conduction [22].

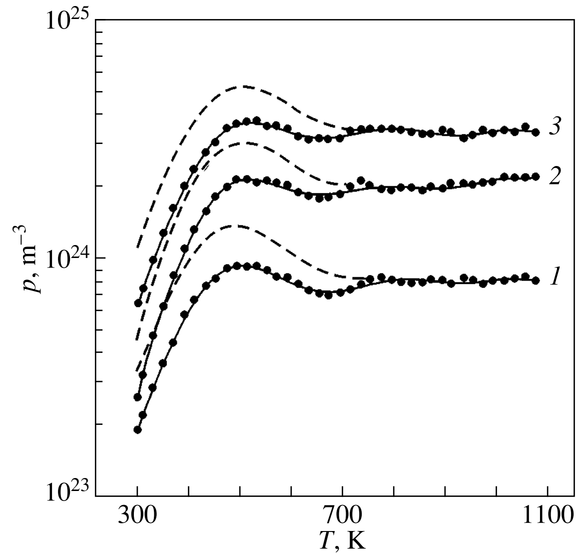

Fig. 4. Temperature dependences of the SP concentration in $La_{1-x}Li_xFeO_3$ calculated with allowance for (points and solid lines) and disregarding (dashed lines) the transformation of their spectrum of electronic states occurring at the paramagnet–antiferromagnet transition for different values of x: (*1*) 0, (*2*) 0.05, and (*3*) 0.1.

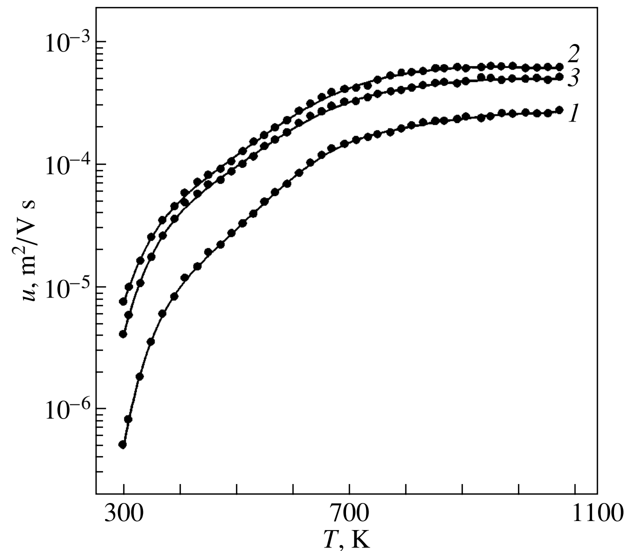

Fig. 5. Temperature dependences of the SP mobility in $La_{1-x}Li_xFeO_3$ for different values of x: (*1*) 0, (*2*) 0.05, and (*3*) 0.1.

4. DISCUSSION OF THE RESULTS

The above results permit us to conclude that the region of existence of the $La_{1-x}Li_xFeO_3$ solid solution prepared in air at atmospheric pressure is limited to 10 mol % and is apparently close to the upper boundary of existence of the $La_{1-x}FeO_3$ nonstoichiometric oxide, which forms for $x \leq 0.075$ [34]. At higher Li concentrations, two-phase samples form, which contain, in addition to the solid solution, the cubic modification of $LiFeO_2$.

In the temperature interval studied, samples 1–3 exhibit p-type hopping conduction. The carriers are

apparently SPs created by the holes that form in the thermal activation of electrons from the π^* band to the close-lying t_β^3 energy levels (Fig. 3), which are separated from the former by a relatively narrow energy gap $E_g \approx 2(E - W) \approx 0.3$ eV (Table 2). As the lithium concentration increases, the electrical resistivity of the samples decreases (Fig. 1). As follows from an analysis of the $\rho(T)$ and $\alpha(T)$ relations, this behavior is associated with the increase in the carrier concentration (Fig. 4) and mobility (Fig. 5).

All temperature dependences of the SP concentration feature a broad maximum in the range 400–600 K, whose magnitude decreases considerably when one takes into account the change the energy spectrum of the samples undergoes at a second-order phase transition (Fig. 4). The fact that this maximum does not disappear altogether can be assigned to the approximations made in attempting to take into account the effect of magnetic ordering for $T < T_N$. In particular, we did not include remanent magnetization of the samples, which appears as a result of the net magnetic moments of each of the two magnetic sublattices being noncollinear. On the other hand, one should not overlook the possibility that, within a broad temperature interval, both below and above T_N, our samples have a domain structure (as do $La_{1-x}Sr_xMnO_3$ samples) and, viewed in terms of their magnetic characteristics, are actually composites consisting of AFM and paramagnetic regions whose fractional concentration varies as one approaches the Néel temperature [7]; in other words, the real temperature dependence of the relative magnetization of each sublattice differs from the relation derived from Eq. (8). A more thorough inclusion of factors capable of affecting the $m(T)$ dependence should result in the disappearance of this maximum. Nevertheless, the approach proposed by us for calculating the carrier concentration for $T < T_N$ offers at least a qualitative interpretation of the phenomena occurring in a sample with increasing temperature.

It is appropriate to note, in particular, that the temperature dependences of carrier concentration in the samples studied are similar to those observed in acceptor semiconductors [23, 32]. At relatively low temperatures, the SP concentration grows with temperature, while at higher temperatures it stabilizes at a certain value, because the number of vacant t_β^3 levels apparently decreases and electron excitation into the e_β^2 levels is made difficult as it requires a higher activation energy.

The increase in SP mobility as the Li concentration increases (Fig. 5) may be related to the correlation among energy states of neighboring polarons increasing as their concentration increases, thus reducing the activation energy W (Table 2) in the corresponding temperature intervals [21]. The same reason probably accounts for the change in W as the sample temperature increases (Table 2).

We note in conclusion that the SP mobility in $LaFeO_3$ for $T < T_N$ calculated with allowance for the spontaneous magnetization of the electronic subsystem differs from our earlier results from [17], where the SP concentration was derived using Eq. (2), which is valid for $T > T_N$. In particular, the dependence of $\ln(uT)$ on T^{-1} obtained in the present study for $LaFeO_3$ (not shown here) does not exhibit a jump when crossing T_N from low temperatures. (In [17], such a jump manifested itself in the fact that the inequality $E \geq W$ did not hold in a certain temperature interval below T_N.) Furthermore, when calculating the SP concentration $p(T)$, the density of states N_V in the band is assumed, following [22], to be equal to the iron atom concentration. In this approximation, the SP concentration is overestimated as compared to the values of p obtained when calculating N_V from Eq. (3). Accordingly, the calculated SP mobility is found to be lower than that obtained in [17].

ACKNOWLEDGMENTS

This study was supported by the Russian Foundation for Basic Research, project no. 01-03-96435.

REFERENCES

1. E. I. Nikulin, V. M. Egorov, Yu. M. Baĭkov, B. T. Melekh, Yu. P. Stepanov, and I. N. Zimkin, Fiz. Tverd. Tela (St. Petersburg) **44** (5), 881 (2002) [Phys. Solid State **44**, 920 (2002)].
2. V. V. Mashkautsan, R. R. Zaĭnullina, N. G. Bebenin, V. V. Ustinov, and Ya. M. Mukovskiĭ, Fiz. Tverd. Tela (St. Petersburg) **45** (3), 468 (2003) [Phys. Solid State **45**, 494 (2003)].
3. N. I. Solin and S. V. Naumov, Fiz. Tverd. Tela (St. Petersburg) **45** (3), 460 (2003) [Phys. Solid State **45**, 486 (2003)].
4. N. N. Loshkareva, A. V. Korolev, T. I. Arbuzova, N. I. Solin, N. A. Viglin, I. B. Smolyak, N. G. Bebenin, Yu. P. Sukhorukov, S. V. Naumov, N. V. Kostromitina, and A. M. Balbashov, Fiz. Tverd. Tela (St. Petersburg) **44** (10), 1827 (2002) [Phys. Solid State **44**, 1916 (2002)].
5. C. N. R. Rao, J. Mater. Chem. **9**, 1 (1999).
6. C. N. R. Rao and J. Gopalakrishnan, *New Directions in Solid State Chemistry. Structure, Synthesis Properties, Reactivity and Materials Design* (Cambridge Univ. Press, Cambridge, 1986; Nauka, Novosibirsk, 1990).
7. É. L. Nagaev, Usp. Fiz. Nauk **166** (8), 833 (1996) [Phys. Usp. **39**, 781 (1996)].
8. L. P. Gor'kov, Usp. Fiz. Nauk **168** (6), 665 (1998) [Phys. Usp. **41**, 589 (1998)].
9. T. Maeder and J. G. Bednorz, J. Eur. Ceram. Soc. **19**, 1507 (1999).
10. M. A. Senaris-Rodriguez and J. B. Goodenough, J. Solid State Chem. **118**, 323 (1995).
11. S. Geller and E. A. Wood, Acta Crystallogr. **9** (7), 563 (1956).

12. G. N. Jonker, Physica (Amsterdam) **22**, 707 (1956).
13. G. V. S. Rao, B. M. Wanklyn, and C. N. R. Rao, J. Phys. Chem. Solids **32** (2), 345 (1971).
14. W. H. Jung and E. Iguchi, J. Phys.: Condens. Matter **7**, 1215 (1995).
15. T. Shimura, T. Hayashi, Y. Inaguma, and M. Itoh, J. Solid State Chem. **124**, 250 (1996).
16. A. E. Teplykh, S. G. Bogdanov, É. Z. Valiev, A. N. Pirogov, Yu. A. Dorofeev, A. A. Ostroushko, A. E. Udilov, V. A. Kazantsev, and A. E. Kar'kin, Fiz. Tverd. Tela (St. Petersburg) **45** (12), 2222 (2003) [Phys. Solid State **45**, 2328 (2003)].
17. S. I. Vecherskiĭ and N. N. Batalov, Zh. Neorg. Khim. **45** (9), 1525 (2000) [Russ. J. Inorg. Chem. **45** (9), 1394 (2000)].
18. L. I. Anatychuk, *Thermal Converters and Thermoelectric Devices* (Naukova Dumka, Kiev, 1979) [in Russian].
19. A. P. Babichev, N. A. Babushkina, A. M. Bratkovskiĭ, *et al.*, in *Physical Quantities. Handbook*, Ed. by I. S. Grigor'ev and E. Z. Meĭlikhov (Énergoatomizdat, Moscow, 1991) [in Russian].
20. M. A. van den Noort, P. J. J. M. van den Put, and J. Schoonman, High Temp. High Press. **20** (2), 197 (1988).
21. N. F. Mott and E. A. Davis, *Electronic Processes in Non-Crystalline Materials*, 2nd ed. (Clarendon, Oxford, 1979; Mir, Moscow, 1982), Vol. 1.
22. D. Appel, in *Polarons*, Ed. by Yu. A. Firsov (Nauka, Moscow, 1975).
23. R. A. Smith, *Semiconductors*, 2nd ed. (Cambridge Univ. Press, Cambridge, 1978; Mir, Moscow, 1982).
24. J. M. Ziman, *Principles of the Theory of Solids*, 2nd ed. (Cambridge Univ. Press, Cambridge, 1972; Mir, Moscow, 1974).
25. M. A. Senaris-Rodriguez and J. B. Goodenough, J. Solid State Chem. **116**, 224 (1995).
26. D. D. Sarma and A. Chainani, J. Solid State Chem. **111**, 208 (1994).
27. M. Abbate, F. M. F. de Groot, J. C. Fuggle, *et al.*, Phys. Rev. B **46** (8), 4511 (1992).
28. P. Mahadevan, N. Shanthi, and D. D. Sarma, J. Phys.: Condens. Matter **9**, 3129 (1997).
29. J. B. Goodenough, J. Appl. Phys. **37** (3), 1415 (1966).
30. É. A. Neĭfel'd, V. E. Arkhipov, N. A. Tumalevich, and Ya. M. Mukovskiĭ, Pis'ma Zh. Éksp. Teor. Fiz. **74** (11), 630 (2001) [JETP Lett. **74**, 556 (2001)].
31. R. White, Usp. Fiz. Nauk **103** (4), 593 (1971).
32. V. L. Bonch-Bruevich and S. G. Kalashnikov, *Physics of Semiconductors* (Nauka, Moscow, 1977) [in Russian].
33. C. Kittel, *Introduction to Solid State Physics*, 5th ed. (Wiley, New York, 1976; Nauka, Moscow, 1978).
34. V. C. Belessi, P. N. Trikalitis, A. K. Lavados, *et al.*, Appl. Catal. A **117**, 53 (1999).

Translated by G. Skrebtsov

Physics of the Solid State, Vol. 46, No. 8, 2004, pp. 1482–1486. Translated from Fizika Tverdogo Tela, Vol. 46, No. 8, 2004, pp. 1441–1445.
Original Russian Text Copyright © 2004 by Aronzon, Granovskiĭ, Nikolaev, Kovalev, Perov, Ryl'kov.

Specific Features of the Hall Effect in Cr/Co Bilayer Films

B. A. Aronzon[1, 2], A. B. Granovskiĭ[3], S. N. Nikolaev[2], D. Yu. Kovalev[1, 2], N. S. Perov[3], and V. V. Ryl'kov[1, 2]

[1] *Institute of Theoretical and Applied Electrodynamics, Russian Academy of Sciences, Moscow, 127412 Russia*
e-mail: kovalev@imp.kiae.ru
[2] *Russian Research Centre Kurchatov Institute, pl. Kurchatova 1, Moscow, 123182 Russia*
[3] *Moscow State University, Vorob'evy gory, Moscow, 119992 Russia*

Received December 10, 2003

Abstract—The Hall effect and magnetoresistance in Cr(50 Å)/Co(200 Å) bilayer films prepared by ion sputtering on a silicon substrate are investigated at room temperature. The planar Hall effect revealed in the bilayer films differs from the planar Hall effect observed usually in that it is symmetric with respect to the sign of the change in the rotation angle of the magnetic moment in the film plane. Under conditions where the symmetric planar Hall effect is realized, the change in the Hall resistance is more than 10% and exceeds the anisotropic magnetoresistance by two orders of magnitude. The hysteresis loops are measured at different orientations of magnetic fields. The planar Hall effect is studied in a weak longitudinal magnetic field. The results obtained demonstrate that the symmetric planar Hall effect is associated with the multidomain structure of the cobalt film in Cr/Co bilayer composites. © *2004 MAIK "Nauka/Interperiodica".*

1. INTRODUCTION

The specific feature of ferromagnetic films lies in the fact that, owing to the magnetoresistance anisotropy, an electric field perpendicular to the direction of current (the Hall voltage or Hall emf) can be induced in these films even when the magnetic moment is entirely aligned with the film plane [1, 2], whereas the anomalous Hall effect is usually observed in a geometry allowing for the perpendicular component of the magnetic moment.

This effect is referred to as the planar Hall effect. For a single-domain film, the planar Hall voltage can be represented in the form [2]

$$V_{PH} = \frac{I_x}{d}(\rho_{\parallel} - \rho_{\perp})\sin\theta\cos\theta. \quad (1)$$

Here, V_{PH} is the Hall voltage induced in the direction (along the Y axis) transverse to the direction of the current I_x passing along the film (the X axis); d is the film thickness; θ is the angle between the direction of the magnetization M and the direction of the current; and $\rho_{\parallel}$ and $\rho_{\perp}$ are the resistivities of the film in the directions parallel and perpendicular to the magnetization direction, respectively [4]: $(\rho_{\parallel} - \rho_{\perp}) \propto M^2$. From relationship (1), it follows that the planar Hall effect is most pronounced in thin films and is determined by the anisotropic magnetoresistance. Note that, if the magnetic field is applied perpendicular to the film plane and there arises a magnetization component aligned parallel to the normal, an additive contribution to the measured signal is made by the anomalous Hall voltage [4]:

$$V_{AH} = \frac{R_s I_x}{d} M\cos\phi, \quad (2)$$

$$V_H = V_{PH} + V_{AH}. \quad (3)$$

Here, R_s is the anomalous Hall constant, ϕ is the angle between the magnetic moment and the normal to the film plane, and V_H is the total measured voltage.[1]

It can be seen from the above relationships that the Hall voltage in ferromagnets is governed by the magnetization behavior and increases with a decrease in the film thickness. It is not accidental that the progress made in spintronics, in which miniature thin-film elements have found application, has given impetus to the investigation and development of the methods based on Hall magnetometry, including the techniques using the planar Hall effect [5–11]. In particular, it has been demonstrated that microcompasses and magnetic sensors with a sensitivity of 1 nT can be devised on the basis of the planar Hall effect (see [5–7] and references therein). In recent works, the planar Hall effect has been used to analyze the complex exchange anisotropy at ferromagnet–antiferromagnet interfaces (specifically in NiFe/FeMn [8] and NiFe/NiMn [9] bilayer structures) and to investigate the magnetization reversal at different directions of a pinning field in spin valves [10].

In this work, we studied the Hall effect in bilayer structures based on cobalt and antiferromagnetic chro-

[1] For 3d transition metals and their alloys, the contribution from the usual Hall effect due to a Lorentz force is negligible.

1063-7834/04/4608-1482$26.00 © 2004 MAIK "Nauka/Interperiodica"

mium. Note that, to date, investigation into the magnetotransport properties of Co/Cr bilayer films has received little attention. This can be explained by the large mismatch between the cobalt and chromium lattices and by the complex structure of the systems formed [12].

2. SAMPLE PREPARATION AND EXPERIMENTAL TECHNIQUE

Samples with one pair of current contacts and two pairs of potential (Hall) contacts had the standard shape of a double cross. The width and length of the conducting channel were $W = 2$ mm and $L = 7$ mm, respectively. The length and width of Hall probes on side faces of the sample were equal to 1.5 and 0.5 mm, respectively. The samples were prepared in a vacuum chamber by ion-beam sputtering of chromium and then cobalt from several targets arranged symmetrically with respect to the sample plane. According to estimates, the angle of incidence of Co and Cr ion beams varied in the range from 20° to 40°. The plane of incidence was, on the average, perpendicular to the direction of the conducting channel. As is known [13], this circumstance favors the appearance of an induced anisotropy with an easy magnetization axis perpendicular to the plane of incidence; i.e., in our case, it is aligned along the sample channel. The films were sputtered onto silicon substrates covered with a thin layer (~1000 Å) of thermal oxide through precisely fabricated nickel masks. The Hall probes were matched accurate to within ~10 μm.

The Hall effect was examined on an automated setup on the basis of a computer. The setup was equipped with an HP3457A precision multimeter. The magnetic field was induced by an electromagnet with a 12-digit dc power supply (20 A), which was also controlled by the computer. For a current of 20 A, the magnetic field strength was approximately equal to 1 T. The voltage between the Hall (V_y) and potential (V_x) probes and the current I_x in the sample were simultaneously measured (in a digital form) at a dc bias voltage in positive and negative magnetic fields H. The results of measurements were used to calculate the sample resistance across the potential probes $R_{xx} = V_x/I_x$ and the transverse resistance $R_{xy} = V_y/I_x$. The current in these measurements did not exceed 4–5 mA. The direction (perpendicular or parallel) of the field with respect to the sample was controlled by measuring the signal of the Hall probes at the maximum strength of the magnetic field (~1 T).

Moreover, in order to determine the easy magnetization axis, the magnetization was studied with the use of a vibrating-coil magnetometer.

3. RESULTS AND DISCUSSION

Figure 1 presents the results of measuring the Hall effect in Cr(50 Å)/Co(200 Å) bilayer films at room temperature in a standard Hall geometry (with the magnetic field applied perpendicular to the sample plane). The experiments were performed in the following way. After aligning the sample plane, a magnetic field with positive polarity and a strength of approximately 2 kOe was applied. Then, the magnetic field strength was decreased at a low rate (~400 Oe/min). The Hall effect was measured with a change in the magnetic field strength, initially, from +2 to –2 kOe and, then, from –2 to + 2 kOe. In this case, the perpendicular magnetic anisotropy could be judged from the hysteresis in the Hall resistance.

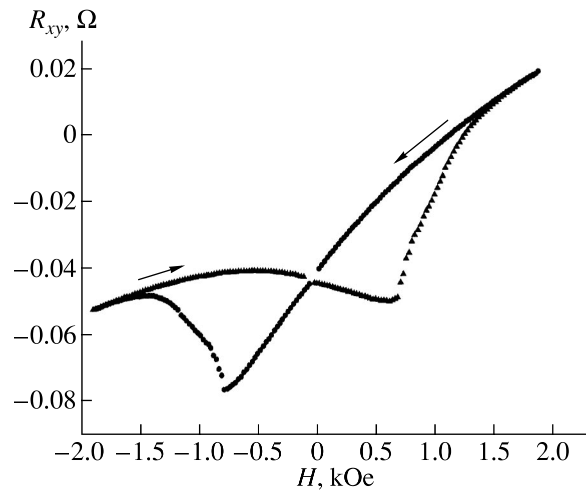

Fig. 1. Magnetic-field dependence of the transverse resistance for a Cr(50 Å)/Co(200 Å) bilayer film. The field is perpendicular to the sample plane. Arrows indicate the direction of change in the magnetic field strength.

It can be seen from Fig. 1 that unusual hysteresis of the Hall voltage is observed in the entire range of field strengths under investigation. Note that similar hysteresis is not observed in Co(200 Å) films without a Cr sublayer. Apparently, the unusual shape of the hysteresis for bilayer films (Fig. 1) suggests the presence of a considerable even (with respect to the magnetic field) component in the transverse resistance or, in other words, the "even" Hall effect $R_a = (R^+_{xy} + R^-_{xy})/2$, where R^+_{xy} and R^-_{xy} correspond to positive and negative fields, respectively. The field dependence of the resistance $R_a(H)$ is plotted in Fig. 2. This dependence was obtained by summing the resistances R_{xy} measured with a change in the magnetic field strength from +2 kOe to 0 and from 0 to –2 kOe. As can be seen from Fig. 2, the resistance R_a considerably increases at small strengths of the magnetic field and then tends to flatten. It should be noted that, in our recent work [14], we observed the manifestation of the even component of the Hall effect in disordered granular ferromagnets (Fe/SiO_2 nanocomposites). In [14], this phenomenon was explained in terms of the percolation mechanism of conduction in these systems and changes in the trajectories of percolation paths of the current under the action of magnetic

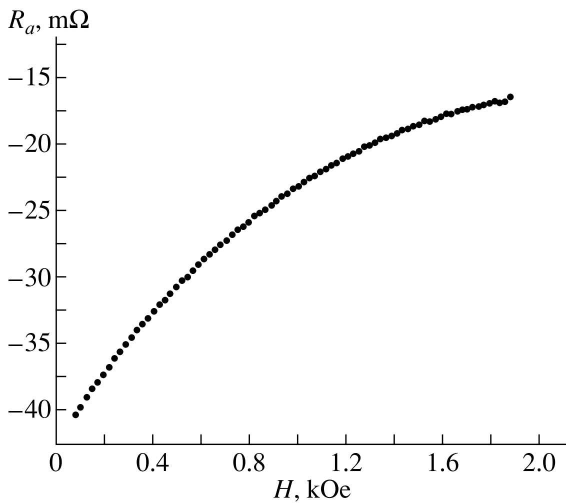

Fig. 2. Magnetic-field dependence of the asymmetry resistance R_a for a Cr(50 Å)/Co(200 Å) bilayer film.

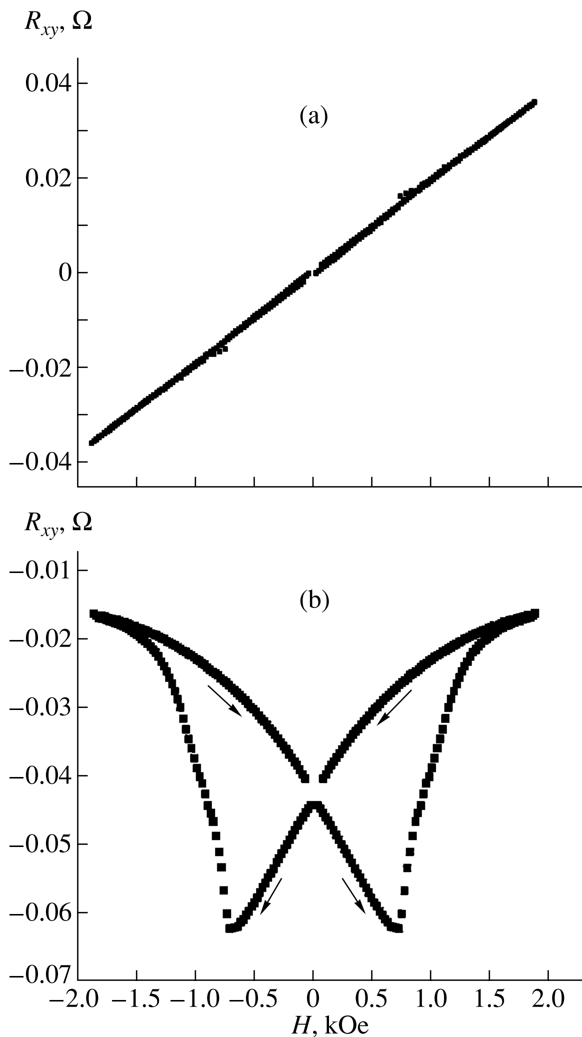

Fig. 3. Magnetic-field dependences of the transverse resistance for the (a) perpendicular and (b) longitudinal magnetization components.

fields. However, the objects studied in the present work are good metals. Consequently, the observed effect should have a different origin. It will be shown below that this effect can be associated with a nontypical behavior of the planar Hall effect.

As follows from relationships (1)–(3), the anomalous Hall voltage is an even function of the magnetization M, whereas the planar Hall voltage is an odd function of the magnetization M. Therefore, if the resistances in the hysteresis loop at field strengths $H < 0$ (see Fig. 1) are subtracted from the corresponding resistances in the hysteresis loop at field strengths $H > 0$, the curve thus obtained will depend only on the perpendicular component of the magnetization. Similarly, when the corresponding resistances in the hysteresis loop are added, the resultant curve will depend only on the in-plane component of the magnetization of the film. By using this procedure, it is easy to reconstruct the dependences of the perpendicular and parallel components of the magnetization [4].

The above procedure was applied to construct the dependences of the transverse resistance associated with the magnetization components oriented perpendicular (Fig. 3a) and parallel (Fig. 3b) to the film plane. A comparison of these dependences shows that the hysteresis of the Hall effect is determined by the in-plane magnetization component. (Note that the residual resistance in Fig. 3b at $H = 0$ should be interpreted as the asymmetry resistance due to a geometrical mismatch of the Hall probes; according to estimates, this mismatch for the given sample can be as large as 4 μm.) It is also worth noting that no hysteresis is observed for the dependence of the transverse magnetization component and this component linearly depends on the field strength over the entire range of field strengths under investigation. This fact indicates that our objects do not exhibit perpendicular anisotropy, which is frequently inherent in CoCr alloys [4, 15].

The measurements carried out with the vibrating-coil magnetometer demonstrated that the easy magnetization axis actually lies in the film plane almost parallel to the conducting channel (the axis of the sample). The hysteresis loops of the magnetization of the sample at different angles between the magnetic field and the axis of the sample are depicted in Fig. 4. The squareness of the loops strongly depends on the field orientation and exhibits a maximum close to unity at an angle of 10° between the magnetic field and the axis of the sample in the film plane (see inset to Fig. 4). Such a dependence suggests that the sample is uniaxial; in this case, the easy magnetization axis deviates from the axis of the sample by an angle of ~10°. The coercive force of the sample is approximately equal to 13 Oe. The magnetization reversal toward the direction of easy magnetization occurs with an increase in the field strength from 12 to 14 Oe. Most likely, this wide range of fields corresponding to the magnetization reversal can be explained by the motion of domain walls, which is vir-

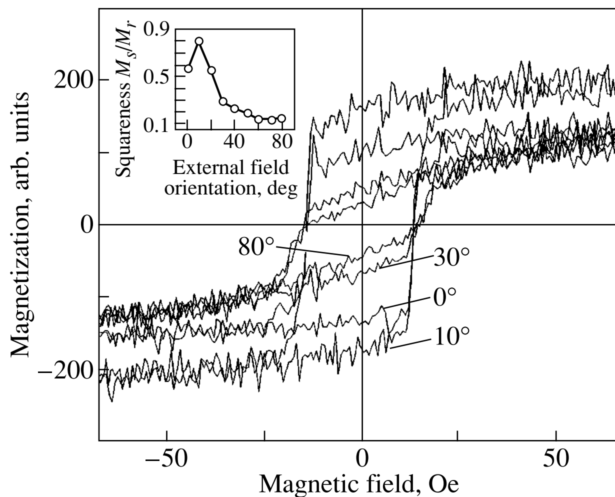

Fig. 4. Magnetization hysteresis loops for different orientations of the magnetic field with respect to the axis of the sample (the direction of current). The external magnetic field is aligned with the sample plane. The inset shows the dependence of the coefficient of squareness on the angle of field orientation.

tually complete at a field strength of the order of 14 Oe. In stronger fields, the magnetic moment gradually completes the rotation to the easy magnetization axis.

The strong influence exerted by the longitudinal magnetization component on the Hall effect (Fig. 3b) stimulated the performance of two series of measurements in a planar geometry. In the first series, the magnetic field was applied parallel to the sample plane and perpendicular to the current passing through the sample (Fig. 5). In the second series, the magnetic field was aligned parallel to both the sample plane and the direction of the current (Fig. 6). It should be noted that negative magnetoresistance is observed in the former case (Fig. 5b), whereas the magnetoresistance is positive in the latter case (Fig. 6b). To put it differently, the behavior of the magnetoresistance has all the traits characteristic of the anisotropic magnetoresistance effect with a small ratio $\Delta\rho/\rho$ (smaller than 0.1%). At the same time, the change in the transverse Hall resistance exceeds 10%. Note also that the observed planar Hall effect is symmetric with respect to the magnetic field and, hence, with respect to the sign of the change in the rotation angle of the magnetic moment. On the other hand, according to relationship (1), the planar Hall effect should be antisymmetric. Possibly, this fact can be explained by the separation of the film into domains due to the interaction of the ferromagnetic (Co) and antiferromagnetic (Cr) components. This situation is typical of Fe/Cr multilayer structures. Recall that a similar symmetric planar Hall effect does not manifest itself in Co films of the same thickness. Certainly, upon separation of the film into domains, expression (1) becomes invalid [16] and the specific features of the planar Hall effect can be completely determined by the domain structure.

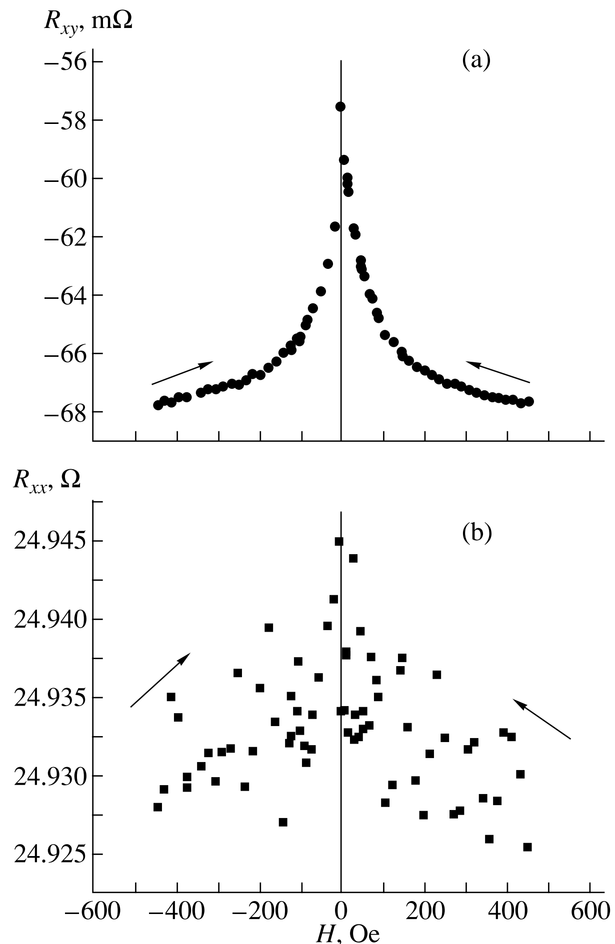

Fig. 5. Magnetic-field dependences of (a) the transverse resistance R_{xy} and (b) the longitudinal resistance R_{xx} for a Cr(50 Å)/Co(200 Å) bilayer film. The external magnetic field is parallel to the sample plane and perpendicular to the direction of the current. Arrows indicate the direction of change in the magnetic field strength.

In order to confirm the above assumption, we performed additional experiments in which a weak constant magnetic field (~10 Oe) was applied in the plane of the Cr(50 Å)/Co(200 Å) bilayer films (along the direction of the current). The field strength was sufficiently strong to decrease the number of domains or to provide an almost homogeneous magnetic state. The sweep field was aligned parallel to the sample plane and perpendicular to the direction of the current. In this case, the field dependence of the transverse resistance R_{xy} differs significantly (Fig. 7). It can be seen from Fig. 7 that the planar Hall effect under these conditions appears to be antisymmetric. A similar situation was previously observed by Ogrin *et al.* [7]. Furthermore, this behavior follows from relationship (1) when taken into account that the planar Hall voltage $V_{PH} \propto \sin\theta$, where θ is the angle between the direction of the current I_x and the direction of the magnetization M. Note that the asymmetry of the dependence in Fig. 7 (i.e., differ-

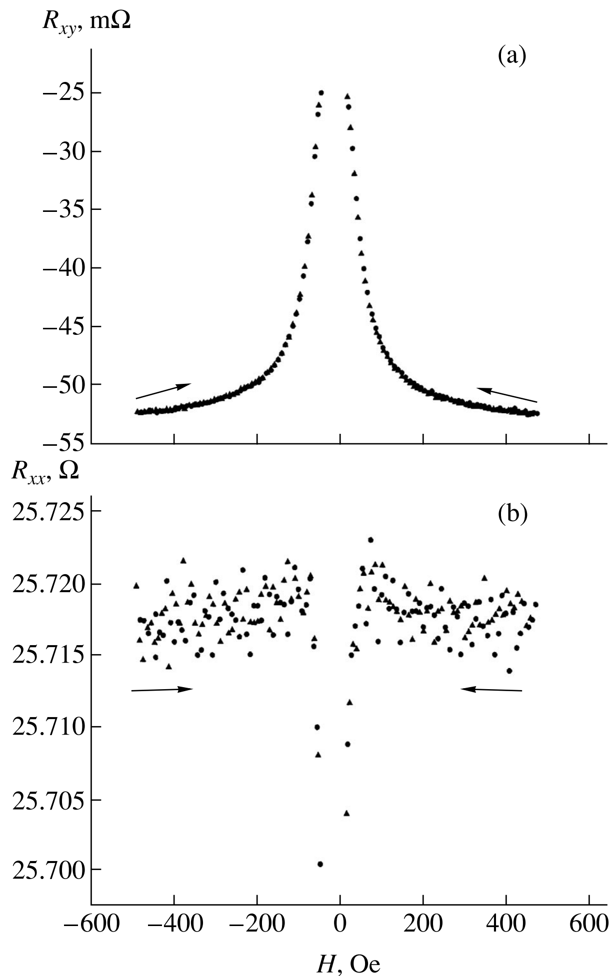

Fig. 6. Magnetic-field dependences of (a) the transverse resistance R_{xy} and (b) the longitudinal resistance R_{xx} for a Cr(50 Å)/Co(200 Å) bilayer film. The external magnetic field is parallel to the sample plane and the direction of the current.

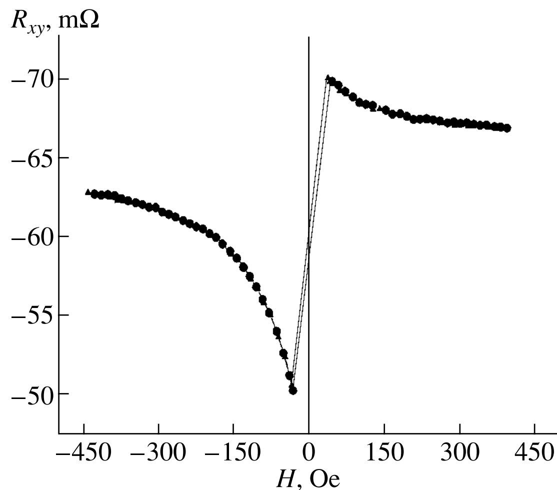

Fig. 7. Magnetic-field dependence of the transverse resistance R_{xy} for a Cr(50 Å)/Co(200 Å) bilayer film in a constant magnetic field (~10 Oe) aligned parallel the direction of the current. The sweep field is parallel to the sample plane and perpendicular to the direction of the current.

ent deviations at the maximum and the minimum from zero magnetic field) can be associated with the fact that the easy magnetization axis makes an angle with the axis of the sample.

4. CONCLUSIONS

Thus, the results obtained in this work demonstrated that the planar Hall effect revealed in Cr(50 Å)/Co(200 Å) bilayer films is symmetric with respect to the sign of the change in the rotation angle of the magnetic moment. The inference was made that this effect is due to the separation of cobalt films into domains and the motion of the domain walls in the magnetic field. Elucidation of the specific features in the observed phenomenon calls for further investigation into the magnetization of materials on the microscopic level [16], which will be performed in the near future.

ACKNOWLEDGMENTS

We would like to thank E.D. Ol'shanskiĭ for his assistance in preparing the samples used in our experiments.

This work was supported by the Russian Foundation for Basic Research, project nos. 03-02-17029, 02-02-16974, and 01-02-16420.

REFERENCES

1. Vu Din Ky and E. F. Kuritsina, Dokl. Akad. Nauk SSSR **160** (1), 77 (1965) [Sov. Phys. Dokl. **10**, 51 (1965)].
2. E. F. Kuritsina and Vu Din Ky, Izv. Akad. Nauk SSSR, Ser. Fiz. **29** (4), 580 (1965).
3. T. R. McGuire and R. I. Potter, IEEE Trans. Magn. **11**, 1018 (1975).
4. D. G. Stinson, A. C. Palumbo, B. Brandt, and M. Berger, J. Appl. Phys. **61** (8), 3816 (1987).
5. F. Montaigne, A. Schuhl, F. Nguyen Van Dau, and A. Encinas, Sens. Actuators A **81**, 324 (2000).
6. C. Christides, S. Stavroyiannis, and D. Niarchos, J. Phys.: Condens. Matter **9**, 7281 (1997).
7. F. G. Ogrin, S. L. Lee, and Y. F. Ogrin, J. Magn. Magn. Mater. **219**, 331 (2000).
8. G. Li, T. Yang, Q. Hu, and W. Lai, Appl. Phys. Lett. **77** (7), 1032 (2000).
9. Z. Q. Lu, G. Pan, W. Y. Lai, D. J. Mapps, and W. W. Clegg, J. Magn. Magn. Mater. **242–245**, 525 (2002).
10. Z. Q. Lu, G. Pan, and Y. K. Zheng, J. Appl. Phys. **91** (4), 2161 (2002).
11. É. M. Épshteĭn, Fiz. Tverd. Tela (St. Petersburg) **44** (7), 1269 (2002) [Phys. Solid State **44**, 1327 (2002)].
12. Th. Zeidler, K. Theis-Brohl, and H. Zabel, J. Magn. Magn. Mater. **187**, 1 (1998).
13. K. Tanahashi, Y. Hosoe, and M. Futamoto, J. Magn. Magn. Mater. **153**, 265 (1996).
14. V. V. Ryl'kov, B. A. Aronzon, A. B. Davydov, D. Yu. Kovalev, and E. Z. Meĭlikhov, Zh. Éksp. Teor. Fiz. **121** (4), 908 (2002) [JETP **94**, 779 (2002)].
15. O. Kitakami and Y. Shimada, Jpn. J. Appl. Phys., Part 1 **40** (6A), 4019 (2001).
16. L. Berger, J. Appl. Phys. **69** (3), 1550 (1991).

Translated by O. Borovik-Romanova

Physics of the Solid State, Vol. 46, No. 8, 2004, pp. 1487–1489. Translated from Fizika Tverdogo Tela, Vol. 46, No. 8, 2004, pp. 1446–1448.
Original Russian Text Copyright © 2004 by Aleksashkin, Berzhanskiĭ, Polulyakh, Turishchev.

Ferromagnetic Resonance in Suspensions of Cobalt-Substituted Magnetite

I. V. Aleksashkin, V. N. Berzhanskiĭ, S. N. Polulyakh, and M. V. Turishchev

Vernadsky Tavrida National University, Yaltinskaya ul. 4, Simferopol, 95007 Ukraine

e-mail: roton@ccssu.crimea.ua

Received October 23, 2003; in final form, December 15, 2003

Abstract—Colloids of cobalt-substituted magnetite are investigated using ferromagnetic resonance. It is found that the ferromagnetic resonance spectrum consists of two spectral lines. The intensity ratio of these lines depends on the size of the magnetic particles. The experimental results are interpreted in the framework of the Raikher–Stepanov theory. It is established that the average radius of particles increases with increasing time.
© 2004 MAIK "Nauka/Interperiodica".

1. INTRODUCTION

Systems of ferromagnetic nanoparticles suspended in a liquid carrier are of special interest for ferromagnetic resonance investigations. In most cases, the ferromagnetic resonance spectrum is a single bell-shaped line with a width of approximately 10^{-1} T. However, in some cases, the ferromagnetic resonance spectrum has a more complex shape and contains a larger number of lines. In particular, Upadhyay *et al.* [1] obtained the ferromagnetic resonance spectrum of a magnetite colloid in a nonaqueous medium. This spectrum exhibits a narrow line against the background of a broad line. The width of the narrower line is one order of magnitude smaller and its intensity is five orders of magnitude lower than those of the broad line. Raikher and Stepanov [2] theoretically analyzed the two-component ferromagnetic resonance spectrum of a magnetic liquid. According to [2], the shape of the ferromagnetic resonance spectrum substantially depends on the parameter $\xi_0 = \mu H/kT$, where μ is the magnetic moment of a particle, H is the magnetic field strength, k is the Boltzmann constant, and T is the temperature. At $\xi_0 < 1$, the ferromagnetic resonance spectrum contains one absorption peak. At $1 < \xi \lesssim 20$, a second low-field peak appears in the spectrum and its intensity increases with an increase in the parameter ξ_0. This is accompanied by a decrease in the intensity of the first peak, which completely disappears at $\xi > 50$. In all cases, the spectral lines have an asymmetric shape. The spectral position of the absorption peaks and the linewidth also depend on the parameter ξ_0 [2].

Each value of the parameter ξ_0 corresponds to a particular height of the absorption peak in the spectrum [2]. Therefore, it is possible to determine the parameter ξ_0 from the height ratio of the peaks measured in the experiments and, hence, to estimate the size of colloidal particles. In contrast to the method described by Folly and de Biasi [3], the above method does not require measurement of the temperature dependences of the height of the absorption peaks and the effective anisotropy constant at low temperatures.

Earlier [4], we carried out magnetometric investigations and revealed that the substitution of cobalt for a small amount of divalent iron (approximately 1%) in magnetite leads to a substantial increase (by approximately two orders of magnitude) in the magnetization of the colloid due to an increase in the average magnetic moment of colloidal particles. Therefore, the magnetic liquids characterized by specified values of the parameter ξ_0 can be prepared by varying the degree of substitution of cobalt for iron.

2. SAMPLE PREPARATION AND EXPERIMENTAL TECHNIQUE

Our experiments were performed with benzene-based magnetic liquids. The magnetic filler was composed of magnetite nanoparticles with oleic acid as a surfactant. Magnetite was synthesized according to the chemical reaction of $FeSO_4$ and $FeCl_3$ aqueous solutions with aqua ammonia as an alkaline agent. The reaction resulted in the precipitation of magnetite, which was then separated from water through centrifugation. In order to prepare the colloid, a solution of oleic acid in benzene was added to the magnetite thus obtained. Doping with cobalt was performed by substituting the cobalt salt for a specified amount of divalent iron sulfate.

The concentration of the magnetic filler in the liquid was determined by weighing the dry residue obtained upon calcination of a sample of known volume. The degree of substitution of cobalt for iron in the sample was equal to 1.5%. The molar concentration of the magnetic filler was 0.33 mol/l, and the volume concentration of the surfactant was 2%.

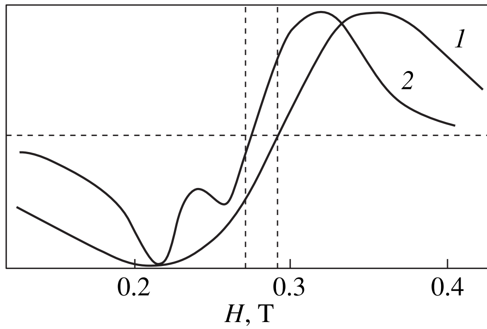

Fig. 1. Experimental ferromagnetic resonance spectra of magnetite colloids (*1*) without substitution and (*2*) with substitution of cobalt for 1.5% Fe^{2+}.

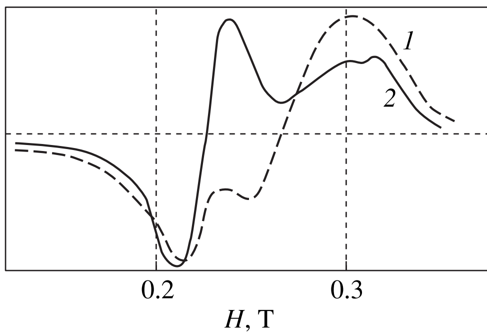

Fig. 2. Evolution of the ferromagnetic resonance line of cobalt-substituted magnetite colloids: (*1*) as-prepared colloid and (*2*) the same colloid 13 days after synthesis.

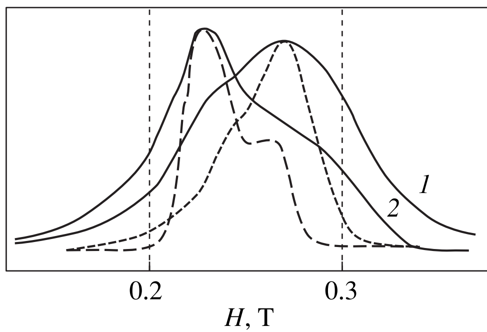

Fig. 3. Integrated spectra of ferromagnetic resonance in magnetic liquids: (*1*) as-prepared sample and (*2*) the same sample 13 days after synthesis. Solid lines represent experimental data, and dashed lines correspond to the results of theoretical calculations.

The ferromagnetic resonance spectra were recorded on an EPR spectrometer at an operating frequency of 9.1 GHz.

3. RESULTS AND DISCUSSION

The ferromagnetic resonance spectrum of the magnetite magnetic liquid measured before doping with cobalt consists of one line with a width of approximately 0.1 T. After doping of the magnetite sample with cobalt, an additional narrow line appears in the ferromagnetic resonance spectrum in the range of weaker fields (Fig. 1).

It can be seen from Fig. 2 that the intensity of the additional line increases with time. Subsequent experiments revealed the complete disappearance of the initial high-field line.

The theoretical calculations performed in [2] demonstrated that, at small parameters ξ_0, the basic mechanism responsible for the broadening of spectral lines is associated with thermal fluctuation broadening. Consequently, the spectral line should be nearly symmetric in shape. This situation corresponds to the experimental spectrum *1* (Fig. 1) of the magnetite colloid before cobalt doping.

As the parameter ξ_0 increases, the fluctuation field decreases and becomes comparable to the anisotropy field H_a; i.e., the magnetic interaction forces become comparable to the thermal fluctuation interaction forces. In this case, the precession of the magnetic moments is affected by the internal fields of anisotropy and the ferromagnetic resonance line becomes asymmetric in shape. This situation is typical of cobalt-substituted magnetite colloids, for which an additional absorption peak is experimentally observed in the low-field range (spectrum *2* in Fig. 1). A further increase in the parameter ξ_0 leads to an increase in the magnetic moment of the particles. As a result, their orientational distribution becomes narrower in a direction almost aligned with the external magnetic field. Up until the orientational distribution in the intermediate cases under consideration becomes completely collinear, the initial high-field peak is retained but decreases in intensity [2]. This situation corresponds to the state of the sample several days after synthesis (Fig. 2). It should be noted that, according to [2], a spectrum consisting of two absorption peaks is a distinguishing feature of ferromagnetic resonance in magnetic liquids. A further increase in the parameter ξ_0 results in an increase in the height of the low-field peak and in complete disappearance of the initial high-field peak [2], which was also observed in the experiments.

Our calculations of the integrated spectra of ferromagnetic resonance in the framework of the theory described in [2] showed that, for the experimental spectra depicted in Fig. 2, the parameter ξ_0 is equal to 0.4 for the as-prepared sample and 13.3 for the same sample 13 days after synthesis (Fig. 3). In these calculations, we used the following parameters: temperature T = 300 K, saturation magnetization M = 477 kA/m, damping factor $\alpha = 0.01$, and ratio of the magnetic anisotropy energy to the Zeeman energy $\varepsilon = 0.2$. In order to deter-

mine the parameter ξ_0, we used the height ratio of the spectral peaks, which was determined from experimental and calculated spectra approximated by a superposition of two lines of Gaussian shape. The disagreement between the experimental widths of the spectral lines and the results of theoretical calculations can be explained in terms of the polydispersity of the particles and the additional mechanisms providing the broadening of the spectral line under the conditions of the experiment.

By assuming the particles to be spherical in shape, the particle radii are found to be 11.6 nm for the as-prepared liquid and 36.5 nm for the same liquid 13 days after synthesis. It follows from the results obtained that particle growth occurs in the studied samples, which can be observed using ferromagnetic resonance.

4. CONCLUSIONS

Thus, the results of our experimental investigations demonstrated that the processes analyzed theoretically in [2] actually take place in magnetic liquids. Thus, ferromagnetic resonance spectroscopy can provide reliable information on the size of magnetic colloidal particles and on the spatial distribution of their anisotropy axes with respect to the external magnetic field.

REFERENCES

1. R. V. Upadhyay, D. Srinivas, and R. V. Mehta, J. Magn. Magn. Mater. **214**, 105 (2000).
2. Yu. Raikher and V. Stepanov, Phys. Rev. B **50** (9), 6250 (1994).
3. W. S. D. Folly and R. S. de Biasi, Braz. J. Phys. **31** (3), 398 (2001).
4. I. V. Aleksashkin, V. N. Berzhanskiĭ, T. A. Vlasova, S. N. Polulyakh, V. I. Ponomarenko, E. D. Pershina, E. V. Potapov, and M. V. Turishchev, in *Abstracts of the 2nd International Scientific Conference on Magnetic Materials and Their Applications (MMP-2002)* (Belorus. Gos. Univ., Minsk, 2002).

Translated by N. Korovin

Physics of the Solid State, Vol. 46, No. 8, 2004, pp. 1490–1495. Translated from Fizika Tverdogo Tela, Vol. 46, No. 8, 2004, pp. 1449–1454.
Original Russian Text Copyright © 2004 by Chebotkevich, Ognev, Grudin.

MAGNETISM
AND FERROELECTRICITY

Structure and Magnetic Anisotropy of Co/Cu/Co Films

L. A. Chebotkevich, A. V. Ognev, and B. N. Grudin
Far East State University, ul. Sukhanova 8, Vladivostok, 690950 Russia
e-mail: lach@phys.dvgu.ru
Received December 16, 2003

Abstract—The energy of the magnetic anisotropy of Co/Cu/Co polycrystalline ultradisperse films is investigated as a function of the thickness of copper and cobalt layers. The influence of the structure parameters (the size and distribution of defects, the period and amplitude of roughnesses) on the surface and volume components of the magnetic anisotropy is analyzed. The parameters of the structure inhomogeneities and their distribution over the film surface are determined from two-dimensional Fourier spectra and electron microscope images of the films. *© 2004 MAIK "Nauka/Interperiodica".*

1. INTRODUCTION

Over the last decade, nanostructured objects have been studied extensively. Research interest expressed in these objects is associated with their widespread use in modern nanotechnology. Considerable recent progress has been achieved in this field owing to significant advances in the technology for producing and studying micro- and nanostructures. Multilayer magnetic structures are of interest not only from the practical standpoint but also as objects with radically new magnetic and magnetoresistive properties. Investigation into the influence of indirect exchange coupling on the magnetic properties of multilayer films is an important problem.

In this work, we investigated the influence of the distribution of structural defects and surface roughnesses on the components of the magnetic anisotropy of Co/Cu/Co films.

2. SAMPLE PREPARATION AND EXPERIMENTAL TECHNIQUE

Samples of Co/Cu/Co films were prepared using magnetron dc sputtering in an argon atmosphere (P_{Ar} = 5×10^{-3} Torr). Films were deposited on naturally oxidized Si(111) single crystals at room temperature. The layer thickness was controlled by the time of sputtering. The rates of deposition of cobalt and copper were equal to 0.10 and 0.08 nm/s, respectively. The structure of the films was investigated using electron microscopy and electron microdiffraction. All the studied films had a polycrystalline structure with a grain size of ~5–6 nm. The magnetization was measured by the induction method with the use of an automated vibrating-coil magnetometer.

The anisotropy field was measured by the ferromagnetic resonance method. The angular dispersion of anisotropy axes φ_a was determined using the technique proposed by Kornev and Borodina [1]. According to this technique, the angular dispersion of the anisotropy axes φ_a was determined from the angle within which the resonance field does not change upon rotation of the film in its plane.

3. EXPERIMENTAL RESULTS AND DISCUSSION

The ferromagnetic resonance method was used to measure the field of magnetic anisotropy of the films: $H_a = (H_r^{h.a} - H_r^{e.a})/2$. Here, $H_r^{h.a}$ and $H_r^{e.a}$ are the resonance fields in the direction of the hard magnetization and easy magnetization axes, respectively. Figure 1 shows the dependences of the constant of induced magnetic anisotropy $K_u = H_a I_{eff}/2$ (where I_{eff} is the magnetization of the film) for $(Co/Cu)_n$ deposited films on the

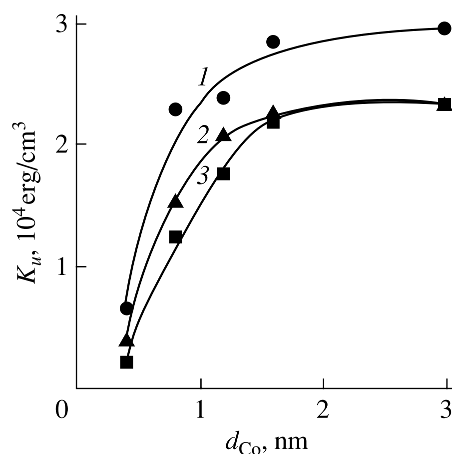

Fig. 1. Dependences of the constant of induced magnetic anisotropy K_u on the thickness of cobalt ferromagnetic layers in Co/Cu(d_{Cu})/Co films. d_{Cu} = (*1*) 0.7, (*2*) 1.0, and (*3*) 1.6 nm.

1063-7834/04/4608-1490$26.00 © 2004 MAIK "Nauka/Interperiodica"

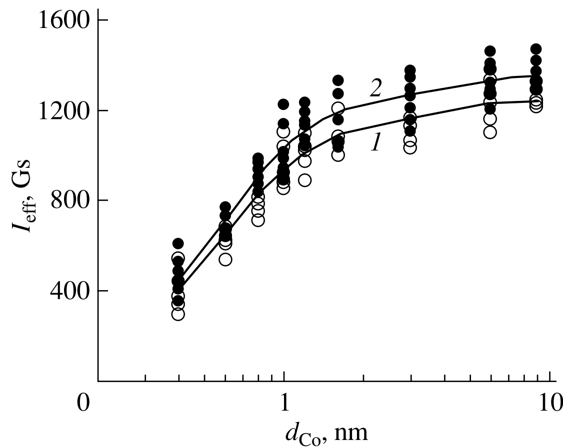

Fig. 2. Variation in the magnetization of Co/Cu/Co films with increasing thickness of the cobalt layers after (*1*) deposition and (*2*) annealing at T_{ann} = 350°C and t_{ann} = 30 min.

thickness of the cobalt layers. The constants of induced magnetic anisotropy K_u were calculated taking into account the dependence of the magnetization on the thickness of the ferromagnetic layers $I_{eff} = f(d_{Co})$ (Fig. 2). As the thickness of the cobalt layers increases, the constant of induced magnetic anisotropy increases to saturation. For samples with a copper layer thickness d_{Cu} = 0.7 nm, the constant of induced magnetic anisotropy reaches a maximum. Possibly, this is associated with the existence of a large number of ferromagnetic bridges in the intermediate copper layer and, consequently, with a local increase in the thickness of the cobalt layers.

The energy of induced magnetic anisotropy $K_{u\,eff}$ can be represented in the form of the phenomenological expression [2, 3]

$$K_{u\,\text{eff}} = K_v + \frac{2K_s}{d_{\text{Co}}},$$

where K_v and K_s are the volume and surface components of the induced magnetic anisotropy, respectively.

The volume component of the magnetic anisotropy K_v is determined by the anisotropic distribution of bulk defects (grain boundaries, chains consisting of grain boundaries, micropores). The surface component of the magnetic anisotropy K_s is governed by the morphology of the Co/Cu interfaces. The coefficient 2 accounts for the fact that each ferromagnetic layer has two interfaces. If the components K_v and K_s are constants, then, according to the phenomenological law, the quantity $K_{u\,eff}d_{Co}$ increases linearly with an increase in the thickness of the ferromagnetic layers. In the case when $d_{Co} = -2K_s/K_v$, the easy magnetization axis undergoes a crossover from the film plane in a direction perpendicular to the surface of the film. The surface component of the magnetic anisotropy $2K_s$ was determined by extrapolating the dependence $K_{u\,eff}d_{Co} = f(d_{Co})$ to zero thickness of the cobalt layer (d_{Co} = 0). Figure 3a shows the dependence $K_{u\,eff}d_{Co} = f(d_{Co})$ for $(Co/Cu)_n$ films with different thicknesses d_{Cu}. The constants of surface anisotropy K_s are presented in Table 1.

After annealing of the samples at a temperature of 350°C for 30 min, the surface component of the magnetic anisotropy in Co/Cu/Co films changes sign (Fig. 3b) This can be associated with the fact that, in annealed films, the intermediate copper layer degrades with an increase in the grain size by a factor of approximately 6 (R = 28–30 nm) and, consequently, many pin holes arise in the nonmagnetic layer. In this situation, ferromagnetic coupling between the layers occurs through pin holes. Therefore, these films can be considered single-layer films with a thickness equal to the total thickness of the ferromagnetic layers. Owing to

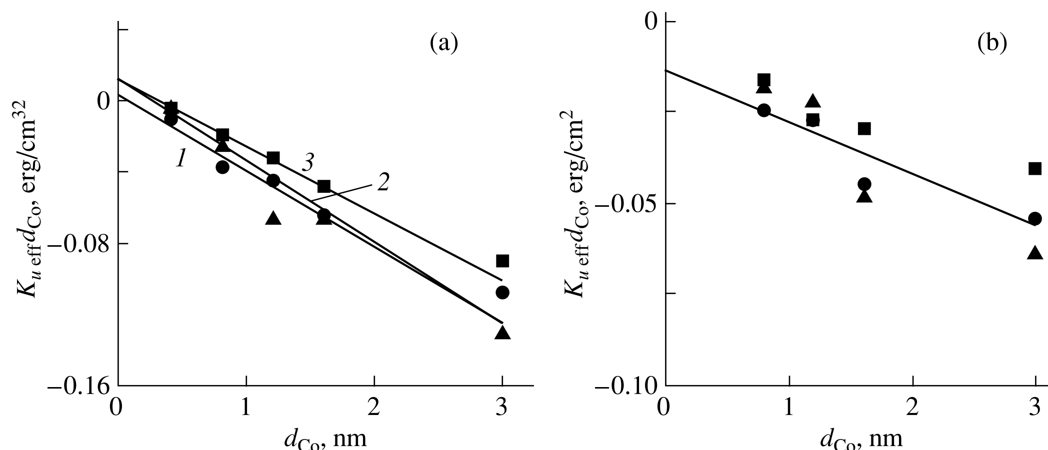

Fig. 3. Dependences of the constant of induced magnetic anisotropy $K_u d_{Co}$ on the thickness of cobalt layers after (a) deposition and (b) annealing at T_{ann} = 350°C and t_{ann} = 30 min for Co/Cu(d_{Cu})/Co films. d_{Cu} = (*1*) 0.7, (*2*) 1.0, and (*3*) 1.6 nm.

Table 1. Magnetic anisotropy of Co/Cu/Co films before and after annealing at T_{ann} = 350°C and t_{ann} = 30 min

d_{Cu}, nm	K_v, 10^4 erg/cm^3				K_s, 10^{-3} erg/cm^3			
	experiment		calculation		experiment		calculation	
	before annealing	after annealing	before annealing	after annealing	before annealing	after annealing	before annealing	after annealing
0.7	7.1				1.3			
1.0	7.5	2.3	7.3	5.7	5.5	–7.0	5.8	–8.6
1.6	6.9				5.0			

the effective increase in the thickness of the cobalt films, the magnetization vector is aligned with the plane of the film.

The volume component of the magnetic anisotropy, which is determined as the slope of the curve $K_{u\,\mathrm{eff}} d_{Co} = f(d_{Co})$, is virtually identical for all films (Table 1). In annealed films, the volume component of the induced magnetic anisotropy decreases.

The surface magnetic anisotropy was estimated on the basis of the real structure of the Co/Cu/Co films. According to Rozenshtern *et al.* [4] and Bruno [5], the surface magnetic anisotropy can be represented in the form $K_s = K_0 + \Delta K$, where K_0 is the constant of surface (boundary) anisotropy for an ideal boundary and ΔK is the anisotropy due to the roughness of the interfaces.

For an ideal interface, the boundary anisotropy in multilayer films is associated with the pseudodipole interaction of atomic pairs and can be represented by the relationship [4] $K_0 = 3aNW$, where a is the lattice constant, N is the number of atoms per unit volume, and $W = W_{CoCo} + W_{CuCu} - 2W_{CoCu}$ is the energy of pseudodipole interaction of the Co–Co, Cu–Cu, and Co–Cu atomic pairs, respectively. The anisotropy constant for the ideal interface is determined to be $K_0 = 8.64 \times 10^{-2}$ erg/cm^2.

The anisotropy of the ideal interface in real films is affected by different factors, such as the roughness of the interfaces between layers, diffusion spreading of the interface, and the nanocrystalline structure.

The contribution from the roughness of the interfaces to the surface component of the magnetic anisotropy was calculated according to the formula [4] $\Delta K_r = -2K_0(\sigma/\lambda)^2$, where σ is the dispersion of the amplitude of roughnesses (the deviation from the mean plane) and λ is the period of roughnesses determined from the statistically processed AFM images of the topography of the film surfaces (Fig. 4). For the samples studied, we obtained $\Delta K_r = -1 \times 10^{-5}$ erg/cm^2.

The contribution from the polycrystalline structure was determined assuming that all orientations of the crystallites are equally probable. Hence, the surface magnetic anisotropy associated with the polycrystalline structure can be represented in the form [4] $\Delta K_p = -0.6K_0 = -5.18 \times 10^{-2}$ erg/cm^2.

Diffusion spreading of the interfaces in the sample occurs during the deposition of layers and subsequent heat treatment. The surface component of the magnetic anisotropy governed by diffusion spreading has the form [4] $\Delta K_d = -K_0(1 - a/h_d)$, where a is the lattice constant and h_d is the depth of diffusion spreading of the interface. For h_d = 1–2 of the interatomic distances, we obtain $\Delta K_d = -2.88 \times 10^{-2}$ erg/cm^2.

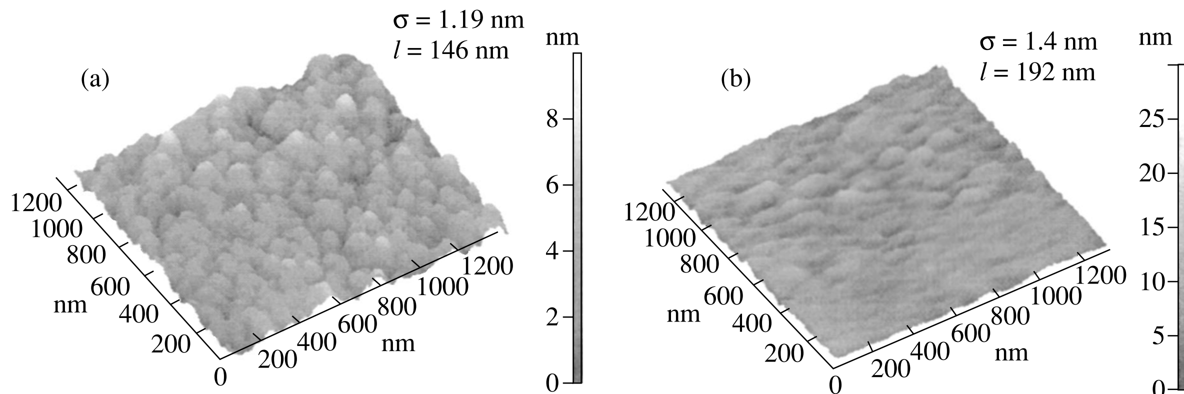

Fig. 4. AFM images of the morphology of the film surface. The dispersion of the amplitude σ and the length l of roughnesses are given in the upper right.

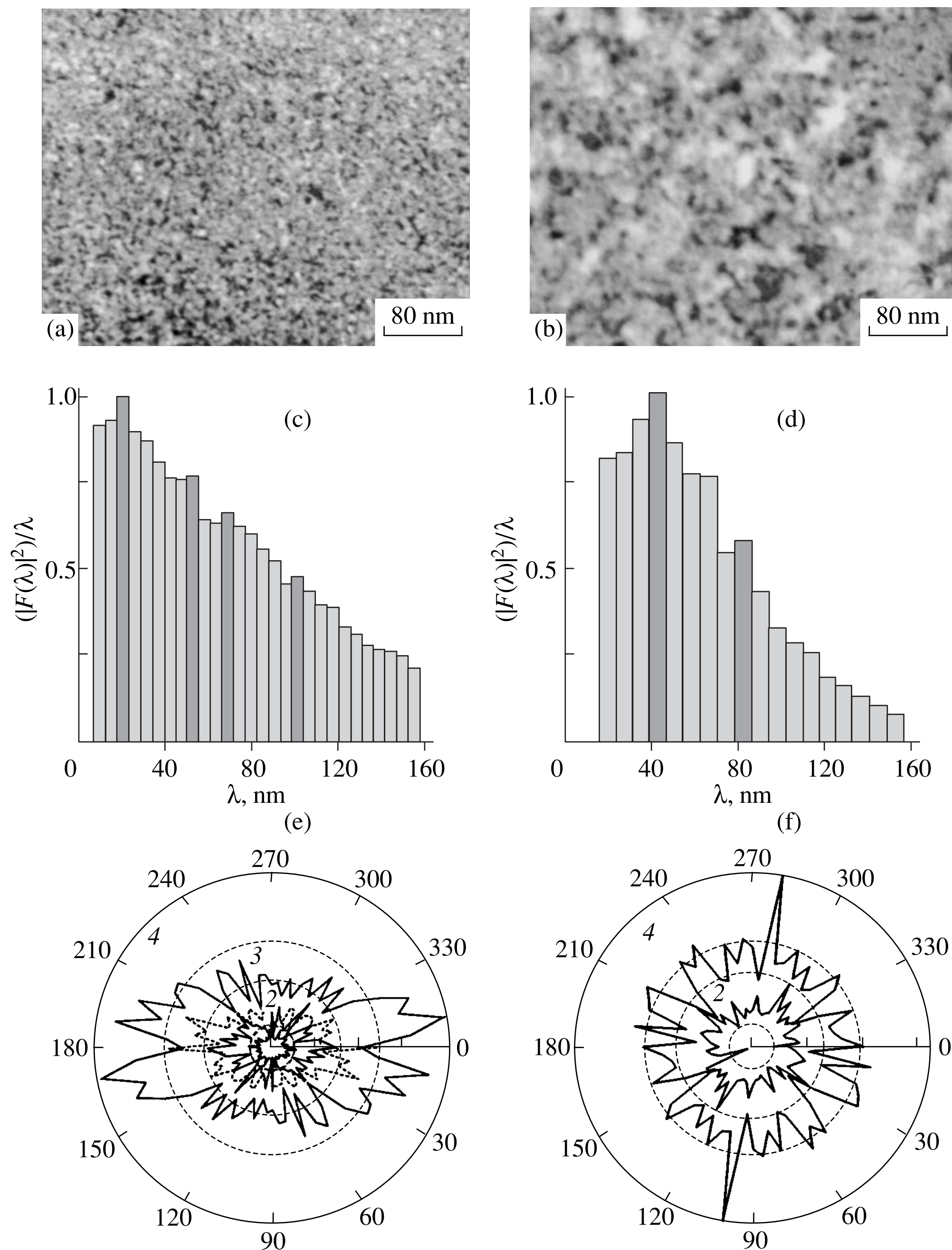

Fig. 5. (a, b) Electron microscope images of the structure of the Co/Cu/Co film, (c, d) the dependences of the integrated energy of frequency characteristics in ring zones on the wavelength, and (e, f) two-dimensional Fourier spectra (a, c, e) before and (b, d, f) after annealing at T_{ann} = 350°C and t_{ann} = 30 min. In panels (e, f), the periods of inhomogeneities λ are plotted along the radii.

In this case, the surface component of the magnetic anisotropy of real interfaces is found to be $K_s = 5.8 \times 10^{-3}$ erg/cm^2. This result agrees with the experimental values of the surface magnetic anisotropy in $(Co/Cu)_n$ films (Table 1).

After annealing at T_{ann} = 350°C, the interfaces of the film undergo degradation due to an increase in the grain size and interdiffusion. Let us assume that the depth h_d of diffusion spreading of the interface in annealed films is comparable to the width of the interface. In this case, the constant of surface magnetic anisotropy K_s changes sign, which agrees with the experimental energy of the surface anisotropy (Table 1).

In order to estimate the volume component of the magnetic anisotropy associated with the distribution of structure inhomogeneities, it is necessary to know not only the linear sizes of the inhomogeneities but also their mutual orientation and distribution in the film. The

Table 2. Parameters characterizing the distribution of structure inhomogeneities over the surface of Co/Cu/Co films

Co/Cu/Co films	Frequency ranges											
	first			second			third			fourth		
	λ_1, nm	γ_1	θ_1, deg	λ_2, nm	γ_2	θ_2, deg	λ_3, nm	γ_3	θ_3, deg	λ_4, nm	γ_4	θ_4, deg
Before annealing	23.4	1.0	–	54	1.6	0	72	2.6	175	104.5	2.3	170
After annealing				44.0	1.1	120	–	–	–	85.0	1.4	100

Table 3. Sizes of structure inhomogeneities

Co/Cu/Co	Frequency ranges							
	first		second		third		fourth	
	l_1, nm	d_1, nm	l_2, nm	d_2, nm	l_3, nm	d_3, nm	l_4, nm	d_4, nm
Before annealing	5	1	10	1	20	1	30	1
After annealing at $T_{\text{ann}} = 350°\text{C}$			74	2			203	

electron microscope images of the films are visualized by the hierarchy of structure inhomogeneities. However, the distribution of defects in multilayer structures are difficult to evaluate quantitatively. In this study, the parameters of structure inhomogeneities were estimated using spectral Fourier analysis of the electron microscope images of the film surfaces. The digital two-dimensional Fourier spectra were calculated on a computer. The two-dimensional Fourier spectrum of each image was separated into 36 ring sectors. In each sector, we determined the mean power of the spectral components, which characterizes the frequency composition of the image. Then, we investigated the spectral energy of structure inhomogeneities in different frequency ranges. For convenience, the integrated frequency characteristics were expressed in equivalent wavelengths λ. Figure 5 shows the dependence of the integrated energy of frequency characteristics in ring zones on the wavelength of spatial inhomogeneities. The spectral Fourier analysis of the electron microscope images of the structure of three-layer films demonstrated that the spectrum of the structure inhomogeneities exhibits several maxima, i.e., several periods in the distribution of inhomogeneities. The distribution of the structure inhomogeneities in the film was estimated from the energy of the spectral components in the radial spectra involving the observed local maxima. The two-dimensional Fourier spectra were used to determine the anisotropy coefficient of the distribution γ of defects in the film and the angle of misorientation θ of defects in different frequency ranges. The parameters of the structure inhomogeneities are presented in Table 2. The inhomogeneities (periods of inhomogeneities) corresponding to local energy maxima can be separated into four types (Table 2). After annealing, the films are characterized by only two local maxima (Fig. 5).

Taking into account the parameters of the structure inhomogeneities of the film before and after annealing, we estimated the contribution of structural defects to the volume component of the magnetic anisotropy K_v.

In order to obtain the total constant of magnetic anisotropy, we determined the anisotropy field. In deposited films, the inhomogeneities involved in the first range are distributed isotropically in the film ($\gamma = 1$) (Fig. 5e). The isotropically distributed defects (stresses) do not contribute to the induced magnetic anisotropy. The precipitated films are characterized by three and, after annealing, two systems of anisotropically distributed defects contributing to the magnetic anisotropy (Table 2, Figs. 5e, 5f). The anisotropy field induced by bulk defects in the deposited film is given by

$$H_a^v = \{H_2^2 + H_3^2 + H_4^2 - 2H_2H_3\cos(\theta_3 - \theta_2) + 2H_4[H_2^2 + H_3^2 - 2H_2H_3\cos(\theta_3 - \theta_2)]^{1/2} \times \cos(\theta_2 - \theta_4 + \gamma)\}^{1/2},$$

$$\gamma = \arccos\frac{H_3\cos(\theta_3 - \theta_2) - H_2}{[H_2^2 + H_3^2 - 2H_2H_3\cos(\theta_3 - \theta_2)]^{1/2}}.$$

For the annealed film, we have

$$H_a^v = [H_2^2 + H_4^2 + 2H_2H_4\cos(\theta_4 - \theta_2)]^{1/2}.$$

Here, H_i are the components of the anisotropy field induced by inhomogeneities of the ith range, which are calculated according to the relationship

$$H_i = 2(N_b - N_a)(\Delta l)^2 c_i / I_{\text{eff}},$$

where N_a and N_b are the demagnetizing coefficients along the a and b axes of the defect, ΔI is the jump in the magnetization at the boundary of the defect, and

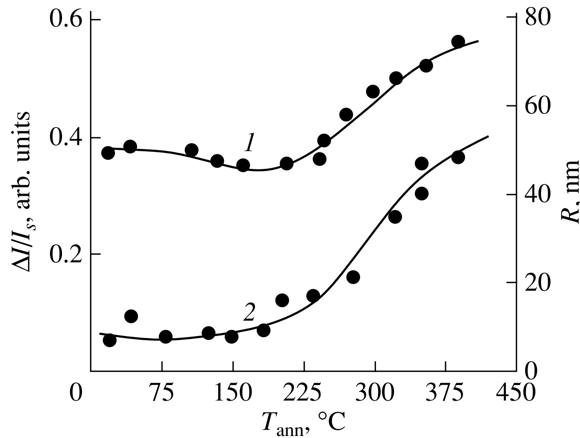

Fig. 6. Dependences of (*1*) the ratio $\Delta I/I_s$ and (*2*) the grain size R on the temperature of annealing of Co/Cu/Co films.

c_i is the concentration of defects of the ith type. Here, $\Delta I = I_s - I_{def}$. Since $I_{eff} = I_sV + I_{def}(1 - V)$, where V is the grain volume, we have $\Delta I = (I_s - I_{eff})/(1 - V)$, where I_s is the reference value and V and I_{eff} are the quantities determined from the experiment (Fig. 6). The concentration of defects in each range was determined from the expressions $c_i = S_i/1\ \text{cm}^2$ and $S_i = S_0n_i$, where $S_0 = ld$ is the surface area of an individual defect in the ith range and $n_i = 1/\lambda_i^2$ is the density of defects in the ith range. Here, l and d are the length and width of defects in the ith range, respectively (Table 3). The calculated volume components of the magnetic anisotropy $K_v = H_a^v I_f/2$ are presented in Table 1. The calculated values agree well with the experimental data.

4. CONCLUSIONS

The results of our investigations can be summarized as follows.

(1) In polycrystalline, fine-grained, and multilayer films, there exists a hierarchy of structure inhomogeneities that differ in terms of their size, periods (density), and distribution over the surface of films.

(2) Heat treatment leads to variations in the size, period, and distribution of structure inhomogeneities in the film.

(3) Long-wavelength roughnesses of the surface do not contribute to the surface anisotropy.

(4) The degradation of the nonmagnetic intermediate layer is accompanied by a change in sign of the surface magnetic anisotropy in Co/Cu/Co films with thin ferromagnetic layers.

(5) The energy components of the surface and volume anisotropies estimated for the real structure of polycrystalline multilayer films agree with the experimental values.

ACKNOWLEDGMENTS

This work was supported from the Russian federal budget within the framework of the program "Research in Priority Areas of Scientific and Technological Development for Civilian Purposes" of the Russian Ministry of Industry (agreement no. 3-02 DVGU in the framework of State Contract no. 40.012.1.1151) and from the federal budget of the Russian Ministry of Education within the framework of the program "Young Scientists of Russia."

REFERENCES

1. Yu. V. Kornev and T. V. Borodina, Fiz. Met. Metalloved. **55** (3), 472 (1983).
2. M. Kowalewski, C. M. Schneider, and B. Heinrich, Phys. Rev. B **47** (14), 8748 (1993).
3. D. Givord, O. F. K. McGrath, C. Meyer, and J. Rothman, J. Magn. Magn. Mater. **157/158**, 245 (1996).
4. D. B. Rozenshtern, M. G. Tetel'man, and A. A. Fraerman, Poverkhnost, No. 4, 15 (1993).
5. P. Bruno, Phys. Rev. B **39**, 865 (1989).

Translated by O. Moskalev

Physics of the Solid State, Vol. 46, No. 8, 2004, pp. 1496–1501. Translated from Fizika Tverdogo Tela, Vol. 46, No. 8, 2004, pp. 1455–1459.
Original Russian Text Copyright © 2004 by Sugakov.

LOW-DIMENSIONAL SYSTEMS
AND SURFACE PHYSICS

Size Distribution and Concentration of Islands of a Condensed Exciton Phase in a Quantum Well

V. I. Sugakov

Institute for Nuclear Research, National Academy of Sciences of Ukraine, Kiev, 03680 Ukraine

e-mail: sugakov@kinr.kiev.ua

Received November 25, 2003

Abstract—A theory describing the formation of condensed-phase regions at a high concentration of excitons in a quantum well is constructed. The condensed phase can be either an exciton or an electron–hole liquid. When the condensed phase and exciton gas coexist, islands of the condensed phase have the shape of disks. A simultaneous solution to the kinetic equation (determining the island sizes) and the diffusion equation for excitons outside the islands is obtained for stationary pumping. It is assumed that the exciton gas is nondegenerate outside the islands. The mutual influence of islands through the concentration fields of excitons is taken into account assuming that the mean radius of islands substantially exceeds the mean distance between them. The radius distribution and concentration of islands are determined as functions of the rate of exciton production and the parameters of the system. It is found that the radius distribution of islands is broadened near the threshold of formation of the condensed phase. *© 2004 MAIK "Nauka/Interperiodica".*

1. INTRODUCTION

Condensation of excitons in quantum wells has been extensively investigated both experimentally [1–7] and theoretically [8–13]. For the most part, these studies have dealt with the Bose–Einstein condensation of excitons. Investigation of excitons in double-well potentials holds much promise. In these systems, the application of an electric field perpendicular to the plane of layers leads to the generation of excitons that consist of electrons and holes located in different layers and have a long lifetime, thus providing a high exciton concentration. Dremin *et al.* [7] studied the luminescence in (GaAl)As crystals with double quantum wells and observed a narrow line against the background of a broad emission band of interwell excitons. This line appeared at the threshold pumping intensity and became narrower with an increase in the pumping intensity. The broad band was assigned to the emission of trapped excitons, and the narrow line was attributed to the emission of excitons in a Bose–Einstein condensed phase.

An indirect (interwell) exciton has a dipole moment. Consequently, indirect excitons separated by large distances experience repulsive dipole–dipole forces. At the same time, the attractive van der Waals forces between indirect excitons are rather strong and can exceed the dipole–dipole repulsion in the range of the order of four or five exciton radii (the specific value depends on the well parameters). As a result, the condensed exciton phase can appear in the system without the formation of a Bose condensate. In a number of theoretical studies [8], it has been demonstrated that the exciton-liquid and exciton-gas phases can coexist in a particular range of parameters of the system. However, the system under consideration is nonequilibrium, which affects the parameters of the condensed phase. Specifically, owing to the finite lifetime of excitons in the range of parameters corresponding to the coexistence of the phases, the sizes of condensed-phase regions should be limited and these regions in a two-dimensional system should have the form of islands surrounded by an exciton gas. The size distribution of condensed exciton phase regions should depend on the kinetic parameters of the system (lifetime, diffusion rate of excitons, etc.). A statistical theory of the size distribution of electron–hole drops in bulk semiconductors was developed in [14–17]. However, the problem for two-dimensional systems was not analyzed.

The aim of the present study was to construct a theory that describes the size distribution of condensed-phase regions and their concentration as a function of the pumping intensity, temperature, and parameters of a two-dimensional system. The theory is applicable in the case when a new phase is either an exciton liquid or an electron–hole liquid. The parameters of the theory are the energy and the surface area per electron–hole pair in the condensed phase. It is assumed that the sizes of condensed-phase regions are considerably larger than the transverse sizes of the system. Therefore, the results obtained can be applied to systems with single-well and double-well potentials. In the calculations, allowance is made for a nonuniform distribution of excitons in the vicinity of condensed-phase islands due to exciton diffusion and the interaction between different condensed-phase islands. This interaction is associated with the effect of an individual island on the exciton density of another island. The calculations are per-

formed under the assumption that the exciton gas in the vicinity of new-phase islands is nondegenerate and the distance between islands is significantly larger than the island sizes.

2. MODEL OF THE SYSTEM. SOLUTION OF THE FOKKER–PLANCK EQUATION FOR THE RADIUS DISTRIBUTION FUNCTION OF EXCITON ISLANDS

Let us consider a two-dimensional system with a high concentration of excitons produced under stationary pumping. Upon first-order phase transitions, the nucleation of a new phase occurs through the formation and growth of nuclei. New-phase regions (islands) should have the shape of disks for which the free energy is at a minimum (Fig. 1). These disks in a two-dimensional system are analogs of drops in a three-dimensional system. New-phase islands are characterized by the minimum critical radius determined by the surface energy and the maximum critical radius governed by the exciton lifetime. It is assumed that the disk radius is considerably larger than the mean free path of excitons. In this case, the spatial distribution of excitons in the vicinity of an island can be obtained from the diffusion equation.

The island size is determined by four processes: the capture of excitons from a region surrounding a disk, the emission of excitons from the island into the environment, the creation of excitons by an external source K, and the annihilation of excitons due to light emission or through other mechanisms. Let n be the number of excitons in the island and $\mathbf{R}_n$ be the radius of the island containing n excitons (or n electron–hole pairs in the case of an electron–hole liquid). The function of the distribution of islands over the particle number will be designated as $f(n)$. With due regard for the above processes, the kinetic equation for the distribution function of excitons can be written in the form

$$\frac{\partial f_n}{\partial t} = -j_{n+1} + j_n. \quad (1)$$

Here, j_n is the probability current of excitons,

$$j_n = (2\pi R_{n-1} W_{fi}(R_{n-1}) c(R_{n-1}) + (n-1)s_0 K) f_{n-1} - 2\pi R_n W_{if}(R_n) c_i - \pi R_n^2 f_n/\tau; \quad (2)$$

$c(R_n)$ and c_i are the concentrations of excitons outside the disk in the vicinity of its surface and inside the island, respectively; $c_i = 1/s_0$; s_0 is the surface area per exciton inside the island; $W_{fi}(R_n)$ and $W_{if}(R_n)$ are the probabilities of the transition of an exciton occurring inside and outside of the island per unit length, respectively; and τ is the exciton lifetime.

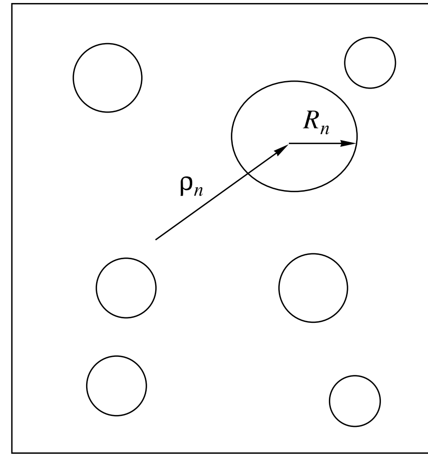

Fig. 1. Distribution of condensed-phase islands in the plane of a quantum well.

According to the principle of detailed balance, the probabilities $W_{fi}(R_n)$ and $W_{if}(R_n)$ are related by the expression

$$\frac{W_{if}(R)}{W_{fi}(R)} = \frac{W_{if}(\infty)}{W_{fi}(\infty)} \exp\left(\frac{\alpha_2}{R}\right), \quad (3)$$

where $W_{fi}(\infty)$ and $W_{if}(\infty)$ are the transition probabilities in the case when the interface between the condensed and gas phases is a straight line, $W_{fi}(\infty)/W_{if}(\infty) = c_i/c_\infty$, and c_∞ is the equilibrium concentration of excitons at a straight-line interface. The value of this equilibrium concentration can be obtained from the equality of the chemical potentials of an exciton in the gas phase and an electron–hole pair in the island; that is,

$$c_\infty = \gamma \frac{m^\bullet \kappa T}{2\pi\hbar^2} \exp(-\varphi/\kappa T). \quad (4)$$

Here, φ is the condensation energy per exciton, $m^\bullet$ is the effective exciton mass, γ is the degeneracy multiplicity of the exciton state, $\alpha_2 = \alpha_l s_0/\kappa T$, and α_l is the surface energy per unit length of the island circumference.

Now, we introduce the radius distribution function $f(R) = f_n dn/dR = 2\pi R_n f_n/s_0$. With a large number of excitons in the island ($n \gg 1$), the kinetic equation (1) for $f(R)$ can be reduced to the Fokker–Planck equation

$$\frac{\partial f(\tilde{R})}{\partial t} = -\frac{\partial}{\partial \tilde{R}}\left(A(\tilde{R}) f(\tilde{R}) - B(\tilde{R}) \frac{\partial}{\partial \tilde{R}} f(\tilde{R})\right), \quad (5)$$

where

$$A(\tilde{R}) = \left(\nu(\tilde{c}(\tilde{R}) - \tilde{c}_\infty \exp(\alpha/(\tilde{R}T))) + \frac{\tilde{R}}{2}(\tilde{c}_K - 1)\right)\frac{1}{\tau}, \quad (6)$$

$$B(\tilde{R}) = \Big(\nu(\tilde{c}(\tilde{R}) - \tilde{c}_\infty \exp(\alpha/(\tilde{R}T))) + \frac{\tilde{R}}{2}(1+\tilde{c}_K)\Big)\frac{1}{4\pi\tau}, \quad (7)$$

and the quantity $\tilde{c}_K = K\tau$ is determined by the pumping intensity and is equal to the exciton concentration that should be observed in the system in the absence of phase formation.

In relationships (5)–(7), we introduced the dimensionless variables

$$\tilde{R} = R/\sqrt{s_0}, \quad \tilde{c}(\tilde{R}) = c(\tilde{R})s_0, \quad \nu = W_{fi}\tau\sqrt{s_0}; \quad (8)$$

the quantities φ and α are expressed in terms of temperature.

In the stationary case, the solution of Eq. (5) has the form

$$f(\tilde{R}) = f_0 \exp\left(\int_0^{\tilde{R}} A(\tilde{R})/B(\tilde{R})d\tilde{R}\right). \quad (9)$$

The nonuniform distribution of excitons in the vicinity of the disk and the contribution from the other disks to the distribution function are taken into account in the exciton concentration $c(R)$ at the disk boundary.

3. SPATIAL DISTRIBUTION OF EXCITONS IN THE VICINITY OF A CONDENSED-PHASE ISLAND

The diffusion equation for the two-dimensional distribution of excitons in the stationary case can be represented in the following form:

$$\Delta_2\tilde{c}(\tilde{\rho}) - \tilde{c}(\tilde{\rho})/\tilde{l} + K = 0, \quad (10)$$

where Δ_2 is the two-dimensional Laplacian, $\tilde{l} = (D\tau/s_0)^{1/2}$ is the dimensionless diffusion coefficient of free excitons, and D is the diffusion coefficient of excitons. Equation (10) will be solved at the boundary conditions which will be determined below for each island. The exciton concentration in the vicinity of a particular island is governed not only by the parameters of the island under consideration but also depends on the other islands. If islands are arranged in random fashion, their concentration fields have cylindrical symmetry. Then, the solution of Eq. (10) can be written in the form

$$\tilde{c}(\tilde{\boldsymbol{\rho}}) = c_K + \sum_{\mathbf{a}} a_{\mathbf{n}} K_0((\boldsymbol{\rho} - \boldsymbol{\rho}_{\mathbf{n}})/l), \quad (11)$$

where $c_K = K\tau$, $K_0(x)$ is the modified Bessel function and $\boldsymbol{\rho}_{\mathbf{n}}$ is the radius vector specifying the position of the $\mathbf{n}$th island.

Now, we consider the concentration field of excitons in the vicinity of a particular island, for example, the island with $\mathbf{n} = \boldsymbol{\rho}_{\mathbf{n}} = 0$. Solution (11) can be represented in the form

$$\tilde{c}(\tilde{\boldsymbol{\rho}}) = c_0 + a_0 K_0(\rho/l), \quad (12)$$

where

$$c_0 = c_K + \sum_{\mathbf{n}\neq 0} a_{\mathbf{n}} K_0((\boldsymbol{\rho} - \boldsymbol{\rho}_{\mathbf{n}})/l). \quad (13)$$

Hereinafter, we will assume that the contribution to the concentration field produced by other islands in the region of the island under investigation is made by a large number of islands. Then, in the last term in formula (13), we can set $\rho \approx 0$ and the sum over $\mathbf{n}$ can be replaced by the integral. As a result, we obtain

$$c_0 = c_K + 2\pi\bar{a}c_N l^2, \quad (14)$$

where $c_N = \frac{N}{S}$ is the island concentration, N is their total number, S is the surface area of the system, and $\bar{a}$ is the coefficient $a_{\mathbf{n}}$ averaged over a large number of islands. In this case, we ignore the correlation in the arrangement of islands and the assumption made corresponds to the self-consistent field approximation.

The boundary condition at the island boundary is determined from the law of conservation of particles: the flux of particles incident on the island must be equal to the difference between the number of excitons captured by the island and the number of excitons escaping from the island; that is,

$$2\pi RD\frac{\partial c(R)}{\partial R} = 2\pi R(W_{fi}c(R) - W_{if}c_i). \quad (15)$$

From relationships (3), (12), and (15), we find that the coefficient a_0 is determined by the formula

$$a_0(R) = -\frac{\nu(c_0 - c_\infty \exp(\alpha/R))}{K_1(R/l)l + \nu K_0(R/l)}. \quad (16)$$

Let us average the left- and right-hand sides of expression (16) over the radius distribution function $f(R)$ of islands. We assume that the distribution function has a sharp maximum at $R = \bar{R}$. This assumption will be confirmed below. After averaging, we have $\bar{a}$ on the left-hand side of expression (16). On the right-hand side of this expression, we replace R by $\bar{R}$. From the derived relationship with allowance made for the dependence of c_0 on a [formula (14)], we obtain the following expression:

$$\bar{a} = -\frac{\nu(c_K - c_\infty \exp(\alpha/\bar{R}))}{lK_1(\bar{R}/l) + \nu K_0(\bar{R}/l) + 2\pi c_N \nu l^2}. \quad (17)$$

As a result, from relationship (9), we find

$$f = f_0 \exp(-F(c_N, R)),$$

where

$$F(c_N, R) = 4\pi \int_0^R \frac{2\nu(c(R) - c_\infty \exp(\alpha/R)) + R(c_K - 1)}{2\nu(c(R) + c_\infty \exp(\alpha/R)) + R(c_K + 1)} R dR, \quad (18)$$

$$c(R) = c_K + 2\pi c_N \bar{a} l^2 + a_0(R) K_0(R/l), \quad (19)$$

and the quantities $a_0(R)$ and $\bar{a}$ are determined by formulas (14), (16), and (17). At a sharp maximum of the distribution function, the mean radius coincides with the most probable radius and can be found from the condition

$$\frac{\partial F(c_N, R)}{\partial R} = 0. \quad (20)$$

The probability that the system contains N islands with radii $R_1, R_2, \ldots, R_N$ can be written as

$$W(N, R_1, R_2, \ldots, R_N) \approx \exp\left(-\sum_i F(c_N, R_i)\right). \quad (21)$$

After integration over the island radius, we obtain the probability of distribution over island numbers:

$$W(N) = W_0 \exp(-\Phi(N)), \quad (22)$$

where

$$\Phi(N) = -N \ln z(c_N),$$

$$z(c_N) = \int_0^\infty \exp(-F(c_N, R)) dR. \quad (23)$$

The most probable concentration of islands is determined by the condition

$$\frac{d\Phi}{dN} = 0. \quad (24)$$

Next, we expand the distribution function $F(c_N, R)$ into a series in the neighborhood of the most probable radius:

$$F(c_N, R) = F(c_N, \bar{R}) + b(R - \bar{R})^2 + \ldots. \quad (25)$$

As a result, we have

$$\Phi(N) = S\psi(c_N), \quad (26)$$

$$\psi(c_N) = c_N\left(F(c_N, \bar{R}) - \frac{1}{2}\ln(\pi/b)\right). \quad (27)$$

For a fixed surface area S of the quantum well, the differentiation in expression (24) with respect to N is equivalent to differentiation with respect to c_N. Formulas (18), (24), and (26) make it possible to determine the mean radius of islands of the condensed exciton phase and their mean concentration.

4. RESULTS OF CALCULATIONS AND DISCUSSION

The function $\psi(c_N)$ has a minimum at a value of c_N that corresponds to the most probable concentration of islands. Qualitatively, the existence of an optimum number of islands can be illustrated as follows. When the condensed and gas phases coexist, the exciton density in the condensed phase is higher than the density of excitons generated by the external source. Therefore, in order to maintain their own size, the islands must trap excitons from surrounding regions. The maximum radius of islands should be limited, because the inflow of excitons is determined by the linear sizes of the island boundary and the number of annihilated excitons is proportional to the surface area of the island. Consequently, the density of islands should not be very high. The density of islands should likewise not be very low, since, at a low density, the probability exists that a new island will be nucleated in the system. In this case, the dependence $\psi(c_N)$ [see expression (26)] exhibits a minimum at the concentration c_N corresponding to the mean concentration of islands. The island parameters were numerically analyzed using the solution of Eq. (24) for a wide range of internal and external parameters. The pumping intensity can be described by the parameter $c_K = K\tau$, i.e., the concentration of excitons produced by pumping in the absence of the condensed phase. The main results obtained can be summarized as follows.

Islands of the new phase arise when the pumping intensity exceeds a critical value dependent on the surface energy, the temperature, and the exciton lifetime.

An increase in the pumping parameter leads to an increase in the mean radius of islands (Fig. 2) and a decrease in the mean distance between them $d = 1/\sqrt{c_N}$ (Fig. 3). However, the radius increases more rapidly than the distance decreases. The results of calculations in dimensionless units are presented in the figures. The unit length (the interparticle distance in the condensed phase) is of the order of several exciton radii. For typical parameters of semiconductors, this estimate approximately corresponds to 100–300 Å. Since the surface energy of condensed-phase islands remains unknown, this quantity was treated as a parameter. For the parameters given in the figure captions, the threshold exciton density is equal to 2×10^9 cm^{-2}. This density is lower than the critical density for Bose–Einstein condensation at the chosen temperature, which justifies the use of the degenerate-gas statistics for excitons. Note that inclusion of the Bose–Einstein statistics can be significant when describing regions inside islands, where the exciton concentration is higher. However, as was noted above in the statement of the problem, the situation in regions inside islands was taken into

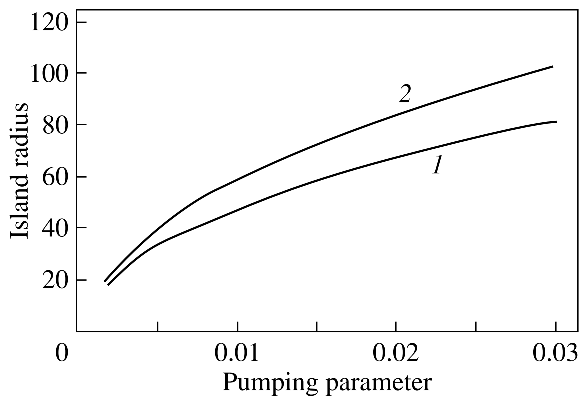

Fig. 2. Dependences of the mean island radius $\bar{R}$ on the pumping parameter c_K. The parameters of the system are as follows: $\varphi = 15$ K, $\alpha_2 = 4$ K, $\nu = 10\,000$, and $l_D = (1)$ 1000 and (2) 1500.

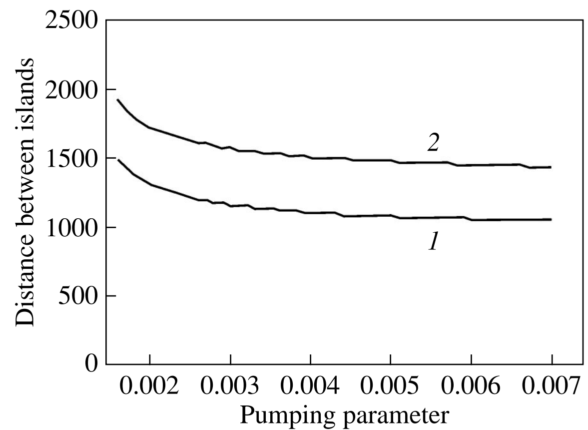

Fig. 3. Dependences of the mean distance d between islands on the pumping parameter c_K. The parameters of the system are the same as in Fig. 2.

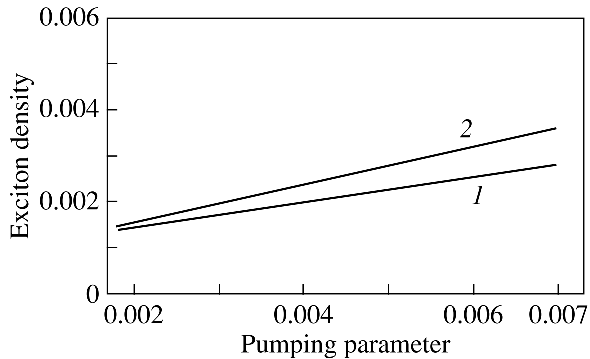

Fig. 4. Dependences of the exciton density c_0 outside the islands on the pumping parameter c_K. The parameters of the system are the same as in Fig. 2.

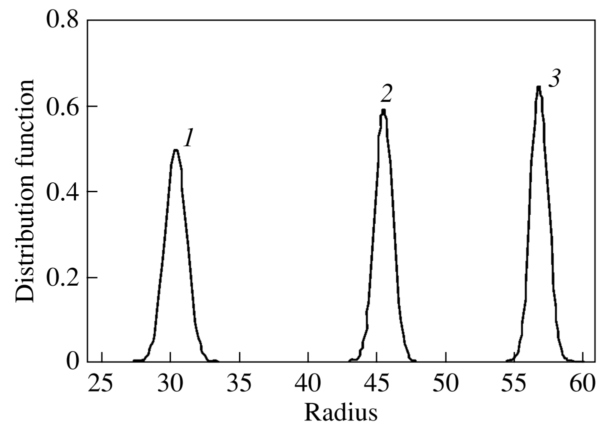

Fig. 5. Radius distribution functions of islands for pumping parameters $c_K = (1)$ 0.004, (2) 0.008, and (3) 0.012. $\varphi = 15$ K, $\alpha_2 = 4$ K, and $\nu = 10\,000$.

account by introducing the phenomenological parameters (the energy and surface area per electron–hole pair).

As the pumping parameter increases, the fraction of excitons in islands increases more rapidly than that in the gas phase (Fig. 4). The exciton density c_0 in the gas phase is severalfold lower than the exciton density c_K in the absence of phase formation.

It can be seen from Fig. 5 that the radius distribution function has a sharp maximum. A decrease in the pumping parameter leads to a broadening of the distribution function. This is associated with the enhancement of the role played by fluctuations with a decrease in the size of the system. The energy per exciton should depend on the size, especially for threshold pumping parameters when the island radii are small. This should result in an increase in the width of the emission bands at threshold pumping intensities. Therefore, the narrowing of emission bands observed in a number of experiments [7] with an increase in the pumping intensity cannot be the sole indication of Bose–Einstein condensation. This narrowing can also be caused by the substantial contribution from fluctuations of radii of small-sized islands at pumping intensities close to the threshold corresponding to the formation of the condensed phase.

When the pumping intensity is high and the mean radius of islands is comparable to the distance between islands, the mean-field approximation used in the present work is inapplicable. In this case, correlations in the island arrangement should be taken into account. The possibility of forming a periodic distribution of

islands at high pumping intensities calls for further investigation.

5. CONCLUSIONS

Thus, the theory constructed in this work for two-dimensional systems makes it possible to determine the mean radius of islands of the condensed exciton phase, the mean distance between islands, and their radius distribution functions. These quantities can be obtained as functions of the pumping intensity, temperature, and parameters of crystals, such as the binding energy and density of excitons in the condensed phase, the surface energy, the diffusion coefficient of excitons, and their lifetime. It was demonstrated that an increase in the pumping intensity leads to a narrowing of the radius distribution function of islands.

ACKNOWLEDGMENTS

This work was supported by the "Nanophysics and Nanoelectronics" program of the National Academy of Sciences of Ukraine and the Ukrainian Ministry of Education and Science (project no. 02.07/147).

REFERENCES

1. T. Fukuzawa, E. E. Mendez, and J. M. Hohg, Phys. Rev. Lett. **64**, 3066 (1990).
2. L. V. Butov, A. Zrenner, G. A. Abstreiter, *et al.*, Phys. Rev. Lett. **64**, 3066 (1994).
3. L. V. Butov, A. C. Gossard, and D. S. Chemla, Nature **418**, 751 (2002).
4. D. Snoke, S. Donev, Y. Liu, L. Pfeiffer, and K. West, Nature **418**, 754 (2002).
5. A. V. Larionov, V. B. Timofeev, J. Hvam, and K. Soerensen, Pis'ma Zh. Éksp. Teor. Fiz. **75**, 233 (2002) [JETP Lett. **75**, 200 (2002)].
6. B. M. Ashkinadze, V. Voznyy, E. Cohen, A. Ron, and V. Umansky, Phys. Rev. B **65**, 073311 (2002).
7. A. A. Dremin, A. V. Larionov, and V. B. Timofeev, Fiz. Tverd. Tela (St. Petersburg) **46**, 168 (2004) [Phys. Solid State **46**, 170 (2004)].
8. Yu. E. Lozovik and O. L. Berman, Pis'ma Zh. Éksp. Teor. Fiz. **64**, 526 (1996) [JETP Lett. **64**, 573 (1996)].
9. H. Chu and Y. C. Chang, Europhys. Lett. **35**, 535 (1996).
10. P. B. Littlewood and Zhu Xuejun, Phys. Scr. T **68**, 56 (1996).
11. P. Stenius, W. Zhao, and A. Imamoglu, Phys. Status Solidi A **164**, 365 (1997).
12. Z. G. Koinov, J. Phys.: Condens. Matter **11**, L127 (1999).
13. Kuan-Ming Hung, Chun-Wei Tseng, and H.-H. Cheng, Physica B (Amsterdam) **298**, 431 (2001).
14. R. N. Silver, Phys. Rev. B **11**, 1569 (1975).
15. V. S. Bagaev, N. V. Zamkovets, L. V. Keldysh, N. N. Sibel'din, and V. A. Tsvetkov, Zh. Éksp. Teor. Fiz. **70**, 1501 (1976) [Sov. Phys. JETP **43**, 783 (1976)].
16. R. M. Westerwelt, Phys. Status Solidi B **74**, 727 (1976).
17. V. I. Sugakov, Mol. Cryst. Liq. Cryst. **384**, 1 (2002).

Translated by O. Borovik-Romanova

Physics of the Solid State, Vol. 46, No. 8, 2004, pp. 1502–1507. Translated from Fizika Tverdogo Tela, Vol. 46, No. 8, 2004, pp. 1460–1464.
Original Russian Text Copyright © 2004 by Koropov.

LOW-DIMENSIONAL SYSTEMS AND SURFACE PHYSICS

Charge Effects in a Metal–Semiconductor Composite System

A. V. Koropov

Institute of Applied Physics, National Academy of Sciences of Ukraine, Sumy, 40030 Ukraine

Received December 4, 2003

Abstract—Small-sized metallic particles contained as inclusions in an *n*-type nondegenerate semiconductor are considered. The problem concerning the potential and charge distributions in this composite system is analyzed in the case where regions depleted in carriers are formed around particles due to contact phenomena and these regions substantially overlap one another. The redistribution of charges among very small metallic particles (R ~ 1–10 nm) is described with due regard for the semiconductor properties of the medium and the volume fraction of particles. © *2004 MAIK "Nauka/Interperiodica".*

The properties of materials in a dispersed state and the physical processes occurring in disperse (and ultradisperse) systems continue to attract research interest (see, for example, [1–3]). Small-sized metallic particles contained as inclusions of a foreign phase in a semiconductor material also belong to these systems.

In such a composite system, we are interested in the phenomena associated with the exchange of free charge carriers through a metal–semiconductor interface. As is known [4], this exchange makes possible equalizing the energies at the Fermi levels in a metal μ_m and a semiconductor μ_s and is accompanied by the formation of space-charge regions around metallic particles. When the number density of metallic particles in the matrix is sufficiently high, the space-charge regions belonging to different particles overlap and the entire volume of the semiconductor appears to be either depleted or enriched in charge carriers. For very small metallic particles (R ~ 1–10 nm), the Fermi energy μ_m strongly depends on R (see the review by Nagaev [2] and [5–8]). This leads to a thermodynamic equilibrium redistribution of charges among particles [6–9].

Under these conditions, the system is characterized by two effects associated with the charge redistribution: (1) the transfer of a number of electrons from the semiconductor to the metal surface (or from the metal to the semiconductor bulk) due to usual contact phenomena at the metal–semiconductor interface and (2) the size effect of charge redistribution among small metallic particles of different size. These effects will be considered within a unified approach. In the framework of the self-consistent approach, the space is divided into domains of influence of individual particles on extracted carriers and the notion of a macroscopic effective medium is introduced. This approach was developed as applied to the problems associated with determining the diffusion [10–12] and heat [13] fluxes on precipitates of a new phase in ensembles.

First, we will consider a single particle in a semiconductor matrix. We assume that the particle is spherical in shape and the matrix is an *n*-type nondegenerate semiconductor.

1. Let us assume that $U(r)$ is the electrostatic potential around a metallic particle of radius R, $\varphi = -eU$ is the potential energy of an electron in the field U, and $(-e)$ is the elementary charge. For brevity, φ will be referred to as the potential. This potential can be described by the equation [4]

$$\Delta\varphi = \frac{4\pi e^2 n_0}{\varepsilon}\{1 - \exp(-\varphi/kT)\}, \tag{1}$$

where n_0 is the carrier density in the semiconductor and ε is the permittivity of the semiconductor. The boundary conditions for Eq. (1) have the form

$$\varphi|_{r=R} = \varphi_0, \quad \varphi|_{r\to\infty} = 0. \tag{2}$$

The quantity φ_0 involved in boundary conditions (2) is equal to the difference between the thermodynamic work functions (reckoned from the Fermi level) of the metal Φ_m and the semiconductor Φ_s [4]:

$$\varphi_0 = \Phi_m - \Phi_s. \tag{3}$$

The charge density σ for the metal is determined from the condition [14]

$$\left.\frac{\varepsilon}{e}\frac{\partial\varphi}{\partial r}\right|_{r=R} = 4\pi\sigma. \tag{4}$$

We will restrict our consideration to the case $\varphi_0 > 0$ where the region depleted in carriers is formed around the particle. Assuming that the inequality $\exp(-\varphi/kT) \ll 1$ is satisfied in the greater part of the region of spatial variation in the potential, Eq. (1) can be rewritten in the form

$$\Delta\varphi = \frac{4\pi e^2 n_0}{\varepsilon}. \tag{5}$$

This approximation, which was introduced by Schottky [15] (see also [4, 16]) in the two-dimensional case,

implies that, in a semiconductor layer, there are no free electrons around the particle (i.e., it is a completely depleted layer). If the thickness of the depleted layer is designated by L, the boundary conditions (2) can be rewritten as

$$\varphi(R) = \varphi_0, \quad \varphi(R+L) = 0, \quad \varphi'_r(R+L) = 0. \quad (6)$$

By solving Eq. (5) with boundary conditions (6) in the range $R \le r \le (R+L)$, we find

$$\varphi = \frac{2\pi e^2 n_0}{3\varepsilon}\left\{r^2 - 3(R+L)^2 + 2\frac{(R+L)^3}{r}\right\}, \quad (7)$$

$$E_r = \frac{4\pi e n_0}{3\varepsilon}\left\{r - \frac{(R+L)^3}{r^2}\right\}, \quad (8)$$

where E_r is the rth component of the electric field vector $\mathbf{E}$ and the thickness L obeys the cubic equation

$$L^3 + \frac{3}{2}L^2 R - \frac{3\varepsilon\varphi_0}{4\pi e^2 n_0}R = 0.$$

Next, we consider two limiting cases of physical interest. For $R \ll L$, we have

$$L = \left(\frac{3\varepsilon\varphi_0}{4\pi e^2 n_0}R\right)^{1/3}. \quad (9)$$

For $R \gg L$, we obtain the Schottky formula [15]

$$L = \left(\frac{\varepsilon\varphi_0}{2\pi e^2 n_0}\right)^{1/2}. \quad (10)$$

In order to obtain numerical estimates, we set $n_0 \sim 10^{20}$ m^{-3}, $\varepsilon \sim 10$, and $\varphi_0/e \sim 1$ V. Then, at $R \ge 10^{-5}$ m, the metallic particle is surrounded by a planar depleted layer $L \sim 3 \times 10^{-6}$ m thick. For $R \le 10^{-7}$ m, the potential around the particle is characterized by a spherical distribution (at $R \sim 10^{-7}$ m, the thickness of the depleted layer $L \sim 10^{-6}$ m exceeds R by one order of magnitude). Setting $R \sim 10^{-7}$ m, we find $E_r(R) \sim 10^{-7}$ V m^{-1} and $E_r(R + L/2) \sim 3 \times 10^5$ V m^{-1}.

Substituting expression (7) into formula (4) gives the charge density at the particle surface:

$$\sigma = -\frac{en_0}{3}\left\{\frac{(R+L)^3}{R^2} - R\right\}. \quad (11)$$

Since the semiconductor at $\varphi_0 > 0$ is depleted in electrons, electrons are in excess on the metal surface ($\sigma < 0$). Formula (11) becomes obvious when changing over to the net charge of the particle:

$$4\pi R^2\sigma = -en_0\left\{\frac{4\pi}{3}(R+L)^3 - \frac{4\pi}{3}R^3\right\}. \quad (12)$$

All free electrons are extracted from the layer of thickness L around the particles and transferred to the particle surface, which determines the charge density σ.

In what follows, we will analyze only small-sized particles ($R \ll L$). In this case, from relationships (9) and (11), we find

$$\sigma = -\frac{\varepsilon\varphi_0}{4\pi e R}. \quad (13)$$

Hence, the excess number of electrons on the particle surface can be represented in the form

$$N_e = \frac{4\pi R^2\sigma}{(-e)} = \frac{\varphi_0}{e^2/\varepsilon R}. \quad (14)$$

Here, $e^2/\varepsilon R$ is equal in order of magnitude to the electrostatic energy acquired by the particle after trapping an electron and φ_0 is the potential energy of an electron in the semiconductor at the interface with the metal. Note that the description of surface charges in terms of their density σ is correct at $N_e \gg 1$. According to expression (14), this leads to the inequality $e^2/\varphi_0\varepsilon R \ll 1$. The same inequality determines the range of applicability of Eq. (5). The relative fluctuation of the quantity N_e can be estimated as $(N_e)^{-1/2} \sim (e^2/\varphi_0\varepsilon R)^{1/2} \ll 1$.

From formula (14), it is easy to verify that, at $\varepsilon \sim 10$ and $\varphi_0/e \sim 1$ V, the surface of the particle $R \sim 10^{-7}$ m in size contains $N_e \sim 10^3$ excess electrons and, hence, $N_e \gg 1$ and $((N_e)^{-1/2} \sim 3 \times 10^{-2} \ll 1$. The density of surface electrons is estimated as $\sigma/(-e) \sim 5 \times 10^{15}$ m^{-2}. For comparison, we note that the density of surface atoms (at the interatomic distance $a \sim 3 \times 10^{-10}$ m) can be estimated as $N_s \sim 10^{19}$ m^{-2}.

The volume of the depleted region around the small-sized metallic particles is given by the approximate formula

$$\frac{4\pi}{3}L^3 = \frac{N_e}{n_0} = \frac{\varepsilon\varphi_0}{e^2 n_0}R. \quad (15)$$

2. Let us now examine a semiconductor containing an ensemble of metallic particles. We assume that particles are uniformly distributed in the semiconductor; i.e., they do not form clusters or regions with a low density. In this case, depleted regions cover the entire volume of the semiconductor and substantially overlap one another when the following condition is satisfied:

$$\frac{4\pi}{3}\int_0^\infty L^3(R)f(R)dR > 1. \quad (16)$$

Here, the size distribution function of particles $f(R)$ is normalized to the particle number density N; that is,

$\int_0^\infty f(R)dR = N$. Substituting relationship (15) into inequality (16) and taking into account that

$$\int_0^\infty Rf(R)dR = N\bar{R}$$

(where $\bar{R}$ is the mean radius of particles), we find the sought criterion for mutual overlapping of depleted layers:

$$\frac{N}{n_0} > \frac{e^2}{\varepsilon\bar{R}\varphi_0}. \quad (17)$$

We introduce the volume fraction η ($\eta < 1$) of metallic particles in the semiconductor:

$$\eta = \frac{4\pi}{3}\int_0^\infty R^3 f(R)dR = N\bar{V},$$

where $\bar{V}$ is the mean volume of metallic particles. Then, criterion (16) can be rewritten in the form of an inequality with respect to the volume fraction:

$$\eta > n_0\bar{V}\frac{e^2}{\varepsilon\bar{R}\varphi_0}. \quad (18)$$

As before, the numerical estimates are made at $n_0 \sim 10^{20}$ m^{-3}, $\varepsilon \sim 10$, $\varphi_0/e \sim 1$ V, and $\bar{R} \sim 10^{-7}$ m. For these parameters, the depleted regions cover the entire volume of the semiconductor at number densities of the metallic particles $N \geq 10^{17}$ m^{-3}.

When condition (17) is satisfied, particles cannot be treated as isolated in the calculation of the potential distribution in the semiconductor and the charge density at the metal surface. To put it differently, particles substantially affect each other through electric fields and form an "electrical" ensemble. We now turn to consideration of this case.

If condition (17) is satisfied, the potential φ in the semiconductor obeys Eq. (5), which can be represented in the form

$$\Delta\psi = -\frac{kT}{l_D^2}. \quad (19)$$

Here, $\psi \equiv \varphi_0 - \varphi$ and l_D is the Debye screening length of the potential (charge) in the semiconductor, which is defined by the expression [4]

$$l_D = \left(\frac{\varepsilon kT}{4\pi e^2 n_0}\right)^{1/2}. \quad (20)$$

The boundary conditions for Eq. (19) must be specified for the surfaces of all particles. By ignoring the size effects, we can write the boundary conditions in the form

$$\psi|_{S_i} = 0, \quad (21)$$

where S_i is the surface of the ith particle in the ensemble.

Now, we use an approach according to which the composite space is divided into domains of influence of individual particles and the notion of a macroscopic effective medium is introduced [10–13]. In this case, the size effects can be disregarded and the distributions of the potential and the radial component E_r of the electric field around a particle can be represented in the form

$$\psi = -kT\frac{r^2 - R^2}{6l_D^2} + \left(\psi^* + kT\frac{R_0^2 - R^2}{6l_D^2}\right)\frac{r - R}{r}\frac{R_0}{R_0 - R}, \quad (22)$$

$$E_r = \frac{1}{r}kT\frac{r}{3l_D^2} - \frac{1}{e}\left(\psi^* + kT\frac{R_0^2 - R^2}{6l_D^2}\right)\frac{R}{r^2}\frac{R_0}{R_0 - R}, \quad (23)$$

where $R_0(R)$ is the radius determining the domain of influence of the particle with size R. The radius R_0 satisfies the integral self-consistent equation

$$\frac{4\pi}{3}\int_0^\infty R_0^3(R)f(R)dR = 1. \quad (24)$$

Equation (24) implies that the domains of influence of individual particles cover the entire volume of the semiconductor matrix. The quantity ψ^*, which is equal to $\psi(r)$ at $r = R_0$, and the radius R_0 are related by the expression

$$\psi^* = kT\frac{R_0^3}{3Rl_D^2}\left(1 - \frac{R}{R_0}\right)^2\left(1 + \frac{1}{2}\frac{R}{R_0}\right). \quad (25)$$

Substituting expression (25) into formulas (22) and (23) gives

$$\psi = -kT\frac{r^2 - R^2}{6l_D^2} + kT\frac{R_0^2}{3l_D^2}\frac{R_0}{R}\left(1 - \frac{R}{r}\right), \quad (26)$$

$$E_r = -\frac{kT}{3el_D^2}\frac{(R_0^3 - r^3)}{r^2} = -\frac{4\pi e n_0}{3\varepsilon}\frac{(R_0^3 - r^3)}{r^2}. \quad (27)$$

By ignoring the dispersion of the distribution function $f(R)$, we obtain

$$R_0(R) = \frac{R}{2}\left\{1 + \left(\frac{\bar{R}}{R}\right)^{2/3}\frac{2 - \eta^{1/3}}{\eta^{1/3}}\right\} \approx \frac{R^{1/3}\bar{R}^{2/3}}{\eta^{1/3}} \gg R. \quad (28)$$

In formula (28), we assume that $\eta^{1/3} \ll 1$. The inequality $\exp(-\varphi^*/kT) \ll 1$ (where $\varphi^* \equiv \varphi_0 - \psi^*$) must be satisfied for the approximation of a completely depleted layer [Eq. (19)] to be applicable. The "contact potential" φ_0 should obey the same condition.

The charge density at the particle surface can be written as

$$\sigma = -\frac{en_0}{3R^2}(R_0^3 - R^3). \quad (29)$$

Hence, it follows that the net charge of the particle can be represented by the relationship

$$4\pi R^2\sigma = -en_0\left(\frac{4\pi}{3}R_0^3 - \frac{4\pi}{3}R^3\right). \quad (30)$$

Relationship (30) is similar to relationship (12) for a single particle and actually describes the law of conservation of electric charge as applied to the particle in the ensemble.

Let us attempt to take into account the size effects associated with the dependence of the Fermi energy μ_m of the metal on the radius R and the high Coulomb energy for small-sized particles. The inclusion of the size dependence of the work function of a small-sized metallic particle (see, for example, [8]) leads to the expressions

$$\Phi_m(R) = \Phi_{mo} - \mu_1 + E_c, \quad (31)$$

$$\mu_1(R) = -\alpha/R \sim R^{-1}. \quad (32)$$

Here, Φ_{mo} is the work function of a bulk metal sample, $\mu_1(R)$ is the size-dependent correction to the Fermi energy of the metal, and E_c is the electrostatic (charge) energy acquired by the particle after the escape of an electron. According to the numerical estimates made by Zakgeĭm *et al.* [17], the energy E_c in a dense ensemble of metallic particles is lower than the electrostatic energy of a single particle $E_{co} = e^2/2\varepsilon R$. This decrease is explained by the polarization of metallic particles surrounding the given particle in the ensemble. However, when the volume fraction η of the metallic phase is sufficiently small, the decrease in the electrostatic energy E_c is insignificant as compared to E_{co}. For example, it was shown for a monodisperse disordered system of metallic particles (see Fig. 3 in [17]) that $\bar{E}_c/E_{co} > 0.9$ at $\eta < 0.05$ (where $\bar{E}_c$ is the mean electrostatic energy of a particle at a fixed volume fraction η). Note that, most likely, the difference between E_c and E_{co} can be disregarded if the inequality $\eta^{1/3} \ll 1$ ($\eta \le 10^{-3}$), which was used in formula (28), is satisfied. Therefore, assuming the volume fraction η to be sufficiently small, we set

$$E_c \approx E_{co} = e^2/2\varepsilon R. \quad (33)$$

The work function of the semiconductor surrounding the metallic particle of radius R in the ensemble can be written in the form

$$\Phi_s(R) = \Phi_{so} + E_{cs}, \quad (34)$$

where Φ_{so} is the work function of a bulk semiconductor sample and E_{cs} is the electrostatic energy of the semiconductor per particle in the domain of influence of the particle with radius R, which appears after the escape of an electron from this domain. It is easy to show that, at $R^3/R_0^3 \ll 1$ (at $\eta \ll 1$), the electrostatic energy E_{cs} is given by the formula

$$E_{cs} = \frac{3}{5}\frac{e^2}{\varepsilon R_0}\left\{1 + O\left(\frac{R^3}{R_0^3}\right)\right\} \approx \frac{3}{5}\frac{e^2}{\varepsilon R_0}. \quad (35)$$

Then, the boundary condition at the particle boundary takes the form

$$\varphi(R) = \Phi_m(R) - \Phi_s(R) = \varphi_0 + \beta_R, \quad (36)$$

where

$$\beta_R \equiv \frac{\alpha}{R} + \frac{e^2}{2\varepsilon R} - \frac{3}{5\varepsilon}\frac{e^2}{R_0(R)}. \quad (37)$$

Now, the problem of the potential distribution in the semiconductor between metallic particles can be formulated as follows. Equation (19) with the aforementioned assumptions is retained. The boundary conditions (21) are replaced by the following conditions:

$$\psi|_{S_i} = -\beta_{R_i}, \quad (38)$$

where R_i is the radius of the ith particle. In this case, the sought distribution of the quantity ψ is determined as the difference between $\psi(r)$ [formula (26)] and the term $\delta\varphi(r)$ [addition to the potential $\varphi(r)$] defined by the relationship

$$\begin{aligned}\varphi_0 - \delta\varphi &= \left\{(\tilde{\varphi} + \beta_R)\left(1 - \frac{R}{r}\right)\frac{l + R_0}{l + R_0 - R} - \beta_R\right\}\theta(R_0 - r) \\ &+ \left\{\tilde{\varphi} - (\tilde{\varphi} + \beta_R)\frac{l}{l + R_0 - R}\frac{R}{r}\exp\left(-\frac{r - R_0}{l}\right)\right\}\theta(r - R_0).\end{aligned} \quad (39)$$

Here, $\tilde{\varphi} \equiv \varphi^* - \bar{\varphi}$, $\bar{\varphi}$ is the potential averaged over the semiconductor volume, l is the macroscopic length of screening of the potential by metallic particles, and $\theta(x)$

is the Heaviside step function. The additional potential $\delta\varphi(r)$ corresponds to the electric field

$$\delta E_r = -(\tilde{\varphi} + \beta_R)\frac{l + R_0}{l + R_0 - R}\frac{R}{er^2}\left\{\theta(R_0 - r) + \frac{l + r}{l + R_0}\exp\left(-\frac{r - R_0}{l}\right)\theta(r - R_0)\right\}, \quad (40)$$

which, in turn, is additional to the field described by expression (27).

By using the easily verified identity

$$\left(1 - \frac{R}{R_0}\right)\frac{l + R_0}{l + R_0 - R} \equiv 1 - \frac{l}{l + R_0 - R}\frac{R}{R_0}, \quad (41)$$

it can be shown that the quantities $\delta\varphi(r)$ and δE_r are continuous at $r = R_0$.

The charge density additional to the density σ [expression (29)] is represented by the relationship

$$\delta\sigma = \frac{\varepsilon}{4\pi}\delta E_r(R) = -\frac{\varepsilon}{4\pi eR}(\tilde{\varphi} + \beta_R)\frac{l + R_0}{l + R_0 - R}. \quad (42)$$

Since the charge with density σ is extracted by the particle only from its own domain of influence [see formula (30)], the quantity $\delta\sigma$ characterizes the charge redistribution among small-sized metallic particles. At $R \ll R_0$, the quantity $\delta\sigma$ can be written in the form

$$\delta\sigma \approx -\frac{\varepsilon}{4\pi eR}\left(\tilde{\varphi} + \frac{\alpha}{R} + \frac{e^2}{2\varepsilon R}\right). \quad (43)$$

The screening length l is described by the formulas derived in [10]. For the parameters $N \sim 10^{17}$ m^{-3} and $\bar{R} \sim 10^{-7}$ m, we find the volume fraction of particles $\eta = (4\pi/3)\bar{R}^3 N \sim 4 \times 10^{-4}$. Then, the numerical estimates give the screening length $l \sim 3 \times 10^{-6}$ m and the quantity $(4\pi/3)l^3 N \approx 10 \gg 1$.

3. Thus, a single metallic particle and an ensemble of metallic particles in an n-type nondegenerate semiconductor were considered in the presence of a contact potential $\varphi_0 > 0$ at the metal. The analysis was performed in the Schottky approximation (the approximation of a semiconductor layer completely depleted in carriers). In the case of a single metallic particle, explicit analytical relationships were derived for the potential $\varphi(r)$ around the particle [formula (7)], the electric field $E_r(r)$ [formula (8)], the thickness of the depleted layer L [formulas (9), (10)], and the charge density σ at the particle surface [formula (11)]. It was shown that, at $R \ll L$ (which is an actual case for nanoparticles), the potential and electric field around the particle are characterized by a virtually spherical distribution.

For a composite system formed by a semiconductor containing small-sized metallic particles, the criterion for mutual overlapping of the depleted layers [inequalities (17), (18)] was formulated. When this criterion holds true, charged metallic particles interact with each other and, hence, form an ensemble. This ensemble was analyzed within an approach according to which the composite space is divided into domains of influence of individual particles and the notion of the macroscopic effective medium is introduced. The use of this approach made it possible to obtain the distributions of the potential and electric field around a particle and the charge density σ at the particle surface without regard for the size effects [formulas (26)–(29)] and with due regard for these effects [formulas (39), (40), (42)] but at a sufficiently small fraction η of the metallic phase. The included size effects are associated with the dependence of the Fermi energy μ_m of the metal on the radius R and the high Coulomb energy E_c for small-sized particles. These effects lead to an additional charge $\delta\sigma$ at the particle surface due to the charge redistribution among small-sized metallic particles [formulas (42), (43)].

Note that the analysis of the composite system within the Schottky approximation does not include screening of the potential by free charge carriers at the Debye length l_D, because all carriers are extracted from the semiconductor by metallic particles. Therefore, there are a macroscopic screening by metallic particles and a screening by immobile charged impurities that remain in the semiconductor after the transfer of carriers to metallic particles. It should also be noted that, when the condition for overlapping of the depleted layers around individual particles [inequalities (17), (18)] is satisfied, the conductivity of the system under consideration in sufficiently weak electric fields should drastically decrease as compared to the conductivity of the semiconductor without particles.

In a p-type semiconductor, a depleted layer around a metallic particle is formed at $\varphi_0 < 0$. The thickness of this layer in the Schottky approximation for a single particle of radius $R \ll L_p$ and a nondegenerate semiconductor can be represented in the form

$$L_p = \left(\frac{3\varepsilon|\varphi_0|}{4\pi e^2 p_0}R\right)^{1/3}, \quad (44)$$

where p_0 is the carrier (hole) density in the semiconductor. Under the condition

$$\frac{N}{p_0} > \frac{e^2}{\varepsilon\bar{R}|\varphi_0|}, \quad \eta > p_0\bar{V}\frac{e^2}{\varepsilon\bar{R}|\varphi_0|}, \quad (45)$$

depleted layers cover the entire volume of the semiconductor. The electric field around the particle is described by relationships similar to those derived above, but with the quantities n_0, L, φ, and E replaced by p_0, L_p, $-\varphi$, and $-E$, respectively. The surface charge density σ_p can be obtained by replacing n_0 by p_0, L by L_p, and σ by $-\sigma_p$.

ACKNOWLEDGMENTS

I would like to thank V.V. Slezov, S.B. Rutkevich, and V.V. Yanovskiĭ for their participation in discussing the results, S.A. Kukushkin for his support, and the reviewer for helpful critical remarks.

REFERENCES

1. S. A. Nepiĭko, *Physical Properties of Small-Sized Metallic Particles* (Naukova Dumka, Kiev, 1985) [in Russian].
2. É. L. Nagaev, Usp. Fiz. Nauk **162** (9), 49 (1992) [Sov. Phys. Usp. **35**, 747 (1992)].
3. V. D. Borman, S. Ch. Laĭ, M. A. Pushkin, V. N. Tronin, and V. I. Troyan, Pis'ma Zh. Éksp. Teor. Fiz. **76** (7), 520 (2002) [JETP Lett. **76**, 444 (2002)].
4. V. L. Bonch-Bruevich and S. G. Kalashnikov, *Physics of Semiconductors*, 2nd ed. (Nauka, Moscow, 1990) [in Russian].
5. É. L. Nagaev, Fiz. Tverd. Tela (Leningrad) **25** (5), 1439 (1983) [Sov. Phys. Solid State **25**, 827 (1983)].
6. L. K. Grigor'eva, N. S. Lidorenko, É. L. Nagaev, and S. P. Chizhik, Pis'ma Zh. Éksp. Teor. Fiz. **43** (6), 290 (1986) [JETP Lett. **43**, 373 (1986)].
7. L. K. Grigor'eva, N. S. Lidorenko, É. L. Nagaev, and S. P. Chizhik, Zh. Éksp. Teor. Fiz. **91** (3), 1050 (1986) [Sov. Phys. JETP **64**, 620 (1986)].
8. P. G. Borzyak, S. A. Gorban', L. K. Grigor'eva, É. L. Nagaev, S. A. Nepiĭko, and S. P. Chizhik, Zh. Éksp. Teor. Fiz. **97** (2), 623 (1990) [Sov. Phys. JETP **70**, 347 (1990)].
9. É. M. Baskin and M. V. Éntin, Pis'ma Zh. Éksp. Teor. Fiz. **70** (8), 510 (1999) [JETP Lett. **70**, 520 (1999)].
10. V. V. Slezov, Fiz. Tverd. Tela (Leningrad) **31** (8), 20 (1989) [Sov. Phys. Solid State **31**, 1289 (1989)].
11. A. V. Koropov, P. N. Ostapchuk, and V. V. Slezov, Fiz. Tverd. Tela (Leningrad) **33** (10), 2835 (1991) [Sov. Phys. Solid State **33**, 1602 (1991)]; Preprint No. 90-50, KhFTI (Kharkov Inst. of Physics and Technology, Kharkov, 1990); Preprint No. 91-16, KhFTI (Kharkov Inst. of Physics and Technology, Kharkov, 1991).
12. V. I. Perekrestov, A. V. Koropov, and S. N. Kravchenko, Fiz. Tverd. Tela (St. Petersburg) **44** (6), 1131 (2002) [Phys. Solid State **44**, 1181 (2002)].
13. A. V. Koropov, S. A. Kukushkin, and D. A. Grigor'ev, Zh. Tekh. Fiz. **69** (7), 53 (1999) [Tech. Phys. **44**, 786 (1999)].
14. L. D. Landau and E. M. Lifshitz, *Course of Theoretical Physics*, Vol. 8: *Electrodynamics of Continuous Media,* 2nd ed. (Nauka, Moscow, 1982; Pergamon, New York, 1984).
15. W. Schottky, Z. Phys. **118** (9–10), 539 (1942).
16. E. V. Buzaneva, *Microstructures in Integrated Electronics* (Radio and Svyaz', Moscow, 1990) [in Russian].
17. D. A. Zakgeĭm, I. V. Rozhanskiĭ, and S. A. Gurevich, Pis'ma Zh. Éksp. Teor. Fiz. **70** (2), 100 (1999) [JETP Lett. **70**, 105 (1999)].

Translated by O. Borovik-Romanova

Physics of the Solid State, Vol. 46, No. 8, 2004, pp. 1508–1519. Translated from Fizika Tverdogo Tela, Vol. 46, No. 8, 2004, pp. 1465–1475.
Original Russian Text Copyright © 2004 by Moskalenko, Yassievich.

Excitons in Si Nanocrystals

A. S. Moskalenko and I. N. Yassievich

Ioffe Physicotechnical Institute, Russian Academy of Sciences, Politekhnicheskaya ul. 26, St. Petersburg, 194021 Russia
e-mail: Irina.Yassievich@mail.ioffe.ru
Received December 16, 2003

Abstract—The states of electron–hole pairs in spherical silicon nanocrystals are theoretically studied using the "multiband" effective-mass approximation in the limit of an infinitely high potential barrier at the boundary. The degeneracy of the states at the top of the valence band is taken into account in the spherical approximation, and the ellipsoidal character of the electronic spectrum in the conduction band is allowed for. Coulomb interaction–induced corrections to the energy of an electron–hole pair are found. *© 2004 MAIK "Nauka/Interperiodica".*

1. INTRODUCTION

Silicon is a basic material for microelectronics; however, its optoelectronic applications are complicated by the fact that its band gap is indirect [1]. It is tempting to overcome this fundamental difficulty, since this would open prospects for integrating silicon-based electronic and optical devices. One possibility is the use of nanocrystalline silicon. In this case, nanocrystals can be radiation sources [2], since the quasi-momentum conservation law for optical transitions is no longer valid due to the violation of translational symmetry [3, 4]; furthermore, nanocrystals can be good sensitizers for radiation by optically active impurities, e.g., erbium ions Er^{3+} [5–7]. Moreover, the use of silicon nanocrystals as photosensitive catalysts of electronic transitions in molecules is in itself of interest for new applications in chemistry and biology [8]. To understand the physical processes involving electrons and holes localized in nanocrystals, it is important to know the structure of their energy spectrum and wave functions.

To date, there have been numerous publications in which the states of electron–hole pairs (excitons) in silicon nanocrystals were investigated theoretically by using the pseudopotential method [9–11], the local-density method [12–14], the tight-binding approximation [15–20], the effective-mass approximation [19, 21–26], and other approaches [27, 28].

In a number of studies of electron–hole states in nanocrystals using the effective-mass approximation [21, 23, 24], an oversimplified description of the structure of the Si valence band top was used. A multiband effective-mass approximation (the **kp** method) taking into account the degeneracy of the Si valence band was first applied to the problem in question in [22]. However, the limiting case of strong spin–orbit interaction [29] was considered in [22], which is not justified for Si, where the spin–orbit splitting energy is 0.04 eV. In [25], the spectrum of electrons and holes was studied (disregarding the Coulomb interaction) in the multiband effective-mass approximation by taking into account the complex structure of the silicon valence band top in the limit of weak spin–orbit interaction. However, the band-mixing effects were taken into account using perturbation theory. It should be noted that the anisotropy of the hole spectrum was neglected [25, 30]. To calculate the electron energy spectrum, the Hamiltonian from [31, 32] was used, which takes into account that the conduction band minimum lies near the X point, where the effects of mixing of the two bands occur. A simple effective-mass approximation was used as a zeroth approximation, and the anisotropy and the effects of mixing of the two lowest conduction bands were taken into account in perturbation theory. Later, the effect of finite height of the potential barrier at the boundary for Si nanocrystals embedded in silicon dioxide was taken into account in [26] and was shown to be able to influence the quantum confinement levels for nanodots of radius smaller than 2.5 nm. In [19, 25, 26], the effect of Coulomb interaction on the energy of electron–hole pairs was disregarded.

In this study, we also apply the multiband effective-mass approximation to calculate the energies and wave functions of electrons and holes in spherical nanocrystals. To describe hole states, we used a generalized Luttinger Hamiltonian in the spherical approximation in the limit of weak spin–orbit interaction [29]. However, in contrast to [25, 26], we find the exact solution rather than use perturbation theory to describe the hole spectrum. We take into account the highly nonspherical (ellipsoidal) character of the electron energy dispersion without using perturbation theory and assume that the effect of the admixture of the upper conduction band on the electronic spectrum in nanodots can be disregarded. The correction introduced by Coulomb interaction between an electron and a hole in the nanocrystal is found in perturbation theory. Furthermore, the jump in the permittivity at the boundary between the nanocrystal and the surrounding material is taken into account.

1063-7834/04/4608-1508$26.00 © 2004 MAIK "Nauka/Interperiodica"

Since the spin–orbit interaction in Si is weak, we neglect the spin-related effects when describing electron and hole states.

2. QUANTUM CONFINEMENT EFFECT FOR ELECTRON STATES

Silicon has a diamond-type lattice and is a semiconductor with an indirect energy band gap, with the conduction band minimum lying at the Δ point near the X point of the Brillouin zone. The space symmetry group of Si is O_h^7, which belongs to the O_h class and is nonsymmorphic since it contains elements with nontrivial translations (by a fraction of a basis lattice vector). This property causes an unavoidable double degeneracy of the band at the X point [33]. It is also known that two lowest conduction bands in Si are nondegenerate at the Δ point and correspond to the Δ_1 and $\Delta_{2'}$ representations, respectively [1, 33]. If the Δ point moves to the surface of the Brillouin zone, it becomes the X point, where, due to the compatibility conditions, the Δ_1 and $\Delta_{2'}$ representations transform into the doubly degenerate X_2 representation or into the doubly degenerate X_4 representation (in the notation from [33]). The X_2 and X_4 representations have a nonzero projection of the momentum matrix element onto the Γ–X axis. For this reason, the band slope at the X point is nonzero and the minimum of the lowest conduction band ($c1$) is shifted from the X point towards the Γ point by a distance of $k_X = 0.15 \times 2\pi/a_{\mathrm{Si}}$, where $a_{\mathrm{Si}} = 0.543$ nm is the lattice parameter for Si. In all, there are six equivalent points corresponding to the conduction band minima in the Brillouin zone. We consider in detail the case where the X point lies on the (001) axis. Accordingly, the minimum of the $c1$ conduction band lies at a distance of $k_0 = 0.85 \times 2\pi/a_{\mathrm{Si}}$ from the Γ point. Thus, the minimum lies near the X point and, in order to describe the energy band structure, we can use the Hamiltonian for the X_2 and X_4 representations (see [33, Eq. (30.51)]):

$$\mathcal{H} = -[A_1\partial_z^2 + A_2(\partial_x^2 + \partial_y^2)]I - A_3\hat{\sigma}_x\partial_x\partial_y - iA_4\hat{\sigma}_z\partial_z, \quad (1)$$

where $\hat{\sigma}_x$ and $\hat{\sigma}_z$ are the Pauli matrices and I is the 2×2 unit matrix. The parameters A_1 and A_2 are expressed in terms of the experimental masses $m_\parallel$ and $m_\perp$: $A_1 = \hbar^2/2m_\parallel$ and $A_2 = \hbar^2/2m_\perp$. The constant A_4 is determined by the relation $|A_4| = 2A_1k_X$. It is convenient to express the constant A_3 in terms of an unknown mass m': $A_3 = \hbar^2/m'$. We note that, since we have neglected the relativistic effects, the band is fourfold degenerate (including spin degeneracy) at the X point. Rewriting Hamiltonian (1) for the point of the Brillouin zone corresponding to the conduction band minimum, we obtain

$$H^{c1, c2} = \begin{pmatrix} H_1 & H_{12} \\ H_{12} & H_2 \end{pmatrix}, \quad (2)$$

where the operators H_1, H_2, and H_{12} are given by

$$H_1 = -\frac{\hbar^2}{2m_\parallel}\partial_z^2 - \frac{\hbar^2}{2m_\perp}(\partial_x^2 + \partial_y^2), \quad (3)$$

$$H_2 = \Delta_c - \frac{\hbar^2}{2m_\parallel}(\partial_z^2 - 4ik_X\partial_z) - \frac{\hbar^2}{2m_\perp}(\partial_x^2 + \partial_y^2), \quad (4)$$

$$H_{12} = -\frac{\hbar^2}{m'}\partial_x\partial_y. \quad (5)$$

The parameter Δ_c determines the energy distance between the conduction bands at the point corresponding to the minimum of the lowest conduction band and is equal to

$$\Delta_c = 2\frac{\hbar^2}{m_\parallel}k_X^2. \quad (6)$$

From this equation, using the Si parameters, we obtain $\Delta_c = 0.5$ eV. Using Hamiltonian (2), we can find a lower bound for the unknown mass $m' \gtrsim 0.1m_\perp$ from the condition that no warping of the conduction band is observed in bulk silicon up to concentrations of 10^{19} cm^{-3}.

To find several lowest electron energy levels in a nanocrystal and the corresponding wave functions, we neglect the admixture of states of the upper conduction band ($c2$) to the $c1$ band states assuming that the matrix element of the operator H_{12} calculated with the wave functions corresponding to these states is much smaller in magnitude than the energy difference between them. Then, for the lower conduction band $c1$, we have the equation

$$\frac{\hbar^2}{2m_\parallel}\frac{\partial^2}{\partial z^2}\psi(x, y, z) + \frac{\hbar^2}{2m_\perp}\left(\frac{\partial^2}{\partial x^2} + \frac{\partial^2}{\partial y^2}\right)\psi(x, y, z) + E\psi(x, y, z) = 0, \quad (7)$$

where ψ is the wave function and E is the corresponding energy. In the approximation of an infinitely high energy barrier at the boundary of the nanocrystal, we have the boundary condition $\psi|_{x^2 + y^2 + z^2 = a^2} = 0$, where a is the radius of the nanocrystal.

Since Eq. (7) has cylindrical symmetry, it is convenient to introduce dimensionless cylindrical coordinates

$$\tilde{\rho} = \frac{\sqrt{x^2 + y^2}}{a}, \quad \phi = \arctan\left(\frac{y}{x}\right), \quad \tilde{z} = \frac{z}{a}. \quad (8)$$

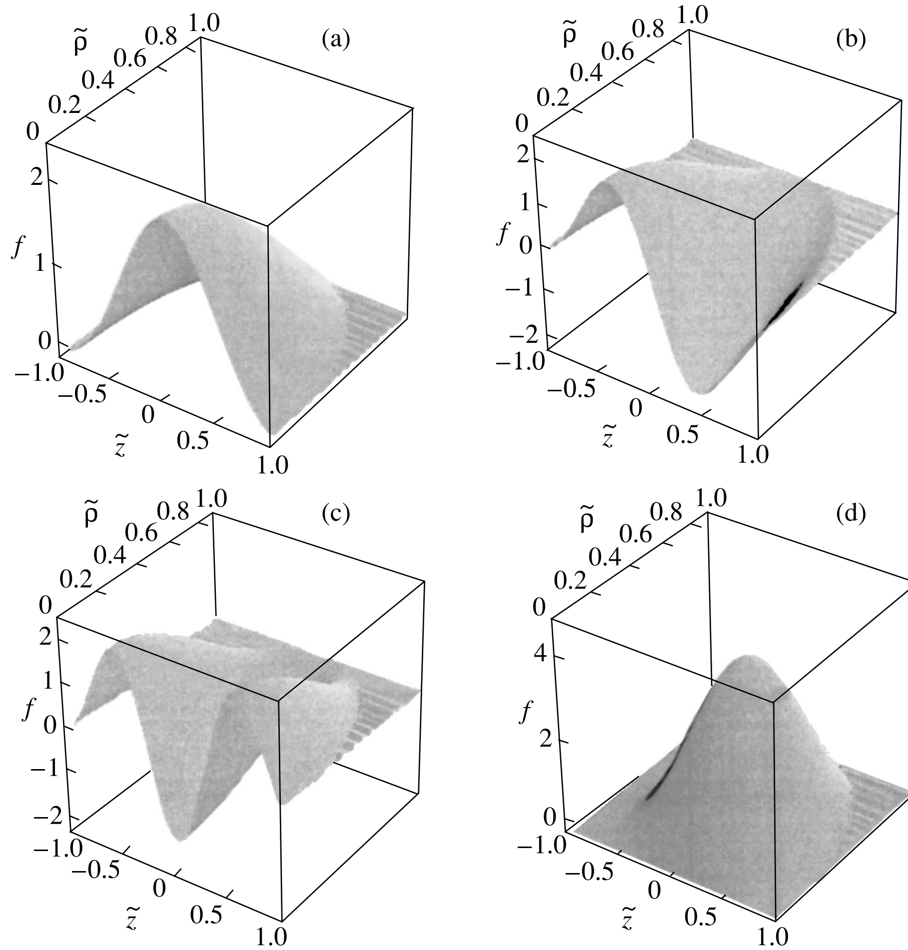

Fig. 1. Wave functions corresponding to the four lowest electron states. (a) $\tilde{E}_0 = 34.30$, $m = 0$; (b) $\tilde{E}_1 = 49.00$, $m = 0$; (c) $\tilde{E}_2 = 67.49$, $m = 0$; and (d) $\tilde{E}_3 = 80.32$, $m = \pm 1$.

In these coordinates, Eq. (7) assumes the form

$$\frac{\partial^2}{\partial \tilde{z}^2}\tilde{\psi}(\tilde{\rho}, \phi, \tilde{z}) + \frac{m_\parallel}{m_\perp}\left(\frac{1}{\tilde{\rho}}\frac{\partial}{\partial \tilde{\rho}}\tilde{\rho}\frac{\partial}{\partial \tilde{\rho}} + \frac{1}{\tilde{\rho}^2}\frac{\partial^2}{\partial \phi^2}\right)\tilde{\psi}(\tilde{\rho}, \phi, \tilde{z}) + \tilde{E}\tilde{\psi}(\tilde{\rho}, \phi, \tilde{z}) = 0, \quad (9)$$

where

$$\tilde{\psi}(\tilde{\rho}, \phi, \tilde{z}) = \psi(a\tilde{\rho}, \phi, a\tilde{z}), \quad \tilde{E} = \frac{2m_\parallel a^2}{\hbar^2}E. \quad (10)$$

The boundary conditions for Eq. (9) are rewritten as

$$\tilde{\psi}|_{\tilde{\rho}^2 + \tilde{z}^2 = 1} = 0 \quad (\tilde{\rho} \ge 0),$$
$$\left.\frac{\partial \psi}{\partial \tilde{\rho}}\right|_{\tilde{\rho} = 0} = 0, \quad \tilde{\psi}|_{\phi = 0} = \tilde{\psi}|_{\phi = 2\pi}. \quad (11)$$

We can search for solutions to Eq. (9) with boundary conditions (11) in the form

$$\tilde{\psi}(\tilde{\rho}, \phi, \tilde{z}) = f(\tilde{\rho}, \tilde{z})\exp(im\phi), \quad (12)$$

where $f(\tilde{\rho}, \tilde{z})$ is a solution to the equation

$$\frac{\partial^2}{\partial \tilde{z}^2}f(\tilde{\rho}, \tilde{z}) + \frac{m_\parallel}{m_\perp}\left(\frac{1}{\tilde{\rho}}\frac{\partial}{\partial \tilde{\rho}}\tilde{\rho}\frac{\partial}{\partial \tilde{\rho}} - \frac{m^2}{\tilde{\rho}^2}\right)f(\tilde{\rho}, \tilde{z}) + \tilde{E}f(\tilde{\rho}, \tilde{z}) = 0 \quad (13)$$

with boundary conditions $f|_{\tilde{\rho}^2 + \tilde{z}^2 = 1} = 0$ and $\partial f/\partial \tilde{\rho}|_{\tilde{\rho} = 0} = 0$. Here, the quantum number m can assume arbitrary integer values.

2.1. Simulation

Taking into account the relationship between the longitudinal and transverse masses in the Si conduction band

$$\frac{m_\parallel}{m_\perp} = \frac{0.916}{0.19} = 4.82, \quad (14)$$

we found the four lowest energy eigenvalues and the corresponding wave functions for Eq. (9) with boundary conditions (11). The results are shown in Fig. 1.

To find the unnormalized energies and wave functions in unnormalized coordinates, we must perform the following transformations:

$$E = \frac{\tilde{E}}{2m_{\parallel}a^2/\hbar^2}, \quad \psi(\rho, \phi, z) = \tilde{\psi}\left(\frac{\rho}{a}, \phi, \frac{z}{a}\right).$$

For further calculations, it is also convenient to normalize the amplitudes of the wave functions.

2.2. Adiabatic Approximation

Since the difference between the transverse and longitudinal electron masses is large (see Eq. (14)), we can use the adiabatic approximation; i.e., we assume that the time scale for transverse motion of an electron is shorter than that for longitudinal motion. This approach is an independent, alternative way of finding the electronic states; therefore, we use it to verify the simulation results and to understand them in more detail. Here, we restrict ourselves to the case of $m = 0$. In the adiabatic approximation, the wave function can be represented as the product $f(\tilde{\rho}, \tilde{z}) = \Phi(\tilde{\rho}, \tilde{z})Z(\tilde{z})$ and Eq. (13) at $m = 0$ takes the form

$$\left(\frac{1}{\tilde{\rho}}\frac{\partial}{\partial\tilde{\rho}}\tilde{\rho}\frac{\partial}{\partial\tilde{\rho}} + \kappa^2(\tilde{z})\right)\Phi(\tilde{\rho}, \tilde{z}) = 0, \tag{15}$$

where $\kappa(\tilde{z})$ is related to $\tilde{E}$ by the equation

$$\frac{\partial^2}{\partial\tilde{z}^2}Z(\tilde{z}) = \left[\frac{m_{\parallel}}{m_{\perp}}\kappa^2(\tilde{z}) - \tilde{E}\right]Z(\tilde{z}). \tag{16}$$

Transforming Eq. (15) and introducing a new coordinate $\xi = \tilde{\rho}\kappa$, we arrive at the equation

$$\left(\frac{\partial^2}{\partial\xi^2} + \frac{1}{\xi}\frac{\partial}{\partial\xi} + 1\right)\Phi = 0. \tag{17}$$

The solutions to this equation bounded at the origin are Bessel functions of zeroth order $\Phi = J_0(\xi) = J_0(\tilde{\rho}\kappa(\tilde{z}))$. The boundary condition $\Phi|_{\tilde{\rho}^2 + \tilde{z}^2 = 1} = 0$ leads to the equation

$$J_0(\sqrt{1 - \tilde{z}^2}\kappa(\tilde{z})) = 0. \tag{18}$$

It follows that

$$\kappa(\tilde{z}) = \frac{\alpha_n}{\sqrt{1 - \tilde{z}^2}}, \tag{19}$$

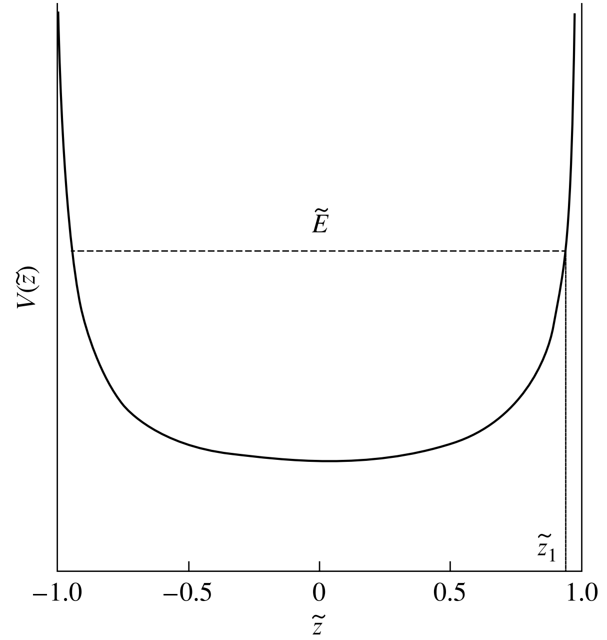

Fig. 2. Motion of a particle with energy $\tilde{E}$ in the potential $V(\tilde{z}) = \frac{m_{\parallel}}{m_{\perp}}\frac{\alpha_n^2}{1 - \tilde{z}^2}$. Here, z is the turning point for classical motion.

where α_n is the nth root of the function $J_0(x)$, $n = 0, 1, 2, \ldots$. Substituting Eq. (19) into Eq. (16), we obtain the equation

$$-\frac{\partial^2}{\partial\tilde{z}^2}Z(\tilde{z}) + \frac{m_{\parallel}}{m_{\perp}}\frac{\alpha_n^2}{1 - \tilde{z}^2}Z(\tilde{z}) = \tilde{E}Z(\tilde{z}) \tag{20}$$

with the boundary conditions $Z|_{\tilde{z} = \pm 1} = 0$. Figure 2 shows in which one-dimensional potential the particle moves according to Eq. (20). Equation (20) cannot be solved analytically, so we solve it using the semiclassical approximation. Let $Z(\tilde{z}) = \exp(i\sigma(\tilde{z}))$, where $\sigma(\tilde{z})$ is a real phase. Using Eq. (20) in the semiclassical limit, we find $\sigma(\tilde{z})$ to be

$$\sigma = \pm\int d\tilde{z}\sqrt{\tilde{E} - \frac{m_{\parallel}}{m_{\perp}}\frac{\alpha_n^2}{1 - \tilde{z}^2}}. \tag{21}$$

The quantization conditions for reflection from the potential barrier yield [34]

$$2\int_0^{\tilde{z}_1} d\tilde{z}\sqrt{\tilde{E} - \frac{m_{\parallel}}{m_{\perp}}\frac{\alpha_n^2}{1 - \tilde{z}^2}} = \pi\left(\frac{1}{2} + N\right). \tag{22}$$

Here, $\tilde{z}_1$ is a turning point (Fig. 2) and the integer nonnegative number N is the number of the level.

Introducing the notation

$$\chi = \sqrt{\frac{\tilde{E}}{\tilde{E} - \frac{m_\parallel}{m_\perp}\alpha_n^2}} \quad (23)$$

$(\tilde{E} = -\frac{m_\parallel}{m_\perp}\alpha_n^2\chi^2/(1-\chi^2))$ and calculating the integral in Eq. (22), we obtain the following equation for the energy:

$$\int_0^{1/\chi} d\tilde{z}\frac{\sqrt{1-\chi^2\tilde{z}^2}}{\sqrt{1-\tilde{z}^2}} = \frac{\pi(1+2N)}{4\sqrt{\frac{m_\parallel}{m_\perp}}\alpha_n}\sqrt{\chi^2-1}. \quad (24)$$

Solving Eq. (24) numerically, we find the energy values for the three lowest electronic levels: $\tilde{E}_0 = 33.54$, $\tilde{E}_1 = 47.31$, and $\tilde{E}_2 = 64.64$. We see that the solutions obtained agree well with the exact numerical solutions (see caption to Fig. 1).

3. QUANTUM CONFINEMENT EFFECT FOR HOLES

To describe the structure of the valence band in silicon, we use a generalization of the Luttinger Hamiltonian in the spherical approximation [35]:

$$\mathcal{H} = -(A+2B)\hbar^2\nabla^2 + 3B\hbar^2(\nabla\cdot\hat{\mathbf{J}})^2 + \frac{1}{3}\Delta\hat{\boldsymbol{\sigma}}\hat{\mathbf{J}} - \frac{1}{3}\Delta. \quad (25)$$

Here, $\hat{\mathbf{J}}$ is the operator of the unit angular momentum, $\hat{\boldsymbol{\sigma}}$ is the operator of the angular momentum 1/2, Δ is the spin–orbit splitting, and

$$A = -\frac{1}{4}\frac{m_h+m_l}{m_h m_l}, \quad B = -\frac{1}{4}\frac{m_h-m_l}{m_h m_l}, \quad (26)$$

where

$$m_h = \frac{m_0}{\gamma_1 - 2\gamma}, \quad m_l = \frac{m_0}{\gamma_1+2\gamma}, \quad (27)$$

$$\gamma = \frac{1}{5}(3\gamma_3 + 2\gamma_2). \quad (28)$$

For Si, the constants γ_1, γ_2, and γ_3 are 4.22, 0.53, and 1.38, respectively [36]. In the limit of infinitesimal spin–orbit splitting, $\Delta \longrightarrow 0$, which can be used for Si, we write Hamiltonian (25) on the basis of the spherical components $u_0 = Z$ and $u_{\pm1} = \mp(1/\sqrt{2})(X \pm iY)$ with the functions X, Y, and Z of the $\Gamma_{25'}$ representation [37] in the following form:

$$H = -(A-B)\hbar^2\nabla^2 I + 3B\hbar^2\begin{pmatrix} -\partial_-\partial_+ & \partial_-\partial_z & \partial_-^2 \\ \partial_+\partial_z & -\partial_z^2 & -\partial_-\partial_z \\ \partial_-^2 & -\partial_+\partial_z & -\partial_-\partial_+ \end{pmatrix}, \quad (29)$$

where I is the 3×3 unit matrix. As eigenfunctions of Hamiltonian (29), we can choose the eigenfunctions ψ_{FM} of the operators of the total angular momentum squared (F^2) and its projection F_z onto the z axis. Here, $\mathbf{F} = \mathbf{L} + \mathbf{J}$, where $\mathbf{L} = -i\mathbf{r} \times \partial_\mathbf{r}$ is the orbital angular momentum operator and $F(F + 1)$ and M are the eigenvalues of F^2 and F_z, respectively.

To find the upper energy levels of holes in a spherical nanocrystal, we consider states with total angular momentum $F = 0, 1$. For $F = 0$, there is only one type of hole state, and it is described by wave functions ψ_{00}^P:

$$\psi_{00}^P(r,\theta,\phi) = R_0^P(r)\sum_{m_1,m_2} C_{1m_1 1m_2}^{00} Y_{1m_1}(\theta,\phi)u_{m_2}, \quad (30)$$

where $R_0^P(r)$ is the radial part of the wave function, $Y_{nm}(\theta, \phi)$ are spherical functions, and $C_{j_1m_1j_2m_2}^{jm}$ are Clebsch–Gordon coefficients [37]. For $F = 1$, there are two types of hole states; they are described by wave functions ψ_{1M}^{SD} and ψ_{1M}^P and are degenerate in quantum number M, which assumes the values –1, 0, 1:

$$\psi_{1M}^{SD}(r,\theta,\phi) = R_1^S(r)Y_{00}(\theta,\phi)u_M + R_1^D(r)\sum_{m_1,m_2} C_{2m_1 1m_2}^{1M} Y_{2m_1}(\theta,\phi)u_{m_2}, \quad (31)$$

$$\psi_{1M}^P(r,\theta,\phi) = R_1^P(r)\sum_{m_1,m_2} C_{1m_1 1m_2}^{1M} Y_{1m_1}(\theta,\phi)u_{m_2}. \quad (32)$$

The functions ψ_{00}^P, ψ_{1M}^{SD}, and $\psi_{1M}^P(r, \theta, \phi)$ were previously used for describing impurity states in semiconductors [29]. The general form of these functions is easily obtained by writing the result from [38] for the case $J = 1$.

We note that only functions (31) are partially composed of functions of s symmetry. The hole state corresponding to the lowest confinement level is described by such a function (below, we show that in our case the admixture of d states for the upper hole level is small). The Schrödinger equation for these functions, $H\psi_{1M}^{SD} =$

$E\psi_{1M}^{SD}$, is reduced to the following system of equations for the radial functions $R_1^S(r)$ and $R_{1M}^D(r)$:

$$A\hbar^2\left[\frac{d^2}{dr^2}+\frac{2}{r}\frac{d}{dr}\right]R_1^S(r) - \sqrt{2}B\hbar^2\left[\frac{d^2}{dr^2}+\frac{5}{r}\frac{d}{dr}+\frac{3}{r^2}\right]R_1^D(r) = -ER_1^S(r), \quad (33)$$

$$-\sqrt{2}B\hbar^2\left[\frac{d^2}{dr^2}-\frac{1}{r}\frac{d}{dr}\right]R_1^S(r) + (A+B)\hbar^2\left[\frac{d^2}{dr^2}+\frac{2}{r}\frac{d}{dr}-\frac{6}{r^2}\right]R_1^D(r) = -ER_1^D(r). \quad (34)$$

Similar equations for a hole bound to a shallow acceptor were derived in [29] using the method of "reduced matrix elements" developed in the theory of angular momenta [37]; in those equations, there are also terms responsible for Coulomb interaction.

The general solution to the system of equations (33) and (34) that does not diverge at $r = 0$ is

$$R_1^S(r) = C_1 j_0(\lambda r/a) + C_2 j_0(\lambda\beta r/a), \quad (35)$$

$$R_1^D(r) = -\frac{1}{\sqrt{2}}C_1 j_2(\lambda r/a) + \sqrt{2}C_2 j_2(\lambda\beta r/a), \quad (36)$$

where C_1 and C_2 are arbitrary coefficients; $j_l(z)$ are spherical Bessel functions, which are expressed in terms of Bessel functions of half-integer argument, $j_l(z) = \sqrt{\pi/2z}J_{l+1/2}(z)$; the positive factor λ is related to the energy E (the energy E is negative) by

$$E = \frac{A\hbar^2}{a^2}(1-\mu)\lambda^2 = -\frac{\hbar^2}{2m_h a^2}\lambda^2; \quad (37)$$

and the coefficient β is defined by

$$\beta = \sqrt{\frac{1-\mu}{1+2\mu}}. \quad (38)$$

Following [29], we introduce here a parameter μ defined by

$$\mu = \frac{B}{A} = 2\frac{\gamma}{\gamma_1}. \quad (39)$$

In the approximation of an infinitely high energy barrier at the boundary of the nanocrystal ($r = a$), we have

$$R_1^S(a) = R_1^D(a) = 0. \quad (40)$$

Solving Eqs. (40), we arrive at the following equation, which determines the possible values of λ and, accordingly, the possible values of the hole energy:

$$j_2(\lambda)j_0(\lambda\beta) + 2j_0(\lambda)j_2(\lambda\beta) = 0. \quad (41)$$

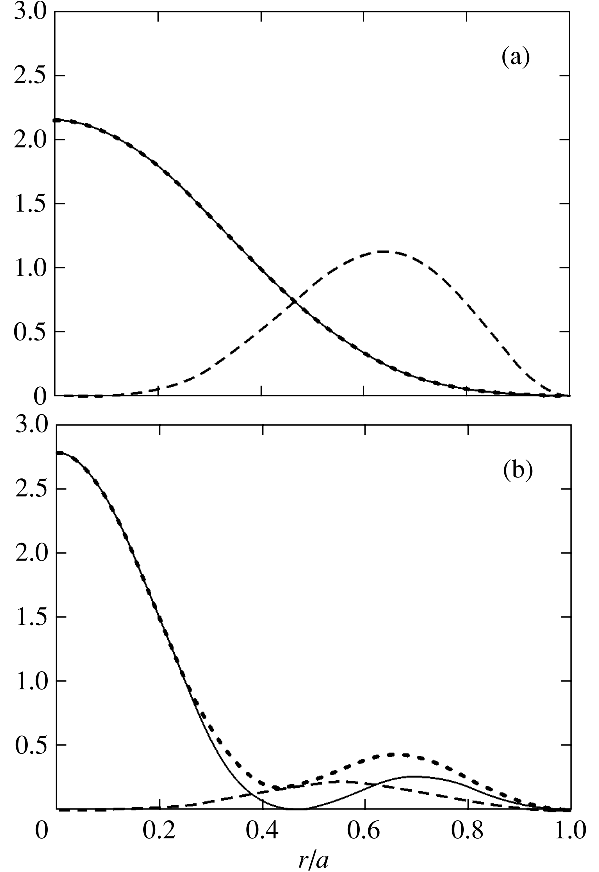

Fig. 3. Probability density for holes as a function of the radius for the states described by the function $\psi_{1M}^S(r, \theta, \phi)$. The solid line shows the contribution of the s state, the dashed line is the contribution of the d state, and the dotted line is the total probability density. (a) $\lambda_0 = 4.286$, when the admixture of d states is small. For clarity, the contribution of d states is scaled by a factor of 100. (b) $\lambda_1 = 6.276$, when the admixture of d states is fairly large ($2s1d$ hybridization).

The roots of this equation can easily be found numerically. For the Si parameters $\gamma_1 = 4.22$, $\gamma_2 = 0.53$, and $\gamma_3 = 1.38$ ($\beta = 0.505$, $\mu = 0.493$) [36], we write out the three smallest roots of Eq. (41), which determine the three upper hole levels corresponding to solutions of the type of Eq. (31):

$$\lambda_0 = 4.286, \quad \lambda_1 = 6.276, \quad \lambda_2 = 9.306. \quad (42)$$

Using these values, we construct the radial wave functions (35) and (36); the square of the modulus of these functions determines the probability density of finding a hole at a given distance from the center of the nanocrystal. As an illustration, Fig. 3 shows the distribution of the radial probability density for two states (λ_0, λ_1) represented by Eq. (31).

We should note the difference between the ground and first excited states of the type considered. For the ground state, the contribution from the d states is small.

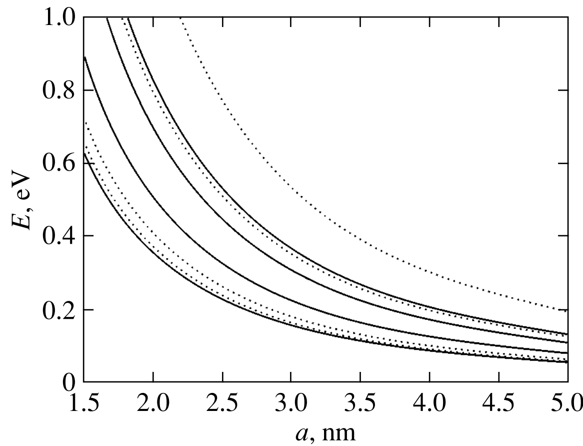

Fig. 4. Dependence of the confinement energy on the nanocrystal radius for the four lowest electron states (solid lines) and the four upper hole states (dashed lines).

Furthermore, we have $j_2(\lambda_0) = 0.245$, $j_2(\lambda_0\beta) = 0.220$, and Eq. (41) is approximately written as $j_0(\lambda\beta) + 2j_0(\lambda) = 0$ (the smallest root of this equation is equal to 4.162). The solution of this equation represents a specific average of the solutions of the equations $j_0(\lambda\beta) = 0$ and $j_0(\lambda) = 0$; these equations determine the energy levels of light and heavy holes, respectively. The factor 2 before $j_0(\lambda)$ corresponds to a twofold degeneracy of the subband of heavy holes. This fact implies that the energy of the lower state can be determined with adequate accuracy if, instead of a complicated valence band structure, we consider (as is done in [24]) a simple band in which the holes have an average mass $m^* = 3m_lm_h/(m_l + 2m_h)$ or if we find the energy to within second-order corrections (as in [25, 26]). For the state corresponding to λ_1, this argument does not hold. It is seen from Fig. 3 that, for this state, the admixture of d states is quite large.

Next, we consider the functions ψ_{00}^{P}. In this case, the Schrödinger equation leads to the following equation, which determines the energy eigenvalues and radial functions:

$$(A + 2B)\hbar^2\left[\frac{d^2}{dr^2} + \frac{2}{r}\frac{d}{dr} - \frac{2}{r^2}\right]R_0^P(r) = -ER_0^P(r), \quad (43)$$

its solution continuous at $r = 0$ has the form $R_0^P(r) = Cj_1(\lambda\beta r/a)$, where C is an arbitrary constant.

The boundary conditions for infinitely high walls lead to the following equation for λ:

$$j_1(\lambda\beta) = 0. \quad (44)$$

The three smallest roots of Eq. (44) are

$$\lambda_0 = 8.892, \quad \lambda_1 = 15.285, \quad \lambda_2 = 22.123. \quad (45)$$

Finally, for the functions ψ_{1M}^{P}, we find the following equation for the hole energy eigenvalues and radial wave functions:

$$(A - B)\hbar^2\left[\frac{d^2}{dr^2} + \frac{2}{r}\frac{d}{dr} - \frac{2}{r^2}\right]R_1^P(r) = -ER_1^P(r). \quad (46)$$

The equation for the energy eigenvalues has the form

$$j_1(\lambda) = 0, \quad (47)$$

and the three smallest roots are

$$\lambda_0 = 4.493, \quad \lambda_1 = 7.725, \quad \lambda_2 = 10.904. \quad (48)$$

For clarity, Fig. 4 shows the dependence of the energy eigenvalues on the nanocrystal radius for the ground and several excited states of electrons and holes.

4. COULOMB SHIFT

To find the energy of an electron–hole pair in a nanocrystal, we must also take into account Coulomb interaction between the electron and the hole. Clearly, this interaction decreases the energy of the electron–hole pair (the exciton effect) in the nanocrystal [39]. We calculate this effect using perturbation theory. The states of the noninteracting electron and hole are taken to be unperturbed states in the nanocrystal. The wave functions of these states are the products of the wave functions of an electron and a hole. Usually, perturbation theory can be applied if the energy level spacings for the unperturbed system are greater than the corrections to these levels.

The unperturbed excitonic states with the lowest energies consist of the lowest electronic state and the uppermost hole state corresponding to the wave function ψ_{1M}^{SD} for the ground exciton state and to ψ_{1M}^{P} for the first excited state. In the absence of spin, both of these exciton states are 18-fold degenerate (six electronic minima and triple degeneracy of hole functions). With allowance for spin, there is a 72-fold degeneracy. Since the separation between the upper hole levels corresponding to the wave functions ψ_{1M}^{SD} and ψ_{1M}^{P} is very small [see Eqs. (42), (48)], the above condition of applicability of perturbation theory is not satisfied. Nevertheless, perturbation theory can be applied to calculate the lower exciton levels, since Coulomb interaction does not mix the corresponding states (Appendix A).

Let the electron and hole be at the points $\mathbf{r}_e$ and $\mathbf{r}_h$, respectively, with respect to the center of a nanocrystal having permittivity κ_1; then, the term corresponding to direct Coulomb interaction to be added to the Hamiltonian of the noninteracting electron and hole is

$$V_1(\mathbf{r}_e, \mathbf{r}_h) = -\frac{e^2}{\kappa_1|\mathbf{r}_e - \mathbf{r}_h|}. \quad (49)$$

For an electron–hole pair in a spherical nanocrystal with permittivity κ_1 surrounded by a material with permittivity κ_2, it is necessary to take into account the additional correction to the Hamiltonian

$$V_2(\mathbf{r}_e, \mathbf{r}_h) = -\frac{e^2}{\kappa_1 a}\sum_{l=0}^{\infty} B_l\left(\frac{r_e r_h}{a^2}\right)^l P_l(\cos\theta) + \frac{e^2}{2\kappa_1 a}\sum_{l=0}^{\infty} B_l\left(\frac{r_e}{a}\right)^{2l} + \frac{e^2}{2\kappa_1 a}\sum_{l=0}^{\infty} B_l\left(\frac{r_h}{a}\right)^{2l}, \quad (50)$$

which appears due to interaction of the electron and the hole with the "image charge" distributed outside the nanocrystal [40]. In Eq. (50), θ is the angle between $\mathbf{r}_e$ and $\mathbf{r}_h$, $P_l(\cos\theta)$ are the Legendre polynomials, and the coefficients B_l are given by

$$B_l = (l+1)\frac{\kappa_1 - \kappa_2}{l\kappa_1 + (l+1)\kappa_2}. \quad (51)$$

It should be noted that, with allowance for spin, Coulomb interaction splits exciton multiplets due to the presence of the exchange integrals. The magnitude of the exchange splitting does not exceed 30 meV and decreases with increasing nanocrystal size [10, 41]. In this study, we neglect the exchange interaction due to its smallness. However, it can be easily taken into account, e.g., if we use the results from [42].

Furthermore, since the symmetry of the lowest electron state is different from spherical, the exciton multiplets split, depending on the absolute value of the hole quantum number M (Appendix A). However, for nanocrystals with a radius exceeding 1 nm, these corrections do not exceed 5 meV. Therefore, they will be disregarded in this study.

In this case, the Coulomb correction to the energy of an electron–hole pair in a nanocrystal can be presented in the form

$$E_C = \int d^3r_e d^3r_h V_1(\mathbf{r}_e, \mathbf{r}_h)\rho^e(\mathbf{r}_e)\rho^h(\mathbf{r}_h) + \int d^3r_e d^3r_h V_2(\mathbf{r}_e, \mathbf{r}_h)\rho^e(\mathbf{r}_e)\rho^h(\mathbf{r}_h), \quad (52)$$

where $\rho^e(\mathbf{r}_e)$ and $\rho^h(\mathbf{r}_h)$ are the probability densities for the electron and hole, respectively. In our notation, we have $\rho^e(\mathbf{r}_e) = |\psi_e(\mathbf{r}_e)|^2$. Neglecting splitting in M due to the nonsphericity of the lowest electron state, we can write $\rho^h(\mathbf{r}_h)$ in the form $\rho^h(\mathbf{r}_h) = [(R_1^S(r_h))^2 + (R_1^D(r_h))^2]/4\pi$ for the states with the hole wave function ψ_{1M}^{SD} and in the form $\rho^h(\mathbf{r}_h) = (R_1^P(r_h))^2/4\pi$ for the states with the hole wave function ψ_{1M}^P (see Appendix A); the functions R correspond to upper hole levels.

Computer calculation of the first term in Eq. (52) yields an exciton ground state energy of $-2.5e^2/\kappa_1 a$. Taking $\kappa_1 = 12$ for the Si permittivity and $\kappa_2 = 4$ for the

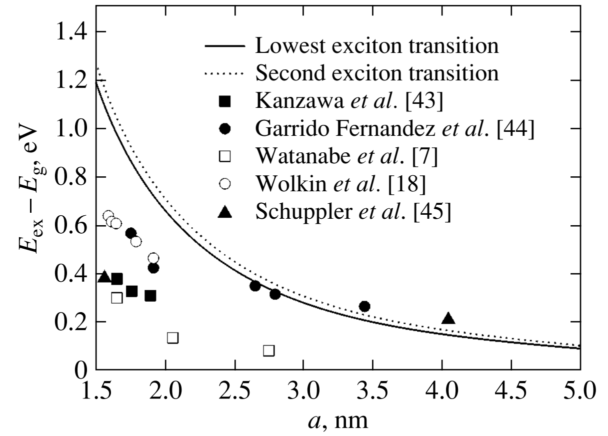

Fig. 5. Dependence of the exciton energy on the nanocrystal radius for the ground (solid line) and first excited multiplet (dashed line) states calculated by using Eqs. (53) and (54). The experimental data obtained from photoluminescence measurements are taken from [7, 18, 43–45].

effective permittivity of the surrounding material (SiO_2 with a high content of Si nanocrystals), we obtain the value $0.2e^2/\kappa_1 a$ for the second term in Eq. (52). Thus, the energy of the exciton multiplet ground state is determined by the formula

$$E_{ex}^0 = E_g + 34.3\frac{\hbar^2}{2m_{\parallel}a^2} + 18.4\frac{\hbar^2}{2m_h a^2} - 2.3\frac{e^2}{\kappa_1 a}. \quad (53)$$

Performing analogous calculations for the first excited exciton multiplet, we obtain $-2.2e^2/\kappa_1 a$ and $0.3e^2/\kappa_1 a$ for the first and second terms in Eq. (52), respectively, and

$$E_{ex}^1 = E_g + 34.3\frac{\hbar^2}{2m_{\parallel}a^2} + 20.2\frac{\hbar^2}{2m_h a^2} - 1.9\frac{e^2}{\kappa_1 a} \quad (54)$$

for the exciton energy. The dependence of the exciton energy on the nanocrystal radius for the ground and first excited exciton multiplets is shown in Fig. 5. Experimental values of the exciton energy in nanocrystals are also shown in this figure.

5. CONCLUSIONS

Our results for the exciton energy agree quite well with the experimental data from [44, 45] on the photoluminescence of silicon nanocrystals of radius $2 < a < 4.5$ nm. There is substantial disagreement with the results from [7] and other studies carried out by the same group. The reason for the low photoluminescence energy of the samples used in [7] remains unclear. It should be noted that the range of nanocrystal radii indicated above has only been studied in a few publications. At present, no reliable experimental data are available for nanocrystals of larger radius.

For small nanocrystals (a < 2 nm), the results obtained in the effective-mass approximation can strongly differ from the experimental data, since the radius of such nanocrystals is fairly close to the Si lattice parameter and the conditions for the validity of the effective-mass approximation are not satisfied. It should be noted that the results obtained in this paper likewise cannot be used for nanocrystals of large radii ($a > 5$ nm), since in this case the exciton binding energy in bulk Si is comparable to or exceeds the confinement energy of electrons and holes. It is known that, in the limit of a large nanocrystal radius, it is necessary to take into account the quantization of the motion of an exciton as a whole [46].

Recently, it was shown [26] that the finiteness of the heights of the potential barriers for electrons and holes at the nanocrystal boundary can affect the energy of an electron–hole pair for small nanocrystal radii, a < 2.5 nm. Furthermore, it is known that the structure of the nanocrystal surface, depending on the environment and on the technological processes, such as passivation by hydrogen and oxidation, affects the nanocrystal radiation spectrum [18, 47]. To compare the experimental spectra with theoretical calculations, it is also necessary to take into account the dispersion in nanocrystal size [24], the difference in the shape of the nanocrystals from a sphere, and also the possibility of the polaron effect [48, 49]. Exact determination of the nanocrystal size is in itself a fairly complex experimental problem. Moreover, for the nanocrystals considered, radiation of a photon due to exciton recombination can occur both with and without the participation of phonons [4, 41]. Finally, many experimental photoluminescence spectra are measured at room temperature. In this case, exciton excited–state recombination is possible, since the energy separation between the ground and first excited states is comparable to or smaller than kT, while the energy separation between the ground and the higher excited states is comparable to kT.

It should be noted that further experimental and theoretical study of the properties of Si nanocrystals is a problem of significant fundamental and applied interest.

APPENDIX A

SYMMETRY PROPERTIES OF COULOMB INTEGRALS

Calculation of the correction to the energy of an electron–hole pair in a nanocrystal due to the interaction $V_1(\mathbf{r}_e, \mathbf{r}_h)$ can be reduced to calculation of integrals of the type

$$\iint dr_1^3 dr_2^3 \frac{1}{|\mathbf{r}_1 - \mathbf{r}_2|} \psi^*_{e,i}(\mathbf{r}_e)\psi^*_{h,j}(\mathbf{r}_h)\psi_{e,i'}(\mathbf{r}_e)\psi_{h,j'}(\mathbf{r}_h), \quad \text{(A1)}$$

where the subscripts i, i', j, and j' enumerate the electron and hole states. To calculate such integrals, it is convenient to use the expansion [38, 39, 50]

$$\frac{1}{|\mathbf{r}_e - \mathbf{r}_h|} = 4\pi \sum_{l=0}^{\infty} \sum_{m=-l}^{l} \frac{1}{2l+1} \frac{r_<^l}{r_>^{l+1}} \times Y_{lm}(\theta_e, \phi_e) Y^*_{lm}(\theta_h \phi_h), \quad \text{(A2)}$$

where θ_e, ϕ_e, θ_h, and ϕ_h are the angles in the spherical coordinate system corresponding to $\mathbf{r}_e$ and $\mathbf{r}_h$, respectively, and $r_>$ is the greater of the quantities r_e and r_h and $r_<$ is the smaller of these quantities. Here, it is convenient to choose the z axis (corresponding to $\theta = 0$ and $\theta = \pi$) along the direction of the longitudinal motion of electrons.

The distance between the zeroth and the first electron level is rather large, while the distance between the zeroth and the first hole level is small; the distance between the first hole level and the second hole level is also comparatively large. Therefore, we will consider only the exciton states originating from the lowest electronic level and the uppermost or first excited hole level. The wave function of the electron ground state does not depend on ϕ (see Eq. (12)). Therefore, when substituting expansion (A2) into Eq. (A1), the sum over m vanishes and only one term corresponding to $m = 0$ survives:

$$K_{j,j'} = 4\pi \iint dr_e^3 dr_h^3 \sum_{l=0}^{\infty} \frac{1}{2l+1} \frac{r_<^l}{r_>^{l+1}} Y_{l0}(\theta_e, \phi_e) \times Y^*_{l0}(\theta_h, \phi_h) |\psi_e(\mathbf{r}_e)|^2 \psi^*_{h,j}(\mathbf{r}_h)\psi_{h,j'}(\mathbf{r}_h). \quad \text{(A3)}$$

For the lowest electron level, we have the symmetry $\psi_e(\mathbf{r}, \theta) = \psi_e(\mathbf{r}, \pi - \theta)$ (Fig. 1). Since the spherical functions have symmetry

$$Y_{lm}(\theta, \phi) = (-1)^l Y_{lm}(\pi - \theta, \pi + \phi), \quad \text{(A4)}$$

for $m = 0$, from Eq. (A4) we have simply $Y_{l0}(\theta, \phi) = (-1)^l Y_{l0}(\pi - \theta, \phi)$, the subscript l in Eq. (A3) assumes only even values.

For the integrals mixing hole states, we have

$$K^{1SD,1P}_{M,M'} = 4\pi \iint dr_e^3 dr_h^3 \sum_{l=0}^{\infty} \frac{1}{2l+1} \frac{r_<^l}{r_>^{l+1}} \times Y_{l0}(\theta_e, \phi_e) Y^*_{l0}(\theta_h, \phi_h) |\psi_e(\mathbf{r}_e)|^2 \Big[R_0^S(r_h) R_1^P(r_h) \times Y_{00}(\theta_h, \phi_h) C^{1M}_{101M} Y_{10}(\theta_h, \phi_h) + R_0^D(r_h) R_1^P(r_h) \times \sum_{m_1, m_2} C^{1M}_{2m_1 1m_2} Y^*_{2m_1}(\theta_h, \phi_h) C^{1M}_{1m_1 1m_2} Y_{1m_1}(\theta_h, \phi_h) \Big] \delta_{M',M}. \quad \text{(A5)}$$

Due to the symmetry of spherical functions (A4) and to the fact that l is even, the integral in Eq. (A5) vanishes,

since the sum of all orbital quantum numbers characterizing the multiplied spherical harmonics is odd.

Thus, Coulomb interaction does not mix the unperturbed exciton states under study but only introduces a correction to their energy. For the lowest exciton state, we have

$$K^{1SD,\,1SD}_{M,\,M'} = 4\pi\iint dr_e^3 dr_h^3 \sum_{l=0}^{\infty}\frac{1}{2l+1}\frac{r_<^l}{r_>^{l+1}}Y_{l0}(\theta_e,\phi_e)$$

$$\times Y^*_{l0}(\theta_h,\phi_h)|\psi_e(\mathbf{r}_e)|^2\Big[(R_1^S(r_h))^2Y^2_{00}(\theta_h,\phi_h) + 2R_1^S(r_h) \quad \text{(A6)}$$

$$\times R_1^D(r_h)Y_{00}(\theta_h,\phi_h)C^{1M}_{201M}Y_{20}(\theta_h,\phi_h) + (R_1^D(r_h))^2$$

$$\times\sum_{m_1,\,m_2}C^{1M}_{2m_11m_2}Y^*_{2m_1}(\theta_h,\phi_h)C^{1M}_{2m_11m_2}Y_{2m_1}(\theta_h,\phi_h)\Big]\delta_{M',\,M}.$$

For $M = \pm1$,

$$C^{1M}_{201M} = \frac{1}{\sqrt{10}},$$

$$\sum_{m_1,\,m_2}C^{1M}_{2m_11m_2}Y^*_{2m_1}(\theta,\phi)C^{1M}_{2m_11m_2}Y_{2m_1}(\theta,\phi) = \frac{1}{4\pi} - \frac{1}{4\sqrt{5\pi}}Y_{20}(\theta,\phi). \quad \text{(A7)}$$

For $M = 0$,

$$C^{1M}_{201M} = -\sqrt{\frac{2}{5}},$$

$$\sum_{m_1,\,m_2}C^{1M}_{2m_11m_2}Y^*_{2m_1}(\theta,\phi)C^{1M}_{2m_11m_2}Y_{2m_1}(\theta,\phi) = \frac{1}{4\pi} + \frac{1}{2\sqrt{5\pi}}Y_{20}(\theta,\phi). \quad \text{(A8)}$$

We see that, because of the nonsphericity of the electronic state, the exciton level splits into two multiplet states, corresponding to $M = \pm1$ and 0.

For the second exciton state, we have

$$K^{1P,\,1P}_{M,\,M'} = 4\pi\iint dr_e^3 dr_h^3 \sum_{l=0}^{\infty}\frac{1}{2l+1}\frac{r_<^l}{r_>^{l+1}}$$

$$\times Y_{l0}(\theta_e,\phi_e)Y^*_{l0}(\theta_h,\phi_h)|\psi_e(\mathbf{r}_e)|^2(R_1^P(r_h))^2 \quad \text{(A9)}$$

$$\times\sum_{m_1,\,m_2}C^{1M}_{1m_11m_2}Y^*_{1m_1}(\theta_h,\phi_h)C^{1M}_{1m_11m_2}Y_{1m_1}(\theta_h,\phi_h)\delta_{M',\,M}.$$

For $M = \pm1$,

$$\sum_{m_1,\,m_2}C^{1M}_{1m_11m_2}Y^*_{1m_1}(\theta,\phi)C^{1M}_{1m_11m_2}Y_{1m_1}(\theta,\phi) = \frac{1}{4\pi} + \frac{1}{4\sqrt{5\pi}}Y_{20}(\theta,\phi). \quad \text{(A10)}$$

For $M = 0$,

$$\sum_{m_1,\,m_2}C^{1M}_{1m_11m_2}Y^*_{1m_1}(\theta,\phi)C^{1M}_{1m_11m_2}Y_{1m_1}(\theta,\phi) = \frac{1}{4\pi} - \frac{1}{2\sqrt{5\pi}}Y_{20}(\theta,\phi). \quad \text{(A11)}$$

Thus, the second level also splits into two multiplet states.

As a result, we can rewrite Eqs. (A6) and (A9) in the form

$$-\frac{e^2}{\kappa_1}K = E_{C1} + \Delta_M, \quad \text{(A12)}$$

where

$$E_{C1} = \int d^3r_e d^3r_h V_1(\mathbf{r}_e,\mathbf{r}_h)|\psi_e(\mathbf{r}_e)|^2 \times[(R_1^S(r_h))^2 + (R_1^D(r_h))^2]/(4\pi) \quad \text{(A13)}$$

for the ground exciton multiplet state,

$$E_{C1} = \int d^3r_e d^3r_h V_1(\mathbf{r}_e,\mathbf{r}_h)|\psi_e(\mathbf{r}_e)|^2(R_1^P(r_h))^2/(4\pi) \quad \text{(A14)}$$

for the first excited exciton multiplet state, and Δ_M is a correction depending on M and related to the presence of overlap integrals between $Y_{20}(\theta_h, \phi_h)$ and the electronic probability density $|\psi_e(\mathbf{r}_e)|^2$ in Eqs. (A6) and (A9). For the ground exciton multiplet state, the correction Δ_M appears only due to a small admixture of hole d states; therefore, in this case, this correction contains additional smallness. For the states differing in the absolute value of the quantum number M, the splitting is approximately $0.035e^2/\kappa_1 a$. For the first excited multiplet state, the splitting is approximately $0.21e^2/\kappa_1 a$.

The calculation of the correction to the energy of an electron–hole pair in a nanocrystal due to the interaction $V_2(\mathbf{r}_e, \mathbf{r}_h)$ given by Eq. (50) is performed in a similar manner; in this case, for the first term in Eq. (50), we used the expansion

$$P_l(\cos\theta) = \frac{4\pi}{2l+1}\sum_{m=-l}^{l}Y_{lm}(\theta_e,\phi_e)Y^*_{lm}(\theta_h,\phi_h), \quad \text{(A15)}$$

where θ is the angle between $\mathbf{r}_e$ and $\mathbf{r}_h$. For the second and third terms in Eq. (50), only components of the hole wave function that are independent of θ and ϕ are important. This part of the Hamiltonian also contains a correction due to nonsphericity of the lowest electronic state; however, since the energy change due to V_2 is sufficiently small compared to the energy change due to V_1 (but is greater than the splitting in M due to V_1), this additional correction can be neglected.

ACKNOWLEDGMENTS

The study was supported by the Russian Foundation for Basic Research, the Russian Academy of Sciences, the President of the Russian Federation (grant no. NSh-2192.2003.2 for supporting leading scientific schools,), INTAS (grant no. 03-51-6486), and a NATO Linkage Grant.

REFERENCES

1. M. Cardona and F. H. Pollak, Phys. Rev. **142**, 530 (1966).
2. L. Pavesi, L. Dal Negro, C. Mazzoleni, G. Franzo, and F. Priolo, Nature **408**, 440 (2000).
3. M. S. Hybertsen, Phys. Rev. Lett. **72**, 1514 (1994).
4. D. Kovalev, H. Heckler, M. Ben-Chorin, G. Polisski, M. Schwartzkopff, and F. Koch, Phys. Rev. Lett. **81**, 2803 (1998).
5. M. Fujii, M. Yoshida, Y. Kanzawa, S. Hayashi, and K. Yamamoto, Appl. Phys. Lett. **71**, 1198 (1997).
6. G. Franzo, V. Vinciguerra, and F. Priolo, Appl. Phys. A **69**, 3 (1999).
7. K. Watanabe, M. Fujii, and S. Hayashi, J. Appl. Phys. **90**, 4761 (2001).
8. D. Kovalev, E. Gross, N. Künzner, F. Koch, V. Yu. Timoshenko, and M. Fujii, Phys. Rev. Lett. **89**, 137401 (2002).
9. S. Ögüt, J. R. Chelikowsky, and S. G. Louie, Phys. Rev. Lett. **79**, 1770 (1997).
10. F. A. Reboredo, A. Franceschetti, and A. Zunger, Phys. Rev. B **61**, 13073 (2000).
11. A. Franceschetti and A. Zunger, Phys. Rev. B **62**, 2614 (2000).
12. B. Delley and E. F. Steigmeier, Phys. Rev. B **47**, 1397 (1993).
13. B. Delley and E. F. Steigmeier, Appl. Phys. Lett. **67**, 2370 (1995).
14. I. Vasiliev, S. Ögüt, and J. R. Chelikowsky, Phys. Rev. B **65**, 115416 (2002).
15. C. Delerue, M. Lanoo, and G. Allan, Phys. Rev. Lett. **76**, 3038 (1996).
16. S. Y. Ren, Phys. Rev. B **55**, 4665 (1997).
17. K. Leung and K. B. Whaley, Phys. Rev. B **56**, 7455 (1997).
18. M. V. Wolkin, J. Jorne, P. M. Fauchet, *et al.*, Phys. Rev. Lett. **82**, 197 (1999).
19. Y. M. Niquet, C. Delerue, G. Allan, and M. Lannoo, Phys. Rev. B **62**, 5109 (2000).
20. J. See, P. Dollfus, and S. Galdin, Phys. Rev. B **66**, 193307 (2002).
21. D. Babic, R. Tsu, and R. F. Greene, Phys. Rev. B **45**, 14150 (1992).
22. T. Takagahara and K. Takeda, Phys. Rev. B **46**, 15578 (1992).
23. J. B. Khurgin, E. W. Forsythe, G. S. Tompa, and B. A. Khan, Appl. Phys. Lett. **69**, 1241 (1996).
24. P. F. Trwoga, A. J. Kenyon, and C. W. Pitt, J. Appl. Phys. **83**, 3789 (1998).
25. V. A. Burdov, Zh. Éksp. Teor. Fiz. **121**, 480 (2002) [JETP **94**, 411 (2002)].
26. V. A. Burdov, Fiz. Tekh. Poluprovodn. (St. Petersburg) **36**, 1233 (2002) [Semiconductors **36**, 1154 (2002)].
27. C. S. Garoufalis, A. D. Zdetsis, and S. Grimme, Phys. Rev. Lett. **87**, 276402 (2001).
28. A. J. Williamson, J. C. Grossman, R. Q. Hood, A. Puzder, and G. Galli, Phys. Rev. Lett. **89**, 196803 (2002).
29. A. Baldereschi and N. O. Lipari, Phys. Rev. B **8**, 2697 (1973).
30. G. Dresselhaus, A. F. Kip, and C. Kittel, Phys. Rev. **98**, 398 (1955).
31. A. A. Kopylov and A. N. Pikhtin, Fiz. Tekh. Poluprovodn. (Leningrad) **11**, 867 (1977) [Sov. Phys. Semicond. **11**, 510 (1977)].
32. A. A. Kopylov, Fiz. Tekh. Poluprovodn. (Leningrad) **16**, 2141 (1982) [Sov. Phys. Semicond. **16**, 1380 (1982)].
33. G. L. Bir and G. E. Pikus, *Symmetry and Strain-Induced Effects in Semiconductors* (Nauka, Moscow, 1972; Wiley, New York, 1975).
34. A. B. Migdal, *Qualitative Methods in Quantum Theory* (Nauka, Moscow, 1975; Benjamin, Reading, Mass., 1977).
35. V. N. Abakumov, V. I. Perel, and I. N. Yassievich, in *Nonradiative Recombination in Semiconductors*, Vol. 33 of *Modern Problems in Condensed Matter Sciences*, Ed. by V. M. Agranovich and A. A. Maradudin (Peterb. Inst. Yad. Fiz., St. Petersburg, 1998; North-Holland, Amsterdam, 1991).
36. A. Dargys and J. Kundrotas, *Handbook on Physical Properties of Ge, Si, GaAs, and InP* (Science and Encyclopedia, Vilnius, 1994).
37. A. R. Edmonds, *Angular Momentum in Quantum Mechanics* (Princeton Univ. Press, Princeton, N.J., 1957; Inostrannaya Literatura, Moscow, 1958).
38. B. L. Gel'mont and M. I. D'yakonov, Fiz. Tekh. Poluprovodn. (Leningrad) **5**, 2191 (1971) [Sov. Phys. Semicond. **5**, 1905 (1971)].
39. L. E. Brus, J. Chem. Phys. **80**, 4403 (1984).
40. V. V. Batygin and I. N. Toptygin, *Problem Book on Electrodynamics* (NITs Regular. Khaot. Din., Moscow, 2002).

41. D. Kovalev, H. Heckler, G. Polisski, and F. Koch, Phys. Status Solidi B **215**, 871 (1999).
42. Al. L. Efros, M. Rosen, M. Kuno, M. Nirmal, D. J. Norris, and M. Bawendi, Phys. Rev. B **54**, 4843 (1996).
43. Y. Kanzawa, T. Kageyama, S. Takeda, M. Fujii, S. Hayashi, and K. Yamamoto, Solid State Commun. **102**, 533 (1997).
44. B. Garrido Fernandez, M. Lopez, C. Garcia, A. Perez-Rodrigues, J. R. Morante, C. Bonafos, M. Carrada, and A. Claverie, J. Appl. Phys. **91**, 798 (2002).
45. S. Schuppler, S. L. Friedman, M. A. Marcus, D. L. Adler, Y.-H. Xie, F. M. Ross, T. D. Harris, W. L. Brown, Y. J. Chabal, L. E. Brus, and P. H. Citrin, Phys. Rev. Lett. **72**, 2648 (1994).
46. Al. L. Éfros and A. L. Éfros, Fiz. Tekh. Poluprovodn. (Leningrad) **16**, 1200 (1982) [Sov. Phys. Semicond. **16**, 767 (1982)].
47. J. P. Wilcoxon, G. A. Samara, and P. N. Provencio, Phys. Rev. B **60**, 2704 (1999).
48. T. Takagahara and K. Takeda, Phys. Rev. B **53**, R4205 (1996).
49. M. A. Odnoblyudov, I. N. Yassievich, and K. A. Chao, Phys. Rev. Lett. **83**, 4884 (1999).
50. J.-B. Xia, Phys. Rev. B **40**, 8500 (1989).

Translated by I. Zvyagin

Physics of the Solid State, Vol. 46, No. 8, 2004, pp. 1520–1527. Translated from Fizika Tverdogo Tela, Vol. 46, No. 8, 2004, pp. 1476–1483.
Original Russian Text Copyright © 2004 by Yugova, Mil'vidskiĭ, Vdovin.

LOW-DIMENSIONAL SYSTEMS AND SURFACE PHYSICS

Defect Formation in $Ge_{1-x}Si_x$/Ge(111) Epitaxial Heterostructures

T. G. Yugova*, M. G. Mil'vidskiĭ, and V. I. Vdovin****

** Giredmet State Research Institute, Moscow, 109017 Russia*

*** Institute for Chemical Problems of Microelectronics, Bol'shoĭ Tolmachevskiĭ per. 5, Moscow, 109017 Russia*

e-mail: icpm@mail.girmet.ru

Received January 12, 2004

Abstract—Selective chemical etching and transmission electron microscopy are used to study the defect formation in $Ge_{1-x}Si_x$/Ge(111) epitaxial heterostructures at $0.01 < x < 0.35$. As the Si content in the solid solution (SS) increases, the dislocation densities in the epitaxial layer, at the interface, and in the near-interface region in the substrate are found to vary nonmonotonically. The difference in the depth distribution of dislocations observed in the heterostructures in three different SS composition ranges is caused by the effect of the SS composition on the kinetics of misfit-stress relaxation, in particular, on the intensity of misfit-dislocation generation and multiplication. It is found that, in the heterostructures grown by hydride epitaxy at 600°C, misfit-dislocation multiplication through a modified Frank–Read mechanism occurs only in the range $0.03 < x < 0.20$. The results obtained are explained in the context of the effect of silicon-rich microprecipitates, which form during the spinodal decomposition of the SS, on dislocation generation and motion in the epitaxial layer. A mechanism is proposed for misfit-dislocation generation by heterogeneous sources in the epitaxial layer; the mechanism is based on the generation of interstitial dislocation loops near microprecipitates. © *2004 MAIK "Nauka/Interperiodica".*

1. INTRODUCTION

Studying the processes of misfit-stress relaxation in epitaxial heterostructures is still a challenging problem in modern semiconductor materials science. Detailed knowledge of the mechanisms of misfit dislocation (MD) generation and multiplication is necessary for the development of new methods for producing strongly relaxed thin buffer layers with low threading dislocation densities [1–4].

The relaxation of misfit stresses in SiGe/Si heterostructures has been the subject of numerous studies (e.g., see reviews [5, 6]). However, various interpretations have been proposed for the phenomena observed in those studies. For example, Houghton [7] proposed a theoretical model of misfit-stress plastic relaxation that was thought to correctly explain the experimental data obtained on single- and multilayer SiGe/Si heterostructures with various Ge contents in the solid solution (SS). According to this model, the activation energies for dislocation generation (Q_n) and slip (Q_v) are independent of the SS composition, effective shear stress τ_{eff}, and the geometry of the stressed epitaxial layer. As a result, the misfit-stress relaxation rate in the heterostructures should be determined by the only parameter ($\tau_{eff}^{4.5}$) depending on the SS composition. However, there are data indicating that stress relaxation in the heterostructures exhibits a more complex dependence on the SS composition. It was shown in [8] that there is a sharp contrast between the kinetics of stress relaxation in $Si_{1-y}Ge_y$/Si heterostructures with a Ge content of ~0.15 and ~0.25. This result was explained as resulting from an increase in the retardation of glide MDs at their intersections with dislocations from orthogonal arrays when the Ge content in the SS increases. In [9], SiGe/Si(100) and GeSi/Ge(100) heterostructures with approximately the same misfit stresses were studied and the dislocation slip velocity was found to be much higher in layers grown on Ge wafers. This result was accounted for by a decrease in Q_v with increasing Ge content in the SS. These findings indicate that the SiGe solution composition has a significant effect on the MD behavior during misfit-stress relaxation. However, the nature of this phenomenon is still unclear.

In studying the processes of stress relaxation, most attention has been concentrated recently on the interaction of dislocations with other dislocations and with point defects and the effect of the microinhomogeneity of the SS on defect formation [6, 10–13]. These phenomena do affect the generation and propagation of MDs in layers. In [6], a mechanism was proposed for MD generation by heterogeneous sources in SiGe/Si heterostructures; the mechanism involved the nucleation of vacancy dislocation loops near Ge-rich precipitates. Unfortunately, the origin of the sufficiently high vacancy concentration in the SiGe layers was not analyzed in [6]. The interaction of MDs with identical Burgers vectors at the intersection points in the MD network formed at the interface brings about the formation of MD multiplication sources through the Frank–

Parameters of the $Ge_{1-x}Si_x$/Ge(111) epitaxial heterostructures under study (x is the Si content in the SS, h is the layer thickness, T is the growth temperature, E_ε is the specific energy of the elastically stressed interface, h_{CR} is the critical layer thickness for MDs to be introduced in the interface, h_{FR} is the critical layer thickness for MD multiplication through the Frank–Read mechanism, and FR means experimental confirmation of the operation of the Frank–Read mechanism)

Parameter	Sample no.											
	1	2	3	4	5	6	7	8	9	10	11	12
x, at. fraction	0.016	0.025	0.030	0.035	0.042	0.064	0.082	0.115	0.135	0.207	0.29	0.315
h, μm	3.5	2.1	1.0	2.5	0.85	0.25	3.5	3.5	2.3	>1.5	2.5	>0.5
T, °C	600									660	705	
E_ε, J/m^2	0.2	0.3	0.2	0.8	0.4	0.3	6.2	12.1	11.0		55.2	
h_{CR}, μm	0.29	0.16	0.13	0.11	0.092	0.054	0.040	0.026	0.022		0.008	
h_{FR}, μm	**2.9**	**1.6**	1.3	**1.1**	0.92	0.54	**0.40**	**0.26**	**0.22**		**0.08**	
FR				+			+	+	+			

Read mechanism. Various versions of the so-called modified Frank–Read mechanism were proposed in [14, 15], where the geometric features of forming dislocation structures were experimentally studied. This mechanism was also studied theoretically using numerical simulation [16]. When studying $Si_{1-y}Ge_y$/Si(100) heterostructures grown by molecular beam epitaxy (MBE) [11] and MBE with a gaseous Ge source [12], we found that MDs multiply through the Frank–Read mechanism in a relatively narrow SS composition range ($0.02 < y < 0.20$). In this range, the heterostructures exhibited a nonmonotonic change in the dislocation density in the layer and the near-interface region in the wafer. This peculiar feature of the Frank–Read mechanism cannot be explained in terms of any well-known models and requires further investigation.

Thus, the question as to which mechanisms of dislocation generation, motion, and multiplication provide misfit-stress plastic relaxation in heterostructures is still an open question and requires further investigation. From this standpoint, GeSi/Ge heterostructures seem to be promising, since they differ in some characteristics from SiGe/Si heterostructures; namely, they have another base component of the SS, strains of other signs in their constituents, and higher plasticity of the wafer. Moreover, these heterostructures have been studied in much less detail. Actually, the dependence of the dislocation slip velocity in the epitaxial layers on the SS composition in GeSi/Ge heterostructures has been studied only in [9]. The goal of this work is to study the formation of a dislocation structure in GeSi/Ge heterostructures over a wide SS composition range. Attention is focused on the effect of the SS composition on the processes of MD generation, motion, and multiplication.

2. EXPERIMENTAL

Epitaxial $Ge_{1-x}Si_x$ solid-solution layers were grown on Ge(111) wafers by hydride epitaxy; the growth technique is described in [17]. The dislocation density in the wafer (substrate) was less than 10^3 cm^{-2}. The basic parameters of the heterostructures grown are given in the table. A sufficiently high growth temperature and a relatively thick SS layer provided misfit-stress relaxation during epitaxial growth.

To solve the problem formulated above, a certain relation between the epitaxial-layer thickness and the lattice mismatch of the heteropair elements must be maintained. The criterion of this relation can be the energy per unit area of the elastically stressed interface [18–20], which is calculated from the formula [21]

$$E_\varepsilon = [2G(1+\gamma)/(1-\gamma)]\varepsilon^2 h, \quad (1)$$

where G and γ are the shear modulus and the Poisson ratio in the isotropic solid, respectively; ε is the elastic strain of the epitaxial layer caused by the mismatch f of the layer and wafer lattice parameters; and h is the layer thickness. The stored energy of the elastically stressed layer determines the value of τ_{eff}, which is the driving force of dislocation generation and motion [7], and the resulting relaxation of misfit stresses in the heterostructure. From this standpoint, in order to study the effect of the SS composition on the formation of a dislocation structure, it is desirable to use heterostructures with the same value of E_ε. In heterostructures where the misfit stress is partially relaxed during epitaxial growth, the interface energy consists of elastically stressed and plastically relaxed components. This heterostructure state is described by the relation

$$\varepsilon = f - \delta, \quad (2)$$

where δ is the portion of strain that is relieved upon the introduction of MDs into the interface. However, in order to make a general estimate of the adequacy of the samples for investigation, it will suffice to use E_ε calculated for an elastically stressed layer. The table lists the values of E_ε calculated from Eq. (1) for the samples

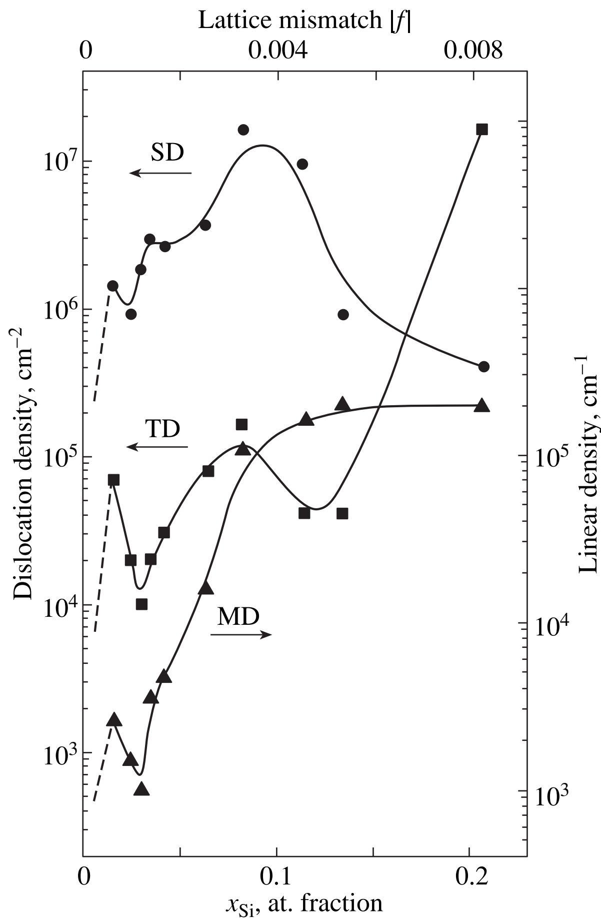

Fig. 1. Dependences of the linear MD density at the interface and the threading-dislocation densities in the layer (TD) and the substrate (SD) on the SS composition in $Ge_{1-x}Si_x$/Ge heterostructures.

under study. For the calculation, we used the values $G = 5.64 \times 10^{11}$ dyn/cm^2 and $\gamma = 0.2$ for Ge [22]. As follows form these data, samples 1–6 exhibit comparable values of E_ε. This fact allows us to correctly compare the dislocation structures formed in these samples. In samples 7–9, we can also compare their structural characteristics. In samples with a higher Si content in the SS (samples 10–12), defects form through other mechanisms, as will be shown below; therefore, the fact that the values of E_ε differ significantly in them is not essential for comparing their structural characteristics with those of other samples.

Structural examination was performed by selective etching of inclined polished sections of the heterostructures in combination with optical interference microscopy and transmission electron microscopy (TEM). We studied the effect of the SS composition on the linear MD density N_{MD} at the interface and the densities of threading dislocations in the layers (N_{TD}) and dislocations in the near-interface region in the substrate (N_{SD}). The dislocation densities in the layers and substrates were determined from dislocation etching pits, which were revealed with an etchant based on $K_3Fe(CN)_6$ and KOH. The linear MD density was measured using electron-microscopic images of longitudinal sections of the heterostructures near the interface.

3. EXPERIMENTAL RESULTS

Figure 1 shows the generalized data characterizing the dislocation density in the $Ge_{1-x}Si_x$/Ge heterostructures as a function of the Si composition in the SS. For the sake of systematization and simplicity, the SS composition range is conventionally divided into three ranges: $x \leq 0.03$, $0.03 < x < 0.20$, and $x > 0.20$. These ranges differ radically in the depth distribution of dislocations in the heterostructures. The third composition range is not shown in Fig. 1, since a one-type dislocation structure with a virtually constant density $N_{TD} \geq 10^9$ cm^{-2} is observed in this range. It should be noted that these ranges are conventional and can shift toward either side depending on the epitaxial growth conditions (layer thickness, growth temperature, substrate orientation, growth technique, etc.).

3.1. Composition Range $x \leq 0.03$

The main characteristic feature of the dislocation structures in the heterostructures in this range is the presence of a flat regular MD network (Fig. 2a) located strictly in the interface plane (Fig. 2b). The trigonal MD network consists of straight 60° dislocation lines oriented along the ⟨110⟩ directions. Note that such a network exhibits asymmetric linear MD density in the dislocation arrays in all three directions. Moreover, the dislocation structures contain groups of parallel MDs with identical Burgers vectors (Fig. 2a), which likely form as a result of dislocation multiplication at the interface through a Hagen–Strunk-like mechanism [23] proposed earlier to describe defect formation in heterostructures with a (100) growth surface. The regular arrangement of MDs at the interface and the absence of dislocation half-loops in the near-interface region in the substrate indicate the absence of MD multiplication through the Frank–Read mechanism. Since the values of N_{MD} in the layers exceed the initial dislocation densities in the substrates, MDs are generated not only by the dislocations growing from these substrates but also by other sources. The high dislocation density, $(1–2) \times 10^6$ cm^{-2}, in the near-interface region in the substrate is caused by the bending of dislocation lines near the intersection points of MDs [24] and the deviation of short dislocation segments from the interface toward the substrate to a depth of ≈0.1 μm (Fig. 2b). It is these tilt dislocation segments that are revealed by chemical etching in the substrate.

In this composition range, as follows from Fig. 1, the dislocation densities in all regions of the heterostructures (N_{MD}, N_{TD}, N_{SD}) decrease with increasing Si

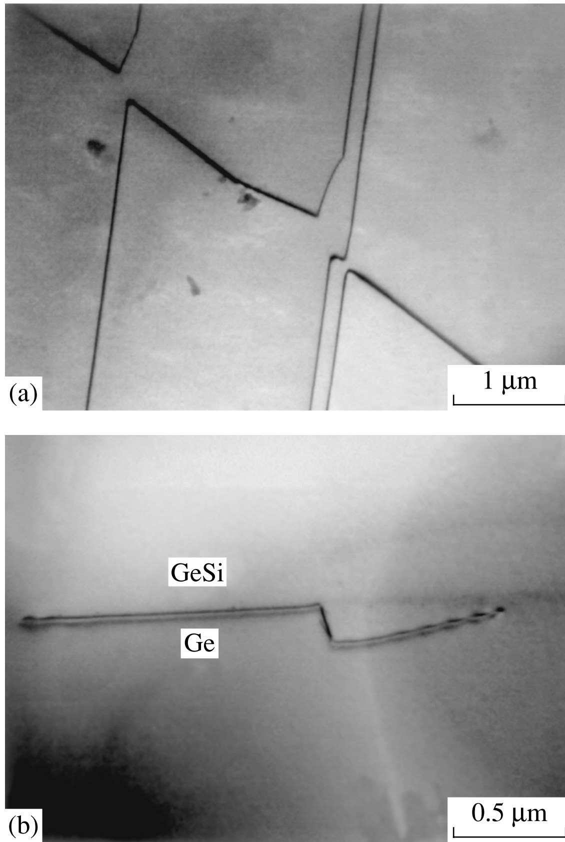

Fig. 2. TEM images of the dislocation structure in (a) longitudinal and (b) transverse sections of the $Ge_{0.984}Si_{0.016}$/Ge heterostructure (SS composition range $x \leq 0.03$).

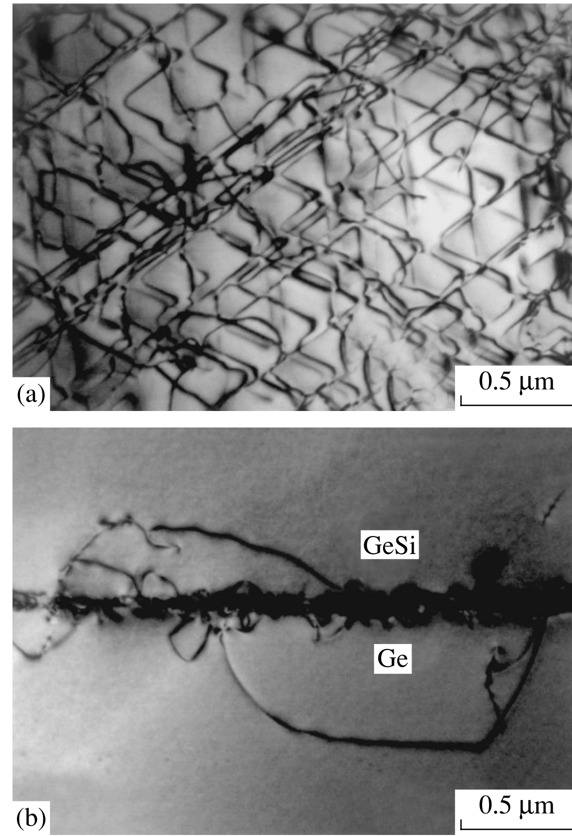

Fig. 3. TEM images of the dislocation structure in (a) longitudinal and (b) transverse sections of the $Ge_{0.918}Si_{0.082}$/Ge heterostructure (SS composition range $0.03 < x < 0.20$).

content in the SS and reach minimum values near $x \approx 0.03$. It should be noted that these concentration curves are more complex, since, near $x \approx 0$, the dislocation densities N_{TD} and N_{SD} must decrease to the initial dislocation density in the substrate and N_{MD} must decrease to zero (these segments are shown by dashed lines in Fig. 1). Therefore, we may expect the curves to bend downward and exhibit a maximum.

3.2. Composition Range $0.03 < x < 0.20$

The main specific feature of the dislocation structure of the heterostructures in this SS composition range is a three-dimensional MD network in the vicinity of the interface. Typical TEM images of the MD network are shown in Fig. 3. As is seen from the image of a longitudinal section, the dense MD network mainly contains regularly arranged dislocation lines along the ⟨110⟩ directions; against the background of these lines, there are many curved segments (Fig. 3a). These curved segments are dislocation half-loops coming from the MD network into both the substrate and the epitaxial layer (Fig. 3b). A stacked MD arrangement takes place at the interface within a 0.1-μm-thick layer. The dislocation density in the substrates of heterostructures is about two orders of magnitude higher than the threading-dislocation density in the layer. These data indicate that MDs in the heterostructures of this composition range multiply through the Frank–Read mechanism. It should be noted that the depth of propagation of the dislocation half-loops into the Ge substrate in the heterostructures with a maximum degree of plastic strain in their substrates does not exceed 2 μm. This value is smaller than the corresponding value (up to 3 μm) for analogous SiGe/Si heterostructures [11].

Earlier [12], we found that a three-dimensional network develops gradually in SiGe/Si heterostructures with increasing layer thickness because of dislocation multiplication in the regular flat MD network that initially forms at the interface. The dislocation multiplication is assumed to begin when a certain “second critical” layer thickness h_{FR} is achieved [25]. According to quantitative estimations, this thickness is an order of magnitude greater than the critical thickness h_{CR} at which MDs are introduced into the interface. The values of h_{CR} calculated by us from the formula given in [7] and the values of h_{FR} ($h_{FR} = 10h_{CR}$) for the samples

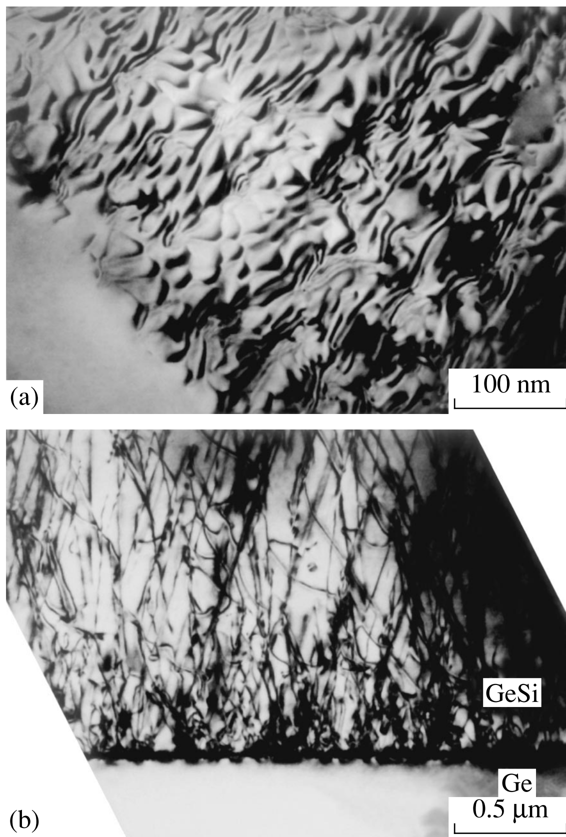

Fig. 4. TEM images of the dislocation structure in (a) longitudinal and (b) transverse sections of the $Ge_{0.71}Si_{0.29}$/Ge heterostructure (SS composition range $x > 0.20$).

under study are listed in the table. The values of h_{FR} that turn out to be smaller than the real layer thickness appear in bold. In the corresponding samples, dislocation multiplication should occur through a modified Frank–Read mechanism. The samples in which dislocation structures characteristic of this multiplication were observed experimentally are marked (as FR) in the lower line of the table. The table shows that, in this composition range, the calculated and experimental data are in good agreement. In samples 5 and 6, which have relatively thin epitaxial layers, flat regular MD networks are formed. In the heterostructures with $h > h_{FR}$ (samples 4, 7–9), well-developed three-dimensional dislocation networks are formed. These results illustrate the evolution of the MD network in GeSi/Ge heterostructures from the flat to a three-dimensional network during layer growth.

Within this composition range, the concentration dependences of the dislocation density are seen to be complex (Fig. 1). The MD density at the interface increases sharply at the beginning of this range and levels off at $x > 0.10$ (at a level of $N_{MD} \approx 2 \times 10^5$ cm^{-1}). In the most of this range, the N_{SD} and N_{TD} concentration curves coincide and have a domelike shape. This shape is caused by a nonmonotonic change in the intensity of MD multiplication with increasing x. In the range $0.03 < x \le 0.8$, the intensity of MD multiplication increases, reaches a maximum at $x \approx 0.8$, and then decreases rapidly. As the Si concentration in the SS increases further ($0.13 < x < 0.20$), the N_{SD} and N_{TD} concentration curves become different. The density N_{SD} decreases to a minimum value because the MD multiplication ceases almost completely (which is supported by the absence of dislocation half-loops in the substrate), whereas N_{TD} increases sharply. These heterostructures have a dense MD network, which is localized near the interface and consists predominantly of irregularly arranged MDs; this likely indicates a transition from layer-by-layer growth of the epitaxial layers to island growth.

3.3. Composition Range $x > 0.20$

In this SS composition range, epitaxial growth proceeds through the island mechanism due to high misfit stresses. Islands grow randomly with respect to each other and the substrate, which is indicated by a moiré pattern with nonparallel fringes of neighboring local regions about 0.1 μm in size. As a result, such heterostructures have a dense irregular MD network at the interface (Fig. 4a) and a forest of threading dislocations ($N_{TD} \ge 10^9$ cm^{-2}) in their epitaxial layers. The substrate has no plastic strain (Fig. 4b). This dislocation structure is characteristic of the whole SS composition range up to $x = 1$.

4. DISCUSSION OF THE RESULTS

The experimental data show that, as the mismatch f increases, the threading-dislocation densities in the substrate and the layer of the $Ge_{1-x}Si_x$/Ge heterostructures and the MD density at the interface vary nonmonotonically. The difference between the depth distributions of dislocations in the SS composition ranges considered above is related to the specific features of MD generation and multiplication in each range. An important factor that depends on the $Ge_{1-x}Si_x$ SS composition and affects the processes of defect formation is the presence of specific microinhomogeneities (caused by the spinodal decomposition of the SS) in the epitaxial layers. The spinodal decomposition occurs at the surface of the growing layer and is accompanied by the formation of a silicon-rich layer of microprecipitates and by its subsequent growth into the layer matrix. The spinodal decomposition intensity depends on the Si content in the SS; namely, the microprecipitate sizes and concentration increase with x. In this paper, we define microprecipitates as Si-rich microinhomogeneities in the SS that are coherent with the layer matrix. Ge-rich microprecipitates in $Si_{1-y}Ge_y$ solid solutions were studied in [6] and found to have a platelike shape.

Elastic stresses in a crystal lattice are known to decrease the enthalpy of formation of intrinsic point defects (vacancies for compressive stresses and interstitials for tensile stresses) and, hence, increase their equilibrium concentration [26]. In $Ge_{1-x}Si_x$/Ge heterostructures, the epitaxial layer undergoes tensile stresses ($f < 0$), since the substrate has a larger lattice parameter. Therefore, the epitaxial layers should be enriched in germanium interstitial atoms (Ge_i). The Ge_i concentration in the SS should increase with the Si content in this solution. Silicon-rich microprecipitates have a smaller lattice parameter than the SS matrix; therefore, potentially, they can be stress concentrators and affect the Ge_i concentration in their local environment. However, in relatively thick epitaxial layers, the hydrostatic (dilatation) component of the stress field should be tensile inside the precipitates and zero in the surrounding matrix. The situation changes radically if a microprecipitate is located in the immediate vicinity of the free surface of the epitaxial layer (when the spacing between the surface and the microprecipitate is smaller or equal to its size). In this case, due to the strong screening of the normal component of the stress field of the microprecipitate by the free surface, the hydrostatic component can become negative in the region between the microprecipitate and the free surface and be positive at the lateral sides of the platelike microprecipitate. These lateral zones can be filled with interstitial atoms, which will be accompanied by the formation of dislocation interstitial loops [27]. This situation occurs in the material under study; indeed, as noted above, microprecipitates form at the surface of an elastically stressed growing layer and the related interstitial-atom Ge_i migration proceeds during the subsequent growth of the microprecipitates into the layer matrix.

Sufficiently large microprecipitates can serve as centers of heterogeneous MD generation when dislocation loops of critical sizes form near them. When such a loop is formed in a plane parallel to the interface, a segment of the loop comes into the inclined {111} slip plane and slides rapidly to the surface of the epitaxial layer under the action of misfit stresses. As a result of breaking of the dislocation line, a 60° half-loop with sliding inclined segments forms at the layer surface. The slip of these inclined segments in the layer leads to the formation of MDs at the interface. An analogous MD generation mechanism (but based on the formation of dislocation vacancy loops near Ge-rich microprecipitates) was considered earlier for SiGe/Si heterostructures [6].

Based on these concepts, we can explain our experimental results as follows. When a growing layer reaches a critical thickness, dislocations growing from the substrate begin to curve toward the interface plane and MDs are formed. This mechanism is the first to manifest itself in all heterostructures irrespective of the SS composition (the f value). MDs also form through heterogeneous dislocation generation at microprecipitates. In the epitaxial layers belonging to the first SS composition range ($x \leq 0.03$), the finest microprecipitates form with a large scatter in size. Therefore, a relatively small addition of the largest microprecipitates manifests itself as centers of heterogeneous MD generation. Since the misfit stresses in the heterostructures are relatively low ($|f| < 1.2 \times 10^{-3}$), we can assume that the concentration of the centers of heterogeneous MD generation in the corresponding layers is virtually constant. Under these conditions, the decrease in dislocation density exhibited by all concentration curves can only be caused by a decrease in the dislocation velocity in the layers with increasing x. This conclusion is experimentally confirmed by the results of measuring the dislocation mobility in these samples [28]. One of the most probable causes of the decrease in the dislocation velocity can be the dragging effect of disperse microprecipitates. This effect is also likely to explain the absence of MD multiplication through the Frank–Read mechanism in the samples belonging to the composition range in question when the layer thickness exceeds the corresponding critical thickness h_{FR} for dislocation multiplication (samples 1, 2).

In the second SS composition range ($0.03 < x < 0.20$), the defect formation changes in character because of a sharp increase in the dislocation generation rate. This is caused, on one hand, by the microprecipitate size and concentration increasing with the Si content in the epitaxial layer and, on the other, by the corresponding increase in the misfit stresses in the heterostructures. As the misfit f increases, the critical dislocation-loop size decreases [6]. As a result, the density N_{MD} in the initially formed regular MD networks at the interface increases with f (samples 5, 6). The MD density detected in the initial networks provides the relaxation of only an insignificant part of the misfit stresses, namely, about 3% for the layers with $x = 0.042$ and $h = 0.85$ μm and 7% for the layers with $x = 0.064$ and $h = 0.25$ μm. The degree of relaxation was estimated from the ratio of the experimental value of N_{MD} to its value calculated assuming complete relaxation of misfit stresses due to the regular arrangement of 60° MDs in the interface plane ($b_{eff} = 1.15$ Å). In such heterostructures, high residual stresses are retained and multiplication sources in the form of dislocation corners bent into the substrate are formed in the regular networks. Therefore, as the layer thickness increases, MD multiplication through the Frank–Read mechanism is activated in these heterostructures.

At $x > 0.08$ in this SS composition range, a further increase in the concentration of dislocation generation centers provides the limiting MD density in the initial network (the concentration curve of N_{MD} levels off). At these MD densities, the intensity of dislocation multiplication decreases sharply and the Frank–Read mechanism is not operative. Similar termination of the Frank–Read mechanism was also observed in

SiGe/Si(100) heterostructures at an MD density in the network of $N_{MD} \approx 8 \times 10^4$ cm^{-1} [15].

Another factor that indirectly depends on the SS composition and affects the defect formation is the epitaxial-layer growth mechanism. In the SS composition range $x < 0.15$, the layer-by-layer growth mechanism, which is optimum for the formation of a regular dislocation structure, is operative. In the SS composition range $0.15 < x < 0.20$ ($6 \times 10^{-3} < |f| < 1 \times 10^{-2}$), this mechanism gradually transforms into the island epitaxial-growth mechanism. In the corresponding heterostructures, irregularly arranged MDs form at the interface and a dense forest of threading dislocations forms in the layer. When the layer grows in the third composition range ($x > 0.20$, ($|f| > 1 \times 10^{-2}$), pronounced island growth takes place; 0.1-μm islands are disoriented with respect to each other. This factor dictates the formation of a threading-dislocation forest in such layers with a virtually constant density $N_{TD} \geq 10^9$ cm^{-2}. In such heterostructures, MDs most likely arise as a result of the generation of dislocation half-loops at the surface of the growing layer [29].

5. CONCLUSIONS

The effect of the solid-solution composition on defect formation in $Ge_{1-x}Si_x$/Ge(111) epitaxial heterostructures produced by hydride epitaxy has been studied. Using TEM and selective etching, we obtained data on the depth distribution of dislocations. The character of the dislocation distribution was shown to be different in three different SS composition ranges ($x \leq 0.03$, $0.03 < x < 0.20$, $x > 0.20$). As the Si content in the SS increases, the densities of threading dislocations in the epitaxial layer and the substrate and the MD density at the interface change nonmonotonically. The formation of a dislocation structure in each composition range is mainly determined by the MD generation rate and the MD multiplication intensity.

We have proposed a mechanism for MD generation from interstitial dislocation loops that form during the coalescence of interstitial Ge_i atoms in the vicinity of Si-rich (compared with the initial SS) platelike microprecipitates that are coherent with the crystalline matrix.

In the heterostructures under study, MD multiplication through a modified Frank–Read mechanism occurs only in the composition range $0.03 < x < 0.20$ at epitaxial-layer thicknesses that are about one order of magnitude larger than the critical thickness. In the initial stages of misfit-stress relaxation in such heterostructures, a flat regular MD network is formed, which transforms into a three-dimensional network in the course of MD multiplication. In this composition range, the MD multiplication intensity changes nonmonotonically as the Si content in the SS increases; namely, the intensity reaches maximum values at $x \approx 0.08$ and virtually vanishes at $x \approx 0.20$.

In the SiGe/Ge heterostructures, MD multiplication through the Frank–Read mechanism has been found to occur just as in SiGe/Si heterostructures, irrespective of the sign of misfit stresses. A characteristic indication of the operation of this mechanism is the propagation of dislocation half-loops from the interface to the substrate.

ACKNOWLEDGMENTS

We thank L.K. Orlov and O.A. Kuznetsov for supplying the epitaxial structures.

This work was supported by the Russian Foundation for Basic Research, project no. 02-02-16692.

REFERENCES

1. T. Hackbarth, H.-J. Herzog, M. Zeuner, G. Höck, E. A. Fitzgerald, M. Bulsara, C. Rosenblad, and H. von Känel, Thin Solid Films **369**, 148 (2000).
2. M. Bauer, K. Lyutovich, M. Oehme, E. Kasper, H.-J. Herzog, and F. Ernst, Thin Solid Films **369**, 152 (2000).
3. C. S. Peng, Z. Y. Zhao, H. Chen, J. H. Li, Y. K. Li, L. W. Guo, D. Y. Dai, Q. Huang, J. M. Zhou, Y. H. Zhang, T. T. Sheng, and C. H. Tung, Appl. Phys. Lett. **72**, 3160 (1998).
4. F. K. LeGoues, MRS Bull., April 38 (1996).
5. Yu. B. Bolkhovityanov, O. P. Pchelyakov, and S. I. Chikichev, Usp. Fiz. Nauk **171**, 689 (2001) [Phys. Usp. **44**, 655 (2001)].
6. D. D. Perovic and D. C. Houghton, Inst. Phys. Conf. Ser. **146**, 117 (1995).
7. D. C. Houghton, J. Appl. Phys. **70**, 2136 (1991).
8. R. Hull and J. C. Bean, Appl. Phys. Lett. **54**, 925 (1989).
9. R. Hull, J. C. Bean, L. J. Peticolas, B. E. Weir, K. Prabhakaran, and T. Ogino, Appl. Phys. Lett. **65**, 327 (1994).
10. R. Hull, E. A. Stach, R. Tromb, F. Ross, and M. Reuter, Phys. Status Solidi A **171**, 133 (1999).
11. V. I. Vdovin, M. G. Milvidskii, T. G. Yugova, K. L. Lyutovich, and S. M. Saidov, J. Cryst. Growth **141**, 109 (1994).
12. T. G. Yugova, V. I. Vdovin, M. G. Milvidskii, L. K. Orlov, V. A. Tolomasov, A. V. Potapov, and N. V. Abrosimov, Thin Solid Films **336**, 112 (1998).
13. V. I. Vdovin, Phys. Status Solidi A **171**, 239 (1999).
14. A. Lefebvre, C. Herbeaux, C. Bouillet, and J. Di Persio, Philos. Mag. Lett. **63**, 23 (1991).
15. F. K. LeGoues, B. S. Meyerson, J. F. Morar, and P. D. Kirchner, J. Appl. Phys. **71**, 4230 (1992).
16. K. W. Schwarz, J. Appl. Phys. **85**, 120 (1999).
17. V. I. Vdovin, O. A. Kuznetsov, M. G. Mil'vidskiĭ, L. K. Orlov, and T. G. Yugova, Kristallografiya **38** (4), 269 (1993) [Crystallogr. Rep. **38**, 573 (1993)].
18. X. W. Liu, A. A. Hopgood, B. F. Usher, H. Wang, and N. S. Braithwaite, J. Appl. Phys. **88**, 5975 (2000).

19. A. R. Powell, S. S. Iyer, and F. K. LeGoues, Appl. Phys. Lett. **64**, 1856 (1994).

20. A. Rockett and C. J. Kiely, Phys. Rev. B **44**, 1154 (1991).

21. J. W. Matthews, J. Vac. Sci. Technol. **12**, 126 (1975).

22. J. P. Hirth and J. Lothe, *Theory of Dislocations* (McGraw-Hill, New York, 1967; Atomizdat, Moscow, 1972).

23. W. Hagen and H. Strunk, Appl. Phys. **47**, 85 (1978).

24. V. I. Vdovin, L. A. Matveeva, G. N. Semenova, M. Ya. Skorohod, Yu. A. Tkhorik, and L. S. Khazan, Phys. Status Solidi A **92**, 379 (1985).

25. R. Beanland, J. Appl. Phys. **72**, 4031 (1992).

26. M. G. Mil'vidskiĭ, N. S. Rytova, and E. V. Solov'eva, in *Problems in Crystallography* (Nauka, Moscow, 1987) [in Russian].

27. M. Yu. Gutkin, I. A. Odiv'ko, and A. G. Sheinerman, J. Phys.: Condens. Matter **15**, 3539 (2003).

28. M. V. Mezhennyi, M. G. Mil'vidskii, and T. G. Yugova, J. Phys.: Condens. Matter **14**, 12997 (2002).

29. E. P. Kvam, Philos. Mag. Lett. **62**, 167 (1990).

Translated by K. Shakhlevich

Physics of the Solid State, Vol. 46, No. 8, 2004, pp. 1528–1532. Translated from Fizika Tverdogo Tela, Vol. 46, No. 8, 2004, pp. 1484–1488.
Original Russian Text Copyright © 2004 by Gaĭsler, Semenova, Sharafutdinov, Kolesov.

LOW-DIMENSIONAL SYSTEMS AND SURFACE PHYSICS

Analysis of Raman Spectra of Amorphous–Nanocrystalline Silicon Films

S. V. Gaĭsler*, O. I. Semenova, R. G. Sharafutdinov***, and B. A. Kolesov******

**Novosibirsk State University, ul. Pirogova 2, Novosibirsk, 630090 Russia*
***Institute of Semiconductor Physics, Siberian Division, Russian Academy of Sciences, pr. Akademika Lavrent'eva 13, Novosibirsk, 630090 Russia*
****Institute of Thermal Physics, Siberian Division, Russian Academy of Sciences, pr. Akademika Lavrent'eva 1, Novosibirsk, 630090 Russia*
*****Nikolaev Institute of Inorganic Chemistry, Siberian Division, Russian Academy of Sciences, pr. Akademika Lavrent'eva 3, Novosibirsk, 630090 Russia*
e-mail: kolesov@che.nsk.su
Received October 30, 2003

Abstract—A new method is proposed for the treatment of Raman spectra of amorphous–nanocrystalline silicon films serving as a major component in solar cells. The method is based on the well-known theory of strong spatial localization (confinement) of phonons and offers the possibility of estimating the fractional content of the amorphous and crystalline phases in a film and the size distribution of nanocrystals. © *2004 MAIK "Nauka/Interperiodica".*

1. INTRODUCTION

Interest in photoelectric solar power converters stems from ecological considerations and the steady reduction of their production costs, which makes them the most promising source of renewable energy. The efforts of researchers and engineers working in the area of solar cell production have been shifting increasingly toward the development of thin-film silicon technology. Deposition of amorphous and microcrystalline silicon layers on low-cost substrates (stainless steel, plastics, glass) appears presently to hold the greatest promise [1–3]. Films prepared in these conditions are usually a mixture of amorphous and microcrystalline silicon. The crystalline phase consists, as a rule, of nanocrystals 30–100 Å in size differing from bulk crystals in terms of their physical properties. The characteristics of thin-film solar cells are governed to a considerable extent by the properties of the silicon layers, which makes monitoring their physical characteristics and phase composition an aspect of paramount importance. Raman spectroscopy is the most appropriate and convenient method for reaching this goal due to its high speed (the time required to measure the spectrum of a Si film is ≈1 min), high spatial resolution (1–2 μm), nondestructive character, and the fact that there is no need for preliminary sample preparation. The spectrum contains complete information on the phase composition of the sample, and the problem actually consists in extracting this information as fully as possible.

The phonon spectrum of nanocrystals is usually described in terms of the model proposed in [4, 5] postulating strong spatial localization (confinement). Assuming spherical crystallites of diameter D and phonon decay following the $\exp(-\alpha r^2 D^2)$ law, the Raman line shape is given by the integral [5]

$$I(\omega) \propto \int \exp\left(-\frac{q^2 D^2}{4}\right) \frac{d\mathbf{q}}{[\omega(\mathbf{q}) - \omega]^2 + (\Gamma_0/2)^2}, \quad (1)$$

where Γ_0 is the natural linewidth of a bulk crystal and $\omega(\mathbf{q})$ is the phonon frequency. The phonon wave vector is expressed in units of $2\pi/a_0$, where a_0 is the silicon lattice constant (0.543 nm).

This expression was employed in [6] to describe an experimental Raman spectrum of a film assuming it to consist of crystallites of one size and the amorphous phase. In analyzing the Raman spectra of porous silicon, the problem was complicated in [7] by assuming a Gaussian size distribution of crystallites and by introducing the corresponding factor into integral (1).

In [8], the ratio between the scattering intensities at frequencies of 520 cm^{-1} (I_c) and 480 cm^{-1} (I_a) in the film spectrum was accepted as a measure of sample crystallinity. Being straightforward and simple to obtain, the I_c/I_a ratio is essentially an abstract parameter that is in no way related to the real film structure. For this reason, the content of the crystalline phase was additionally determined in [8] by deconvoluting the spectrum into four components, two of which corresponded to the amorphous phase and the other two, to crystallites 35 and 200 Å in size.

This communication pursues a somewhat different goal. We believed it essential to estimate this distribution from the spectra themselves, rather than to preset

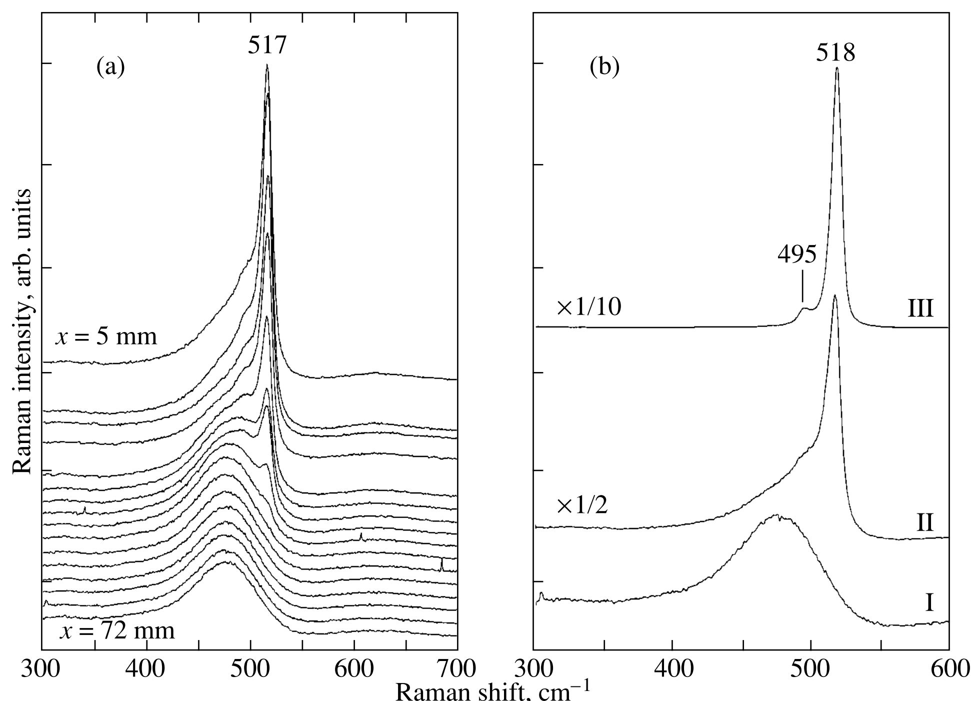

Fig. 1. (a) Raman spectra obtained from different regions of the same silicon film at different distances from its edge and (b) typical Raman spectra of films. Intensity of spectrum II is halved (×1/2), and that of spectrum III is reduced by ten times (×1/10).

the nanoparticle size distribution in advance in analyzing various Raman spectra of amorphous–nanocrystalline silicon films. Our approach would enable one to extract as fully as possible the information contained in a spectrum and to correct the technological conditions of film deposition.

2. EXPERIMENTAL

The amorphous–nanocrystalline silicon films under study were prepared using the gas-jet electron-beam plasma-enhanced chemical vapor deposition technology (GJEB PE CVD) [9]. The film thickness was derived from reflectance spectra in the near IR region (800–2000 nm, UV 3101PC spectrophotometer, Shimadzu) and varied within 300–600 nm.

Raman spectra were measured with a Triplemate SPEX spectrometer equipped with a liquid nitrogen–cooled LN 1340PB (Princeton Instruments) multichannel CCD camera. The spectra were excited by a 488-nm argon laser line with a power at the sample surface of no greater than 5 mW. The excitation wavelength was chosen so as to reduce the light penetration depth and prevent formation of the substrate spectrum, and the excitation power was low in order to preclude light-induced sample crystallization. The sample was placed in the focal plane of a microscope whose objective, (LD EPIPLAN, 40/0.60 Pol. Zeiss), with an operating distance of 2 mm and an aperture of 0.6, served to focus the laser beam and collect the scattered radiation. The laser beam spot on the sample surface was 2 μm in diameter. In the experiments, 180° scattering geometry was used. Raman spectra of films were measured with a resolution of 5 cm^{-1}.

3. RESULTS

Figure 1a presents Raman spectra of a film obtained for different values of the distance x (in mm) from the edge of the film facing the nozzle of the gas source, and Fig. 1b shows typical Raman spectra, two of which (I, II) are those shown in Fig. 1a and the third (III) was measured on a film prepared in different technological conditions.

One readily sees that Raman spectra reflect either solely an amorphous state with a broad band peaking at ~475 cm^{-1} (Fig. 1b, I), an amorphous–nanocrystalline state (Fig. 1b, II), or again a predominantly nanocrystalline phase (Fig. 1b, III). The Raman band peak position of nanoparticles varies from 514 to 518 cm^{-1}; i.e., it is always lower than the phonon frequency in a bulk crystal (520 cm^{-1}). Note the feature at 495 cm^{-1} in spectra II and III (Fig. 1b), whose origin still remains to be established.

4. ANALYSIS OF THE RAMAN SPECTRA

To describe the structure of a film, namely, the degree of its crystallinity and the nanocrystal size distribution, we introduce a trial function. To do this, we use Eq. (1) to calculate the line profiles for nanocrystals

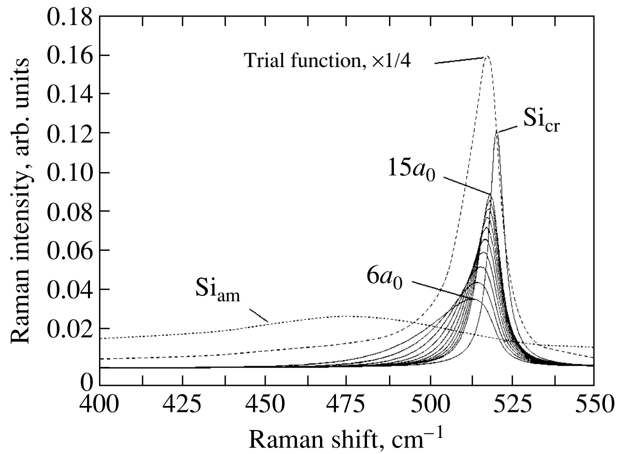

Fig. 2. Calculated profiles of Raman spectra from particles with different diameters (solid lines) and from the amorphous phase. All spectra are normalized against unit integrated intensity. Dashed line is a trial function (see text). The intensity for the trial function is reduced by four times (×1/4).

with a diameter of $6a_0$ (3.3 nm), $7a_0$, etc., up to $15a_0$ and assign the same integrated intensity of unity to each line. The lower limit corresponds to particles ~3 nm in diameter, and the upper limit, to ~8 nm. Identification of particles less than 3 nm in diameter with crystalline formations is questionable. The profiles calculated for nanocrystals with diameters above $15a_0$ are close to one another and to the spectrum of a bulk crystal in terms of peak position and halfwidth and thus can be replaced by the latter. The spectrum of crystalline silicon obtained under the same conditions as the spectra of the other samples has a Lorentzian profile centered at 520 cm^{-1} with a halfwidth of 6 cm^{-1}. The calculated profiles are presented in Fig. 2. Also shown is a band corresponding to the amorphous phase, likewise with a unit intensity, and representing not a calculated Gaussian or a Lorentzian profile but rather an envelope of an experimental spectrum of a pure amorphous phase (bottom spectrum in Fig. 1a) intended to take into account the scattering from acoustic phonons and second-order scattering from combination tones. The amorphous and the nanocrystalline components are normalized in the same way, which finds justification in the fact that the integrated intensities (scattering cross sections) of both components are similar, I_c/I_a = 0.95 [6]. (In actuality, the integrated Raman line intensity of a crystal is about seven times that of the amorphous phase, which should be assigned to a difference not in the scattering cross section but rather in the absorption coefficient and, accordingly, in the depth of exciting-light penetration into the sample.) Summing up all the profiles, we obtain a trial function (Fig. 2). The contribution of each component to the experimental spectrum can be estimated by reduction, i.e., by mathematically dividing the experimental spectrum by a trial function. Figure 3a illustrates the reduction of typical spectra I, II, and III from Fig. 1b. Each of the spectra gives an idea of the phase contents and the distribution of particles in size. Because each of the spectra contains a large fraction of the amorphous phase (100% for spectrum I), one can make them still more revealing by subtracting spectrum I

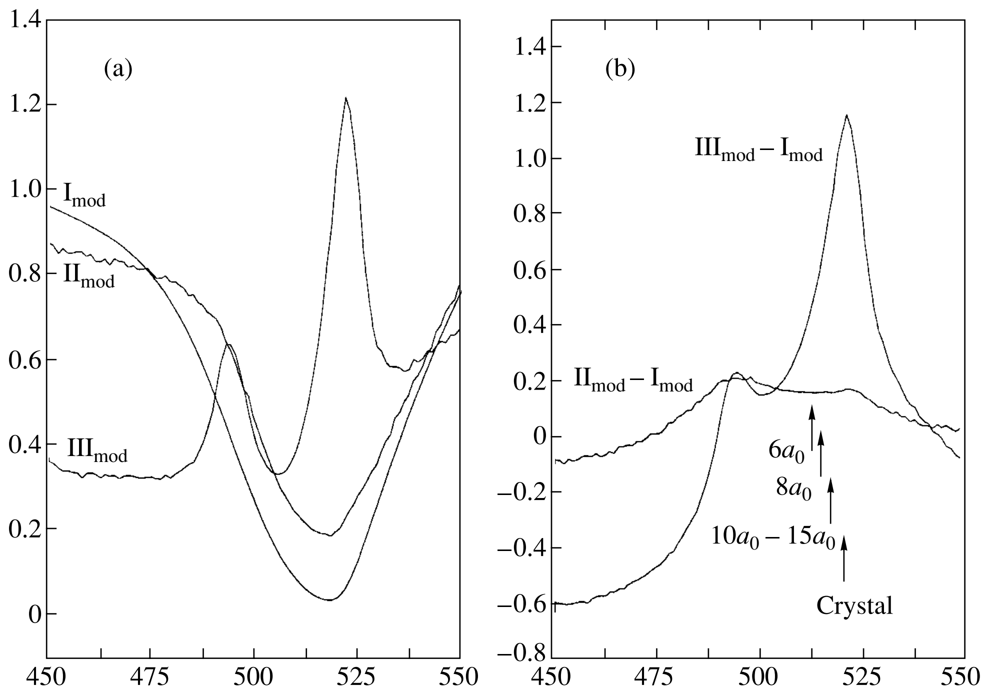

Fig. 3. (a) Reduction of the typical Raman spectra presented in Fig. 1b and (b) the difference between the reduced spectra (see text).

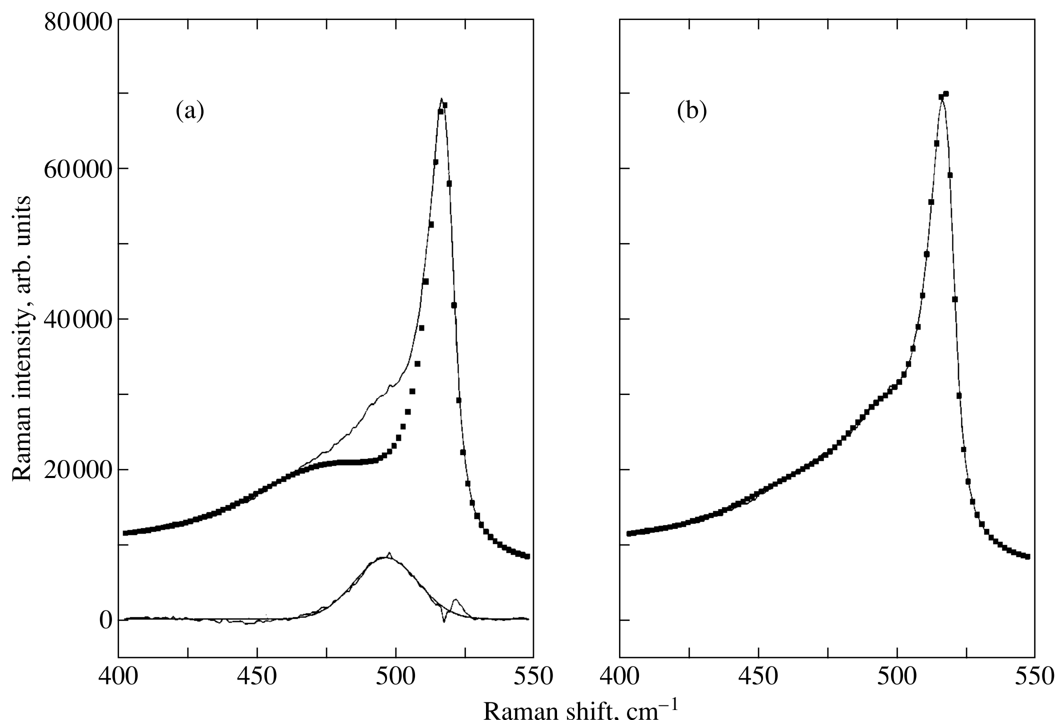

Fig. 4. (a) Comparison of the reconstructed Raman spectrum (without scattering at the *L* point) with the experimental spectrum (above), and the difference between the experimental and calculated spectra (below). (b) Same with scattering at the *L* point added. Solid line is experiment, and points are calculation.

from spectra II and III. The result of this procedure is displayed in Fig. 3b. Of most interest is the reduction of spectrum II, because spectra of this type are frequently met in studies of films and are the most difficult to interpret. As is evident from the distributions in Fig. 3, the fraction of the amorphous phase in the sample characterized by spectrum II is ~90%. The size distribution of nanoparticles is practically uniform, with a very weakly pronounced decrease in the fraction of large particles and of the bulk crystal. This may be used as a basis to attempt to reconstruct the experimental spectrum by adding up the corresponding fractions of "single-particle" functions and the amorphous phase (Fig. 2). The sum of the Raman spectra of nine fractions of the amorphous phase, particles $7a_0$, $8a_0$, $\ldots 14a_0$ in size (one fraction for each size), a 1/2 fraction of particles $15a_0$ in size, and a 1/4 fraction of the crystalline phase (i.e., of all nanoparticles more than 8 nm in size) is presented in Fig. 4a. We readily see that the reconstructed Raman spectrum is in accord with experiment in the frequency region corresponding to the amorphous phase and nanocrystals but disagrees with the experimental spectrum in the intermediate region 490–500 cm^{-1}. The application of scattering profiles to particles $6a_0$ or less in diameter, which have a strong and extended low-frequency wing, results in a considerable deviation of the calculated spectrum from the experimental spectrum in the range 400–480 cm^{-1}. The difference between the two spectra (Fig. 4a, bottom) is a Gaussian centered at 496 cm^{-1} with a halfwidth of 23 cm^{-1}. A similar feature, but shaped as a well-resolved spectral band, becomes manifest in the sample with a large (~60%) content of the nanocrystalline phase (spectrum III in Fig. 1b). It is well known that, at the center of the Brillouin zone of silicon, there may be one threefold degenerate vibration mode F_{2g}, which includes two transverse and one longitudinal optical phonon. When moving along the dispersion curve toward one of the high-symmetry points, this vibration splits into the TO and LO modes, whose frequencies at the L point are 493 and ~400 cm^{-1}, respectively [10]. Thus, the TO(L)-phonon frequency practically coincides with the position of the feature observed in the Raman spectra of films (495 cm^{-1} for the line in spectrum III in Fig. 1b). First-order Raman scattering at the zone-edge critical points is forbidden, but in nanocrystals the wave-vector selection rules are violated because of the decrease in the phonon correlation length, thus making such scattering possible. The same effect is responsible for the detection of frequency-shifted localized phonon modes at the zone center in nanocrystals. The phonon density of states and the vibration frequencies at the critical points in silicon have been repeatedly studied both theoretically and experimentally (see, e.g., [11]).

Figure 4b presents an experimental and a reconstructed spectrum with inclusion of the scattering at the L point. In this case, the agreement between the two spectra is quite satisfactory.

To sum up, Raman spectra contain complete information on the phase composition and structure of amorphous–crystalline films, which can be extracted through special treatment of the spectral data.

ACKNOWLEDGMENTS

The authors are deeply indebted to V.A. Gaĭsler (ISP, SD RAS) for useful discussions and valuable comments.

This study was supported by INTAS, project no. 01-2257.

REFERENCES

1. K. R. Catchpole, M. J. McCann, K. J. Weber, and A. W. Blakers, Sol. Energy Mater. Sol. Cells **68** (2), 173 (2001).
2. Yoshihiro Hamakawa, Sol. Energy Mater. Sol. Cells **74** (1), 13 (2002).
3. R. B. Bergmann and J. H. Werner, Thin Solid Films **403–404**, 162 (2002).
4. H. Richter, Z. P. Wang, and L. Ley, Solid State Commun. **39** (5), 625 (1981).
5. L. H. Campbell and P. M. Fauchet, Solid State Commun. **58** (10), 739 (1986).
6. V. G. Golubev, V. Yu. Davydov, A. V. Medvedev, A. B. Pevtsov, and N. A. Feoktistov, Fiz. Tverd. Tela (St. Petersburg) **39** (8), 1348 (1997) [Phys. Solid State **39**, 1197 (1997)].
7. Md. N. Islam and K. Satyendra, Appl. Phys. Lett. **78** (6), 715 (2001).
8. T. Kamei, P. Stradins, and A. Matsuda, Appl. Phys. Lett. **74** (12), 1707 (1999).
9. R. Sharafutdinov, S. Khmel, O. Semenova, S. Svitasheva, R. Bilyalov, and J. Poortmans, in *Proceedings of the 29th IEEE Photovoltaic Specialists Conference, New Orleans, USA, 2002* (IEEE, New York, 2002), p. 1178.
10. M. Balkanski and M. Nusimovici, Phys. Status Solidi **5**, 635 (1964).
11. M. Cardona, in *Light Scattering in Solids*, Ed. by M. Cardona and G. Guntherodt, 2nd ed. (Springer, Berlin, 1982; Mir, Moscow, 1984), Vol. 2.

Translated by G. Skrebtsov

Physics of the Solid State, Vol. 46, No. 8, 2004, pp. 1533–1537. Translated from Fizika Tverdogo Tela, Vol. 46, No. 8, 2004, pp. 1489–1493.
Original Russian Text Copyright © 2004 by Artamonov, Baĭdullaeva, Vlasenko, Vuĭchik, Litvin, Mozol', Strel'chuk.

LOW-DIMENSIONAL SYSTEMS AND SURFACE PHYSICS

Atomic-Force Microscopy and Raman Scattering Studies of Laser-Induced Structural Disordering on the *p*-CdTe Surface

V. V. Artamonov, A. Baĭdullaeva, A. I. Vlasenko, N. V. Vuĭchik, O. S. Litvin, P. E. Mozol', and V. V. Strel'chuk

Institute of Semiconductor Physics, National Academy of Sciences of Ukraine, pr. Nauki 45, Kiev, 03028 Ukraine
e-mail: baidulla@yahoo.com
Received December 10, 2003

Abstract—Atomic-force spectroscopy and Raman scattering are applied to study structural modification of the *p*-CdTe (111) surface under exposure to pulsed multimode ruby laser radiation of nanosecond duration and a power density below the material-melting and destruction thresholds. It is shown that irradiation of crystals produces nanometer quasi-ordered surface nanoclusters 1.0–11.3 nm in height with a lateral size of 41–336 nm. Possible mechanisms of their formation are discussed. © *2004 MAIK "Nauka/Interperiodica".*

1. INTRODUCTION

Laser irradiation of solids produces both isolated point (vacancies and interstices) and extended defects. Accumulation of these defects and their interaction intricately depend on the local temperature effects, irradiation dose, defect density, material properties, and other factors. The interaction between defects and the elastic strain field can bring about the formation of surface ordered structures, such as periodic structures and clusters ranging in linear size from a few micrometers to several nanometers [1–5]. The formation of such micrometer-sized structures caused by laser irradiation of semiconducting Si crystals has been explained in terms of two mechanisms: in-plane ordering of dislocation–strain instabilities and redistribution of dislocations between various atomic planes due to strain-induced drift of vacancies [3, 4].

A defect–deformation theory of the laser-induced structural modification of the semiconductor surface caused by the interaction between defects via the elastic strain field was proposed in [1, 2]. According to this theory, when the externally controlled concentration of laser-induced defects exceeds a threshold value, periodic structures or clusters of nanometer size are formed on the surface of solids.

In the case of binary compounds, in particular, CdTe, such nanometer-scale structures were not formed under laser irradiation. Therefore, it is urgent to search for the conditions under which laser irradiation of CdTe crystals causes the formation of low-dimensional ordered surface structures, as this would be promising for the development of modern optoelectronic engineering.

In this paper, we report on atomic-force spectroscopy and Raman spectroscopy studies of the laser-induced structural modification of surface layers of CdTe crystals grown by synthesis from Cd and Te vapors [6].

2. EXPERIMENTAL

Samples were irradiated at room temperature by single nanosecond pulses ($\tau = 2 \times 10^{-8}$ s) from a multimode Q-switched ruby laser with a pulse power density I below the surface destruction and melting thresholds ($I_1 = 3$ MW/cm^2 and $I_2 = 4.5$ MW/cm^2, respectively). The irradiation dose $D = NI\tau$ was changed by varying the number of pulses N.

The crystal surface morphology before and after irradiation was studied with a NanoScope IIIa (Digital Instruments) atomic-force microscope (AFM) operating in the tapping mode. Silicon probes with a nominal tip radius of ~10 nm were used for measurements. Raman scattering spectra were measured at $T = 80$ K using a setup based on a DFS-24 spectrometer. Raman spectra were excited by an Ar^+-laser beam with wavelength $\lambda_{ex} = 488.0$ nm and power $P < 50$ mW. The accuracy of determining the spectral position of phonon lines in the Raman spectra was improved by simultaneously recording the plasma lines and was no worse than 0.3 cm^{-1}.

We note that optical radiation of the ruby laser is absorbed in a thin CdTe surface layer of thickness $d \sim \alpha^{-1} \approx 10^{-4}$–$10^{-5}$ cm (the absorptivity is $\alpha = 6 \times 10^4$ cm^{-1} [7]). For this reason, it is expected that the main changes in the structural properties of CdTe will occur in a thin layer, whose thickness is defined by the value of α^{-1} and the thermal diffusion length (0.1–0.7 μm [8]).

1063-7834/04/4608-1533$26.00 © 2004 MAIK "Nauka/Interperiodica"

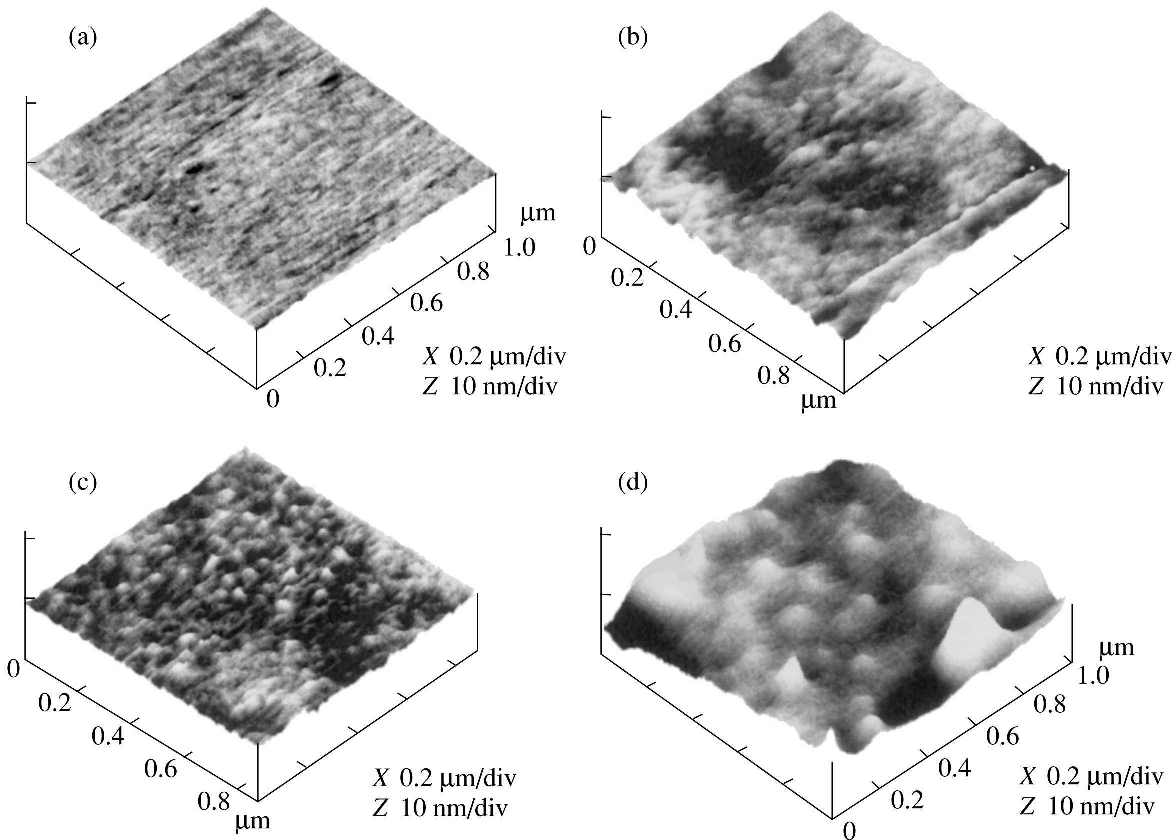

Fig. 1. AFM images of the surface of a CdTe crystal (a) in the initial state, (b) after irradiation with a dose $D_1 = 0.6$ J/cm^2 before and (c) after removal of the Te layer, and (d) after irradiation with a dose $D_2 = 0.9$ J/cm^2 before removal of the Te layer.

3. EXPERIMENTAL RESULTS

Figure 1 shows the AFM images of surface fragments (1 × 1 μm) obtained before and after laser irradiation of *p*-CdTe (111) crystals. The arithmetic mean roughness of the nonirradiated sample surface was ~0.056 nm; i.e., the crystal surface can be considered to be atomically smooth (Fig. 1a). Irradiation with a dose D_1 = 0.6 J/cm^2 brought about the formation of a microrelief and of nanoclusters against its background in the shape of smoothed hills with a lateral size of ~47 nm and an average height of ~1.0 nm (Fig. 1b). In this case, the arithmetic mean surface roughness increased to ~0.205 nm. The smoothed nanocluster shape is caused by a thin tellurium layer formed at the sample surface after irradiation [9]. After the Te film was removed (to this end, the irradiated samples were etched in a 1-N KOH solution in methanol), AFM studies were repeated. Figure 1c demonstrates that nanoclusters with a lateral size of ~41 nm and an average height of ~1.01 nm became more distinct on the sample surface after removal of the Te film. The arithmetic mean roughness of the surface after such treatment changed insignificantly. Furthermore, nanoclusters are ordered along certain directions, forming a quasiperiodic surface microrelief.

As the irradiation dose is increased to D_2 = 0.9 J/cm^2, larger nanoclusters are formed and their size variance increases. Their lateral size and average height before removal of the Te layer changed from ~185 to 256 nm and from ~2.0 to ~5.1 nm, respectively. After removal of the Te film, the lateral size and height of the clusters changed from ~164 to ~336 nm and from ~2.2 to ~11.3 nm, respectively (Fig. 1d). The arithmetic mean surface roughness was ~0.837 nm. It should be noted that the sizes and the character of the size distribution of nanoclusters depend on both the irradiation dose and uniformity of the laser beam spot.

Figure 2 shows the Raman spectra of CdTe exposed to a pulsed laser beam, and the inset shows AFM images of 30 × 30-μm fragments of the sample surface irradiated with a dose D_2 = 0.9 J/cm^2.

The spectrum of the initial sample (curve *1* in Fig. 2) contains only the longitudinal optical (LO) phonon band of CdTe, ν_{LO}(CdTe) ≈ 168 cm^{-1}. According to the selection rules for Raman scattering (in the backscattering geometry), scattering by LO and TO phonons is allowed in the case of the (111) crystal plane [10]. The fact that scattering by TO phonons was not observed in the Raman spectra under consideration is likely due to

the resonance conditions for excitation near the photonic gap $E_0 + \Delta_0$ [11]. The latter factor causes a significant increase in the LO(CdTe) band intensity due to the Fröhlich mechanism of electron–phonon coupling (in comparison to the TO(CdTe) band).

In the Raman spectrum of a sample irradiated with a dose D_1 = 0.6 J/cm^2, the LO(CdTe) band shifts to lower frequencies ($\Delta\nu \approx 2.4$ cm^{-1}) and its half-width increases (curve *2* in Fig. 2). In the low-frequency region of the Raman spectra, Rayleigh scattering is observed to occur, which is caused by elastic scattering of light from extended defects, the distance between which (≥10 μm) is smaller than the beam spot diameter (~100 μm). Such an extended defect is, e.g., a dislocation network, which can form during elastic stress relaxation [12] (see inset to Fig. 2). The formation of nanoclusters of fairly large density between dislocation lines in the irradiated samples (Fig. 1), as well as the fact that the thickness ($d \approx 1/2\alpha$) of the layer probed in Raman scattering is comparable to surface relief inhomogeneities, suggests that the main contribution to the Raman spectrum comes from the beam-modified surface layer. The Raman spectrum of the sample irradiated with a dose D_i contains not only the LO(CdTe) bands but also additional bands at ~123 and ~141 cm^{-1}, corresponding to the A_1 and E vibrational modes of trigonal tellurium. The large half-width of the observed Te lines and their low-energy shift with respect to the lines from single-crystal Te are manifestations of the size effects characteristic of a polycrystalline Te structure with very small crystallites [13–15]. We note that the Te absorptivity in the wavelength range under study reaches 10^6 cm^{-1}. Therefore, the mere fact that the LO(CdTe) band is observed in the presence of a Te film allows us to conclude that the Te film thickness is several tens of angstroms. After the Te film was removed from the sample surface, only the LO(CdTe) band was observed in the Raman spectrum (curve *3* in Fig. 2). In this case, the half-width of the LO(CdTe) band remains unchanged and its small shift is due to a decrease in mechanical stresses caused by the tellurium film.

The possible formation of oxides comprising the elements was also examined. The frequencies of characteristic vibrations of oxides should be much higher than those observed in our case [16]. Comprehensive measurements of Raman spectra in the frequency range 500–800 cm^{-1}, where intense bands of TeO_2 and $CdTeO_3$ should be observed [17], revealed no traces of them.

Figure 2 (curves *4*, *5*) shows Raman spectra of CdTe exposed to a laser beam with a dose D_2 = 0.9 J/cm^2. An increase in the irradiation dose causes a stronger low-frequency shift of the LO(CdTe) band and an appreciable decrease in its intensity (curve *4* in Fig. 2). It is worth noting that, in this case, in comparison with dose D_1, the bands of the tellurium A_1 and E modes shift to higher frequencies by ~2 cm^{-1} and their intensities

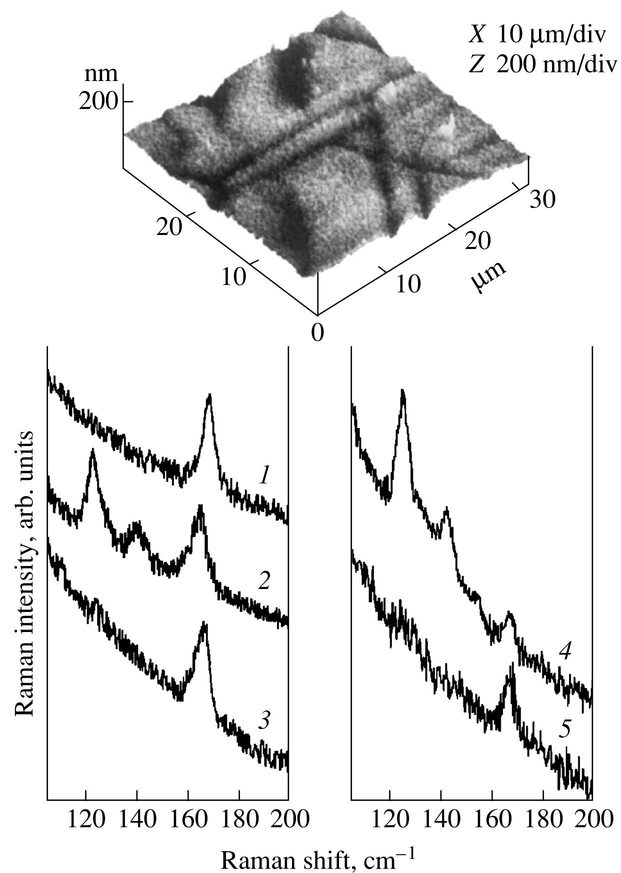

Fig. 2. Raman scattering spectra of crystalline CdTe (*1*) in the initial state, (*2*) after irradiation with dose D_1 before and (*3*) after removal of the Te layer, and (*4*) after irradiation with dose D_2 before and (*5*) after removal of the Te layer. The inset shows an AFM image of the sample irradiated with dose D_2 on the 30 × 30-μm scale.

increase. This fact can be due to both an increase in the stresses in the Te film and an increase in its thickness. In [18], it was shown that the frequencies of Te phonon bands decrease as the compressive stress increases. Hence, the fact that the experimentally determined phonon frequencies exceed the values characteristic of crystalline tellurium suggests that the tellurium film is under tensile stress [18].

4. DISCUSSION

The Te film formation at the irradiated sample surface is associated with the preferred removal of cadmium atoms from a surface layer. Mass-spectrometric studies of the composition of atomic flows during laser processing of CdTe showed that the number of Cd atoms exceeds the number of Te atoms by four times as a steady flow is established [19]. Thus, the surface layer exposed to a laser beam is depleted by cadmium and an amorphous Te film arises at the surface. We performed Auger spectrum studies of CdTe before and after laser irradiation, which showed that exposure of CdTe crys-

tals to nanosecond laser pulses with a power density below the destruction or melting threshold not only causes evaporation of Cd as a more volatile component but also changes the defect structure of the surface region [12]. The Auger electron spectra, like the Raman spectra, did not reveal any traces of oxides of the elements comprising the crystal. Excess tellurium forms an amorphous p-type film, which eventually crystallizes [5, 9]. The generation of point defects gives rise to elastic stresses propagating to a crystal depth of 2–3 μm. As the corresponding critical stresses are reached, their relaxation can result in the formation of relief surface structures. Their sizes depend on stresses, i.e., on the density of generated defects. Relaxation of these stresses was considered the cause of the formation of a micrometer-sized dislocation structure associated with the band at λ_{max} = 840 nm, which arises in photoluminescence spectra as a result of a recombination involving cationic point defects in CdTe crystals exposed to a laser beam [12]. It is interesting that dislocation networks begin to appear at an irradiation dose D = 0.32 J/cm^2 [5, 12], which is appreciably lower than the dose at which nanometer-sized clusters form. Therefore, the formation of the observed nanostructures can be explained in terms of the self-organization of defects due to screening of the strain field by point defects [2]. This circumstance arises as a certain critical point-defect density is reached. The density of defects generated by laser irradiation, as estimated using a formula from [3], is ~10^{19} cm^{-3}, which corresponds to the first critical value for screening of the elastic interaction between point defects [2]. In this case, defects are assembled into nanometer-sized clusters, which are self-trapped in strain wells. The formation of surface nanoclusters observed during irradiation of CdTe crystals with dose D_1 is likely caused by this mechanism. The increase in the nanocluster size at the higher dose D_2 can be associated with an increase in the doze at which the critical defect density is reached [2]. Thus, there are lower and upper limits of laser irradiation doses at which nanometer-sized clusters form at the CdTe crystal surface.

The structural disordering of the CdTe surface layer can be studied by analyzing the changes in the frequency and profile of the LO line in the Raman spectra in terms of the model of spatial correlation of phonons [13–15]. In the case under consideration, the band LO(CdTe) profile was analyzed after subtracting the Rayleigh scattering background.

This model assumes phonon localization in nanoclusters, which weakens the selection rules for the wave vector **q** for first-order Raman scattering (**q** = 0); i.e., transitions with **q** ≠ 0 become allowed. The latter factor results in broadening of the LO band, its asymmetry, and a low-frequency shift of the maximum.

Under the assumption that nanoclusters are homogeneous in a spherical region of diameter L (the correlation length) and that the localization factor for the phonon wave functions is Gaussian, the first-order Raman scattering intensity can be written as [13–15]

$$I(\nu) \propto \int_{L_1}^{L_2} N(L)dL \int_0^1 \frac{\exp(-q^2L^2/4a^2)}{[\nu - \nu(q)]^2 + (\Gamma_0/2)^2} d^3q,$$

where q is measured in units of $2\pi/a$, a is the lattice constant, Γ_0 = 3.5 cm^{-1} is the natural half-width of the LO-phonon line for the initial CdTe crystal, $\nu(q)$ describes the dispersion of phonon branches, and $N(L)$ is the Gaussian size distribution of nanocrystallites. We note that, within this model, correct results can be obtained if the spherical nanocrystallites are less than 50 nm in size.

An AFM study shows that the nanocrystal size is rather large; therefore, the lateral confinement of LO phonons is negligible. For this reason, we relate the broadening, asymmetry, and shift of the LO line to a change in the nanocluster size along the direction perpendicular to the crystal surface. Using the results from [9], we estimated the change in the average CdTe nanocluster size as a function of the irradiation area. For irradiation doses D_1 and D_2, the average nanocluster size is found to be ~7.5 and ~9.0 nm, respectively. The difference between the nanocluster sizes determined from the Raman spectra and AFM data can be explained as follows. The AFM data characterize only the inhomogeneity scale of the surface relief, while the Raman spectra are also formed by deeper surface regions extended to a certain crystal depth [12]. Furthermore, the measured average nanocluster size can also be affected by resonant enhancement of scattering from LO phonons in nanoclusters of certain sizes. Therefore, the nanocluster size determined by analyzing the LO(CdTe) line is only a rough estimate.

5. CONCLUSIONS

Thus, we have studied the structural modification of CdTe surface layers under nanosecond-pulsed laser radiation. It was shown that laser irradiation causes the formation of a thin tellurium film on the surface, as well as the generation of point defects and their subsequent clustering, which results in the formation of CdTe nanoclusters in the surface region. The sizes and the size distribution of surface nanoclusters depend on the laser radiation dose absorbed by the CdTe crystal.

REFERENCES

1. V. I. Emel'yanov and I. M. Panin, Fiz. Tverd. Tela (St. Petersburg) **39** (11), 2029 (1997) [Phys. Solid State **39**, 1815 (1997)].
2. V. I. Emel'yanov, Fiz. Tverd. Tela (St. Petersburg) **43** (4), 637 (2001) [Phys. Solid State **43**, 663 (2001)].
3. B. L. Volodin and B. I. Emel'yanov, Izv. Akad. Nauk SSSR, Ser. Fiz. **55** (7), 1274 (1991).

4. A. F. Banishev, B. L. Volodin, B. I. Emel'yanov, and K. S. Merzlyakov, Fiz. Tverd. Tela (Leningrad) **32** (9), 2529 (1990) [Sov. Phys. Solid State **32**, 1469 (1990)].
5. A. Baidullaeva, A. I. Vlasenko, A. V. Lomovtsev, and P. E. Mozol', in *Proceedings of International Conference on Extended Defects in Semiconductors, EDS-2002* (Bolonia, Italy, 2002), Abstracts, Part 1, p. 61.
6. B. A. Bulakh and S. M. Krasikova, Izv. Akad. Nauk SSSR, Neorg. Mater. **9** (7), 1112 (1973).
7. R. O. Bell, M. Toulermonde, and P. Siffert, J. Appl. Phys. **50** (1), 313 (1979).
8. S. A. Akhmanov, V. I. Emel'yanov, N. I. Koroteev, and V. N. Seminogov, Usp. Fiz. Nauk **147** (4), 675 (1985) [Sov. Phys. Usp. **28**, 1084 (1985)].
9. V. V. Artamonov, M. Ya. Valakh, A. P. Litvinchuk, and V. V. Strel'chuk, Poverkhnost, No. 1, 46 (1989).
10. M. Cardona, in *Light Scattering in Solids*, Ed. by M. Cardona and G. Guntherodt, 2nd ed. (Springer, Berlin, 1982; Mir, Moscow, 1984), Vol. 2.
11. Z. C. Feng, S. Perkowitz, J. M. Wrobel, and J. J. Dubovski, Phys. Rev. B **39** (17), 12997 (1989).
12. V. N. Babentsov, A. Baĭdullaeva, A. I. Vlasenko, S. I. Gorban', B. K. Dauletmuratov, and P. E. Mozol', Fiz. Tekh. Poluprovodn. (St. Petersburg) **27** (10), 1618 (1993) [Semiconductors **27**, 894 (1993)].
13. H. Richter, Z. P. Wang, and L. Ley, Solid State Commun. **39** (5), 625 (1981).
14. F. H. Pollak and R. Tsu, Proc. SPIE **452**, 25 (1983).
15. H. S. Mavi, B. G. Rasheed, A. K. Shukla, S. C. Abbi, and K. P. Jain, J. Phys. D **34**, 292 (2001).
16. A. S. Pine and G. Dressehaus, Phys. Rev. B **5** (10), 4087 (1972).
17. D. N. Bose and M. Holtz, Mater. Lett. **5** (7/8), 291 (1987).
18. W. Richter, J. B. Renucci, and M. Cardona, Phys. Status Solidi B **56** (1), 223 (1973).
19. J. J. Dubovski, P. K. Bhat, D. F. Williams, and P. Becla, J. Vac. Sci. Technol. A **4**, 1879 (1986).

Translated by A. Kazantsev

Physics of the Solid State, Vol. 46, No. 8, 2004, pp. 1538–1541. Translated from Fizika Tverdogo Tela, Vol. 46, No. 8, 2004, pp. 1494–1497.
Original Russian Text Copyright © 2004 by Bernatskiĭ, Pavlov.

Field Desorption of a Potassium–Gold Film on Tungsten

D. P. Bernatskiĭ and V. G. Pavlov

Ioffe Physicotechnical Institute, Russian Academy of Sciences, Politekhnicheskaya ul. 26, St. Petersburg, 194021 Russia

e-mail: bernatskii@ms.ioffe.rssi.ru, vpavlov@ms.ioffe.rssi.ru

Received November 18, 2003

Abstract—The formation and destruction of alloys and chemical compounds of gold with potassium occurring in their coadsorption on tungsten have been studied by continuous-mode field-desorption microscopy, field-emission microscopy, and time-of-flight mass analysis of the products of field-induced desorption. The effect of an electric field on these processes was investigated. Monatomic and cluster ions of potassium and its compounds with gold were found to appear in fields too weak for field desorption to set in. Chemical reactions give rise to autooscillations in the field desorption of potassium. *© 2004 MAIK "Nauka/Interperiodica".*

1. INTRODUCTION

Chemical compounds of gold with alkali metals exhibit unique physical and chemical properties [1–4]. They feature the largest bonding ionicity among all compounds of metals with metals. The volume of a compound is far less than the sum of the volumes of the starting components and even less than the volume of one of the components, the alkali metal. The electrical properties of the compounds are also unusual in that, depending on the actual composition and external conditions, they can behave as conductors, semiconductors, or insulators.

The unusual properties of the gold compounds and alloys with alkali metals should be particularly manifest on the surface and at interfaces, where the structure and the number of nearest neighbor gold and alkali metal atoms undergo a sharp change. Among these specific features, one could class the recently discovered increase in the diffusion rate under illumination [5] and autooscillations of the field-desorption ionic current [6].

The investigation of films of gold compounds with alkali metals also has application potential, because regions differing in conductivity type can be obtained in one film by slightly varying the chemical composition. Studying the effect of an electric field on the growth and destruction of films with scanning tunneling and atomic force microscopy may prove to be of particular interest in nanotechnology.

2. EXPERIMENTAL

Experiments were conducted with an ultrahigh-vacuum field-emission microscope, which can operate in the field-electron and field-desorption microscopy modes and perform time-of-flight mass analysis of the products of field desorption. Continuous-mode field-desorption images were obtained with potassium and cesium used as imaging substances. The base pressure in the instrument did not exceed 10^{-10} mm Hg. Emission images and time-of-flight spectra were recorded from the screens of the microscope and a storage oscillograph, respectively, with a video camera and fed to a computer for subsequent treatment and analysis.

A film of a gold compound with potassium was prepared on the surface of a tungsten tip from the gold and potassium atoms adsorbed on the tip. The potassium was deposited from a commercial IKO-34-9 directly heated source. Tantalum foil sources were fabricated for the deposition of gold. A piece of gold wire of 0.999 purity was placed on the source after degassing the source by heating in vacuum. To deposit the gold, the tip holder was positioned such that the apex of the tip faced the source. The adsorbates were deposited on the tip surface with the substrate maintained at room temperature.

The adsorbate surface concentration and the quality of the film formed were judged from the *I*–*V* characteristics of field electron emission (by determining the work function), as well as from field electron and desorption images and field desorption mass spectra.

3. RESULTS AND DISCUSSION

The field desorption mass spectra obtained directly after potassium and gold adsorption exhibited only single- and multiatomic potassium ions (K^+, K_2^+, K_3^+).

Field desorption of potassium from a surface with a gold–potassium adsorbate mixture revealed autooscillation effects [6]. These effects consisted in periodic variations of the ionic current and of the desorption images under constant experimental conditions. The image variations were shown in a periodic appearance and disappearance of desorption zones, their broadening and narrowing, migration over the tip surface, and local variations in the desorption intensity. The variations were observed at gold surface concentrations less than a monolayer or near the edge of a thicker gold film.

1063-7834/04/4608-1538$26.00 © 2004 MAIK "Nauka/Interperiodica"

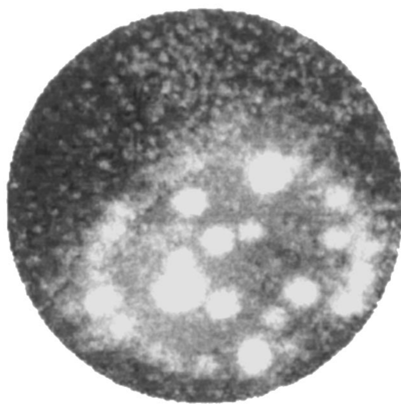

Fig. 1. Gold islands on the (110)W face (continuous-mode field-desorption image). Imaging adsorbate is cesium, imaging field is 1.5×10^7 V/cm, and $T = 500$ K.

Films of a gold compound with potassium were formed when the temperature increased to 500–800 K; they were visualized by field electron and field desorption images and were evident from mass spectra. Accordingly, films were prepared in three regimes: with no field applied, in a field desorbing the potassium, and in a field high enough to obtain field electron images. The order in which the adsorbates were deposited was also varied (first gold, then potassium, and in the reverse sequence). Gold was deposited under various angles of rotation of the tip relative to the gold source. Gold was applied either to the entire surface or to part of it. In the latter case, heating performed after the gold deposition resulted in surface diffusion of gold with a sharp front of propagation and the formation of islands behind the front. Field electron images of the gold film on tungsten had a weak contrast because of the adsorbate and the substrate having similar work functions; the diffusion front and the islands appearing in the continuous-mode field-desorption images were more distinct (Fig. 1).

Our experiments did not reveal any noticeable effect of the sequence in which the adsorbates were deposited and of the electric field on the formation and quality of the film thus formed. The film properties depended only on the amount of adsorbed gold. As already mentioned, in field desorption of mixtures of the gold and potassium adsorbates (desorbing fields $F < 10^8$ V/cm), only potassium ions were observed. After heating ($T >$ 500 K) and subsequent cooling to room temperature, signals of molecular ions containing gold atoms appeared in the field-desorption mass spectra (Fig. 2). Furthermore, such heating (giving rise to the formation of a film of the potassium–gold surface compound) brought about a substantial rise in the surface diffusion rate of potassium atoms and in the brightness of continuous-mode field-desorption images.

Destruction of a film and decomposition of the potassium–gold chemical compound by an electric field was studied by analyzing continuous-mode field-desorption images (Fig. 3) and mass spectra of the desorption products (Fig. 2). Three stages in the film destruction were detected. In the first stage (fields of 2.0–2.5 V/nm), the spectra contained potassium ion signals only. The desorption zone revealed in the field-desorption images expanded from the center of the image to its periphery with increasing voltage and receded with decreasing voltage, with the image recovering its prior pattern (Figs. 3a, 3b). This behavior of the images is characteristic of continuous-mode field-desorption of alkali metals [7, 8]. This cycle could be repeated many times without any noticeable changes in the images.

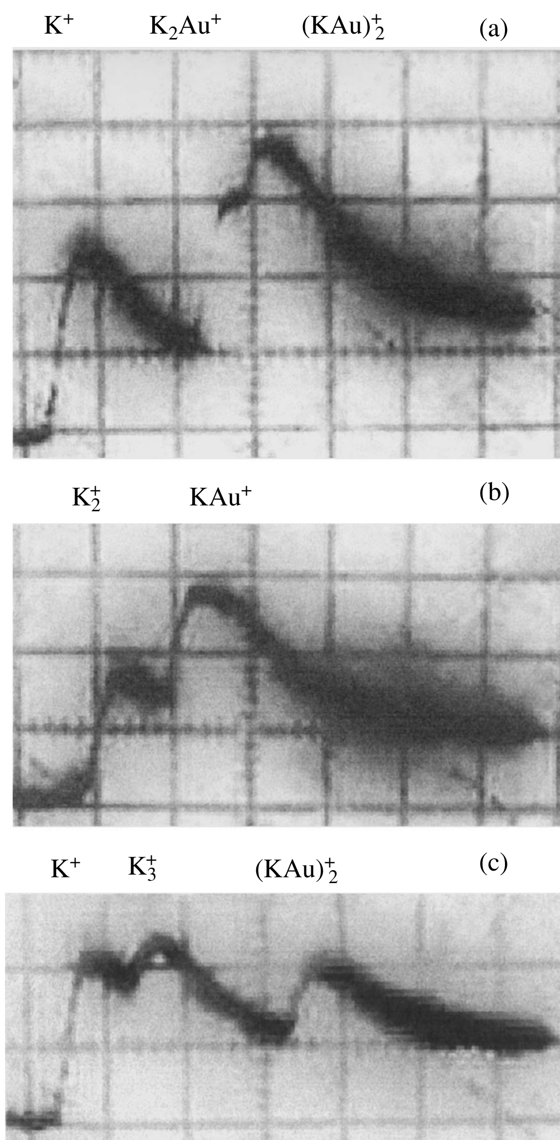

Fig. 2. Typical mass spectra of the desorption products escaping from a KAu film in the course of its destruction in an electric field. Detected ion composition: (a) K^+, K_2Au^+, $(KAu)_2^+$; (b) K_2^+, KAu^+; and (c) K^+, K_3^+, $(KAu)_2^+$.

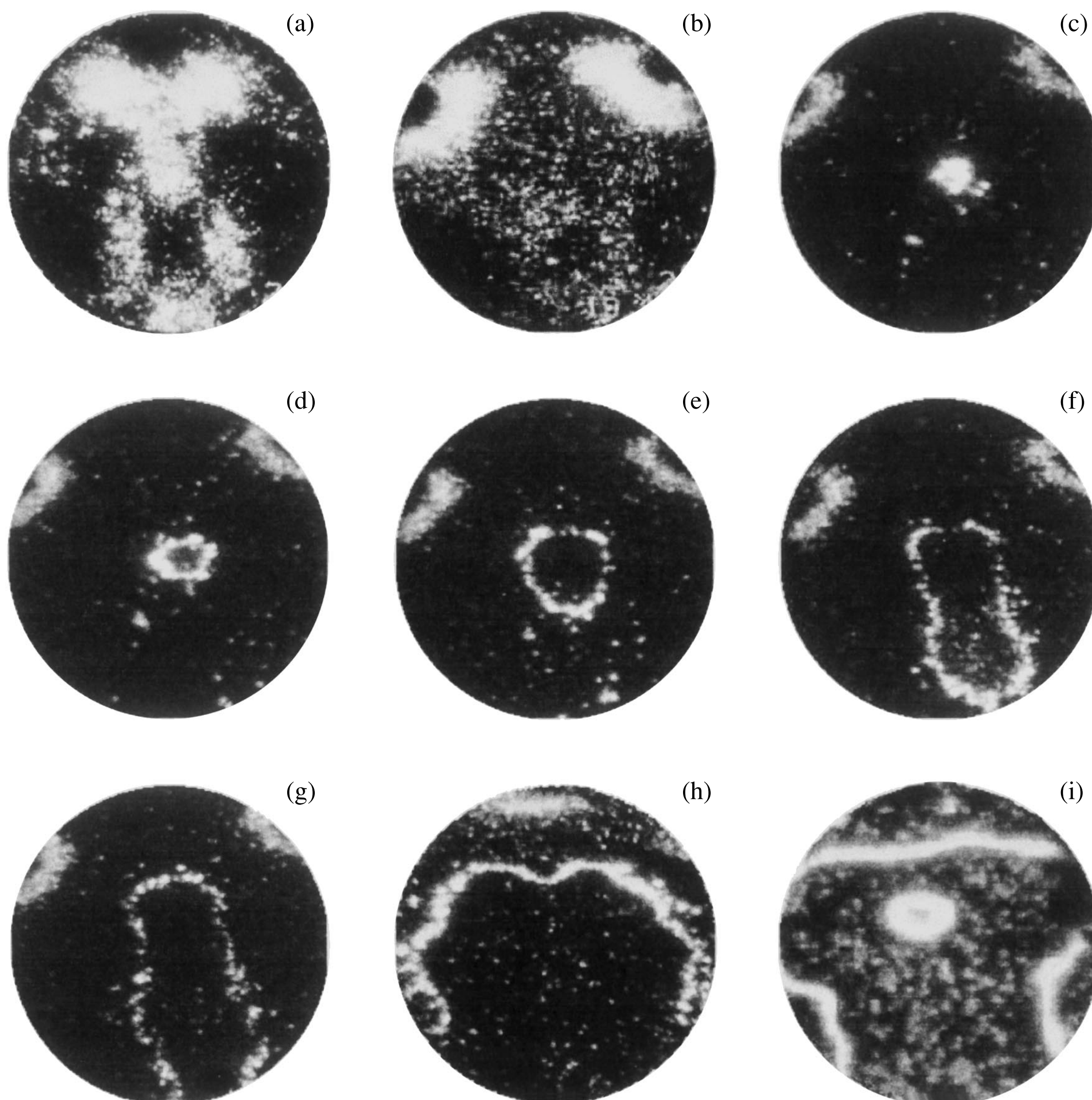

Fig. 3. Continuous-mode field-desorption images of electric field–induced destruction of a KAu film for different values of the field strength: (a) 2.5, (b) 2.8, (c–f) 4.0, (g, h) 4.6, and (i) 5.2 V/nm.

This stage is interpreted by us as indicating desorption of the potassium adsorbed on the surface of the gold–potassium compound film.

The second stage was observed to occur in fields of 3.0–3.5 V/nm (i.e., 20–30% higher than in the first stage). This stage resembled the first stage of destruction in terms of its pattern; namely, there was an expanding front of desorption and only potassium ions were present in the spectra. The only differences were a lower desorption current and a sharper boundary of the desorption zone. It is believed that in this stage the excess potassium atoms that are dissolved in the KAu film become extracted and desorbed.

In the next stage, occurring in fields about twice those of the first stage (4–6 V/nm), the chemical compound decomposes and the film breaks down. The mass spectra now contain signals not only from the potassium ions but also from molecular (cluster) ions, including potassium and gold atoms. Figure 2 illustrates time-of-flight spectra containing cluster ion signals. The ion mass is estimated from the time taken by the ion to cross the distance from the tip to the detector, which is derived from the rising part of the peak [9]. The occurrence frequency of a peak reflects the fractional content of the corresponding ion species in the desorption flux. Most of the oscillograms obtained contained only peaks due to potassium ions. The amount of cluster ions containing gold atoms does not exceed a few percent of that of the alkali metal ions.

Destruction of a film of the KAu compound starts at the passage of the desorption front expanding from the maximum-field region at the tip apex (Figs. 3c–3i) and

continues as the voltage is increased, which becomes manifest in the desorption of potassium ions and cluster ions of the K_nAu_m type from the whole surface of the tip. Experiments with thick films revealed the second front of destruction of the KAu compound (Fig. 3i). A continuous-mode field-desorption image indicates the onset of film destruction with increasing desorbing field by the appearance of a bright spot at the image center (Fig. 3c), which transforms immediately into a rapidly expanding ring (Figs. 3d–3f). When the ring breaks up at the edge of the image (Fig. 3g), the front stops. If the desorbing voltage is increased, the desorption front moves gradually toward the edge of the image (Fig. 3i) and eventually escapes beyond it.

The processes observed can be explained as follows. When the field is raised to the level corresponding to Fig. 3c, the adsorbed potassium escapes from all of the imaged tip surface and potassium and, partly, gold from the KAu film start desorbing near the tip apex. Three zones form on the surface: (1) near the tip vertex within a ring, which corresponds to the partially destroyed and potassium-depleted KAu compound with no adsorbed potassium present; (2) outside the ring, a zone that can be identified with the unaffected compound, in which the potassium diffusing from the tip side surface is desorbed by the field (the lifetime of adsorbed potassium is short in this zone) and cannot reach the ring; and (3) the side surface of the tip, which is coated by the KAu film with potassium adsorbed on the surface. At the boundary between the first and second zones, a step (ring) forms, which enhances the field. The local field enhancement at the step makes film destruction possible not only in the region of the maximum field, at the tip vertex (Fig. 3c), but also in weaker fields. The ring expands, and, as it approaches the third zone or merges with it (Fig. 3g), adsorbed potassium can now diffuse from the tip sides directly to the first zone, i.e., the area of the surface compound depleted in potassium. The binding energy of potassium atoms to the surface and their lifetime in the zone of the partially decomposed compound are apparently higher than those on the surface of the original undamaged compound; therefore, the potassium migrating over the first zone is more likely to reach the step. The processes occurring at the step (surface diffusion, field desorption, decomposition and recovery of the surface compound) become balanced in a dynamic equilibrium, after which the desorption front stabilizes (Fig. 3g).

As the voltage is lowered, the decomposed film is partially recovered through the influx of potassium atoms from the tip sides. After several cycles of a rise and decrease in voltage (decomposition–recovery of the film), the restoration of the film degrades noticeably, which may be assigned to gold escaping from the desorbing cluster ions. The original gold concentration at the tip vertex can be restored through heating to the temperature at which surface diffusion of gold sets in, but in these conditions all of the potassium desorbs thermally from the surface.

4. CONCLUSIONS

Thus, for the specific example of a KAu film, we have shown that, by properly varying the electric field, the local composition (and, hence, the electronic properties) of gold compounds with alkali metals can be changed. The changes are induced by field desorption of atomic and cluster (molecular) ions and can be reversible (with only the alkali metal being removed) or irreversible (if the cluster ions containing gold atoms also desorb).

ACKNOWLEDGMENTS

The authors are indebted to V.I. Paleev for useful discussions.

This study was supported by the Russian federal program “Surface Atomic Structures,” project no. 1152.

REFERENCES

1. W. Spicer, A. H. Sommer, and J. C. White, Phys. Rev. **115**, 57 (1959).
2. W. Spicer, Phys. Rev. **125**, 1297 (1962).
3. R. E. Watson and M. Weinert, Phys. Rev. B **49**, 7148 (1994).
4. T. A. Rodriguez, J. Hrbek, Y.-W. Yang, M. Kuhn, and T. K. Sham, J. Vac. Sci. Technol. A **11**, 2029 (1993).
5. M. V. Knat’ko, V. I. Paleev, and M. N. Lapushkin, Zh. Tekh. Fiz. **68** (10), 104 (1998) [Tech. Phys. **43**, 1231 (1998)].
6. D. P. Bernatskiĭ and V. G. Pavlov, Pis’ma Zh. Tekh. Fiz. **26**, 22 (2000) [Tech. Phys. Lett. **26**, 233 (2000)].
7. D. P. Bernatskiĭ, Yu. A. Vlasov, and V. G. Pavlov, Zh. Tekh. Fiz. **57**, 2257 (1987) [Sov. Phys. Tech. Phys. **32**, 1366 (1987)].
8. D. P. Bernatskii and V. G. Pavlov, Phys. Low-Dimens. Semicond. Struct., No. 7, 93 (1997).
9. D. P. Bernatskiĭ, Yu. A. Vlasov, and V. G. Pavlov, Pis’ma Zh. Tekh. Fiz. **12**, 806 (1986) [Sov. Tech. Phys. Lett. **12**, 333 (1986)].

Translated by G. Skrebtsov

Physics of the Solid State, Vol. 46, No. 8, 2004, pp. 1542–1547. Translated from Fizika Tverdogo Tela, Vol. 46, No. 8, 2004, pp. 1498–1503.
Original Russian Text Copyright © 2004 by Ageev, Afanas'eva, Potekhina.

LOW-DIMENSIONAL SYSTEMS AND SURFACE PHYSICS

Oxidation Kinetics of Thin Titanium Films Grown on Tungsten

V. N. Ageev, E. Yu. Afanas'eva, and N. D. Potekhina

Ioffe Physicotechnical Institute, Russian Academy of Sciences, Politekhnicheskaya ul. 26, St. Petersburg, 194021 Russia
e-mail: afanaseva@ms.ioffe. rssi.ru

Received December 16, 2003

Abstract—Growth of thin Ti films on (100)W and the kinetics of their oxidation are studied using thermal-desorption spectroscopy and Auger electron spectroscopy. Titanium films grow nearly layer by layer on the (100)W face at room temperature. The activation energy for desorption of Ti atoms decreases from 5.2 eV for coverage θ = 0.1 to 4.9 eV in a multilayer film. Oxidation of a thin (θ = 6) titanium film starts with dissolution of oxygen atoms in its bulk to the limiting concentration for a given temperature, after which the film oxidizes to TiO, with the TiO_2 oxide starting to grow when exposure of the film to oxygen is prolonged. The thermal desorption of oxides follows zero-order kinetics and is characterized by desorption activation energies of 5.1 (TiO) and 5.9 eV (TiO_2). *© 2004 MAIK "Nauka/Interperiodica".*

1. INTRODUCTION

The TiO_2 oxide has been employed as an effective catalyst for photocatalytic splitting of water [1] and organic compounds in polluted air and wastewaters [2]. This accounts for the large number of publications dealing with studies of the initial stages in the oxidation of single crystals [3–6], polycrystalline ribbons [7–10], and thin titanium films deposited on a substrate [11–16]. In those studies, various methods were invoked, among them Auger electron spectroscopy (AES) [4, 8, 14, 16], UV photoelectron spectroscopy (UVPES) [3, 4, 12], low-energy electron diffraction (LEED) [3, 15, 16], work function measurements [3, 5, 8, 11], electron-stimulated desorption (ESD) [5], electron energy loss spectroscopy (EELS) [4, 16], secondary ion mass spectrometry (SIMS) [7], and x-ray photoelectron spectroscopy (XPS) [9, 10, 12, 16]. Nevertheless, there is still apparent disagreement in the interpretation of data bearing on the chemical composition of the oxide growing in the initial stage of oxidation and on its distribution over the substrate volume. In particular, some authors believe that, in the initial stages of adsorption, oxygen penetrates into the near-surface layer and only after this does it chemisorb on the surface [3, 8, 11, 17]. Other researchers conclude that oxygen originally builds up on the surface [5, 7, 18, 19]. There is also discrepancy concerning the stoichiometric composition of the oxides forming in the course of oxidation. Some publications report the growth of oxide TiO_2 under long exposure to oxygen [4, 20]; others [8, 12, 21] assume the formation of oxides TiO and Ti_2O_3; and, finally, in [3, 5, 9, 10, 22], a mixture of various oxides is said to have been revealed. The opinion is given that the composition of oxides on a surface is affected by surface pretreatment [9, 16], by the oxygen pressure at which oxidation is carried out [23], and by the substrate temperature [10].

This communication reports on thermal-desorption spectroscopy (TDS) and AES studies of the growth of thin Ti films on a patterned, predominantly (100)-oriented tungsten ribbon and their oxidation kinetics in an oxygen environment.

2. EXPERIMENTAL

Measurements were carried out with TDS and AES (for more details, see [24, 25]). The experimental setup consists of the following main parts. The products of thermal desorption were detected by a pulsed time-of-flight mass spectrometer. The magnitudes of fluxes of Ti atoms and TiO and TiO_2 molecules were determined from the Ti^+ (mass-48 line of the mass spectrum), TiO^+ (mass-64 line), and TiO_2^+ (mass-80 line) ion currents, respectively. The mass spectrometer resolution was ~60, which permitted reliable identification of these ions.

The Auger spectra were measured with a 120° quasi-spherical retarding-field analyzer. The amount of deposited titanium was derived from the intensity of the differentiated Ti(*LMM*) Auger line at 387 eV. The degree of W screening by titanium was determined from measurements of the differentiated W(*NNV*) Auger line at 169 eV. The primary electron energy was 1.3 keV, the electron beam modulation voltage was ~3 eV, and the primary beam electron density did not exceed 1.3×10^{-3} A/cm^2.

The substrates were patterned tungsten ribbons with a predominantly (100)-oriented surface measuring $0.01 \times 1.0 \times 30$ mm. The ribbons were cleaned of carbon by annealing in oxygen at a pressure of ~10^{-6} Torr and at a ribbon temperature of ~1600 K for one hour, and the oxygen was flash desorbed at T = 2500 K in vacuum. The titanium was deposited by ablation from

two titanium rods measuring 0.7 × 0.7 × 30 mm and located parallel to the W ribbon on both its sides. The rods were heated by a dc electric current.

A deposited titanium film was oxidized at a constant temperature and an oxygen pressure of 10^{-7}–10^{-6} Torr. The amount of deposited titanium was determined from the deposition time at a constant flux and monitored using TDS and AES. The ribbon temperature was measured in the high temperature region with an optical micropyrometer and in the low-temperature range by linearly extrapolating the heating-current dependence of the ribbon temperature to room temperature. The ribbon heating rate could be varied from 20 to 2000 K s^{-1}, with the time dependence of the temperature being close to linear. The deviation from linearity in the range 1300–2000 K did not exceed 30 K.

A tungsten ribbon and titanium rods were fixed to a manipulator, making it possible to displace the ribbon surface under study between the entrance to the mass spectrometer source and the entrance to the energy analyzer. The base pressure in the instrument was ~10^{-10} Torr.

3. EXPERIMENTAL RESULTS

3.1. Growth of a Ti Film on W(100)

Figure 1 presents plots relating the Auger signal intensity of Ti (387 eV) and W (169 eV) to the amount of deposited titanium. The initial linear portion in the plots is replaced by a break indicating the completion of filling of one monolayer. In accordance with a study on thin Ti film growth on W(110) [26], one Ti monolayer screens the W Auger signal by a factor 0.56. When Ti is applied to a substrate at $T = 300$ K, the Ti Auger signal saturates after the deposition of about six monolayers, with the W Auger signal dropping to zero. These graphs argue for the layer-by-layer growth of a film at $T = 300$ K. Analogous plots obtained at the tungsten temperature $T = 1100$ K coincide with those measured at $T = 300$ K, before the formation of a monolayer coverage. For larger amounts of deposited Ti, the Ti Auger signal saturates at a lower level, with the W Auger signal still being observed after the deposition of six monolayers. This suggests a growth of three-dimensional Ti formations on the W surface at $T = 1100$ K after completion of the monolayer coverage.

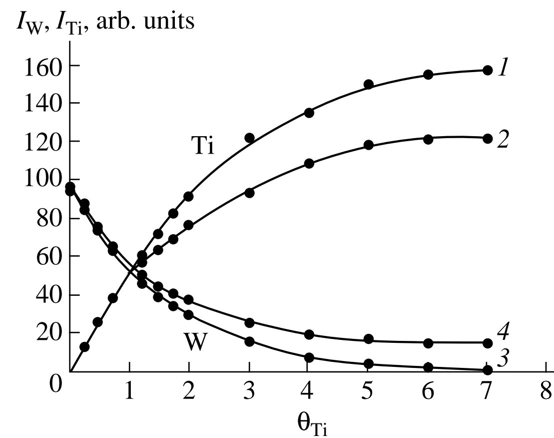

Fig. 1. Auger peak intensities of (*1*, *2*) Ti and (*3*, *4*) W plotted vs. the amount of deposited Ti (in monolayers) at substrate temperature (*1*, *3*) $T = 300$ and (*2*, *4*) 1100 K.

Figure 2 displays the dependences of the Ti Auger signal on the annealing temperature measured for different initial coverages θ_0. For coverages $\theta_0 \leq 2$ MLs, the Ti Auger signal remains practically constant up to 1330 K, after which the signal intensity diminishes gradually due to the thermal desorption of Ti. The dissolution of Ti in the bulk of W can be neglected [26]. For $\theta_0 = 6$ MLs, the annealing curve exhibits features in the temperature region $T = 600$–800 K apparently caused by changes in the film structure, possibly by the formation of Ti clusters. For $T > 1330$ K, the Auger signal starts to decay as a result of thermal desorption. The

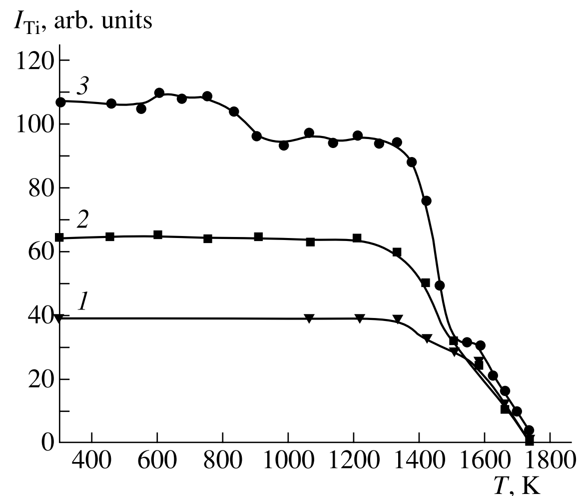

Fig. 2. Auger peak intensities of Ti plotted vs. annealing temperature (annealing at each point was performed for 1 min) for various initial Ti coverages θ_0: (*1*) 1, (*2*) 2, and (*3*) 6 MLs.

shoulder in the curve at $T = 1550$ K is probably associated with desorption from a submonolayer coating persisting through the breakup of Ti clusters.

Figure 3 plots thermal-desorption spectra of Ti atoms obtained for different titanium coverages θ_0 on W(100) at $T = 300$ K. For $\theta_0 > 1$, the thermal-desorption spectra exhibit two maxima. First, the high-temperature maximum grows with increasing coverage to reach saturation at one-monolayer coverage. After this, a low-temperature maximum appears, whose intensity increases in proportion to θ_0. For $\theta_0 > 2.5$, the rising parts of the thermal-desorption curves associated with this maximum coincide, which is indicative of zero-order desorption kinetics, a feature usually observed under layer-by-layer evaporation. The graph of $\ln(-d\theta/dt)$ versus $1/T$ drawn for the rising part of the

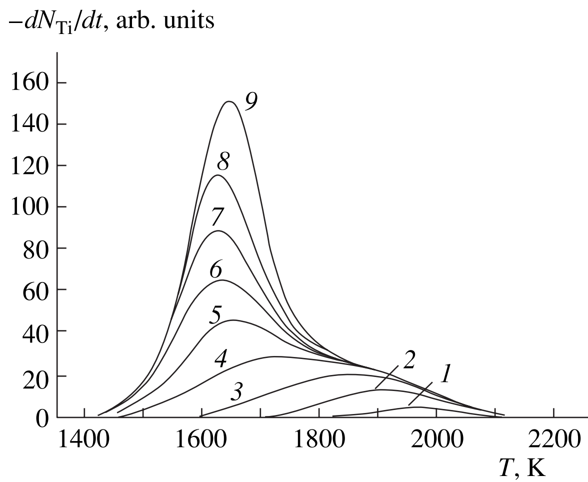

Fig. 3. Thermal-desorption spectra of Ti atoms escaping from the W surface for different coverages θ_0: (*1*) 0.1, (*2*) 0.4, (*3*) 0.85, (*4*) 1.4, (*5*) 1.85, (*6*) 2.3, (*7*) 2.75, (*8*) 3.2, and (*9*) 3.8 MLs. Adsorption temperature T = 300 K; heating rate 200 K s^{-1}.

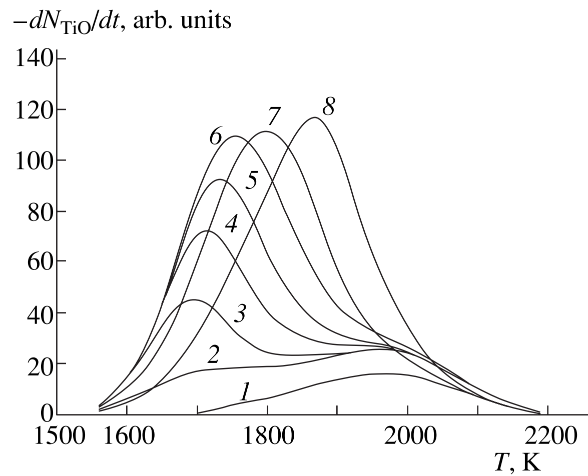

Fig. 4. Thermal-desorption spectra of TiO obtained for various oxidation times of a Ti film θ = 6 ML thick deposited at T = 300 K. Pressure $P(O_2) = 10^{-7}$ Torr; oxidation temperature T = 1100 K. Oxidation time t: (*1*) 4, (*2*) 6, (*3*) 8, (*4*) 10, (*5*) 13, (*6*) 16, (*7*) 22, and (*8*) 30 min. Heating rate 200 K s^{-1}.

low-temperature maximum is fitted well by a straight line, whose slope yields the activation energy for desorption of Ti atoms $E_2 = 4.9 \pm 0.2$ eV. This value is close to the titanium sublimation heat, 4.87 eV [27]. The $\ln[(-d\theta/dt)/\theta]$ versus $1/T$ graphs drawn for the high-temperature phase remain straight lines only for $\theta_0 <$ 0.15. From their slope, the desorption activation energy is found to be $E_1 = 5.2 \pm 0.2$ eV. As the coverage increases, the maxima in the desorption curves of the high-temperature phase shift toward lower temperatures, which can be tentatively ascribed to lateral repulsive interactions in the adlayer.

3.2. Oxidation of Ti Films Deposited on W

Figure 4 shows thermal-desorption spectra of TiO molecules obtained after oxidation of a Ti film deposited on a tungsten substrate at T = 300 K to a coverage θ_0 = 6 MLs. The oxidation was conducted at an oxygen pressure $P(O_2) \cong 10^{-7}$ Torr and a substrate temperature T = 1100 K. Thermal-desorption spectra of TiO molecules, similar to those of Ti atoms, have a two-phase shape but are shifted toward higher temperatures. Hence, TiO molecules are bound to the substrate more strongly than Ti atoms. The rising parts of the thermal-desorption curves obtained within the oxidation time interval from 8 to 16 min coincide, which indicates the desorption kinetics to be zero-order. From the slope of the $\ln(-d\theta/dt)$ versus $1/T$ dependence drawn for the rising part of the TiO molecule desorption curves, the activation energy for desorption is found to be 5.1 ± 0.2 eV. The rising parts of the desorption curves obtained under oxidation for more than 20 min (curve *7* in Fig. 4) are shifted toward higher temperatures, with TiO_2 molecules appearing in the mass spectrum. Therefore, the deviation from zero-order desorption kinetics for TiO molecules can be due to the rate of their desorption being affected by a growing layer of oxide TiO_2, which, as will be shown later, desorbs at a higher temperature.

The number of desorbing TiO molecules grows linearly with increasing oxidation time at constant oxygen pressure and substrate temperature and gradually approaches saturation (Fig. 5). Such a linear dependence implies that the rate-limiting stage in the oxidation process is not the oxygen diffusion but the reaction at the interface. As follows from Fig. 5, TiO molecules start to desorb with a certain delay. Figure 6 plots the dependences of the number of desorbing TiO molecules versus oxidation time at T = 1100 K for Ti films

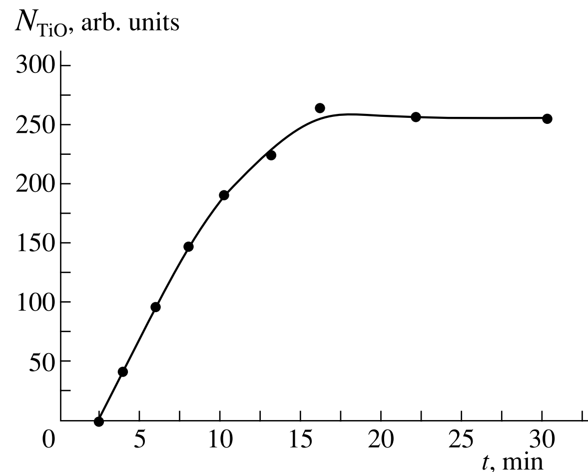

Fig. 5. Dependence of the number of desorbing TiO molecules on oxidation time. The oxidation was performed at an oxygen pressure $P(O_2) = 10^{-7}$ Torr and T = 1100 K.

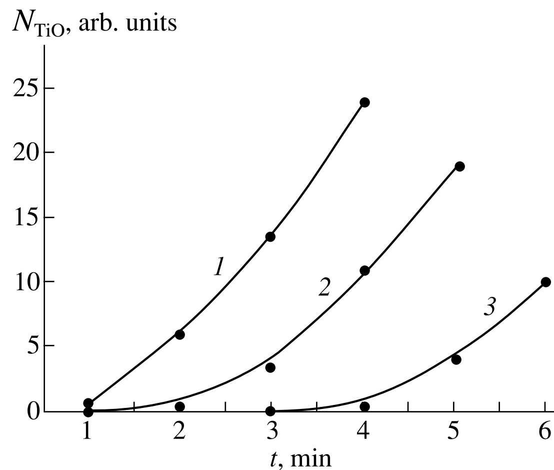

Fig. 6. Initial parts of the graphs relating the number of flash-desorbed TiO molecules to oxidation time, obtained for Ti films of various thickness θ_0: (*1*) 4, (*2*) 8, and (*3*) 16 MLs. The oxidation was performed at T = 1100 K and an oxygen pressure $P(O_2) = 10^{-7}$ Torr.

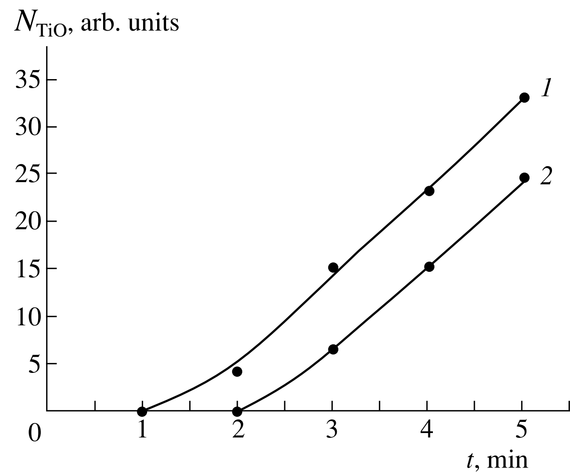

Fig. 7. Initial parts of the graphs relating the number of flash-desorbed TiO molecules to oxidation time, obtained for oxidation temperature (*1*) T = 1100 and (*2*) 300 K. Oxygen pressure $P(O_2) = 10^{-7}$ Torr; Ti film thickness θ_0 = 4 MLs.

of various thickness. The delay in the onset of formation of TiO molecules is seen to increase with the thickness of the deposited Ti film. Furthermore, the delay time decreases with increasing oxidation temperature at constant oxygen pressure and Ti film thickness (Fig. 7). Therefore, it follows that the delay originates from the dissolution of oxygen atoms in the bulk of the Ti film until a certain limiting concentration is reached. Estimates based on the TiO desorption delay times in the course of Ti oxidation show that the concentration of oxygen dissolved in the bulk of the Ti film at T = 1100 K is ~10%, which agrees with the literature data [28].

Figure 8 illustrates the dependence of the number of desorbed TiO molecules on the oxidation temperature under constant exposure of a 6-ML-thick Ti film to oxygen. We readily see that the number of TiO molecules grows slowly in the temperature interval from 300 to 1000 K, to pass through a maximum at T = 1300 K. The decrease in the number of TiO molecules for $T >$ 1300 K is apparently connected with the desorption of Ti atoms (Fig. 2). The increase in the number of TiO molecules with temperature suggests that there is a potential barrier associated with the reaction proceeding at the interface between TiO and Ti.

Long exposures of a Ti film to oxygen bring about desorption of TiO_2 molecules. Figure 9 plots the number of desorbing TiO and TiO_2 molecules versus the oxidation time at T = 1100 K and a pressure $P(O_2) \approx 10^{-6}$ Torr for a 6-ML-thick titanium film deposited at T = 300 K. The delay time required to saturate the bulk of the Ti film with oxygen decreases with increasing oxygen pressure (cf. Fig. 5). For short oxidation times, only the TiO molecules desorb; their number grows linearly with oxidation time. The thermal-desorption spectra of TiO (Fig. 10) exhibit filling of the high-temperature phase, followed by a rise in the low-temperature desorption phase (curves *1*, *2*). The plot attains a maximum (curve *1* in Fig. 9) apparently when oxide TiO grows through the Ti film. In the vicinity of the maximum, TiO_2 molecules start to desorb, which signals the onset of a new stage in the film oxidation. The maximum in the dependence of the number of desorbing TiO molecules on oxidation time does not fully coincide in position with the onset of growth of TiO_2 molecules, which is possibly caused by nonuniformities in the thickness or structure of the Ti film. The dependence of the number of desorbing TiO_2 molecules on oxidation time (curve *2* in Fig. 9) reaches saturation when oxide TiO_2 grows through the Ti film. This is

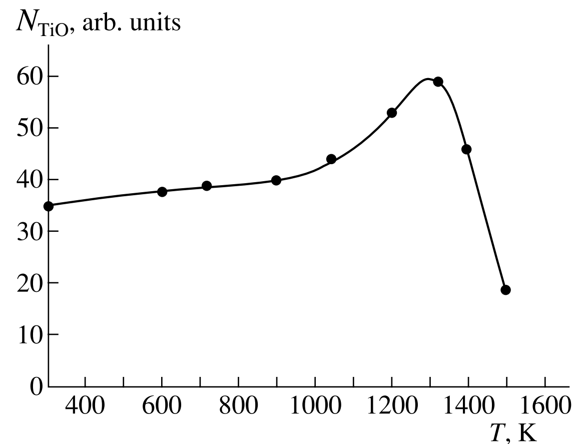

Fig. 8. Number of flash-desorbed TiO molecules plotted vs. oxidation temperature. A Ti film θ_0 = 6 ML thick was oxidized at an oxygen pressure $P(O_2) = 10^{-7}$ Torr for t = 4 min.

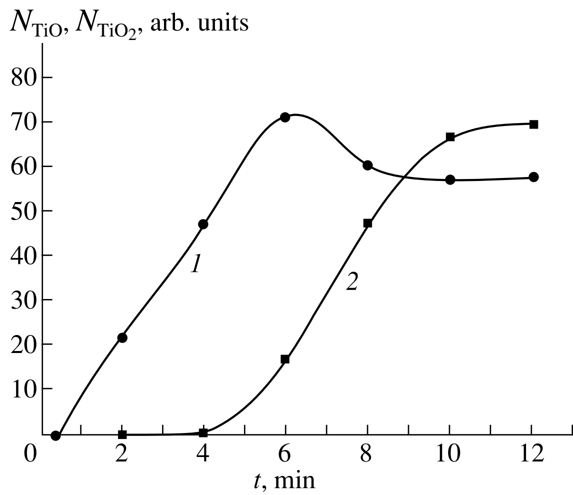

Fig. 9. Oxidation-time dependence of the number of (*1*) TiO and (*2*) TiO_2 molecules flash-desorbed from a Ti film θ_0 = 6 ML thick, obtained through oxidation at T = 1100 K and $P(O_2) = 10^{-6}$ Torr.

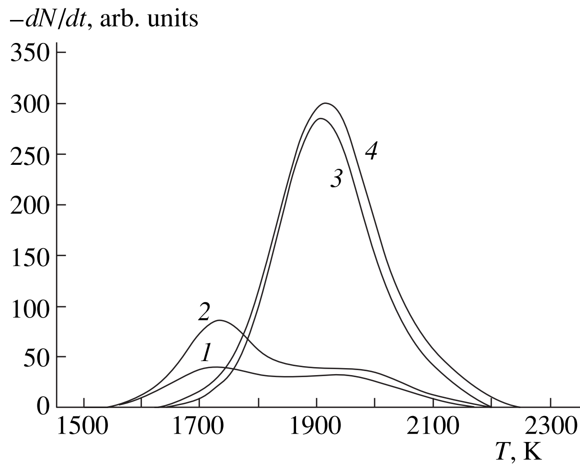

Fig. 10. Thermal-desorption spectra of (*1–3*) TiO and (*4*) TiO_2 obtained for different oxidation times of a Ti film θ = 6 ML thick deposited on W at T = 300 K. The oxidation was performed at an oxygen pressure $P(O_2) = 10^{-6}$ Torr and T = 1100 K. Oxidation time *t*: (*1*) 1.5, (*2*) 2, and (*3*, *4*) 10 min. Heating rate 200 K s^{-1}.

accompanied by a slight decrease in the signal corresponding to the TiO molecule desorption, which remains flat thereafter. Thermal-desorption spectra obtained for TiO and TiO_2 in this region (for $t \geq 10$ min) practically coincide in shape and are in the same position on the temperature scale (curves *3*, *4* in Fig. 10). This gives us grounds to maintain that the TiO^+ ions observed in the mass spectrum in this case originate from dissociative ionization of TiO_2 molecules caused by the electron beam in the mass spectrometer source. The activation energy for the desorption of TiO_2 molecules derived from the rising part of the thermal-desorption curve under the assumption of zero-order desorption kinetics is found to be 5.9 ± 0.2 eV. This value is higher than the activation energy for desorption of TiO molecules, 5.1 ± 0.2 eV, determined from the rising part of the low-temperature peak without the formation of TiO_2.

4. DISCUSSION OF THE RESULTS

Titanium films on W(100) grow nearly layer by layer at T = 300 K. For $T \geq 900$ K, a film grows through the Stranski–Krastanow mechanism, with a Ti monolayer first forming on the surface and three-dimensional clusters growing on it thereafter.

Oxidation of a Ti film in an oxygen environment is accompanied, under flash desorption, by the appearance of TiO^+ and TiO_2^+ ions in the mass spectrum, with the former ions appearing first and the TiO_2^+ ions being seen only after long exposures. Note that thermal-desorption mass spectra obtained in the final stage of oxidation always have TiO_2^+ and TiO^+ ions. In this case, however, the TiO^+ ions form primarily in the dissociation of TiO_2 molecules by electron impact, with the heat of the reaction $TiO_2^{(g)} \longrightarrow TiO^{(g)} + O$ being 6.3 eV, as estimated from the Hess law [29]. Observation of this reaction in the mass spectrometer correlates with the thermal-desorption spectra of TiO_2 and TiO molecules having identical shape and occupying the same position on the temperature scale.

TiO_2 molecules desorb following the zero-order kinetics (as do TiO molecules in the absence of TiO_2 desorption). These desorption processes require 5.9 and 5.1 eV, respectively, for their activation, which is close to the corresponding heats of sublimation of oxides TiO_2 and TiO [27, 30].

Decay of other oxides could also give rise to the appearance of TiO and TiO_2 molecules in the gas phase. These reactions are [30]

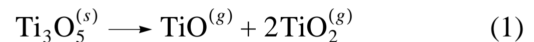

$$Ti_3O_5^{(s)} \longrightarrow TiO^{(g)} + 2TiO_2^{(g)} \quad (1)$$

(with a heat of reaction of 18.8 eV) and

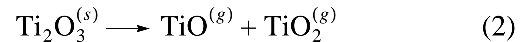

$$Ti_2O_3^{(s)} \longrightarrow TiO^{(g)} + TiO_2^{(g)} \quad (2)$$

(with a heat of reaction of 12.8 eV).

However, we believe it to be unlikely that the kinetics of thermal desorption of different molecules (TiO, TiO_2) are characterized by the same activation energy and prefactor in the desorption rate constant, as follows from the thermal-desorption spectra (curves *3*, *4* in Fig. 10). We are of the opinion that the simultaneous appearance of TiO and TiO_2 in thermal desorption observed with long oxidation times is associated with the desorption of oxide TiO_2 followed by its breakup in electron impact ionization.

The oxidation of a Ti film proceeds in a fairly complex manner. First, oxygen dissolves in the Ti film until an equilibrium solution forms at a given temperature. Under a flash, the oxygen is apparently removed thermally in the form of atoms and, therefore, is difficult to detect because of its high chemical activity. The accumulation time of this oxygen increases with Ti film thickness but decreases with increasing substrate temperature (Figs. 6, 7). After this stage of oxygen buildup in the titanium film has come to completion, further absorption of oxygen brings about the formation of oxide TiO, which grows through the Ti film. As the oxidation is continued, TiO oxidizes to TiO_2.

Although a latent period in the oxide desorption under the adsorption of oxygen has been observed earlier for a number of high-melting metals, in all those cases oxygen accumulated on the surface of the metal [31–33]; in our case, however, this period is associated with the fact that the reaction can occur only after oxygen has reached the limiting concentration in the bulk of the titanium film.

5. CONCLUSIONS

Thus, we have carried out AES and TDS studies on the mechanism of growth and the thermal stability of a Ti film on W(100). At room temperature, a Ti film was shown to grow layer by layer. A transition to three-dimensional formations in the deposited film occurs at $T \geq 900$ K. A Ti film is thermally stable up to $T \sim 1300$ K. Oxidation at $T = 1100$ K of a film deposited at room temperature to $\theta = 6$ MLs brings about dissolution of oxygen atoms in the bulk of the Ti film, which is followed by growth of oxide TiO evaporating with a heat of sublimation of 5.1 ± 0.2 eV. The rate of formation of this oxide is rate-limited by the reaction at the Ti–TiO interface. In the next stage, TiO_2 starts to grow; its heat of evaporation is 5.9 ± 0.2 eV. The presence of a particular oxide phase is detected unambiguously from the products of thermal desorption and the position of their thermal-desorption peaks on the temperature scale.

ACKNOWLEDGMENTS

The authors express sincere gratitude to N.R. Gall' and V.G. Pavlov for useful discussions.

This study was supported by the Russian Foundation for Basic Research (project no. 03-02-17523) and the Russian federal program "Surface Atomic Structures" (project no. 1152).

REFERENCES

1. A. Fujishima and K. Honda, Nature **37**, 238 (1972).
2. A. L. Lisebigler, G. Lu, and J. T. Jates, Jr., Chem. Rev. **95**, 735 (1995).
3. D. M. Hanson, R. Stockbauer, and T. E. Madey, Phys. Rev. B **24** (10), 5513 (1981).
4. E. Bertel, R. Stockbauer, and T. E. Madey, Surf. Sci. **141**, 355 (1984).
5. A. Takano and K. Ueda, Surf. Sci. **242**, 450 (1991).
6. C. Ocal and S. Ferrer, Surf. Sci. **178**, 850 (1986).
7. P. H. Dawson, Surf. Sci. **65**, 41 (1977).
8. D. Brugnian, C. Argile, M. G. Barthes-Labrousse, and G. E. Read, Surf. Sci. **141**, 639 (1984).
9. A. Azouley, N. Shamir, E. Fromm, and M. H. Mintz, Surf. Sci. **370**, 1 (1997).
10. G. Lu, S. L. Bernasek, and J. Schwartz, Surf. Sci. **458**, 80 (2000).
11. W. Brearly and N. A. Surplice, Surf. Sci. **64**, 372 (1977).
12. A. Platau, L. I. Johansson, A. L. Hugstrom, S. E. Karlsson, and S. B. M. Hagstrom, Surf. Sci. **63**, 153 (1977).
13. M. Martin, W. Mader, and E. Fromm, Thin Solid Films **250**, 61 (1994).
14. I. Vaquila, M. C. G. Passeggi, Jr., and J. Ferron, Phys. Rev. B **55** (20), 13925 (1997).
15. W. S. Oh, C. Xu, D. Y. Kim, and D. W. Goodman, J. Vac. Sci. Technol. A **15**, 1710 (1997).
16. O. Guo, W. S. Oh, and D. W. Goodman, Surf. Sci. **437**, 49 (1999).
17. R. L. Strong and J. L. Erskine, J. Vac. Sci. Technol. A **3**, 1428 (1985).
18. B. T. Jonker, J. F. Morar, and R. L. Park, Phys. Rev. B **24** (6), 2951 (1981).
19. S. Aduru and J. W. Rabalais, Langmuir **3**, 543 (1987).
20. D. E. Eastman, Solid State Commun. **10**, 933 (1972).
21. H. D. Shih and F. Jona, Appl. Phys. **12**, 311 (1977).
22. L. Porte, M. Demosthenous, and T. M. Duc, J. Less-Common Met. **56**, 183 (1977).
23. J. S. Corneille, J.-W. He, and D. W. Goodman, Surf. Sci. **338**, 211 (1995).
24. V. N. Ageev and E. Yu. Afanas'eva, Poverkhnost, No. 7, 30 (1987).
25. V. N. Ageev and E. Yu. Afanas'eva, Fiz. Tverd. Tela (St. Petersburg) **39** (8), 1484 (1997) [Phys. Solid State **39**, 1318 (1997)].
26. M.-Ch. Wu, J. S. Corneille, and D. W. Goodman, Surf. Sci. Lett. **255**, L536 (1991).
27. *Thermodynamic Properties of Particular Substances: Handbook*, Ed. by V. P. Glushko, L. V. Gurevich, N. V. Veĭts, *et al.*, 3rd ed. (Nauka, Moscow, 1978–1982).
28. E. Fromm and E. Gebhardt, *Gase und Kohlenstoffin Metallen* (Springer, Berlin, 1976; Metallurgiya, Moscow, 1980).
29. *Course of Physical Chemistry*, Ed. by Ya. I. Gerasimov *et al.* (Khimiya, Moscow, 1964) [in Russian].
30. E. K. Kazenas and Yu. V. Tsvetkov, *Oxide Evaporation* (Nauka, Moscow, 1997) [in Russian].
31. V. N. Ageev and N. I. Ionov, Zh. Tekh. Fiz. **38** (7), 1149 (1968) [Sov. Phys. Tech. Phys. **13**, 950 (1968)].
32. N. P. Vas'ko and Yu. G. Ptushinskiĭ, Ukr. Fiz. Zh. **13**, 347 (1968).
33. V. N. Ageev, Zh. Tekh. Fiz. **40** (8), 1743 (1970) [Sov. Phys. Tech. Phys. **15**, 1355 (1970)].

Translated by G. Skrebtsov

Physics of the Solid State, Vol. 46, No. 8, 2004, pp. 1548–1553. Translated from Fizika Tverdogo Tela, Vol. 46, No. 8, 2004, pp. 1504–1508.
Original Russian Text Copyright © 2004 by Zakharov, Vakulenko.

POLYMERS
AND LIQUID CRYSTALS

Rapid Viscous Flow of a Nematic Liquid Crystal in the Vicinity of the Nematic–Smectic *A* Transition

A. V. Zakharov and A. A. Vakulenko

Institute for Problems of Mechanical Engineering, Russian Academy of Sciences, Bol'shoĭ pr. 61, Vasil'evskiĭ Ostrov, St. Petersburg, 199178 Russia

Received November 10, 2003

Abstract—The resistance to shear flow is investigated theoretically for polar liquid crystals, such as 4-*n*-octyl-4'- and 4-*n*-octyloxy-4'-cyanobiphenyls. It is established that the lowest resistance to shear flow at temperatures in the vicinity of the nematic–smectic *A* phase transition point T_{NA} is observed when the nematic director is oriented perpendicular to both the flow velocity vector and the flow velocity gradient. The three Miesowicz shear viscosity coefficients η_i (i = 1–3) at temperatures close to the phase transition temperature (tens of millikelvins from T_{NA}) and far from this transition are calculated in the framework of the Ericksen–Leslie theory. The decrease in the viscosity coefficients in the order $\eta_2 > \eta_1 > \eta_3$ is explained by the fact that fluctuations of the local smectic order in the nematic phase lead to a singular behavior of the viscosity coefficient η_2, whereas the other two viscosity coefficients η_1 and η_3 are not affected by order parameter fluctuations. *© 2004 MAIK "Nauka/Interperiodica".*

1. INTRODUCTION

As is shown in recent works [1–4], the theoretical approach to describing dissipation processes in liquid crystals continues to attract considerable research attention. A number of qualitative and quantitative advances have been made within the molecular theory of rheological properties of nematic liquid crystals upon shear flow at temperatures far from the temperature of the nematic–smectic *A* phase transition (*N–SmA* transition) [5–9]. However, the theory describing the rheology of nematic liquid crystals in the vicinity of this transition at temperatures differing from the temperature T_{NA} by several tens of millikelvins is far from complete. Since fluctuations of the local smectic order parameter in the vicinity of the *N–SmA* second-order phase transition lead to singularities in both the Frank elastic constants and the rotational viscosity coefficient γ_1 [10–12], it can be expected that the Miesowicz shear viscosity coefficients η_i (i = 1–3) should also possess singularities in the vicinity of the temperature T_{NA} [12]. Actually, when the nematic director **n** is oriented parallel to the flow velocity **v** ($\mathbf{n} \parallel \mathbf{v}$) and perpendicular to the velocity gradient ($\mathbf{n} \perp \nabla v$), the lowest resistance to nematic flow (the smallest viscosity coefficient η_2 [13]) is observed in the nematic liquid crystal. Among the other two viscosity coefficients, η_1 and η_3, the coefficient η_1 ($\mathbf{n} \parallel \nabla v$, $\mathbf{n} \perp \mathbf{v}$) is the largest and the value of the coefficient η_3 ($\mathbf{n} \perp \nabla v$, $\mathbf{n} \perp \mathbf{v}$) is close to that measured in the isotropic phase. Outside the pretransition temperature range, the temperature dependences of the shear viscosities are approximately parallel to each other [13]. The viscosities of nematic liquid crystals upon cooling can deviate from this behavior in the vicinity of the *N–SmA* phase transitions at temperatures of the order of tens of millikelvins above the temperature T_{NA}. Fluctuations of the order parameter of the forming smectic *A* phase lead to a singular behavior of the viscosity coefficient η_2, whereas the other two viscosity coefficients η_1 and η_3 are not affected by order parameter fluctuations [11, 12]. Physically, this is explained by the fact that the viscosity coefficients η_1 and η_2 change places; i.e., at temperatures differing from the temperature T_{NA} by less than tens of millikelvins, the lowest resistance to flow is observed when the director is perpendicular to both the velocity gradient and the flow direction. Our recent theoretical investigation [4] into the behavior of the rotational viscosity coefficient γ_1 in the vicinity of the phase transition of 4-*n*-octyl-4'-cyanobiphenyl (8CB) showed that the critical behavior of the rotational viscosity coefficient γ_1^c should be expected only in the temperature range $0 < t < 10^{-3}$ (hereafter, we will use the dimensionless temperatures $t = T/T_{NA} - 1$), which is lower than 306.7 K ($T_{NA} \approx 306.5$ K for 8CB). On the basis of this result and other theoretical data [11, 12], we can assume that presmectic anomalies in the behavior of the coefficient η_2 should also be expected in the same temperature range $0 < t < 10^{-3}$. In the present work, the temperature difference between the phase transition temperature T_{NA} and the temperature of the nematic phase at which the coefficient η_2 exhibits pretransition anomalies will be determined within a theory based on the results obtained earlier for the director rotation in the vicinity of the *N–SmA* phase transition [4, 6, 11, 12].

1063-7834/04/4608-1548$26.00 © 2004 MAIK "Nauka/Interperiodica"

2. THEORY

The orientation of the director **n** in a shear flow is determined by the balance of the torques acting on the director. For a rapid shear flow, the elastic torques are ignored [4] and the torque of the viscous forces can be represented, according to the Leslie–Ericksen theory [8, 9], in the general form $\mathbf{T}_{vis} = -\mathbf{n} \times [\gamma_1 \mathbf{N} + \gamma_2 \mathbf{M} \cdot \mathbf{n}]$, where γ_1 and γ_2 are the rotational viscosity coefficients, $\mathbf{N} = d\mathbf{n}/dt - \mathbf{W} \cdot \mathbf{n}$ is the vector of the rate of change in the director with respect to the nematic flow, $2\mathbf{M} = \nabla\mathbf{v} + (\nabla\mathbf{v})^T$, and $-2\mathbf{W} = \nabla\mathbf{v} - (\nabla\mathbf{v})^T$. Here, **M** and **W** are the symmetric and antisymmetric parts of the tensor of the flow velocity gradient, respectively; the superscript T indicates the transposition of the matrix corresponding to $\nabla\mathbf{v}$; and $d\mathbf{n}/dt = \frac{\partial n}{\partial t} + \mathbf{v} \cdot \nabla\mathbf{n}$. In a one-dimensional model (the x–y plane is determined by the liquid-crystal flow in the x direction and the velocity gradient in the y direction; z is the vortex axis), we have $\mathbf{v} = v\mathbf{i} \equiv \dot{\gamma} y \mathbf{i}$. As a result, the torque of the viscous forces can be represented in the following form:

$$\mathbf{T}_{vis} = -\mathbf{n} \times \left[\gamma_1 \frac{\partial \mathbf{n}}{\partial t} + \dot{\gamma}\mathbf{m}\right], \quad (1)$$

where the vector **m** has the components $(\alpha_2 n_y, \alpha_3 n_x, 0)$ and the Leslie viscosity coefficients α_2 and α_3 are related to the rotational viscosity coefficients through the expressions $\alpha_2 = (\gamma_2 - \gamma_1)/2$ and $\alpha_3 = (\gamma_1 + \gamma_2)/2$.

The dynamic behavior of the director **n** $(\cos\theta, \sin\theta)$ in the shear plane can be reduced to two cases. In the first case, the hydrodynamic torque

$$\begin{aligned} T_{vis} &= \gamma_1 \frac{\partial \theta}{\partial t} + \frac{1}{2}(\gamma_1 + \gamma_2 \cos\theta_{bulk})\dot{\gamma} \\ &= \gamma_1 \frac{\partial \theta}{\partial t} + (\alpha_3 \cos^2(\theta_{bulk}) - \alpha_2 \sin^2(\theta_{bulk}))\dot{\gamma} \end{aligned} \quad (2)$$

per unit volume of the nematic shear flow becomes zero when the director is oriented at the equilibrium angle θ_{eq} with respect to the flow velocity **v** [8, 9]; that is,

$$\theta_{eq} = \frac{1}{2}\cos^{-1}\left(-\frac{\gamma_1}{\gamma_2}\right) = \tan^{-1}\left(\sqrt{\frac{\alpha_3}{\alpha_2}}\right). \quad (3)$$

This condition is satisfied at $|\gamma_2| > |\gamma_1|$. In the second case at $|\gamma_1| > |\gamma_2|$, the director continuously rotates in the shear plane.

Let us consider the Miesowicz viscosity coefficients η_i (i = 1–3) for a plane flow. These coefficients are defined as the ratio between the yx component of the stress tensor $\sigma_{yx}^{(i)}$ and the shear rate $\dot{\gamma}$ [8, 9]:

$$\eta_i = -\frac{\sigma_{yx}^{(i)}}{\dot{\gamma}}. \quad (4)$$

The indices i = 1, 2, and 3 correspond to the cases where the director **n** is parallel to the $-x$, $-y$, and $-z$ axes, respectively. The Miesowicz and Leslie viscosity coefficients are related by the expressions [13]

$$\eta_1 = \frac{1}{2}(\alpha_3 + \alpha_4 + \alpha_6), \quad \eta_2 = \frac{1}{2}(-\alpha_2 + \alpha_4 + \alpha_5), \quad \eta_3 = \frac{1}{2}\alpha_4. \quad (5)$$

From relationship (3), it follows that, at $|\gamma_1| < |\gamma_2|$ or $\alpha_3 < 0$ (because the inequality $\alpha_2 < 0$ is almost always satisfied), the stationary solution to the torque balance equation [see Eq. (1)] leads to orientation of the director **n** in the $\mathbf{v}$–∇v shear plane at a small angle θ_{eq} to the flow direction. As the temperature T_{NA} is approached (upon cooling), an enhancement of order parameter fluctuations gives rise to a torque $\mathbf{T}_{fl}$ acting on the director **n**. At shear rates $\dot{\gamma}\tau \ll 1$ (τ is the maximum time of structural relaxation), the inclusion of the torque $\mathbf{T}_{fl}$ induced by the order parameter fluctuations leads to a new torque balance equation [11, 12]: $\mathbf{T}_{vis} + \mathbf{T}_{fl} = 0$, where

$$\begin{aligned} \mathbf{T}_{fl} &= -A\mathbf{n} \times \mathbf{j} \\ &= -\left[-\frac{\pi}{2}\frac{k_B T}{l^2 \xi_{\|}}(\dot{\gamma}\tau)(\mathbf{n} \cdot \hat{\mathbf{v}}) + O((\dot{\gamma}\tau)^2)\right]\mathbf{n} \times \mathbf{j}. \end{aligned} \quad (6)$$

Here, $\xi_{\|} = \xi$ is the correlation length of the smectic order, $\hat{\mathbf{v}} = \mathbf{v}/|\mathbf{v}|$, and l is the interlayer spacing in the SmA phase. Physically, the appearance of the torque $\mathbf{T}_{fl}$ is associated with the influence of shear flow on fluctuation regions. This implies that, in the region of thermal fluctuations with $\mathbf{n} \parallel \mathbf{v}$ [2], the shear flow tends to rotate layers, which results in a change in the interlayer spacing and induces the restoring torque $\mathbf{T}_{fl}$. By contrast, the shear flow does not disturb the internal structure through fluctuations at the director orientations i = 2 and 3. A comparison of the two torque balance equations with due regard for relationships (2) and (6) shows that the smallest effect in order of magnitude of $\dot{\gamma}\tau$ is reduced to the renormalization of γ_1 and α_3 ($\sim\eta_2$); that is,

$$\bar{\gamma}_1 = \gamma_1 + \alpha_3^{C1}, \quad \bar{\alpha}_3 = \alpha_3 + \alpha_3^{C1} = \alpha_3 + \frac{\pi}{4}\frac{k_B T}{l^2}\frac{\tau}{\xi}. \quad (7)$$

Here, α_3 and γ_1 are the initial values (without regard for fluctuations) of the Leslie and rotational viscosity coefficients, respectively. By using the dynamic similarity method, Jahnig and Brochard [11] revealed that the relaxation time τ can be approximated by the expression $\tau \sim \xi^{3/2}$ and the correlation length $\xi = \xi_{\|}$ in a smectic A liquid crystal in the range of reduced temperatures close to the critical point can be approximated by the relationship $\xi = \xi_0 t^{-\nu}$, where ξ_0 is the dimension factor and $\nu = \nu_{\|}$ is the corresponding critical exponent. This

suggests that, at shear rates $\dot{\gamma}\tau \ll 1$, the quantities $\bar{\gamma}_1$, α_3^{C1}, and $\bar{\eta}_1$ diverge as $\tau/\xi \sim t^{-\nu/2}$ in the vicinity of the phase transition temperature T_{NA}. Since the inequality $\alpha_3 < 0$ is satisfied virtually for all nematic liquid crystals [14], the result obtained predicts that the effective value of $\bar{\alpha}_3$ should change sign in the neighborhood of the temperature T_{NA} and the lowest resistance to the nematic flow should be observed when the director is oriented perpendicular to both the flow velocity and the flow velocity gradient and can be calculated from relationship (4) or (5) for η_2.

It should be noted that there exists one more approach to the description of the pretransition contribution to the Leslie viscosity coefficient α_3. According to this approach, in the hydrodynamic regime $q_0\xi_{\parallel} \ll 1$, the critical contribution α_3^C to the corresponding Leslie coefficient can be written in the form [10, 11]

$$\alpha_3^{C2} = \gamma_1^{C2} = \frac{\pi}{4}\frac{k_B T}{\xi_0}\sqrt{\frac{\rho_m}{K_1}}t^{\nu-1}, \tag{8}$$

where $q_0 = 2\pi/l$, K_1 is the elastic lateral bending strain, and ρ_m is the density of the material. The correlation lengths of the smectic A phase $\xi_{\parallel}$ in 8CB and 4-*n*-octyloxy-4'-cyanobiphenyl (8OCB) at temperatures close to the critical point were measured using high-resolution x-ray scattering by Davidov *et al.* [15]. The results obtained in the range of reduced temperatures $5 \times 10^{-7} < t < 2 \times 10^{-2}$ are as follows: $\xi_0 = 0.37$ nm and $\nu = 0.67$ for 8CB, $\xi_0 = 0.42$ nm and $\nu = 0.62$ for 8OCB, and interlayer spacing in the smectic A phase $l \approx 2.0$ nm for both liquid crystals. The critical contributions α_3^C (or γ_1^C) were calculated by Karat and Madhusudana [16] with the use of the parameters $\rho_m = 1000$ kg/m^3 and $K_1 = 10$ and 8 pN for the 8CB and 8OCB compounds, respectively. Since the elastic lateral bending strain does not exhibit an anomalous behavior in the vicinity of the temperature T_{NA}, both values of K_1 were measured at the phase transition temperatures T_{NA} of these compounds. It should be emphasized that fluctuations of the local smectic order parameter upon an *N*–*SmA* second-order phase transition according to relationships (5), (7), and (8) lead to a singularity only in the behavior of the viscosity coefficient η_2, whereas the other two Miesowicz viscosity coefficients η_1 and η_3 are not affected by the new structure. This suggests that the disturbing effect associated with the fluctuations of the local smectic order parameter manifests itself in the singular behavior of γ_1. Note that the analytical expressions for the rotational viscosity coefficient can be written in two forms: $\bar{\gamma}_1$ in the vicinity of the phase transition temperature T_{NA} can diverge either as $\sim t^{\nu/2}$ or as $\sim t^{\nu-1}$. Therefore, only comparison with experimental data on $\bar{\gamma}_1$ makes it possible to choose the appropriate form for describing the pretransition anomaly in the behavior of $\bar{\gamma}_1$. As the starting point, it is necessary to calculate the pure contribution to the viscosity coefficient $\bar{\gamma}_1$, namely, the viscosity coefficient γ_1.

For this purpose, we will use the statistical-mechanics approach to the theory of rotational viscosity γ_1 [6]. In terms of this theory, the antisymmetric part of the phenomenological stress tensor $\bar{\sigma}^a = 1/2(\alpha_2 - \alpha_3) \times (\mathbf{nN} - \mathbf{Nn}) + 1/2(\alpha_5 - \alpha_6)(\mathbf{nn} \cdot \mathbf{M} - \mathbf{M} \cdot \mathbf{nn}) = 1/2S[(\gamma_1\mathbf{N} + \gamma_2\mathbf{n} \cdot \mathbf{M}) \times \mathbf{n}]$ (where S is the Levi-Civitá tensor) can be represented as the mean equivalent microscopic tensor $\bar{\sigma}^a$ on the basis of the Zubarev method of a nonequilibrium statistical operator [17].

In essence, this approach is as follows: autocorrelations of the microscopic stress tensor are considered according to Fialkowski [7], and additional correlations of both the stress tensor with the director and the flow with the order parameter tensor are also taken into account. As a result, the rotational viscosity coefficient γ_1 can be calculated as a function of the density ρ, order parameter $\bar{P}_2$, and temperature T [6, 18, 19] and has the form

$$\gamma_1 = \frac{k_B T}{D_\perp}s\rho f(\bar{P}_2), \tag{9}$$

where $D_\perp$ is the coefficient of rotational self-diffusion with respect to the short molecular axes, $\rho = N/V$ is the number density of molecules, $s = (b^2 - 1)/(b^2 + 1)$ (b is the length-to-width ratio of molecules) is the geometric factor of molecules, and the function f is written in the form

$$f(\bar{P}_2) = \bar{P}_2^2\frac{9.54 + 2.77\bar{P}_2}{2.88 + \bar{P}_2 + 12.56\bar{P}_2^2 + 4.69\bar{P}_2^3 - 0.74\bar{P}_2^4}.$$

The mean value of the symmetric part $\bar{\sigma}^s$ of the stress tensor can be calculated by averaging its microscopic equivalent $\bar{\sigma}^s_{\text{micr}}$ using the equilibrium orientational distribution function $\phi(\mathbf{a})$ from the formula $\bar{\sigma}^s = \int \bar{\sigma}^s_{\text{micr}}\phi(\mathbf{a})d\mathbf{a}$, where $\mathbf{a}$ is the orientation of the long molecular axis. In turn, the expression for the coefficient γ_2 can be written as [5, 18, 19]

$$\gamma_2 = -\frac{k_B T}{D_\perp}s\rho\bar{P}_2. \tag{10}$$

The Leslie coefficients α_i ($i = 2, \ldots, 6$) are expressed in terms of the microparameters and macroparameters of

Relaxation times τ_{00}^{1}, rotational diffusion coefficients $D_{\perp}$, and order parameters for 8CB [4] and 8OCB [18] nematic liquid crystals

8CB (T_{NA} = 306.5 K); T, K	306.72	306.80	308.00	310.00	312.00
τ_{00}^{1} (ns)	19	20	27.8	22.7	18.6
$D_{\perp} \times 10^{7}$ (s^{-1})	13	12.3	8.4	9.4	11.3
P_2			0.57	0.053	0.44
P_4			0.14	0.12	0.06
P_6			0.07	0.05	0.03
8OCB (T_{NA} = 339.5 K); T, K	340		345		350
τ_{00}^{1} (ns)	30.4		19.5		12.1
$D_{\perp} \times 10^{7}$ (s^{-1})	7.55		9.43		11.71
P_2	0.55		0.47		0.38
P_4	0.20		0.15		0.10
P_6	0.05		0.03		0.02

the nematic liquid crystal as follows [5]:

$$\alpha_2 = -g\left(1+\frac{1}{\lambda}\right)\bar{P}_2, \quad \alpha_3 = -g\left(1-\frac{1}{\lambda}\right)\bar{P}_2,$$
$$\alpha_4 = g\frac{2s}{35}(7-5\bar{P}_2-2\bar{P}_4),$$
$$\alpha_5 = g\left[\frac{s}{7}(3\bar{P}_2+\bar{P}_4)+\bar{P}_2\right], \quad (11)$$
$$\alpha_6 = g\left[\frac{s}{7}(3\bar{P}_2+\bar{P}_4)-\bar{P}_2\right],$$

where $\bar{P}_{2L}$ (L = 1, 2) are the even-rank order parameters, $1/\lambda = -\gamma_1/\gamma_2 = \cos(2\theta_{eq})$, $g = k_B T \rho / D_{\perp}$, and the Leslie coefficients in expressions (11) satisfy the Onsager–Parodi relation $\alpha_2 + \alpha_3 = \alpha_6 - \alpha_5$.

Consequently, according to relationships (9)–(11), the rotational viscosity coefficients γ_1 and γ_2 and the Leslie coefficients α_i appear to be inversely proportional to the rotational self-diffusion coefficient $D_{\perp}$. Note that, in the limit of high temperatures, the statistical-mechanics approach predicts that $\gamma_1 \sim \bar{P}_2^2$. This behavior of the rotational viscosity coefficient is consistent with the mean-field theory [13]. It should be noted that, although the order parameters for almost all cyanobiphenyls were measured with a high accuracy [20], determination of the mobility constants for rotational diffusion remains considerably complicated.

By using the short-time expansion of the orientational time correlation functions $\Phi_{mn}^{L}(t) = \Phi_{mn}^{L}(\infty) + [\Phi_{mn}^{L}(0) - \Phi_{mn}^{L}(\infty)]\exp(-t/\tau_{mn}^{L})$, the relaxation time τ_{00}^{1} can be represented in the form [18]

$$\tau_{00}^{1} = \left[D_{\perp}\frac{2-2\bar{P}_2}{1+2\bar{P}_2}\right]^{-1}. \quad (12)$$

Here, the first-rank functions (L = 1) can be determined by the dielectric spectroscopic techniques and the orientational time correlation functions with L = 2 enter into the expressions for the nuclear spin relaxation rate and Raman band shapes. The experimental dielectric spectroscopic data obtained by Bose *et al.* [21] were used to calculate the complex permittivity $\epsilon^*(\omega) = \mathrm{Re}\,\epsilon(\omega) - i\,\mathrm{Im}\,\epsilon(\omega)$ for the 8CB compound in the frequency range 100 kHz $\le \omega \le$ 10 GHz. The experimental data on the complex permittivity $\epsilon_{\parallel}^{*}(\omega)$ parallel to the director **n** allow us to calculate the relaxation time τ_{00}^{1} with respect to the short axes of the 8CB molecules. In turn, these relaxation times and the order parameters $\bar{P}_2$ obtained from the polarized laser Raman scattering data [20] can be used to calculate the rotational self-diffusion coefficient $D_{\perp}$ from formula (12). In [18], the dynamic ($D_{\perp}$) and structural ($\bar{P}_{2L}$ at L = 1–3) characteristics of the 8OCB compound over a wide temperature range corresponding to the nematic phase were determined by NMR spectroscopy. The temperature dependences of the relaxation time τ_{00}^{1}, the rotational self-diffusion coefficient $D_{\perp}$, and the order parameter are presented in the table. In order to calculate the Leslie coefficients α_i of these nematic liquid crystals, the length and width of their molecules were chosen equal to ~2.0 and 0.6 nm, respectively [15]. The number density of molecules ρ for the 8OCB and 8CB compounds in the temperature range of the nematic phase was taken

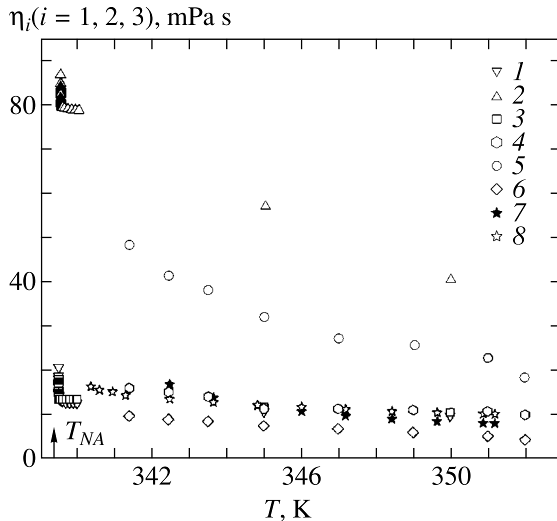

Fig. 1. Temperature dependences of the Miesowicz viscosity coefficients η_i (i = 1–3) for the 8OCB compound. Results of calculations from formulas (5), (7), and (8): (*1*) η_1, (*2*) η_2, and (*3*) η_3. Experimental data: (*4*) η_1, (*5*) η_2, (*6*) η_3 [22], (*7*) η_1, and (*8*) η_3 [23].

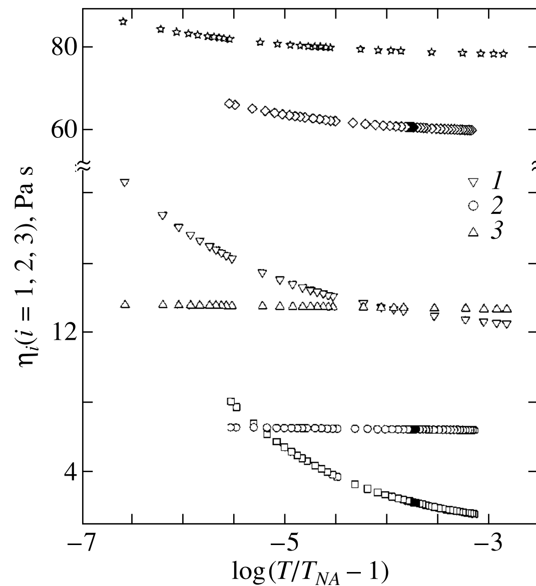

Fig. 2. Temperature dependences of the Miesowicz viscosity coefficients η_i (i = 1–3) calculated from formulas (5), (7), and (8) in the vicinity of the *N–SmA* phase transition [$-7 < \log(T/T_{NA} - 1) < -3$] for the 8CB and 8OCB compounds: (*1*) η_2 for 8OCB, (*2*) η_2 for 8CB, and (*3*) η_3 for 8OCB. Stars indicate η_1 for 8OCB, rhombuses correspond to η_1 for 8CB, and squares represent η_3 for 8CB.

equal to 1.8×10^{27} m^{-3}. The temperature dependences of the Miesowicz viscosity coefficients η_i (i = 1–3) calculated from relationships (5), (7), and (8) for the 8OCB compound are depicted in Fig. 1. The experimental data in [14, 22, 23] were obtained by direct measurements in the temperature range corresponding to the nematic phase of the 8OCB compound. In the temperature range far from the phase transition temperature ($\log t > -4$ or at temperatures 10 mK above the temperature T_{NA}), the calculated and measured Miesowicz viscosity coefficients indicate that the smallest viscosity coefficient η_2 ($\eta_2 < \eta_1 < \eta_3$) is observed when the nematic-flow velocity **v** is parallel to the director **n**. The temperature dependences $\eta_i(T)$ for the two liquid crystals are parallel to each other, except in the temperature range in the vicinity of the clearing point [13]. The dependences $\eta_i(T)$ deviate from this behavior in the neighborhood of the temperature T_{NA}. As can be seen from the temperature dependences $\eta_i(T)$ in the range $-7 < \log t < -3$ (Fig. 2), the viscosity coefficients $\eta_1(T)$ and $\eta_2(T)$ change places and the lowest resistance to the flow is observed when the director is oriented perpendicular to both the flow velocity **v** and the flow velocity gradient ∇v. It should be noted that, according to the experimental data on the viscosity coefficients $\eta_2(T)$ and $\eta_1(T)$ for the nematic phase of the 8CB compound, the viscosity coefficients $\eta_1(T)$ and $\eta_2(T)$ change places only at $T_c \approx 343.64$ K and the lowest resistance to the shear flow upon cooling is observed when the director is oriented perpendicular to both the flow velocity vector and the flow velocity gradient (i.e., $\eta_2 > \eta_1 > \eta_3$). In turn, the independent experimental measurement of the rotational viscosity coefficient γ_1 (Fig. 3) in the vicinity of the phase transition temperature T_{NA} for the 8CB compound demonstrates that the above exchange of places of the coefficients occurs at temperatures $\log t < -3$ or at temperatures lower than 306.6 K ($T_{NA} \sim 306.5$ K for 8CB). The viscosity coefficients η_2 calculated from relationships (5), (7), and (8) indicate that the viscosity

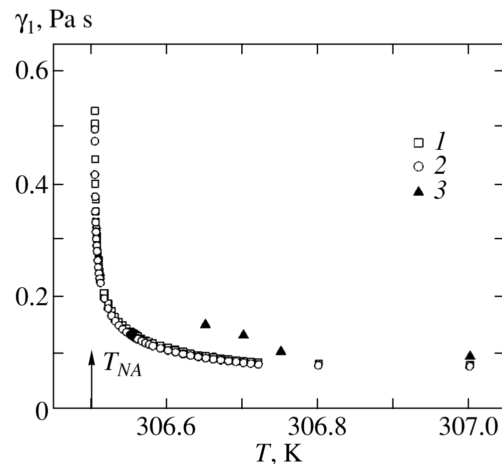

Fig. 3. Temperature dependences of the rotational viscosity coefficient γ_1 calculated from (*1*) formulas (5) and (7) and (*2*) formulas (5) and (8) in the vicinity of the *N–SmA* phase transition [$-7 < \log(T/T_{NA} - 1) < -3$] for the 8CB compound. Symbols *3* are the experimental data taken from [23, 24].

coefficients η_1 and η_2 change places at log*t* = –5.25 (≈306.502 K) for the 8CB compound and log*t* = –4 (≈339.540 K) for the 8OCB compound. It should be noted that the use of formulas (7) and (8) to calculate the contributions made to the rotational viscosity coefficient γ_1 by fluctuations of the local smectic order parameter leads to virtually identical results in the temperature range $-7 < \log t < -3$ (Fig. 3).

3. CONCLUSIONS

Thus, the performed calculations of the Miesowicz viscosity coefficients made it possible to describe the viscous hydrodynamics in the vicinity of the *N–SmA* phase transition more adequately.

ACKNOWLEDGMENTS

This work was supported by the Russian Foundation for Basic Research, project no. 01-03-32084.

REFERENCES

1. A. Madsen, J. Als-Nielsen, and G. Grübel, Phys. Rev. Lett. **90**, 085701 (2003).
2. G. Rienäcker, M. Kröger, and S. Hess, Phys. Rev. E **66**, 040702R (2002).
3. D. L. Cheung, S. J. Clark, and M. R. Wilson, Chem. Phys. Lett. **356**, 140 (2002).
4. A. V. Zakharov, A. A. Vakulenko, and J. Thoen, J. Chem. Phys. **118**, 4253 (2003).
5. N. Kuzuu and M. Doi, J. Phys. Soc. Jpn. **52**, 3486 (1983).
6. A. V. Zakharov, Phys. Lett. A **193**, 471 (1994).
7. M. Fialkowski, Phys. Rev. E **58**, 1955 (1998).
8. J. L. Ericksen, Arch. Ration. Mech. Anal. **4**, 231 (1960).
9. F. M. Leslie, Arch. Ration. Mech. Anal. **28**, 265 (1968).
10. P. G. de Gennes, Solid State Commun. **10**, 783 (1972).
11. F. Jahnig and F. Brochard, J. Phys. (Paris) **35**, 301 (1974).
12. R. F. Bruinsma and C. R. Safinya, Phys. Rev. A **43**, 5377 (1991).
13. P. G. de Gennes and J. Prost, *The Physics of Liquid Crystals*, 2nd ed. (Oxford Univ. Press, Oxford, 1995; Mir, Moscow, 1977), p. 360.
14. A. G. Chmielewski, Mol. Cryst. Liq. Cryst. **132**, 319 (1986).
15. D. Davidov, C. R. Safinya, M. Kaplan, *et al.*, Phys. Rev. B **19**, 1657 (1979).
16. P. P. Karat and N. V. Madhusudana, Mol. Cryst. Liq. Cryst. **40**, 239 (1977).
17. D. N. Zubarev, *Nonequilibrium Statistical Thermodynamics* (Nauka, Moscow, 1971; Consultants Bureau, New York, 1974).
18. A. V. Zakharov and R. Dong, Phys. Rev. E **63**, 011704 (2001).
19. A. V. Zakharov, A. V. Komolkin, and A. Maliniak, Phys. Rev. E **59**, 6802 (1999).
20. T. Kobayashi, H. Yoshida, A. D. Chandani, *et al.*, Mol. Cryst. Liq. Cryst. **77**, 267 (1986).
21. T. K. Bose, B. Campbell, S. Yagihara, *et al.*, Phys. Rev. A **36**, 5767 (1987).
22. H. J. Coles and M. S. Sefton, Mol. Cryst. Liq. Cryst. Lett. **4** (5), 123 (1987).
23. H. Graf, H. Kneppe, and F. Schneider, Mol. Phys. **77**, 521 (1992).
24. J. Jadzyn and G. Czechovski, J. Phys.: Condens. Matter **13**, L261 (2001).

Translated by O. Borovik-Romanova

Physics of the Solid State, Vol. 46, No. 8, 2004, pp. 1554–1559. Translated from Fizika Tverdogo Tela, Vol. 46, No. 8, 2004, pp. 1509–1513.
Original Russian Text Copyright © 2004 by Aver'yanov.

Correlation of the Molecular Structure of Discotic Nematic Liquid Crystals with Their Orientational Order and Specific Features of the Nematic–Isotropic Phase Transition

E. M. Aver'yanov

Kirensky Institute of Physics, Siberian Division, Russian Academy of Sciences, Akademgorodok, Krasnoyarsk, 660036 Russia

e-mail: aver@iph.krasn.ru

Received November 14, 2003

Abstract—The orientational order parameter S of molecules in high-temperature discotic nematic liquid-crystal phases of triphenylene derivatives is investigated as a function of the length of side flexible molecular chains at different temperatures. It is established that the orientational order parameters S in the range of the transition from the nematic phase to the isotropic liquid phase (the N_D–I transition) are smaller than those predicted from the molecular-statistical theory and computer simulation. It is shown that the N_D–I transition is close to both the isolated Landau point and the tricritical point (regardless of the chemical structure of the molecules and the anisotropy of dispersion intermolecular interactions). Consistent explanations are offered for a number of experimental findings, such as the anomalously small changes in the enthalpy and entropy upon the N_D–I transition (as compared to those revealed upon the N–I transition in calamitic nematic liquid crystals), the anomalously strong response of the isotropic phase of discotic nematic liquid crystals to external fields (thermodynamically conjugate to the order parameter S) and the long relaxation times of this response, and the formation of cybotactic discotic molecular clusters in the isotropic phase in the vicinity of the N_D–I transition. *© 2004 MAIK "Nauka/Interperiodica".*

1. INTRODUCTION

The phase transition from a discotic nematic phase to an isotropic liquid phase (the N_D–I transition) in liquid crystals consisting of disk-shaped molecules is one of the most intriguing phenomena in the physics of liquid crystals. This transition has been the subject of extensive experimental studies [1–12], molecular-statistical theoretical investigations [13–17], and computer simulation [18–23]. Disk-shaped molecules forming a discotic nematic phase consist of a planar central aromatic core with a relatively large radius and radial flexible aliphatic chains of specific length [24, 25]. In a uniaxial nonpolar homogeneously oriented discotic nematic phase, the preferred axes **l** of disk-shaped molecules are normal to the molecular planes and are predominantly oriented along the director **n**. The degree of orientational ordering in liquid-crystal molecules is characterized by the order parameter $S = \langle 3\cos^2\theta - 1\rangle/2$, where θ is the angle between the vectors **l** and **n** and the brackets $\langle\ldots\rangle$ indicate statistical averaging.

Discotic nematic liquid crystals are characterized by anomalously small changes in the enthalpy $\Delta H = 0.02$–0.6 kJ/mol upon the N_D–I phase transition [3–8, 12] as compared to the enthalpy change $\Delta H = 1$–6 kJ/mol [26] observed upon the N–I phase transition in calamitic nematic liquid crystals, which consist of rodlike or lathlike molecules. From the Landau–de Gennes expansion for the thermodynamic potential of a nematic liquid crystal into a series in powers of the parameter S, that is,

$$\Delta\Phi = a(T-T^*)S^2/2 - BS^3/3 + CS^4/4 + ES^5/5 + DS^6/6 + \ldots, \quad (1)$$

we obtain the following expression:

$$\Delta H = aS_{NI}^2 T_{NI}/2, \quad (2)$$

where T_{NI} is the temperature of the N_D–I phase transition ($T_{NI} > T^*$) and $S_{NI} = S(T_{NI})$). Hence, it follows that the smallness of the change in the enthalpy ΔH can be associated either with the small values of S_{NI} and the similarity of the N_D–I phase transition to the second-order transition or with the smallness of the factor a. Both variants lead to a number of physical consequences. Since the specific features of the N_D–I phase transition are governed by the structural features of disk-shaped molecules, this problem can be solved by analyzing the available data on the influence of molecular properties on the temperature dependence of the orientational order parameter $S(T)$. There are only a few works devoted to the investigation of the dependence $S(T)$ for discotic nematic liquid crystals with the use of refractometry [6, 9–11] and IR spectroscopy [12].

In this work, the dependence $S(T)$ for the discotic nematic phase of two high-temperature triphenylene

derivatives was investigated using the anisotropy of diamagnetic susceptibility of these compounds. Consideration was given to the structural features of the chosen molecules and their ordering, which are responsible for the strong coupling of the orientational and conformational degrees of freedom of molecules in the discotic nematic phase. A correlation was revealed between the dependence $S(T)$ and molecular properties. The results obtained were compared with those predicted from the molecular-statistical theory and computer simulation. Consistent explanations were offered for the known features of the N_D–I phase transition.

2. OBJECTS OF INVESTIGATION AND THEIR SPECIFIC FEATURES

Owing to the relatively dense molecular packing in the nematic phase, the shape of the molecules determines the anisotropy of their local coordination environment. In calamitic nematic liquid crystals, the vector **n** is perpendicular to the direction of the shortest intermolecular distance which is comparable to the transverse size of rodlike molecules. At the same time, in the discotic nematic liquid crystals, the vector **n** is aligned parallel to the direction of the shortest intermolecular distance which is comparable to the thickness of disk-shaped molecules. This difference in the local anisotropy of the calamitic nematic and discotic nematic phases, along with the structural–chemical features of discotic molecules, accounts for the fact that the conformational state of side chains of these molecules in the discotic nematic phase has a more profound effect on the order parameter S and the dependence $S(T)$ as compared to that in the calamitic nematic phase.

The loose structure of discotic molecules with the statistical symmetry axis $C_n \parallel \mathbf{l}$ ($n \geq 3$) is characterized by large-sized holes between side chains of the molecules, which is a prerequisite for a high conformational mobility of the chains. As the chain length increases, the free volume per chain of a discotic molecule increases rapidly, which also enhances their conformational mobility.

In the discotic nematic phase, the planar aromatic cores of the molecules are equivalent to the planes restricting the conformational mobility of the chains of neighboring molecules along the director. However, the mobility in the directions normal to the director remains sufficiently high and is restricted only by steric repulsion of adjacent chains of the same molecule or by the engagement of chains of the neighboring molecules. An increase in the degree of orientational order of molecular axes **l** with respect to the director **n** or in the order parameter S leads to a decrease in the number of conformational states responsible for the deviation of the chains from the core plane. This favors an increase in the anisotropy of the molecular shape and enhances anisotropic steric intermolecular interactions. On the other hand, the thermal conformational mobility of the chains results in a decrease in their contribution to the energy of the anisotropic intermolecular interaction and has a disordering effect on the molecular cores. The above factors are responsible for the interrelation between the orientational order of molecules and the conformational state of their chains in the nematic phase. In turn, this interrelation should manifest itself in the dependence of the magnitude and the temperature behavior of the order parameter S on the chain length, especially in the case when the mesophase has a high temperature corresponding to a high thermal mobility of the molecular chains.

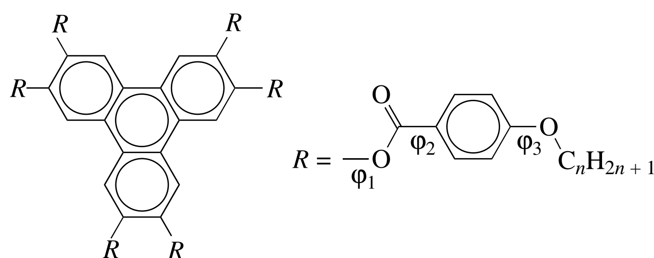

Fig. 1. Structure of *n*OBT molecules.

On this basis, the compounds of the homologous series of 2,3,6,7,10,11-hexakis(4-*n*-alkyloxybenzoyloxy)triphenylenes (*n*OBT) at $n = 6$ and 11 [1] were chosen as the objects of our investigation. The structure of *n*OBT molecules is shown in Fig. 1.

The molecules of these compounds with an identical number of side chains differ from those studied earlier in [9–11] in terms of the point group of statistical symmetry C_3, the chemical structure, the polar properties of the aromatic cores, and the free volume per chain in an individual molecule. For each fragment R, the angle φ_1 between the plane of the triphenylene core and the plane of the O(O)C bridging group varies from 61° to 81° [7]. The angle $\varphi_2 = 0$ between the plane of the O(O)C electron-acceptor fragment and the phenyl ring provides the π conjugation of this fragment to the phenyl ring and the electron-donor alkoxy chain. This results in an increase in the anisotropy of molecular polarizability. The distribution function $f(\varphi_3)$ has a maximum at the angle $\varphi_3 = 0$ [7]. Therefore, for the methylene chain fragments that are adjacent to the molecular core and predominantly adopt a *trans* conformation, the carbon backbone lies in the plane making the angle $\varphi_4 = \varphi_1$ with the plane of the triphenylene core. As the length of the chains increases, their side fragments deviate from the core plane. This leads to an increase in the thickness of the molecule and a decrease in the anisotropy of the molecular shape. The anisotropy of steric intermolecular interactions also decreases.

Among the known compounds [25], the 6OBT homolog has one of the highest temperature discotic nematic phases. The nematic phase of the 11OBT

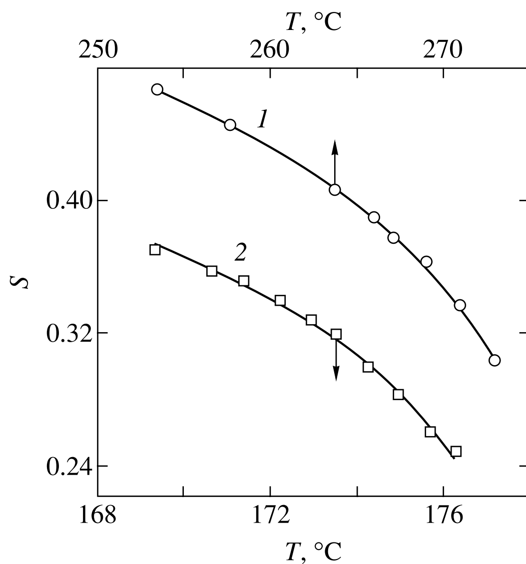

Fig. 2. Temperature dependences of the order parameter S in the discotic nematic phase for nOBT homologs at n = (*1*) 6 and (*2*) 11. Solid lines represent the results of interpolation according to relationships (3) and (4).

homolog is also observed at temperatures considerably above the limiting temperature $T_l = T_{NI}(n \longrightarrow \infty) \approx$ 60°C at which the molecular chains do not affect the phase transition point T_{NI} for this homologous series [27]. For all homologs of the nOBT series, the inequality $T_{NI}(n) > T_l$ holds true and an increase in n is accompanied by a monotonic decrease in the temperature $T_{NI}(n)$. This implies a decrease in the anisotropy of intermolecular interactions that stabilize the nematic order of molecules. There is a scatter in the data available in the literature on the phase transition temperatures $T_{NI}(n)$ for compounds of the nOBT series [1, 5, 12, 24, 25]; however, this scatter is not related to the anisotropic properties of the discotic nematic phase on the scale of the reduced temperature $\Delta T = T_{NI} - T$.

3. ORIENTATIONAL ORDER OF THE NEMATIC PHASE AND SPECIFIC FEATURES OF THE N_D–I PHASE TRANSITION

The molecules under consideration are statistically uniaxial, and the anisotropy $\Delta\chi_m = (\chi_\parallel^m - \chi_\perp^m) < 0$ of the diamagnetic susceptibility tensor of a discotic nematic liquid crystal is determined only by the order parameter S [11]. The components $\chi_\parallel^m$ and $\chi_\perp^m$ correspond to the magnetic field directions parallel and perpendicular to the director. For the 6OBT and 11OBT homologs, there are data on the dependence of the specific diamagnetic anisotropy $\Delta\chi_m(T)$ for the discotic nematic phase oriented in a magnetic field [1]. These dependences were obtained from the relationship $\Delta\chi_m = 3(\chi_i^m - \chi_\perp^m)$ under the assumption that the diamagnetic susceptibility χ_i^m in the isotropic phase coincides with the average diamagnetic susceptibility in the nematic phase $\bar{\chi}_m = (\chi_\parallel^m + 2\chi_\perp^m)/3$, which does not depend on the temperature and the degree of molecular ordering. Since the contribution of alkyl chains to the anisotropy of diamagnetic polarizability of the studied molecules is negligible [28], the dependences $\Delta\chi_m(T)$ can be used to determine the order parameter S:

$$S(T) = \Delta\chi_m(T)/\Delta\chi_{m0}. \tag{3}$$

Here, the value of $\Delta\chi_{m0} = \Delta\chi_m$ ($T = 0$, $S = 1$) can be determined from the approximate relationship

$$\Delta\chi_m(T) = \Delta\chi_{m0}(1 - T/T_H)^\beta, \tag{4}$$

which was theoretically justified in terms of expansion (1) [9–11]. Here, we have $T_H > T_{NI}$. Figure 2 shows the dependences $S(T)$ thus calculated with parameters $\Delta\chi_{m0} = -(1.267 \pm 0.027) \times 10^{-7}$ cm^3/g, $T_H = 550 \pm 0.27$ K, and $\beta = 0.241 \pm 0.007$ for the 6OBT compound and $\Delta\chi_{m0} = -(0.811 \pm 0.082) \times 10^{-7}$ cm^3/g, $T_H = 451 \pm 0.38$ K, and $\beta = 0.248 \pm 0.027$ for the 11OBT compound. The order parameters for each homolog at the highest temperatures correspond to the values of S_{NI} [1]. It can be seen from Fig. 2 that the dependences $S(T)$ are approximated well by expressions (3) and (4). For identical differences $\Delta T = T_{NI} - T$, the order parameter S for the 11OBT homolog with long chains is smaller than that for the 6OBT homolog with short chains (especially at temperatures close to the phase transition point T_{NI}). This indicates that the thermal mobility of chains has a disordering effect on the orientational order of the molecular cores in the range of the N_D–I phase transition. For the intermediate homolog 8OBT of the studied series with the phase transition temperature T_{NI} = 238°C and a wide range of existence of the nematic phase, the order parameters $S(\Delta T)$, which were obtained from the data on the dichroism of the IR absorption band at frequency ν = 1603 cm^{-1} for homeotropically oriented samples, vary in the range from 0.27 to 0.6 [12]. For identical differences ΔT, these order parameters fall in the range between the corresponding values for the 6OBT and 11OBT homologs. Therefore, an increase in the chain length of the nOBT homologs leads to a monotonic decrease in the order parameter S in the range of the N_D–I phase transition. A similar decrease in the order parameter S with an increase in the chain length was observed earlier for the low-temperature reentrant discotic nematic phase of truxene derivatives [29] and, most likely, can be considered a general property of discotic nematic liquid crystals.

The values of β = 0.24–0.25 for the above homologs are close to those determined for the previously studied liquid crystals [6, 9–11] with a different molecular

structure and different parameters $A = 3(\gamma_t - \gamma_l)/(\gamma_l + 2\gamma_t)$, where γ_l and γ_t are the longitudinal (along the **l** axis) and transverse components of the molecular polarizability, respectively. The parameter A characterizes the relative anisotropy of the molecular polarizability and dispersion intermolecular interactions in the nematic phase. The close values of β indicate that the steric intermolecular repulsion plays a decisive role in the orientational ordering of discotic nematic liquid crystals, as is the case with calamitic nematic liquid crystals.

The experimental values of the order parameter $S(\Delta T)$ for the homologs under consideration and the compounds studied earlier in [6, 9–12] are considerably smaller than the parameters predicted from the Maier–Saupe molecular-statistical theory [13], especially in the vicinity of the phase transition temperature T_{NI}. The approaches based on generalizing this theory with a more detailed analysis of the anisotropic intermolecular interactions [14–16] and intermolecular correlations of short-range order [17] lead to overestimated values of $S(\Delta T)$ and do not offer correct interpretation of the experimental data. The molecular dynamics simulation of a system of particles in the form of oblate ellipsoids of revolution [21–23] predicts the sequence of the I–N_D–Col_{hd} phase transitions with the order parameter $S_{NI} = 0.5$–0.7 and large values of $S = 0.7$–0.95 for the discotic nematic phase. These results differ significantly from the experimental data. Therefore, the experimentally observed features in the dependence $S(\Delta T)$ for discotic nematic liquid crystals cannot be explained without considering the structural features of real discotic molecules and intramolecular degrees of freedom in the framework of the molecular-statistical theory and in the computer simulation.

The sequence of the I–N_D–Col_{hd} phase transitions was also predicted by the Monte Carlo method for an athermic system of disk-shaped particles (cut spheres with diameter D_s and thickness L) at $L/D_s < 0.14$ [20]. However, in this system, the N_D–I phase transition is a weak first-order transition with the order parameter $S_{NI} = 0.3$–0.4. For a system of N disk-shaped particles in a volume V with $L = 0$ and an effective density $\rho = ND_s^3/V$ [18, 19], the order parameter $S_{NI} \approx 0.37$ corresponds to the temperature of the N_D–I phase transition at $\rho = \rho_{NI}$ and the dependence $S(\rho)$ in the discotic nematic phase is approximated well by the relationship $S \sim (\rho - \rho_1)^\beta$, where $\beta = 0.23 \pm 0.03$. Here, the quantities ρ_1 and β are similar to the quantities T_H and β in formula (4). The small difference between the calculated and experimental values of β confirms the above assumption regarding the role played by the steric intermolecular interactions in the ordering of the discotic nematic phase.

Therefore, when changing over from models of ellipsoidal molecules with a three-dimensional shape ($D = 3$) [17, 21–23] to models of disk-shaped molecules with a small thickness (dimension $D \approx 2$) [18, 19], the calculated parameters S_{NI} and β approach the experimental values. The loose structure of discotic molecules with large-sized holes between radial side chains suggests that the shape of these molecules has a dimension $D < 2$. The value of D depends on statistical symmetry of molecules, the structure of the molecular core, the number of flexible chains, and their length. This ensures a mutual penetration of the chains of neighboring molecules in the nematic phase (similar to engaged gears) and hinders the rotation of molecules about the **l** axes and their sliding relative to one another in planes normal to the director. This type of intermolecular correlation, which is not taken into account or described in any of the known theoretical approaches or computer simulation, corresponds to the high viscosity of discotic nematic liquid crystals, which exceeds the viscosity of calamitic nematic liquid crystals by one or two orders of magnitude [4].

The experimental dependences $S(\Delta T)$ for calamitic and discotic nematic liquid crystals over the entire range of existence of the mesophase are described with a high accuracy in terms of expansion (1) with inclusion of the terms up to S^6 [9–11]. Note that, at $B \neq 0$, the contribution from the term $\sim S^5$ is insignificant. Since the values of β for discotic nematic liquid crystals are close to 0.25, both coefficients B and C in expansion (1) are small; i.e., the N_D–I phase transition is close to the isolated Landau point ($B = 0$) and the tricritical point ($C = 0$). The smallness of the coefficients B and C for discotic liquid-crystal molecules can be due to the dimension of these molecules ($D < 2$) and the interrelation between the orientational order of the molecules and the conformational state of their flexible chains. The former factor is associated with the mutual penetration and engagement of the neighboring molecules located in the plane normal to the director. This factor brings about the formation of molecular associates with an effective biaxial shape, which leads to a decrease in the coefficient B [30]. The interrelation between the order parameter S and the conformational mobility of chains provides a decrease in the coefficient C [11].

The order parameters S_{NI} for the discotic nematic liquid crystals considered in this paper and studied earlier in [6, 9–12] are smaller than those for calamitic nematic liquid crystals. However, the difference is insignificant. Therefore, the anomalously small changes in the enthalpy ΔH [expression (2)] upon the N_D–I phase transition, as compared to the enthalpy change observed upon the N–I phase transition, are determined primarily by the smallness of the factor a for the discotic nematic liquid crystals. In turn, the smallness of the factor a suggests a considerable bare correlation length ξ_0 for equilibrium thermal fluctuations of the order parameter S. For the isotropic phase, the bare correlation length can be represented in the form $\xi_{0i} = (L/aT^*)^{1/2}$ [10]. In the one-constant approximation of the elasticity theory, the parameter L and the

elastic modulus K of the nematic liquid crystal are related by the expression $K = 2S^2L$ [28]. Since the elastic moduli (like the order parameters S) for calamitic and discotic nematic liquid crystals are close to each other [3–5], the correlation length ξ_{0i} for the discotic nematic liquid crystals should be severalfold greater than $\xi_{0i} \approx 6$ Å for the calamitic nematic liquid crystals [31] and should be comparable to the diameter of disk-shaped molecules.

According to the x-ray scattering data [1, 4], the mean intermolecular distance along the director **n** in the discotic nematic phase $d_{\parallel} \approx 4.5$ Å is substantially smaller than the molecular diameter. Structurally, from the inequality $\xi_{0i} \gg d_{\parallel}$ for discotic nematic liquid crystals, it follows that the isotropic and nematic phases should contain cybotactic molecular clusters with a strong correlation of several molecules along the director **n**. This is confirmed by the x-ray scattering data obtained for *n*OBT homologs with polar molecules [1] and other liquid crystals with nonpolar molecules [4]. The latter circumstance implies that the polarity of discotic molecules is not a controlling factor in the formation of cybotactic clusters.

The small values of the enthalpy change ΔH indicate a small change in the entropy $\Delta\Xi = \Delta H/T_{NI}$. In turn, the smallness of the entropy change $\Delta\Xi$ means that cybotactic clusters consisting of several molecules rather than individual molecules serve as structural units upon the N_D–I phase transition. Moreover, this transition is attended by an insignificant transformation of the local structure of the material. This inference is consistent with the aforementioned consequences of the smallness of the factor a.

The factor a characterizes the susceptibility $\chi_i = (\partial^2\Phi/\partial S^2)^{-1}_{S=0} = [a(T - T^*)]^{-1}$ of the isotropic phase of the nematic liquid crystal to external actions and determines the amplitude of anomalous changes in the anisotropic properties of this phase in response to external fields (thermodynamically conjugate to the order parameter S) as the temperature of the I–N_D phase transition is approached [10, 11]. Furthermore, the smallness of the factor a indicates long relaxation times $\tau \sim \chi_i$ [32] for anisotropic properties induced by external fields in the isotropic phase for a fixed difference $T - T^*$. This explains not only the anomalously high birefringence $\Delta n \sim \chi_i$, which is induced by shear flow in the isotropic phase of the discotic liquid crystal [8] with an anomalously small value of $\Delta H = 20 \pm 10$ J/mol, but also the large Kerr constant $B \sim \chi_i$ for the electric birefringence Δn_E in the isotropic phase of the discotic nematic liquid crystal in the vicinity of the phase transition temperature T_{NI} and the long relaxation time $\tau \sim \chi_i$ for the quantity Δn_E as compared to the relaxation time characteristic of calamitic nematic liquid crystals [4].

4. CONCLUSIONS

Thus, the above analysis of the experimental data on the properties of discotic and calamitic nematic liquid crystals has demonstrated that the difference in their properties and the specific features of the N_D–I phase transition are associated with the structural features of loose discotic molecules and can be consistently explained in terms of the smallness of the factor a in expansion (1).

REFERENCES

1. A. M. Levelut, F. Hardouin, H. Gasparoux, C. Destrade, and N. H. Tinh, J. Phys. (Paris) **42** (1), 147 (1981).
2. C. Baumann, J. P. Marcerou, J. C. Rouillon, and J. Prost, J. Phys. (Paris) **45** (3), 451 (1984).
3. T. W. Warmerdam, R. J. M. Nolte, W. Drenth, J. C. van Miltenburg, D. Frenkel, and R. J. J. Zijlstra, Liq. Cryst. **3** (8), 1087 (1988).
4. M. Ebert, D. A. Jungbauer, R. Kleppinger, T. H. Wendorff, B. Kohne, and K. Praefcke, Liq. Cryst. **4** (1), 53 (1989).
5. T. J. Phillips, J. C. Jones, and D. G. McDonnell, Liq. Cryst. **15** (2), 203 (1993).
6. T. J. Phillips and J. C. Jones, Liq. Cryst. **16** (5), 805 (1993).
7. P. Hindmarsh, M. J. Watson, M. Hird, and J. W. Goodby, J. Mater. Chem. **5** (12), 2111 (1995).
8. T. J. Phillips and V. Minter, Liq. Cryst. **20** (2), 243 (1996).
9. E. M. Aver'yanov, Pis'ma Zh. Éksp. Teor. Fiz. **61** (10), 796 (1995) [JETP Lett. **61**, 815 (1995)].
10. E. M. Aver'yanov, Zh. Éksp. Teor. Fiz. **110** (5), 1820 (1996) [JETP **83**, 1000 (1996)].
11. E. M. Aver'yanov, *Local-Field Effects in Optics of Liquid Crystals* (Nauka, Novosibirsk, 1999) [in Russian].
12. H. Monobe, S. Mima, T. Sugino, Y. Shimizu, and M. Ukon, Liq. Cryst. **28** (8), 1253 (2001).
13. G. E. Feldkamp, M. A. Handschi, and N. A. Clark, Phys. Lett. A **85** (6/7), 359 (1981).
14. K. Singh, U. P. Singh, and S. Singh, Liq. Cryst. **3** (5), 617 (1988).
15. T. K. Lahiri and S. Singh, Indian J. Phys. A **66** (5), 619 (1992).
16. K. Singh, N. S. Padney, and T. K. Lahiri, Liq. Cryst. **26** (7), 999 (1999).
17. K. Singh, S. Singh, and T. K. Lahiri, Liq. Cryst. **27** (11), 1431 (2000).
18. D. Frenkel and R. Eppenga, Phys. Rev. Lett. **49** (15), 1089 (1982).
19. R. Eppenga and D. Frenkel, Mol. Phys. **52** (6), 1303 (1984).
20. J. A. C. Veerman and D. Frenkel, Phys. Rev. A **45** (8), 5632 (1992).
21. M. D. de Luca, M. P. Neal, and C. M. Care, Liq. Cryst. **16** (2), 257 (1994).
22. A. P. J. Emerson, G. R. Luckhurst, and S. G. Whatling, Mol. Phys. **82** (1), 113 (1994).

23. M. A. Bates and G. R. Luckhurst, J. Chem. Phys. **104** (17), 6696 (1996).
24. C. Destrade, P. Foucher, H. Gasparoux, N. H. Tinh, A. M. Levelut, and J. Malthete, Mol. Cryst. Liq. Cryst. **106**, 121 (1984).
25. K. Praefcke, EMIS Datarev. Ser. **25**, 17 (2000).
26. A. P. Kapustin, *Experimental Investigations of Liquid Crystals* (Nauka, Moscow, 1978) [in Russian].
27. E. M. Aver'yanov, Zhidk. Krist. Ikh Prakt. Ispol., No. 1, 25 (2003).
28. W. H. de Jen, *Physical Properties of Liquid Crystalline Materials* (Gordon and Breach, New York, 1980; Mir, Moscow, 1982).
29. E. M. Aver'yanov, Zh. Strukt. Khim. **38** (1), 89 (1997).
30. E. M. Aver'yanov, Fiz. Tverd. Tela (St. Petersburg) **45** (5), 943 (2003) [Phys. Solid State **45**, 990 (2003)].
31. M. A. Anisimov, *Critical Phenomena in Liquids and Liquid Crystals* (Nauka, Moscow, 1987) [in Russian].
32. L. D. Landau and E. M. Lifshitz, *Course of Theoretical Physics*, Vol. 5: *Statistical Physics*, 3rd ed. (Nauka, Moscow, 1976; Pergamon, Oxford, 1980), Part 1.

Translated by O. Borovik-Romanova

Physics of the Solid State, Vol. 46, No. 8, 2004, pp. 1560–1568. Translated from Fizika Tverdogo Tela, Vol. 46, No. 8, 2004, pp. 1514–1521.
Original Russian Text Copyright © 2004 by Larin.

Phase Diagram of Transitions from an Isotropic Phase to Nematic and Smectic (Uniaxial, Biaxial) Phases in Liquid Crystals with Achiral Molecules

E. S. Larin

Research Institute of Physics, Rostov State University, pr. Stachki 194, Rostov-on-Don, 344090 Russia

e-mail: eslarin@ip.rsu.ru

Received December 30, 2003

Abstract—The phase diagrams of transitions from an isotropic phase to nematic and smectic phases are investigated within a simple phenomenological model of the Landau thermodynamic potential. The conditions of the isomorphic phase transition between two uniaxial smectic phases and the direct transition from the isotropic phase to the uniaxial and biaxial smectic phases are determined. The behavior of the order parameters is described along different thermodynamic paths. The theoretical results are discussed using the example of liquid-crystal phases in compounds with banana-shaped achiral molecules. *© 2004 MAIK "Nauka/Interperiodica".*

1. INTRODUCTION

Phases (mesophases) in liquid crystals are characterized by orientational and partial positional orders and, according to the Friedel classification [1], can be separated into two main types, namely, nematic (N) and smectic (Sm) phases. In a nematic phase, anisotropic molecules (rods, disks) are predominantly oriented along a preferred direction **n**, which is referred to as the director. The centers of gravity of liquid-crystal molecules are disordered, as is the case with the simple isotropic (I) liquid. There are two types of nematic liquid crystals with achiral molecules that differ in terms of their physical properties, namely, uniaxial (N_u) and biaxial (N_b) nematic liquid crystals [2–8]. The specific features of the phase diagram (PD) of transitions between these phases were investigated within the Landau theory of phase transitions by Prostakov *et al.* [9].

Smectic liquid crystals have a layered structure and are separated into three main types: SmA, SmC, and SmB [2]. In the structure of smectic liquid-crystal phases, apart from the orientational order, there exists a partial translational order with a specific spacing between layers. Inside each layer, molecules are oriented, but their centers of gravity are disordered, so that each layer can be represented as a two-dimensional liquid [2].

Recent investigations revealed a biaxial smectic phase in liquid crystals with achiral molecules [10–14]. For this phase, it is possible to choose a direction characterizing the biaxiality of the phase with the unit vector **m** lying in the layer plane ($\mathbf{m} \perp \mathbf{p}$, where **p** is the vector normal to the smectic layer). In this case (for nonpolar molecules), the phase is invariant with respect to the transformation $\mathbf{m} \longrightarrow -\mathbf{m}$. According to de Gennes [2], this smectic phase is designated as C_M. In [13, 14], the corresponding smectic phase was denoted by Sm A_b. In what follows, we will use the latter abbreviation, because it characterizes the phase properties completely; namely, the letter A indicates the director orientation $\mathbf{n} \parallel \mathbf{p}$ and the letter b stands for the phase biaxiality. Therefore, the uniaxial smectic phase with $\mathbf{n} \parallel \mathbf{p}$ will be designated as Sm A_u. The particular interest expressed by researchers in investigating the properties of Sm A_b phases is explained by two main factors. First, a number of phases that have hitherto been classified as SmC phases can appear to be Sm A_b phases according to their optical biaxiality [15, 16]. Second, in recent works [13, 14], it was revealed that the Sm A_b phases with achiral molecules exhibit ferroelectric properties.

In this work, the specific features of the phase diagram of liquid crystals and the behavior of a number of physical quantities upon transitions from an isotropic phase to uniaxial nematic, uniaxial smectic A, and biaxial smectic A phases were investigated in the framework of the Landau theory of phase transitions. The possibility of a direct transition occurring from an isotropic phase to a uniaxial A smectic phase was theoretically studied in [15–24]. In particular, Prostakov [24] proposed a simple model of Landau transitions from an isotropic phase to uniaxial smectic A and uniaxial nematic phases. In the present work, the model of the Landau potential in the fourth order was used to determine the conditions for the existence of a smectic A phase and to describe a number of transitions, such as (i) a transition between two isostructural phases Sm A_u(I) and Sm A_u(II), which differ in the degree of ordering of molecular orientation and the thickness of smectic layers; (ii) Sm A_u–Sm A_b–N_u phase transitions; and (iii) a direct I–SmA_b phase transition. Moreover, we analyzed

all types of phase diagrams that are possible within the proposed model and the behavior of the order parameters along different thermodynamic paths (TP).

2. MODEL OF THE THERMODYNAMIC POTENTIAL

The formation of nematic and smectic phases from an isotropic liquid phase can be adequately described within the phenomenological approach in the framework of the Landau theory of phase transitions [25]. The symmetry of an isotropic phase (praphase) composed of achiral molecules is described by the space group $G_0 = T(3) \times O(3)$, where $T(3)$ is the translation group and $O(3)$ is the full orthogonal group in three-dimensional space. For a phase transition to a nematic phase, the order parameter, which can be transformed according to the irreducible representation of the G_0 group, is a symmetric traceless tensor of second rank, $Q_{ik}(\mathbf{r})$ [2]. The tensor field $Q_{ik}(\mathbf{r})$ describes both the degree of order (the degree of molecular orientation) and the orientation (direction) of molecules at each point $\mathbf{r}$. In the homogeneous case, it is assumed that the tensor Q_{ik} does not depend on $\mathbf{r}$. This approximation holds for the majority of nematic liquid crystals with achiral molecules for which the Frank elastic constants K_i (i = 1–3) are positive in sign [2, 21].

Let us choose the coordinate system $\mathbf{e}_i$, $i = x, y, z$ (where $\mathbf{e}_i$ are the unit vectors along the x, y, and z axes, respectively), in which Q_{ik} is the diagonal tensor; that is,

$$Q_{xx} = -1/2(\eta_1 - \sqrt{3}\eta_2), \quad Q_{yy} = -1/2(\eta_1 + \sqrt{3}\eta_2), \\ Q_{zz} = \eta_1, \quad Q_{ik} = 0, \quad i \neq k, \quad i, k = x, y, z. \tag{1}$$

From relationships (1), it follows that the director $\mathbf{n}$ is aligned parallel to the z axis. Now, we introduce the triad of orthogonal vectors $\mathbf{n}$, $\mathbf{m}$, and $\mathbf{l} = \mathbf{m} \times \mathbf{n}$, for which $n_i = (\mathbf{e}_i'\mathbf{e}_z)$, $m_i = (\mathbf{e}_i'\mathbf{e}_y)$, and $l_i = (\mathbf{e}_i'\mathbf{e}_x)$. Then, the tensor Q_{ik} takes the form

$$Q_{ik} = 1/2\eta_1(3n_in_k - \delta_{ik}) + \sqrt{3}/2\eta_2(l_il_k - m_im_k). \tag{2}$$

The changeover to layered smectic phases leads to violation of the continuous translational symmetry G_0 of the isotropic phase. For the smectic A phase under consideration, the violation occurs only in one direction, for example, along the z axis. In this case, the phase transition is described by a two-component order parameter, which is a one-dimensional density wave along the direction $\mathbf{q} \parallel \mathbf{z}$ [2], that is,

$$\psi(\mathbf{r}) = \rho_0 + |\Psi|\exp(iqz), \tag{3}$$

where ρ_0 is the density in the absence of layers and $|\Psi|$ is the modulus determining the strength of the smectic order parameter. The wave number can be represented as $q = 2\pi/d$, where d is the interlayer spacing. In the general case, the modulus $|\Psi|$ depends on the x, y, and z coordinates. We assume that the modulus $|\Psi|$ does not depend on $\mathbf{r}$.

By retaining only the terms up to the fourth order in the integer rational basis set of invariants, which involves both order parameters, we find that the thermodynamic potential depends on the following seven functions:

$$I_1 = Q_{il}Q_{li}, \quad I_2 = Q_{im}Q_{ml}Q_{li}, \\ I_3 = |\psi|^2, \quad I_4 = (\nabla_i\psi)(\nabla_i\psi^*), \\ I_5 = |\Delta\psi|^2, \quad I_6 = Q_{ik}(\nabla_i\psi)(\nabla_k\psi^*), \\ I_7 = Q_{im}Q_{mk}(\nabla_i\psi)(\nabla_k\psi^*). \tag{4}$$

In the present formulation of the problem, the biaxiality is determined only by the orientational order parameter Q_{ik} and the inhomogeneity is governed only by the smectic order parameter $\Psi(z)$. Physically, the presence of the invariant I_6 among invariants (4) means that the smectic ordering is accompanied by orientational ordering. With the use of expressions (1) and (3), invariants (4) can be rearranged into the form

$$I_1 = 2/3(\eta_1^2 + \eta_2^2), \quad I_2 = 3/4(\eta_1^3 - 3\eta_1\eta_2^2), \tag{5}$$

$$I_4 = q^2|\Psi|^2, \quad I_5 = q^4|\Psi|^2, \\ I_6 = \eta_1 q^2|\Psi|^2, \quad I_7 = \eta_1^2 q^2|\Psi|^2. \tag{6}$$

By retaining the terms up to the fourth order in the order parameter in the expression for the thermodynamic potential, we obtain a simple model potential similar to that derived in [24]:

$$\Phi(\eta_1, \eta_2; |\Psi|, q) = a_1(\eta_1^2 + \eta_2^2) + b_1(\eta_1^3 - 3\eta_1\eta_2^2) \\ + a_2(\eta_1^2 + \eta_2^2)^2 + \alpha_1^*|\Psi|^2 + \alpha_2|\Psi|^4 \\ + \lambda_1|\Psi|^2q^2 + \lambda_2|\Psi|^2q^4 + \gamma_1^*\eta_1q^2|\Psi|^2 \\ + \gamma_2(\eta_1^2 + \eta_2^2)|\Psi|^2 + \gamma_3^*\eta_1^2q^2|\Psi|^2. \tag{7}$$

Compared to the potential proposed in [24], the potential Φ defined by expression (7) includes the additional term $\gamma_3^*\eta_1^2q^2|\Psi|^2$.

3. MODELS OF LIQUID-CRYSTAL PHASES

The system of equations of state for the model thermodynamic potential (7) has the form

$$\frac{\partial\Phi}{\partial\eta_1} = 2a_1\eta_1 + 3b_1(\eta_1^2 - \eta_2^2) + 4a_2(\eta_1^2 + \eta_2^2)\eta_1 \\ + \gamma_1^*|\Psi|^2q^2 + \gamma_2|\Psi|^2\eta_1 + \gamma_3^*|\Psi|^2\eta_1^2 = 0,$$

$$\frac{\partial\Phi}{\partial\eta_2} = 2\eta_2[a_1 - 3b_1\eta_1 + 2a_2(\eta_1^2 + \eta_2^2) + \gamma_2|\Psi|^2] = 0,$$
$$\frac{\partial\Phi}{\partial|\Psi|} = 2|\Psi|[\alpha_1 + 2\alpha_2|\Psi|^2 - 2\lambda_2 q^4 + \gamma_2(\eta_1^2 + \eta_2^2)] = 0, \quad (8)$$
$$\frac{\partial\Phi}{\partial q} = 2|\Psi|^2 q(\lambda_1 + 2\lambda_2 q^2 + \gamma_1^*\eta_1 + \gamma_3^*\eta_1^2) = 0$$

and admits the solutions corresponding to the following phases.

The isotropic phase exists under the conditions

$$\eta_1 = \eta_2 = 0, \quad |\Psi| = 0. \quad (9)$$

The uniaxial nematic phases can be observed when the following conditions are satisfied:

$$\begin{gathered} N_u^+: \quad \eta_1 > 0, \quad \eta_2 = 0 \\ (\eta_2 = \pm\sqrt{3}\eta_1, \eta_1 < 0), \quad |\Psi| = 0; \\ N_u^-: \quad \eta_1 < 0, \quad \eta_2 = 0 \\ (\eta_2 = \pm\sqrt{3}\eta_1, \eta_1 > 0), \quad |\Psi| = 0. \end{gathered} \quad (10)$$

The $\mathrm{Sm}A_u^{\pm}$ uniaxial smectic phases is observed when

$$\eta_1 \neq 0, \quad \eta_2 = 0, \quad |\Psi| \neq 0, \quad q \neq 0. \quad (11)$$

The Sm A_b biaxial smectic phase exists under the following conditions:

$$\begin{gathered} \eta_1 \neq 0, \quad \eta_2 \neq 0, \quad |\Psi| \neq 0, \quad q \neq 0, \\ \eta_2^2 - 3\eta_1^2 = (\gamma_1^* q^2|\Psi|^2 + \gamma_3^*\eta_1 q^2|\Psi|^2)/3b_1. \end{gathered} \quad (12)$$

As will be shown below, the model under consideration describes the sequence of the I–Sm A_u^+–Sm A_b–N_u^+ phase transitions. In this case, the behavior of the biaxiality in the biaxial smectic A phase is similar to the behavior of the biaxiality described for the biaxial nematic phase in [9], because the biaxiality of the system is governed only by the orientational order parameter. The biaxiality reaches a maximum at $3\eta_2^2 = \eta_1^2$ and vanishes in the lines corresponding to the Sm A_u^+–Sm A_b and Sm A_b–N_u^+ phase transitions.

4. PHASE DIAGRAM

In order to construct the phase diagram, it is necessary to determine the stability regions for each phase (9)–(12) in the space of variable parameters of the model thermodynamic potential Φ (7). The global minimum of the model (all phases exist at finite order parameters), which is obtained by the method proposed in [9], requires that the following conditions be satisfied:

$$\begin{gathered} a_2 > 0, \quad \alpha_2 > 0, \quad \lambda_2 > 0, \\ \gamma_2 + \gamma_3^* > -2\sqrt{a_2}\alpha_2 + \gamma_1^{*2}/4\lambda_2. \end{gathered} \quad (13)$$

In the model potential Φ (7), the parameters a_1, α_1, λ_1, and b_1 are variable parameters that depend on the external conditions and determine the space of the complete phase diagram. As a rule, experimental phase diagrams are represented by two-dimensional diagrams in which the pressure P, temperature T, and concentration c serve as variable parameters. Such two-dimensional phase diagrams can be obtained from the complete n-dimensional diagram (in our case, $n = 4$) through the transformation $R^n(a_i) \longrightarrow R^2(x_1, x_2)$, where $x_i = T, P$, or c and $i = 1, 2$. The simplest variant of the transformation $R^n \longrightarrow R^2$ can be written in the form

$$\begin{gathered} \lambda_1 = \text{const}, \quad b_1 = \text{const}, \\ a_1 = a_1^0 + a_1^1 x_1 + a_1^2 x_2, \quad \alpha_1 = \alpha_1^0 + \alpha_1^1 x_1 + \alpha_1^2 x_2. \end{gathered} \quad (14)$$

The assumption that λ_1 = const is justified, because the layer thickness in the experiments only weakly depends on external conditions [in our model, owing to the interaction with the orientational order parameter (15)]. The assumption that b_1 = const (hereinafter, $b_1 < 0$ for definiteness) is supported by the fact that, at $b_1 < 0$ and $b_1 > 0$, the topological features of the phase diagram $R^2(a_1, \alpha_1)$ are retained upon the change $\eta_1 \longrightarrow -\eta_1$. In this case, from the system of equations of state, we find

$$q^2 = -(\lambda_1 + \gamma_1\eta_1^* + \gamma_3^*\eta_1^2)/4\lambda_2. \quad (15)$$

Substitution of this relationship into formula (7) gives

$$\begin{aligned} F(\eta_1, \eta_2; |\Psi|) &= a_1(\eta_1^2 + \eta_2^2) + b_1(\eta_1^3 - 3\eta_1\eta_2^2) \\ &+ a_2(\eta_1^2 + \eta_2^2)^2 + \alpha_1|\Psi|^2 + \alpha_2|\Psi|^4 + \gamma_1\eta_1|\Psi|^2 \\ &+ \gamma_2(\eta_1^2 + \eta_2^2)|\Psi|^2 + \gamma_3\eta_1^2|\Psi|^2, \end{aligned} \quad (16)$$

where

$$\alpha_1 = \alpha_1^* - \lambda_1^2/4\lambda_2, \quad \gamma_1 = -\lambda_1\gamma_1^*/4\lambda_2,$$
$$\gamma_3 = -\lambda_1\gamma_3^*/2\lambda_2 - \gamma_1^2/4\lambda_2.$$

The model of the effective thermodynamic potential $F(\eta_1, \eta_2; |\Psi|)$ (16) for the uniaxial and biaxial smectic A phases should be analyzed with due regard for the additional condition following from the reality condition $q^2 > 0$ [see relationship (15)], that is,

$$\lambda_1 + \gamma_1^*\eta_1 + \gamma_3^*\eta_1^2 < 0. \quad (17)$$

In order to construct the phase diagram for different model parameters γ_1, γ_2, and γ_3, we first determine the complete bifurcation set of the parameters a_1^b and α_1^b

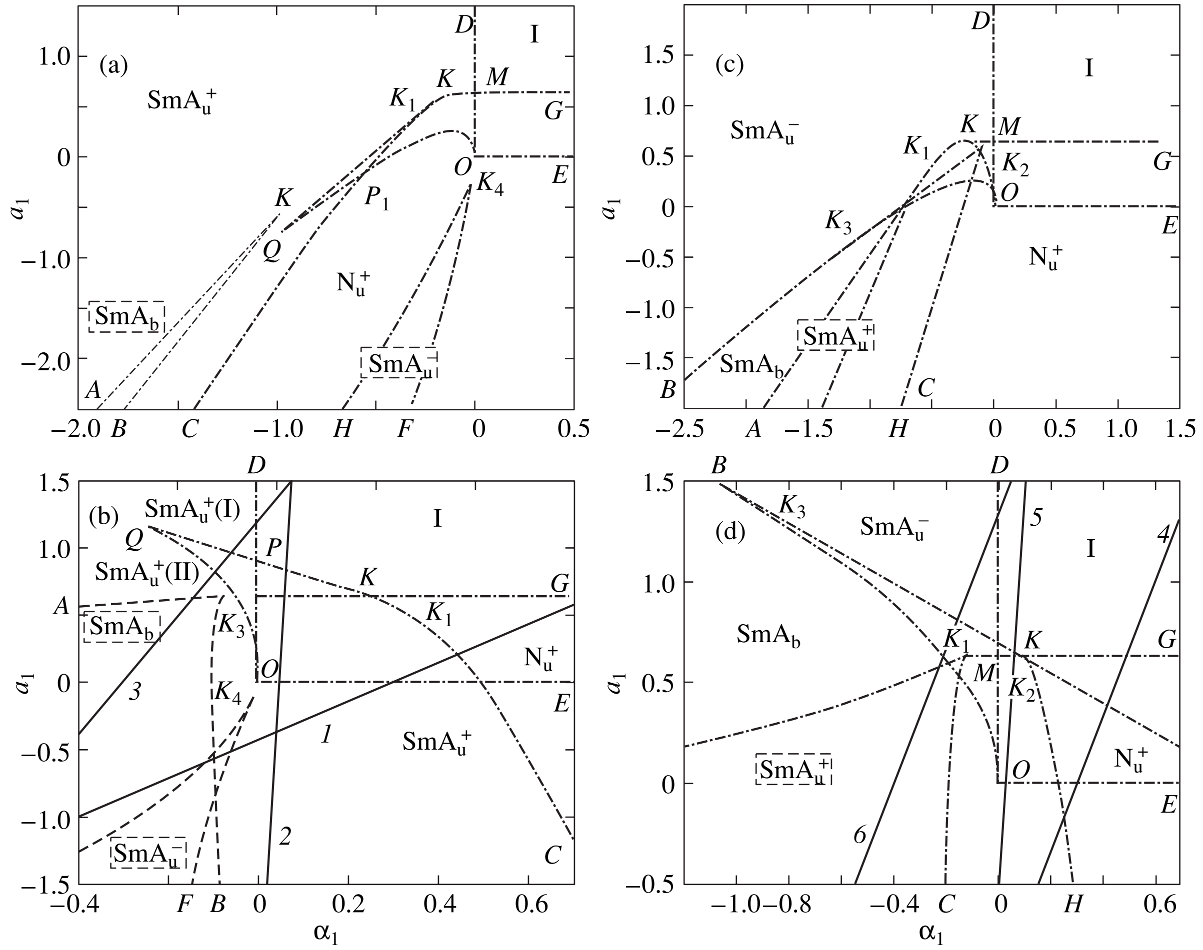

Fig. 1. Phase diagrams in the model of the thermodynamic potential $F(\eta_1, \eta_2; |\Psi|)$ (16) at different values of parameters γ_1 and γ_2: (a) $\gamma_1 = -0.25$ and $\gamma_2 = 2$, (b) $\gamma_1 = -0.7$ and $\gamma_2 = -0.3$, (c) $\gamma_1 = 0.5$ and $\gamma_2 = 1.3$, and (d) $\gamma_1 = 0.5$ and $\gamma_2 = -0.3$. Dot-dashed lines indicate the loss of stability of the phases. Solid straight lines represent the thermodynamic paths at different parameters k and α_0 [relationship (34)]: *(1)* TP_1 ($k = 0.8$, $\alpha_0 = 0.3$), *(2)* TP_2 ($k = 0.02$, $\alpha_0 = 0.05$), *(3)* TP_3 ($k = 0.25$, $\alpha_0 = -2.5$), *(4)* TP_4 ($k = 0.2$, $\alpha_0 = 0.3$), *(5)* TP_5 ($k = 0.1$, $\alpha_0 = 0.05$), and *(6)* TP_6 ($k = 0.3$, $\alpha_0 = -0.4$).

in $R^2(a_1, \alpha_1)$ from the degeneracy conditions for the matrix of second derivatives of the potential $F(\eta_1, \eta_2; |\Psi|)$ with respect to the order parameters (Hessian H_{ik}).

The bifurcation set $B^{\mathrm{B}}(a_1^b, \alpha_1^b) \in R^2(a_1, \alpha_1)$ can be found from the condition $\det\|H_{ik}\| = 0$ for the order parameters obtained for each phase from the system of the equations of state (8)–(12). The problem associated with constructing the phase diagram is reduced to determination of the subset of the parameters a_1^{PD} and $\alpha_1^{\mathrm{PD}} \in B^{\mathrm{PD}}$, which lead to degeneracy of the solutions of the system of the equations of states corresponding to minima of the thermodynamic potential $F(\eta_1, \eta_2; |\Psi|)$ (16).

The parameters a_1^{PD} and $\alpha_1^{\mathrm{PD}} \in B^{\mathrm{PD}}$ determine the conditions for the loss of stability of an equilibrium (absolute minimum) or metastable (local minimum) state of the system.

(i) For the isotropic phase, we have

$$\eta_1 = 0, \quad \eta_2 = 0, \quad \Psi = 0, \quad a_1 \geq 0, \quad \alpha_1 \geq 0. \quad (18)$$

Equations (18) describe the *OE* and *MD* lines (Fig. 1).

(ii) The uniaxial nematic phase is characterized by the order parameters

$$\eta_1 \neq 0, \quad \eta_2 = 0, \quad \Psi = 0.$$

The degeneracy conditions for the solutions of the equation of state are given by

$$\mathrm{Det}\|H_{ik}\| = (-18b_1\eta_1)\eta_1(3b_1 + 8a_2\eta_1) \times \eta_1^2[\alpha_1 + \gamma_1\eta_1 + (\gamma_2 + \gamma_3)\eta_1^2] = 0. \quad (19)$$

The discriminant equation (the *KG* line in Fig. 1) determined by the condition $3b_1 + 8a_2\eta_1 = 0$ has the form

$$a_1(\mathrm{N_u}) = 9b_1^2/32a_2. \quad (20)$$

This equation in the phase diagram $R^2(a_1, \alpha_1)$ describes the reality region of the solutions to the equation of state of the uniaxial nematic phase, that is,

$$2a_1 + 3b_1\eta_1 + 4a_2\eta_1^2 = 0. \quad (21)$$

In the phase diagram $R^2(a_1, \alpha_1)$, between the lines corresponding to relationships (18) and (21), there exist two solutions of Eq. (21) for a given a_1, namely, one maximum and one minimum ($\eta_{1\min} > \eta_{1\max}$), and one minimum at $a_1 < 0$. For the model under consideration, the condition $-18b_1\eta_1 \geq 0$ following from relationships (18) leads to $\eta_1 > 0$ at $b_1 < 0$. A similar condition for domains with $\eta_2 = \pm\sqrt{3}\eta_1$ gives $\eta_1 < 0$. The stability condition with respect to fluctuations of the order parameter Ψ [equality of the expression in the square brackets in formula (19) to zero] results in the equation for the *KC* line (Fig. 1):

$$a_1 = -\frac{3}{2}b_1\eta_1 - 2a_2\eta_1^2, \ \ \alpha_1 = -\gamma_1\eta_1 - (\gamma_2 + \gamma_3)\eta_1^2. \quad (22)$$

The *GK* and *KC* lines are joined at the *K* point and form a smooth *GKC* line:

$$\begin{aligned} \alpha_1(K) &= [\gamma_1 + (\gamma_2 + \gamma_3)3b_1/8a_2]/3b_1/8a_2, \\ a_1(K) &= 9b_1^2/32a_2. \end{aligned} \quad (23)$$

The stability region of the $\mathrm{N_u^+}$ uniaxial nematic phase is bounded by the *GKC* line (Fig. 1). In the *GMOE* (Figs. 1a, 1b, 1d) and *GKC* (Fig. 1b) regions, the isotropic and $\mathrm{N_u^+}$ phases coexist. The first-order transition between these phases occurs along the line described by the expression

$$a_1(I-N) = b_1^2/4a_2. \quad (24)$$

(iii) Let us now consider the uniaxial smectic A phase.

The condition $\det\|H_{ik}\| = 0$ for the uniaxial smectic A phase takes the form

$$\begin{aligned} |H_{ik}| &= \frac{\partial^2 F}{\partial\eta_2^2}\left[\frac{\partial^2 F}{\partial\eta_1^2}\frac{\partial^2 F}{\partial\Psi^2} - \left(\frac{\partial^2 F}{\partial\eta_1\partial\Psi}\right)^2\right] \\ &= 4\left(-9b_1\eta_1 - \frac{(\gamma_1 + 2\gamma_3\eta_1)\Psi^2}{\eta_1}\right) \\ &\times\left\{4\eta_1^2\Delta_1 + 2\eta_1[3b_1\alpha_2 - 2(\gamma_2+\gamma_3)\gamma_1]\right. \\ &\left. + \gamma_1^2 + \frac{2\alpha_2\gamma_1\Psi^2}{\eta_1}\right\}\Psi^2 = 0, \end{aligned} \quad (25)$$

where $\Delta_1 = 4a_2\alpha_2 - (\gamma_2 + \gamma_3)^2$ and, together with Eqs. (26), determines the complete bifurcation set of the parameters a_1^{B} and α_1^{B}. From condition (25), it follows that, at $|\Psi| = 0$ and $\eta_1 = 0$, the degeneracy condition is determined as $\alpha_1 = 0$. By setting the expression in the curly brackets in formula (25) equal to zero, we obtain the discriminant for $R^2(a_1, \alpha_1)$. This discriminant in the parametric form can be expressed through the equations

$$\begin{aligned} \alpha_1 &= \frac{-\eta_1^2}{\gamma_1}\{4\Delta_1\eta_1 - 3[\gamma_1(\gamma_2+\gamma_3) - 2a_2b_1]\}, \\ a_1 &= \frac{1}{4\alpha_2\eta_1}\{\alpha_1\gamma_1 + [2(\gamma_2+\gamma_3)\alpha_1 + \gamma_1^2]\eta_1 \\ &\quad + 3[\gamma_1(\gamma_2+\gamma_3) - 2\alpha_2b_1]\eta_1^2 - 2\Delta_1\eta_1^3\}. \end{aligned} \quad (26)$$

The K_1QO line [Eqs. (26)] has a cusp Q (Figs. 1a, 1b) at

$$\eta_1(Q) = \frac{\gamma_1(\gamma_2+\gamma_3) - 2\alpha_2b_1}{2\Delta_1}. \quad (27)$$

The line that corresponds to the condition for loss of stability of the uniaxial smectic A phase with respect to fluctuations of η_2 ($\partial^2F/\partial^2\eta_2 \geq 0$), with allowance made for the effective equation of state (26), is described by the relationship

$$\alpha_1 = -\gamma_1\eta_1 - (\gamma_2+\gamma_3)\eta_1^2 + \frac{18b_1\alpha_2\eta_1^2}{\gamma_1 + 2\gamma_2\eta_1}. \quad (28)$$

The line corresponding to the condition $|\Psi|^2 \geq 0$ (at $\eta_1 \neq 0$) coincides with that determined by relationships (23), is tangent to the discriminant line at the K_1 point, and then merges with this line. At $\gamma_1 < 0$, there is an interval of values of the parameters a_1 and α_1 in which two stable solutions for the $\mathrm{SmA_u^+}$ phase coexist (P_1QK_1, $\gamma_2 > 0$, Fig. 1a; *OPQ*, $\gamma_2 > 0$, Fig. 1b). In these regions, the isostructural first-order phase transition can occur between the two smectic phases $\mathrm{SmA_u^+}$(I) and $\mathrm{SmA_u^+}$(II) [η_1(AI) < η_1(AII)]. The line of this transition ends at a critical point of the liquid–vapor type. The $\mathrm{SmA_u^+}$(I) and $\mathrm{SmA_u^+}$(II) phases differ in terms of the orientational order parameter, the layer thickness, and the order parameter $|\Psi|$ (Fig. 2). The K_1 point is the tricritical point of the $\mathrm{SmA_u^+}$–I transition at which the second-order transition (CK_1 line in Figs. 1a, 1b) becomes a first-order transition. At $\gamma_1 > 0$, the $\mathrm{SmA_u^-}$ phase can border on the $\mathrm{SmA_b}$ biaxial smectic phase.

(iv) Now, we analyze the biaxial smectic A phase.

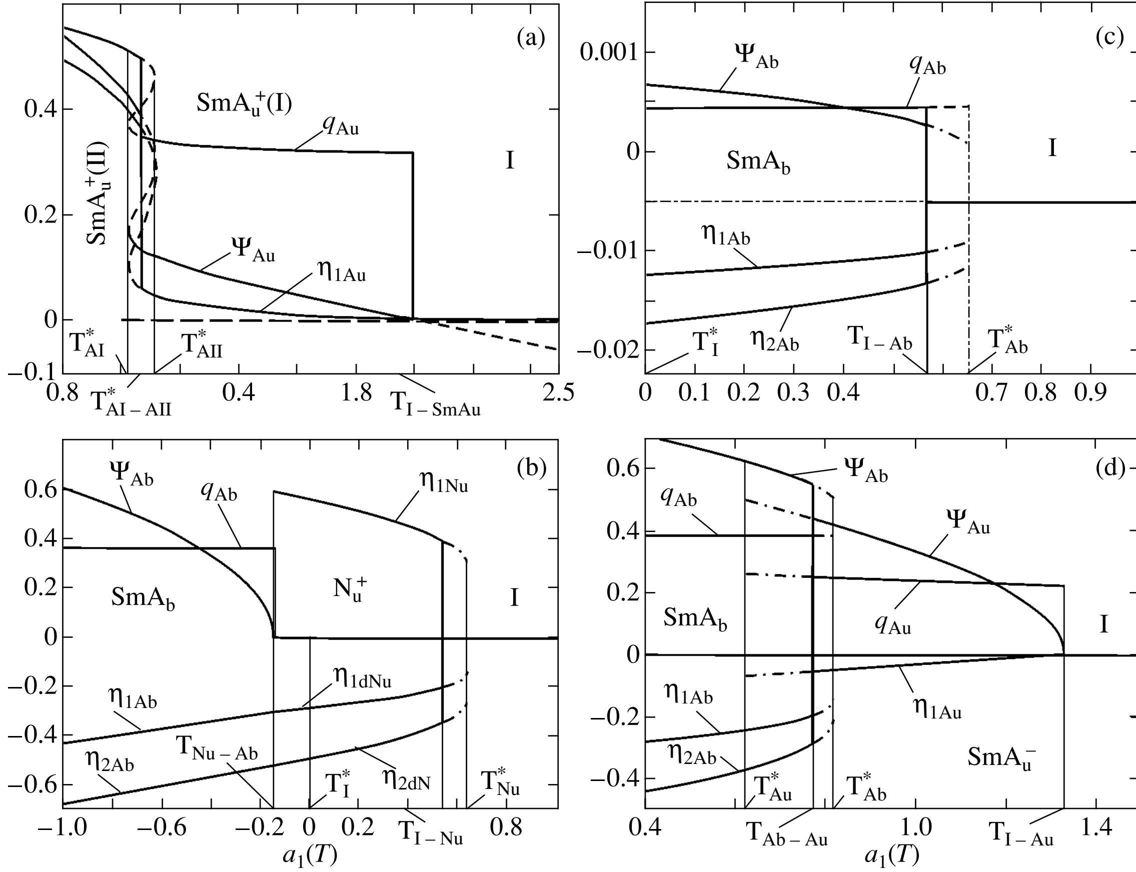

Fig. 2. Dependences of the order parameters η_1, η_2, $|\Psi|$, and q (ordinate axis) on the parameter a_1 for different phases along the thermodynamic paths (a) TP_3, (b) TP_4, (c) TP_5, and (d) TP_6.

The effective equation of state for η_1 in the biaxial smectic A phase (at $\gamma_3 = 0$) can be written in the form

$$12\Delta_2 b_1\eta_1^2 - 2(9\alpha_2 b_1^2 + 3b_1\gamma_1\gamma_2 + a_2\gamma)\eta_1 + a_1(6\alpha_2 b_1 + \gamma_1\gamma_2) - \alpha_1(3b_1\gamma_2 + 2a_2\gamma_1) = 0. \quad (29)$$

For the biaxial smectic A phase, we have

$$\det\|H_{ik}\| = 32\eta_2^2\Psi^2\eta_1 b_1 \times [12b_1\Delta_2\eta_1 - (9\alpha_2 b_1^2 + 3b_1\gamma_1\gamma_2 + a_2\gamma_1^2)], \quad (30)$$

where $\Delta_2 = 4a_2\alpha_2 - \gamma_2^2$.

According to relationship (30), the conditions for loss of stability of the biaxial smectic A phase are as follows. Making allowance for the effective equation of state (29), the $A_{\mathrm{Sm\,A_b}}$ discriminant curve

$$\eta_1 = \frac{9\alpha_2 b_1^2 + 3b_1\gamma_1\gamma_2 + a_2\gamma_1^2}{12b_1\Delta_2} \quad (31)$$

can be represented by a straight line.

The $B_{\mathrm{Sm\,A_b}}$ line corresponds to $|\Psi| = 0$. At $\eta_2 = 0$, the condition for loss of stability of the biaxial smectic A phase coincides with condition (22) for the uniaxial nematic phase. At $\eta_2 \neq 0$, there appears an additional condition

$$a_1 = 3b_1\eta_1 - 8a_2\eta_1^2, \qquad \alpha_1 = -\gamma_1\eta_1 - 4\gamma_2\eta_1^2. \quad (32)$$

The $C_{\mathrm{Sm\,A_b}}$ line at $\eta_2 = 0$ and $|\Psi| \neq 0$ coincides with the line that corresponds to the condition for loss of stability of the uniaxial smectic A phase [relationship (28)]. There can exist four topologically different types of phase diagrams depending on the signs and ratios of the nonvariable parameters b_1, γ_1, γ_2, and γ_3 (Fig. 1; $a_2 = 4$, $\alpha_2 = 0.5$, $b_1 = -0.2$, $\gamma_3 = 0$).

(i) At $\gamma_1 < 0$ (Figs. 1a, 1b), the phase diagram $R^2 = (a_1, \alpha_1)$ contains stability regions of the I, N_u^+, and SmA_u^+ phases and regions of the metastable SmA_u^- and SmA_b phases (shown by dotted rectangles). As follows from the equation of state (29), in the region of the

SmA_u^+ phase, the isostructural first-order transition is possible between the two isomorphic smectic phases SmA_u^+ (I) and SmA_u^+ (II) at $b_1 < \gamma_1(\gamma_2 + \gamma_3)/2a_2$ ($\eta_1 > 0$). The direct first-order transition to the SmA_u^+ phase can occur at $\gamma_2 < 0$ (Fig. 1b). The first-order transition between the N_u^+ and SmA_u^+ phases transforms into a second-order transition at the tricritical point J_1.

(ii) The situation observed in the phase diagram $R^2 = (a_1, \alpha_1)$ at $\gamma_1 > 0$ (Figs. 1c, 1d) differs fundamentally from the results obtained in [21, 22, 24]. In this case, there exist stability regions of the I, N_u^+, SmA_u^-, and SmA_b phases, whereas the SmA_u^+ phase is metastable. The transitions from the N_u^+ and SmA_u^- phases to the SmA_b biaxial smectic phase (at the K_2 and K_3 tricritical points, respectively) can be first- and second-order phase transitions. The I–SmA_b direct first-order transition is possible. At $\gamma_2 > 0$ (Fig. 1c), there exists a first-order phase transition between the N_u^+ and SmA_u phases.

5. BEHAVIOR OF THE ORDER PARAMETERS ALONG THE THERMODYNAMIC PATHS

The performed analysis of the phase diagram (Fig. 1) makes it possible to investigate the behavior of physical quantities and order parameters along different thermodynamic paths. The thermodynamic path in the phase diagram $R^2(a_1, \alpha_1)$ is represented by a straight line described by the dependence of the variable parameters a_1 and α_1 on one external variable [for example, $x_1 = x_2 = T$ in relationships (14)]. In this case, the dependences $a_1 = a_1(T)$ and $\alpha_1 = \alpha_1(T)$ can be represented in the form [24]

$$a_1(T) = a_N(T - T_N^*), \quad \alpha_1(T) = \alpha_A(T - T_A^*), \quad (33)$$

where a_N and α_A are constants and T_N^* and T_A^* are the temperatures of the loss of stability of the isotropic phase upon transition to the uniaxial nematic and uniaxial smectic A phases, respectively.

Relationship (33) can be written as

$$\alpha_1 = \alpha_0 + ka_1, \quad (34)$$

where $\alpha_0 = \alpha_A(T_N^* - T_A^*)$ and $k = \alpha_N/\alpha_A$.

Figure 2 depicts the dependences of the orientational order parameter $\eta = (\eta_1, \eta_2)$, the smectic order parameter $|\Psi|$, and $q = 2\pi d^{-1}$ in several phases at different values of α_0 and k along the thermodynamic paths:

$$\begin{gathered} TP_1\colon I - N_u^+ - SmA_u^+; \quad TP_2\colon -I - SmA_u^+; \\ TP_3\colon -I - SmA_u^+(I) - SmA_u^+(II); \\ TP_4\colon I - N_u^+ - SmA_b; \quad TP_5\colon I - SmA_b; \\ TP_6\colon I - SmA_u^- - SmA_b. \end{gathered} \quad (35)$$

Note that the behavior of the order parameters along the thermodynamic paths TP_3–TP_6 has not been studied previously. The main features observed in the above dependences along these paths can be summarized as follows.

(1) Along the thermodynamic path TP_3 (Fig. 2a), the direct first-order transition from the isotropic phase to the SmA_u^+ uniaxial smectic A phase is observed at $T_{I-SmA_u^+}$. In our model, the nematic and smectic order parameters increase from zero and the layer thickness $d(q_{A_u})$ increases jumpwise with a decrease in the temperature. The isomorphic transition accompanied by a jumpwise change in the quantities η_{1A_u}, $|\Psi|_{A_u}$, and q_{A_u} occurs at T_{AI-AII} (Fig. 2a).

(2) Along the path TP_4, the I–N_u^+ first-order phase transition takes place at $T_{I-N_u^+}$. In the N_u^+ phase, the director (domains) can have three different orientations in the chosen laboratory coordinate system:

$$\text{I: } \eta_{1N_u} > 0, \quad \eta_{2N_u} = 0 \quad (Q_{zz}, Q_{xx} = Q_{yy});$$

$$\text{II: } \eta_{2N_u} = \sqrt{3}\eta_{1N_u} \quad (Q_{yy}, Q_{xx} = Q_{zz});$$

$$\text{III: } \eta_{2N_u} = -\sqrt{3}\eta_{1N_u} \quad (Q_{xx}, Q_{yy} = Q_{zz}).$$

It should be noted that the z axis specifies the orientation of smectic layers $\mathbf{p} = (0, 0, p_z)$ and the director in domains I, II, and III is aligned along the z, y, and x axes, respectively. Upon an N_u–SmA_b phase transition (first-order or second-order transition; K is the tricritical point) at ($T = T_{N_u-SmA_b}$), the director, which is determined in the biaxial phase by the eigenvector with the largest eigenvalue of the tensor [9], lies in the plane of smectic layers. As the temperature of the SmA_u^- phase is approached (Fig. 2c), the biaxiality reaches a maximum and becomes equal to zero upon an SmA_b–SmA_u^- phase transition. In this case, the director is oriented perpendicular to the layer plane. Upon an N_u–SmA_b second-order phase transition, the dependences $\eta_1(a_1)$ and $\eta_2(a_1)$ exhibit kinks.

(3) Along the path TP_5, the direct first-order transition from the isotropic phase to the biaxial smectic A phase is observed at T_I–SmA_b (Fig. 2c).

(4) The phase transition from the isotropic phase to the biaxial smectic A phase can occur through the intermediate SmA_u^- phase (thermodynamic path TP_6). The SmA_u^- phase with symmetry $D_{\infty h}^z$ (Fig. 2d) is formed in compounds with discotic molecules. The director perpendicular to the plane of disks is oriented normally to layers ($Q_{zz} < 0$, $Q_{yy} = Q_{xx}$). In the $\mathrm{SmA_b}$ biaxial smectic phase (D_{2h}), in the vicinity of the transition (for small biaxiality of the molecules), the director is perpendicular to layers and the biaxiality vector **m** lies in the layer plane. In the stability region of the biaxial smectic A phase, the director in the line determined by the conditions $Q_{yy} - Q_{xx} = Q_{zz} - Q_{xx}$ changes the orientation by $\pi/2$ and is aligned along the orientation of rodlike molecules.

The results obtained at $b_1 < 0$ are topologically identical to those for the phase diagram and the behavior of the order parameters at $b_1 > 0$ when the N_u^+ and SmA_u^- phases are replaced by N_u^- and SmA_u^+ phases, respectively.

6. DISCUSSION

The investigation performed in terms of the simple model of thermodynamic potential (7) revealed a number of new features in the transitions from the isotropic phase to the nematic and smectic phases (compare with [18–24]).

(1) The isotropic phase can undergo a direct first-order transition to the uniaxial smectic A phase. This transition occurs at $T = T_A^*$ along the thermodynamic paths TP_2 and TP_6 (Figs. 1c, 2a, 2d) under the following conditions:

$$\alpha_1(\mathrm{I} - \mathrm{Sm\,A_u}) = 0, \quad a_1(\mathrm{I} - \mathrm{Sm\,A_u}) > a_1(\mathrm{I} - \mathrm{N_u}); \\ T_A^* > T_N^* + a_N b_1^2/4a_2 a_A \alpha_A. \tag{36}$$

At $\alpha_1 = 0$ and $a_1 > a_1(\mathrm{I–N_u})$, upon a first-order phase transition, the smectic order parameter $|\Psi|$ is primary and the nematic order parameter $\eta = (\eta_1, 0)$ arises as a secondary order parameter due to the interaction $\gamma_1\eta_1|\Psi|^2$ ($\eta_1 \approx |\Psi|^2$ in the vicinity of the phase transition). The thickness d of smectic layers increases jumpwise to a final value at the phase transition point. In the experiments, the $\mathrm{I–SmA}_u^+$ direct transition was observed as a first-order transition [26–32] upon which both the nematic and smectic order parameters arise in a jumpwise manner. Such a transition becomes possible when condition (36) or the inequality $\alpha_2 < 0$ is satisfied for the corresponding compounds. Note that, in this case, the term $\alpha_3|\Psi|^6$ should be taken into account.

(2) The SmA_u^+(I)–SmA_u^+(II) isomorphic phase transition is attended by a stepwise increase in the nematic and smectic order parameters, which leads to an increase in the thickness of smectic layers. The line of this transition ends at a critical point Q of the liquid–vapor type (Figs. 1a, 1b).

(3) In recent years, liquid crystals with achiral mesogens $\mathrm{BC_a}$ have been investigated extensively [13, 14, 26–35]. It is in these compounds that the biaxial smectic phase has been found [13 14, 26–32]. A $\mathrm{BC_a}$ molecule (mesogen) has biaxial symmetry C_{2v} and consists of two spherocylinders oriented along the unit vectors $\mathbf{e}_1$ and $\mathbf{e}_2$ [$\mathbf{e}_1\mathbf{e}_2 = \cos(180°–\gamma) = –\cos\gamma$]. This dimer molecule is uniaxial at $\gamma = 0$ and biaxial at $\gamma \neq 0$ [33]. At small angles γ, the molecule (rod) is aligned along the z axis (N_u^+ phase). At large angles γ, the vector perpendicular to the plane of the molecule (disk) is oriented along the z axis (N_u^- phase). At intermediate angles γ, there arises an N_b nematic biaxial phase, which is not considered in our model. The SmA_u^+, SmA_u^-, and $\mathrm{SmA_b}$ smectic phases are formed in a similar manner.

(4) In our case ($b_1 < 0$), the director **n** of the $\mathrm{BC_a}$ molecule in the biaxial smectic A phase upon an N_u^+–$\mathrm{SmA_b}$ transition lies in the plane of smectic layers. It is this orientation that was experimentally found by Sadashiva *et al.* [29]. The compound studied in [29] is the first example of a single-component system with $\mathrm{BC_a}$ molecules that form the liquid-crystal phase under consideration. The smectic phases ($\mathrm{SmA_u}$ uniaxial phase, $\mathrm{SmA_b}$ biaxial phase) found in this compound differ from those observed in mixtures of rodlike and $\mathrm{BC_a}$ molecules in which the director is oriented perpendicular to the layers [28]. Note that, at $b_1 > 0$, the SmA_u^+ phase can undergo a transition to the $\mathrm{SmA_b}$ phase. In this case, the director of $\mathrm{BC_a}$ molecules is perpendicular to the smectic layers.

In conclusion, it should be noted that, in order to describe the N_b biaxial nematic phase, strong nonlinear interactions (terms up to the sixth order) should be included in the Landau potential, whereas the formation of the $\mathrm{SmA_b}$ biaxial smectic A phase can be described with due regard for terms up to the fourth order. The reason for this is that the biaxiality in the biaxial smectic A phase is stabilized through the secondary interaction of two order parameters (invariant $\gamma_1\eta_1|\Psi|^2$); as a result, more highly nonlinear interactions are effectively taken into account [34, 35]. The inclusion of terms up to the sixth order in the nematic order parameter in the Landau potential will make it possible to describe the N_b–$\mathrm{SmA_b}$ and N_b–N_u first- and second-order transitions.

ACKNOWLEDGMENTS

I would like to thank Prof. H. Pleiner and Prof. H. Takezoe for kindly supplying the results of investigations into the properties of compounds with banana-shaped molecules.

This work was supported by the Russian Foundation for Basic Research, project no. 03-05-65409.

REFERENCES

1. G. Friedel, Ann. Phys. (Leipzig) **18** (2), 273 (1922).
2. P. de Gennes, *The Physics of Liquid Crystals* (Clarendon, Oxford, 1974; Mir, Moscow, 1977).
3. M. J. Frieser, Phys. Rev. Lett. **24** (19), 1041 (1970).
4. L. J. Yu and A. Saup, Phys. Rev. Lett. **45** (12), 1000 (1980).
5. H. Finkelmann, H. Ringdorf, and I. H. Wendorf, Macromol. Chem. Phys. **179**, 237 (1978).
6. S. Chandrasekhar, Mol. Cryst. Liq. Cryst. **124**, 1 (1985).
7. J. Malthete, L. Liehert, and A. M. Levelut, Acad. Sci., Paris **303**, 1073 (1986).
8. S. Singh, Phys. Rep. **324** (1), 107 (2001).
9. A. E. Prostakov, E. S. Larin, and M. B. Stryukov, Kristallografiya **47** (6), 1048 (2002) [Crystallogr. Rep. **47**, 1041 (2002)].
10. H. R. Brand and H. Pleiner, J. Phys. (Paris) **41**, 553 (1991).
11. H. Luebe and H. Finkelmann, Macromol. Chem. Phys. **192**, 1317 (1991).
12. R. Meyer and W. L. McMillan, Phys. Rev. A **9** (2), 899 (1974).
13. T. Niori, T. Sekino, J. Watanabe, T. Furukawa, and H. Takezoe, J. Mater. Chem. **6** (11), 1231 (1996).
14. T. Sekino, T. Niori, J. Watanabe, S. W. Choi, Y. Takanishi, H. Takezoe, and M. Sone, Jpn. J. Appl. Phys. **36**, L1201 (1997).
15. H. R. Brand and H. Pleiner, Macromolecules **25** (12), 7223 (1992).
16. W. L. McMillan, Phys. Rev. A **4** (3), 1238 (1971).
17. H. R. Brand and H. Pleiner, Macromol. Rapid Commun. **12**, 539 (1991).
18. W. L. McMillan, Phys. Rev. A **6** (3), 936 (1972).
19. F. T. Lee, H. T. Tan, Yu. M. Shih, and C.-W. Woo, Phys. Rev. Lett. **31** (18), 1117 (1973).
20. S. A. Pikin and V. L. Indenbom, Usp. Fiz. Nauk **125** (2), 251 (1978) [Sov. Phys. Usp. **21**, 487 (1978)].
21. E. E. Gorodetskiĭ and V. É. Podniek, Kristallografiya **29** (6), 1054 (1984) [Sov. Phys. Crystallogr. **29**, 618 (1984)].
22. J. Lelidis and G. Durand, Phys. Rev. Lett. **73** (5), 672 (1994).
23. P. K. Mukhergjee, H. R. Brand, and H. Pleiner, Eur. J. Phys. E **4** (3), 293 (2001).
24. A. E. Prostakov, Kristallografiya **47** (5), 922 (2002) [Crystallogr. Rep. **47**, 856 (2002)].
25. L. D. Landau and E. M. Lifshitz, *Course of Theoretical Physics*, Vol. 5: *Statistical Physics,* 3rd ed. (Nauka, Moscow, 1978; Pergamon, 1980), Parts 1 and 2.
26. D. R. Link, G. Natale, R. Shao, J. E. Maclennan, N. A. Clark, E. Korbova, and D. M. Walbal, Science **278** (5345), 1924 (1997).
27. D. M. Walba, E. Korblova, R. Shao, J. E. Maclennan, D. R. Link, M. A. Glaser, and N. A. Clark, Science **288** (5474), 2181 (2000).
28. R. Pratibha, B. K. Sadashiva, and N. V. Madhusudana, Science **288** (5474), 2184 (2000).
29. B. K. Sadashiva, R. A. Reddy, R. Pratibha, and N. V. Madhusudana, Chem. Commun. **20**, 2140 (2001).
30. A. Eremin, S. Diele, G. Pelzl, H. Nadasi, W. Weissflog, J. Salfetnikova, and H. Kresse, Phys. Rev. E **64**, 051707 (2001).
31. P. K. Maiti, Y. Lansac, M. A. Glaser, and N. A. Clark, Phys. Rev. Lett. **88**, 065504 (2002).
32. M. W. Schroder, S. Diele, N. Panchenko, W. Weissflog, and G. Pelzl, J. Mater. Chem. **12** (10), 1331 (2002).
33. P. J. Camp, M. P. Allen, and A. J. Masters, J. Chem. Phys. **111** (9), 9871 (1999).
34. Yu. M. Gufan, O. D. Lalakulich, G. M. Vereshkov, and G. Sartori, in *Proceedings of International Conference on Symmetry and Perturbation Theory, SPT-I* (World Sci., Singapore, 2001).
35. A. Sergienko, Yu. M. Gufan, and S. Urazhdin, Phys. Rev. B **65**, 144104 (2002).

Translated by O. Borovik-Romanova

Physics of the Solid State, Vol. 46, No. 8, 2004, pp. 1569–1573. Translated from Fizika Tverdogo Tela, Vol. 46, No. 8, 2004, pp. 1522–1525.
Original Russian Text Copyright © 2004 by Enyashin, Ivanovskaya, Makurin, Ivanovskiĭ.

Modeling of the Structure and Electronic Structure of Condensed Phases of Small Fullerenes C_{28} and Zn@C_{28}

A. N. Enyashin, V. V. Ivanovskaya, Yu. N. Makurin, and A. L. Ivanovskiĭ

Institute of Solid-State Chemistry, Ural Division, Russian Academy of Sciences,
ul. Pervomaĭskaya 91, Yekaterinburg, 620219 Russia
e-mail: ivanovskii@ihim.uran.ru
Received October 31, 2003

Abstract—A comparative analysis of the stability factors and electronic structure of two possible crystalline forms of small fullerene C_{28} and endohedral fullerene Zn@C_{28} with diamond and lonsdaleite structures is performed using a cluster model. Atoms of elements that, when placed inside C_{28} cages, have no significant effect on the stability of free small-fullerene molecules are shown to be able to dramatically change the electronic properties and reactivity of the C_{28} skeleton and to be favorable for forming small-fullerene crystalline modifications, which are covalent crystals. In contrast, if the presence of foreign atoms inside C_{28} cages stabilizes the isolated nanoparticles, then molecular crystals (such as C_{60} fullerites) are formed due to weak van der Waals forces. © *2004 MAIK "Nauka/Interperiodica".*

The discovery of small fullerene C_{28} [1] in 1993 in the form of the U@C_{28} endohedral complex has stimulated theoretical and experimental studies on its stability and the development of methods for producing it in the free state and in the form of various complexes. Analysis of the electronic structure and stability of fullerene C_{28} has shown that it is more stable than its isomers in the form of a ring or a planar layer [2–4]. However, this fullerene is a radical with four unpaired electrons ($S = 2$) [5], which are localized on the atoms shared by pentagons (Fig. 1). This state is responsible for the high reactivity of the C_{28} polyhedral nanoparticle.

The C_{28} cage can be stabilized by forming endohedral fullerenes M@C_{28} in which M atoms are in the M^{4+} configuration (e.g., *d* elements Ti, Zr, Mo, W, Ru, Os; *f* elements U, Ce, Th, Pu; *p* elements Si, Ge) [5–9]. Endohedral fullerenes with other M atoms are unstable and reactive. The C_{28} fullerene can also be stabilized by replacing part of the carbon atoms with atoms of other elements. It was shown in [5, 10] that heterofullerenes $C_{24}B_4$ and $C_{24}N_4$ with symmetry T_d are stable particles with closed electron shells.

Finally, C_{28} becomes stable when its free valences are saturated through linking with hydrogen or halogen atoms, alkyl groups, etc., on the outer side of the fullerene to form an exohedral fullerene. Saturation is also attained when C_{28} molecules are joined together to form polymers, films, or crystals [5, 11].

It has been found that the formation of $[C_{28}]_n$ polymer chains and diamond-structure C_{28} crystals (so-called hyperdiamonds) is favored energetically [11]. Energy-band calculations showed [12] that hyperdiamond C_{28} is a semiconductor with a band gap of ~1.5 eV; its lattice parameter, elastic modulus, and density were calculated in [13]. When doped, hyperdiamond C_{28} is suggested to undergo a transition to a superconducting state; estimates of the electron–phonon interaction constants [14] show that the critical temperature of alkali metal–doped phases M_xC_{28} is approximately eight times higher than that of fullerides M_xC_{60}. However, attempts to synthesize hyperdiamond C_{28} have not yet met with success.

In this paper, we perform a comparative analysis of the electronic structure and stability factors of two possible crystalline modifications of C_{28} with diamond- and lonsdaleite-type structures, as well as of analogous crystals of endohedral complex Zn@C_{28}. It is well known that zinc is not a stabilizer of small fullerenes; therefore, the properties of endohedral fullerene Zn@C_{28} and C_{28} are similar in many ways.

We described the C_{28} and Zn@C_{28} crystals with diamond and lonsdaleite structures (space groups $Fd3m$, $P63/mmc$) using clusters $(C_{28})_5H_{12}$ and $(Zn@C_{28})_5H_{12}$ with symmetries T_d and C_{3v}, respectively (Fig. 1). The boundary conditions are imposed by introducing hydrogen atoms, which "close" the unsaturated bonds of the clusters. The total energies E_{tot} of the clusters and the energies of molecules C_{28}, Zn@C_{28}, $C_{28}H_4$, and Zn@$C_{28}H_4$ are calculated using the AM1 method [15] within the Hartree–Fock approximation for fully optimized geometry. The electronic structure of the model clusters is found following the self-consistent electron density functional method and the discrete-variation technique with a numerical atomic orbital basis [16, 17]. The Gunnarsson–Lundqvist local exchange-corre-

1063-7834/04/4608-1569$26.00 © 2004 MAIK "Nauka/Interperiodica"

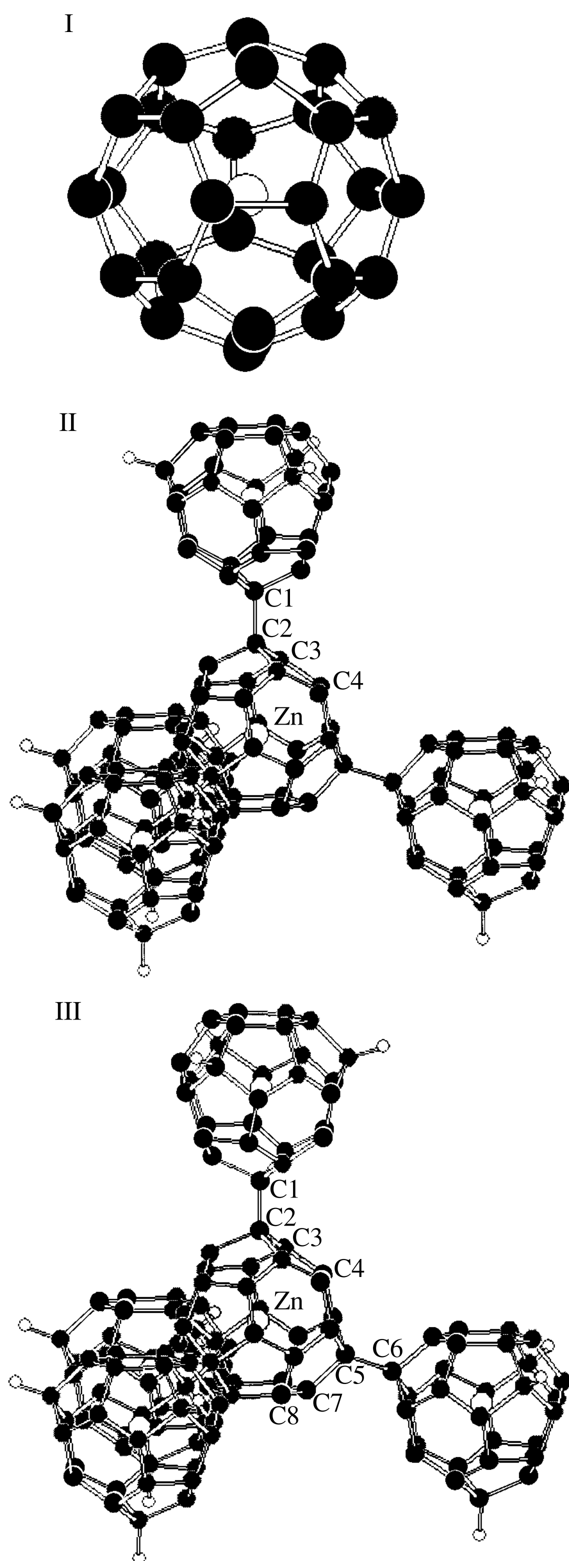

Fig. 1. (I) Fullerene $Zn@C_{28}$ and (II, III) clusters $(Zn@C_{28})_5H_{12}$ modeling (II) diamond- and (III) lonsdaleite structure crystals with T_d and C_{3v} symmetry, respectively.

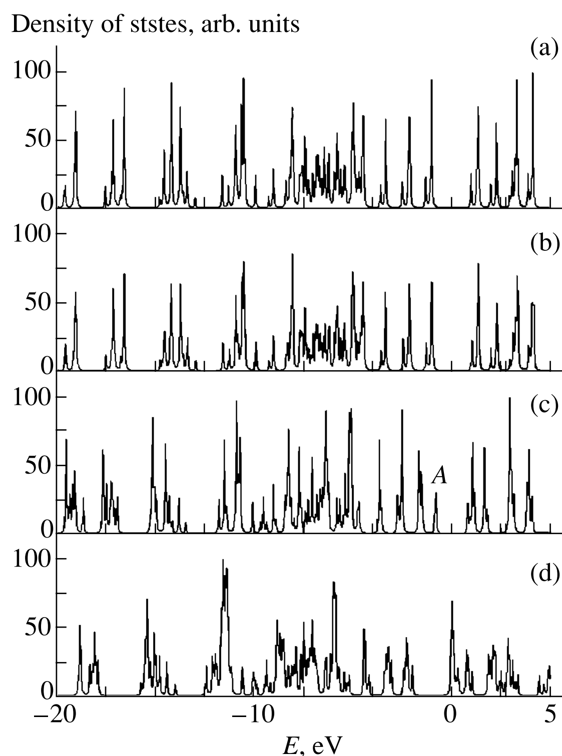

Fig. 2. Calculated electron densities of states of various crystals (structures): (a) C_{28} (diamond), (b) C_{28} (lonsdaleite), (c) $Zn@C_{28}$ (diamond), and (d) $Zn@C_{28}$ (lonsdaleite). The Fermi level corresponds to zero energy.

lation potential [18] is used. The basis atomic orbitals are determined by solving the Hartree–Fock–Slater equation for isolated atoms. In calculating the matrix elements, numerical integration is carried out using 96000 points (1000 points for each of the C and H atoms and 2000 points for each of the Zn atoms), and the energy levels are determined with an accuracy of better than 0.1 eV.

Knowing the total energies of fullerenes C_{28} and $Zn@C_{28}$ and their clusters $(C_{28})_5H_{12}$ and $(Zn@C_{28})_5H_{12}$ (Table 1), we can find the energy of association of fullerenes ΔE_{tot} (per fullerene mole) by first calculating the bonding energy of the C–H bond, E(C–H), for the systems in question (Table 2). For example, the energy ΔE_{tot} of association of C_{28} fullerenes is defined as

$$\Delta E_{tot} = E_{tot}((C_{28})_5)/5 - E_{tot}(C_{28}),$$

where

$$E_{tot}((C_{28})_5) = E_{tot}((C_{28})_5H_{12}) - 12E(\text{C–H}),$$

$$E(\text{C–H}) = E_{tot}(C_{28}H_4) - E_{tot}(C_{28}) - 4E(\text{H}).$$

It can be seen from Table 2 that the formation of the C_{28} and $Zn@C_{28}$ crystals is favored in all cases ($\Delta E_{tot} < 0$). It is significant that the values of the energy of association ΔE_{tot} for the diamond- and lonsdaleite-structure C_{28} crystals are very close to each other; they differ by

Table 1. Total energies E_{tot} of the C_{28} and $Zn@C_{28}$ fullerenes and clusters modeling diamond- and lonsdaleite-structure crystals (AM1 calculations)

System (symmetry)	$-E_{tot}$, kcal/mol	System (symmetry)	$-E_{tot}$, kcal/mol
C_{28}	81976.3997	$Zn@C_{28}$	82439.3854
$C_{28}H_4$	83378.8486	$Zn@C_{28}H_4$	83820.9341
$(C_{28})_5H_{12}$ (T_d)	414307.5974	$(Zn@C_{28})_5H_{12}$ (T_d)	416512.6825
$(C_{28})_5H_{12}$ (C_{3v})	414306.5933	$(Zn@C_{28})_5H_{12}$ (C_{3v})	416814.3787

Table 2. Differences ΔE_{tot} between the total energies of free fullerenes C_{28} and $Zn@C_{28}$ and of their crystalline modifications (AM1 calculations)

Reaction*	$-\Delta E_{tot}$, kcal/mol
C_{28} (gas) ⟶ C_{28} (solid) (1)	43.6505
C_{28} (gas) ⟶ C_{28} (solid) (2)	43.4497
$Zn@C_{28}$ (gas) ⟶ $Zn@C_{28}$ (solid) (1)	34.2218
$Zn@C_{28}$ (gas) ⟶ $Zn@C_{28}$ (solid) (2)	94.5611

* Formation of C_{28} (solid) and $Zn@C_{28}$ (solid) crystals with (1) diamond or (2) lonsdaleite structure.

Table 3. Lattice constants a and c and density ρ of the C_{28} and $Zn@C_{28}$ crystalline modifications (AM1 calculations)

System*	a, nm	c, nm	ρ, g/cm^3
C_{28} (1)	1.6110	–	1.07
C_{28} (2)	1.1292	1.8462	1.10
$Zn@C_{28}$ (1)	1.6074	–	1.28
$Zn@C_{28}$ (2)	1.1427	1.8542	1.27

* (1) Diamond and (2) lonsdaleite structures.

less than ~0.2 kcal/mol. Therefore, experimentally, it will be difficult to prepare C_{28} crystals with these structures in the uncombined state (e.g., hyperdiamond C_{28} predicted in [12, 13]). The disordered (amorphous) C_{28} phase will most likely be formed (see also [19]).

For endohedral fullerene $Zn@C_{28}$, the difference in the energy of association between crystals with different structures is large (more than 60 kcal/mol), with the lonsdaleite-structure $Zn@C_{28}$ crystal being more likely to form. Therefore, atoms placed inside the C_{28} cages can significantly change the reactivity of the C_{28} skeleton, thereby shifting the equilibrium toward the formation of a particular crystalline modification.

Table 3 lists the values of the lattice constants a and c and density of hypothetical crystals of fullerenes C_{28} and $Zn@C_{28}$ calculated for the optimized geometry of the model clusters. According to our calculations, a = 1.611 nm for hyperdiamond, which agrees well with the results of DFT–LDA energy band calculations (1.64 nm [12]) and thereby supports the validity of the model used. The density of the C_{28} and $Zn@C_{28}$ crystals turns out to be about one-third that of diamond (Table 3).

The calculated densities of states of the crystalline modifications of C_{28} and $Zn@C_{28}$ are very close to one another (Fig. 2). In the C_{28} crystals, the quasi-core C2s states with an admixture of the C2p states form a set of bands in the range from –20 to –13 eV below the Fermi level, E_F. The uppermost occupied band consists predominantly of the C2p states responsible for σ and π bonds in the C_{28} fullerenes, with the π bonds being associated with the well-defined peaks in the density of states near E_F. The bottom of the conduction band is formed by the C2p states. Both crystalline modifications of C_{28} exhibit an energy spectrum typical of a semiconductor, with a band gap of about 2 eV.

The electronic energy spectra of the analogous $Zn@C_{28}$ crystals differ significantly. On the whole, the relative position and widths of the bands corresponding to the carbon 2s and 2p states are similar to those for the

Table 4. Bond populations for carbon atoms in the C1–C8 positions (Fig. 1) in the C_{28} and $Zn@C_{28}$ crystalline modifications calculated using the discrete variation method

System*	Bond**	Population, e	Bond	Population, e	Bond	Population, e
C_{28} (1)	C1–C2	0.372	C2–C3	0.431	C3–C4	0.830
$Zn@C_{28}$ (1)	C1–C2	0.371	C2–C3	0.452	C3–C4	0.927
C_{28} (2)	C1–C2	0.365	C2–C3	0.406	C3–C4	0.547
	C5–C6	0.370	C5–C7	0.433	C7–C8	0.533
$Zn@C_{28}$ (2)	C1–C2	0.367	C2–C3	0.410	C3–C4	0.444
	C5–C6	0.343	C5–C7	0.452	C7–C8	0.526

* (1) Diamond and (2) lonsdaleite structures.
** The Zn–C1,2 interactions correspond to antibonding (bond population is negative).

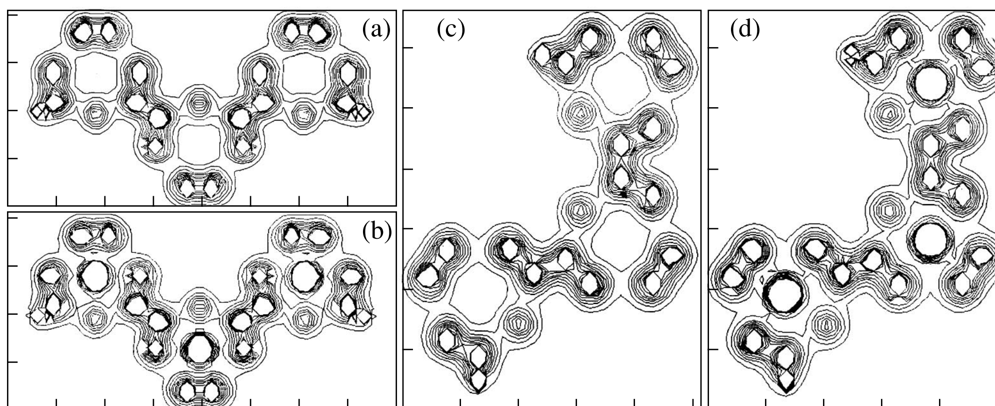

Fig. 3. Electron density distributions (a, b) in diamond-structure crystals of (a) C_{28} and (b) Zn@C_{28} and (c, d) in lonsdaleite-structure crystals of (c) C_{28} and (d) Zn@C_{28}.

C_{28} crystals. However, in the energy spectrum of hyperdiamond Zn@C_{28}, the filled band of Zn4*s* states (Fig. 2, peak A) lies above the uppermost filled carbon π bands. As a result, the band gap in this phase narrows to ~1.6 eV. The Zn3*d* states lie in the range from –20 to –16 eV.

The lonsdaleite-structure Zn@C_{28} crystal has an energy spectrum typical of metals. The carbon density of states is also analogous to that in the lonsdaleite-structure C_{28} crystal; however, the position of the zinc energy levels differs significantly from that in hyperdiamond: the Zn3*d* states lie in the range from –12 to –11 eV, and the Zn4*s* and C2*p* states form a mixed-type band crossing the Fermi level.

The interatomic interactions in the C_{28} and Zn@C_{28} crystals are covalent in character (Fig. 3) and are determined mainly by the overlap between the C2*s* and C2*p* states and between different C2*p* states. The bond population is significant between the carbon atoms that form the hexagons of the C_{28} cage. Weaker bonds are formed between the atoms of these rings and the atoms shared by three pentagons. The atoms via which fullerenes link are bonded even more weakly (Table 4). However, the populations of these bonds are comparable in magnitude, which fundamentally distinguishes the crystals under study from "classical" fullerites (e.g., fcc-C_{60}); the latter are molecular crystals where individual molecules are linked via van der Waals forces [20–23]. The Zn atoms are not bonded to the carbon atoms.

Thus, comparative analysis of the electronic structures and stability of the crystalline modifications of fullerene C_{28} and endohedral fullerene Zn@C_{28} has shown that, while a Zn atom placed inside a C_{28} cage does not have a significant effect on the stability of the free small-fullerene molecule, it can dramatically change the reactivity of the C_{28} skeleton and the electronic properties of its crystalline modifications and render fabrication of the latter impracticable. It is important that these modifications are covalent crystals in which the interactions are due to hybridization between states of carbon atoms belonging to neighboring fullerenes. One might expect that, in the case where *M* atoms placed inside C_{28} cages stabilize the isolated nanoparticles, such endohedral fullerenes can be used to fabricate molecular crystals in which nanoparticles interact via van der Waals forces, as is the case in C_{60} fullerites.

ACKNOWLEDGMENTS

This study was supported by the state program of support for leading scientific schools of the Russian Federation, project no. NSh 829.2003.3.

REFERENCES

1. T. Guo, M. D. Diener, Y. Chai, M. J. Alford, R. E. Haufler, S. M. McClure, T. Ohno, J. H. Weaver, G. E. Scuseria, and R. E. Smalley, Science **257**, 1661 (1993).
2. C. Piskoti, J. Yarger, and A. Zettl, Nature **393**, 771 (1998).
3. T. Guo, R. E. Smalley, and G. E. Scuseria, J. Chem. Phys. **99**, 352 (1993).
4. P. R. C. Kent, M. D. Towler, R. J. Needs, and G. Rajagopal, Phys. Rev. B **62**, 15394 (2000).
5. Yu. N. Makurin, A. A. Sofronov, A. I. Gusev, and A. L. Ivanovsky, Chem. Phys. **270**, 293 (2001).
6. B. I. Dunlap, O. D. Haeberlen, and N. Roesch, J. Phys. Chem. **96**, 9095 (1992).
7. M. R. Pederson and N. Laouini, Phys. Rev. B **48**, 2733 (1993).
8. K. Jackson, E. Kaxiras, and M. R. Pederson, Phys. Rev. B **48**, 17556 (1993).
9. K. Jackson, E. Kaxiras, and M. R. Pederson, J. Phys. Chem. **98**, 7805 (1994).

10. Z. Chen, H. Jiao, M. Buehl, A. Hirsch, and W. Thiel, Theor. Chem. Acc. **106**, 352 (2001).
11. K. Choho, G. Van de Woude, G. Van Lier, and P. Geerlings, J. Mol. Struct.: THEOCHEM **417**, 265 (1997).
12. E. Kaxiras, L. M. Zeger, A. Antonelli, and Y. Juan, Phys. Rev. B **49**, 8446 (1994).
13. D. M. Bylander and L. Kleinman, Phys. Rev. B **47**, 10967 (1993).
14. N. Breda, R. A. Brogila, G. Colo, G. Onida, D. Provasi, and E. Viggezzi, cond-mat/0001133.
15. M. J. S. Dewar, E. G. Zoebisch, and E. F. Healy, J. Am. Chem. Soc. **107**, 3902 (1985).
16. E. Baerends, D. E. Ellis, and P. Ros, Chem. Phys. **2**, 41 (1973).
17. M. R. Press and D. E. Ellis, Phys. Rev. B **35**, 4438 (1987).
18. O. Gunnarsson, B. I. Lundqvist, and P. Ros, Phys. Rev. B **13**, 4274 (1976).
19. W. J. Zhu, Z. Y. Pan, Y. K. Ho, and Y. X. Wang, J. Appl. Phys. **88**, 6836 (2000).
20. F. Diederich and M. Gomez-Lopez, Chem. Soc. Rev. **28**, 263 (1999).
21. K. E. Geckeler and S. Samal, Polym. Int. **48**, 743 (1999).
22. M. Prato, Top. Curr. Chem. **199**, 173 (1999).
23. P. Moriarty, Rep. Prog. Phys. **64**, 297 (2001).

Translated by Yu. Epifanov

Physics of the Solid State, Vol. 46, No. 8, 2004, pp. 1574–1576. Translated from Fizika Tverdogo Tela, Vol. 46, No. 8, 2004, pp. 1526–1528.
Original Russian Text Copyright © 2004 by Pukha, Varganov, Mikhaĭlov, Drozdov.

Effect of Bismuth Nanolayers on the Oriented Growth of Fullerene C_{60} on an Amorphous Substrate

V. E. Pukha, V. V. Varganov, I. F. Mikhaĭlov, and A. N. Drozdov

Kharkov Polytechnic Institute National Technical University, ul. Frunze 21, Kharkov, 61002 Ukraine

e-mail: puch@kpi.kharkov.ua

Received November 5, 2003

Abstract—The effect of a bismuth sublayer with an effective thickness of 0.5 to 4 nm on the structure of C_{60} fullerene films grown on amorphous substrates (silicon covered with a natural oxide layer; glass) using the quasi-closed-volume method is studied. An x-ray diffraction study of fullerene films showed that the intensity ratio between the (220) and (111) peaks depends nonmonotonically on the sublayer thickness. In the bismuth sublayer thickness range 0.5–2.0 nm, fullerene films are found to exhibit a growth texture with the ⟨110⟩ axis; the average crystallite size was ~20 μm. The quality of the texture can be improved by varying the fullerene growth temperature. © *2004 MAIK "Nauka/Interperiodica".*

1. INTRODUCTION

The fabrication of oriented C_{60} fullerene films on traditional substrates in electronics (silicon, germanium, gallium arsenide) offers possibilities for the use of fullerene C_{60} in nanotechnologies. Perfectly textured C_{60} films have been produced only on layered substrates with an appropriate structural geometry, e.g., on mica [1–3]. The quasi-closed-volume method enables one to obtain a highly perfect ⟨111⟩ texture in C_{60} fullerene films grown on mica substrates. The typical rocking-curve half-width for (111) reflections of the films was 0.25°–0.5°, and the maximum reflectivity for FeK_α radiation reached 12%, which is close to the theoretical value for fullerenes [3]. Only Makarova *et al.* [1] succeeded in growing a fullerene film with (111) texture on an amorphous substrate; however, the grain size of the film did not exceed a few micrometers.

To grow textured films on nonoriented substrates, the substrate surface is frequently covered with a surface-active substance (surfactant), such as bismuth, antimony, or arsenic. With an antimony sublayer 0.5 nm thick, C_{60} fullerene films with ⟨111⟩ texture were obtained in [4] with grains several micrometers in size. For growing a fullerene film, bismuth is more preferable as a surfactant, because it has a larger atomic radius and, hence, a smaller diffusion coefficient for diffusion into the fullerite and substrate. According to [5], in the initial stage of bismuth sublayer growth, dimers Bi_2 are observed to unite into linear chains, which are favorable for forming a texture in C_{60} films.

In this work, we study the influence of bismuth nanolayers on the texture and grain size of C_{60} fullerene films grown on glass and on the natural amorphous oxide covering a (100) single crystal silicon.

2. EXPERIMENTAL TECHNIQUE

C_{60} fullerene films were grown on a bismuth nanolayer using the quasi-closed-volume method. A vertical quartz tube with two graphite bases at its ends was used as an evaporation chamber. Inside the chamber, substrates were placed near the top base and an evaporator was placed on the bottom base. The evaporator consisted of a graphite crucible (closed with a graphite cap with calibrated holes) and a channel transporting bismuth vapor from an evaporation molybdenum cell loaded with metallic bismuth. When the cell was removed, the channel in the bottom base of the evaporation chamber was closed off with a heated shutter. The crucible of the evaporator, the quartz walls of the evaporation chamber, the evaporation cell, and the substrates were heated by external tungsten heaters. A pumping-out system based on an Orbitron-type getter-ion pump was used, which provided a residual pressure of lower than 10^{-5} Pa in a pumped volume. C_{60} films were grown at a residual pressure of lower than 5×10^{-4} Pa.

As substrates, cover glasses and (100) single-crystal silicon plates covered with natural amorphous oxide were used. Substrates were washed in distilled water, acetone, and n-hexane. Prior to depositing a bismuth sublayer, substrates were heated in vacuum to a temperature of 673 K. The initial materials to be evaporated were fullerene C_{60} of purity higher than 99.98% and bismuth of purity higher than 99.99%. A bismuth nanolayer was deposited at a substrate temperature T_s = 400 K, with the bismuth being completely evaporated in the evaporation cell, which was located under the channel transporting bismuth vapor. Bismuth sublayers differing in thickness were obtained by varying the amount of bismuth in the evaporation cell. After deposition of a sublayer, the substrate temperature was

1063-7834/04/4608-1574$26.00 © 2004 MAIK "Nauka/Interperiodica"

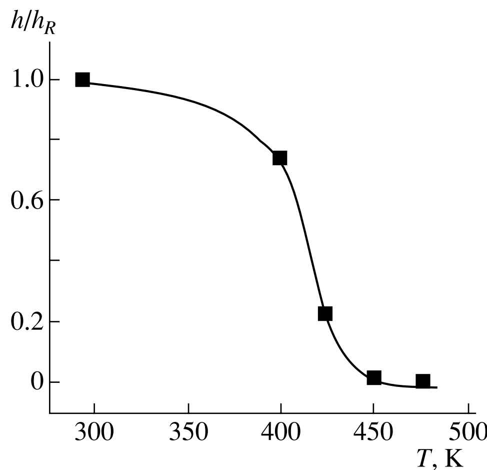

Fig. 1. Dependence of the effective bismuth sublayer thickness h on the substrate temperature (h_R is the thickness of a bismuth sublayer deposited at a substrate temperature of 273 K).

increased to 550–560 K (which is higher than the melting point of bismuth) and a fullerene film 15 to 100 μm thick was grown on the substrate.

The effective thickness of bismuth sublayers was determined from the intensity of the BiL_α analytic line in the x-ray fluorescence spectrum using a Sprut 2 spectrometer. The perfection of texture was judged from the peak-intensity ratio between the (220) and (111) reflections. X-ray diffraction studies were performed in the θ–2θ geometry using a DRON-3M diffractometer (CuK_α radiation monochromatized in the diffracted beam by reflecting from the (002) plane of graphite).

3. RESULTS AND DISCUSSION

Since the condensation coefficient of bismuth differs from unity above room temperature [6], we experimentally determined the dependence of the effective sublayer thickness on the substrate temperature for a fixed amount of bismuth charged into the evaporation cell and with the evaporation regime held constant (Fig. 1). As the temperature increases, this thickness sharply decreases starting from 400 K and the condensation coefficient approaches zero and does not exceed 1% at 450 K. In the temperature range 400–450 K, the condensation coefficient decreases by approximately 1% as the temperature decreases by one kelvin. Therefore, the temperature should be kept constant very accurately in order to exactly dose the amount of bismuth for the sublayer. The highest substrate temperature at which the condensation coefficient does not vary significantly with temperature is 400 K. At this temperature, the sublayer thickness is dictated by the amount of bismuth charged into the evaporation cell and can be closely controlled by this amount.

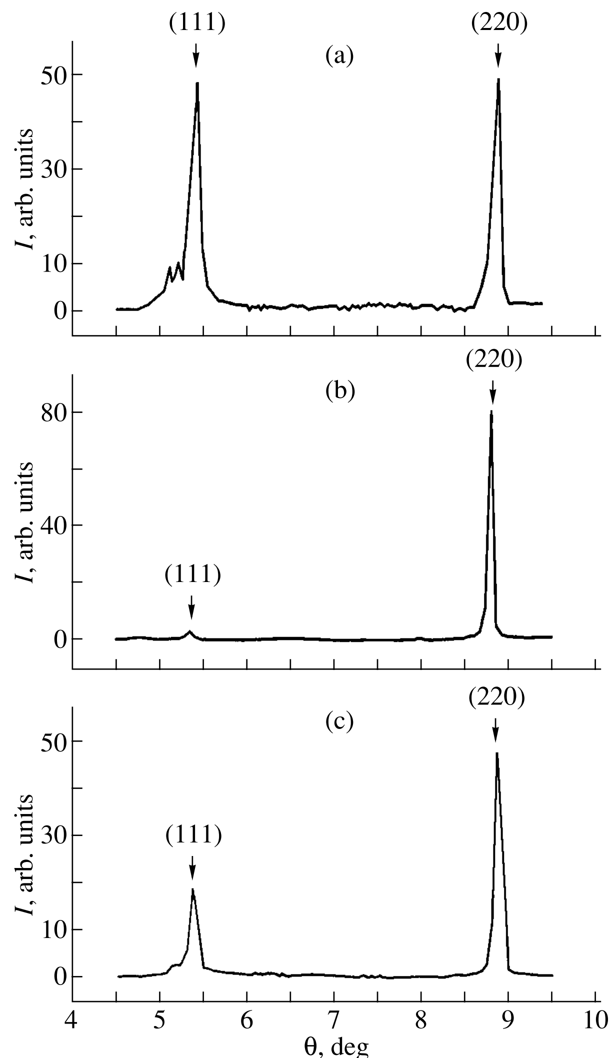

Fig. 2. Variations in intensity of the (111) and (220) x-ray diffraction peaks from C_{60} fullerene films grown on a bismuth sublayer with thickness (a) $h = 0$, (b) 0.5, and (c) 1.5 nm.

An x-ray diffraction study of fullerene films grown on a bismuth nanolayer revealed a difference in peak intensity between the (220) and (111) reflections (Fig. 2). In the absence of a sublayer, their peak-intensity ratio is close to unity, which is typical of a polycrystal without texture (Fig. 2a). The presence of a nanolayer causes this ratio to increase sharply up to 20–30 (Fig. 2b), which indicates the formation of texture with the ⟨110⟩ axis. Such texture is observed in the case of both silicon and glass substrates. Texture arises only in a limited range of bismuth sublayer thicknesses (0.5 to 2 nm) and almost disappears as the thickness increases (Fig. 2c). It is of great importance that, in this thickness range, the texture can be improved (up to $I_{220}/I_{111} = 120$) by varying the temperature conditions of fullerene growth, while outside this range a noticeable texture cannot be achieved (Fig. 3). The (110) texture peak half-width can be decreased to a few kelvins,

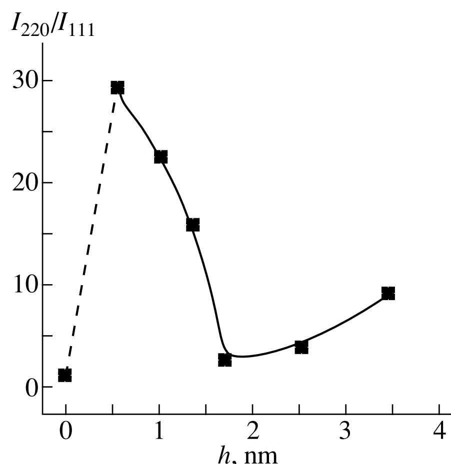

Fig. 3. Intensity ratio between the (220) and (111) reflections from fullerene as a function of the bismuth sublayer thickness.

which indicates that the C_{60} fullerene can grow through autoepitaxy on amorphous substrates.

We grew fullerene films at temperatures exceeding the bismuth melting temperature; therefore, the oriented growth of C_{60} is not caused by the sublayer crystal structure. Crystallographic (110)-type planes of a fullerene fcc lattice are not habit planes; therefore, this type of texture is unlikely to arise spontaneously. The formation of texture can be due to the presence of bismuth dimer nanofilaments. If the sublayer thickness is small, dimers and nanofilaments of bismuth cover only part of the free substrate surface (being located primarily on defects with broken bonds). During deposition of fullerene C_{60} under conditions of a quasi-closed volume, where evaporation of fullerene from a substrate is comparable in rate to its condensation, C_{60} molecules can deposit predominantly along bismuth nanofilaments in the initial stage of film growth. C_{60} molecule chains arranged along bismuth nanofilaments can serve as a basis for forming the [110] close-packing directions of the growing fullerite crystal. As the sublayer thickness increases, the bismuth sublayer transforms into a set of islands through coalescence. In this case, C_{60} molecules condense for the most part on liquid bismuth droplets and on the amorphous substrate surface, in which there is no nanoscale relief in the form of bismuth filaments and dimers; therefore, texture does not form.

In the presence of a bismuth nanolayer, the grain size in fullerene films increased up to 20 μm and on the substrate surface there were crystallites 100 μm in size, which occupied several percent of the surface area. Note that, in films deposited on substrates without a bismuth sublayer, the crystallite size did not exceed 1 μm. The increase of the crystallites in size is probably due to bismuth concentrating primarily on defects of the substrate and deactivating broken bonds on its surface. This process decreases the quantity of nucleation centers and enhances fullerene diffusion over the substrate surface, which results in enlarged grains and improves the structure of growing films.

4. CONCLUSIONS

The growth of fullerene films with (110) orientation is most likely due to the formation of ordered bismuth nanostructures on the amorphous substrate surface. The coarsening of grains in fullerite is associated with the deactivation of broken bonds in amorphous silicon oxide by adsorbed bismuth; this process decreases the quantity of nucleation centers and enhances surface diffusion of fullerene.

ACKNOWLEDGMENTS

This study was supported by the Ukrainian state scientific research program "Fullerene Compositions Forming from Fluxes of Component Particles of Higher Energy," project no. M5462.

REFERENCES

1. T. L. Makarova, I. B. Zakharova, T. I. Zubkova, and A. Ya. Vul', Fiz. Tverd. Tela (St. Petersburg) **41** (2), 354 (1999) [Phys. Solid State **41**, 319 (1999)].
2. V. A. Dudkin, A. S. Vus, V. E. Pukha, E. Zubarev, and O. Vovk, Mol. Cryst. Liq. Cryst. **361**, 245 (2001).
3. I. F. Mikhailov, V. E. Pukha, O. V. Sobol, and V. V. Varganov, Funct. Mater. **10** (2), 266 (2003).
4. J. G. Hou, Wentao Xu, Wang Haiqian, and Yang Li, J. Appl. Phys. **84**, 2906 (1998).
5. M. Naitoh, H. Shimaya, S. Nishigaki, N. Oishi, and F. Shoji, Surf. Sci. **377–379**, 899 (1997).
6. *Handbook of Thin Technology*, Ed. by L. I. Maissel and R. Glang (McGraw-Hill, New York, 1970; Sovetskoe Radio, Moscow, 1977), Vol. 1.

Translated by Yu. Epifanov

Physics of the Solid State, Vol. 46, No. 8, 2004, pp. 1577–1582. Translated from Fizika Tverdogo Tela, Vol. 46, No. 8, 2004, pp. 1529–1534.
Original Russian Text Copyright © 2004 by Lisenkov, Ponomareva, Chernozatonskiĭ.

Basic Configuration of a Single-Wall Carbon Nanotube *Y* Junction of D_{3h} Symmetry: Structure and Classification

S. V. Lisenkov, I. V. Ponomareva, and L. A. Chernozatonskiĭ
Émanuel Institute of Biochemical Physics, Russian Academy of Sciences, Moscow, 119991 Russia
e-mail: lisenkov@sky.chph.ras.ru
Received August 5, 2003; in final form, December 29, 2003

Abstract—The structure of single-wall carbon nanotube *Y* junctions of symmetry D_{3h} containing topological defects in the form of six heptagons or three octagons located immediately in the junction region of each pair of nanotubes forming the *Y* junctions is investigated, and their classification is suggested. It is shown that the pairs of heptagons in a *Y* junction formed by nanotubes of the "zigzag" type can be arranged in two ways and can be transformed into one another by using the (6, 7, 7, 6) $\rightleftharpoons$ (7, 6, 7, 6) Stone–Wales transformation and that the octagon and pairs of heptagons in a *Y* junction formed by nanotubes of the "armchair" type can be transformed into one another by introducing or removing a C_2 cluster. A method for constructing such *Y* junctions is suggested. © *2004 MAIK "Nauka/Interperiodica".*

1. INTRODUCTION

After the discovery of carbon nanotubes (CNTs) by Iijima [1], numerous experimental [2–6] and theoretical [6–10] studies of CNT-based multiterminal structures, namely, junctions of *L*, *X*, *Y*, and *T*-types, have been carried out. It has been shown that such structures can be used as nanotransistors and nanodiodes [11–18].

It is known that, depending on their diameter and chirality, which are determined by the chiral vector (n, m), where n and m are integers [19], single-wall CNTs can be either conducting [of the (n, n) or (n, m) type with $n = m + 3q$)] or semiconducting [of the (n, m) type with $n \neq m + 3q$, where q is an integer]. Thus, multiterminal junctions can be formed from nanotubes of different conductivity. In 1992, the possible formation of a continuous junction from two different nanotubes through the introduction of a pentagon–heptagon pair was predicted [7, 8]. If one of the two nanotubes is metallic and the other is semiconducting, then their heterojunction is a rectifying diode [20, 21]. Such two-terminal junctions have recently been observed [22, 23].

In order to use *Y* junctions in electronic devices, one needs high-yield fabrication of junctions that are uniform in shape and size; therefore, the first experimental observations of CNT *Y* junctions [2] did not attract special attention from scientists because of the difficulties involved in fabricating uniform structures. Only quite recently have controlled methods for producing *Y* junctions been developed, using aluminum patterns [3] and also through the pyrolysis of organometallic products [5]. Using the former of these methods [3], *Y* junctions were fabricated with a "stem" exceeding the "branches" in diameter and with an acute angle between them; CNT *Y* junctions with equal angles (120°) between all nanotubes were synthesized by chemical vapor deposition [5].

2. STRUCTURE AND CLASSIFICATION OF *Y* JUNCTIONS

From a topological point of view, the formation of nanotube *Y* junctions is possible only in the presence of topological defects between the nanotubes forming a junction. As a rule, these defects are pentagons, heptagons, and octagons. The number of topological defects in such *Y* junctions can be defined by the Euler formula for polyhedrons of an arbitrary type G [24]:

$$N(7) + 2N(8) - N(5) = 12G - 12, \quad (1)$$

where $N(5)$, $N(7)$, and $N(8)$ are the total numbers of pentagons, heptagons, and octagons, respectively. The number of hexagons in such a polyhedron is arbitrary. If two *Y* junctions are joined perfectly, a closed second-order surface is formed. For such a surface, the total number of defects is twice that for each of the two *Y* junctions forming this surface:

$$N(5) = 2n(5), \quad N(7) = 2n(7), \quad N(8) = 2n(8), \quad (2)$$

where $n(5)$, $n(7)$, and $n(8)$ are the numbers of pentagons, heptagons, and octagons in such a *Y* junction. Using Eq. (2), Eq. (1) can be written in the form

$$n(7) + 2n(8) - n(5) = 6. \quad (3)$$

We note that pentagons, in pairs with additional heptagons, can be present in a *Y* junction; however, the presence of such pairs is not obligatory. Therefore, in this study, we set $n(5) = 0$.

We consider only CNT *Y* junctions of symmetry D_{3h} (a C_3 axis of third order, three symmetry planes σ_v con-

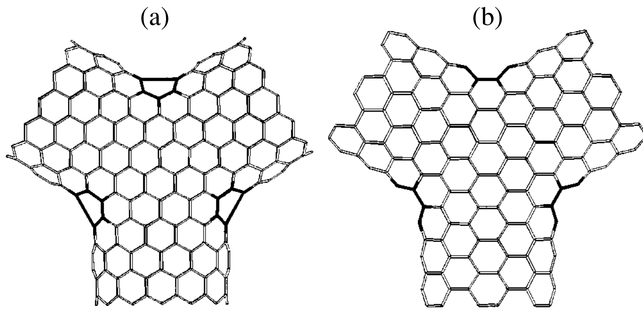

Fig. 1. Y_b junctions of (a) (12, 0) CNTs of the zigzag type, six-heptagon defects; and (b) (6, 6) CNTs of the armchair type, three-octagon defects. Defects are indicated by thick lines.

taining this axis, and a symmetry plane perpendicular to it) consisting of nonchiral nanotubes either of the (n, n) armchair type or of the (n, 0) zigzag type. They contain defects located in the regions of the nanotube coupling (Fig. 1). We call these CNT junctions basic Y_b junctions (the subscript b means basic), since other Y junctions of symmetry D_{3h} can be obtained from them using different transformations (transformations of the Stone–Wales type; introducing/removing atoms, atomic clusters, or hexagon rings).

The Y_b junctions are formed of nanotubes of one type with equal pairs of indices. Moreover, only nanotubes with even indexes n can take part in the formation of such a junction because of the presence of symmetry planes of the D_{3h} symmetry group; $n \geq 2$ for nanotubes of the armchair type and $n \geq 4$ for nanotubes of the zigzag type. Due to the presence of a third-order symmetry axis, only two possible sets of topological defects exist in Y_b junctions, namely, six heptagons or three octagons (two heptagons or one octagon between each pair of nanotubes). All possible variations of defect configurations in the region of coupling of different pairs of nanotubes forming a Y_b junction are shown in Fig. 2.

As seen from Fig. 2, two heptagons can occupy two different positions in the regions of coupling of nanotubes of the zigzag type (Figs. 2a, 2b); they can be transformed into one another by the (6, 7, 7, 6) $\rightleftharpoons$ (7, 6, 7, 6) Stone–Wales transformation [25]. Out of the two arrangements of heptagons, we choose the configuration corresponding to Fig. 2a as the basic arrangement. We note that an octagon (Fig. 2c) cannot be transformed into two heptagons and vice versa either by using a Stone–Wales transformation or by removing or adding a C_2 cluster. It follows that, for Y_b junctions of nanotubes of the zigzag type, the basic sets of defects are six heptagons (the location of each pair of heptagons is shown in Fig. 2a) and three octagons (the location of each octagon is shown in Fig. 2c).

In Y_b junctions consisting of nanotubes of the armchair type, one octagon (Fig. 2d) can be converted into two heptagons (Fig. 2e or 2f) by introducing a C_2 cluster connecting the two heptagons. Inverse conversion is

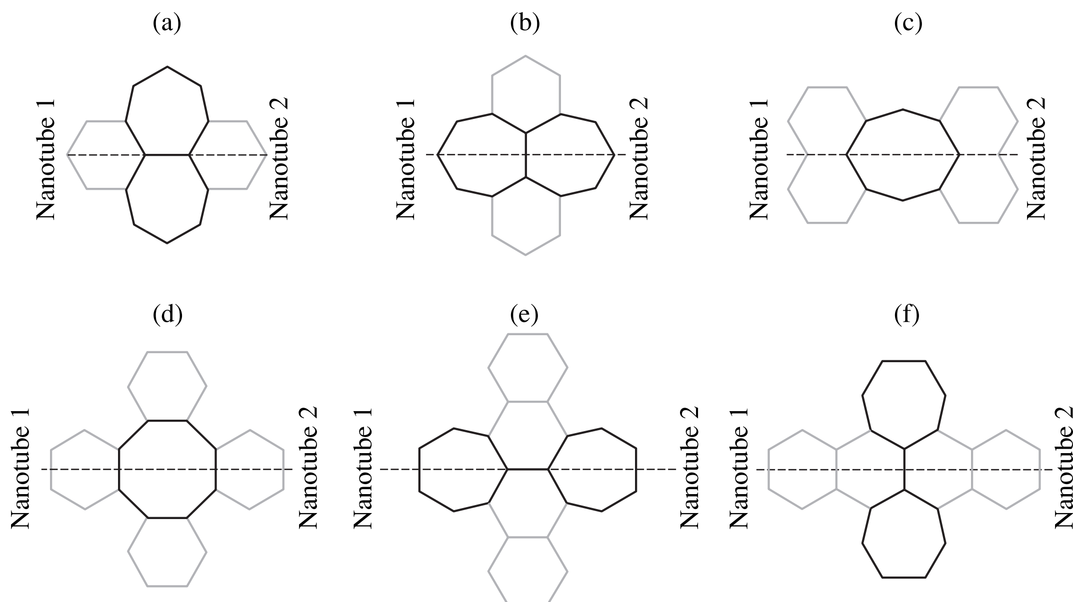

Fig. 2. Configurations of defects between the nanotubes forming Y_b junctions. Nanotubes of the zigzag type: (a, b) two heptagons and (c) an octagon. Nanotubes of the armchair type: (d) an octagon and (e, f) two heptagons. The (a $\rightleftharpoons$ b) defect conversion is realized by the (6, 7, 7, 6) $\rightleftharpoons$ (7, 6, 7, 6) Stone–Wales transformation, and the (d $\rightleftharpoons$ e and d $\rightleftharpoons$ f) defect conversion is accomplished by introducing or removing a C_2 cluster. The dashed line shows the intersection of the Y junction with the symmetry plane σ_v. Defects are indicated by thick lines.

possible by removing the C_2 cluster. Accordingly, we choose an octagon as the basic defect for nanotube junctions of this type. Therefore, for Y_b junctions of nanotubes of the armchair type, we should consider three octagons as the basic set of defects (the location of each octagon is shown in Fig. 2d). Using this set, we can obtain Y_b junctions with six heptagons in two versions corresponding to the location of each pair either according to Fig. 2e or according to Fig. 2f.

Now, we consider the structure of Y_b junctions in detail. In the case of Y_b junctions consisting of nanotubes of the zigzag type, the third-order symmetry axis can pass either through one of the atoms of the two-point basis of the hexagonal mesh or through the center of the hexagon ring. We will refer to the two points of a Y_b junction through which the C_3 axis passes as the interface. The junction under study can have three different types of interfaces (A, B, C), each of which has its own system of basis vectors. We associate the ($\mathbf{a}_1$, $\mathbf{a}_2$, $\mathbf{a}_3$) system with an interface of the A type, the ($\mathbf{b}_1$, $\mathbf{b}_2$, $\mathbf{b}_3$) system with an interface of the B type, and the ($\mathbf{c}_1$, $\mathbf{c}_2$, $\mathbf{c}_3$) system with an interface of the C type. The center of each system of basis vectors coincides with one of the points of the interface (Figs. 3a–3c). The lengths of the basis vectors satisfy the relationship

$$|\mathbf{a}_i| = |\mathbf{b}_i| = |\mathbf{c}_i| = a_{\text{C–C}}, \quad i = 1, 2, 3, \tag{4}$$

where $a_{\text{C–C}}$ is the distance between the neighboring atoms in the graphite plane.

Y_b junctions of nanotubes of the armchair type have only one type of interface (D) and, accordingly, one system of basis vectors (d_1, d_2, d_3) (Fig. 3d). The vectors $\mathbf{d}_1$, $\mathbf{d}_2$, and $\mathbf{d}_3$ satisfy the relation

$$|\mathbf{d}_i| = (\sqrt{3}/2)a_{\text{C–C}}. \tag{5}$$

The classification is based on the following parameters of Y_b junctions: the nanotube type (zigzag or armchair), the defect type (six heptagons or three octagons), and the interface type (A, B, C, or D). We note that these three parameters are not independent. Therefore, to define the structure of Y_b junctions unambiguously, it is necessary and sufficient to know any two of these three parameters.

To find the relation between the parameters determining a Y_b junction of nanotubes of the zigzag type, we note that the type of an interface (A, B, C) is repeated if the nanotube index n is changed by 6. Thus, the indices n of nanotubes having the same interface type form an arithmetic progression whose common difference is 6. The formula for the kth term of this progression is

$$n_k = n_0 + 6(k-1), \tag{6}$$

where $n_k = n$ is the nanotube index in the Y_b junction, n_0 is the minimum value of the nanotube index in the Y_b junction having an interface of the given type, and k is the number of the term of the arithmetic progression. Thus, for a Y_b junction with a set of topological defects in the form of six heptagons, we have $n_0 = 6$ for an interface of the A type, $n_0 = 8$ for an interface of the B type, and $n_0 = 10$ for an interface of the C type. We form three arithmetic progressions: $n = 6 + 6(k-1)$ for an interface of the A type, $n = 8 + 6(k-1)$ for an interface of the B type, and $n = 10 + 6(k-1)$ for an interface of the C type. If we express k in formulas (4)–(6) in terms of n, we obtain an efficient method for determining the interface type from the nanotube index n: the sequence number of the term in the arithmetic progression is an integer; therefore, from the three formulas corresponding to the three different interface types, we can choose the term in which the number k is an integer and thus determine the interface type from the nanotube index n. Likewise, we can derive formulas for finding the type of interface of topological defects in the form of three octagons.

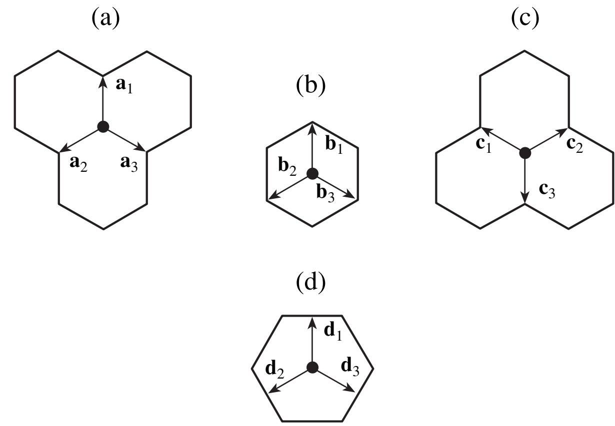

Fig. 3. Interface types and the related systems of basis vectors for CNT Y_b junctions. Nanotubes of the zigzag type: (a) A type, (b) B type, and (c) C type. Nanotubes of the armchair type: (d) D type. $\mathbf{a}_i$, $\mathbf{b}_i$, $\mathbf{c}_i$, and $\mathbf{d}_i$ are the basis vectors.

Table 1. Relations between the three main parameters of Y_b junctions: the nanotube type (zigzag or armchair), the defect type (six heptagons or three octagons), and the interface type (A, B, C, D)

k	Interface type	
	six heptagons	three octagons
1	2	3
	(n, 0) zigzag type	
$(n+2)/6$	C	A
$n/6$	A	B
$(n-2)/6$	B	C
	(n, n) armchair type	
$n/2$	–	D

Note: $k > 0$ is an integer, and n is the first nanotube index.

Table 2. Numbers of atoms in the connectors of Y_b junctions

Type of defects	Number of atoms in the connector	
	$(n, 0)$ nanotube	(n, n) nanotube
Six heptagons	$(n + 4)^2/2 - 6$ Fig. 2a	$3(n^2 + 2n + 4)/2$, $n \geq 4$ Fig. 2e
"	$(n + 10)^2/2 - 48$ Fig. 2b	$3(n^2 + 14n + 4)/2$ Fig. 2f
Three octagons	$(n + 6)^2/2 - 18$	$3(n^2 + 6n)/2$

Note: References to the figures, where the configuration of heptagons in the connector is shown, are given in brackets.

These formulas are given in the first column of Table 1. The upper part of this table corresponds to Y_b junctions formed by nanotubes of the zigzag type, and the lower part corresponds to Y_b junctions formed by nanotubes of the armchair type. The second and third columns contain information on the type of interface corresponding to each arithmetic progression for different defect types.

To facilitate the construction of Y_b junctions, we introduce a pointer vector $\mathbf{R}_L$ for defects (the subscript $L = H$ for a heptagon and $L = O$ for an octagon); the origin of the vector coincides with the origin of the system of basis vectors, and this vector ends at the defect (at a vertex of a heptagon or at the middle of an octagon side). The magnitude of the pointer vector is a function of the nanotube index n; for a nanotube of the zigzag type, we have

$$|\mathbf{R}_H| = \frac{n}{2} - 2, \quad (7)$$

$$|\mathbf{R}_O| = \frac{n}{2} - 1; \quad (8)$$

and for a nanotube of the armchair type, we have

$$|\mathbf{R}_O| = n - 1. \quad (9)$$

Below, we describe an algorithm that permits us to construct a Y_b junction by using the pointer vector.

Thus, once any two of the three main parameters of a Y_b junction are known, we can uniquely determine its structure using the third parameter taken from Table 1. The defect configurations are shown in Figs. 2a, 2c, and 2d.

We describe one of the possible algorithms for constructing Y_b junctions with the given nanotube type and nanotube index n.

(1) In Table 1, we choose the part that corresponds to the given type of nanotubes forming the Y_b junction (zigzag or armchair).

(2) Substituting the nanotube index n into the formulas in the first column, we determine the table row for which the number k is an integer.

(3) At the intersection of the row chosen at step 2 and the column corresponding to the given set of defects, we find the interface type for the Y_b junction.

(4) We determine the magnitude of the pointer vector corresponding to the given set of defects (see Eqs. (7)–(9)).

(5) Next, we construct the system of basis vectors for the given interface type in the hexagon mesh (Fig. 3) and plot the pointer vectors $\mathbf{R}_L$ along each basis vector.

(6) From the hexagon mesh, we cut a triangular fragment at whose vertices there are hexagons at which the pointer vectors end. These hexagons are replaced by defects (heptagons for $\mathbf{R}_H$ and halves of octagons for $\mathbf{R}_O$). Then, the triangle obtained is mirror reflected in a plane perpendicular the C_3 axis. Finally, we superpose the vertices of these two triangles.

The figure thus obtained is a pattern for forming a Y_b junction, since it contains all topological defects that determine its geometrical shape. We call such a pattern a connecter of three nanotubes [8].

Table 2 lists the number of atoms in the connecter for Y_b junctions.

In the next section, we discuss two examples, which clarify the scheme of the construction of Y_b junctions.

3. EXAMPLES OF THE CONSTRUCTION OF Y_b JUNCTIONS

3.1. An Example of the Construction of Y_b Junctions of Zigzag-Type Nanotubes

Let us construct a (12, 0)–(12, 0)–(12, 0) Y_b junction with topological defects in the form of six heptagons by applying our algorithm.

(1) The upper part of Table 1 corresponds to a nanotube of the zigzag type. The nanotube index is $n = 12$.

(2) We sequentially substitute the number 12 into the three formulas for k (rows 1–3 of Table 1) and choose the row for which k is an integer. For $n = 12$, we have $k = 2$ in the second row.

(3) Since the topological defects are six heptagons, the Y_b junction has an interface of the A type (the intersection of the second row and the second column).

(4) Using formula (7), we determine the magnitude of the pointer vector, $|\mathbf{R}|_H = 4$.

(5) The system of basis vectors ($\mathbf{a}_1$, $\mathbf{a}_2$, $\mathbf{a}_3$) is associated with an interface of the A type. We construct this system of basis vectors in the hexagon mesh (Fig. 3a) and plot the pointer vector $\mathbf{R}_H = 4\mathbf{a}_i$ along each of the vectors $\mathbf{a}_1$, $\mathbf{a}_2$, and $\mathbf{a}_3$ (Fig. 4a).

(6) From the hexagon mesh, we cut the triangle at whose vertices there are hexagons at which the pointer vectors end. Then, we replace these hexagons with heptagons (Fig. 4b). Next, we reflect this triangle in a plane perpendicular to the C_3 axis and superimpose the

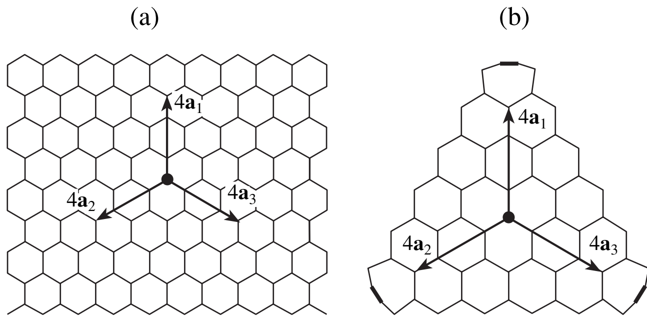

Fig. 4. Construction of a (12, 0)-nanotube Y_b junction (schematic). (a) A system of basis vectors of the A type with the pointer vector $\mathbf{R}_H = 4\mathbf{a}_i$, and (b) a triangular fragment of the hexagon mesh after the replacement of hexagons lying at the ends of the pointer vectors by heptagons. Thick lines are the heptagon bonds that determine the superimposition.

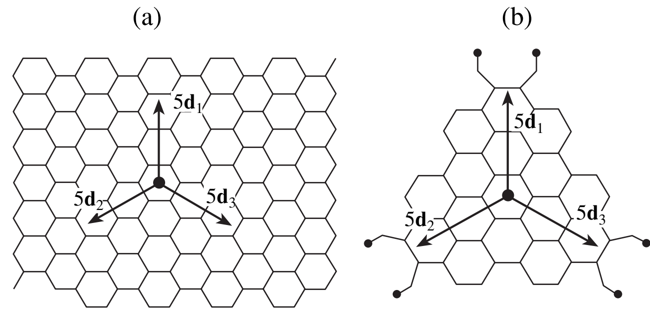

Fig. 5. Construction of a (6, 6)-nanotube Y_b junction (schematic). (a) A system of basis vectors of the D type with the pointer vector $\mathbf{R}_O = 5\mathbf{d}_i$, and (b) a triangular fragment of the hexagon mesh after the replacement of hexagons lying at the ends of the pointer vectors by halves of octagons. Solid circles are the octagon atoms that determine the superimposition.

obtained triangles on the bonds (Fig. 4b). As a result, we obtain the connector of the (12, 0)–(12, 0)–(12, 0) Y_b junction. By joining (12, 0) nanotubes to each of the three connector terminals, we obtain the Y_b junction shown in Fig. 1a.

We note that, in order to construct a Y_b junction with topological defects in the form of six heptagons located in accordance with Fig. 2b, we must perform the (6, 7, 7, 6) $\rightleftharpoons$ (7, 6, 7, 6) Stone–Wales transformation for each pair of heptagons.

3.2. An Example of the Construction of a Y_b Junction from Nanotubes of the Armchair Type

We outline the construction of a (6, 6)–(6, 6)–(6, 6) Y_b junction with topological defects in the form of three octagons. We perform the construction using the above algorithm.

(1) The lower part of Table 1 corresponds to a nanotube of the armchair type; the first nanotube index is 6.

(2) There is only one type of interface (the D type) for Y_b junctions of nanotubes of the armchair type.

(3) Using Eq. (9), we determine the magnitude of the pointer vector, $|\mathbf{R}_O| = 5$.

(4) To construct a Y_b junction with an interface of the D type, we construct the system of basis vectors $\mathbf{d}_1$, $\mathbf{d}_2$, and $\mathbf{d}_3$ and plot the pointer vector $\mathbf{R}_O = 5\mathbf{d}_i$ along each basis vector (Fig. 5a).

(5) From the hexagon mesh, we cut the triangle at whose vertices there are hexagons at which the pointer vectors end. Then, we replace these hexagons with halves of octagons (Fig. 5b). Next, we reflect this triangle in a plane perpendicular to the C_3 axis and superimpose the obtained triangles on the octagon atoms (solid circles in Fig. 5b). Thus, we obtain the (6, 6)–(6, 6)–(6, 6) connector of the Y_b junction. By joining the (6, 6) nanotubes to each of the three connector terminals, we obtain the Y_b junction shown in Fig. 1b.

We note that, if we want to construct a Y_b junction with topological defects in the form of six heptagons (in any version), we need to construct a Y_b junction with defects in the form of three octagons and then add three C_2 clusters (Figs. 2d, 2e).

4. CONCLUSIONS

We have suggested a classification of CNT Y junctions of symmetry D_{3h} with the basic configuration that contain topological defects in the form of six heptagons or three octagons in the regions of coupling of each pair of nanotubes. As a basis for the classification, we chose a one-to-one correspondence between the three main parameters of the Y_b junction, namely, the nanotube type, the defect type, and the interface type. These main parameters determine the electronic and transport properties of the junctions considered [17]; therefore, knowledge of the one-to-one correspondence between them is effective for constructing nanochain elements and studying the properties of such junctions. We have shown that, in such basic Y_b junctions, conversion of defects into one another is possible by applying a Stone–Wales transformation or by removing a C_2 cluster. On the basis of the suggested classification, we have developed an effective method for constructing basic Y_b junctions.

ACKNOWLEDGMENTS

The authors thank I.V. Stankevich (Institute of Organoelement Compounds, Russian Academy of Sciences) for useful discussions and valuable comments.

This study was supported by the Russian scientific and technical program “Promising Directions in Condensed Matter Physics” (section “Fullerenes and

Atomic Clusters"), the Russian program "Low-Temperature Quantum Structures" (project no. 9.21), and INTAS (grant no. 00-237).

REFERENCES

1. S. Iijima, Nature **345** (6348), 56 (1991).
2. D. Zhou and S. Seraphin, Chem. Phys. Lett. **238** (4–6), 286 (1995).
3. J. Li, C. Papadopoulos, and J. Xu, Nature **402** (6759), 253 (1999).
4. P. Nagy, R. Ehlich, L. B. Biro, and J. Gjulai, Appl. Phys. A **70** (4), 481 (2000).
5. B. C. Satishkumar, P. J. Thomas, A. Govindraj, and C. N. R. Rao, Appl. Phys. Lett. **77** (16), 2530 (2000).
6. M. Terrones, F. Banhart, N. Grobert, J. C. Charlier, H. Terrones, and P. M. Ajayan, Phys. Rev. Lett. **89** (7), 075505 (2002).
7. B. I. Dunlap, Phys. Rev. B **46** (3), 1933 (1992).
8. L. A. Chernozatonskii, Phys. Lett. A **170** (1), 37 (1992).
9. G. E. Scuseria, Chem. Phys. Lett. **195** (5–6), 534 (1992).
10. L. A. Chernozatonskii, Phys. Lett. A **172** (3), 173 (1992).
11. M. Menon and D. Srivastava, Phys. Rev. Lett. **79** (22), 4453 (1997).
12. C. Papadopoulos, A. Rakitin, J. Li, A. S. Vedeneev, and J. M. Xu, Phys. Rev. Lett. **85** (16), 3476 (2000).
13. A. N. Andriotis, M. Menon, D. Srivastava, and L. Chernozatonskii, Phys. Rev. B **65** (16), 165416 (2002).
14. G. Treboux, P. Lapstun, and K. Silverbrook, Chem. Phys. Lett. **306** (5–6), 402 (1999).
15. A. N. Andriotis, M. Menon, D. Srivastava, I. Ponomareva, and L. Chernozatonskii, Phys. Rev. Lett. **91**, 145501 (2003).
16. G. Treboux, P. Lapstun, Z. Wu, and K. Silverbrook, J. Phys. Chem. B **103** (41), 8671 (1999).
17. G. Treboux, J. Phys. Chem. B **103** (47), 10378 (1999).
18. A. N. Andriotis, M. Menon, D. Srivastava, and L. Chernozatonskii, Phys. Rev. Lett. **87** (6), 066802 (2001).
19. R. Saito, M. Fujita, G. Dresselhaus, and M. S. Dresselhaus, Phys. Rev. B **46** (3), 1804 (1992).
20. P. Lambin, A. Fonseca, J. Vigneron, J. B. Nagy, and A. A. Lucas, Chem. Phys. Lett. **245** (1), 85 (1995).
21. L. Chico, V. H. Crespi, L. X. Benedict, S. G. Louie, and M. L. Cohen, Phys. Rev. Lett. **76** (6), 971 (1996).
22. J. Han, M. P. Anantram, R. Jaffe, J. Kong, and H. Dai, Phys. Rev. B **57** (23), 14983 (1998).
23. Z. Yao, H. W. C. Postma, L. Balants, and C. Dekker, Nature **402** (6759), 273 (1999).
24. V. H. Crespi, Phys. Rev. B **58** (19), 12671 (1998).
25. A. J. Stone and D. J. Wales, Chem. Phys. Lett. **128** (5–6), 501 (1986).

Translated by I. Zvyagin